LLE 2007 Annual Report

UR
LLE

October 2006 – September 2007

$\rho R = 200$ mg/cm^2

Shot
47206

Instrument
cutoff

Normalized yield
(Protons/MeV)

Energy (MeV)

Cover Photos

Upper left: Robert Earley and Dale Guy working on the OMEGA off-axis parabola inserter system.

Middle left: Mark Wittman with the advanced target characterization system.

Middle center: Aitoff projection of the variation in ice-layer-thickness uniformity for an LLE DT-filled capsule showing submicron uniformity.

Lower left: David Canning is shown aligning optics in the OMEGA EP grating compressor chamber.

Upper right: Secondary proton spectrum from an OMEGA high-density cryogenic capsule implosion that achieved an areal density of ~200 g/cm^2.

Middle right: High-school student interns participating in the 2007 LLE Summer High School Research Program in the OMEGA EP Laser Bay.

Lower right: View of the OMEGA target chamber along the H3 port direction.

LLE 2007 Annual Report

UR
LLE

October 2006 – September 2007

Inertial Fusion Program and National Laser Users' Facility Program

Contents

Executive Summary

The fiscal year ending in September 2007 concluded the fifth year of the five-year renewal of Cooperative Agreement DE-FC52-92F19460 with the U.S. Department of Energy. This annual report serves as the final report for the Agreement and summarizes progress in laser-fusion research at the Laboratory for Laser Energetics (LLE) during the past fiscal year. It also reports on LLE's progress on laser, optical materials, and advanced technology development; work on the OMEGA EP (extended performance) laser project; operation of OMEGA for the National Laser Users' Facility (NLUF) and other external users; and programs focusing on the education of high school, undergraduate, and graduate students during the year.

Progress in Laser-Fusion Research

The laser-fusion research program at the University of Rochester's Laboratory for Laser Energetics (LLE) is focused on the National Nuclear Security Administration's (NNSA's) Campaign-10 inertial confinement fusion (ICF) ignition and experimental support technology, operation of facilities (OMEGA), and the construction of OMEGA EP—a high-energy petawatt laser system. While LLE is the lead laboratory for research into the direct-drive approach to ICF ignition, it also takes a lead role in certain indirect-drive tasks within the National Ignition Campaign.

During this past year progress in the laser-fusion research program was made in three principal areas: OMEGA direct-drive and indirect-drive experiments and targets; development of diagnostics for experiments on OMEGA, OMEGA EP, and the National Ignition Facility (NIF); and theoretical analysis and design efforts aimed at improving direct-drive-ignition capsule designs and advanced ignition concepts such as fast ignition and shock ignition.

1. National Ignition Campaign Experiments

In FY07, LLE scientists in collaboration with scientists from the Massachusetts Institute of Technology (MIT) Plasma Science and Fusion Center (PSFC) inferred, for the first time, a neutron-averaged areal density in excess of 200 mg/cm^2

from direct-drive cryogenic D_2 implosions on the OMEGA laser. This set of measurements completed an NNSA Level-2 milestone and demonstrated conclusively that hydrogen can be compressed to fuel densities required for both indirect- and direct-drive-ignition capsules. The neutron-averaged areal density was inferred from the energy loss of secondary protons produced in the core along five different directions. The measured particle spectra were in close agreement with *LILAC* 1-D code predictions, indicating that the fuel assembly proceeded according to 1-D simulations up to the peak density of the implosions, i.e., ~140 g/cc (or approximately 700 times the density of liquid deuterium). Results of these experiments were presented at the 49th Annual Meeting of the American Physical Society Division of Plasma Physics and have been submitted for publication.

Experiments were conducted on OMEGA to investigate the energy coupling and implosion symmetry achieved in an indirect (hohlraum)-driven target using a multicone geometry and elliptical phase plates (p. 212). Indirect-drive-ignition target designs planned for the National Ignition Facility (NIF) aim at concurrent objectives of minimizing laser-energy losses due to stimulated Brillouin scattering (SBS) or stimulated Raman scattering (SRS) and maximizing the capsule drive symmetry. The OMEGA experiments, which used specially designed phase plates that produced elliptical irradiation patterns on the hohlraum wall, demonstrated significant improvement in coupling. The improved coupling correlates with reduced losses from SRS and SBS. In the same experiments, the implosion symmetry was investigated for the first time using a multicone laser drive smoothed with phase plates.

OMEGA planar direct-drive experiments investigated the role of preheat in the stabilization of the Rayleigh–Taylor (RT) instability. Compression of an ICF target is very sensitive to any preheat experienced by the driven target. Nonlocal-electron preheat is a potentially major source of preheat for ICF targets (caused by electrons with energies of ~10 keV and hot electrons with energies of ~100 keV). The RT-instability growth rate of target modulations at the ablation surface is sensitive to pre-

heat because the increased ablation velocity (caused by target decompression) reduces the RT growth. The experiments showed significant reduction in the RT growth rate for short-wavelength (i.e., less than 30-μm) perturbations driven by high-intensity (1×10^{15} W/cm^2) compared to lower-intensity (5×10^{14} W/cm^2) UV irradiation. These results were presented at the 49th Annual Meeting of the American Physical Society Division of Plasma Physics and will be submitted for publication.

The speed and heating of convergent shocks are of fundamental importance for the design of ignition and high-gain ICF capsules. Strong, spherically converging shocks are formed by the rapid deposition of energy on the capsule's surface (laser energy in the case of direct-drive or x rays in the case of indirect-drive targets). All of the generated shocks must propagate through hot, already-shocked material; this adds uncertainty in the shock speed and strength. In collaboration with MIT PSFC, the products of two nuclear-reaction types induced by the central collapse of convergent shocks were measured temporally and spectrally on OMEGA (p. 148). Observations of these products provided information about the speed and heating of the shocks, as well as the state of the imploding capsule at the time of shock collapse. Comparison of these data to predictions from 1-D hydrodynamic simulations revealed numerous differences that will be used in the future to develop improved models for these implosions.

A comprehensive set of experiments was completed on OMEGA (p. 1) to track the flow of laser energy in a target. Time-resolved measurements of laser absorption in the corona were performed on imploding directly driven capsules. The mass ablation rate was inferred using time-resolved Ti K-shell spectroscopy of stationary (nonimploding), solid CH spherical targets that were configured with a buried tracer layer of Ti. Shock heating was also measured. A detailed comparison of the experimental results and the simulations indicates that a time-dependent flux limiter in the thermal transport model is required to simulate the laser-absorption measurements.

In another collaborative OMEGA experiment with MIT PSFC, nuclear measurements of fuel–shell mix in inertial confinement implosions were carried out (p. 14). The extent of fuel–shell mix was probed in imploded capsules containing a deuterated plastic (CD) layer and filled with pure ^{3}He. Spectral measurements of the high-energy protons produced by the D-^{3}He fusion reaction were used to constrain the level of mix at shock time, to demonstrate that some of the fuel mixes with the CD layer, and that capsules with a higher initial fill density or thicker shells are less susceptible to the effects of mix.

2. *Target Diagnostics for OMEGA, OMEGA EP, and the NIF*

To improve the understanding and predictions of the shock-heated and compressed temperature and density conditions in the main fuel layer of an imploding capsule, exploratory experiments were undertaken on OMEGA by LLE scientists in collaboration with Rutherford Appleton Laboratory, Oxford University, and LLNL scientists to measure the temperature and ionization conditions in shock-heated and compressed targets using noncollective spectrally resolved x-ray scattering (p. 191). The shock-heated shell is predicted to have plasma conditions in the warm dense matter (WDM) regime. Measuring WDM conditions is challenging because the temperature of the plasma is too low (~10 eV) to emit x rays and dense plasmas cannot be optically probed. The experiments succeeded in determining an upper limit of $Z = 2$ and $T_e = 20$ eV for the ionization and electron temperature, respectively, of directly driven, Br-doped CH foils. The experiments demonstrated that x-ray scattering is a promising technique to probe spatially averaged plasma conditions in the DT shell of an imploding target during the laser irradiation to determine the shell adiabat.

Current designs for both direct-drive-ignition (DDI) and indirect-drive-ignition (IDI), high-gain ICF targets require a layer of condensed (cryogenic) hydrogen fuel that adheres to the inner surface of a spherical ablator. NIF ignition capsules (both DDI and IDI) require a total root-mean-square (rms) deviation of less than 1 μm in the uniformity of the DT-ice layer. Measurement of the ice-layer radius over the entire surface of the capsule with submicron resolution is required to verify that this specification has been met. LLE scientists developed an improved system for three-dimensional characterization of spherical cryogenic capsules using ray-trace analysis of multiple shadowgraph views (p. 46). A 3-D ray-tracing model was incorporated into the backlit optical shadowgraph analysis (the primary diagnostic for ice-layer characterization of transparent targets at LLE). The result was an improved self-consistent determination of the hydrogen/vapor surface structure for cryogenic targets.

Neutron core imaging will be used on NIF implosions to identify ignition-failure mechanisms such as poor implosion symmetry or inadequate convergence/areal density. Neutron imaging on OMEGA is obtained by placing an appropriate aperture in front of a spatially sensitive neutron detector [see, for example, the report on the Commissariat à l'Énergie Atomique (CEA) work on p. 270]. Similar systems will be used on the NIF. LLE, in collaboration with CEA, LLNL, and LANL, has conducted an optimization study (p. 203) to understand the

effects and trade-offs of the neutron-imaging system's component tolerances on the overall quality of the system.

3. Theoretical Analysis and Design

Ignition target designs based on a wetted-foam ablator offer higher coupling efficiency for NIF DDI capsules than is possible with conventional solid-DT-ablator capsules. Simulations were carried out on the performance of wetted-foam targets driven by 1 MJ on the NIF (p. 26). A stability analysis was performed using the two-dimensional hydrodynamic code *DRACO*. A nonuniformity budget analysis was constructed and suggests that two-dimensional smoothing by spectral dispersion (SSD) or an alternative scheme using multiple frequency modulators (presented at the 49th Annual Meeting of the American Physical Society Division of Plasma Physics) may reduce single-beam nonuniformities to levels required for ignition.

To produce ignition with direct-drive targets at the 1-MJ level, NIF capsules require relatively thin shells (initial aspect ratio ~5) driven at high velocities (~4×10^7 cm/s). The performance of such implosions is sensitive to the growth of RT instability on the ablation front. Low-velocity implosions with low in-flight aspect ratio (IFAR) have good stability properties during the acceleration phase. However, such targets would fail to ignite for moderate driver energies because the hot-spot temperature and pressures are too low. In collaboration with the University of Rochester Fusion Science Center (FSC), we have investigated (p. 234) the possibility of using a spherically converging shock wave propagating through the shell during the coasting phase of the implosion to enhance the compression of the hot spot and significantly improve ignition conditions. The ignitor shock is launched at the end of the laser pulse and must collide with the return shock near the inner shell surface. We show that a two-step ignition scheme can be configured by combining a fuel-assembly laser pulse and a shock-driving power spike. Such configurations can lead to a significant reduction in the energy required for ignition and high gain.

Fast ignition is another two-step ignition scheme that uses fast electrons (or protons) to heat an assembled high-density fuel core. In direct-drive fast ignition, the high-energy driver used for the compression is a conventional short-wavelength ($\lambda < 0.53$ μm) laser while a high-intensity laser (power ~ petawatts) with a longer wavelength ($\lambda > 0.53$ μm) is used to produce the high-energy charged particles. During FY07 we conducted comprehensive hydrodynamic simulations of ignition and burn for direct-drive fast-ignition fusion targets (p. 74).

The simulations show that even modest-sized UV-laser drivers (for the target compression), with an energy of ~100 kJ, can produce a fuel assembly yielding maximum gain close to ~60 with the appropriate ignition laser pulse. At a total energy of ~1 MJ, the total gain of the optimized fast-ignition target is ~160 for an ignition pulse of ~100 kJ. The basis of these designs will be tested on OMEGA EP beginning in FY09.

Lasers, Optical Materials, and Advanced Technology

In recent years, the output power of fiber lasers has increased to levels in excess of a kilowatt. These lasers are widely used in high-power applications such as material processing and industrial manufacturing. Nonlinear effects such as SBS and SRS and self-focusing can limit the power scalability in fibers. Self-focusing can lead to beam-quality degradation through a process called filamentation. Filamentation has been studied extensively in semiconductor lasers over the past two decades; however, little such work has been done in fiber lasers. A theoretical model for the filamentation effect in a large-mode-area (LMA) fiber laser is discussed starting on p. 55. This model predicts the output-power thresholds at which the filamentation will occur for a given set of optical-fiber parameters; a simplified threshold expression is also provided. The results are consistent with previous experiments.

Although the damage threshold of fiber lasers is increased with the use of LMA's, their increased mode area in traditional step-index fibers introduces higher-order transverse modes that can potentially degrade the laser beam. Many designs of LMA fibers for high-power applications have been developed for beam-quality control. These design features have included internal structures, external structures, refractive-index, and gain-dopant designs in multimode fibers. However, the impact of transverse spatial-hole burning (THSB) on beam quality has largely been ignored. As a beam with nonuniform transverse intensity distribution propagates through the fiber, the gain becomes more saturated where the intensity is highest. As the gain sampled by each transverse mode changes, the net beam profile, and thus the beam quality, changes. At high power this effect becomes pronounced due to heavily saturated population inversion. We report (p. 120) on measurements of the beam-quality factor for an ASE source based on an ytterbium-doped LMA multimode fiber as a function of pump power. A localized multimode model is presented containing spatially resolved gain and a modal decomposition of the optical field. Numerical simulations are performed with this model and compared to the experimental results. The comparison validates the model and demonstrates TSHB's impact on beam quality.

We report on comprehensive experimental and theoretical studies of the time-resolved generation and detection of coherent acoustic phonons (CAP's) in very high quality GaN single crystals (p. 88). These studies were performed using a femtosecond, two-color, all-optical pump/probe technique. Very good agreement is observed between the theoretical modeling and experimental measurements, indicating that this approach makes it possible to successfully generate nanoscale acoustic waves at the surface of bulk semiconductors and, simultaneously, to nondestructively probe the material's structure deep below the surface. This approach should be very promising in producing and detecting CAP waves in a large variety of bulk semiconductor materials.

Holographic volume Bragg gratings (VBG's) represent a new class of robust, highly efficient, and spectrally selective optical elements that are recorded in photo-thermo-refractive glass. VBG's have extremely high spectral and angular dispersions that are higher than any dispersive elements previously used. VBG's are stable at elevated temperatures, have a high optical-damage threshold similar to that of bulk glass materials, and have a high diffraction efficiency and low losses, allowing their use in laser resonators. In collaboration with scientists from OptiGrate and the College of Optics and Photonics/CREOLE, University of Central Florida, we report (p. 115) on the demonstration of instrument-limited suppression of out-of-band amplified spontaneous emission (ASE) in a Nd:YLF diode-pumped regenerative amplifier (DPRA) using a VBG element as a spectrally reflective element. A VBG with 99.4% diffraction efficiency and a 230-pm-FWHM reflection bandwidth produced a 43-pm-FWHM output spectral width in an unseeded DPRA compared to 150-pm FWHM in the same DPRA with no VBG.

In a second article (p. 135) by the same collaborative team as above we report on analytical and experimental studies of pump-induced temporal contrast degradation in optical parametric chirped-pulse amplifiers (OPCPA's). OPCPA systems will be playing an increasingly important role in the exploration of the new regimes of laser–matter interaction at intensities in excess of 10^{22} W/cm^2. Such experiments can be adversely affected by laser light present before the main pulse. The temporal contrast of the laser pulse is the ratio of the peak power of the main pulse to the power of the light in some predetermined temporal range before the main pulse. Incoherent laser and parametric fluorescence can significantly degrade the contrast of the pulse. In this report we quantify the effect of incoherent pump-pulse ASE on contrast degradation in OPCPA systems and present an experimental technique using VBG crystals to mitigate this problem.

Polycrystalline ceramics such as chemical-vapor–deposited (CVD) silicon carbide, polycrystalline alumina, and aluminum oxynitride display a great potential for advanced optical applications in severe environments that require high hardness, high toughness, and excellent thermal properties. These materials are nominally fully dense, and there is growing interest in grinding and ultimately polishing them to nanometer levels of surface microroughness. We have developed a procedure (p. 98) for estimating subsurface damage depth induced by deterministic microgrinding of hard polycrystalline optical ceramics with diamond-bonded tools. This estimate comes from tracking the evolution of surface microroughness with the amount of material removed by multiple MRF spots of increasing depth into the surface. This technique also provides information regarding the specimen microstructure (i.e., grain size), mechanical properties (hardness and fracture roughness), and the grinding conditions (i.e., abrasive size used), from extended spotting with the MRF process.

Key to the success of a multipetawatt laser such as OMEGA EP is the ability to produce meter-scale, high-optical-quality, high-damage-resistance, high-efficiency, multilayer dielectric diffraction (MLD) gratings. The specific requirements for OMEGA EP are a diffraction efficiency greater than 95%, peak-to-valley wavefront quality of less than $\lambda/10$ waves, and a laser damage threshold greater than 2.7 J/cm^2 for 10-ps pulses. The multilayer dielectric grating consists of a film of SiO$_2$ etched to form a grating structure with 1740 lines per millimeter. The structure resides on top of a multilayer dielectric high-reflector stack composed of alternating layers of SiO$_2$ and HfO$_2$. The cleanliness of this structure is of paramount importance to its survivability. An article starting on p. 228 describes the results of an investigation conducted by LLE to further optimize a final MLD diffraction grating cleaning process called "piranha clean" that will increase laser-damage resistance to meet LLE specifications.

Status and Progress of OMEGA EP

The OMEGA EP project is in its fifth year. In FY07 an allocation of $2.25 million completed the $89 million funding required for the project. The project will be completed in April 2008.

The first quarter of FY07 was highlighted by the start of shot operations. Propagating shots on Beamline 1 were used to characterize spatially resolved gain profiles for the amplifier chain. The amplifiers and laser diagnostics met all performance objectives with high reliability. Beamline 1 was also tested for amplification of the broadband short-pulse

source. The spectral transmittance of a chirped-pulse source beam with 8-nm bandwidth was characterized. Analysis of the spectral transmittance data indicated that there were no spectral anomalies in the four-pass beamline. This is a favorable and important result for the short-pulse performance of the OMEGA EP beamlines.

In the second quarter of FY07, progress was highlighted by the completion of the spatial-filter vacuum vessel subsystem. These tubes are a vital component of the architecture of the beamline, used to transport and image the high-power beam from one portion of the laser to the next. There are 108 individually welded and machined tube sections, custom fabricated to OMEGA EP requirements. Center sections include access features to the pinhole regions that proved to be very useful during the initial alignment and commissioning operations. Also during this second quarter the grating compressor internal structures, on the project critical path, started to arrive at LLE.

Acquisition of the grating compressor internal structure concluded in the third quarter, approximately one year behind initial plans. Delays in the acquisition are largely attributable to managing potential contamination sources. Contamination in any form is a serious threat to the performance of the compressor optics—a threat that was minimized through the control of materials and fabrication processes. Ultimately, the tables were successfully cleaned to the LLE-required precision cleaning standard and installed during the third quarter. This allowed the installation of the internal assemblies to begin. All eight of the tiled-grating assemblies were completed and tested offline in preparation for the compressor loading. Also during the third quarter, two of the remaining three beams were activated to ~3-kJ IR energy at the beamline output calorimeters.

During the fourth quarter of FY07 the fourth and final beamline was activated to ~3-kJ IR energy level. Loading of grating compressor optics continued, along with the assembly and installation of the UV diagnostic systems. At the end of FY07, 68 of the 104 optical assemblies were loaded into the grating compressor chamber. Alignment was completed through the four main alignment paths to the primary compressor optics. Each of the two Fizeau interferometer arms that will be used to verify grating tiling within the vacuum vessel was completed as were the up-collimators that send full aperture infrared beams to the grating and transport paths. The optical alignment made good progress in part due to the internal structure design flexibility, allowing temporary alignment fixtures to be placed in a variety of locations.

Overall, the project completed most objectives for FY07 and continues to make satisfactory progress toward project completion. In addition to having operated the beamlines with trained and qualified operators, the project is successfully operating all key enabling technologies. Development is complete, engineering is complete, and by the end of the year all of the following project elements will have achieved operating status:

- optical parametric chirped-pulse-amplification front-end sources
- deformable mirrors and wavefront-control systems
- plasma-electrode Pockels cells (double pulse)
- 40-cm-aperture disk amplifiers
- 41-cm × 141-cm-aperture tiled gratings
- diffractive color correctors
- frequency-conversion crystals

National Laser Users' Facility (NLUF) and External Users' Programs

More than half (54%) of the OMEGA shots in FY07 were dedicated to external users including the NLUF programs, LLNL, LANL, SNL, CEA, and AWE (Atomic Weapons Establishment).

FY07–FY08 NLUF Experiments

Fiscal year 2007 was the first year of a two-year period of performance for the NLUF projects approved for FY07–FY08 funding and OMEGA shots. A total of 121 shots were conducted for six NLUF projects. Their progress is detailed beginning on p. 242 in the following reports:

- *Recreating Planetary Core States on OMEGA in FY07* (R. Jeanloz, University of California, Berkeley)

- *Experimental Astrophysics on the OMEGA Laser* (R. P. Drake, University of Michigan)

- *Laboratory Experiments on Supersonic Astrophysical Flows Interacting with Clumpy Environments* (P. Hartigan, Rice University)

- *Multiview Tomographic Study of OMEGA Direct-Drive-Implosion Experiments* (R. Mancini, University of Nevada, Reno)

- *Monoenergetic Proton Radiography of Laser–Plasma-Generated Fields and ICF Implosions* (R. D. Petrasso and C. K. Li, Massachusetts Institute of Technology)

- *X-Ray Compton Scattering on Compressed Matter* (R. Falcone and H. J. Lee, University of California at Berkeley)

FY07 LLNL OMEGA Experimental Programs

In FY07, LLNL led 422 target shots on the OMEGA Laser System; this rate was 9.3% higher than the planned allocation. Approximately 57% of these LLNL-led shots were dedicated to advancing the National Ignition Campaign (NIC) in preparation for future experiments on the NIF; the remainder were dedicated to experiments for the high-energy-density science (HEDS) program. Objectives of the OMEGA NIC Campaigns included the following:

- *Laser–plasma interaction studies in physical conditions relevant for the NIF ignition targets*

- *Studies of the impact of x-ray flux originating from outside the laser entrance hole (LEH) on the radiation temperature of a hohlraum*

- *Characterization of the properties of warm, dense matter—specifically radiatively heated Be*

- *Studies of the physical properties of capsules based on Cu-doped Be and high-density carbon*

- *Determination of the ablator performance during the implosion of NIC-candidate ablators*

- *Experiments to detect and study second-shock-melting, high-density carbon*

- *High-resolution measurements of velocity nonuniformities created by microscopic pertubations in NIF ablator materials*

The LLNL HEDS campaigns included the following experiments:

- *Quasi-isentropic (ICE) drive used to study material properties such as strength, equation of state, phase, and phase-transition kinetics under high pressure*

- *Late-time hohlraum-filling studies*

- *Laser-driven dynamic hohlraum (LDDH) implosion experiments*

- *The development of an experimental platform to study nonlocal thermodynamic equilibrium (NLTE) physics using direct-drive implosions*

- *Opacity studies of high-temperature plasmas under LTE conditions*

- *Development of long-duration, point-apertured, point-projection x-ray backlighters*

- *Studies of improved hohlraum heating efficiency using cylindrical hohlraums with foam walls*

FY07 LANL OMEGA Experimental Programs

During FY07, LANL fielded a range of experiments on OMEGA to study ICF and high-energy-density laboratory plasma (HEDLP) physics. LANL conducted 192 target shots, 21.5% higher than the planned allocation.

As reported starting on p. 259, the LANL-led campaigns included the following experiments:

- *Studies of radiation transport in inhomogeneously mixed media where discrete particles of random size are randomly dispersed in a host material*

- *Off-Hugoniot experiments to explore the hydrodynamic evolution of embedded layers subject to radiative heating*

- *NIF Platform #5—aimed at developing x-ray diagnostic techniques to measure temperature in future NIF radiation transport experiments*

- *The "symergy" experiment to test the concept of using thin shells to quantify asymmetry during the foot of NIF ignition drive pulse*

- *The "convergent ablator" campaign, to characterize the ablator performance in scaled NIF capsules*

- *Laser–plasma interaction experiments*

- *The "Hi-Z" experiment to study the effects of instability growth and the resulting mix*

- *Studies of reaction history using a double laser pulse*

- *"DT ratio—^{3}He" experiment to investigate the effect of helium on yield and reaction history of DT implosions*

- *The "beta-mix" experiment to develop a radiochemical diagnostic to study mix in NIF experiments*

FY07 SNL OMEGA Experimental Programs

During FY07, SNL scientists led 15 target shots on the OMEGA laser—36% more than the nominal allocation. The SNL experiments focused on measurements of the high-density carbon ablation rate conducted on planar ablator samples driven by radiation from a halfraum. These experiments are reported on pp. 268–269.

FY07 CEA OMEGA Experimental Programs

During FY07, CEA scientists led 40 experiments on OMEGA (equal to the nominal allocation). Reports on the experiments begin on p. 270 and include the following:

- *Measurements of wall and laser-spot motion in cylindrical hohlraums*

- *Development of neutron imaging on OMEGA*

- *Neutron flux and duration measurements with CVD diamond detectors*

FY07 AWE OMEGA Experimental Programs

AWE scientists conducted 26 OMEGA target shots in FY07—30% more than the nominal allocation. The experiments were focused on studies of radiation transport through enclosed spaces with inwardly moving walls—key to understanding the physics of laser-heated hohlraums.

FY07 Laser Facility Report

The OMEGA facility conducted 1514 target shots for a variety of users in FY07 (see Fig. 1). The OMEGA Availability and Experimental Effectiveness averages for the year were 92.8% and 95.9%, respectively. Highlights of the year included the following:

- *A total of 27 D_2 and 17 DT low-adiabat cryogenic target implosions that required high-contrast pulse shapes were performed.*

- *An offline OMEGA frequency-conversion-crystal (FCC) tuning test bed was developed.*

- *More than 25 new or significantly modified target-diagnostic systems were qualified for use on the OMEGA Experimental Facility in FY07. These diagnostics supported LLE, LLNL, LANL, AWE, and CEA experiments.*

- *Significant modifications were made to the OMEGA Laser Facility in FY07 to integrate the OMEGA EP short-pulse beam into the OMEGA target chamber.*
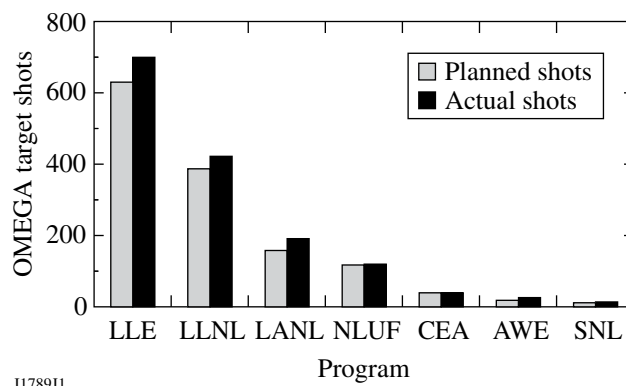
I1789J1

Figure 1
FY07 OMEGA target shot summary.

Education at LLE

As the only major university participant in the National ICF Program, education continues to be an important mission for the Laboratory. A report on this year's Summer High School Research Program is described in detail on p. 238. Fourteen students participated in this year's program. The William D. Ryan Inspirational Teacher Award was presented to Mr. Christian Bieg, a physics teacher at Fairport High School.

Graduate students are using the OMEGA laser for fusion research and other facilities for HED research and technology development. They are making significant contributions to LLE's research activities. Twenty-nine faculty from five departments collaborate with LLE's scientists and engineers. Presently, 77 graduate students are involved in research projects at LLE, and LLE directly sponsors 42 students pursuing Ph.D. degrees via the NNSA-supported Frank Horton Fellowship Program in Laser Energetics. Their research includes theoretical and experimental plasma physics, high-energy-density physics, x-ray and atomic physics, nuclear fusion, ultrafast optoelectronics, high-power-laser development and applications, nonlinear optics, optical materials and optical fabrications technology, and target fabrication.

Approximately 68 undergraduate students participated in work or research projects at LLE this past year. Student projects include operational maintenance of the OMEGA Laser System; work in laser development, materials, and optical-thin-film–coating laboratories; and programming, image processing,

and diagnostic development. This is a unique opportunity for students, many of whom will go on to pursue a higher degree in the area in which they gained experience at the Laboratory.

In addition, LLE directly funds research programs within the MIT Plasma Science and Fusion Center, the State University of New York (SUNY) at Geneseo, the University of Nevada, Reno, and the University of Wisconsin. These programs involve a total of approximately 16 graduate students, 27 undergraduate students, and 7 faculty members.

Robert L. McCrory
Director, Laboratory for Laser Energetics
Vice Provost, University of Rochester

Laser Absorption, Mass Ablation Rate, and Shock Heating in Direct-Drive Inertial Confinement Fusion

Introduction

Inertial confinement fusion (ICF) occurs when a spherical shell target containing cryogenic thermonuclear fuel (i.e., DT) is imploded.[1–9] The implosion is initiated by the ablation of material from the outer surface using either intense laser beams (direct drive)[3,5,6,8,9] or x rays produced in a high-Z enclosure (indirect drive).[4,7] The ablated shell mass forms a coronal plasma that surrounds the target and accelerates the shell inward via the rocket effect. When the higher-density shell converges toward the target center and is decelerated by the lower-density fuel, a hot spot forms. Compression by the cold, dense shell causes the pressure and DT fusion reaction rate of the hot spot to increase. It is predicted that the α-particle fusion products will deposit sufficient energy in the hot spot to launch a thermonuclear burn wave out through the cold, dense fuel in the shell just prior to stagnation when the areal density of the hot spot exceeds 0.3 g/cm^2 and the hot-spot temperature reaches 10 keV (Ref. 4). Energy gain with hot-spot ignition depends on the implosion velocity of the shell V_{imp}, the shell areal density ρR_{shell} at the time of burn, and the in-flight shell adiabat $\alpha = P_{\text{fuel}}/P_{\text{Fermi}}$, defined as the ratio of the pressure in the main fuel layer P_{fuel} to the Fermi-degenerate pressure P_{Fermi}.[4,10–12]

A physical understanding of the energy transport from the laser to the target is required to develop capsule designs that can achieve energy gain with ICF. An experimental investigation of direct-drive energy coupling is the subject of this article. The 60-beam, 30-kJ, 351-nm OMEGA Laser System[13] is used to irradiate millimeter-scale, spherical and planar plastic and cryogenic D$_2$ and DT targets on nanosecond time scales with peak intensities I ranging from 10^{13} to 10^{15} W/cm^2. High levels of laser drive uniformity are achieved with 2-D smoothing by spectral dispersion (SSD) and polarization smoothing (PS).[14] The three major parts of energy coupling—laser absorption, electron thermal transport, and shock heating of the target—were diagnosed with a wide variety of experiments. The experimental results are compared with the simulations of the 1-D hydrodynamics code *LILAC*,[15] which is used to design ignition targets for the 1.8-MJ, 351-nm, 192-beam National Ignition Facility (NIF).[16] The initial design of a direct-drive-ignition target relies on 1-D simulations

to optimize the energetics of the implosion. Subsequent calculations are performed with the 2-D hydrodynamics code *DRACO* to mitigate the deleterious effects of hydrodynamic instabilities on target performance.[17] Energy coupling to the target is primarily a 1-D effect; therefore, comparisons of experimental results with 1-D *LILAC* simulations are presented. The physics of direct-drive energy coupling is similar for plastic and cryogenic targets. The initial coupling is identical since cryogenic targets have a thin plastic ablator; however, the subsequently formed lower-Z, hydrogen-isotope, coronal plasma absorbs less laser energy. Plastic targets reduce the complexity and cost of the experiment and increase the shot rate.

ICF target acceleration and deceleration are realized when hot, low-density plasma pushes against cold, high-density plasma, making the target implosion inherently susceptible to the Rayleigh–Taylor (RT) hydrodynamic instability.[4–9,18–20] High-gain, direct-drive ICF target implosions require accurate predictions of the shell adiabat α since it defines the minimum energy needed for hot-spot ignition and the amount of ablative stabilization in the RT growth rate. The shell adiabat is tuned by varying the temporal pulse shape of the laser irradiation. The minimum energy for hot-spot ignition scales as $E_{\text{min}} \propto \left(\alpha^{1.8}/V_{\text{imp}}^{5.8}\right)$ (Refs. 11 and 12); hence, low-adiabat implosions with high-implosion velocities require less laser energy to ignite. A higher adiabat at the ablation front reduces the RT growth rate $\gamma_{\text{RT}} = \alpha_{\text{RT}}\sqrt{kg} - \beta_{\text{RT}}V_a$, where α_{RT} and β_{RT} are constants, k is the wave number of the perturbation, and g is the target acceleration (Refs. 18 and 19), by increasing the ablative stabilization term,[21,22] which is proportional to the velocity of the ablation front with respect to the unablated shell V_a. The ablation velocity depends on the shell adiabat $V_a \propto \alpha^{3/5}$ (Ref. 19). A balance must be struck between the laser energy and the shell stability constraints to choose a shell adiabat.

A schematic of direct-drive energy coupling is presented in Fig. 109.1. After the initial breakdown of the target surface with the intense laser beams, the laser light no longer propagates to the ablation front. Instead, the expanding coronal plasma forms a critical electron density $n_{\text{cr}} = \pi m c^2/e^2 \lambda_L^2$, where m is the

electron mass, c is the speed of light, e is the electron charge, and λ_L is the laser wavelength, and the laser energy is absorbed primarily via inverse bremsstrahlung in the underdense corona having electron densities less than the critical density $n_e \leq n_{cr}$, where $n_{cr}(\lambda_L = 351\text{ nm}) = 9 \times 10^{21}\text{ cm}^{-3}$. The fraction of laser energy absorbed in the corona, f_{abs}, is inferred from measurements of the scattered light.
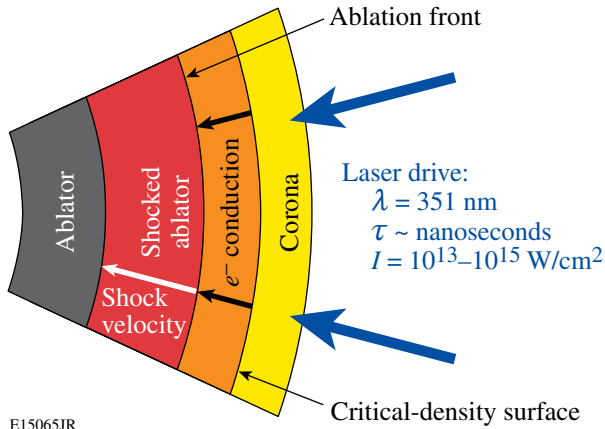
Figure 109.1
Diagram illustrating the flow of energy from the laser to the target in direct-drive ICF. Typical laser irradiation conditions are listed. The laser energy is absorbed in the corona at densities less than the critical density via inverse bremsstrahlung. Thermal electron conduction transports the absorbed energy to the ablation front. Laser ablation launches a shock wave in the ablator or shell of the target.

As shown in Fig. 109.1, the energy flows from the critical-density surface to the ablation front via electron thermal transport. This process is calculated in *LILAC*[15] using a flux-limited thermal transport model.[23] The efficiency η_{hydro} of this process can be obtained by comparing the mass ablation rate $\dot{m}$ to the measured laser absorption fraction f_{abs}.[4] The mass ablation rate is inferred from time-resolved x-ray burnthrough measurements of laser-driven targets with buried high-Z tracer layers.[24–34] To eliminate the early burnthrough due to the RT instability growth,[34] the measurements are performed on solid, plastic spherical targets. In contrast to an accelerating, spherical shell target with a buried high-Z layer, a solid target does not accelerate and is not susceptible to the RT instability; therefore, the burnthrough measurement will be affected only by the laser ablation. The effects of the Richtmyer–Meshkov instability on the burnthrough experiments presented here have been estimated to be negligible. Both the ablation pressure P and the mass ablation rate depend on the amount of energy coupled to the ablation front: $P \propto (f_{abs}\eta_{hydro}I)^{2/3}$ and $\dot{m} \propto (f_{abs}\eta_{hydro}I)^{1/3}$, and the implosion velocity is proportional to the ratio of the ablation pressure to the mass ablation rate $V_{imp} \propto (P/\dot{m})$ (Ref. 4).

The laser ablation process launches a shock wave into the target that compresses and heats the shell (Fig. 109.1). This primary source of heating determines the adiabat for the bulk of the shell. X-ray radiation and energetic electrons provide additional but lower levels of shell heating. Diagnosing the plasma conditions in the shock-heated shell and modeling its equation of state are challenging since they straddle the boundaries between Fermi-degenerate, strongly coupled, and weakly coupled plasmas (i.e., $10^{23}\text{ cm}^{-3} < n_e < 10^{24}\text{ cm}^{-3}$ and 10 eV < T_e < 40 eV). Such plasmas are too cold to emit x rays and too dense to be probed with optical Thomson scattering. The amount of shock heating in planar-CH-foil targets was diagnosed with time-resolved x-ray absorption spectroscopy[35–37] and noncollective spectrally resolved x-ray scattering.[38]

The implosion can be divided into four stages: shock propagation, acceleration phase, deceleration phase, and peak compression. This article concentrates on the first two stages, when the laser irradiates the target and when the shell adiabat is set. It is organized as follows: A description of the 1-D hydrodynamics code and its predictions are presented in **1-D Hydrodynamics Code** (p. 2). The scattered-light measurements are presented in **Laser-Absorption Experiment** (p. 3). The laser-driven burnthrough measurements are described in **Mass-Ablation-Rate Experiment** (p. 5). The shock-heating measurements are presented in **Shock-Heating Experiment** (p. 8). Throughout this article, the highly reproducible experimental results achieved with a high level of laser drive uniformity are shown to constrain the modeling of direct-drive energy transport from the laser to the target. The limitations of the flux-limited thermal-transport model[23] and further improvements in the modeling are presented in **Discussion** (p. 11). A nonlocal treatment of the thermal transport, which is in progress,[39] is expected to improve agreement between the simulation and the experiment.

1-D Hydrodynamics Code
Direct-drive implosions on the OMEGA Laser System are routinely simulated with the 1-D hydrodynamics code *LILAC*.[15] This code is used to design high-gain, direct-drive implosions for the NIF.[6,8,9] The electron thermal conduction that throttles the energy flow in direct-drive ICF is challenging to model.[23,39,40] As described below, it is currently simulated with a flux-limited thermal-transport model. The main objective of this detailed investigation is to tune the physics models in *LILAC* by comparing the predicted laser absorption, mass ablation rate, and shock heating with the measured quantities. Accurate simulations of OMEGA experiments will instill confidence in the target designs for the NIF.

A detailed description of *LILAC* can be found elsewhere[15] with the main features of the code described in this section. Laser absorption is calculated using a ray-trace algorithm that models inverse bremsstrahlung. Transport of radiation is modeled through multigroup diffusion with the Los Alamos National Laboratory Astrophysical Tables[41] providing the opacities. The *SESAME* tables are used to model the equation of state. *LILAC* uses a flux-limited Spitzer–Härm[42] electron-thermal-conduction model that calculates the effective heat flux q_{eff} using a sharp cutoff model [i.e., $q_{eff} = \min(q_{SH}, f q_{FS})$]. The heat flux is proportional to the temperature gradient $q_{SH} = -\kappa\nabla T_e$. In the region where $q_{SH} > q_{FS}$, the heat flux is calculated as a fraction f of the free stream limit $q_{FS} = n T_e V_T$, where κ is the heat conductivity, T_e is the electron temperature, $V_T = \sqrt{T_e/m_e}$ is the thermal electron velocity, and n_e is the electron density. The coefficient f is commonly referred to as a "flux limiter." Typical values of f for simulations of direct-drive experiments are $0.04 < f < 0.1$. The larger the flux limiter, the closer the heat flux is to the classical Spitzer–Härm limit.

The classical heat-transport theory of Spitzer–Härm is valid when the mean free path of the electron is much smaller than the temperature-gradient length of the plasma. This is not a good approximation for the steep gradients near the critical density in direct-drive ICF. Nonlocal energy-transport calculations have been proposed using Fökker–Planck codes to model the heat flux in direct-drive ICF when the temperature scale length is a few electron mean free paths;[40] however, until recently such calculations have been implemented with limited success in hydrodynamics codes.[43] A new nonlocal-transport model using a simplified Boltzmann equation (Krook model) has been developed and incorporated in *LILAC*.[39]

Laser-Absorption Experiment

The fraction of laser energy absorbed in the corona is inferred from power measurements of the 351-nm light scattered from spherical implosions[44–47] of cryogenic D_2 and plastic-shell targets.[48] Scattered light is detected behind two focusing lenses in the full-aperture backscatter stations (FABS) of beams 25 and 30: time-resolved spectra and calorimetric measurements are recorded.[49] Time-resolved spectra of the scattered light collected between the focusing lenses are also recorded. The scattered light is assumed to be distributed uniformly over 4π since the calculated deviations from isotropy are in the 1% to 2% range. As shown in Fig. 109.2, there is good agreement (within ±2% rms) between time-integrated
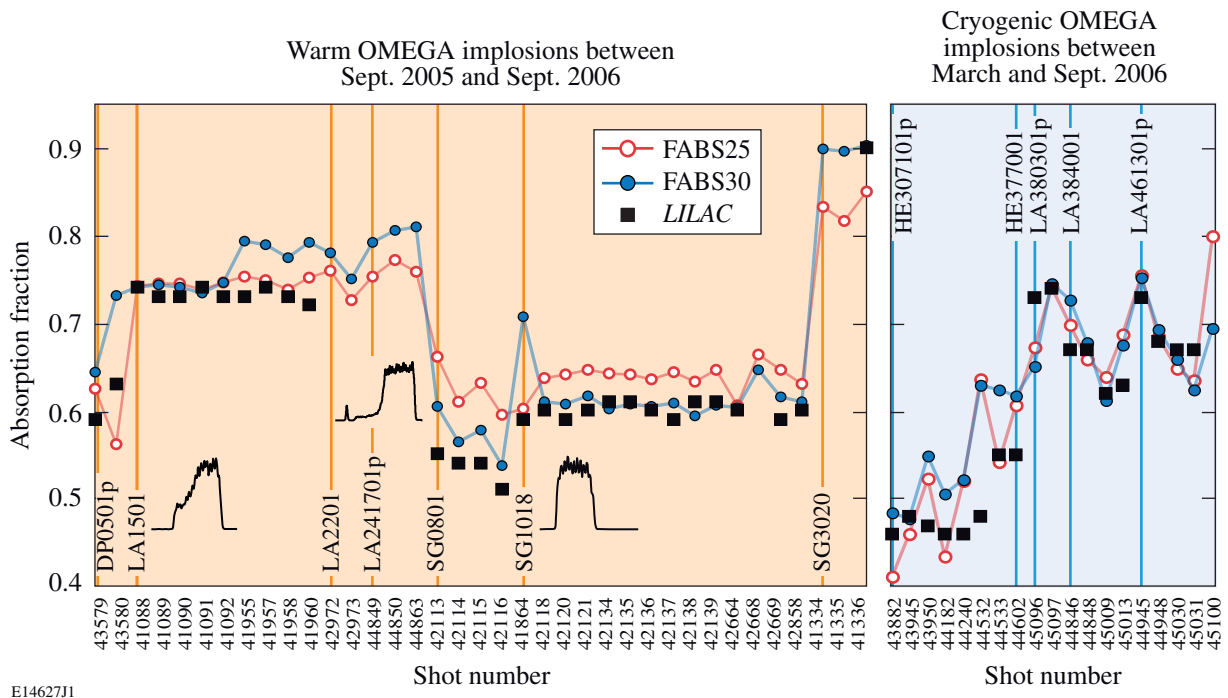

Figure 109.2
Time-integrated laser-absorption fraction measured on OMEGA for a variety of targets, laser pulse shapes, and irradiation energies. Good agreement is observed between the *LILAC* prediction (square symbols) and the measurements recorded in beams 25 and 30 (circle symbols) with the full-aperture backscatter stations (FABS25 and FABS30).

absorption data and the *LILAC* predictions for a wide variety of targets, laser pulse shapes, and irradiation energies. (The overall accuracy of the FABS calorimetry is estimated at 1% to 2% rms. Systematic errors of ≤3% between the calorimeters in the two FABS stations arise from the shot-to-shot variations in the transmissions of the blast shields protecting the OMEGA focus lenses that are coated with target debris from experiments. These errors are calibrated and corrected during routine system maintenance every few weeks.)

Since the shell adiabat is tuned by varying the temporal pulse shape of the laser irradiation, power measurements of the scattered light are essential to characterize the drive. The time-resolved scattered-light spectrum presented in Fig. 109.3(a) was recorded for the shaped laser pulse drive shown on a linear scale in Fig. 109.3(a) and a log scale in Fig. 109.3(b). The laser pulse has a low-intensity foot followed by a higher-intensity main drive. The shell adiabat is set during the foot portion of the pulse. A comparison of the time histories of the measured, spectrally integrated, scattered-light signal and the *LILAC* prediction is shown in Fig. 109.3(b). Two flux limiters were considered: $f = 0.06$ and $f = 0.1$. Overall the *LILAC* prediction for the scattered-light power is in good agreement with the measurement over more than three orders of magnitude; however, some differences (10% of the absolute scattered-light fraction) are observed that could affect the shock dynamics

(i.e., shock timing and shock strength). It is difficult to ascribe a single rms error estimate to the time-resolved absorption (or scattered-light) measurements. The absorption and scattering processes are affected by detailed coronal plasma conditions created by the incident laser pulse shape. During the first 100 ps of the laser pulse and at low intensities, the discrepancy can be as high as 50% or more without affecting the time-integrated absorption, while later in the plasma evolution, nonlinear effects can instantaneously lead to enhanced scattering of up to 10%. These discrepancies are well outside the experimental error bars, which depend on the dynamic range and the recording intensities on the streak camera. The discrepancy revealed with the scattered-light power is not evident in shock-velocity measurements, which can discriminate between the flux limiters under consideration.[39,50]

The measured absorption is systematically higher than predicted during the first 100 to 200 ps of the laser pulse. This is difficult to see in Fig. 109.3(b) because of the compressed time scale. The higher absorption at early times during the initial plasma formation is more apparent with a double-picket laser pulse (i.e., a train of two 100-ps laser pulses separated by 400 ps with ~12 J/beam in the first pulse and ~18 J/beam in the second pulse) experiment. The double-picket laser pulse shape is presented in Fig. 109.4(a), with the resulting streaked spectrum of the measured scattered light shown in Fig. 109.4(b).

E15205aJR
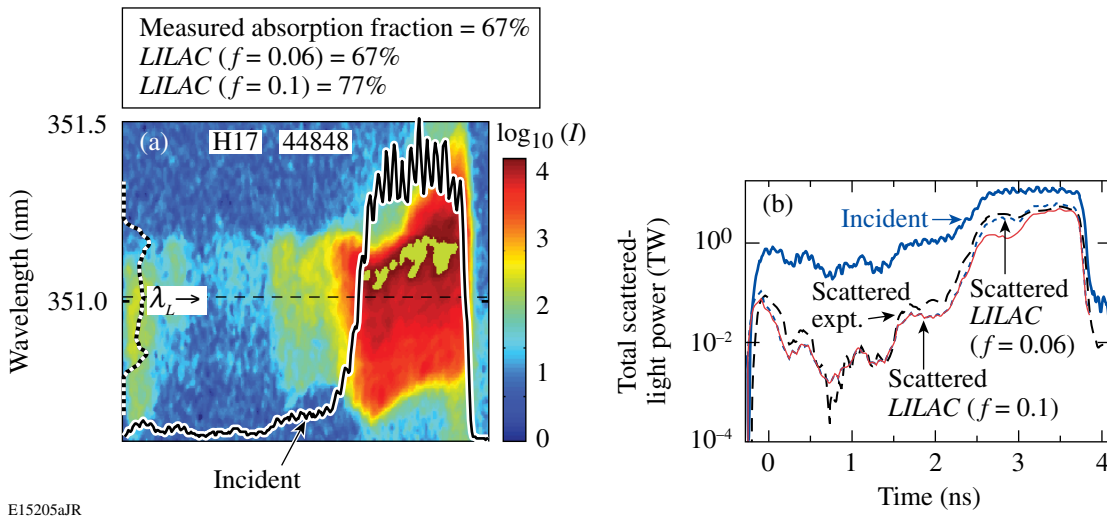
Figure 109.3

(a) Time-resolved spectral measurement of 351-nm scattered laser light for a shaped laser pulse irradiating a spherical DT cryogenic implosion target having a 95-μm-thick cryogenic DT layer inside a 5.4-μm-thick CD shell. The incident pulse shape (solid curve) and the broad incident spectrum (dotted curve) are overplotted on linear scales. (b) Spectrally integrated power measurement of scattered laser light (dashed curve) recorded with a laser pulse shape (bold solid curve) incident on target. *LILAC* predictions for two flux limiters are shown: $f = 0.06$ (dotted curve) and $f = 0.1$ (solid curve). Time-integrated laser absorption fractions are listed for the three scattered-light curves.
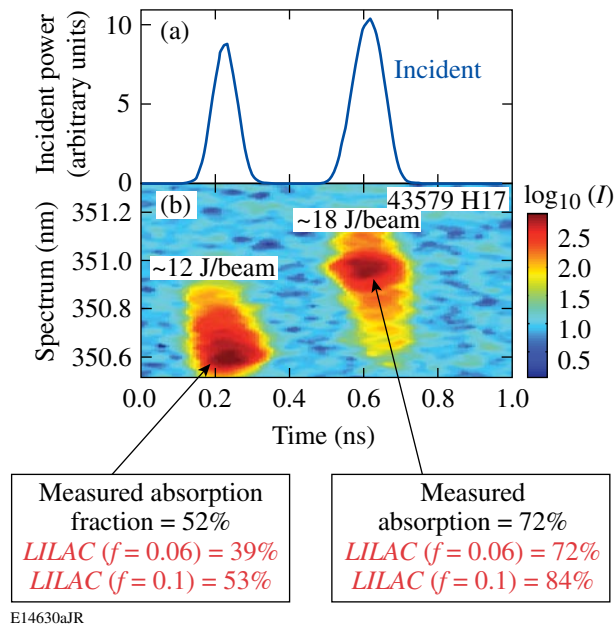
Figure 109.4
(a) Intensity of double-picket laser pulse shape irradiating a spherical plastic target, and (b) associated time-resolved, spectral measurement of scattered laser light. Measured time-integrated laser absorption fractions are listed for the two 100-ps picket pulses and compared with the *LILAC* predictions for two flux limiters ($f = 0.06$ and $f = 0.1$). The first pulse has ~12 J/beam and the second pulse has ~18 J/beam.

Although the 52% temporally integrated absorption fraction inferred from the experiment for the first peak is higher than the 39% *LILAC* prediction with $f = 0.06$, a simulation with a higher flux limiter of $f = 0.1$ (predicted absorption fraction = 53%) matches the experimental result. After the corona is established with the first pulse, the measured absorption fraction of the second pulse (72%) is matched with the lower flux limiter (predicted absorption fraction = 72%), while the higher flux limiter of $f = 0.1$ overpredicts an absorption fraction of 84%. Therefore, the flux limiter needs to vary in time to simulate the measured absorption fraction. Fökker–Planck simulations have predicted a time-varying flux limiter.[43] The enhanced absorption at early times is likely due to resonance absorption at very low $I\lambda_L^2 < 10^{13}\ \text{W}\mu\text{m}^2/\text{cm}^2$ with concomitant low energetic electron production ($T_h < 10$ keV). In the overall energetics this enhanced absorption is negligible; however, the energetic electrons can deposit their energy in the shell.

The time-resolved scattered-light spectra shown in Figs. 109.3(a) and 109.4(b) contain significant information. The initial rapid blue shift in the spectra is directly related to the rapid buildup of the plasma corona whose optical path length decreases as the plasma size increases. This is most easily

seen in Fig. 109.4(b) where the incident laser bandwidth was very narrow compared to the scattered-light spectra shown. In addition, the broad incident spectrum presented in Fig. 109.3(a) (dotted line) changes dramatically during the high-intensity part of the laser pulse, indicating that nonlinear processes are changing the spectra and possibly the scattered-light levels. A detailed investigation of these spectra is currently underway.

Mass-Ablation-Rate Experiment

The mass ablation rate is inferred from time-resolved x-ray burnthrough measurements[24–34] of solid, spherical plastic targets with buried tracer layers of Ti. Hydrodynamic instabilities are expected to have negligible effects on the inferred mass ablation rate since these targets do not accelerate. The 1-D simulations show that the shell trajectory of an imploding target has a negligible effect on the mass ablation rate for the 1-ns square laser pulse; therefore, the non-accelerating, solid, spherical burnthrough target is predicted to have a mass ablation rate similar to the shell target. The target shown in Fig. 109.5 is irradiated with 60 beams smoothed with 2-D SSD and PS,[14] using a 23-kJ, 1-ns square laser pulse with a peak intensity of 1×10^{15} W/cm². The ablation time is measured for three ablator thicknesses (2, 5, and 8 μm) to sample the mass ablation rate at different times during the laser pulse. It is predicted that the mass ablation rate for the 1-ns square laser pulse, having near-constant laser irradiation, has small temporal variations; therefore, the burnthrough experiment is not preferentially sampling particular times during the laser pulse. The mass ablation rate is inferred from the onset of the K-shell emission of the ablated Ti tracer layer. Prior to ablation the Ti layer is too cold to emit x rays; however, as the Ti is ablated into the hot corona, a significant fraction of

Drive intensity: 1×10^{15} W/cm²
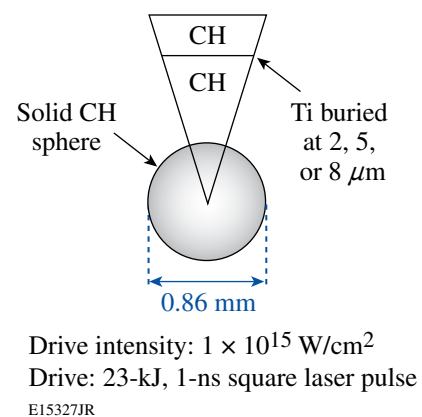Drive: 23-kJ, 1-ns square laser pulse

Figure 109.5
Diagram of nonaccelerating target used for laser-driven burnthrough experiment. The solid, spherical plastic (CH) target has a buried tracer layer of Ti (0.1 μm thick). The target specifications and laser irradiation conditions are shown.

its population is ionized to the He-like and H-like charge states and emits K-shell emission in the 4.5- to 5.5-keV photon energy range. The experimental signature of burnthrough is given by the Ti He_α emission.

Time-resolved, Ti K-shell spectroscopic measurements were performed with x-ray streak cameras[51] outfitted with a Bragg crystal spectrometer that used a flat RbAP (rubidium acid phthalate) crystal to disperse the spectrum onto a gold photocathode. The time axis for the streaked x-ray spectra was established as follows: The streak speed of the camera is calibrated using a temporally modulated ultraviolet laser pulse (i.e., a sequence of eight consecutive Gaussian laser pulses having a 548-ps period). The temporal resolution, defined by the streak speed and the photocathode slit width, is 50 ps. Defining the time $t = 0$ is challenging because the initial x-ray emission from the target is below the detection threshold of the diagnostic. Using the 4.5-keV x-ray continuum emission as a timing fiducial, the absolute timing is determined by synchronizing the measured pulse with the simulated one as described below. The synchronization is performed for each flux limiter under consideration since the temporal shape of the x-ray pulse depends on the flux limiter. The standard deviation of the difference between the measured and simulated x-ray pulse duration is 50 ps; therefore, the uncertainty in the measured burnthrough time is estimated to be ±50 ps. The spectra

recorded for the 2-μm CH ablator are shown in Fig. 109.6(a). The laser strikes the target at $t = 0$ ns and the onset of the Ti He_α signature burnthrough emission occurs around 0.3 ns. A similar measurement is presented in Fig. 109.6(b) for the 8-μm CH ablator. The spectral resolving power ($E/\Delta E \sim 50$) is limited by source broadening but is clearly high enough to resolve the prominent Ti K-shell emissions. The streaked spectra presented in Fig. 109.6 show that the burnthrough occurs later for the target with the thicker CH ablator, as expected.

Weak Ca K-shell emissions are observed in the burnthrough x-ray spectra of Fig. 109.6. Calcium is a surface contaminant of the solid plastic target introduced during production of the sphere. The calcium layer is ablated into the coronal plasma and emits K-shell emission around the same time as Ti. It is an experimental artifact that does not affect the measured burnthrough time.

The x-ray emission from the corona is simulated by post-processing the *LILAC* prediction with the time-dependent atomic physics code *Spect3D*.[52] As mentioned above, the x-ray continuum emission from the target during the first few hundred picoseconds is below the detection threshold of the diagnostic; therefore, the absolute timing of the measurement is established by synchronizing the measured x-ray continuum in the 4.5-keV range with the *LILAC/Spect3D* prediction. The
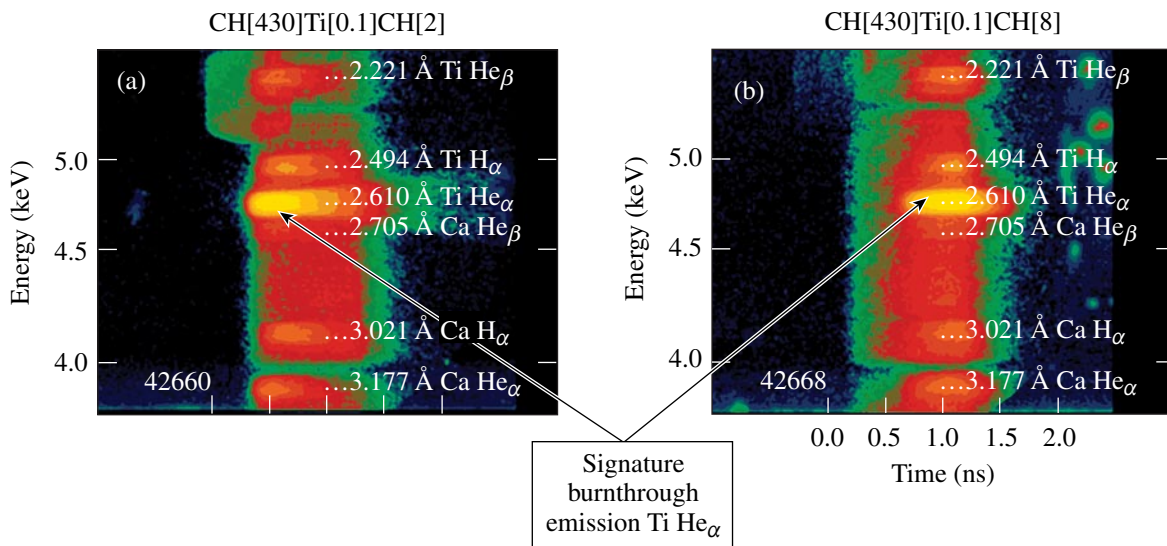
Figure 109.6
(a) Streaked x-ray spectrum recorded on a laser-driven burnthrough experiment with the prominent Ti K-shell emissions identified for the 2-μm-thick CH ablator. The mass ablation rate is inferred from the signature Ti He_α emission. (b) Streaked x-ray spectrum for the 8-μm-thick CH ablator. Calcium is a surface contaminant of the solid plastic target introduced during production of the sphere. The calcium layer is ablated into the coronal plasma and emits K-shell emission around the same time as Ti.

synchronized x-ray pulses are shown in Fig. 109.7(a) for the 8-μm CH ablator. In Fig. 109.7(b), the temporal evolution of the Ti He$_\alpha$ emission predicted with *LILAC/Spect3D* is compared with the measured burnthrough emission for the 8-μm CH ablator. Two flux limiters ($f = 0.06$ and $f = 0.1$) were considered, and the experimental results are closer to the predictions with the higher flux-limiter value. Comparisons of the predicted

and measured burnthrough times for these two flux limiters are presented in Fig. 109.8 for the ablators under consideration. The burnthrough time is defined as the time at which the Ti He$_\alpha$ emission reaches 10% of its peak intensity. It is clear from Fig. 109.8 that the burnthrough experiment is more consistent with the higher mass ablation rate of the *LILAC* prediction with $f = 0.1$. A flux limiter of $f = 0.1$ was also needed to simulate the
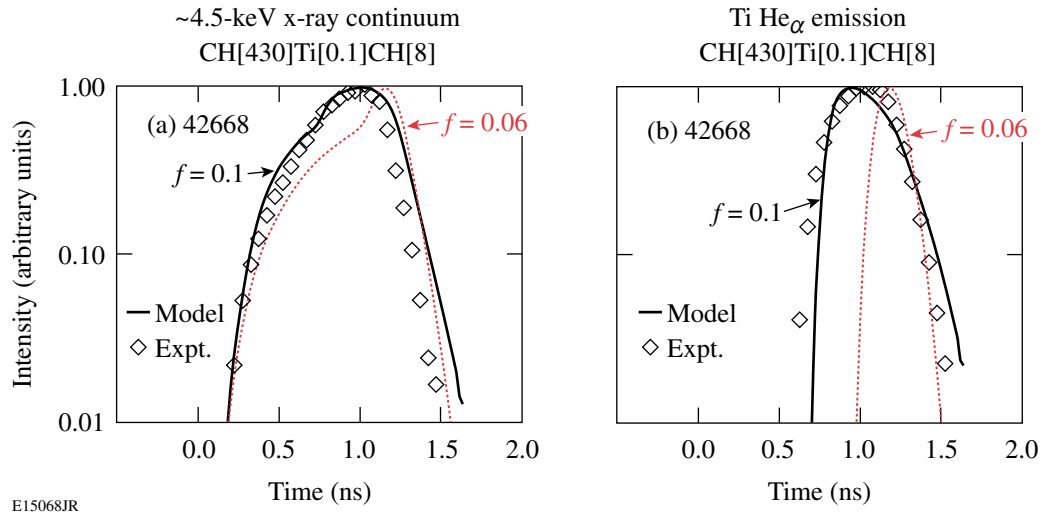
Figure 109.7

(a) Time histories of the measured (diamond symbols) and simulated (dotted curve for $f = 0.06$ and solid curve for $f = 0.1$) x-ray continuum in the ~4.5-keV range, and (b) time histories of the measured (diamond symbols) and simulated (dotted curve for $f = 0.06$ and solid curve for $f = 0.1$) Ti He$_\alpha$ emission for the laser-driven burnthrough experiment.
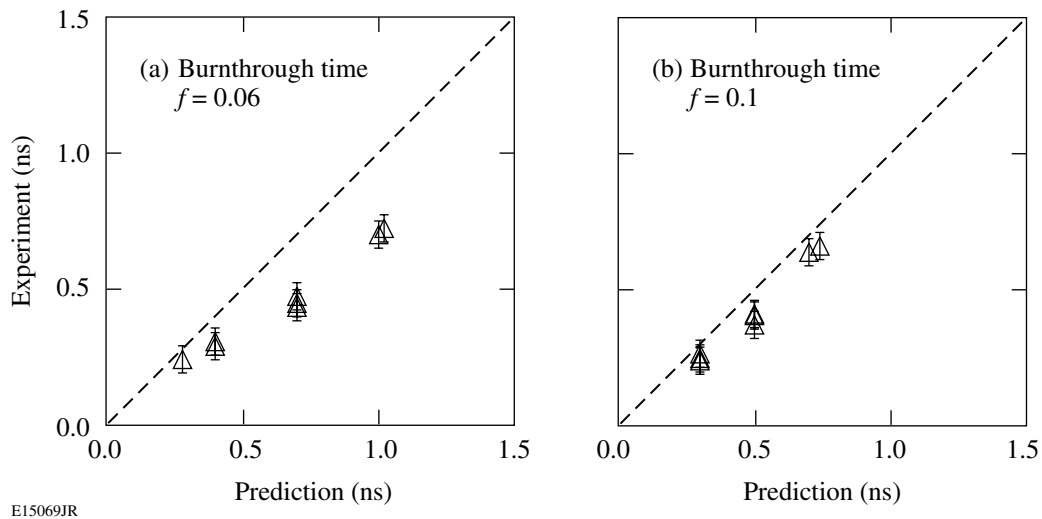
Figure 109.8

A comparison of the measured laser-driven burnthrough time and (a) the *LILAC* prediction with a flux limiter $f = 0.06$ and (b) the *LILAC* prediction with a flux limiter $f = 0.1$ for the three ablators under consideration.

ablation-front perturbation oscillations for Richtmyer–Meshkov instability experiments on OMEGA.[39,53]

Shock-Heating Experiment

The shock wave launched by laser ablation into the target is the primary source of heating for the bulk of the shell. X-ray radiation and energetic electrons from the corona can provide additional heating to portions of the shell near the ablation front. The amount of shock heating in planar-CH-foil targets was diagnosed using two techniques: time-resolved x-ray absorption spectroscopy and noncollective spectrally resolved x-ray scattering. A detailed description of the latter experiment can be found elsewhere.[38] The results of the former experiment will be briefly described in this section; however, a more detailed version will be published separately.[37] Planar geometry is a good approximation for the shell during the shock-propagation stage of the implosion since convergence can be neglected. It also provides better diagnostic access than a spherical shell target.

Local shell conditions were measured using time-resolved x-ray absorption spectroscopy of plastic foil targets with a buried tracer layer of Al as shown in Fig. 109.9. As the shock wave propagates through the Al, it compresses and ionizes the Al. The buried depth of the tracer layer is varied to probe the plasma conditions in different regions of the target. As shown in Fig. 109.10, Al $1s$–$2p$ x-ray absorption spectroscopy of a CH planar target with a buried Al tracer layer (1 to 2 μm thick) was performed with a point-source (i.e., <100-μm) Sm backlighter irradiated with laser intensities of ~10^{16} W/cm^2. The overall

thickness (~50 μm) of the drive foil was chosen to delay the acceleration phase until after the absorption spectra were recorded, minimizing the influences of hydrodynamic instabilities on the measurements. The direct-drive target was irradiated with up to 18 laser beams that were smoothed with phase plates, 2-D SSD, and PS.[14] The overlapped intensity had a uniform drive portion with a 400-μm diameter and peak intensities in the range of 10^{14} to 10^{15} W/cm^2. The Sm M-shell emission in the 1.4- to 1.7-keV range overlaps the bound–bound absorption features of Al near 1.5 keV and probes the uniform drive portion of the target.[35]
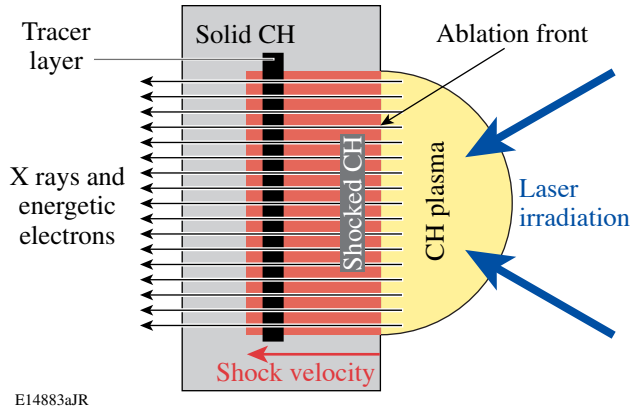
E14883aJR

Figure 109.9
Diagram of the target used to diagnose the shock-heated conditions of a direct-drive ICF target. X-ray radiation and energetic electrons provide additional heating. X-ray absorption spectra of buried high-Z tracer layer are used to diagnose the plasma conditions in the shock-heated target. The position of the layer is varied to probe different regions of the target.
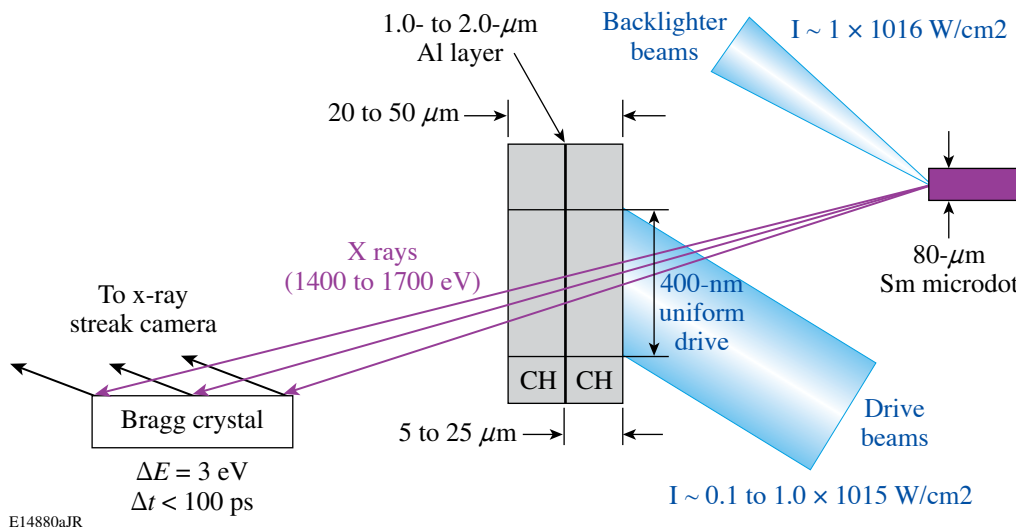
E14880aJR

Figure 109.10
Layout of the Al $1s$–$2p$ absorption-spectroscopy experiment showing the Sm backlighter, the plastic drive foil with the buried Al layer, and the Bragg crystal spectrometer.

The frequency-dependent transmission of the shock-heated Al layer, obtained from the ratio $I(\nu)/I_0(\nu) = e^{[-\mu(\nu, n_e, T_e)\rho\Delta L]}$ of the transmitted backlighter spectrum $I(\nu)$ to the incident Sm spectrum $I_0(\nu)$, depends on the mass absorption coefficient μ and the areal density of the Al layer $\rho\Delta L$. The absorption coefficient is sensitive to variations in n_e and T_e for the shock-heated conditions under consideration.[36] The high electron densities cause the spectral line shapes of the bound–bound absorption features to be Stark-broadened beyond the instrumental spectral resolution (~3 eV). The incident and transmitted spectra were recorded with an x-ray streak camera[51] outfitted with a Bragg crystal spectrometer that used a flat RbAP crystal to disperse the spectrum onto a low-density CsI photocathode. The temporal resolution of the measurement was ~100 ps.

The sensitivity of the absorption spectroscopy to variations in the electron temperature is illustrated in Fig. 109.11. The predicted Al $1s$–$2p$ absorption spectra, obtained by post-processing the *LILAC* simulation for shot #44116 with the time-dependent atomic physics code *Spect3D*,[52] are compared to the electron temperature in the Al layer. The target had a 1-μm-thick Al layer buried at a depth of 10 μm in a 50-μm-thick CH target and was irradiated with a 1-ns square laser pulse having a peak intensity of 1×10^{15} W/cm^2. A flux limiter of 0.06 was used for the simulation. The electron temperature in the Al layer was calculated as follows: The *LILAC/Spect3D* spectra

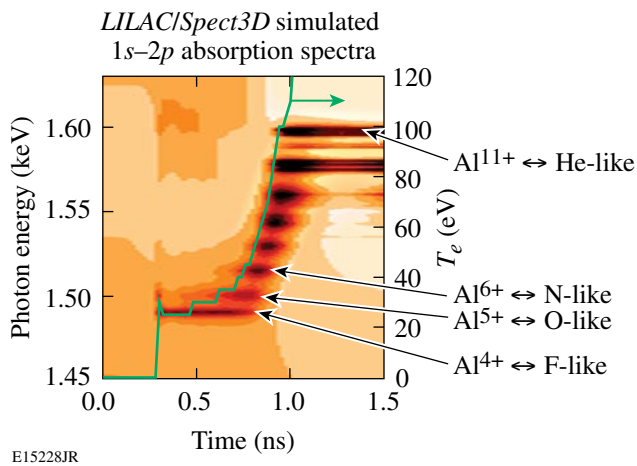were compared with spectra calculated with the time-dependent atomic physics code PrismSPECT[52] assuming uniform shell conditions for various combinations of n_e and T_e. The best fit between the *LILAC/Spect3D* spectra and PrismSPECT was determined based on a least-squares-fitting routine, which inferred n_e and T_e simultaneously. The accuracy of the T_e inference is 10%, while the uncertainty of the n_e inference is about a factor of 2. The stair step in the simulated electron temperature observed in Fig. 109.11 around 0.5 ns is due to the discrete electron temperatures considered in the spectral fitting routine. Higher-charge states of Al are ionized in succession and absorb in $1s$–$2p$ transitions as the shell T_e increases. At time $t = 0$ ns, the laser irradiation of the target begins. When the shock propagates through the buried Al layer, the sharp rise in the temperature ionizes the Al and the lowest-charge states of Al (i.e., F-like and O-like) are observed in $1s$–$2p$ absorption. The second rise in electron temperature at 0.75 ns occurs when the heat front penetrates the Al layer and ultimately ionizes it to the K shell. The minimum electron temperature that can be currently diagnosed using this technique is ~10 eV.

Time-resolved x-ray absorption spectroscopy was performed using a 50-μm-thick target with a 1- or 2-μm-thick Al layer buried at a depth of 10 μm. Two laser intensities were studied: 1×10^{14} W/cm^2 generating a 10-Mbar shock and 1×10^{15} W/cm^2 generating a 50-Mbar shock. The predicted, shocked mass density in the Al layer for the higher intensity drive is ~8 g/cm^3. The streaked x-ray spectra are presented in Fig. 109.12 with the prominent absorption features identified. The cold K edge of Al can be observed prior to the shock arrival at the Al layer. The diagnostic utility of the temperature and density dependence of the K-edge shift is currently being studied. Only the F-like Al $1s$–$2p$ absorption feature is observed with the lower drive intensity [Fig. 109.12(a)]. The three lowest-charge states (F-like, O-like, and N-like) appear in absorption when shock heated by the higher intensity [Fig. 109.12(b)]. The Sm backlighter and the CH/Al/CH target have the same 1-ns square laser pulse drive, but the Sm backlighter was fired 200 ps earlier than the drive foil to optimize the backlighter brightness for the shock-heating period of the Al layer. The higher charge states associated with the heat-front penetration that are predicted in Fig. 109.11 are not observed in Fig. 109.12(b) because the Sm backlighter was off at that time. The temporal onset of the $1s$–$2p$ absorption depends on the buried depth of the Al layer and the shock velocity.

The measured spectral line shapes were compared with simulated absorption spectra calculated with *LILAC* and *Spect3D*.

LILAC/Spect3D simulated $1s$–$2p$ absorption spectra

E15228JR

Figure 109.11

Temporal evolution of the Al $1s$–$2p$ absorption spectrum simulated with *LILAC* using $f = 0.06$ and *Spect3D* for shot #44116. The target had a 1-μm-thick Al layer buried at a depth of 10 μm in a 50-μm-thick CH target and was irradiated with a 1-ns square laser pulse having a peak intensity of 1×10^{15} W/cm^2. The predicted electron temperature in the Al layer is also plotted (solid curve). Higher-charge states of Al are ionized in succession and absorb in $1s$–$2p$ transitions as T_e increases.

A detailed description can be found elsewhere.[37] Reasonable agreement was observed for the lower drive intensity; however, the higher-charge states were observed in the measured absorption spectrum compared to the simulated absorption spectrum for the higher drive intensity. This indicates that the measured electron temperature is higher than the prediction. The measured spectra were compared with simulated spectra calculated with PrismSPECT[52] assuming uniform shell conditions for various combinations of n_e and T_e. The best fit to the measured spectra was determined based on a least-squares-fitting routine, which inferred n_e and T_e simultaneously. The electron density inferred from the higher laser drive intensity was 1×10^{24} cm^{-3}

and for the lower drive intensity was 5×10^{23} cm^{-3}, consistent with the 1-D predictions. The time history comparing the predicted electron temperature with the measurements is shown in Fig. 109.13. Again, the simulated electron temperature was calculated as follows: (1) *LILAC* was post-processed with *Spect3D* and (2) the simulated absorption spectra were fitted with PrismSPECT, assuming uniform electron temperature and density in the Al layer. These calculations were performed

Figure 109.12
Time-resolved x-ray absorption spectra recorded for drive intensities of (a) 1×10^{14} W/cm^2 and (b) 1×10^{15} W/cm^2. The prominent absorption features are identified.

Figure 109.13
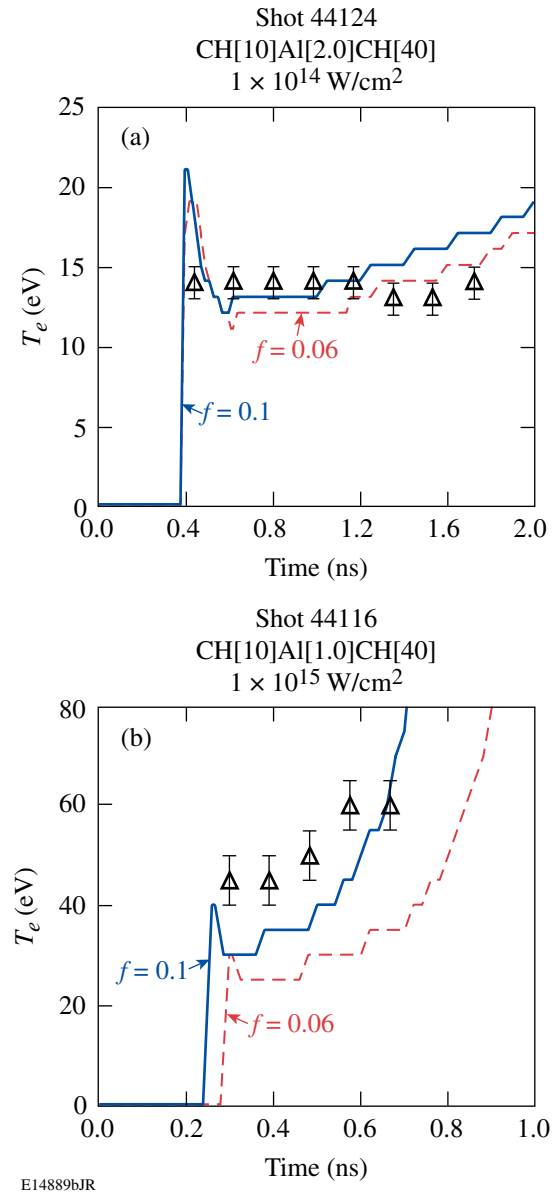Comparison of time-resolved electron temperature in the Al layer inferred from the experiment (triangles) with *LILAC* simulations using $f = 0.06$ (dashed curves) and $f = 0.1$ (solid curves) for drive intensities of (a) 1×10^{14} W/cm^2 and (b) 1×10^{15} W/cm^2.

for two flux limiters (f = 0.06 and f = 0.1). For the lower drive intensity the predicted electron temperatures for both flux limiters are close to the time-resolved electron temperatures inferred from the measured absorption spectra [Fig. 109.13(a)]. These experimental measurements are consistent with the results from the noncollective spectrally resolved x-ray scattering experiment of a similar drive foil: an upper limit of T_e = 20 eV was inferred in those experiments.[38] The time-resolved electron temperatures inferred from the measured absorption spectra are higher than the simulated ones for the 1×10^{15} W/cm^2 drive intensity [Fig. 109.13(b)]. The simulation with the higher flux limiter predicts more shock heating and an earlier penetration of the heat front. The initial level of measured shock heating is higher than the simulation with f = 0.1; however, the timing of the heat-front penetration is similar.

Discussion

The experimental results indicate that the energy transport from the critical density to the ablation front cannot be described by flux-limited diffusion and may be nonlocal. The role of nonlocal thermal transport is twofold: (1) It results in an effective time-dependent flux limiter that influences the laser absorption fraction, the shock timing, and the shock-heated conditions. (2) It results in preheat through the transport of energetic electrons, which would increase the shell temperature. All of the experimental results presented in this article were compared with *LILAC* simulations having flux limiters of f = 0.06 and f = 0.1. The measurements are accurate enough to distinguish between these two models. In some cases the simulations with the higher flux limiter were closer to the experimental observables. A higher flux limiter was needed to reduce the discrepancies between the simulations and measurements for the early-time laser absorption, the mass ablation rate with laser irradiation of 1×10^{15} W/cm^2, and the shock heating with laser irradiation of 1×10^{15} W/cm^2. Preheat due to energetic electrons and x rays from the corona may explain shock heating at laser irradiation of 1×10^{15} W/cm^2. These observations are consistent with the effects of nonlocal electron thermal transport.[39] Other effects influencing the measurements also need to be investigated. The higher early-time laser absorption may be caused by resonance absorption,[54] which is not included in the *LILAC* prediction. *LILAC* may be underestimating the predicted electron temperature due to shock heating. The accuracy of modeling the electron temperature in the Al layer needs to be investigated. The simulations with the lower flux limiter of f = 0.06 were close to the measurements of shock heating at laser irradiation of 1×10^{14} W/cm^2. This could be consistent with a nonlocal electron thermal transport if the preheat is negligible at the lower intensity.

This detailed comparison of the results from the experiment and *LILAC* reveals the limitations of a flux-limited thermal-transport model for direct-drive ICF: a single-flux limiter cannot explain all the experimental observables. Laser absorption measurements indicate a time-dependent flux limiter is required. However, a nonlocal treatment of the thermal transport currently under development[39] is expected to improve agreement between the simulations and the experimental results.

Conclusion

An investigation of direct-drive energy coupling was conducted to tune the physics models of the 1-D hydrodynamics code *LILAC*. The flow of energy from the laser to the target was inferred by measuring the laser absorption fraction, the mass ablation rate, and the amount of shock heating. The highly reproducible experimental results achieved with a high level of laser drive uniformity constrain the modeling of direct-drive energy coupling. All of the experimental results were compared with *LILAC* simulations having flux limiters of f = 0.06 and f = 0.1. The detailed comparison reveals the limitation of a flux-limited thermal-transport model for direct-drive ICF: a single-flux limiter cannot explain all the experimental observables. Furthermore, simulations of laser absorption measurements need a time-dependent flux limiter to match the data. The experimental results indicate that the energy transport from the critical density to the ablation front is probably nonlocal. A nonlocal treatment of the thermal transport in *LILAC* is expected to improve the agreement between the simulations and the experimental results.

REFERENCES

1. J. Nuckolls *et al.*, Nature **239**, 139 (1972).

2. J. D. Lindl, R. L. McCrory, and E. M. Campbell, Phys. Today **45**, 32 (1992).

3. R. L. McCrory, J. M. Soures, C. P. Verdon, F. J. Marshall, S. A. Letzring, S. Skupsky, T. J. Kessler, R. L. Kremens, J. P. Knauer, H. Kim, J. Delettrez, R. L. Keck, and D. K. Bradley, Nature **335**, 225 (1988).

4. J. D. Lindl, *Inertial Confinement Fusion: The Quest for Ignition and Energy Gain Using Indirect Drive* (Springer-Verlag, New York, 1998).

5. S. E. Bodner, D. G. Colombant, J. H. Gardner, R. H. Lehmberg, S. P. Obenschain, L. Phillips, A. J. Schmitt, J. D. Sethian, R. L. McCrory, W. Seka, C. P. Verdon, J. P. Knauer, B. B. Afeyan, and H. T. Powell, Phys. Plasmas **5**, 1901 (1998).

6. P. W. McKenty, V. N. Goncharov, R. P. J. Town, S. Skupsky, R. Betti, and R. L. McCrory, Phys. Plasmas **8**, 2315 (2001).

7. J. D. Lindl *et al*., Phys. Plasmas **11**, 339 (2004).

8. P. W. McKenty, T. C. Sangster, M. Alexander, R. Betti, R. S. Craxton, J. A. Delettrez, L. Elasky, R. Epstein, A. Frank, V. Yu. Glebov, V. N. Goncharov, D. R. Harding, S. Jin, J. P. Knauer, R. L. Keck, S. J. Loucks, L. D. Lund, R. L. McCrory, F. J. Marshall, D. D. Meyerhofer, S. P. Regan, P. B. Radha, S. Roberts, W. Seka, S. Skupsky, V. A. Smalyuk, J. M. Soures, K. A. Thorp, M. Wozniak, J. A. Frenje, C. K. Li, R. D. Petrasso, F. H. Séguin, K. A. Fletcher, S. Padalino, C. Freeman, N. Izumi, J. A. Koch, R. A. Lerche, M. J. Moran, T. W. Phillips, G. J. Schmid, and C. Sorce, Phys. Plasmas **11**, 2790 (2004).

9. R. L. McCrory, S. P. Regan, S. J. Loucks, D. D. Meyerhofer, S. Skupsky, R. Betti, T. R. Boehly, R. S. Craxton, T. J. B. Collins, J. A. Delettrez, D. Edgell, R. Epstein, K. A. Fletcher, C. Freeman, J. A. Frenje, V. Yu. Glebov, V. N. Goncharov, D. R. Harding, I. V. Igumenshchev, R. L. Keck, J. D. Kilkenny, J. P. Knauer, C. K. Li, J. Marciante, J. A. Marozas, F. J. Marshall, A. V. Maximov, P. W. McKenty, J. Myatt, S. Padalino, R. D. Petrasso, P. B. Radha, T. C. Sangster, F. H. Séguin, W. Seka, V. A. Smalyuk, J. M. Soures, C. Stoeckl, B. Yaakobi, and J. D. Zuegel, Nucl. Fusion **45**, S283 (2005).

10. R. Betti, K. Anderson, T. R. Boehly, T. J. B. Collins, R. S. Craxton, J. A. Delettrez, D. H. Edgell, R. Epstein, V. Yu. Glebov, V. N. Goncharov, D. R. Harding, R. L. Keck, J. H. Kelly, J. P. Knauer, S. J. Loucks, J. A. Marozas, F. J. Marshall, A. V. Maximov, D. N. Maywar, R. L. McCrory, P. W. McKenty, D. D. Meyerhofer, J. Myatt, P. B. Radha, S. P. Regan, C. Ren, T. C. Sangster, W. Seka, S. Skupsky, A. A. Solodov, V. A. Smalyuk, J. M. Soures, C. Stoeck, W. Theobald, B. Yaakobi, C. Zhou, J. D. Zuegel, J. A. Frenje, C. K. Li, R. D. Petrasso, and F. H. Séguin, Plasma Phys. Control. Fusion **48**, B153 (2006).

11. M. C. Herrmann, M. Tabak, and J. D. Lindl, Nucl. Fusion **41**, 99 (2001).

12. R. Betti, K. Anderson, V. N. Goncharov, R. L. McCrory, D. D. Meyerhofer, S. Skupsky, and R. P. J. Town, Phys. Plasmas **9**, 2277 (2002).

13. T. R. Boehly, D. L. Brown, R. S. Craxton, R. L. Keck, J. P. Knauer, J. H. Kelly, T. J. Kessler, S. A. Kumpan, S. J. Loucks, S. A. Letzring, F. J. Marshall, R. L. McCrory, S. F. B. Morse, W. Seka, J. M. Soures, and C. P. Verdon, Opt. Commun. **133**, 495 (1997).

14. S. P. Regan, J. A. Marozas, R. S. Craxton, J. H. Kelly, W. R. Donaldson, P. A. Jaanimagi, D. Jacobs-Perkins, R. L. Keck, T. J. Kessler, D. D. Meyerhofer, T. C. Sangster, W. Seka, V. A. Smalyuk, S. Skupsky, and J. D. Zuegel, J. Opt. Soc. Am. B **22**, 998 (2005).

15. J. Delettrez, R. Epstein, M. C. Richardson, P. A. Jaanimagi, and B. L. Henke, Phys. Rev. A 36, 3926 (1987); J. Delettrez, Can. J. Phys. **64**, 932 (1986).

16. J. Paisner *et al*., Laser Focus World **30**, 75 (1994).

17. P. B. Radha, V. N. Goncharov, T. J. B. Collins, J. A. Delettrez, Y. Elbaz, V. Yu. Glebov, R. L. Keck, D. E. Keller, J. P. Knauer, J. A. Marozas, F. J. Marshall, P. W. McKenty, D. D. Meyerhofer, S. P. Regan, T. C. Sangster, D. Shvarts, S. Skupsky, Y. Srebro, R. P. J. Town, and C. Stoeckl, Phys. Plasmas **12**, 032702 (2005).

18. H. Takabe *et al*., Phys. Fluids **28**, 3676 (1985).

19. R. Betti, V. N. Goncharov, R. L. McCrory, and C. P. Verdon, Phys. Plasmas **5**, 1446 (1998).

20. S. P. Regan, J. A. Delettrez, V. N. Goncharov, F. J. Marshall, J. M. Soures, V. A. Smalyuk, P. B. Radha, R. Epstein, V. Yu. Glebov, P. A. Jaanimagi, D. D. Meyerhofer, T. C. Sangster, W. Seka, S. Skupsky, C. Stoeckl, D. A. Haynes, Jr., J. A. Frenje, C. K. Li, R. D. Petrasso, and F. H. Séguin, Phys. Rev. Lett. **92**, 185002 (2004).

21. V. N. Goncharov, J. P. Knauer, P. W. McKenty, P. B. Radha, T. C. Sangster, S. Skupsky, R. Betti, R. L. McCrory, and D. D. Meyerhofer, Phys. Plasmas **10**, 1906 (2003).

22. K. Anderson and R. Betti, Phys. Plasmas **10**, 4448 (2003).

23. R. C. Malone, R. L. McCrory, and R. L. Morse, Phys. Rev. Lett. **34**, 721 (1975).

24. W. Seka, J.-L. Schwob, and C. Breton, J. Appl. Phys. **42**, 315 (1971).

25. F. C. Young *et al*., Appl. Phys. Lett. **30**, 45 (1977).

26. B. Yaakobi and T. C. Bristow, Phys. Rev. Lett. **38**, 350 (1977).

27. B. H. Ripin *et al*., Phys. Fluids **23**, 1012 (1980).

28. M. H. Key, R. G. Evans, and D. J. Nicholas, Rutherford Appleton Laboratory, Chilton, Didcot, Oxon, England, Report RL-78-020/XAB (1978).

29. B. Yaakobi, T. Boehly, P. Bourke, Y. Conturie, R. S. Craxton, J. Delettrez, J. M. Forsyth, R. D. Frankel, L. M. Goldman, R. L. McCrory, M. C. Richardson, W. Seka, D. Shvarts, and J. M. Soures, Opt. Commun. **39**, 175 (1981).

30. T. J. Goldsack *et al*., Opt. Commun. **42**, 55 (1982); T. J. Goldsack *et al*., Phys. Fluids **25**, 1634 (1982).

31. M. H. Key *et al*., Phys. Fluids **26**, 2011 (1983).

32. A. Hauer *et al*., Phys. Rev. Lett. **53**, 2563 (1984).

33. J. Delettrez, R. Epstein, M. C. Richardson, P. A. Jaanimagi, and B. L. Henke, Phys. Rev. A **36**, 3926 (1987).

34. D. K. Bradley, J. A. Delettrez, and C. P. Verdon, Phys. Rev. Lett. **68**, 2774 (1992).

35. D. J. Hoarty *et al*., J. Quant. Spectrosc. Radiat. Transf. **99**, 283 (2006).

36. T. R. Boehly, J. A. Delettrez, J. P. Knauer, D. D. Meyerhofer, B. Yaakobi, R. P. J. Town, and D. Hoarty, Phys. Rev. Lett. **87**, 145003 (2001).

37. H. Sawada, S. P. Regan, R. Epstein, D. Li, V. N. Gonchraov, P. B. Radha, D. D. Meyerhofer, T. R. Boehly, V. A. Smalyuk, T. C. Sangster, B. Yaakobi, and R. C. Mancini, "Investigation of Direct-Drive Shock Heating Using XRay Absorption Spectroscopy," to be submitted to Physics of Plasmas.

38. H. Sawada, S. P. Regan, D. D. Meyerhofer, I. V. Igumenshchev, V. N. Goncharov, T. R. Boehly, T. C. Sangster, V. A. Smalyuk, B, Yaakobi, G. Gregori, S. H. Glenzer, and O. L. Landen, "Diagnosing Direct-Drive, Shock-Heated Plastic Planar Foils with Noncollective Spectrally Resolved X-Ray Scattering," to be submitted to Physics of Plasmas.

39. V. N. Goncharov, O. V. Gotchev, E. Vianello, T. R. Boehly, J. P. Knauer, P. W. McKenty, P. B. Radha, S. P. Regan, T. C. Sangster, S. Skupsky, V. A. Smalyuk, R. Betti, R. L. McCrory, D. D. Meyerhofer, and C. Cherfils-Clérouin, Phys. Plasmas **13**, 012702 (2006).

40. A. R. Bell, R. G. Evans, and D. J. Nicholas, Phys. Rev. Lett. **46**, 243 (1981).

41. W. F. Huebner *et al.*, Los Alamos National Laboratory, Los Alamos, NM, Report LA-6760-M (1977).

42. L. Spitzer, Jr. and R. Härm, Phys. Rev. **89**, 977 (1953).

43. A. Sunahara, J. A. Delettrez, C. Stoeckl, R. W. Short, and S. Skupsky, Phys. Rev. Lett. **91**, 095003 (2003).

44. W. Seka, L. M. Goldman, M. C. Richardson, J. M. Soures, K. Tanaka, B. Yaakobi, R. S. Craxton, R. L. McCrory, R. Short, E. A. Williams, T. Boehly, R. Keck, and R. Boni, in *Plasma Physics and Controlled Nuclear Fusion Research 1982* (IAEA, Vienna, 1983), Vol. I, pp. 131–137.

45. J. M. Soures, T. C. Bristow, H. Deckman, J. Delettrez, A. Entenberg, W. Friedman, J. Forsyth, Y. Gazit, G. Halpern, F. Kalk, S. Letzring, R. McCrory, D. Peiffer, J. Rizzo, W. Seka, S. Skupsky, E. Thorsos, B. Yaakobi, and T. Yamanaka, in *Laser Interaction and Related Plasma Phenomena*, edited by H. J. Schwarz, H. Hora, M. J. Lubin, and B. Yaakobi (Plenum Press, New York, 1981), Vol. 5, pp. 463–481.

46. W. Seka, R. S. Craxton, J. Delettrez, L. Goldman, R. Keck, R. L. McCrory, D. Shvarts, J. M. Soures, and R. Boni, Opt. Commun. **40**, 437 (1982).

47. M. C. Richardson, R. S. Craxton, J. Delettrez, R. L. Keck, R. L. McCrory, W. Seka, and J. M. Soures, Phys. Rev. Lett. **54**, 1656 (1985).

48. W. Seka, V. N. Goncharov, J. A. Delettrez, D. H. Edgell, I. V. Igumenshchev, R. W. Short, A. V. Maximov, J. Myatt, and R. S. Craxton, "Time-Dependent Absorption Measurements in Direct-Drive Spherical Implosions," to be submitted to Physics of Plasmas.

49. S. P. Regan, D. K. Bradley, A. V. Chirokikh, R. S. Craxton, D. D. Meyerhofer, W. Seka, R. W. Short, A. Simon, R. P. J. Town, B. Yaakobi, J. J. Caroll III, and R. P. Drake, Phys. Plasmas **6**, 2072 (1999).

50. T. R. Boehly, E. Vianello, J. E. Miller, R. S. Craxton, T. J. B. Collins, V. N. Goncharov, I. V. Igumenshchev, D. D. Meyerhofer, D. G. Hicks, P. M. Celliers, and G. W. Collins, Phys. Plasmas **13**, 056303 (2006).

51. D. H. Kalantar *et al.*, in *22nd International Congress on High-Speed Photography and Photonics*, edited by D. L. Paisley and A. M. Frank (SPIE, Bellingham, WA, 1997), Vol. 2869, pp. 680–685.

52. Prism Computational Sciences, Inc., Madison, WI 53711.

53. O. Gotchev, V. N. Goncharov, J. P. Knauer, T. R. Boehly, T. J. B. Collins, R. Epstein, P. A. Jaanimagi, and D. D. Meyerhofer, Phys. Rev. Lett. **96**, 115005 (2006).

54. W. L. Kruer, *The Physics of Laser–Plasma Interactions, Frontiers in Physics*, Vol. 73, edited by D. Pines (Addison-Wesley, Redwood City, CA, 1988).

Nuclear Measurements of Fuel–Shell Mix in Inertial Confinement Fusion Implosions on OMEGA

Introduction

Turbulent mix is a vital concern in inertial confinement fusion (ICF)[1,2] since it can quench the nuclear burn in the hot spot prematurely, or even extinguish it entirely. The saturation of Rayleigh–Taylor (RT) instability growth at a density interface leads to small-scale, turbulent eddies that in turn lead to mixing of the high- and low-density materials.[3] These mixing processes can disrupt the formation of the low-density hot spot, lowering its temperature and reducing its volume. The resulting lower nuclear production can fail to ignite the capsule. Understanding the extent of mix under different conditions is a crucial step toward mitigating its adverse effects.

A substantial and sustained effort to understand hydrodynamic instabilities and mix has been ongoing for many decades, due in large part to their heavy impact on ICF. Reviews of the literature on experimental, computational, and theoretical work on hydrodynamic instabilities and mix can be found on, for example, the first page of Refs. 4 and 5. Related work on mix in ICF implosions includes papers by Li,[6] Radha,[7] Regan,[8] and Wilson,[9] as well as many others.

This article reviews and extends aspects of the work published by Li *et al.*[6] over a wider range of capsule parameters. In addition, we calculate a quantitative upper limit on the null result published by Petrasso *et al.*[10] of the amount of mix at the time of shock collapse, which occurs before the onset of the deceleration phase. Results from time-dependent nuclear production history measurements of the mix region will be published elsewhere.[11] A brief review of the causes and effects of mix can be found in the next section. The remaining sections (1) describe the experimental setup, (2) present experimental observations, (3) describe the constraint on the amount of fuel–shell mix between shock collapse and deceleration-phase onset, and (4) summarize our results.

Causes and Effects of Mix

When a fluid of density ρ_1 accelerates a heavier fluid of density ρ_2, the fluid interface is RT unstable. The rapid growth of initial perturbations sends spikes of the heavy fluid into the light fluid, while bubbles of the light fluid penetrate into the heavy fluid. The exponential growth eventually saturates into a nonlinear regime where the spike and bubble amplitudes grow quadratically in time. As the spikes and bubbles continue to interpenetrate, velocity shear between the two fluids results in further instability (the drag-driven Kelvin–Helmholtz instability), causing the spike tips to "mushroom" and roll up on increasingly finer scales, increasing the vorticity of the flow and eventually leading to mixing of the two fluids on the atomic scale.

In ICF, both the acceleration and deceleration phases have RT-unstable surfaces.[2] The low-density ablating mass pushes against the high-density "payload" during the acceleration phase, and after further convergence and compression, the high-density shell is stopped by the low-density hot spot during the deceleration phase. Initial perturbations are seeded by laser and target surface nonuniformities, and growth of these perturbations during the acceleration phase can feed through to the inner surface and contribute to seeding perturbations for the deceleration phase.[2]

Unmitigated RT growth during the acceleration phase can eventually break through the shell, compromising its compressibility and reducing the attainable areal density of the assembled target at stagnation. RT growth during the deceleration phase can send spikes of cold, dense fuel into the central hot spot, potentially disrupting its formation. Even if the spikes do not reach the center, their penetration and the resultant mixing of the cold, dense shell with the low-density hot spot will cool the outer regions of the hot spot, reducing the volume participating in nuclear production.

Experimental Setup

Direct-drive implosions were conducted on OMEGA,[12] with 60 beams of frequency-tripled (351 nm) UV light in a 1-ns square pulse and a total energy of 23 kJ. One-THz-bandwidth smoothing by spectral dispersion and polarization smoothing of the laser beam were used.[13] The beam-to-beam energy imbalance was typically between 2% and 4% rms. The spherical capsules had diameters between 860 and 940 μm, plastic-shell thicknesses of 20, 24, or 27 μm, and a surface coating of 0.1 μm of aluminum.

Three target configurations were used (Fig. 109.14): The reference "CH" capsules had shells made of plastic (CH) and a gaseous fill of D_2 and ^{3}He. "CD" capsules had gaseous fills of pure ^{3}He, and a shell made mostly of CH, except for a 1-μm layer of deuterated plastic (CD) on the inner surface. "CD offset" capsules are like the CD capsules, except that the 1-μm CD layer is offset from the inner surface by 1 μm of CH. The composition of the ordinary plastic consists of an H to C ratio of 1.38, and the deuterated plastic has a D to C ratio of 1.56 (Ref. 6).
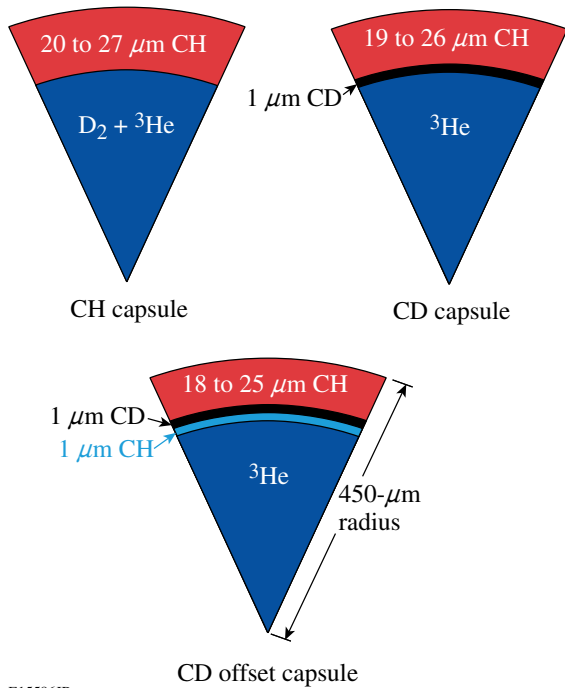
Figure 109.14

0.5 or 2.5 mg/cm^3 of pure ^{3}He gas fills a 20- to 27-μm-thick plastic shell with a 1-μm deuterated layer either adjacent to the inner surface (CD capsule) or offset from the inner surface by 1 μm (CD offset capsule). The reference (CH capsule) contains D^{3}He gas and has no deuterated layer. Whereas CH capsules will produce D^{3}He protons whenever the fuel gets sufficiently hot, CD capsules will produce only D^{3}He protons if the fuel and shell become atomically mixed.

The pure ^{3}He gases were filled to initial pressures of 4 and 20 atm at a temperature of 293 K, corresponding to initial mass densities (ρ_0) of 0.5 and 2.5 mg/cm^3. The D_2–^{3}He gas is an equimolar mixture of D to ^{3}He by atom and is filled to a hydrodynamically equivalent initial pressure as the pure-^{3}He fill, as described in Ref. 14. Because fully ionized D and ^{3}He have the same value of $(1 + Z)/A$, mixtures with the same mass density will also have the same total particle density and equation of state and can be considered hydrodynamically equivalent. For

the 4- and 20-atm ^{3}He fills, the hydrodynamically equivalent D_2–^{3}He pressures are 3.6 and 18 atm, respectively.

Hydrodynamic simulations of capsule implosions using the 1-D code *LILAC*[15] showed only minor differences in the timing and profiles between the equivalent CH and CD implosions. The convergence ratio C_r, defined as the initial inner capsule radius over the fuel–shell interface radius at the time of stagnation, for capsules with different shell thicknesses and initial fill density is shown in Table 109.I.

Table 109.I: Predicted convergence ratio C_r calculated by *LILAC* for different capsule parameters. Capsules with higher convergence ratios are expected to be more susceptible to mix. The convergence ratio does not differ significantly between CH and CD capsules.

ρ_0 (mg/cm^3)	Thickness (μm)	C_r (1-D)
0.5	20	38.0
0.5	24	35.2
0.5	27	31.5
2.5	20	14.9
2.5	24	14.5
2.5	27	13.8

The following primary nuclear reactions can occur in targets containing both D_2 and ^{3}He:

$$D + D \rightarrow {}^3He + n(2.45 \text{ MeV}),$$
$$D + D \rightarrow T + p(3.0 \text{ MeV}), \qquad (1)$$
$$D + {}^3He \rightarrow {}^4He + p(14.7 \text{ MeV}),$$
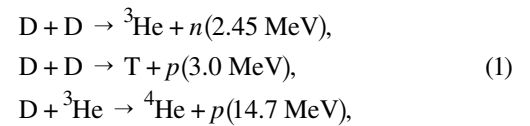
where the number in parentheses is the mean birth energy of the second product.

The set of capsules shown in Fig. 109.14 is ideal for studying the nature and extent of turbulent mix in ICF implosions. Whereas implosions of CH capsules will produce D^{3}He protons whenever the fuel gas gets sufficiently hot, heating alone is not sufficient for D^{3}He production in CD and CD offset capsules. To produce measurable D^{3}He yields, these capsules require in addition the mixing of the fuel and shell on an atomic scale. Measurement or absence of the D^{3}He yield in implosions of CD offset capsules can be used to ascertain the extent into the shell that turbulent mixing processes reach.

Fuel–shell mix is not a requirement to produce DD-*n* yields in CD and CD offset implosions, but measurement of the DD-*n* yield provides a useful way to determine if the CD layer was heated to temperatures near 1 keV.

The primary diagnostics for this study were wedged-range-filter (WRF) spectrometers,[16] to measure the D^{3}He proton yield and spectrum, and neutron time-of-flight (nTOF) scintillator detectors,[17] to measure the DD-n yield. On a given shot, up to six WRF spectrometers were used simultaneously to improve the estimate of the D^{3}He yield.[16] The D^{3}He proton spectrum measured from implosions of D^{3}He-filled CH capsules often shows two distinct components, corresponding to D^{3}He proton emission shortly after the collapse of the converging shock and to emission during the deceleration phase, about 300 ps later.[10,18]

Experimental Results

1. Yield Measurements

Turbulent mixing of the fuel and shell is demonstrated by measurements of finite D^{3}He yields (Y_p) in ^{3}He-filled, CD capsules (see Fig. 109.15 and Ref. 6). The shock component, apparent in the spectrum of the CH capsule implosion above 14 MeV, is absent in the CD capsule. All D^{3}He yields reported in this section for CH

capsules will include only the compression component; the shock component will be considered in the following section.

The D^{3}He yields from CD capsules are at least two orders of magnitude higher than would be expected by the interaction of thermal ^{3}He ions penetrating through the CD layer surface,[6] even with enhanced surface area resulting from a RT-perturbed surface. The D^{3}He yields are at least three orders of magnitude higher than the maximum that would be expected if some ^{3}He had diffused into the CD layer between the times of fabrication and implosion.[6] For yields as high as have been observed, there must be a region that has been heated to at least 1 keV and where the fuel and shell have experienced atomic mix.

Significant D^{3}He yield from CD-offset implosions demonstrates that there is substantial mixing of the fuel with the "second" 1-μm layer of the shell (Fig. 109.16). Thermal ^{3}He ions cannot penetrate through the first micron of the shell to produce

Figure 109.15
D^{3}He proton spectra from a CH capsule (shot 37642) and from a CD capsule (shot 32828) with 2.5-mg/cm^3 initial fill density. The high D^{3}He yield from CD implosions demonstrates the existence of fuel–shell mix. The CD implosion yield, although substantially less than the yield from the CH implosion, is much higher than what would be expected in the absence of turbulent fuel–shell mix.
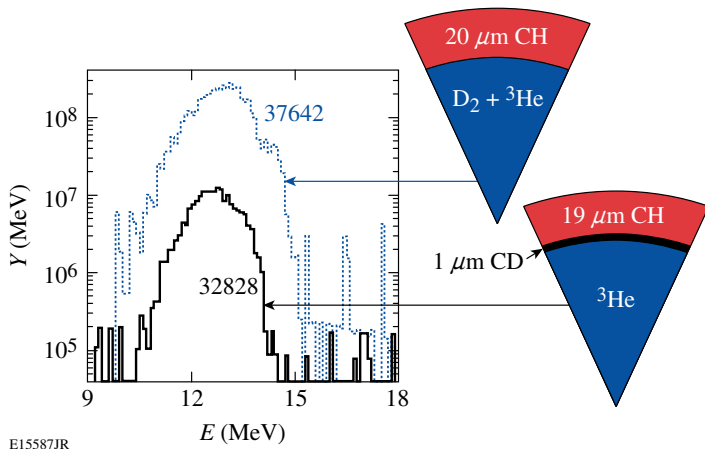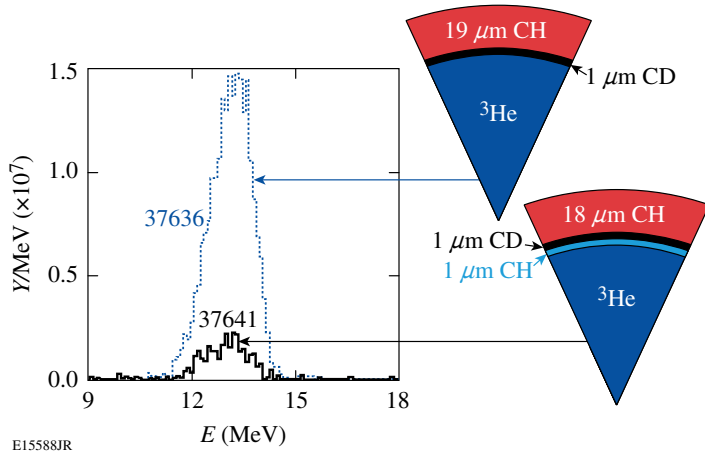

Figure 109.16
D^{3}He proton spectra from a CD capsule (shot 37636) and from a CD offset capsule (shot 37641) with 0.5-mg/cm^3 initial fill density. The D^{3}He yield drops by only a factor of 5 to 10 when the CD layer is offset from the inner surface by 1 μm, demonstrating that a substantial amount of the second micron of the shell is mixed with the fuel.

these yields, so the second micron must be exposed to the fuel by bubble growth and then mixed through turbulent processes.

The decreasing yields for increasing ρ_0 in CD capsules contrast strongly with the increasing yields for increasing initial ρ_0 in the reference CH capsules (see Fig. 109.17). This is evidence that the extent of mix is reduced for increasing initial fill density, since Y_p in CD implosions is lower, even though the core conditions are more favorable for nuclear production, as seen by the higher value of Y_p for CH implosions. Y_p in CD-offset implosions decreases by an additional factor of 5 and 10 compared to inner CD capsule implosions for 0.5 and 2.5 mg/cm^3 fills, respectively.

The lower DD-n yield (Y_n) for CD implosions with higher ρ_0 indicates that less heating of the CD layer occurred in these implosions. Additional heating of the inner surface of the shell can occur through thermal conduction from and turbulent mix with the hot fuel. The lower Y_n supports the picture of reduced mix for higher-density fills.

Yields in both CH and CD implosions decrease with increasing shell thickness (Fig. 109.18). Thicker shells decrease Y_p by a larger factor in CD capsules compared to CH capsules, which suggests that the effects of mix are diminished. However, Y_n decreases by a smaller factor in CD capsules, which may be due to temperature effects dominating mix effects for the neutron yield in such implosions.

2. Areal Density Measurements

Evidence for a delay in nuclear production can be found through measurement of the compression of the target at bang time by

E15589JR
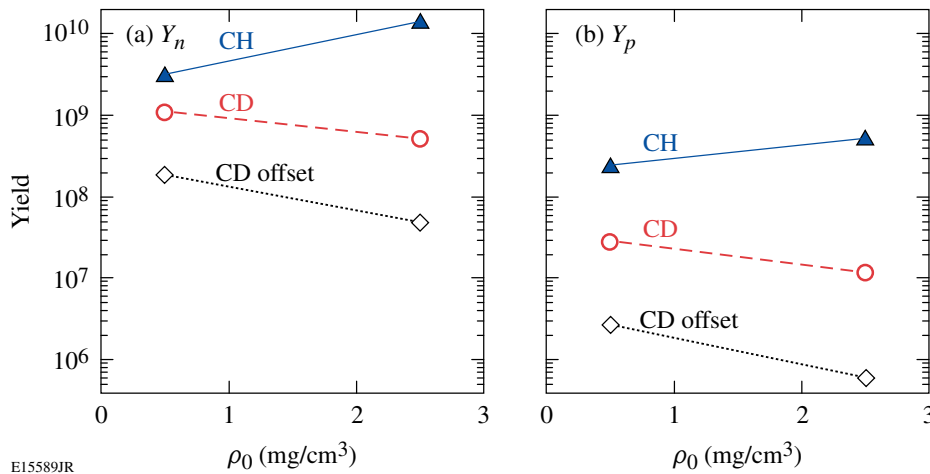
Figure 109.17
(a) DD-n and (b) D^{3}He yields from CH (solid triangles), CD (open circles), and CD-offset (open diamonds) implosions as a function of initial fill density for 20-μm-thick shells. Yields from CD and CD-off-set implosions decrease with increasing fill density, in contrast to the increasing yields from CH implosions. Points show the mean of each shot ensemble, where the standard error in the mean is smaller than the size of the markers.

E15590JR
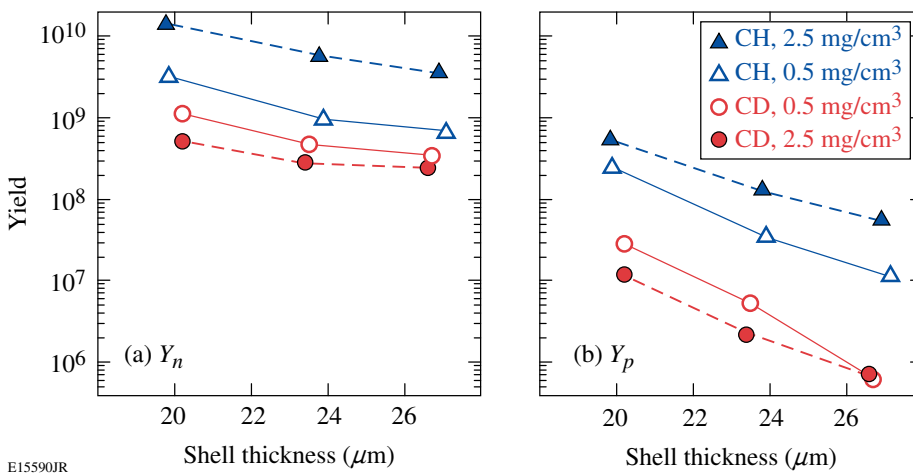
Figure 109.18
(a) DD-n and (b) D^{3}He yield in CH (triangles) and CD (circles) capsules with low (open markers) and high (solid markers) ρ_0 as a function of shell thickness. Capsules with lower ρ_0 are more susceptible to mix for all shell thicknesses.

means of the areal density ρR. Areal density is inferred from the mean downshift of the D³He proton spectrum from the birth energy of 14.7 MeV, so the inferred ρR is an average measurement of ρR over the time of nuclear production. Because the capsule continues to compress, and ρR to increase, throughout the deceleration phase, one would expect that if bang time occurs during a later stage of the deceleration phase for an otherwise equivalent implosion, then the average ρR would be higher.[11,18] As seen in Fig. 109.19, the inferred burn-averaged ρR is higher for implosions of CD capsules than for CH capsules. This is qualitatively consistent with the later bang times measured for CD capsules.

The experimental results of these experiments are summarized in Table 109.II. The mean and standard error are shown of
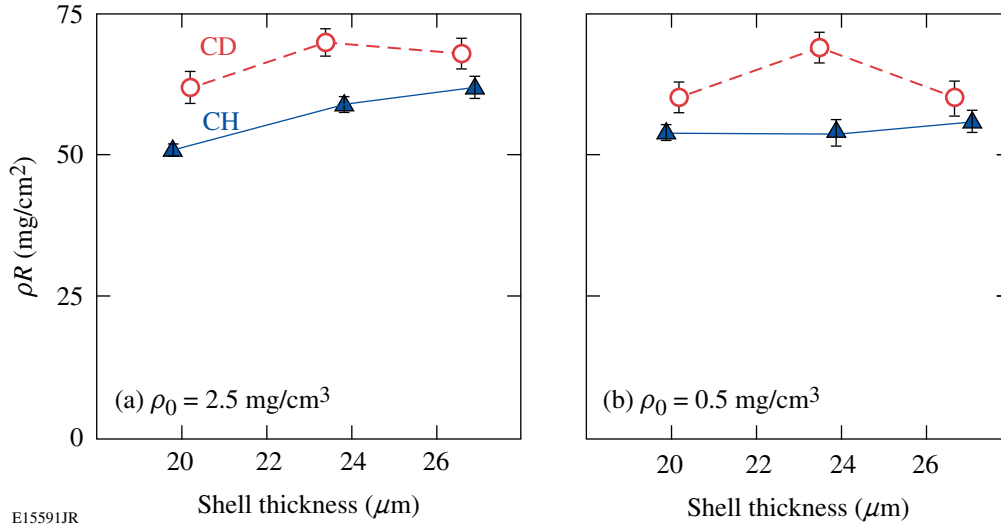
Figure 109.19
Mean and standard error of ρR's for CH (solid markers) and CD (open markers) implosions as a function of shell thickness with (a) high- and (b) low-density fills. The D³He burn-averaged ρR is consistently higher for CD capsules.

E15591JR

Table 109.II: Experimental yield and areal density results of CH, CD, and CD-offset capsule implosions. The values shown are the mean and standard error of all shots in a particular ensemble, with the yield errors expressed as a percent of the mean. The quoted D³He yield and areal density for CH capsules include the compression component only.

| Type	ρ_0 (mg/cm³)	Thickness (μm)	Number of shots	Y_n ($\times 10^8$)	Error (%)	Y_p ($\times 10^7$)	Error (%)	ρR (mg/cm²)	Error
CH	0.5	19.9	17	31.3	6	24.3	11	54	1.5
CH	0.5	23.9	9	9.6	6	3.5	12	54	2.3
CH	0.5	27.1	8	6.7	7	1.13	30	56	2.0
CH	2.5	19.8	61	142	4	54.4	5	51	1.0
CH	2.5	23.8	26	58	5	13.2	8	59	1.3
CH	2.5	26.9	16	35	5	5.6	8	62	2.0
CD	0.5	20.2	7	10.8	10	2.9	10	60	2.4
CD	0.5	23.5	5	4.7	7	0.54	9	69	2.6
CD	0.5	26.7	2	3.4	7	0.06	7	60	3.1
CD	2.5	20.2	11	5.2	8	1.25	13	62	2.8
CD	2.5	23.4	7	2.7	15	0.22	19	70	2.4
CD	2.5	26.6	4	2.4	5	0.07	4	68	2.7
CD-off	0.5	19.2	3	1.9	17	0.28	28	52	1.7
CD-off	0.5	23.7	2	1.2	14	–	–	–	–
CD-off	2.5	18.4	5	0.5	24	0.06	14	55	3.0
CD-off	2.5	22.8	3	1.2	49	–	–	–	–

the DD-n and D^{3}He yields (Y_n and Y_p) and the areal density ρR inferred from the mean downshift of 14.7-MeV D^{3}He protons for CH, CD, and CD-offset capsules. Also shown is the number of shots of each kind. The mean is the average of measured values within a given shot ensemble, and the standard error is the standard deviation of the measurements divided by the square root of the number of shots.

Constraint on the Possibility of Mix During the Coasting Phase

Comparative analysis of D^{3}He-p spectra from CH and CD implosions can be used to place an upper bound on the possible amount of mix at shock time. For the representative spectrum of a CH capsule shown in Fig. 109.20, the total yield in the region from 14.2 to 14.7 MeV, corresponding to the shock component, is $1.7 \pm 0.2 \times 10^7$, or $3.7 \pm 0.3\%$ of the total yield. The yield in the same region of the representative spectrum from a CD capsule comes to $2.6 \pm 2.5 \times 10^4$, equal to $0.14 \pm 0.13\%$ of the total yield, and is consistent with zero.

Figure 109.20
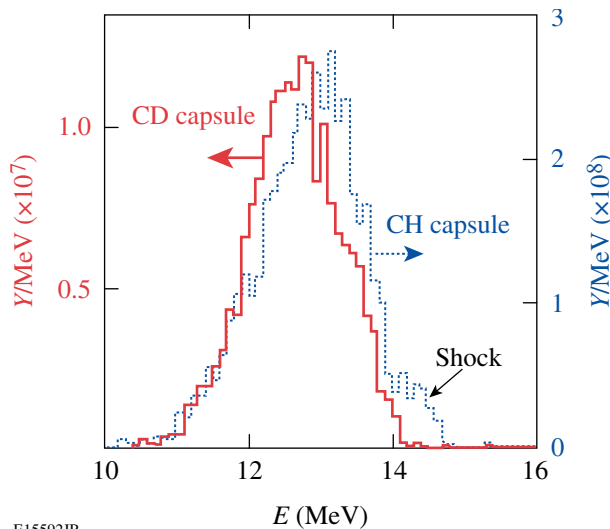D^{3}He proton spectra from implosions of 20-μm-thick shells filled with 2.5 mg/cm^3 of fuel with CH (shot 37642, dotted) and CD (shot 32828, solid) shell configurations. The shock component of the CH implosions comes to 3.7% of the total yield, whereas the shock component contribution to the CD implosion spectrum is consistent with zero.

The "shock yield" of the CD implosion ($\leq 2.6 \times 10^4$) comes to, at most, 0.15% of the shock yield of the corresponding CH implosion (1.7×10^7). This yield ratio can be used to constrain the deuterium fraction by atom $f_D \leq 0.05\%$ in the fuel of the CD implosion during shock burn, by application of Eq. (5) in Ref. 14. Equation (5) assumes that f_D is uniform through the

fuel region, so it does not preclude the more likely physical situation of deuterium concentrations higher than the above constraint in the outer, cooler region of the fuel.

Summary

The extent of fuel–shell mix has been shown to include a substantial amount of the shell from the inner first and second micron of the original material using ^{3}He-filled, CD-shell target implosions. The observed yields are higher than is consistent with diffusive mixing, so they must be the result of turbulent mixing down to the atomic scale.

The improved stability of capsules with higher initial fuel density and thicker initial shells has been confirmed by comparing the yield trends of CH, CD, and CD-offset capsules. Increasing the capsule fill density decreased the D^{3}He and DD-n yields for CD capsules and increased the yields for CH capsules, thereby demonstrating that the extent of mix is reduced for increasing initial fill density.

The D^{3}He shock yield in CD capsules with high initial fill density was constrained to be less than 0.14% of the total D^{3}He yield, and the average atomic fraction of deuterium in the fuel during the shock burn has been constrained to be less than 0.05% and is consistent with zero.

REFERENCES

1. J. Nuckolls *et al.*, Nature **239**, 139 (1972).

2. S. Atzeni and J. Meyer-ter-Vehn, *The Physics of Inertial Fusion: Beam Plasma Interaction, Hydrodynamics, Hot Dense Matter, International Series of Monographs on Physics* (Clarendon Press, Oxford, 2004).

3. P. E. Dimotakis, Annu. Rev. Fluid Mech. **37**, 329 (2005).

4. G. Dimonte, Phys. Plasmas **6**, 2009 (1999).

5. A. J. Scannapieco and B. Cheng, Phys. Lett. A **299**, 49 (2002).

6. C. K. Li, F. H. Séguin, J. A. Frenje, S. Kurebayashi, R. D. Petrasso, D. D. Meyerhofer, J. M. Soures, J. A. Delettrez, V. Yu. Glebov, P. B. Radha, F. J. Marshall, S. P. Regan, S. Roberts, T. C. Sangster, and C. Stoeckl, Phys. Rev. Lett. **89**, 165002 (2002).

7. P. B. Radha, J. Delettrez, R. Epstein, V. Yu. Glebov, R. Keck, R. L. McCrory, P. McKenty, D. D. Meyerhofer, F. Marshall, S. P. Regan, S. Roberts, T. C. Sangster, W. Seka, S. Skupsky, V. Smalyuk, C. Sorce, C. Stoeckl, J. Soures, R. P. J. Town, B. Yaakobi, J. Frenje, C. K. Li, R. Petrasso, F. Séguin, K. Fletcher, S. Padalino, C. Freeman, N. Izumi, R. Lerche, and T. W. Phillips, Phys. Plasmas **9**, 2208 (2002).

8. S. P. Regan, J. A. Delettrez, F. J. Marshall, J. M. Soures, V. A. Smalyuk, B. Yaakobi, V. Yu. Glebov, P. A. Jaanimagi, D. D. Meyerhofer, P. B. Radha, W. Seka, S. Skupsky, C. Stoeckl, R. P. J. Town, D. A. Haynes, Jr., I. E. Golovkin, C. F. Hooper, Jr., J. A. Frenje, C. K. Li, R. D. Petrasso, and F. H. Séguin, Phys. Rev. Lett. **89**, 085003 (2002).

9. D. C. Wilson, C. W. Cranfill, C. Christensen, R. A. Forster, R. R. Peterson, H. M. Hoffman, G. D. Pollak, C. K. Li, F. H. Séguin, J. A. Frenje, R. D. Petrasso, P. W. McKenty, F. J. Marshall, V. Yu. Glebov, C. Stoeckl, G. J. Schmid, N. Izumi, and P. Amendt, Phys. Plasmas **11**, 2723 (2004).

10. R. D. Petrasso, J. A. Frenje, C. K. Li, F. H. Séguin, J. R. Rygg, B. E. Schwartz, S. Kurebayashi, P. B. Radha, C. Stoeckl, J. M. Soures, J. Delettrez, V. Yu. Glebov, D. D. Meyerhofer, and T. C. Sangster, Phys. Rev. Lett. **90**, 095002 (2003).

11. J. R. Rygg, J. A. Frenje, C. K. Li, F. H. Séguin, R. D. Petrasso, V. Yu. Glebov, D. D. Meyerhofer, T. C. Sangster, and C. Stoeckl, "Time-Dependent Nuclear-Measurements of Fuel–Shell Mix in Inertial Confinement Fusion," submitted to Physical Review Letters.

12. T. R. Boehly, D. L. Brown, R. S. Craxton, R. L. Keck, J. P. Knauer, J. H. Kelly, T. J. Kessler, S. A. Kumpan, S. J. Loucks, S. A. Letzring, F. J. Marshall, R. L. McCrory, S. F. B. Morse, W. Seka, J. M. Soures, and C. P. Verdon, Opt. Commun. **133**, 495 (1997).

13. S. Skupsky and R. S. Craxton, Phys. Plasmas **6**, 2157 (1999).

14. J. R. Rygg, J. A. Frenje, C. K. Li, F. H. Séguin, R. D. Petrasso, J. A. Delettrez, V. Yu. Glebov, V. N. Goncharov, D. D. Meyerhofer, S. P. Regan, T. C. Sangster, and C. Stoeckl, Phys. Plasmas **13**, 052702 (2006).

15. J. Delettrez, R. Epstein, M. C. Richardson, P. A. Jaanimagi, and B. L. Henke, Phys. Rev. A **36**, 3926 (1987).

16. F. H. Séguin, J. A. Frenje, C. K. Li, D. G. Hicks, S. Kurebayashi, J. R. Rygg, B.-E. Schwartz, R. D. Petrasso, S. Roberts, J. M. Soures, D. D. Meyerhofer, T. C. Sangster, J. P. Knauer, C. Sorce, V. Yu. Glebov, C. Stoeckl, T. W. Phillips, R. J. Leeper, K. Fletcher, and S. Padalino, Rev. Sci. Instrum. **74**, 975 (2003).

17. R. A. Lerche and T. J. Murphy, Rev. Sci. Instrum. **63**, 4880 (1992).

18. J. A. Frenje, C. K. Li, F. H. Séguin, J. Deciantis, S. Kurebayashi, J. R. Rygg, R. D. Petrasso, J. Delettrez, V. Yu. Glebov, C. Stoeckl, F. J. Marshall, D. D. Meyerhofer, T. C. Sangster, V. A. Smalyuk, and J. M. Soures, Phys. Plasmas **11**, 2798 (2004).

Measured Magnetic-Field Evolution and Instabilities in Laser-Produced Plasmas

The stability of plasmas with magnetic (B) fields is a critical issue for basic and applied plasma physics; instabilities may lead to important (and sometimes catastrophic) changes in plasma dynamics.[1] Intensive studies of various instabilities have been conducted for a wide range of plasmas and fields, particularly in the areas of magnetic-confinement plasmas[2] and space physics.[3] In laser-produced, high-energy-density (HED) laboratory plasmas, however, experimental studies of B-field–related instabilities have been rare because of limitations in experimental methods. In particular, resistive instabilities, a large category of macroscopic instabilities, have not been observed previously in this regime, partly because they are not important in the hot, low-resistivity plasmas usually studied.[4]

In the experiments described here, monoenergetic proton radiography was used for the first time to study the time evolution of the B-field structure that is generated by the interaction of a long-pulse, low-intensity laser beam with plasma. This work focuses on the qualitative and quantitative study of the physics involved in field evolution and instabilities over a time interval much longer than the laser pulse length, and B fields generated by laser–plasma interactions experience a tremendous dynamic range of plasma conditions. While the laser is on, we study field generation (via $\nabla n_e \times \nabla T_e$),[4–6] growth, and the balance between energy input and losses. After the laser turns off, laser absorption at the critical surface ends and the plasma cools down. Fields start to decay and dissipate, and field diffusion [$\nabla \times (D_m \nabla \times \mathbf{B})$, where D_m is the magnetic diffusion coefficient[4–6]] becomes increasingly important relative to convection [$\nabla \times (\mathbf{v} \times \mathbf{B})$, where $\mathbf{v}$ is the plasma fluid velocity[4–6]] as the cooling plasma becomes more resistive. At these later times, physical processes associated with resistivity tend to dominate over fluid effects, particularly around the bubble edge where the plasma β values, a ratio of thermal to field energies, are smaller than one.

The approach described here allows us to make a direct comparison of proton images recorded at different times, to measure field evolution, to address different physics processes in different regimes, and, most importantly, to identify resistiv-ity-induced instabilities. Most previous work in this field has involved high-intensity, short-pulse lasers[7] or long-pulse lasers with limited diagnostic measurements.[8] Preliminary measurements we made while a laser beam was on have recently been published,[9] but the work described here uniquely covers times extending well past the end of the laser pulse and reveals important new phenomena that were not previously seen and are not predicted by two-dimensional (2-D) simulation codes. The first observation of repeatable, asymmetric structure around the plasma bubbles at late times provides important insights into pressure-driven magnetohydrodynamic (MHD) instabilities in resistive plasmas,[2] while the first observation of nonrepeatable chaotic structure within the plasma bubble provides likely evidence of the electron thermal instability.[10] Simulations[11] of these experiments with the 2-D hydrodynamic code *LASNEX*[12,13] and hybrid PIC code *LSP*[14] have been performed; they are qualitatively useful for interpreting the observations but diverge from our measurements (particularly after the laser beam is off).

The setup of the experiments performed on OMEGA[15] is illustrated schematically in Fig. 109.21. B fields were generated through laser–plasma interactions on a plastic (CH) foil by a single laser beam (henceforth called the *interaction beam*) with a wavelength of 0.351 μm, incident 23° from the normal
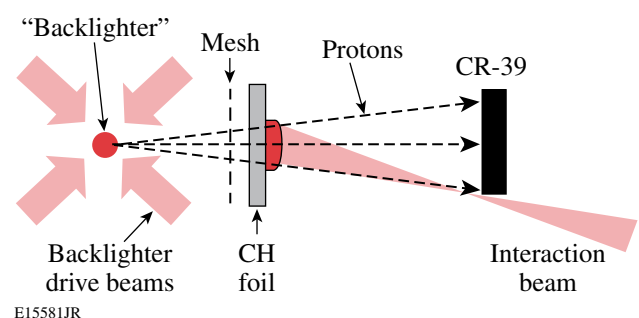
E15581JR

Figure 109.21

Schematic illustration of the experimental setup for face-on proton radiography. Distances from the backlighter are 1.3 cm for the mesh, 1.5 cm for the CH foil (5 μm thick), and 30 cm for the CR-39 detector.

direction. The laser had a 1-ns-long square pulse, an energy of ~500 J, and a spot diameter of 800 μm determined by phase plate SG4 (defined as 95% energy deposition),[16] resulting in a laser intensity of the order of 10^{14} W/cm^2.

The fields were studied with monoenergetic proton radiography, using a backlighter that produced protons at the two discrete energies of 14.7 MeV and 3 MeV (fusion products of the nuclear reactions D + ^{3}He → α + p and D + D → T + p, respectively, generated from D^{3}He-filled, exploding-pusher implosions driven by 20 OMEGA laser beams).[9,17] The duration of the backlighter was ~150 ps, and the timing of the interaction laser was adjusted in different experiments so the arrival of the backlighter protons at the foil would occur with different delays after the laser interaction beam was turned on. Separate radiographs made with the two proton energies were recorded simultaneously using stacked CR-39 detectors arranged with filters so that only one detector was sensitive to each energy.[18] A nickel mesh (60 μm thick with a 150-μm hole-to-hole spacing) was used to divide the backlighter protons into discrete beamlets, and, for the 14.7-MeV protons, the deflections of these beamlets due to fields in laser-induced plasmas on CH foils were measured in the images.

Images made with these monoenergetic-proton backlighters have distinct advantages over images made with broadband sources: measured image dimensions and proton beamlets deflections provide unambiguous quantitative information about fields; detectors can be optimized; and the backlighter is isotropic (simultaneous measurements can be made in multiple directions[17] and the source can be monitored at any angle).

Face-on images made with D^{3}He protons are shown in Fig. 109.22(a). The laser timing was adjusted so that these 14.7-MeV protons arrived at the foil at various times between 0.3 ns and 3 ns after the laser interaction beam was turned on. Since the interaction-beam pulse was 1 ns square with ~0.1-ns rise and decay times, the data covered two time intervals: 0.3 to 0.9 ns when the laser was on, and 1.2 to 3 ns when the laser was off. Each image shows how the proton beamlets are deflected while passing through the magnetic field that formed around the plasma bubble generated by the interaction beam, as described previously.[9,11,17]

While the interaction beam is on, each image has a sharp circular ring where beamlets pile up after passing through the edges of the plasma bubble where the maximum B fields were generated. The deflection of each beamlet is proportional to the integral $\left| \int \mathbf{B} \times d\ell \right|$ (where $d\ell$ is the differential pathlength along the proton trajectory), and this integral is highest at the edge of the bubble. Beamlets in the center of each image undergo less radial deflection, indicating that the integral $\left| \int \mathbf{B} \times d\ell \right|$ is much smaller there. These features are well reproduced by *LASNEX + LSP* simulations, as shown in Fig. 109.22(b) (0.3 to 0.9 ns). Figure 109.23(a) shows the
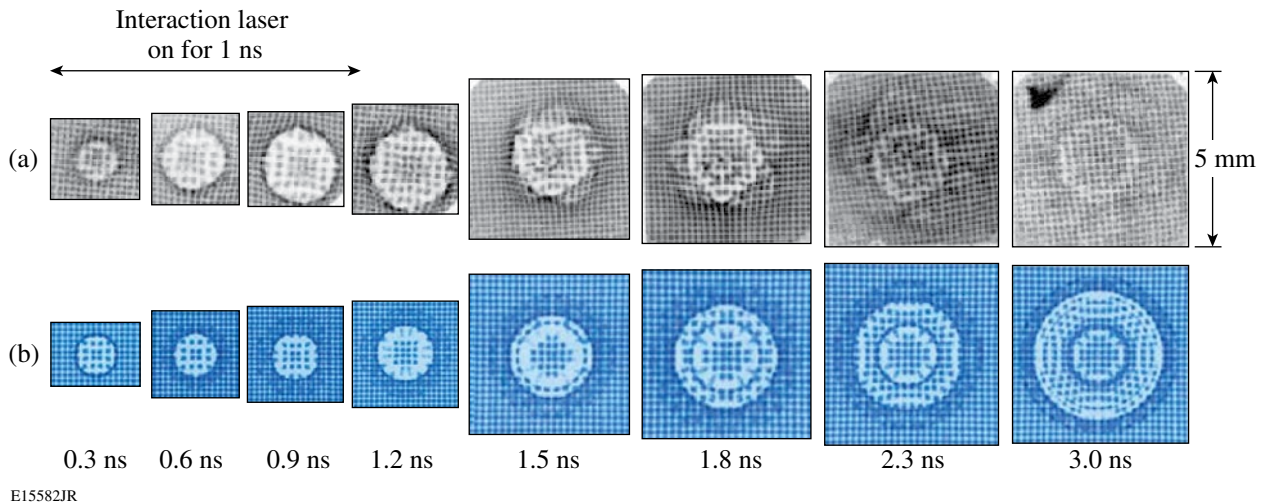
Figure 109.22

(a) Measured face-on D^{3}He proton images showing the spatial structure and temporal evolution of the B fields generated by laser–plasma interactions. Each image is labeled by the time interval between the arrival of the interaction beam at the foil and the arrival of the imaging protons. The images illustrate the transition from 2-D symmetric expansion of magnetic fields, during a 1-ns laser illumination, to a more-asymmetric 3-D expansion after the laser turned off and the plasma cooled and became more resistive; this asymmetry is conjectured to be driven by a resistive MHD interchange instability. (b) Images simulated by *LASNEX + LSP* for the conditions that produced the experimental images shown in (a).

magnetic field predicted in these simulations in a plane perpendicular to the foil at 0.6 ns. The protons would travel from right to left in the plane of this field map, and the maximum line integrals would be at the edges.

At times after the laser beam is off, the simulations do not track the data as well. As shown in Fig. 109.22(b) (1.5 to 3 ns), simulations predict that the proton images have a double ring structure. The outer ring comes from the outer edge of the plasma bubble where large ∇T_e occurred; the inner ring comes from the toroidal magnetic field at the edge of the hole burned into the plastic by the interaction laser, as seen in Fig. 109.23(b) for 1.5 ns. Figure 109.23(b) shows that the simulations also predict a second plasma bubble with a surface B field on the rear face of the foil after the laser has completely burned through; the direction of this field is reversed relative to the field on the front of the foil, but the simulated images show no major feature associated with this field because it is relatively weak.

At 2.3 ns in Fig. 109.22, the data and simulation are generally similar to each other. They each have an inner ring that corresponds to the burnthrough field, as described above, though it is a little smaller in the simulation than in the data. They each show a boundary farther out that corresponds to the outer surface of the bubble, but in the data it is strikingly asymmetric while in the simulation it is round because the code is limited to a 2-D structure.

We believe this is the first direct observation of the pressure-driven, resistive MHD interchange instability in laser-produced HED plasmas at the interface between the bubble and field.

This instability, which involves the interchange of field between the inside and outside of the bubble surface, occurs when the plasma is resistive and there is unfavorable field curvature ($\mathbf{\kappa} \cdot \nabla p > 0$, where $\mathbf{\kappa} = \mathbf{B} \cdot \nabla \mathbf{B}/B^2$ is the field-line curvature and ∇p is the pressure gradient).[2] It makes sense that the instability occurs only after the laser is off, when the cooling plasma becomes more resistive.

There are strong similarities in the angular structure of this region from one image to the next (five to ten cycles over the 360° around the bubble), in spite of the fact that the images are from different shots. It seems that once the power input from the laser disappears, the plasma bubble quickly becomes asymmetric, but something systematic must be seeding the asymmetry. The physics behind this process is conjectured to be highly localized resonance absorption of linearly polarized laser light caused by obliquely incident light (23° from the normal) in an inhomogeneous ($\nabla n_e \neq 0$) plasma.[19] This phenomenon merits future experimental and theoretical investigation.

Another type of instability is apparent during the interval from 1.5 to 2.3 ns, where the distributions of beamlets near the image centers have some chaotic structure. The structures are quite different in each of the three images in this time interval, and since these images are from different shots, it would appear that the structure is random. We note that our earlier work[9] showed that a similar chaotic structure would occur if the laser was on and if no laser phase plates were used; phase plates either prevented the chaotic structure from forming as long as the laser was on or reduced its amplitude sufficiently that it was not visible until it had a chance to grow over a longer time
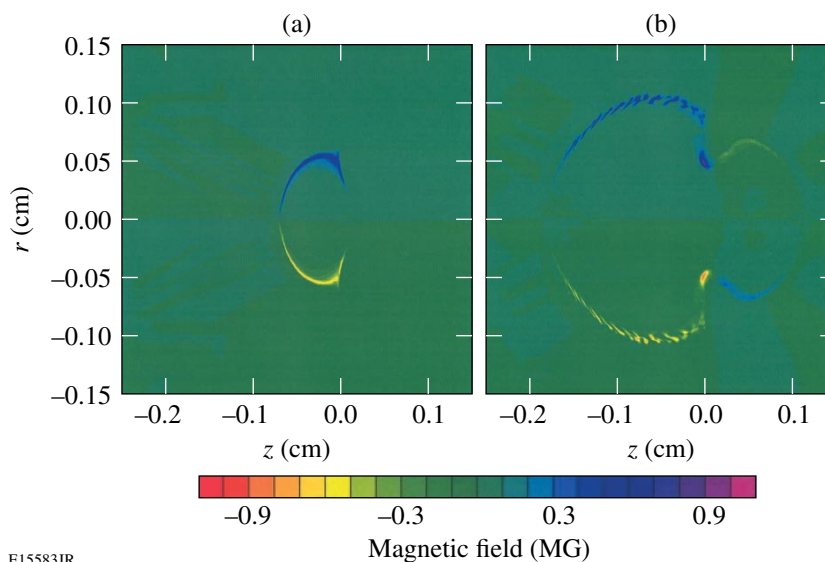
Figure 109.23
Time evolution of *LASNEX*-simulated *B*-field strength on a cross section of the plasma bubble in a plane perpendicular to the foil at (a) ~0.6 ns, when the laser was on, and (b) ~1.5 ns, when the laser was off. In each case, the horizontal coordinate z is the distance from the foil (assuming the laser is incident from the left), and the vertical coordinate r is the distance from the central axis of the plasma bubble. When the laser is on, strong fields occur near the edge of the plasma bubble. After the laser pulse, strong fields also appear near the edge of the hole burned into the foil by the laser and weaker fields (with the opposite direction) appear on the backside of the foil.

E15583JR

period (possibly due to the electron thermal instability when the plasma cools and becomes more resistive, driven by heat flow and leading to a random filamentary structure of n_e and T_e, as well as B fields[10]). The phase plates presumably result in a more-uniform temperature profile and a reduced medium-scale random structure associated with localized regions of strong $\nabla n_e \times \nabla T_e$ (Refs. 9 and 16).

Similar features are seen as late as our last image at 3 ns, although by this time the field strengths have diminished so that the amplitudes of all beamlet displacements are small. Although both simulation and experiment show a continued expansion of the plasma bubble at late times, leading to convective losses, the beamlet displacements in the data are much smaller than those in the simulation, indicating that fields have dissipated much more quickly than predicted. However, since the data reveal a 3-D structure after the laser is off, we have to realize that 2-D computer codes simply cannot model this time interval (although they are still useful for aiding qualitative interpretation of the images, particularly the role of the burnthrough hole in producing a static pattern in the images). Experimental measurements such as those shown here are therefore doubly important since they directly reveal previously unpredicted physical phenomena and also provide invaluable information for benchmarking true 3-D code development in the future.

Quantitative conclusions can be drawn from the images by measuring the sizes of features in the images and the displacements ξ of individual beamlet positions in the images. The displacements ξ of individual beamlet positions in the images result from the Lorenz force $\left| \int \mathbf{B} \times d\ell \right|$ and represent not lateral displacements at the foils but angular deflections from interactions with fields near the foil leading to lateral displacement at the detector. The actual bubble size is thus not determined directly by the apparent size in the image because the image of the bubble is magnified by radial beamlet displacements. The position of the actual bubble edge is inferred by determining the locations that the beamlets in the pileup region would have had in the image without displacement. The result of this analysis is shown in Fig. 109.24(a), where the radius at late times (when the bubble is asymmetric) represents an angular average. We see that the bubble radius grows linearly while the laser is on and then continues to expand after the laser is off. In addition to the radii of the plasma bubble, Fig. 109.24(a) also shows the radius of the burnthrough holes. Once the laser is off, this radius changes very little.

The maximum displacement ξ in each image represents the maximum value of $\left| \int \mathbf{B} \times d\ell \right|$; the values from the images of

Fig. 109.22(a) are plotted in Fig. 109.24(b). The maximum value of this integral occurs at the end of the laser pulse, and it decays thereafter; the value predicted by *LASNEX* does not decay as fast. We note that while the laser is on, this maximum occurs at the outside of the plasma bubble, but after the laser is off, the maximum occurs at the edge of the burnthrough hole.

In summary, we have measured the spatial structure and temporal evolution of magnetic fields generated by laser–plasma interactions for the first time over a time interval that is long compared to the laser pulse duration, using monoenergetic proton radiography. Our experiments demonstrated that while a long-pulse, low-intensity laser beam illuminates a plastic foil, a hemispherical plasma bubble forms and grows linearly, surrounded by a symmetric, toroidal B field. After the laser pulse turns off, the bubble continues to expand, but field strengths decay and field structure around the bubble edge becomes asymmetric due, presumably, to the resistive MHD interchange instability. A significant part of that asymmetric structure is repeatable in different experiments, indicating that the asymmetry must have been seeded by some aspect of the experiment, like resonance absorption of obliquely incident, linearly polar-

E15584JR
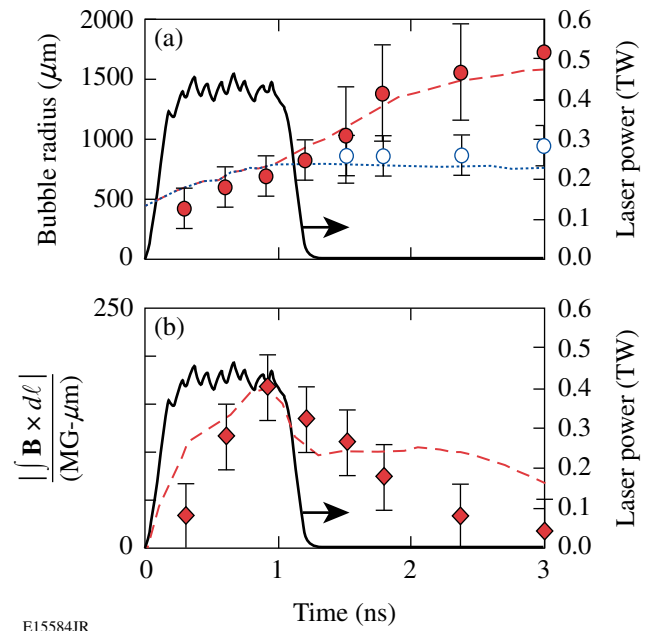
Figure 109.24

(a) Evolution of sizes at the foil, inferred from the images, for the plasma bubble radius (solid circles) and the burnthrough hole (open circles), compared with simulations (dashed and dotted lines, respectively). (b) Evolution of the maximum measured value of $\left| \int \mathbf{B} \times d\ell \right|$ (diamonds), compared with *LASNEX* simulations (dashed line). The solid lines in both (a) and (b) represent the 1-ns OMEGA laser pulse.

ized laser light by an inhomogeneous plasma. Nonrepeatable chaotic structure forms at the center of the plasma bubble after the laser is off, possibly due to a resistivity-induced electron thermal instability. *LASNEX + LSP* simulations agree fairly well with data while the interaction laser is on, aiding the interpretation of the measured images, but the 2-D limitation of these simulations prevents them from predicting some large 3-D structures that develop after the laser is off.

ACKNOWLEDGMENT

REFERENCES

1. B. B. Kadomstev, in *Reviews of Plasma Physics*, edited by M. A. Leontovich (Consultants Bureau, New York, 1966), Vol. 2, pp. 153–199.

2. J. P. Freidberg, *Ideal Magnetohydrodynamics* (Plenum Press, New York, NY, 1987).

3. W. Baumjohann and R. A. Treumann, *Basic Space Plasma Physics* (Imperial College Press, London, 1996).

4. S. Eliezer, *The Interaction of High-Power Lasers with Plasmas* (Institute of Physics Publishing, Bristol, England, 2002).

5. M. G. Haines, Phys. Rev. Lett. **78**, 254 (1997).

6. S. I. Braginskii, in *Reviews of Plasma Physics*, edited by Acad. M. A. Leontovich (Consultants Bureau, New York, 1965), Vol. 1, p. 205.

7. J. A. Stamper *et al.*, Phys. Rev. Lett. **26**, 1012 (1971); D. G. Colombant and N. K. Winsor, Phys. Rev. Lett. **38**, 697 (1977); A. Raven, O. Willi, and P. T. Rumsby, Phys. Rev. Lett. **41**, 554 (1978); M. Borghesi *et al.*, Phys. Rev. Lett. **81**, 112 (1998); A. J. Mackinnon, P. K. Patel, R. P. Town, M. J. Edwards, T. Phillips, S. C. Lerner, D. W. Price, D. Hicks, M. H. Key, S. Hatchett, S. C. Wilks, M. Borghesi, L. Romagnani, S. Kar, T. Toncian, G. Pretzler, O. Willi, M. Koenig, E. Martinolli, S. Lepape, A. Benuzzi-Mounaix, P. Audebert, J. C. Gauthier, J. King, R. Snavely, R. R. Freeman, and T. Boehly, Rev. Sci. Instrum. **75**, 3531 (2004); U. Wagner *et al.*, Phys. Rev. E **70**, 026401 (2004).

8. M. G. Drouet and R. Bolton, Phys. Rev. Lett. **36**, 591 (1976); M. A. Yates *et al.*, Phys. Rev. Lett. **49**, 1702 (1982).

9. C. K. Li, F. H. Séguin, J. A. Frenje, J. R. Rygg, R. D. Petrasso, R. P. J. Town, P. A. Amendt, S. P. Hatchett, O. L. Landen, A. J. Mackinnon, P. K. Patel, V. A. Smalyuk, T. C. Sangster, and J. P. Knauer, Phys. Rev. Lett. **97**, 135003 (2006).

10. M. G. Haines, Phys. Rev. Lett. **47**, 917 (1981).

11. R. P. J. Town *et al.*, Bull. Am. Phys. Soc. **51**, 142 (2006).

12. G. B. Zimmerman and W. L. Kruer, Comments Plasma Phys. Control. Fusion **2**, 51 (1975).

13. P. D. Nielsen and G. B. Zimmerman, Lawrence Livermore National Laboratory, Livermore, CA, UCRL-53123 (1981).

14. D. R. Welch *et al.*, Nucl. Instrum. Methods Phys. Res. A **464**, 134 (2001).

15. T. R. Boehly, D. L. Brown, R. S. Craxton, R. L. Keck, J. P. Knauer, J. H. Kelly, T. J. Kessler, S. A. Kumpan, S. J. Loucks, S. A. Letzring, F. J. Marshall, R. L. McCrory, S. F. B. Morse, W. Seka, J. M. Soures, and C. P. Verdon, Opt. Commun. **133**, 495 (1997).

16. T. J. Kessler, Y. Lin, J. J. Armstrong, and B. Velazquez, in *Laser Coherence Control: Technology and Applications*, edited by H. T. Powell and T. J. Kessler (SPIE, Bellingham, WA, 1993), Vol. 1870, pp. 95–104.

17. C. K. Li, F. H. Séguin, J. A. Frenje, J. R. Rygg, R. D. Petrasso, R. P. J. Town, P. A. Amendt, S. P. Hatchett, O. L. Landen, A. J. Mackinnon, P. K. Patel, V. Smalyuk, J. P. Knauer, T. C. Sangster, and C. Stoeckl, Rev. Sci. Instrum. **77**, 10E725 (2006).

18. F. H. Séguin, J. L. DeCiantis, J. A. Frenje, S. Kurebayashi, C. K. Li, J. R. Rygg, C. Chen, V. Berube, B. E. Schwartz, R. D. Petrasso, V. A. Smalyuk, F. J. Marshall, J. P. Knauer, J. A. Delettrez, P. W. McKenty, D. D. Meyerhofer, S. Roberts, T. C. Sangster, K. Mikaelian, and H. S. Park, Rev. Sci. Instrum. **75**, 3520 (2004).

19. W. L. Kruer, *The Physics of Laser Plasma Interactions* (Westview Press, Boulder, CO, 2003).

Performance of the 1-MJ, Wetted-Foam Target Design
for the National Ignition Facility

Introduction

The primary mission of the National Ignition Facility (NIF)[1] is to demonstrate fusion ignition via inertial confinement fusion (ICF).[2] In the direct-drive[3,4] approach to ICF, a spherical target is illuminated by a number of laser beams arranged symmetrically in a configuration that provides adequate drive symmetry. The target shell is accelerated inward as its outer layers expand due to ablation. After the end of the laser pulse, shock dynamics and compression of the contained gas cause the shell to decelerate. During both the acceleration and deceleration phases of the implosion, the target is subject to Rayleigh–Taylor (RT) instability (see Ref. 3 and references therein)—first on the outer, then the inner surface of the shell. The acceleration-phase instability is seeded by the roughness of the outer surface of the shell, by nonuniformities in the illumination profiles of the individual beams, by beam mispointing, by energy imbalance and mistiming between the various beams, by the drive nonuniformity inherent in the geometric arrangement of the beams, and by the feedout of perturbations to the ablation surface from the inner surface of the shell by means of rarefaction waves. The deceleration-phase RT instability is seeded by the initial roughness of the inner surface of the shell and by nonuniformities that feed through to the inner surface by laser-driven shocks. Target-fabrication techniques have been developed to improve the target-surface smoothness, including the use of β-layering of the DT-ice surface.[5] The single-beam nonuniformities may be reduced through various beam-smoothing methods, such as smoothing by spectral dispersion (SSD),[6] polarization smoothing,[7] or distributed phase plates.[8] Even with these techniques, a target must be designed in such a way as to remain integral during the implosion and uniform enough to produce a hot spot that can initiate a burn wave in the fuel of the shell.

In this article, we present a target design that uses a plastic foam ablator saturated with deuterium–tritium (DT) ice (so-called "wetted foam"). Due to the dependence of inverse bremsstrahlung absorption on the atomic number ($\kappa \sim \langle Z^2 \rangle / \langle Z \rangle$ see Ref. 9), the wetted foam has a higher laser-coupling efficiency than pure DT. Plastic foam shells were originally proposed as a matrix for liquid DT fuel.[10] Others[11,12] proposed the use of foam as an ablator, in conjunction with a high-atomic-number material. In these designs, radiation from the high-atomic-number material preheats the foam, increasing the ablation velocity and reducing outer-surface instability. In the design presented here, the wetted foam is used primarily because of the increase in laser absorption.[13] Other proposed uses of foam include target designs for inertial fusion energy,[14] as well as for reduction of laser imprint.[15]

The stability of this design with respect to the primary sources of target and drive nonuniformity has been determined using two-dimensional (2-D) simulations with the hydrocode *DRACO*.[16] To weigh the effects of these different sources, a nonuniformity-budget analysis is performed in the manner of McKenty *et al.*[17] This analysis maps nonuniformity from different sources to a parameterization of the inner-shell-surface spectrum at the end of the acceleration phase, which in turn allows prediction of target performance. Following a description of the design in the next section, the tolerance of the design to nonuniformity sources is presented; the results from integrated simulations including ice and surface roughness, multiple-beam nonuniformity (primarily due to port geometry and power imbalance between beams), and imprint are shown; and, finally, the conclusions from the nonuniformity-budget analysis and the integrated simulations are presented.

The 1-MJ, Wetted-Foam Design

The 1.5-MJ, all-DT, direct-drive point design for symmetric drive on the NIF, shown in Fig. 109.25(a), consists of a DT shell surrounded by a thin layer of plastic (CH; see Ref. 17). The same design, scaled to an incident energy of 1 MJ, and the 1-MJ wetted-foam design are shown in Figs. 109.25(b) and 109.25(c). An incident energy of 1 MJ has been chosen to match energy restrictions to reduce the risk of damage to the NIF's optical elements. Table 109.III shows that the laser absorption, averaged over the length of the laser pulse, is ~60% to 65% for the all-DT designs. When part of the DT shell is replaced by a $CH(DT)_4$ wetted-foam ablator, the higher-average atomic number of the ablator results in an absorption of 86%

(Table 109.III). This allows a greater fraction of the incident laser energy to be converted to shell kinetic energy, allowing a thicker shell to be driven. The resulting 1-D gain for the 1-MJ, wetted-foam target is ~10% higher than that of the 1.5-MJ, all-DT design.
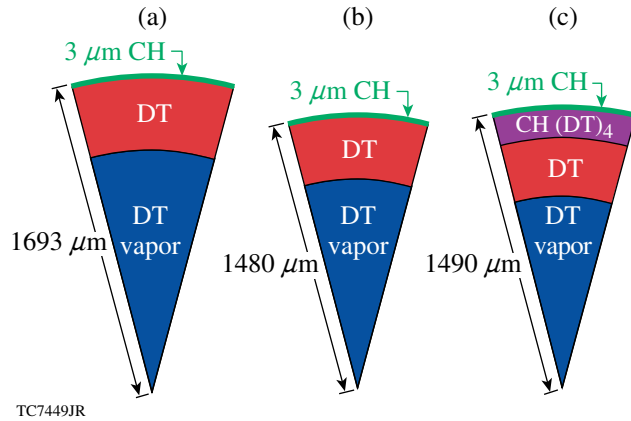

TC7449JR

Figure 109.25
(a) The 1.5-MJ, all-DT, direct-drive target design for the NIF, (b) the same design scaled for an incident laser energy of 1 MJ, and (c) the 1-MJ, wetted-foam design. The wetted-foam shell is 326 μm thick, with 216 μm of pure DT fuel.

Table 109.III: Properties of the 1.5-MJ, all-DT; 1-MJ, all-DT; and 1-MJ, wetted-foam designs. Here A is the rms bubble amplitude at the end of the acceleration phase and ΔR is the in-flight shell thickness.

	All-DT	Scaled, All-DT	Wetted-foam
Energy (MJ)	1.5	1	1
Target radius (μm)	1695	1480	1490
Absorption (%)	65	59	86
$A/\Delta R$ (%)	30	33	11
Gain	45	40	49

The density of $CH(DT)_4$ is 304 mg cm^{-3}, corresponding to a dry-foam density of 120 mg cm^{-3}, given that during the freezing process the liquid DT contracts in volume by 17%, leaving voids in the wetted-foam layer. This is only 22% greater than the density of pure DT ice. This dry-foam density provides higher absorption, while not generating enough radiation to appreciably raise the fuel isentrope (as measured by the adiabat α, given by the ratio of the pressure to the cold Fermi-degenerate pressure). The wetted-foam-layer thickness ensures that the foam is entirely ablated by the end of the laser pulse. In an ignition design such as this, the first laser-driven shock, whether steady or, for picket designs, decaying, determines the shell adiabat. This is the only strong laser-driven shock, and it is the only shock to encounter unmixed foam and DT. High-resolution hydrodynamic simulations modeling the wetted-foam mixture have shown that after the initial undercompression behind the first shock,[18] the flow variables asymptote to within a few percent of the Rankine–Hugoniot values for ICF-relevant shock strengths.[19] These simulations demonstrate that the fluctuation decay scale length behind the shock is less than 2 μm, where this scale length is defined for a quantity q as $Lq = dr/d\ln\langle q \rangle$, and $\langle q \rangle$ is the average of q in the shock frame in the direction perpendicular to the shock [see Eq. (1) of Ref. 19]. These findings allow the wetted-foam layer to be modeled as a homogeneous mixture in the simulations described here.

Assuming an ICF shell remains intact during the acceleration phase, the most dangerous modes during deceleration are those that feed through from the outer to the inner surface. Modes feed through attenuated by a factor exp($-k\Delta R$), where k is the wave number and ΔR is the shell thickness; the long-wavelength modes with $k \sim 1/\Delta R$ feed through most effectively. The number N of e-foldings of growth experienced by these modes during acceleration may be approximated by $N \sim \gamma\Delta t \sim (kgt^2)^{1/2}$, where γ is the growth rate over the time period Δt during which the shell is accelerated by the laser pulse, which is proportional to the classical growth rate for long-wavelength modes. Writing this in terms of the distance traveled by the shell, which is proportional to the initial outer shell radius R_0, $N \sim (R_0/\Delta R)^{1/2} \equiv (\text{IFAR})^{1/2}$, where IFAR is the in-flight aspect ratio of the imploding shell. This is related to the implosion velocity v and the average shell adiabat by IFAR $\sim v^2/\langle\alpha\rangle^{3/5}$ (Ref. 3). These relations show that the integrity of the shell during acceleration depends on the IFAR. The shell stability can be improved by lowering the implosion velocity or lowering the IFAR by increasing the shell thickness, which is equivalent to raising the average adiabat, since $\Delta R \sim \langle\alpha\rangle^{3/5}$. For a target where the adiabat is a constant function of shell mass, increasing the adiabat reduces the fuel compressibility and target gain. For a design such as this one, which has a shaped adiabat, N is reduced by a term proportional to $v(\alpha_{out}/\langle\alpha\rangle)^{0.6}$, where α_{out} is the ablator adiabat.[20] The shell instability of the wetted-foam design is reduced from that of a 1-MJ-scaled, all-DT design by lowering the shell velocity by ~60 μm/ns (see Table 109.IV). As a result, the shell is less unstable during the acceleration phase, and the rms bubble amplitude divided by the shell thickness $A/\Delta R$, computed from 1-D simulations using a postprocessor,[21] is lower by a factor of 3 for the 1-MJ, wetted-foam design.

The increase in shell mass has the added benefit of raising the areal density of the shell at the time of ignition, making the shell more robust to deceleration-phase instabilities. Any RT growth on the inner edge of the shell during deceleration delays the onset of ignition, effectively lowering the shell velocity.[22] The inward motion of the shell at the time of ignition is necessary to offset the tremendous pressure the expanding burn wave exerts on the shell. If left unimpeded, the pressure of the burn wave would decompress the shell prematurely, quenching any possibility of high gain. In addition, decreasing the implosion velocity decreases the work done compressing the hot spot and reduces the hot-spot temperature. Further, a reduction in hot-spot temperature reduces the effects of ablative stabilization of the deceleration-phase RT instability. Due to these effects, the minimum energy needed for ignition scales with IFAR as $E_{ign} \sim (IFAR)^{-3}$ (Ref. 20). The margin, defined as the inward-moving kinetic energy at ignition divided by the peak inward kinetic energy, is a measure of the additional kinetic energy of the shell above that needed for ignition. As seen in Table 109.IV, the decrease in IFAR and increase in shell mass have the effect of lowering the margin for the wetted-foam design. As will be shown in the following section, this design tolerates 1.75 μm of ice roughness, suggesting sufficient margin.

The laser pulse shape, shown in Fig. 109.26, uses an initial high-intensity picket to generate a decaying shock. As this shock propagates through the shell, its strength decreases to that supported by the foot, causing the level of shock heating to decrease from the ablator to the inner edge of the shell. This shapes the adiabat,[23] producing a high-ablator adiabat of ~10 while retaining a low-fuel adiabat of ~2. (Other adiabat-shaping techniques include the use of a relaxation picket where the

Table 109.IV: The wetted-foam design's shell is thicker than that of the all-DT design scaled to 1 MJ. This reduces shell instability and increases the areal density, but at the cost of a lower margin.

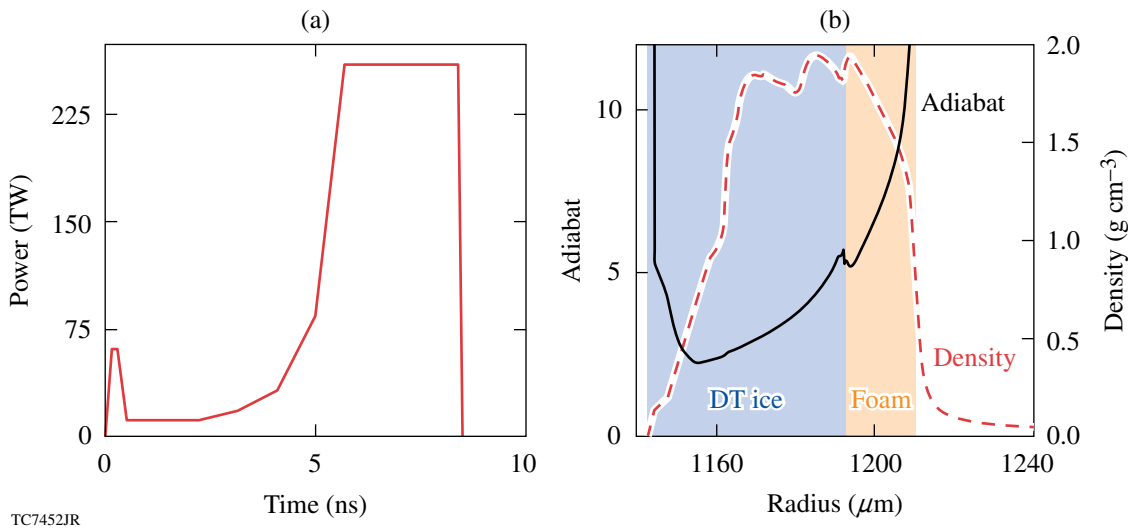|	V (μm/ns)	ΔR (μm)	IFAR	$A/\Delta R$ (%)	Areal density ρR (g/cm^2)	Margin (%)
1-MJ, all-DT	430	285	69	33	1.1	45
Wetted-foam	372	323	28	11	1.4	30

Figure 109.26
(a) The laser pulse and (b) the adiabat and mass density of the shell shortly after shock breakout. The laser pulse consists of an initial intensity spike or "picket" followed by a foot of low constant intensity and a rise to a high-power drive pulse.

TC7452JR

laser intensity is zero between the picket and the foot pulse,[24] and a series of such isolated picket pulses preceding the main drive pulse.[12]) This technique reduces the shell instability and laser imprint during the acceleration phase since the ablation velocity is proportional to $\alpha^{3/5}$ (see Ref. 3). At the same time, it maintains the low-fuel adiabat needed to compress the fuel and achieve ignition. The picket also lowers imprint by decreasing the duration of the period of acceleration due to the outer CH layer and by increasing the rate of growth of the conduction zone between the ablation and critical surfaces.[25]

This design is robust to shock mistiming, critical for a successful ICF target design. The shock timing depends on accurate modeling of the equation of state (EOS) of the wetted-foam mixture and the DT. The effect on 1-D gain of changing either the foot length or power is shown in Fig. 109.27. These simulations show a reduction in gain of less than 10% for a variation in the foot-pulse length of ±250 ps, well within the NIF specification[26] of 100 ps. A change in power of ±4%, comparable to the NIF specification, produces a gain reduction of ~8%. It is anticipated that the shock timing will be verified experimentally using the materials of interest.

Nonuniformity-Budget Analysis

Four sources of nonuniformity contribute to the RT instability during the implosion. These include inner-surface DT-ice roughness, outer-surface roughness, and single-beam and multiple-beam nonuniformity. To gauge their relative importance and estimate their effects on target gain in an integrated simulation incorporating all four, a nonuniformity budget has been developed.[17,27] McKenty et al.[17] found that target gain may be approximated as a function of a weighted average of the inner-surface ice spectrum at the end of the acceleration phase,

$$\overline{\sigma} = \sqrt{a\sigma^2_{\ell < 10} + \sigma^2_{\ell > 9}},$$

regardless of the source of the ice perturbations. The low-mode weighting factor is $a = 0.06$. (The end of the acceleration phase is taken as the time when the ablation-front acceleration changes sign, shortly after the end of the laser pulse.) In 2-D simulations of the wetted-foam design incorporating various levels and spectral indices of ice roughness, it was found that this weighting factor provides reasonable scaling for this design as well.

This spectral weighting is based on the different effects that short-wavelength modes have on the hot spot. Any mode growth increases the hot-spot surface area, enhancing the cooling due to thermal conduction with the shell. For short wavelengths, the spikes of a single-mode perturbation on the inner surface of the shell lie close enough together that they cool below the temperatures at which they can contribute to α-particle generation. For these modes, the hot-spot size is effectively reduced by the physical extent of the perturbation.[28] Gain reduction becomes independent of wavelength for these high modes depending only on mode amplitude. Kishony and Shvarts[28] show that this behavior occurs for modes with $\ell > 9$. Because the dependence of yield on $\overline{\sigma}$ is independent of the source of the nonuniformity, the target gain may be estimated by adding the contributions to $\overline{\sigma}$ in quadrature and using the gain as a function of $\overline{\sigma}$ found, for instance, from simulations of just initial ice roughness.

Each of the sources of nonuniformity was simulated in 2-D. The laser-energy deposition was modeled using a straight-line ray-trace algorithm. To incorporate the reduction of coupling due to refraction, the absorbed energy determined from a 1-D simulation was used as the incident energy in 2-D simulations. This method provides a drive that closely replicates the adiabat
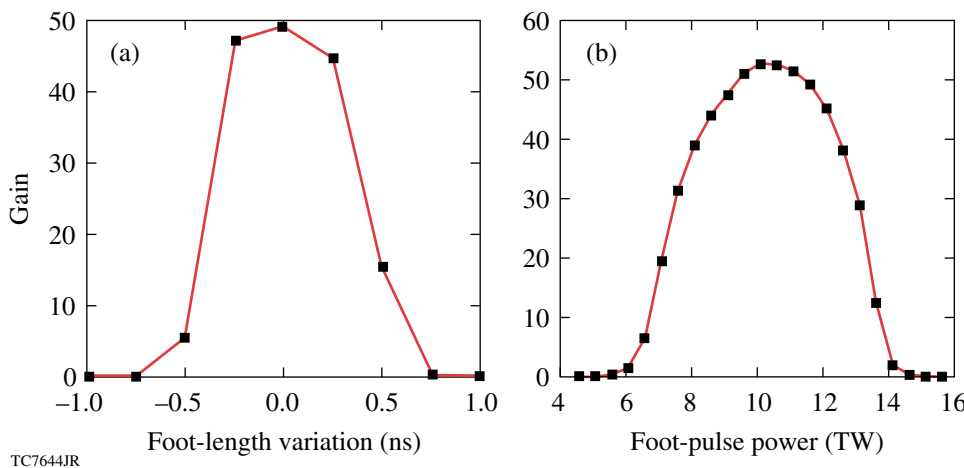

Figure 109.27
Sensitivity of the wetted-foam design's 1-D target gain to (a) deviation in the foot-pulse length and (b) foot-pulse power.

TC7644JR

in the 1-D simulation. The pulse was truncated to ensure that the acceleration-phase stability, as determined using a 1-D postprocessor,[21] and the shell areal density at the time of ignition remained the same, and the implosion velocity differed by only 3%. Without refraction, however, the conduction zone is smaller, leading to more-efficient imprint.[29] It is expected that when these simulations are repeated using refractive laser-energy deposition, the target will be somewhat less sensitive to single-beam nonuniformity.

1. Initial DT-Ice Surface Roughness

The amplitude spectrum of initial inner-surface ice roughness has been found for cryogenic D_2 targets fabricated at LLE and is approximated here by a power law in mode number $A_\ell = A_0 \ell^{-\beta}$, where $\beta \sim 2$. The power for these modes lies primarily in $\ell < 50$. A series of 2-D simulations of ice-surface roughness were performed for various spectral amplitudes A_0 and power-law indices β, including modes 2 to 50. The resolution used for these simulations was about eight zones per wavelength for $\ell = 50$. The target gain as a function of initial rms ice roughness for $\beta = 2$ is shown in Fig. 109.28(a). This target was found to withstand 1.75 μm of initial ice roughness with little degradation in performance. When a power-law index of 1.5 was used, this design showed greater tolerance to ice roughness than the 1.5-MJ design presented in Ref. 17. This is most likely because of the higher areal density, 1.4 g cm^{-2}, of the wetted-foam design.

Figure 109.28(b) shows the shell at the time of ignition, when the hot-spot ion temperature has reached 10 keV. The density contours show that the hot spot is primarily distorted by modes 2 to 6. The dependence of gain on $\bar{\sigma}$ is shown in Fig. 109.29. It can be seen that this 1-MJ design can tolerate a $\bar{\sigma}$ of slightly less than 1 μm, compared with ~2 μm for the 1.5-MJ design of Ref. 17. For $\bar{\sigma} \gtrsim 0.8$ μm in the wetted-foam design, the RT

TC7457JR
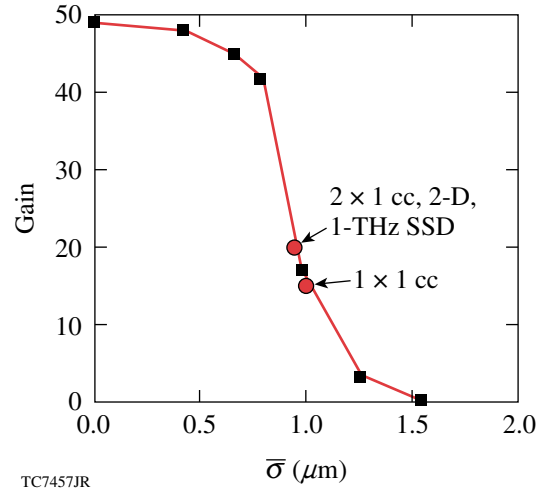
Figure 109.29
The dependence of gain on the parameter $\bar{\sigma}$ is shown, determined from simulations of initial ice-layer roughness for an ice spectrum with a power-law index of $\beta = 2$.

TC7455JR
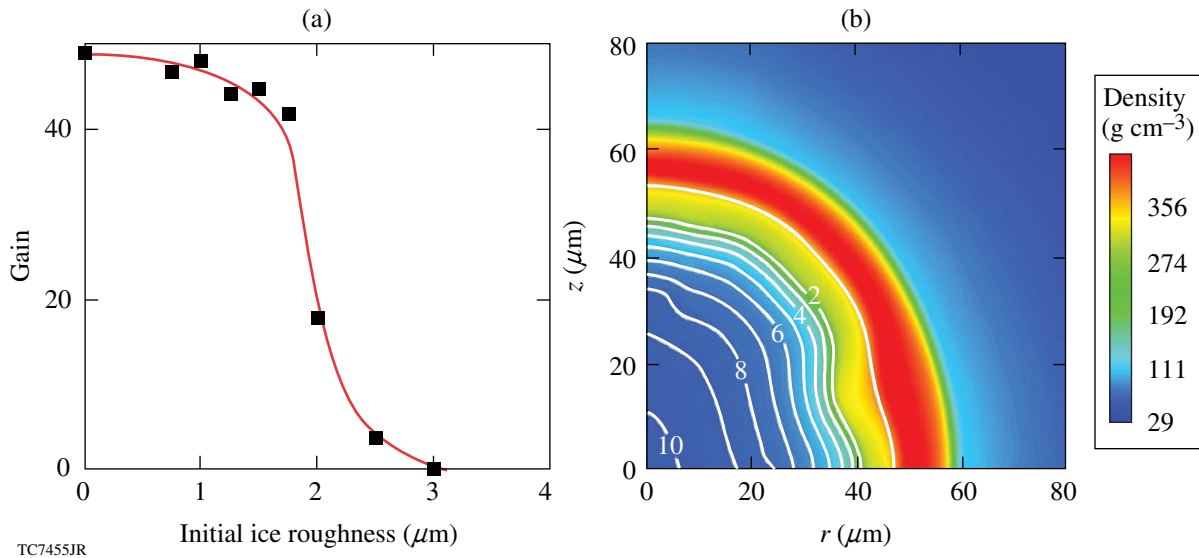
Figure 109.28
(a) The gain as a function of initial ice roughness for a power-law index of 2. This target tolerates an rms ice roughness of ~1.75 μm before deviation from the 1-D gain. (b) The shell at the time of ignition for the case of 1.75-μm-rms ice roughness is also shown. The gray scale shows mass density, and contour lines indicate ion temperature in keV. Note that the hot spot is primarily distorted by modes 2 to 6.

growth delays the onset of ignition, which consumes part of the margin leading to a lower burnup fraction at ignition.[22] The lower tolerance of this design compared to the 1.5-MJ design is due to the reduction in margin caused by the lowering of the incident laser-driver energy.

2. Outer-Surface Roughness

Foam-target fabrication at General Atomics has made significant strides in the past few years. Resorcinol-formaldehyde foam shells with submicron pore sizes (less than 0.25 μm) and thin (~5-μm) CH overcoats have been diagnosed using atomic-force microscopy.[30] The measured mode-amplitude spectrum shows spectral dependence roughly proportional to ℓ^{-2}, with most of the power in modes less than ten. The overall rms roughness for these foam shells has been shown to be as low as ~450 nm, about four times larger than that of the NIF's CH-surface standard roughness (Ref. 17 and references therein).

A 2-D simulation incorporating this surface spectrum, modeled as ribbon modes, resulted in a $\overline{\sigma}$ value of 0.38 μm and demonstrated negligible reduction in target gain. By comparison, a simulation using the NIF standard with an rms of ~115 nm produced a $\overline{\sigma}$ of 0.08 μm.

3. Multiple-Beam Nonuniformity

Multiple-beam nonuniformity, often referred to as beam-to-beam power imbalance, is caused by at least five sources of drive nonuniformity: variations in the power between the different laser beams, drive asymmetry caused by the geometry of the beam port locations and beam overlap, beam-pointing errors, and variations in beam timing. The nonuniformity spectrum has been determined as a function of time for the first four of these contributions for the wetted-foam laser pulse by spherical-harmonic decomposition of the illumination pattern of the beams projected onto the surface of the target. A harmonic modal spectrum is produced by combining all m modes in quadrature for each mode number ℓ. The symmetric NIF direct-drive port geometry contributes a constant perturbation, primarily in mode $\ell \le 6$. Beam mistiming, which is expected to have an rms value of 30 ps on the NIF,[26] produces perturbations in modes $\ell = 1$ to 3, primarily during the rise and fall of the picket. Despite these perturbations, the mistiming of the picket was found to have a small effect on target performance.[31] The imbalance in energy between beams is expected to be ~8% rms on the NIF. The resulting perturbations are dominated by modes 2 to 12, with an amplitude of ~1%. The 2-D simulations described here include the effects of power imbalance between beams, beam overlap, and port geometry.

A series of six 2-D power-balance runs were performed. These simulations included modes 2 to 12, with 44 zones per wavelength of mode 12. They were performed using power-balance histories[17] adapted to the wetted-foam-design laser pulse. They produced an average reduction in gain of ~6%, with a $\overline{\sigma}$ of about 0.11 μm.

4. Single-Beam Nonuniformity

Single-beam nonuniformity or imprint is the source of nonuniformity capable of causing the greatest reduction in target yield, depending on the level of beam smoothing used. Illumination perturbations contribute to imprint through the perturbation in the laser-drive shock front and the acceleration perturbation in the post-shock region, which causes lateral flow in the shock-compressed material.[32] These produce secular growth during the foot pulse that seeds RT growth during the drive pulse. Several methods have been developed for reducing imprint. On the NIF these include SSD, distributed phase plates, and polarization smoothing. In the 2-D imprint simulations, we have modeled the effects of all three smoothing techniques. The DPP spectrum is modeled using an analytical fit for the laser speckle,[33] with amplitudes reduced to account for the effects of polarization smoothing and 40-beam overlap for the NIF's 192-beam system.

Two-dimensional SSD is modeled using a nondeterministic algorithm where the phase of each mode is assigned randomly every modal coherence time. The coherence time is given by a 2-D generalization of the formula $t_c = \left[\Delta\nu \sin\left(n_c \pi \ell / \ell_{max}\right) \right]^{-1}$ (Ref. 34), where $\ell_{max} = 2\pi R_0 / \delta$ is the mode number corresponding to half the speckle size δ, $\Delta\nu$ is the SSD bandwidth, and n_c is the number of color cycles on the laser system. The randomly chosen phases for each mode repeat after a number of coherence times, which depends on the mode number and the angular divergence in each dimension, implementing the asymptotic level of smoothing achievable by SSD. This asymptotic limit is much larger for 1-D SSD than for 2-D, resulting in much greater imprint, as will be seen below. For long-wavelength modes the number of statistically independent speckle patterns is small enough that a single simulation does not fully sample the ensemble of possible phase choices. For this reason, many of the runs here were repeated several times.

The reduction in growth rate due to ablative stabilization means the ablation-front mode spectrum due to imprint decreases with increasing mode number (see, e.g., Fig. 4 of Ref. 32). When this spectrum feeds through to the inner surface of the ice, there is an additional reduction in amplitude for increasing mode number due to the attenuation factor

exp($-k\Delta R$). The ice spectrum at the end of the acceleration phase is shown in Fig. 109.30 for a simulation modeling the effects of imprint from modes $\ell = 2$ to 200. Due to the initial mode-number dependence in the imprint spectrum and the feedthrough attenuation, modes above $\ell = 100$ contribute less than 1% to the overall rms. For this reason, additional 2-D imprint runs were performed including only modes up to 100. To reduce the simulation time, only even modes are modeled in

TC7465JR

Figure 109.30

The DT-ice-roughness spectrum on the inner surface of the shell at the end of the acceleration phase for a simulation modeling the effects of imprint in modes up to $\ell = 200$. Due to the mode-number dependence on the imprint spectrum and feedthrough attenuation, modes above $\ell \sim 100$ contribute negligibly to the total rms.

these simulations, with the amplitudes of the odd modes added in quadrature. These simulations use a resolution of 14 zones per wavelength at $\ell = 100$, which has been found to be sufficient to resolve the smallest perturbation wavelengths.

The characteristic smoothing time T for SSD, given by the inverse of the smoothing rate, is related to the key SSD parameters by $T \sim (\nu_m n_c \delta)^{-1} \sim (\Delta\nu n_c)^{-1}$, where ν_m is the modulator depth. To determine the dependence of target performance on smoothing time, we have performed simulations for four different levels of SSD bandwidth: 1.33 THz, 0.89 THz (referred to here and elsewhere as "1-THz" SSD), 590 GHz, and 295 GHz. These all use one color cycle in each direction and modulator frequencies of 15.4 GHz and 2.81 GHz. The shell at the end of the acceleration phase is shown for each of these simulations in Fig. 109.31. The dependence of imprint on the bandwidth is clearly seen in the level of perturbation on the outer shell surface: whereas the shell from the 1.3-THz simulation is intact and relatively unperturbed, that from the ~0.3-THz simulation is completely broken up. The $\bar{\sigma}$ values for imprint alone are shown in Fig. 109.31: 0.37 μm, 0.86 μm, 0.96 μm, and 2.3 μm for 1.3 THz, 0.9 THz, 0.6 THz, and 0.3 THz, respectively. For comparison, the $\bar{\sigma}$ value from a simulation with 2-D, 1-THz SSD with two color cycles in one direction and one in the other is just 0.43 μm, half of that found with one color cycle in each direction and the same bandwidth. When the $\bar{\sigma}$ values from the simulations shown in Fig. 109.31 are combined in quadrature with those due to energy imbalance, port geometry and beam overlap, foam surface roughness, and 1-μm initial ice roughness, they are increased to 0.74 μm, 1.07 μm, 1.15 μm, and 2.43 μm. The projected gain factors from these sums are 39, 12, 8, and 0.008, respectively.
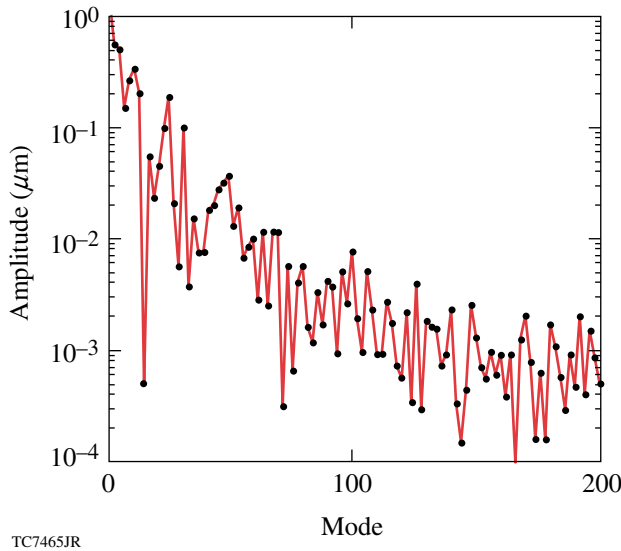
TC7458JR

Figure 109.31

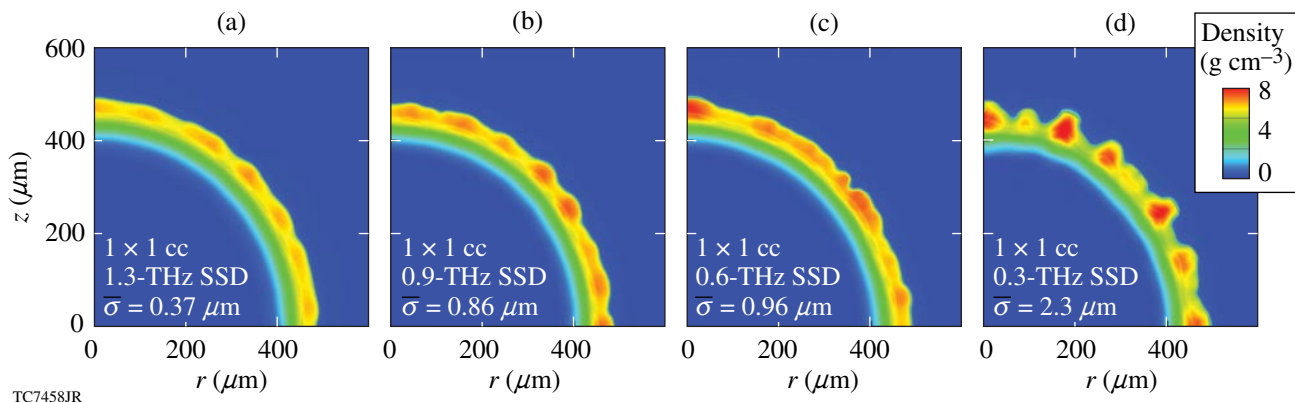The shell is shown at the end of the acceleration phase for 2-D simulations of imprint modes 2 to 100, with one color cycle of SSD in each dimension and descending levels of bandwidth, showing the reduction in smoothing and the performance parameter $\bar{\sigma}$ just from imprint.

The SSD parameters that are currently anticipated for the NIF are much different from those required for an all-DT, direct-drive target at 1.5 MJ (Ref. 17), which we will refer to here as "2×1 SSD." The 2×1 SSD parameters are 2 and 1 color cycles in each direction, modulator frequencies of 15.4 GHz and 2.81 GHz, and a total UV bandwidth of 0.89 THz found by summing the individual bandwidths in quadrature. The anticipated NIF parameters for use with indirect-drive ignition (IDI) are 1-D SSD with 1.35 color cycles, a modulator frequency of 17 GHz, and a UV bandwidth of 185 GHz. These two sets of parameters have been simulated in 2-D, along with two intermediate levels of SSD: the 2×1 parameters but with just one color cycle in each direction ("1×1" SSD), and 2×1 SSD reduced to one dimension with two color cycles ("2×0" SSD). The shells at the end of the acceleration phase from multimode imprint simulations incorporating these levels of SSD are shown in Fig. 109.32. These simulations include all four sources of nonuniformity. The values of $\overline{\sigma}$ for these four simulations are 0.94 μm for the 2×1 SSD case, 1.0 μm for 1×1 SSD, 2.0 μm for 2×0 SSD, and 7.3 μm for IDI SSD. The projected gain factors for these integrated simulations are 21, 16, 0, and 0, respectively.

Integrated Simulations

Three integrated simulations were performed. The first two include drive asymmetry due to power imbalance and port geometry, surface roughness (370 nm), 0.75-μm initial ice roughness with a power-law index of $\beta = 2$, and single-beam imprint. The third uses a different initial ice spectrum with 2-D, 2×1 SSD beam smoothing and is discussed below.

The smoothing modeled in the first two simulations was polarization smoothing and either 2-D, 2×1 or 1-D, 2×0 SSD.

The targets from these simulations, at the end of the acceleration phase and near the time of peak compression, are shown in Fig. 109.33. The 2-D SSD case has a much less perturbed shell at the end of acceleration than the 1-D SSD simulation. As a result, its hot spot is much more uniform at peak compression, showing primarily distortions with modes less than or equal to 6. The hot spot at this time (9.4 ns) is approximately 40 μm in size, and the neutron-averaged areal density is 1.31 g/cm^3. By comparison, the 1-D SSD simulation shows large perturbations at the end of acceleration that produce distortions over a wide spectral range at peak compression (9.3 ns). These distortions in the shell produce a more-distorted inner shell surface and lower ion temperatures at stagnation than in the 2-D SSD case and prevent the target from achieving gain greater than 1.

Smoothing levels due to 2-D and 1-D SSD are very different, even for long-wavelength modes. The shortest mode that can be smoothed by SSD is given by $\ell_{\min} = 2\pi R_0 / (2F\Delta\theta) \sim 4$ (Ref. 35), where F is the focal distance (7.7 m for the NIF) and $\Delta\theta^2 = \Delta\theta_1^2 + \Delta\theta_2^2$ is the effective far-field divergence, approximated by summing the contributions from each direction in quadrature. For 2×1, 2-D SSD, smoothing is effective above mode 4, and above mode 6 for 2×0, 1-D SSD. This is demonstrated in Fig. 109.34(a), which shows the smoothing due to SSD at 1 ns for modes up to 50. Note that even though the difference between 1-D and 2-D smoothing is small for modes less than 10, these modes also see less thermal smoothing[29] and a greater decoupling time than shorter-wavelength modes. Both 1-D and 2-D SSD smooth at the same rate prior to asymptoting. The difference in smoothing between 1-D and 2-D SSD is due to the difference in the asymptotic level. This is shown for mode number 22 in Fig. 109.34(b). For this
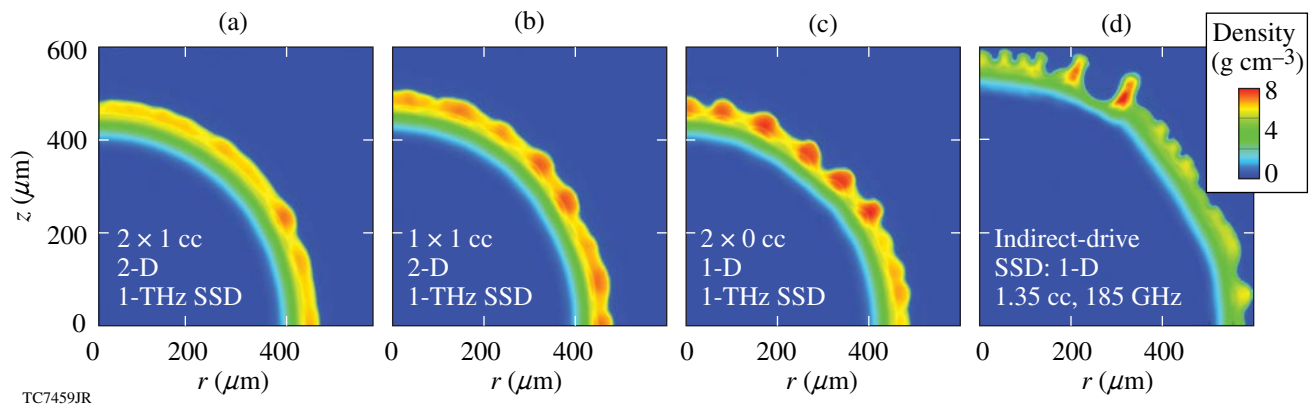
Figure 109.32
The shell at the end of the acceleration phase is shown for four 2-D simulations incorporating different sets of SSD parameters. These are integrated simulations that also include the effects of energy imbalance, foam-surface nonuniformity, and 1 μm of ice roughness.
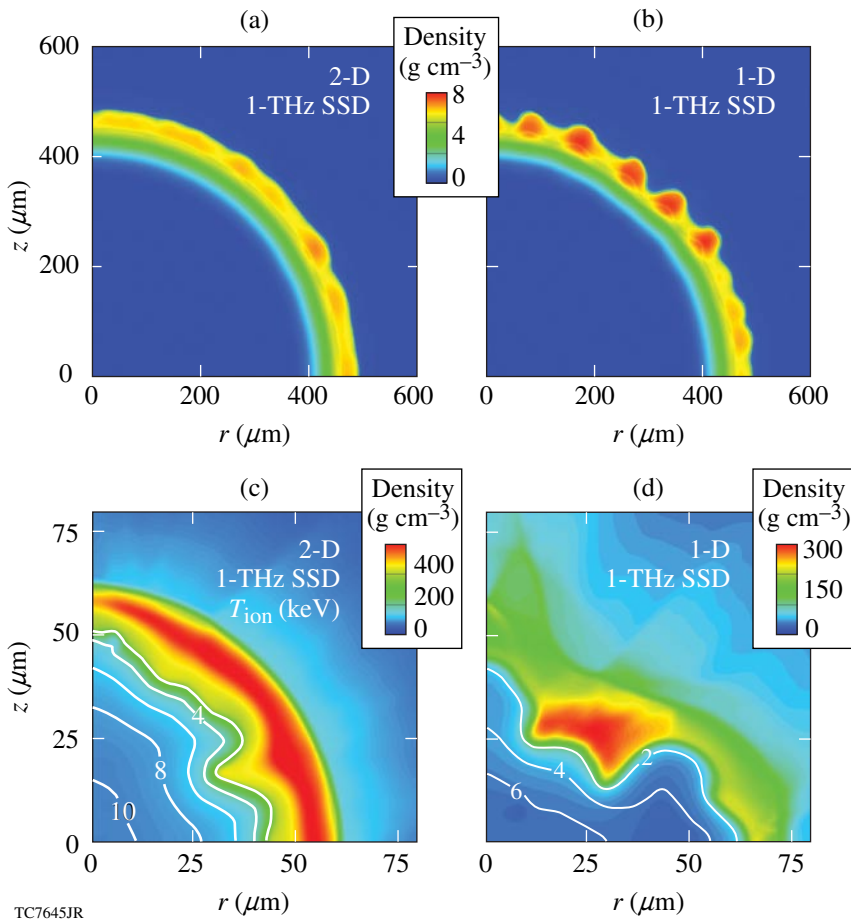
Figure 109.33
The shell is shown at the end of the acceleration phase [(a) and (b)] and near the time of peak compression [(c) and (d)] for the 2×1 and 2×0 SSD configurations, including all sources of nonuniformity. Unlike the integrated simulations shown in Fig. 109.32, these were run to completion. The high level of nonuniformity at the end of the acceleration phase and the highly distorted hot spot in the 2×0 case demonstrate the importance of 2-D SSD smoothing for target performance. The 2×1 simulation achieved a gain of 20, compared to a gain of less than 1 for the 2×0 case.
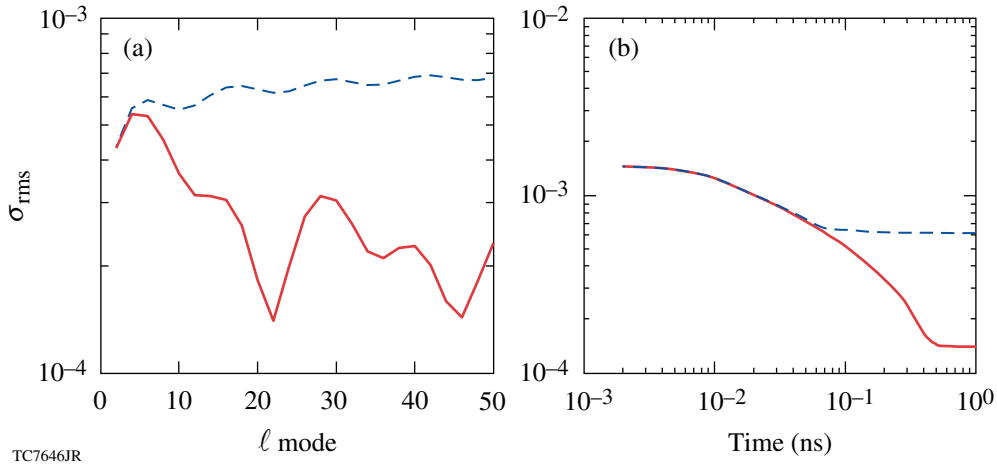
Figure 109.34
The smoothing due to SSD is shown in terms of (a) the mode number at 1 ns and (b) the perturbation for mode $\ell = 22$ as a function of time. Solid lines are 2-D SSD and dashed lines are 1-D SSD. These demonstrate the difference in the asymptotic level of smoothing for 1-D and 2-D SSD, as well as the level of smoothing for low mode numbers.

mode, the asymptotic level is reached at 70 ps for 1-D SSD and at 0.5 ns for 2-D SSD.

The third completed integrated simulation had the same nonuniformity levels and beam smoothing as the 2×1 just discussed, with an initial ice roughness of 1 μm and an ice power-law spectral index of $\beta = 1$. This was chosen to approximate the spectra of cryogenic DT capsules produced at LLE, which have less power in the low modes because of the different layering process. While the ice roughness was higher for this simulation than for the integrated 2-D SSD simulation described above, the lower power-law index reduces the spectral power in the low modes relative to the high modes. The combined effect is to produce a hot spot at peak compression, shown in Fig. 109.35, which is similar to that of the 2×1 SSD integrated simulation shown in Fig. 109.33(c), although with a smaller and more distorted hot spot. The gain factor of this simulation was 27. This shows that, for a smaller power-law index, the target can tolerate a greater ice roughness with little reduction in gain.

TC7660JR

Figure 109.35
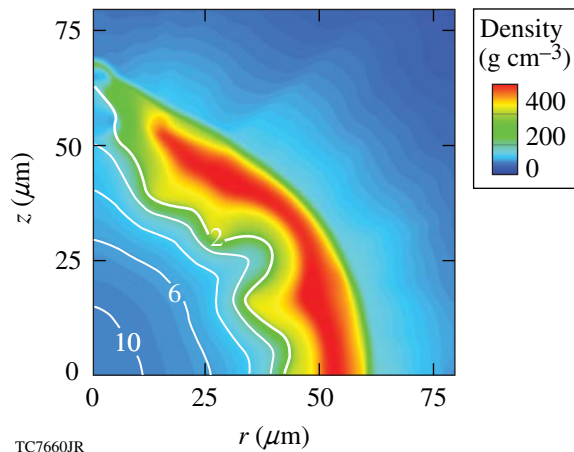The shell is shown at peak compression for a simulation using 2-D, 2×1, 1-THz SSD with 1-μm initial ice roughness and an ice spectral index of 1. The resulting 2-D gain is 27.

Conclusions

An ignition target design using a wetted-foam ablator to couple greater laser energy into the target has been presented for use on the NIF with 1 MJ of incident laser energy. This design makes use of a thicker shell and lower implosion velocity to reduce the effects of imprint. A nonuniformity-budget analysis indicates that imprint, with 2-D, 2×1 color-cycle, 1-THz SSD smoothing, produces an effective nonuniformity $\overline{\sigma}$ that is slightly larger than that of the other sources of non-

uniformity, namely, power imbalance, outer-surface roughness, and ice roughness. With 1×1 SSD the effective nonuniformity is more than twice that from other sources.

Simulations suggest that this design will ignite and achieve gain only if 2-D SSD is used to smooth single-beam illumination nonuniformities. The need for 2-D SSD has been found in other target-design performance studies as well.[17,36] Integrated simulations including imprint, surface and ice roughness, and beam-to-beam power imbalance were completed for two levels of SSD: 2×1 and 2×0, and 0.75-μm initial ice roughness with a power-law index of $\beta = 2$. The former achieved a gain of 32 compared to less than 1 for the latter. The difference in performance is due primarily to the difference in the asymptotic level of smoothing for 2-D and 1-D SSD. A third integrated simulation was completed using 1-μm initial ice roughness with a power-law index of $\beta = 1$, meant to approximate the ice spectra found in DT cryogenic targets at LLE. This simulation also ignited, achieving a gain factor of 27. This indicates that greater ice nonuniformity may be tolerated if combined with a smaller spectral index.

REFERENCES

1. J. Paisner *et al*., Laser Focus World **30**, 75 (1994).

2. J. Nuckolls *et al*., Nature **239**, 139 (1972).

3. J. D. Lindl, Phys. Plasmas **2**, 3933 (1995).

4. S. Atzeni and J. Meyer-ter-Vehn, *The Physics of Inertial Fusion: Beam Plasma Interaction, Hydrodynamics, Hot Dense Matter*, International Series of Monographs on Physics (Clarendon Press, Oxford, 2004).

5. A. J. Martin, R. J. Simms, and R. B. Jacobs, J. Vac. Sci. Technol. A **6**, 1885 (1988); J. K. Hoffer and L. R. Foreman, Phys. Rev. Lett. **60**, 1310 (1988).

6. S. Skupsky, R. W. Short, T. Kessler, R. S. Craxton, S. Letzring, and J. M. Soures, J. Appl. Phys. **66**, 3456 (1989).

7. T. R. Boehly, V. A. Smalyuk, D. D. Meyerhofer, J. P. Knauer, D. K. Bradley, C. P. Verdon, and D. Kalantar, in *Laser Interaction and Related Plasma Phenomena*, edited by G. H. Miley and E. M. Campbell (American Institute of Physics, New York, 1997), Vol. 406, pp. 122–129.

8. Y. Lin, T. J. Kessler, and G. N. Lawrence, Opt. Lett. **20**, 764 (1995).

9. T. W. Johnston and J. M. Dawson, Phys. Fluids **16**, 722 (1973).

10. L. M. Hair *et al.*, J. Vac. Sci. Technol. A **6**, 2559 (1988); R. A. Sacks and D. H. Darling, Nucl. Fusion **27**, 447 (1987).

11. D. G. Colombant *et al.*, Phys. Plasmas **7**, 2046 (2000).

12. M. Tabak, *ICF Program Annual Report 1989 (U)*, Lawrence Livermore National Laboratory, Livermore, CA, UCRL-LR-116901-88/80, 141 (1989).

13. S. Skupsky, R. Betti, T. J. B. Collins, V. N. Goncharov, D. R. Harding, R. L. McCrory, P. W. McKenty, D. D. Meyerhofer, and R. P. J. Town, in *Inertial Fusion Sciences and Applications 2001*, edited by K. Tanaka, D. D. Meyerhofer, and J. Meyer-ter-Vehn (Elsevier, Paris, 2002), pp. 240–245.

14. J. D. Sethian *et al.*, Nucl. Fusion **43**, 1693 (2003).

15. M. Desselberger *et al.*, Phys. Rev. Lett. **74**, 2961 (1995).

16. P. B. Radha, V. N. Goncharov, T. J. B. Collins, J. A. Delettrez, Y. Elbaz, V. Yu. Glebov, R. L. Keck, D. E. Keller, J. P. Knauer, J. A. Marozas, F. J. Marshall, P. W. McKenty, D. D. Meyerhofer, S. P. Regan, T. C. Sangster, D. Shvarts, S. Skupsky, Y. Srebro, R. P. J. Town, and C. Stoeckl, Phys. Plasmas **12**, 032702 (2005).

17. P. W. McKenty, V. N. Goncharov, R. P. J. Town, S. Skupsky, R. Betti, and R. L. McCrory, Phys. Plasmas **8**, 2315 (2001).

18. G. Hazak *et al.*, Phys. Plasmas **5**, 4357 (1998).

19. T. J. B. Collins, A. Poludnenko, A. Cunningham, and A. Frank, Phys. Plasmas **12**, 062705 (2005).

20. R. Betti, K. Anderson, T. R. Boehly, T. J. B. Collins, R. S. Craxton, J. A. Delettrez, D. H. Edgell, R. Epstein, V. Yu. Glebov, V. N. Goncharov, D. R. Harding, R. L. Keck, J. H. Kelly, J. P. Knauer, S. J. Loucks, J. A. Marozas, F. J. Marshall, A. V. Maximov, D. N. Maywar, R. L. McCrory, P. W. McKenty, D. D. Meyerhofer, J. Myatt, P. B. Radha, S. P. Regan, C. Ren, T. C. Sangster, W. Seka, S. Skupsky, A. A. Solodov, V. A. Smalyuk, J. M. Soures, C. Stoeck, W. Theobald, B. Yaakobi, C. Zhou, J. D. Zuegel, J. A. Frenje, C. K. Li, R. D. Petrasso, and F. H. Séguin, Plasma Phys. Control. Fusion **48**, B153 (2006).

21. V. N. Goncharov, P. McKenty, S. Skupsky, R. Betti, R. L. McCrory, and C. Cherfils-Clérouin, Phys. Plasmas **7**, 5118 (2000).

22. W. K. Levedahl and J. D. Lindl, Nucl. Fusion **37**, 165 (1997).

23. V. N. Goncharov, J. P. Knauer, P. W. McKenty, P. B. Radha, T. C. Sangster, S. Skupsky, R. Betti, R. L. McCrory, and D. D. Meyerhofer, Phys. Plasmas **10**, 1906 (2003); K. Anderson and R. Betti, Phys. Plasmas **10**, 4448 (2003).

24. K. Anderson and R. Betti, Phys. Plasmas **11**, 5 (2004); R. Betti, K. Anderson, J. Knauer, T. J. B. Collins, R. L. McCrory, P. W. McKenty, and S. Skupsky, Phys. Plasmas **12**, 042703 (2005).

25. T. J. B. Collins and S. Skupsky, Phys. Plasmas **9**, 275 (2002).

26. O. S. Jones *et al.*, in *NIF Laser System Performance Ratings*, Supplement to Third Annual International Conference on Solid State Lasers for Application to Inertial Confinement Fusion (SPIE, Bellingham, WA, 1998), Vol. 3492, pp. 49–54.

27. V. N. Goncharov, S. Skupsky, P. W. McKenty, J. A. Delettrez, R. P. J. Town, and C. Cherfils-Clérouin, in *Inertial Fusion Sciences and Applications 99*, edited by C. Labaune, W. J. Hogan, and K. A. Tanaka (Elsevier, Paris, 2000), pp. 214–219.

28. R. Kishony and D. Shvarts, Phys. Plasmas **8**, 4925 (2001).

29. S. E. Bodner, J. Fusion Energy **1**, 221 (1981).

30. J. Hund and A. Nikroo, General Atomics, private communication (2006).

31. R. Epstein, T. J. B. Collins, J. A. Delettrez, V. N. Goncharov, J. P. Knauer, J. A. Marozas, P. W. McKenty, P. B. Radha, and V. A. Smalyuk, Bull. Am. Phys. Soc. **50**, 114 (2005).

32. V. N. Goncharov, S. Skupsky, T. R. Boehly, J. P. Knauer, P. McKenty, V. A. Smalyuk, R. P. J. Town, O. V. Gotchev, R. Betti, and D. D. Meyerhofer, Phys. Plasmas **7**, 2062 (2000).

33. R. Epstein, J. Appl. Phys. **82**, 2123 (1997).

34. J. E. Rothenberg, J. Opt. Soc. Am. B **14**, 1664 (1997).

35. S. Skupsky and R. S. Craxton, Phys. Plasmas **6**, 2157 (1999).

36. S. V. Weber, S. G. Glendinning, D. H. Kalantar, M. H. Key, B. A. Remington, J. E. Rothenberg, E. Wolfrum, C. P. Verdon, and J. P. Knauer, Phys. Plasmas **4**, 1978 (1997).

High-Intensity Laser Interactions with Mass-Limited Solid Targets and Implications for Fast-Ignition Experiments on OMEGA EP

Introduction

Picosecond laser–solid interaction at relativistic intensities has generated a high level of experimental[1–5] and theoretical[6–9] interest in recent years. This is due to its relevance to the fast-ignitior (FI) scheme for achieving inertial confinement fusion (ICF)[10,11] and to backlighter development for the x-ray radiography of dense materials.[12,13]

The interaction of high-intensity, $I \sim (10^{18}$ to $10^{21})$ W/cm^2, picosecond laser pulses with solid targets produces copious energetic electrons. Remarkable conversion efficiencies of up to 40% of the incident laser energy have been reported,[1,14] with characteristic electron energies ranging from ~100 keV up to several MeV.[14–16]

When these energetic electrons propagate into the bulk of a solid target, hard-x-ray bremsstrahlung and characteristic inner-shell line emission are produced [the first observations of K$_\alpha$ radiation from picosecond laser–produced plasmas were presented as early as 1979 (Ref. 17)]. The brightness of this radiation, either continuous or line emission, makes it valuable for x-ray radiography of ICF implosions, a primary motivation for the recent experiments of Theobald *et al.*, reported in Ref. 18. This article investigates, using semi-analytic and implicit-hybrid particle-in-cell (PIC) modeling,[19,20] the K-shell line emission from mass-limited targets and compares the predictions with these experiments.

The inner-shell line emission provides information on the energetic electrons produced in the interaction and its subsequent transport and heating of the target.[1,4,21–37] The main conclusion is that mass-limited targets of mid-Z elements provide an excellent "test bed" for FI physics due to simplifications afforded by the near-perfect hot-electron refluxing and by the effects on the line emission caused by the target heating.

Electron "refluxing" within the target, due to reflection from the surface sheath fields, is well known[9,28,29] and is connected to the generation of fast protons and ions.[30,31] When considering the generation of secondary radiation, this effect has not always been taken into account, e.g., Refs. 32–34. Unlike the case of proton acceleration,[9,28] the effect of hot electrons refluxing on the K-shell production efficiency has not been described, rather the emphasis has been placed on the energy dependence of the K-shell ionization cross section[34] and the competition with penetration depth and reabsorption of the characteristic radiation,[26,35] which is appropriate for massive targets.

It is shown here that the K-shell yields, per joule of hot electrons, of mass-limited targets are insensitive to the hot-electron spectrum and laser intensity. This is valid as long as the hot-electron stopping is classical and arises because of the energy dependence of the K-shell ionization cross section and electron range. It requires that relativistic corrections to the K-shell ionization cross section are accounted for.[36] The intensity dependence of K-shell production efficiency, expressed per joule of incident laser energy, is sensitive to the hot-electron conversion efficiency $\eta_{L \to e}(I)$. The experimental K$_\alpha$ yields from Ref. 18 are found to be consistent with the model if an intensity-independent hot-electron conversion efficiency of $\eta_{L \to e} = 10\%$ is assumed over the range $10^{18} < I < 10^{20}$ W/cm^2.

Volumetric heating of reduced-mass targets[18] is predicted to be sufficient that ionization of the copper M shell will strongly affect the ratio of K$_\beta$ to K$_\alpha$ emission.[21] Three-dimensional *LSP* calculations,[19,20] including the relevant atomic processes,[27] have been performed for parameters of the RAL (Rutherford Appleton Laboratory) experiments and spatially resolved images of both K$_\alpha$ and K$_\beta$ emission have been produced. It is shown that these measurements can be used to infer the degree of bulk heating and provide a *consistency check* on the hot-electron conversion efficiency obtained by fitting the absolute K$_\alpha$-photon yields. A comparison between the predicted ratio of K$_\beta$- to K$_\alpha$-photon production, for $\eta_{L \to e} = 10\%$, with the experimentally observed ratios is not conclusive. Rather, it suggests the usefulness of the technique, which will be pursued in future experiments on OMEGA EP currently under construction at LLE.[38]

The following sections (1) summarize the Theobald *et al.*[18] experiments, (2) describe a semi-analytic model for K-shell line emission in mass-limited targets, (3) compare the modeling pre-

dictions with the RAL experiments, (4) present the *LSP* calculations of volumetric heating, and (5) present the conclusions.

RAL PW and 100-TW Experiments

Pulses of 1.06-μm laser light from either the RAL Petawatt (PW) or the 100-TW Facility were focused with an *f*/3 off-axis parabola to ~10- to 100-μm spots onto Cu foil targets, achieving laser intensities between 3×10^{18} to 4×10^{20} W/cm^2. The foil thicknesses ranged between $d = 1$ to 75 μm, and the areas from $A = 0.01$ to 8.0 mm^2, resulting in target volumes of $V = 10^{-5}$ to 10^{-1} mm^3. The pulse durations ranged from 0.4 to 10 ps. Inner-shell emission and resonance-line emission occurred in these experiments. The K$_\alpha$ and K$_\beta$ lines are emitted by the inner-shell transitions when an L- or M-shell electron fills a vacancy in the K shell, respectively, and the corresponding excess energy is radiated away by a photon in competition with Auger decay. Both x rays and energetic electrons may produce K-shell vacancies, assuming that the radiation has sufficient energy to excite above the K edge (for Cu, $h\nu > 9$ keV). Indirect inner-shell emission due to absorption of continuous x-ray radiation that is produced while suprathermal electrons decelerate in the target is negligible for elements with an atomic number $Z < 30$ (Refs. 37 and 39). Energetic electrons are the main contribution to K$_\alpha$ and K$_\beta$ production in high-intensity, ultrashort, laser–solid interaction with low- and mid-*Z* materials.[24,26] X-ray spectra were collected, and the total number of K$_\alpha$ and K$_\beta$ photons emitted, per unit laser energy, were obtained as described in Theobald *et al*.[18] The resonance-line emission is not discussed here.

In contrast with previous experiments using massive targets, absorption of the characteristic x rays is modest. As a result, the mechanism controlling the intensity dependence of the K$_\alpha$ yield is no longer the interplay between the electron penetration depth relative to the K-photon attenuation length as in earlier experiments.[26,40] A different model is required to predict the K-shell yield and its dependence on interaction parameters.

Description of a Semi-Analytic Model

The absolute K-shell photon yield N_k is the sum of the yield from two hot-electron populations: (1) electrons that escape from the target after losing only part of their energy (*l*), and (2) electrons that reflux, losing all of their energy to the target (*r*), i.e., $N_k = (N_k)_l + (N_k)_r$. The distinction is of significance only for targets thinner than the expected electron range in the material. For copper, this corresponds to targets thinner than a few millimeters for interaction intensities of ~10^{19} W/cm^2.

A simple estimate of the "refluxing efficiency," which is the ratio of the number of electrons stopped in the target to the total, $\eta_r = (N_e - N_l)/N_e$, can be given roughly by estimating the capacitance of the target. Assuming the target is a perfectly conducting thin disk in vacuum, $C = 8 \, \epsilon_0 r \sim 70.8 \times 10^{-12} \, r$ farads, where r is the radius of the disk in meters, then a loss of $N_l = 4.42 \times 10^{11}$ (r/1 mm) (V/1 MV) electrons is required to produce a potential drop V in a target of radius r. This will be modified if the target is not isolated, for example, by a conducting target stalk. The required potential is determined self-consistently so that, for Boltzmann-distributed electrons at a temperature T, the potential satisfies $N_l = N_e \exp(-eV/T)$. This leads to the equation $\exp(-\Phi) = \kappa\Phi$, where $\Phi = eV/T$ and κ is given by $\kappa = 7.08 \times 10^{-2} rT^2/(\eta_{L\to e} E_L)$, where r is in mm, T is in MeV, and E_L is in joules. This can be solved for Φ, giving the refluxing efficiency $\eta_r = 1 - \exp(-\Phi)$, with the results for varying laser intensity and foil radius shown in Fig. 109.36. Note that the efficiency is extremely high for the parameters of the RAL experiments, $\eta_r > 90\%$.
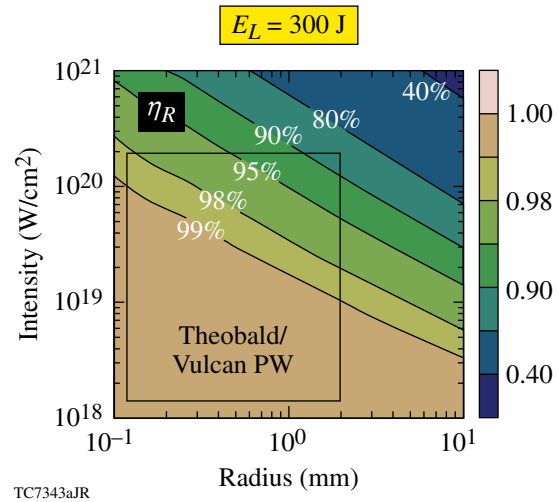
Figure 109.36
Refluxing efficiency obtained from the capacitance model. The hot-electron temperature is assumed to depend on laser intensity according to the ponderomotive scaling.[6]

The refluxing electrons are prevented from escaping by the self-consistent electromagnetic fields, so that the electron stopping can be treated as if the electrons were propagating in an infinite medium. The K-photon yield $(N_k)_r$ is computed by integrating along the path of electrons whose initial energies are described by an energy distribution $f(E_0)$ as long as (1) energy loss is accurately described with a continuous slowing-down formula (dE/ds), and (2) cold cross sections $\sigma_K(E)$ for K-shell ionization are appropriate (note that for copper $Z = 29$, only direct K-shell ionization is significant[37]). The contribution to the total yield N_k due to refluxing electrons $(N_k)_r$ is then given by

TC7343aJR

$$(N_k)_r = (\eta_r N_e) \int_0^\infty dE_0 f(E_0) \int_{E_0}^0 dE \omega_k n_{Cu} \sigma_k \left(\frac{dE}{ds}\right)^{-1} \quad (1)$$

$$= (\eta_r N_e) n_{Cu} \omega_k \int_0^\infty dE_0 f \int_0^{s(E_0)} ds \sigma_k \left[E(E_0, s)\right], \quad (2)$$

where N_e is the total number of hot electrons, ω_k is the fluorescence yield ($\omega_k = 0.44$ for Cu)[41] (the fraction of K-ionization events resulting in K-quantum emission), and n_{Cu} is the number density of copper atoms in the target. The contribution from the "loss" electrons $(N_k)_l$ is similarly obtained to the above but by replacing η_r with $1-\eta_r$ and truncating the electron path length s in the integral Eq. (2) whenever it exceeds the target thickness $s(E_0) \rightarrow s_{max} = \min[s(E_0), d]$ (if the target is thick enough so that multiple scattering is important, an accurate calculation of this term would require a Monte Carlo calculation). To distinguish between the K-emission lines, e.g., K_β, $K_{\alpha 1}$, $K_{\alpha 2}$, etc., of corresponding energies $\epsilon_{K_i} = 8.906$, 8.048, and 8.028 keV, respectively, the relative emission probabilities p_i are introduced, defined according to $N_{K_i} = p_i N_k$, where "i" stands for either "β," "α_1," or "α_2." The probabilities are taken to be $p_a(= \Sigma_{i=\alpha_1,\alpha_2} p_i)$, $p_\beta = 0.88$, 0.12, respectively, whose values correspond to cold Cu at solid density.[42] From this model the electron-to-K-photon generation efficiency $\eta_{e \rightarrow k}$ is determined. This is defined as $E_k = \eta_{e \rightarrow k} E_e$, where the energy in electrons is given by $E_e = N_e \langle E_e \rangle$, and in K photons by $E_k = \epsilon_k N_k$. Here ϵ_k is the average fluorescence energy $\epsilon_K = \sum_i p_i \epsilon_{K_i}$ (8.14 keV for copper) and $\langle E_e \rangle = \int dE E f(E)$ is the average electron energy, resulting in

$$\eta_{e \rightarrow k} = n_{Cu} \omega_k \frac{\epsilon_k}{\langle E_e \rangle}$$

$$\times \left\{ \eta_r \int_0^\infty dE_0 f(E_0) \int_0^{s(E_0)} ds \sigma_k \left[E(E_0, s)\right] \right.$$

$$\left. + (1 - \eta_r) \int_0^\infty dE_0 f \int_0^{s_{max}} ds \sigma_k \left[E(E_0, s)\right] \right\}. \quad (3)$$

A direct comparison between the experimental production efficiency (yield/laser joule) and the calculated generation efficiency is not straightforward. The experimentally observable quantity $N_{k,obs}$ requires a knowledge of the detector solid angle, the filter, and detector efficiency.[18] Given this, the efficiency

$$\eta_{e \rightarrow k} = \frac{\epsilon_k \left(N_{k,obs} / f_{abs}\right)}{\eta_{L \rightarrow e} E_L} \quad (4)$$

may be computed only if the K-shell photon reabsorption fraction f_{abs} and the hot-electron production efficiency $\eta_{L \rightarrow e} = E_e / E_L$ are known. E_L is the energy in the laser pulse. The absorption fraction f_{abs} can be easily computed,[43] but the electron-production efficiency is subject to a great deal of uncertainty.[1] In principle, this could depend on many factors, $\eta_{L \rightarrow e} = \eta_{L \rightarrow e}(I_L, E_L, \nabla \log n, \ldots)$, where, for example, I_L is the laser intensity, E_L is the laser energy, and $\nabla \log n_e$ is the electron-plasma density scale length.[31,44] For current purposes it is either treated as a free "fitting" parameter, or taken to be a function of laser intensity only, with the dependence as given by Ref. 27, a fit to data obtained on the Nova Petawatt.[1] The predicted efficiency, obtained using Eq. (3), requires further specification of the hot-electron spectrum $f(E)$. Exponentially distributed electron energies are assumed, $f(E)dE = (1/T) \exp(-E/T)dE$, and the laser intensity connected to the temperature T, equal to the average energy for an exponential distribution, $\langle E \rangle = T$, using the "ponderomotive scaling" of Wilks,[6,45] $T = 0.511 \left[\left(1 + I_{18} \lambda_{\mu m}^2 / 1.37 \right)^{1/2} - 1 \right]$ MeV. Different intensity-temperature scalings have been proposed in the literature.[46,47] The calculations have also been performed with a relativistic Maxwellian (Jüttner) distribution,[48] leading to no change in the overall conclusions.

Equation (3), using ITS (Integrated Tiger Series) data for hot-electron stopping power and K-shell ionization cross sections,[49,50] the fluorescence probability, and the relative emission probabilities, taken together with the absorption fraction, the refluxing fraction, the hot-electron conversion efficiency, the hot-electron distribution function, and hot-electron temperature scaling as described in the text fully defines the model. From this the conversion efficiency of laser energy to K photons $\eta_{L \rightarrow k}$ can be computed with no free parameters.

Comparison Between the Modeling and RAL Experimental Results

Figure 109.37 shows K_α-photon yield, per joule of laser energy, as a function of laser intensity from the model described above with constant hot-electron conversion efficiencies of $\eta_{L \rightarrow e} = 10\%$ and 20% (solid curves). The predicted K_α production efficiency is almost independent of laser intensity over the range $I = 2 \times 10^{18}$ to 2×10^{20} W/cm^2 and takes the value $(\eta_{L \rightarrow k})_{model} \sim 4 \times 10^{-4}$ for $\eta_{L \rightarrow e} = 10\%$. This is consistent with experimental data taken from shots with 200 to 500 J of laser energy on a 20-μm-thick target (black triangles). Although not the case in Fig. 109.38, the experimental data are usually corrected for absorption and not the model predictions. The independence of efficiency on hot-electron temperature (laser intensity) over the experimental range of intensities can

be understood if perfect refluxing is assumed: the number of K-shell photons per electron is essentially given by the product of the range $s_0 \equiv s(E_0) = \int_{E_0}^{0} dE (dE/ds)^{-1}$ and the probability
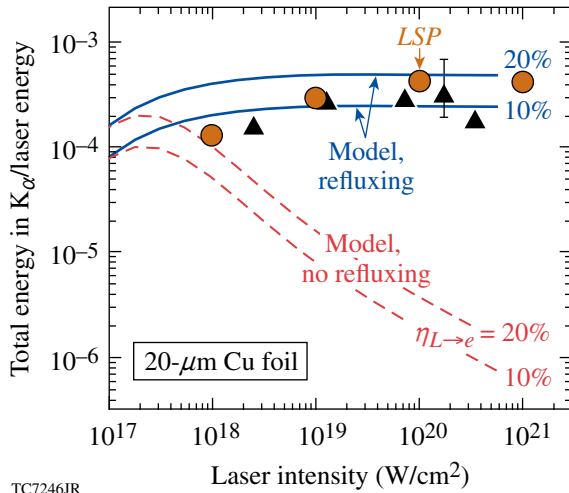

Figure 109.37
K_α production efficiency versus laser intensity for 20-μm-thick foils. The semi-analytic model with refluxing and a 10% hot-electron conversion efficiency (lower solid line) agrees with the *LSP* calculation (circles) and the experimental data (triangles). Also shown are the model predictions with no refluxing (dashed lines). The predictions, and not the data, have been corrected for reabsorption in the target.
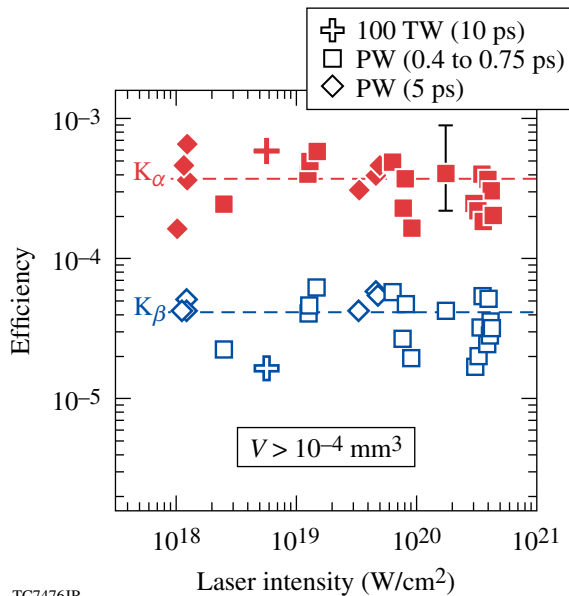

Figure 109.38
Experimental K_α (solid markers) and K_β (open markers) production efficiency as a function of laser intensity for both the 100-TW laser system (crosses) and the PW laser for short pulses (squares) and long pulses (diamonds). Only targets having a volume greater than 10^{-4} mm^3 are shown.

of K-shell emission per unit path $\omega_k n_{Cu} \sigma_k(E_0)$ [Eq. (1)]. When normalized by E_0, this product is a very weak function of the electron energy, provided that the relativistic corrections to the cross section $\sigma_k(E)$ are properly taken into account.[51] If the refluxing is ignored, $\eta_r \to 0$, then the dashed curves result. The *LSP* predictions, shown as circles in Fig. 109.37, are very similar to the semi-analytic model. This is to be expected because *LSP* uses the same cross sections as the model and the stopping is found to be due to classical collisions and not anomalous mechanisms. The discrepancies are a result of the approximations in the *LSP* collision model.[20]

Agreement can be obtained only for high refluxing efficiency, $\eta_r \sim 100\%$, leading to the broad conclusion that reduced-mass targets produce the same number of K photons as targets of infinite thickness (but without the reabsorption). It follows that the K-shell yield is independent of the target geometry (volume). As Fig. 109.38 shows, this is actually observed.

Figure 109.38 shows both the K_α- (solid markers) and K_β-photon production efficiencies (open markers) from both the 100-TW system (crosses) and the RAL PW (squares and diamonds) as a function of laser intensity for a range of target geometries having volumes $10^{-4} < V < 10^0$ mm^3. (The target thicknesses employed were 20 μm for the 100-TW shots, 5 to 75 μm for the PW shots with 5-ps pulses, and 5 to 25 μm for the PW shots with 0.4- to 0.75-ps pulses.) The yields are essentially constant and the ratio of K_β/K_α is consistent with the expected cold matter value $N_{K_\beta}/N_{K_\alpha} = 0.14$. The predictions of the semi-analytic model with $\eta_{L \to e} = 10\%$ are shown as dashed lines.

A hot-electron conversion efficiency of 10% is lower than the $\eta_{L \to e} \sim (20\%-40\%)$ quoted in the literature for these intensities, e.g., in Ref. 15. Reference 1 suggests that the conversion efficiency $\eta_{L \to e}$ rises significantly with laser intensity with efficiencies of $\eta_{L \to e} \sim 40\%$ for laser intensities of 10^{20} W/cm^2. Figure 109.39 shows the predicted K_α yield from the model as a function of laser intensity when the functional form of $\eta_{L \to e}$ is fit to the Nova PW data.[1,27] The solid lines are lines of constant conversion efficiency $\eta_{L \to e}$ and the shaded area, bounded by the dashed curves, is the prediction of the model with a reasonable allowance made for scatter in the data of Ref. 1. With the conversion efficiency prescribed in this way, there are no free parameters in the model.

The discrepancy between the simple model and the experiment at high, $I \gtrsim 1 \times 10^{19}$ W/cm^2, and low, $I \sim 10^{18}$ W/cm^2, intensities might have several causes. Additional energy-loss
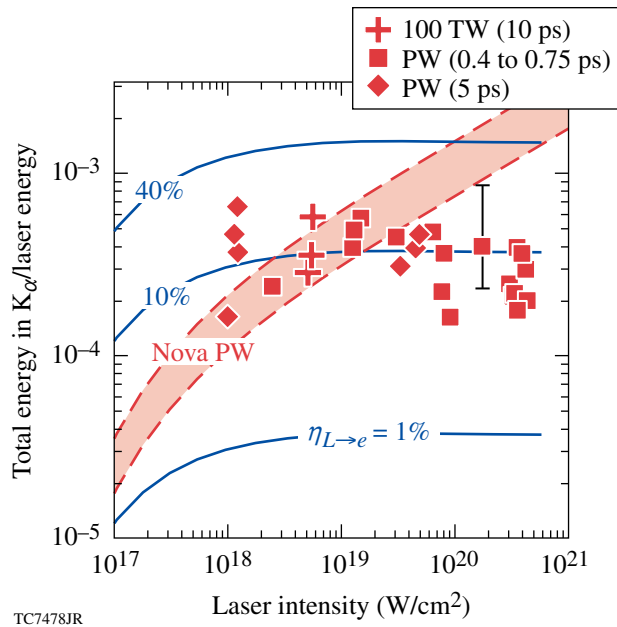
Figure 109.39

Experimental K_α production efficiency from the 100-TW system (crosses) and PW laser system with short pulses (squares) and long pulses (diamonds) as a function of laser intensity. The predictions of the semi-analytic model with hot-electron conversion efficiencies taken from a fit to Nova PW data are indicated by the shaded area bounded by dashed lines. The solid curves are lines of constant hot-electron conversion efficiency.

channels for the hot electrons such as the acceleration of protons (or ions) from the back side of the target, "anomalous" stopping mechanisms such as resistive inhibition,[52] or current filamentation instabilities, presumably becoming more important at higher intensities[9] are potential candidates. Large magnetic fields could bottle energy up at the surface,[53] where the plasma is too hot to produce K photons.

An experimentally verifiable consistency check on the inferred hot-electron conversion efficiencies, computed by fitting the absolute K_α yields, can be made by considering the volumetric heating created by the hot electrons. The collisional dissipation of the fast electrons, or the return current of the slower electrons, will volumetrically heat the foil on the picosecond time scale. The heating on this time scale, the same time scale as the K-shell emission, can be due only to the hot electrons and will be a measure of their energy content. The target heating can be quantified by measuring the ratio of K_β to K_α emission N_{K_β}/N_{K_α} because for the expected temperature rise $T \gtrsim 100$ eV, significant ionization of the M shell is expected[21] (Fig. 109.40). Smaller-mass targets are expected to achieve higher temperatures since an equal amount of energy is deposited in a smaller volume.[21]

Figure 109.40 shows the ionization degree Z^* for solid-density copper as a function of temperature according to the Thomas–Fermi model.[54] The main part of the figure shows an estimate of the line ratio as a function of temperature based on this ionization (the cold ratio has been weighted by the relative population of the M shell). It is not straightforward to estimate the ratio of the absolute K_α and K_β yields because the heating rate is a function of time and space, as is the hot-electron population. To take this properly into account we have performed *LSP* calculations.
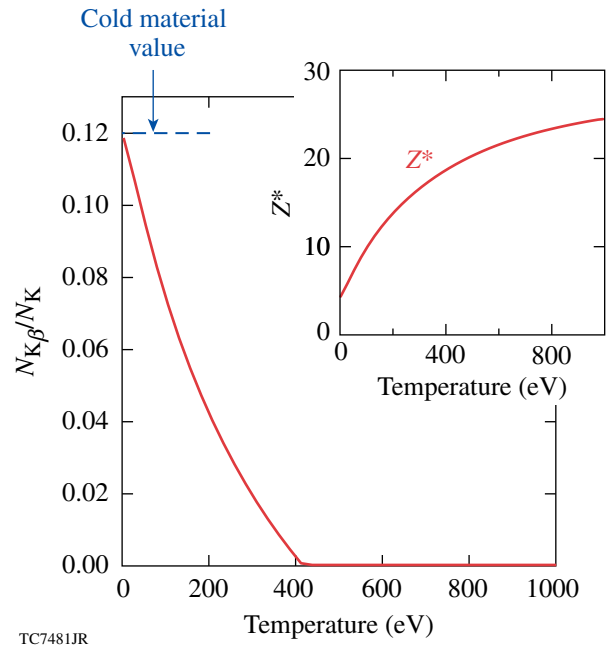
Figure 109.40

Reduction in the ratio of K_β to total K-emission probability as a function of plasma temperature, based on the Thomas–Fermi average ionization state Z^* (inset).

LSP Calculations of Volumetric Target Heating

Three-dimensional numerical calculations of target heating and K-shell emission were performed using *LSP*.[19,20] The targets were square copper foils of either (80×80) μm^2 or (160×160) μm^2 area, and either 10 μm or 20 μm in thickness. The hot-electron source was prescribed, as is usual in MC and implicit-hybrid calculations.[26,53] Electrons from the cold bulk were promoted in energy inside a region defined laterally by the laser spot and extending to a depth of 0.5 μm into the target. The rate of promotion was defined so that the power translated into the electrons was a constant fraction $\eta_{L\to e}$ of the assumed incident laser power. The energy spectrum of the promoted electrons was an isotropic Maxwellian with an average energy defined according to the local laser intensity on the surface of

the foil (assuming the ponderomotive scaling). A realistic laser spot shape was assumed, taken from Ref. 55, where 50% of the energy is contained within a characteristic diameter, $a_0 \sim$ 16 μm. A radial temperature dependence of the hot electrons resulted from the assumed axial symmetry of the spot, similar to that of Ref. 26. The total injected hot-electron kinetic energy was taken to be either 10 or 30 J, with a pulse duration of 0.5 or 1.5 ps, respectively. This held the average laser intensity over the central spot constant at $I = 1.2 \times 10^{19}$ W/cm^2. The total duration of the simulations was 15 ps and the targets were either 10 or 20 μm thick. Inter- and intra-species collisions are included in the calculation,[19,20] the effect of which is to slow the hot particles and to heat the initially cold target. It was observed that $\gtrsim$90% of the hot-electron energy was converted into thermal energy of the target primarily as a result of direct e–e collisions, with only a few percent being either lost or converted into electromagnetic-field energy.

Figure 109.41 shows the peak temperatures attained by 20-μm-thick targets that have been taken on a slice transverse to the target normal at a depth of 5 μm. In the left (right)-hand column, 10 (30) J of energy was introduced into hot electrons. The target volume was 1.28×10^{-4} (5.12×10^{-4}) mm^3 in the first (second) row. The smallest target reaches a peak tempera-
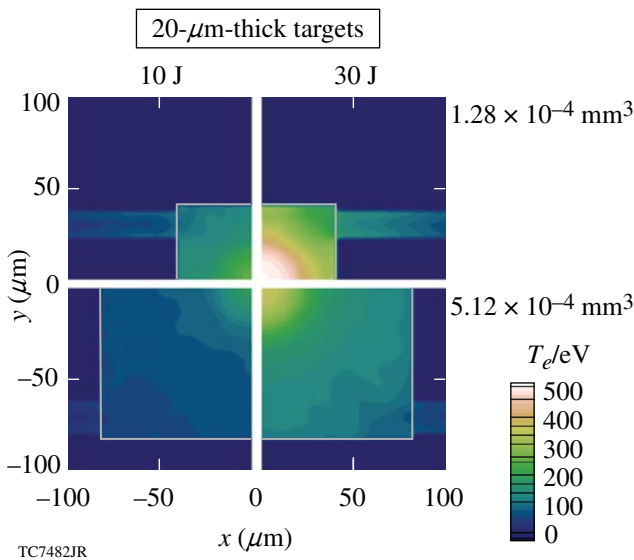

Figure 109.41
The images show target heating from four 3-D *LSP* calculations on a slice perpendicular to the target normal taken at a depth of 5 μm from the target surface. The heating was computed with 10 J and 30 J of energy in hot electrons (columns) and for target volumes of $V = 1.28 \times 10^{-4}$ and 5.12×10^{-4} mm^3 (rows). Only one quadrant of each foil was modeled, the remainder completed by assuming symmetry about the x and y axes.

ture of ~500 eV, while the most massive ~100 eV. Only one quadrant of each foil was modeled, the remainder completed by assuming symmetry about the x and y axes. *LSP* assumes an ideal equation of state (EOS) for the various particle species. Here, the temperatures have been renormalized assuming a Thomas–Fermi EOS.

1. Reasons for the Absence of Enhanced Stopping in the *LSP* Calculations

The stopping power of hot electrons can be increased above that due to particle collisions by the presence of resistive electric fields.[8,52] The current carried by the hot, laser-produced electrons far exceeds the Alfvén-limiting current for vacuum propagation, $I_A = 17\gamma_b\beta_b$kA,[56] where β_b is the beam velocity normalized to the speed of light, $\beta_b = v_b/c$, and γ_b is the relativistic gamma factor $\gamma_b = (1 + \beta_b^2)^{-1/2}$. Estimating the current according to $I \sim \eta_{L \to e}\, eI_L A/T_{hot} = 25$ MA for $I_L = 10^{19}$ W/cm^2, $A = \pi \times (20)^2$ μm^2, $\eta_{L \to e} = 0.2$, and $T_{hot} = 1$ MeV. This is several hundred times larger than the Alfvén limit $I_{hot} \sim 560\left[2.7/(\gamma_b\beta_b)\right]I_A$.

Such beams cannot propagate unless there is a compensating return current. In metals and plasmas, the return current is naturally provided by cold electrons. The cold current represents a drag on the hot component through the resistive electric field $\vec{E} = \vec{j}/\sigma$, where σ is the electrical conductivity (assuming scalar conductivity and neglecting the Hall term). The resistive electric field $E \cong j/\sigma$ may be estimated to be ~2 × 10^5 kV/cm for the above parameters. This would stop a 1-MeV electron in ~50 μm. In making this estimate, a conductivity of $\sigma = 1 \times 10^6$ Ω^{-1}m^{-1} has been assumed. This value is representative of the minimum conductivity of copper (other mid-Z metals are similar). Typically this minimum occurs at a few 100 eV, thereafter increasing with temperature $\sigma \sim T_e^{3/2}$ according to the Spitzer value.

Resistive inhibition would be expected to be dominant, if the characteristic range due to the resistive electric field is small compared with the range due to binary collision events s_0. The range estimated above is shorter than the range in copper of $s_0 = 700$ (3800) μm for 1.0 (5.0)-MeV electrons, respectively. In the current experiments, this is not the full story. In the thin-foil case, $d < s_0$, the "resistive" range should instead be compared with the foil thickness d. This is because refluxing hot electrons can contribute significantly to the return current for times greater than a hot-electron transit time. For this reason the *LSP* calculations indicate that resistive inhibition is not an important effect for the parameters of the experiments of Ref. 18. This is further borne out by the predictions of the semi-analytic model that are consistent with the usual stopping power.

Sources of plasma resistivity that are not currently modeled by *LSP*, such as ion-acoustic turbulence, possibly resulting from instability of the return current, have the potential to modify this picture. If the anomalous resistivity were to be a few times larger than the maximum resistivity quoted above, then the resistive range would become smaller than the typical target thickness. This could substantially reduce the contribution of hot electrons to the return current.

2. Effect of Target Heating on K-Shell Line Ratios

The effect of target heating on the relative emission probability of the K_β line has been estimated by adjusting the emission probability p_{K_β} in the *LSP* calculations, according to Fig. 109.40, using the local temperature at the time when the emission process took place. The *LSP* predictions for the line ratio N_{K_β}/N_{K_α}, for three target volumes and 10 (30) J of hot-electron energy, are shown by the light upper (dark lower) open diamonds in Fig. 109.42. Figure 109.42 also shows the experimentally determined ratio of K_β to K_α yield N_{K_β}/N_{K_α} from the RAL 100-TW (crosses) and RAL PW (squares, diamonds, and circles) as a function of target volume.
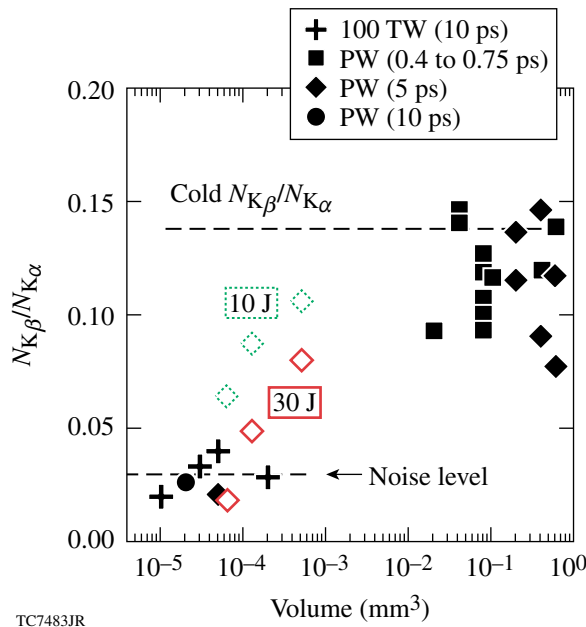
Figure 109.42

Experimental ratio of K_β to K_α yield N_{K_β}/N_{K_α} from the RAL 100-TW (crosses) and RAL PW (squares, diamonds, and circles) as a function of target volume. The open diamonds show *LSP* predictions in the cases of 10 J of energy in hot electrons (upper light) and 30 J (lower dark).

The scatter in the experimental data is too large for the consistency check to be conclusive, especially considering that the experimental K_β signals, for target volumes $V \lesssim 10^{-4}$ mm,

are very close to the noise level of the detector at ~3%. It can be said, however, that the PW data are not inconsistent with a hot-electron conversion efficiency of 10%. For example, the close agreement of the 30-J calculations with the experimental data point (shot 5021803) at $V = 5 \times 10^{-5}$ mm^3, where the energy in the central spot was ~150 J.

3. Spatially Resolved K-Shell Emission

The spatial distribution of the K-shell emission reflects the trajectories of the hot electrons[57] and also the volumetric heating profile. Although the K-shell emission was not imaged in Ref. 18, images of the K_α emission from the *LSP* calculation can be produced (Fig. 109.43).
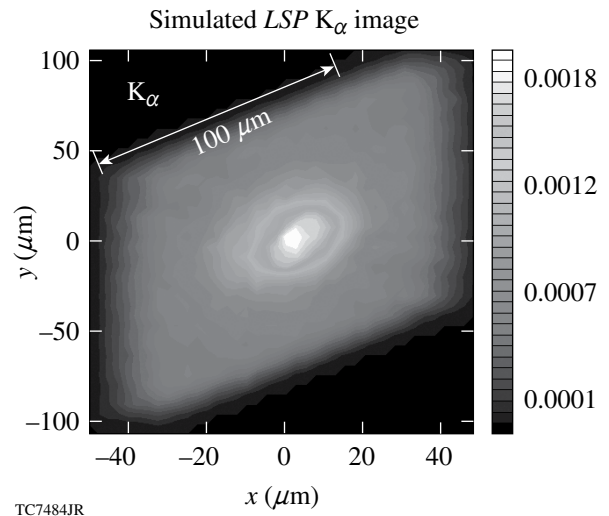
Figure 109.43

Image of K_α emission obtained from 3-D *LSP* calculations.

Conclusions

A semi-analytic model has been developed, and implicit-hybrid particle-in-cell code simulations (*LSP*)[19,20] have been performed to study fast-electron propagation, inner-shell x-ray photon production, and heating of mid-*Z*, mass-limited targets.

For the conditions considered, motivated by RAL experiments,[18] hot-electron flow within the target is dominated by refluxing at the electrostatic sheath at the target surface. This effect is responsible for the observed absolute x-ray yield. The semi-analytic model has been used to demonstrate the insensitivity of the yield to target geometry and hot-electron temperature under the conditions of hot-electron refluxing and classical stopping.

The experimental K_α yields are consistent between both models and experiment for an intensity-independent electron

conversion efficiency of ~10%. This result raises some concerns since 15% to 50% conversion efficiencies have been reported in the literature, e.g., Refs. 1, 6, 7, and 15. Surface fields[18] or anomalous stopping mechanisms, e.g., Ref. 58, might prevent hot electrons from penetrating to the cold interior of the target where they can efficiently produce K_α photons. If this were the case, a higher hot-electron conversion efficiency would be required to produce the observed K_α yields.[18] Target expansion is not a likely explanation for the discrepancy because it is responsible for only a few-percent decrease in the target density over the period of K_α emission. The ratio of K_β to K_α line emission is related to the degree of target heating that may be used as a consistency check on the hot-electron conversion efficiency.

Three-dimensional *LSP* calculations of volumetric target heating have been performed giving predictions for line ratios as a function of hot-electron conversion efficiency. At present, the experimental data set is not sufficiently precise to conclusively choose between the predictions; however, it does suggest the usefulness of the technique, which will be pursued in future experiments on OMEGA EP.

ACKNOWLEDGMENT

REFERENCES

1. M. H. Key, M. D. Cable, T. E. Cowan, K. G. Estabrook, B. A. Hammel, S. P. Hatchett, E. A. Henry, D. E. Hinkel, J. D. Kilkenny, J. A. Koch, W. L. Kruer, A. B. Langdon, B. F. Lasinski, R. W. Lee, B. J. MacGowan, A. MacKinnon, J. D. Moody, M. J. Moran, A. A. Offenberger, D. M. Pennington, M. D. Perry, T. J. Phillips, T. C. Sangster, M. S. Singh, M. A. Stoyer, M. Tabak, G. L. Tietbohl, M. Tsukamoto, K. Wharton, and S. C. Wilks, Phys. Plasmas **5**, 1966 (1998).

2. P. A. Norreys *et al*., Phys. Plasmas **6**, 2150 (1999).

3. K. A. Tanaka *et al*., Phys. Plasmas **7**, 2014 (2000).

4. J. A. Koch *et al*., Phys. Rev. E **65**, 016410 (2001).

5. R. B. Stephens *et al*., Phys. Rev. E **69**, 066414 (2004).

6. S. C. Wilks *et al*., Phys. Rev. Lett. **69**, 1383 (1992).

7. B. F. Lasinski *et al*., Phys. Plasmas **6**, 2041 (1999).

8. L. Gremillet *et al*., Phys. Plasmas **9**, 941 (2002).

9. Y. Sentoku *et al*., Phys. Rev. Lett. **90**, 155001 (2003).

10. M. Tabak *et al*., Phys. Plasmas **1**, 1626 (1994).

11. N. G. Basov, S. Yu. Gus'kov, and L. P. Feokistov, J. Sov. Laser Res. **13**, 396 (1992).

12. O. L. Landen *et al*., Rev. Sci. Instrum. **72**, 627 (2001).

13. H.-S. Park *et al*., Rev. Sci. Instrum. **75**, 4048 (2004).

14. K. Yasuike *et al*., Rev. Sci. Instrum. **72**, 1236 (2001).

15. K. B. Wharton *et al*., Phys. Rev. Lett. **81**, 822 (1998).

16. R. Kodama *et al*., Phys. Plasmas **8**, 2268 (2001).

17. J. D. Hares *et al*., Phys. Rev. Lett. **42**, 1216 (1979).

18. W. Theobald, K. Akli, R. Clarke, J. Delettrez, R. R. Freeman, S. Glenzer, J. Green, G. Gregori, R. Heathcote, N. Izumi, J. A. King, J. A. Koch, J. Kuba, K. Lancaster, A. J. MacKinnon, M. Key, C. Mileham, J. Myatt, D. Neely, P. A. Norreys, H.-S. Park, J. Pasley, P. Patel, S. P. Regan, H. Sawada, R. Shepherd, R. Snavely, R. B. Stephens, C. Stoeckl, M. Storm, B. Zhang, and T. C. Sangster, Phys. Plasmas **13**, 043102 (2006).

19. D. R. Welch *et al*., Nucl. Instrum. Methods Phys. Res. A **464**, 134 (2001).

20. D. R. Welch *et al*., Phys. Plasmas **13**, 063105 (2006).

21. G. Gregori *et al*., Contrib. Plasma Phys. **45**, 284 (2005).

22. F. Pisani *et al*., Phys. Rev. E **62**, R5927 (2000).

23. E. Martinolli *et al*., Phys. Rev. E **73**, 046402 (2006).

24. H. Chen, B. Soom, B. Yaakobi, S. Uchida, and D. D. Meyerhofer, Phys. Rev. Lett. **70**, 3431 (1993).

25. A. Rousse *et al*., Phys. Rev. E **50**, 2200 (1994).

26. D. C. Eder *et al*., Appl. Phys. B **70**, 211 (2000).

27. R. P. J. Town *et al*., Nucl. Instrum. Methods Phys. Res. A **544**, 61 (2005).

28. A. J. Mackinnion *et al*., Phys. Rev. Lett. **88**, 215006 (2002).

29. H. Chen and S. C. Wilks, Laser Part. Beams **23**, 411 (2005).

30. S. P. Hatchett, C. G. Brown, T. E. Cowan, E. A. Henry, J. S. Johnson, M. H. Key, J. A. Koch, A. B. Langdon, B. F. Lasinski, R. W. Lee, A. J. MacKinnon, D. M. Pennington, M. D. Perry, T. W. Phillips, M. Roth, T. C. Sangster, M. S. Singh, R. A. Snavely, M. A. Stoyer, S. C. Wilks, and K. Yasuike, Phys. Plasmas **7**, 2076 (2000).

31. R. A. Snavely, M. H. Key, S. P. Hatchett, T. E. Cowan, M. Roth, T. W. Phillips, M. A. Stoyer, E. A. Henry, T. C. Sangster, M. S. Singh, S. C. Wilks, A. MacKinnon, A. Offenberger, D. M. Pennington, K. Yasuike, A. B. Langdon, B. F. Lasinski, J. Johnson, M. D. Perry, and E. M. Campbell, Phys. Rev. Lett. **85**, 2945 (2000).

32. U. Teubner, I. Uschmann, P. Gibbon, D. Altenbernd, E. Föster, T. Feurer, W. Theobald, R. Sauerbrey, G. Hirst, M. H. Key, J. Lister, and D. Neely, Phys. Rev. E **54**, 4167 (1996).

33. D. Salzmann *et al*., Phys. Rev. E **65**, 036402 (2002).

34. F. Ewald, H. Schwoerer, and R. Sauerbrey, Europhys. Lett. **60**, 710 (2002).

35. Ch. Reich *et al.*, Phys. Rev. Lett. **84**, 4846 (2000).

36. H. Kolbenstvedt, J. Appl. Phys. **38**, 4785 (1967).

37. M. Green, Solid-State Electron. **3**, 314 (1961).

38. C. Stoeckl, J. A. Delettrez, J. H. Kelly, T. J. Kessler, B. E. Kruschwitz, S. J. Loucks, R. L. McCrory, D. D. Meyerhofer, D. N. Maywar, S. F. B. Morse, J. Myatt, A. L. Rigatti, L. J. Waxer, J. D. Zuegel, and R. B. Stephens, Fusion Sci. Technol. **49**, 367 (2006).

39. M. Green and V. E. Cosslett, J. Phys. D **1**, 425 (1968).

40. T. Feurer, W. Theobald, R. Sauerbrey, I. Uschmann, D. Altenbernd, U. Teubner, P. Gibbon, E. Förster, G. Malka, and J. L. Miquel, Phys. Rev. E **56**, 4608 (1997).

41. W. Bambynek *et al.*, Rev. Mod. Phys. **44**, 716 (1972).

42. S. M. Seltzer, in *Monte Carlo Transport of Electrons and Photons*, edited by T. M. Jenkins, W. R. Nelson, and A. Rindi (Plenum Press, New York, 1988), Chap. 7, pp. 153–181.

43. Assuming that the hot-electron density within the foil is uniform, we can estimate the absorption fraction by $f_{abs} = (L_a/d)[1 - \exp(-d/L_a)]$ with the linear attenuation length $L_a = 22.3$ μm for K_α photons.

44. M. I. K. Santala *et al.*, Phys. Rev. Lett. **84**, 1459 (2000).

45. G. Malka and J. L. Miquel, Phys. Rev. Lett. **77**, 75 (1996).

46. D. W. Forslund, J. M. Kindel, and K. Lee, Phys. Rev. Lett. **39**, 284 (1977).

47. F. N. Beg *et al.*, Phys. Plasmas **4**, 447 (1997).

48. F. Juettner, Ann. Phys. **34**, 856 (1911).

49. M. J. Berger, in *Methods in Computational Physics: Advances in Research and Applications*, edited by B. Alder, S. Fernbach, and M. Rotenberg, Volume 1: Statistical Physics (Academic Press, New York, 1963), pp. 135–215.

50. The total K-shell ionization cross section is from Ref. 36, and, unlike the cross section in Refs. 37 and 39, it is good for relativistic electron energies.

51. C. Hombourger, J. Phys. B, At. Mol. Opt. Phys. **31**, 3693 (1998).

52. A. R. Bell *et al.*, Plasma Phys. Control. Fusion **39**, 653 (1997).

53. R. J. Mason, E. S. Dodd, and B. J. Albright, Phys. Rev. E **72**, 015401(R) (2005).

54. R. M. More, Adv. At. Mol. Phys. **21**, 305 (1985).

55. P. K. Patel, M. H. Key, A. J. Mackinnon, R. Berry, M. Borghesi, D. M. Chambers, H. Chen, R. Clarke, C. Damian, R. Eagleton, R. Freeman, S. Glenzer, G. Gregori, R. Heathcote, D. Hey, N. Izumi, S. Kar, J. King, A. Nikroo, A. Niles, H.-S. Park, J. Pasley, N. Patel, R. Shepherd, R. A. Snavely, D. Steinman, C. Stoeckl, M. Storm, W. Theobald, R. Town, R. Van Maren, S. C. Wilks, and B. Zhang, Plasma Phys. Control. Fusion **47**, B833 (2005).

56. H. Alfvén, Phys. Rev. A **55**, 425 (1939).

57. Ch. Reich *et al.*, Phys. Rev. E **68**, 056408 (2003).

58. M. Honda, J. Meyer-ter-Vehn, and A. Pukhov, Phys. Rev. Lett. **85**, 2128 (2000).

Three-Dimensional Characterization of Spherical Cryogenic Targets Using Ray-Trace Analysis of Multiple Shadowgraph Views

Introduction

In the laser-driven direct-drive approach to inertial confinement fusion (ICF), energy from many individual high-power lasers is delivered to a spherical target, causing a spherically symmetric implosion.[1] The 60-beam, 30-kJ OMEGA Laser System[2] is used to study direct-drive ignition (DDI), where the laser energy is deposited directly onto the target. For indirect-drive ignition (IDI), the laser energy is directed onto a metal container (a *hohlraum*) surrounding the target, creating x rays that deposit the energy onto the target.[3,4] IDI is inherently less efficient than DDI but has less-restrictive symmetry requirements on the laser illumination.

Current designs for both DDI and IDI high-gain ICF targets require a layer of condensed hydrogen fuel that adheres to the inner surface of a spherical shell ablator. Photon energy delivered to the target ablates its outer surface, and the ablation pressure drives the fuel layer inward, compressing both it and the gaseous fuel at the target's center. The drive pressure is varied in time such that the fuel density is compressed by a factor of as much as 4000 while remaining relatively cold. Shock waves resulting from the drive-pressure history, along with compressive work, heat the gaseous-core "hot spot" to the high temperatures needed to initiate burning the fuel.

As the fuel layer is compressed and decelerates, perturbations on the inner ice surface act as amplitude seeds for the Rayleigh–Taylor instability[5,6] on the inner surface. The nonlinear growth of this deceleration-phase instability mixes the cold compressed fuel layer with the hot-spot fuel vapor, reducing fusion yield or preventing ignition.[7–10] Asymmetry-induced hydrodynamics can reduce the performance of ICF targets to well below that predicted by 1-D modeling.[11] Ignition requirements impose strong constraints on the illumination uniformity and on the sphericity of the target.[12]

The degrading effect of an inner-ice-surface perturbation on implosion performance depends on the perturbation's mode number, which is the ratio of the capsule's circumference to the wavelength of the perturbation. The surface roughness is charac-terized in terms of a mode spectrum analogous to Fourier analysis. Since the target geometry is spherical, spherical harmonics $Y_{\ell m}(\theta,\varphi)$ form the basis functions used for the mode spectrum. Accurate surface characterization of ice layers requires reliable measurement of the layer's surface with submicron resolution at many points distributed over the surface of a target. Hydrodynamic codes then calculate capsule implosion performance using the measured surface mode power spectrum. The benchmarking of calculated target performance with experimental results is essential for designing ignition-scale targets and specifying their allowable surface roughness with confidence.

The DDI specifications[12] for the National Ignition Facility (NIF)[13] require a total root-mean-square (rms) deviation of less than 1 μm for an ice layer with less than 0.25-μm rms from Fourier modes higher than $n = 10$. An ice-layer rms deviation of less than 1 μm is also required for successful IDI on the NIF.[14] Measurement of the ice-layer radius over the entire surface with submicron resolution is required to verify success or failure at achieving the required specifications.

This article describes the optical backlit shadowgraphic 3-D characterization of cryogenic direct-drive-target ice layers at LLE using ray-trace analysis of the shadowgrams. The following sections (1) briefly describe the principles and equipment used to record a cryogenic-target shadowgram at LLE; (2) analyze the resolution of shadowgram measurements; (3) describe three-dimensional ice-layer reconstruction from multiple target views using the conventional assumption that the shadowgram bright ring can be directly related to the ice thickness based on spherically symmetric calculations; and (4) present a shadowgram analysis to which nonspherically symmetric ray tracing is added, thereby improving the 3-D ice-layer reconstruction by self-consistently calculating the effects of ice-layer asymmetries and roughness on the position of the bright ring in each view. The conclusions are presented in the final section.

Shadowgraphic Characterization of Ice Layers

Optical backlit shadowgraphy is the primary diagnostic used to measure ICF target ice-layer roughness.[15–25] A shadow-

graph records the image of the light rays passing through a backlit target. The rays are reflected and refracted at the shell wall and ice-layer surfaces. Some rays are focused into characteristic rings. Ray-trace modeling of a typical cryogenic target using the *PEGASUS* code[26] has identified the specific reflections/refractions responsible for the brightest rings (see Fig. 109.44). The most-prominent ring or "bright ring" is the result of a single internal reflection off the inner solid/vapor interface of the ice layer. The position of the bright ring in the shadowgraph is directly correlated with the position of the inner surface of the ice layer and allows the nonuniformity of the inner surface to be characterized.

A high-magnification, high-fidelity backlit optical shadowgraphy system (see Fig. 109.45) is used to diagnose the ice-layer quality. A 627-nm red-light–emitting diode (LED) provides the backlighting. A 50- to 100-μs pulse drives the LED to illuminate (~f/5) the target. Imaging optics (~f/6) magnify the target image on a DALSA charge-coupled-device (CCD) camera

(12 bit, 1024 × 1024) (Ref. 27) such that the camera typically images about 1.2 μm per pixel. The camera is triggered by the same pulse that drives the LED.

A sample shadowgram of an LLE cryogenic D$_2$ target suspended from a beryllium "C-mount" by four threads of spider silk is shown in Fig. 109.46. The strong unbroken bright ring and mostly featureless central spot are indicative of the high quality of this ice layer. Two inner rings are also clearly visible.

Resolution of Shadowgram Rings

The analysis of the target image in an individual shadowgram consists of accurately determining the target center, unwrapping the image into polar coordinates, and measuring the radial positions of both the target edge and the bright ring's peak intensity. Details of this procedure are published elsewhere.[21] Here, the accuracy and resolution of these measurements are discussed.

E13425cJR

Figure 109.44
Ray-trace modeling of a cryogenic target has identified the sources of the most-intense rings. The bright ring (b) is by far the most intense.

E13424JR2
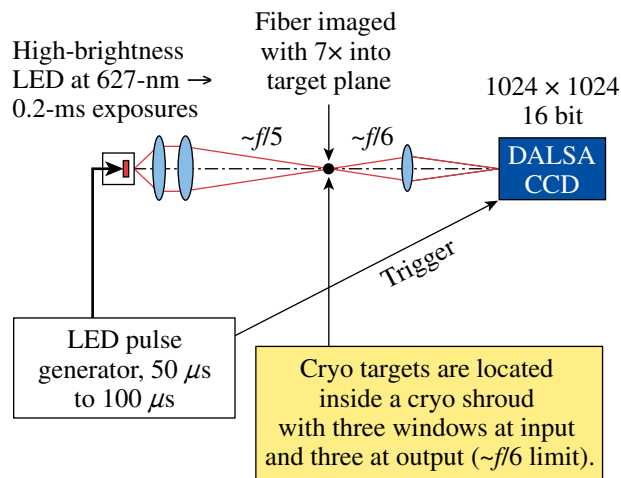
Figure 109.45
The LLE Cryogenic Target Characterization Stations are based on a diffuse f/5 source and f/6 imaging optics.

E15438JR
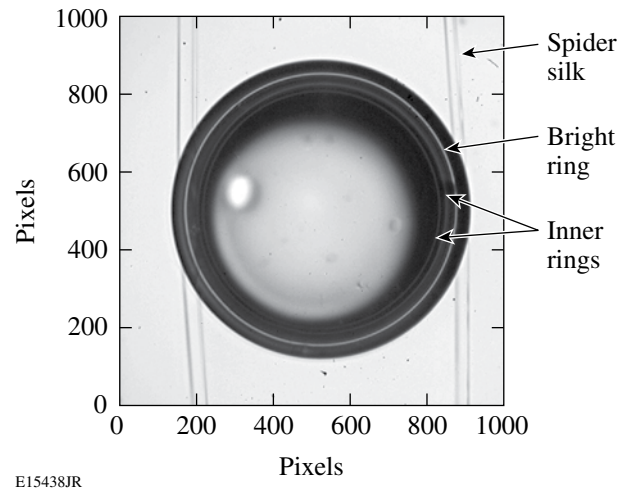
Figure 109.46
Shadowgraph of a cryogenic target (876-μm outer diameter, 4.2-μm shell thickness, 79-μm ice thickness) in a logarithmic scale. The fainter inner rings are clearly visible in the image. The bright-ring signal-to-noise ratio is typically over 20, and the effects of noise are reduced by the shadowgraph analysis routines.[21] The offset of the light rays passing through the center of the target is due to an asymmetry in the spread of the illumination, which has little effect on the position of the bright ring.

Previously, by examining the bright-ring-measurement scatter for very smooth liquid hydrogen layers,[21] the resolution of the measurements was estimated to be about 0.1 pixel (~0.12 μm). The high resolution of the bright-ring measurements has been verified using precision calibration targets as described here. The calibration targets are simulated target images of photolithographed chrome on glass.[28] A simulated image consists of a "perfectly" circular edge along with a bright ring (plus two fainter inner rings) with a known variation in radial position. The radial variation of the rings was calculated, using the linearized formula discussed in the next section, for an ice surface with a surface-deviation, Fourier-mode power spectrum of

$$P_n = Cn^{-2} \tag{1}$$

for Fourier modes $n = 1$ to 100, where C was chosen such that the spectrum meets the DDI specification. The phase of each Fourier mode was randomized. This power spectrum and the calculated bright-ring position are shown in Fig. 109.47. The precision calibration target was photolithographed with a manufacturing tolerance of 0.1 μm. A shadowgram of this target taken in one of OMEGA's Cryogenic Target Characterization Stations is shown in Fig. 109.48. This image has been analyzed using LLE's standard shadowgram analysis routines, and the results are shown in Fig. 109.47. The measured bright-ring positions have a mean error of less than 0.1 μm (within the manufacturing tolerances of the calibration target), and the total rms error of the ring measurement is about 0.01 μm.

It is clear that the bright-ring position can be very accurately measured in the characterization station shadowgrams. The relationship of that ring position with the radius of the actual ice surface producing the ring is discussed in the next section.
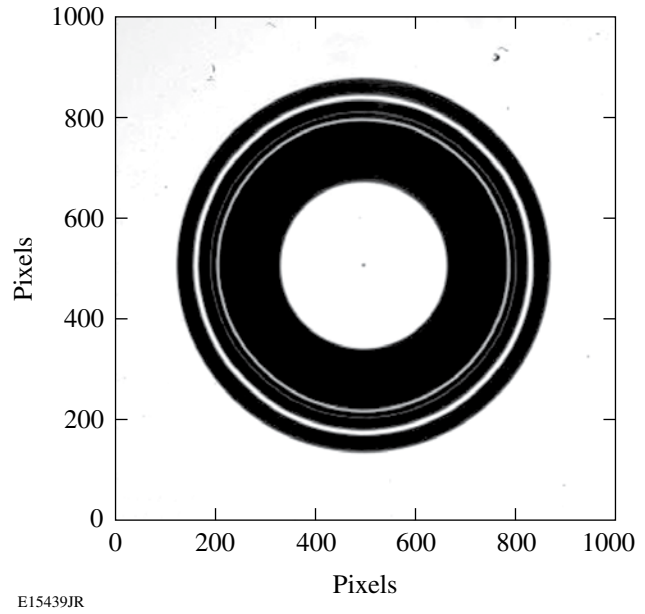
E15439JR

Figure 109.48
Shadowgraph of the photolithographed chrome-on-glass "dot-surrogate" target. The outer edge is a perfect circle to within the manufacturing tolerance (0.1 μm). The rings are simulated by uniform-thickness gaps in the dot. The inner rings are fainter than the bright ring because their gap width is less. The radial positions of the rings vary around the target and are calculated for an ice surface whose roughness meets the DDI requirements.
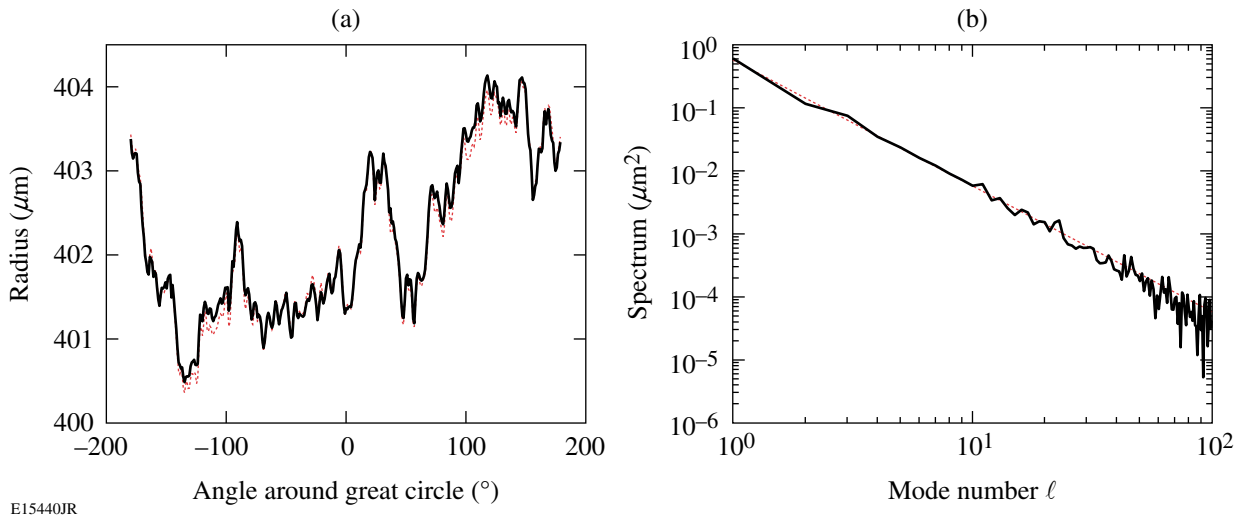
E15440JR

Figure 109.47
The measured (solid) bright ring for the simulated dot-surrogate target is an excellent match to the design specification (dotted) in terms of both (a) radial position and (b) power spectrum.

Three-Dimensional Ice-Layer Reconstruction Using Multiple Shadowgraph Views

An important feature of LLE's Cryogenic Target Shadowgraphy System is the use of multiple views of the target to fully characterize the ice surface. Multiple views allow a far-more-complete surface characterization than is possible from a single view. Even with three mutually orthogonal views, it can be shown that there is only a small chance of detecting many local ice defects.[29]

In the LLE Cryogenic Target Characterization Stations, the targets are rotated to provide a large number of different views for a single camera. The maximum number of views is limited only by the step size of the rotation stepper motor, which is a few tenths of a degree. Shadowgrams are typically recorded at 15° intervals, producing a total of 48 independent views between two cameras in each characterization station. The two cameras have approximately orthogonal views: one camera views the target center from an angle of 26.56° above the equator and the second camera, located 109.96° azimuthally from the first, views the target center from 12.72° above the equator. These view angles are determined by the location of the layering sphere windows that are aligned with the OMEGA target chamber's viewing ports, which are used to center the target at shot time. These views are not optimum for target characterization. An off-the-equator viewing angle always results in unviewable regions surrounding the rotation poles; these unviewable "polar caps" are apparent in Fig. 109.49(a).

The standard method of shadowgram analysis assumes that the ice surface position along a great circle perpendicular to the shadowgraph view can be uniquely determined from the observed bright-ring position for that view[17,22–25] by characterizing the ice-to-bright-ring relationship using a ray-trace study of spherically symmetric targets with varying ice thickness. At LLE, ray-trace modeling of a typical cryogenic target using the *PEGASUS* code[26] has identified how the shadowgram ring positions vary with the target parameters such as the shell outer radius and thickness, the D_2-ice thickness, the shell index of refraction, and the D_2 index of refraction. The *PEGASUS* code is two dimensional and assumes spherical symmetry in the target. A linearized formula derived from this modeling is used to determine the inner-ice-surface radius from the position of the bright ring for given target parameters.

A 3-D representation of the ice layer can be constructed from the ice-surface positions determined from the multiple shadowgram views. Figure 109.49 shows a target's inner ice surface reconstructed from a target rotation of 24 separate views. The surface is dominated by low-mode-number asymmetries, but very different Fourier modes are observed for any given great circle. For this data set, the ice-surface 1-D rms roughness of the individual great-circle observations varies from 2.6 μm to 5.3 μm with an average value of 3.5 μm. This particular data set was selected for the following reasons:

- The outer surface is very smooth and symmetric and should have little effect on the bright ring.

- The optical distortion from collection optics was well minimized for these images.

- The bright ring is smooth and has few breaks.

(a) (b) (c)

E15441JR

Deviation from spherical (μm): 10, 5, 0, −5, −10

min = −8.0 μm, max = 7.9 μm
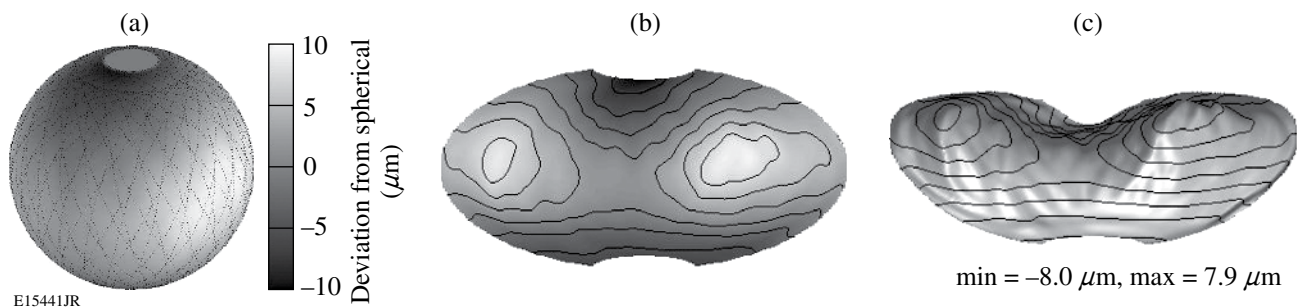
Figure 109.49
Three-dimensional representation of a cryogenic inner ice surface (μm) displayed (a) on a spherical surface, (b) using the Aitoff projection with contour lines, and (c) using the Aitoff projection with surface elevation. These displays are constructed by interpolating all the individual data from the many great-circle observations to an evenly spaced (θ,ϕ) surface grid. The dotted lines in (a) show the location of the actual great circles observed in the individual shadowgraphs. The "polar caps" crossed by none of the great-circle observations are clearly visible.

As mentioned earlier, computer modeling of a spherical implosion, including instability growth, requires an ice-roughness spectrum described in terms of spherical-harmonics-basis functions $Y_{\ell m}(\theta, \phi)$ on the ice surface:

$$R(\theta, \phi) = \sum_{\ell = 0}^{\infty} \sum_{m = -\ell}^{\ell} A_{\ell m} Y_{\ell m}(\theta, \phi) \quad (\mu m). \quad (2)$$

This description gives a Legendre-mode power spectrum and total surface variance of

$$P_{\ell} = \frac{1}{4\pi} \sum_{m = -\ell}^{\ell} \left| A_{\ell m} \right|^2 \quad (\mu m), \quad (3)$$

$$\sigma_{rms}^2 = \sum_{\ell = 1}^{\infty} P_{\ell} \quad (\mu m^2), \quad (4)$$

respectively. The P_{ℓ} spectrum represents an average over all azimuthal modes.

The P_{ℓ} spectrum for high mode numbers can be inferred from the Fourier power spectra of the many great circles observed. If one assumes that the surface perturbations are randomly distributed, the great-circle 1-D Fourier-mode power spectrum, averaged over many great circles, can be mapped[30] to an equivalent Legendre-mode power spectrum. The assumption of randomly distributed perturbations limits the applicability of the mapping to higher mode numbers. At LLE the ice-surface positions are directly fit to spherical harmonics to determine the lower mode numbers (up to some ℓ_{max}).[21]

The results of a direct $Y_{\ell m}(\theta, \phi)$ fit are shown in Figs. 109.50 and 109.51 for a fit up to $\ell_{max} = 10$. The surface reconstruction in Fig. 109.51 based on the low-mode-number fit is a good match to the data shown in Fig. 109.49. The Legendre power spectrum P_{ℓ} corresponding to this fit along with the higher mode numbers determined by the mapping method is displayed in Fig. 109.50. Target reconstructions using the standard analysis have successfully detected low-mode asymmetries in the ice layer, allowing the identification and correction of the sources of the layering sphere temperature isotherm asymmetries that cause them.[31]

The maximum mode number fit, ℓ_{max}, is limited by the largest space between sampled points on the surface. For typical LLE targets, the largest gap in the surface data occurs at the unviewable polar cap of the target. The maximum mode number that can be reliably fit is also reduced by the many smaller surface gaps between great-circle measurements, noise in the data, uneven surface weighting (sections crossed by several great circles are more heavily weighted), and the fact that the data do not agree

E15442JR

Figure 109.50
Legendre-mode power spectrum P_{ℓ} of the ice surface. The dots correspond to the low-mode-number (up to $\ell_{max} = 10$) direct fit. The circles result from mapping the average Fourier-mode spectrum of the many great circles.

min = –8.4 μm, max = 7.8 μm

E15443JR

Figure 109.51
Three-dimensional reconstruction of a cryogenic inner ice surface (μm) based on a direct $Y_{\ell m}(\theta, \phi)$ fit to the measured data (up to $\ell_{max} = 10$) (a) using the Aitoff projection with contour lines and (b) using the Aitoff projection with surface elevation. A comparison with Fig. 109.49 shows that the low-mode features are well matched by the fit. Although the actual great-circle data are used in the fitting, the results are mapped to an evenly spaced (θ, ϕ) surface grid using the $Y_{\ell m}$ coefficients for better display.

at "cross-over" points (see the next section). The sum of these effects typically limits the direct surface fit to mode numbers up to about $\ell_{max} = 10$. The exact limit varies with each data set. The results of fitting too high an ℓ_{max} are shown in Figs. 109.52 and 109.53, where the fit has been extended to $\ell_{max} = 16$. The power spectrum in Fig. 109.52 is rising as mode numbers approach

ℓ_{max}, a trend not observed in the Fourier analysis of the bright rings. The combination of a too high ℓ_{max} along with the spaces between data circles and data mismatch at the great-circle cross-over points produces a fit with more structure than seen in the individual bright rings. This increased structure and "crinkling" are evident in Fig. 109.53.

E15444JR

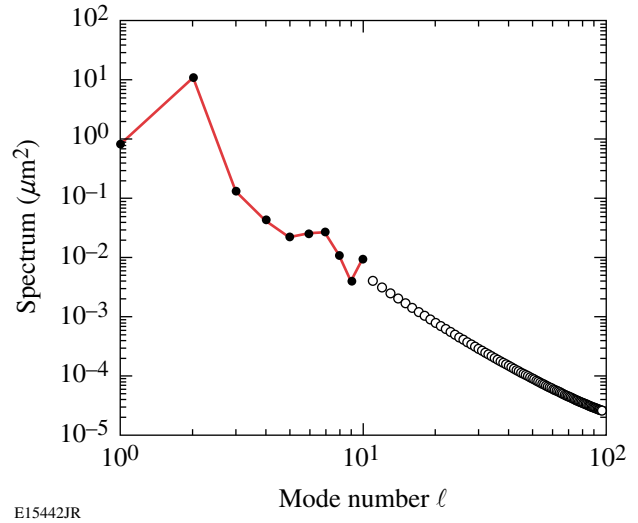**Figure 109.52**
Legendre-mode power spectrum P_ℓ of the ice surface. The dots correspond to the low-mode-number (up to $\ell_{max} = 16$) direct fit. The circles result from mapping the average Fourier-mode spectrum of the many great circles.
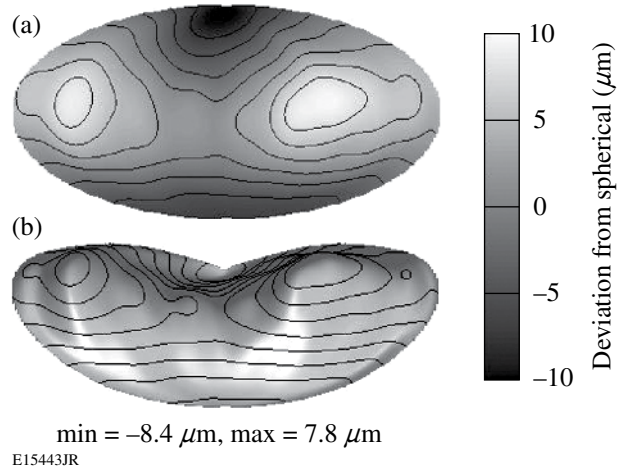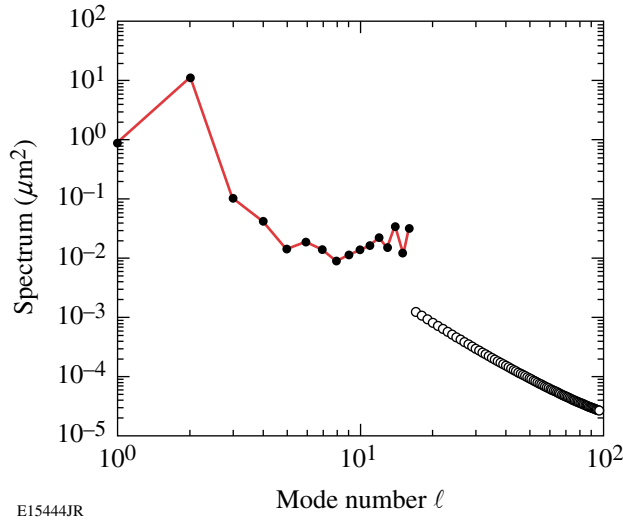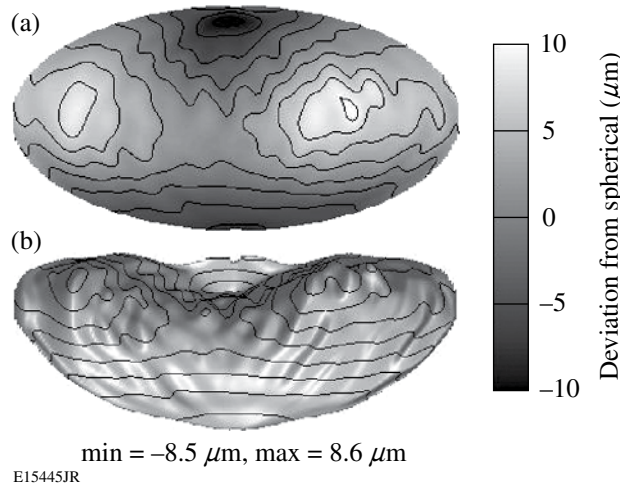

min = –8.5 μm, max = 8.6 μm

E15445JR

Figure 109.53
Three-dimensional reconstruction of a cryogenic inner ice surface (μm) based on a direct $Y_{\ell m}(\theta,\phi)$ fit to the measured data (up to $\ell_{max} = 16$) (a) using the Aitoff projection with contour lines and (b) using the Aitoff projection with surface elevation. A comparison with Fig. 109.49 shows a large amount of mid-mode noise in the fit.

Ray-Trace Analysis

Despite the success of the standard analysis, it is well known[18–20,24] that the assumption that the ice-surface position along a great circle perpendicular to the shadowgraph view can be directly correlated to the observed bright-ring position for that view is valid only for perfectly spherical symmetry. Kozioziemski *et al.*[18] showed that a shift in the ice layer along the viewing axis will alter the bright-ring position and "significantly shift the apparent ice-layer thickness." This effect can be easily seen in Fig. 109.54, which shows the ray path of the bright ring for a target layer shifted along the viewing axis. For imperfect ice layers, Koch *et al.*[19,20] note that "correlation depends on the height and curvature of the imperfection." To illustrate this, the bright-ring radii predicted by 3-D ray tracing of a simulated ice surface constructed from spherical harmonics for opposing views are shown in Fig. 109.55. The predicted bright rings show general similarities in the low-mode structures but differ greatly in the higher-mode detail. This explains why the ice surfaces determined by the standard method do not agree at the cross-over points of the views.

If the shadowgrams were viewed along the equator and exactly opposing views could be measured, the average position of two bright rings would show a good correlation to the ice-surface position along the great circle perpendicular to the views.[32] In this case the standard method can accurately be applied to the averaged bright ring. If one has nonequatorial views, exactly opposing views cannot be recorded. A study of two above-the-equator views in the Cryogenic Target Characterization Stations for OMEGA rotated 180° about the polar
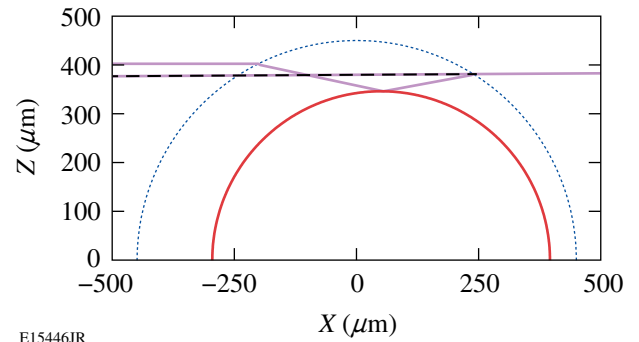
E15446JR

Figure 109.54
The ray path that produces the bright ring in a target where the ice surface is shifted along the line of view shows how asymmetries affect the bright ring. When viewed from the right, the bright ring appears lower than when viewed from the left. The standard analysis would determine a quite-different ice thickness for each view. For an unshifted layer, the rays on both sides would be at the same height and the bright ring would appear the same for both views.
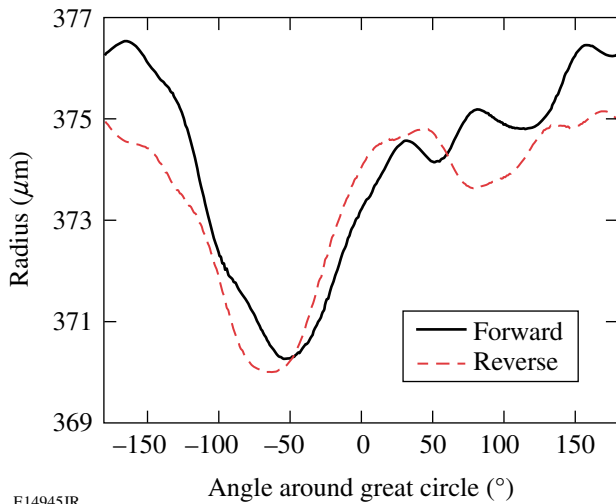
E14945JR

Figure 109.55
Bright-ring radii predicted by 3-D ray tracing of an asymmetric ice surface for opposing views show very different structures. The standard method of shadowgram analysis assumes that both views will be identical and will depend solely on the ice radius at the great circle perpendicular to the view. In fact, the bright-ring radii also depend on the angle of the ice surface relative to each view, and the bright ring may not be centered on rays that strike the ice surface at the great circle.

axis showed that only the lowest modes can be determined with any accuracy by averaging two bright rings.[33]

To self-consistently and accurately determine the 3-D ice surface from shadowgram bright-ring measurements requires the modeling of the effect that the ice-surface asymmetries and defects have on the bright-ring position and including this modeling into the shadowgram analysis. Kozioziemski *et al.*[18] accomplished this in a limited fashion by using interferometry to measure the P1 ice-layer mode along the viewing axis, then correcting the bright-ring position for the effect of the P1 based on a ray-trace study. The ray-trace shadowgram analysis at LLE uses 3-D ray tracing to simultaneously fit the bright-ring measurements for all views (typically 48 different views) to a multimode (up to $\ell = 18$) spherical-harmonic representation of the ice layer.

Producing a simulated full shadowgram for a nonspherically symmetric ice layer can take days of CPU time[20,24] due to the large number of ray-trace calculations required. For this fitting analysis, where many iterations of varying a large number of spherical-harmonic components is required, an alternative was found based on the observation that for spherically symmetric targets, the peak intensity of the bright ring is centered on rays whose paths on both sides of the target are along the viewing axis. This is a poor approximation for asymmetric layers such as a melted layer that is very offset from the view angle, but it

is a good approximation for the quasi-symmetrical case of a typical well-layered OMEGA cryogenic target.

With the above assumption, one need only follow one ray for each measured bright-ring position used in the fitting. The rays are launched backward from the measured bright-ring positions along their viewing angles and followed through the target and out the other side where the divergences of the rays' final paths from the view angles are recorded. Nonlinear fitting iterations are employed to adjust the spherical-harmonic description of the ice surface, minimizing the divergence of all the rays from the viewing angles. Typical total fitting times are of the order of several hours to a day, depending on the number of measurements (typically 180 points from each of 48 views) and the number of spherical-harmonic components fit, which varies as $(\ell_{max} + 1)^2$. The nonlinear fitting routine constrains the maximum peak-to-valley variation of the ice surface to be similar to the maximum variation in the bright-ring position, preventing large peak-to-valley structures from occurring on the surface between the data rings or in the polar cap.

An example of the results from the ray-trace analysis with $\ell_{max} = 16$ is shown in Figs. 109.56–109.58. The ice-surface Legendre-mode power spectrum is well behaved up to this ℓ_{max} (Fig. 109.56), and the surface reconstructs show less anomalous structure (Fig. 109.57) than the standard method.
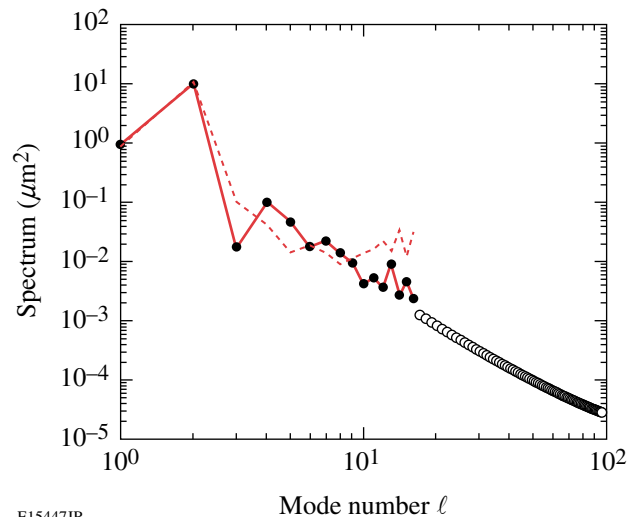
E15447JR

Figure 109.56
Legendre-mode power spectrum P_ℓ of the ice surface. The solid dots correspond to the low-mode-number (up to $\ell_{max} = 16$) ray-trace fit while the dashed line redisplays the standard method fit (up to $\ell_{max} = 16$). The ray-trace analysis is well behaved up to higher mode numbers than the standard method. The circles are the result from mapping the average Fourier-mode spectrum of the many great circles to determine the higher Legendre modes.

(a)

(b)
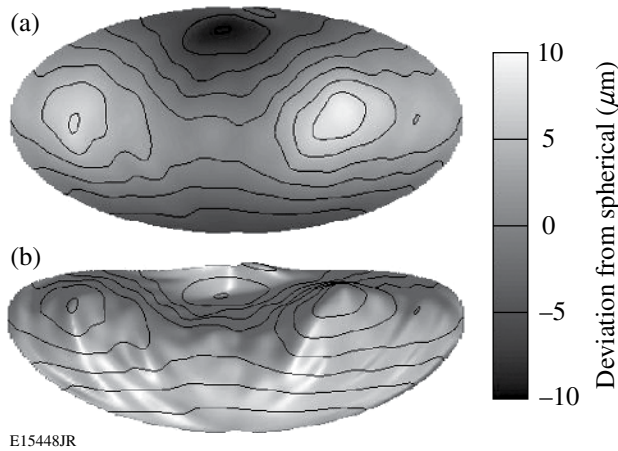
E15448JR

Figure 109.57
Three-dimensional reconstruction of a cryogenic inner ice surface (μm) based on a ray trace $Y_{\ell m}(\theta,\phi)$ fit to the measured data (up to $\ell_{max} = 16$) (a) using the Aitoff projection with contour lines and (b) using the Aitoff projection with surface elevation. This ray-trace fit shows less-artificial structure than the standard fit of Fig. 109.53.
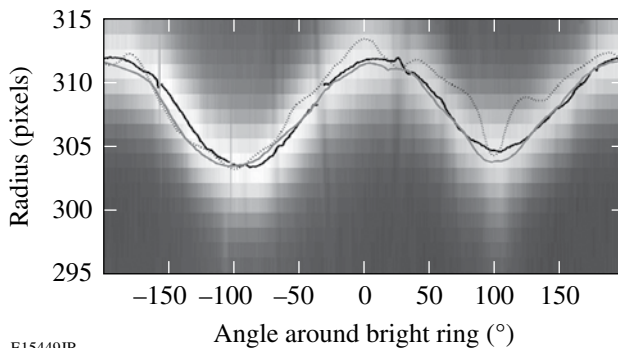
E15449JR

Figure 109.58
Unwrapping of a sample bright ring in polar coordinates shows that the measured bright-ring positions (black line) are much better matched by the predicted bright-ring positions using the ray-trace analysis ice surface (gray line) than by the bright ring predicted using the ice surface determined by the standard method (dotted line).

Figure 109.58 shows a measured bright ring taken from one of the 48 different views of a D_2-ice layer in an OMEGA cryogenic target. The ice surface determined using the standard method with $\ell_{max} = 16$ (Fig. 109.53) would produce the bright ring shown by the dotted line according to ray-trace calculations using that surface. The standard deviation between the measured bright rings for the 48 different views and their standard method predictions is 1.5 μm.

The ice surface determined by the ray-trace analysis (Fig. 109.57) gives the bright-ring prediction shown by the solid gray line in Fig. 109.58. This surface produces a much better match to the observed bright ring. The standard deviation between the measured bright rings for the 48 different views and their ray-trace analysis predictions is 0.8 μm, a reduction of 45% from the standard method.

Summary and Discussion

It has been shown that the bright-ring position can be measured very precisely, but accurately correlating the bright-ring position to an ice-surface position is difficult. The standard method of applying spherically symmetric bright-ring calculations is inaccurate for asymmetric ice layers. Incorporating asymmetric ray tracing directly into the bright-ring analysis allows a self-consistent fitting of the bright rings from multiple views to an ice surface. Ray-tracing analysis reduced the error between the measured bright rings (for 48 different views) and those predicted for the fitted ice surface by 45% in comparison with the ice surface determined by the standard analysis.

It may be possible to further improve the performance of the ray-trace shadowgram analysis by

- modeling the bright-ring position, directly taking into account the uncollimated illumination of the actual shadowgraphy instead of assuming that the ring is centered on rays parallel to the viewing angles,

- fitting the optical differences between the views (magnification, focal position, etc.),

- adding some localized (e.g., spherical wavelet) defects to the ice-surface fitting to account for bright-ring features too localized to be fit by spherical harmonics and a reasonable ℓ_{max}, and

- including the effects of outer-surface perturbations on the bright ring that are believed to be responsible for some sharp features in the bright ring.

It is important to note that as the ice-layer quality improves and becomes more symmetric, the accuracy of the standard method improves. Initial studies of DT cryogenic targets for OMEGA[34] indicate that beta-layered DT targets are very smooth and symmetric and good candidates for accurate standard analyses. These very symmetric layers may still benefit from ray-trace analysis by isolating the effects of outer-surface perturbations on the bright ring that can be even larger than the actual ice-surface effects.

LLE is building a cryogenic fill-tube target station that will allow validation of this ray-trace modeling and shadowgram

analysis. The station will possess target rotation capabilities and equatorial views for both shadowgraphy and x-ray phase-contrast[35] layer diagnostics, allowing a direct comparison of ray-trace shadowgraphic analysis with (1) the standard analysis; (2) the standard analysis using averaged bright rings from opposing views; and (3) x-ray-phase-contrast direct measurements of the ice surface.

ACKNOWLEDGMENT

REFERENCES

1. J. Nuckolls *et al.*, Nature **239**, 139 (1972).

2. T. R. Boehly, D. L. Brown, R. S. Craxton, R. L. Keck, J. P. Knauer, J. H. Kelly, T. J. Kessler, S. A. Kumpan, S. J. Loucks, S. A. Letzring, F. J. Marshall, R. L. McCrory, S. F. B. Morse, W. Seka, J. M. Soures, and C. P. Verdon, Opt. Commun. **133**, 495 (1997).

3. J. D. Lindl, Phys. Plasmas **2**, 3933 (1995).

4. J. D. Lindl, *Inertial Confinement Fusion: The Quest for Ignition and Energy Gain Using Indirect Drive* (Springer-Verlag, New York, 1998), Chap. 6, p. 61.

5. Lord Rayleigh, Proc. London Math Soc. **XIV**, 170 (1883).

6. G. Taylor, Proc. R. Soc. London Ser. A **201**, 192 (1950).

7. V. Lobatchev and R. Betti, Phys. Rev. Lett. **85**, 4522 (2000).

8. M. C. Herrmann, M. Tabak, and J. D. Lindl, Phys. Plasmas **8**, 2296 (2001).

9. R. Betti, K. Anderson, V. N. Goncharov, R. L. McCrory, D. D. Meyerhofer, S. Skupsky, and R. P. J. Town, Phys. Plasmas **9**, 2277 (2002).

10. R. P. J. Town and A. R. Bell, Phys. Rev. Lett. **67**, 1863 (1991).

11. D. D. Meyerhofer, J. A. Delettrez, R. Epstein, V. Yu. Glebov, V. N. Goncharov, R. L. Keck, R. L. McCrory, P. W. McKenty, F. J. Marshall, P. B. Radha, S. P. Regan, S. Roberts, W. Seka, S. Skupsky, V. A. Smalyuk, C. Sorce, C. Stoeckl, J. M. Soures, R. P. J. Town, B. Yaakobi, J. D. Zuegel, J. Frenje, C. K. Li, R. D. Petrasso, D. G. Hicks, F. H. Séguin, K. Fletcher, S. Padalino, C. Freeman, N. Izumi, R. Lerche, T. W. Phillips, and T. C. Sangster, Phys. Plasmas **8**, 2251 (2001).

12. P. W. McKenty, V. N. Goncharov, R. P. J. Town, S. Skupsky, R. Betti, and R. L. McCrory, Phys. Plasmas **8**, 2315 (2001).

13. W. J. Hogan, E. I. Moses, B. E. Warner, M. S. Sorem, and J. M. Soures, Nucl. Fusion **41**, 567 (2001).

14. S. W. Haan *et al.*, Fusion Sci. Technol. **49**, 553 (2006).

15. J. K. Hoffer *et al.*, Fusion Technol. **30**, 529 (1996).

16. J. D. Sheliak *et al.*, Fusion Technol. **30**, 83 (1996).

17. D. N. Bittner *et al.*, Fusion Technol. **35**, 244 (1999).

18. B. J. Kozioziemski *et al.*, in *Inertial Fusion Sciences and Applications 2003*, edited by B. A. Hammel, D. D. Meyerhofer, J. Meyer-ter-Vehn, and H. Azechi (American Nuclear Society, La Grange Park, IL, 2004), pp. 762–765.

19. J. A. Koch *et al.*, Fusion Technol. **38**, 123 (2000).

20. J. A. Koch *et al.*, Fusion Sci. Technol. **43**, 55 (2003).

21. D. H. Edgell, W. Seka, R. S. Craxton, L. M. Elasky, D. R. Harding, R. L. Keck, and M. D. Wittman, Fusion Sci. Technol. **49**, 616 (2006).

22. I. V. Aleksandrova *et al.*, J. Phys. D: Appl. Phys. **37**, 1163 (2004).

23. E. R. Koresheva *et al.*, Nucl. Fusion **46**, 890 (2006).

24. F. Lamy *et al.*, Fusion Sci. Technol. **48**, 1307 (2005).

25. F. Gillot *et al.*, Fusion Sci. Technol. **49**, 626 (2006).

26. S. Jin, *2002 Summer Research Program for High School Juniors at the University of Rochester's Laboratory for Laser Energetics*, Rochester, NY, LLE Report No. 329, LLE Document No. DOE/SF/19460-479 (2003).

27. DALSA, Waterloo, Ontario, Canada, N2V 2E9 (http://www.dalsa.com).

28. APPLIED IMAGE, Inc., Rochester, NY 14609, (http://www.applied-imagegroup.biz).

29. R. B. Stephens *et al.*, Fusion Sci. Technol. **45**, 210 (2004).

30. S. Pollaine and S. Hatchett, Nucl. Fusion **44**, 117 (2004).

31. D. R. Harding, D. D. Meyerhofer, S. J. Loucks, L. D. Lund, R. Janezic, L. M. Elasky, T. H. Hinterman, D. H. Edgell, W. Seka, M. D. Wittman, R. Q. Gram, D. Jacobs-Perkins, R. Early, T. Duffy, and M. J. Bonino, Phys. Plasmas **13**, 056316 (2006).

32. G. Balonek, *2004 Summer Research Program for High School Juniors at the University of Rochester's Laboratory for Laser Energetics*, University of Rochester, Rochester, NY, LLE Report No. 337, LLE Document No. DOE/SF/19460-590 (2005).

33. R. Wu, *2005 Summer Research Program for High School Juniors at the University of Rochester's Laboratory for Laser Energetics*, University of Rochester, Rochester, NY, LLE Report No. 343 (2006).

34. T. C. Sangster, R. Betti, R. S. Craxton, J. A. Delettrez, D. H. Edgell, L. M. Elasky, V. Yu. Glebov, V. N. Goncharov, D. R. Harding, D. Jacobs-Perkins, R. Janezic, R. L. Keck, J. P. Knauer, S. J. Loucks, L. D. Lund, F. J. Marshall, R. L. McCrory, P. W. McKenty, D. D. Meyerhofer, P. B. Radha, S. P. Regan, W. Seka, W. T. Shmayda, S. Skupsky, V. A. Smalyuk, J. M. Soures, C. Stoeckl, B. Yaakobi, J. A. Frenje, C. K. Li , R. D. Petrasso, F. H. Séguin, J. D. Moody, J. A. Atherton, B. D. MacGowan, J. D. Kilkenny, T. P. Bernat, and D. S. Montgomery, "Cryogenic DT and D$_2$ Targets for Inertial Confinement Fusion," to be published in Physics of Plasmas (invited).

35. D. S. Montgomery, A. Nobile, and P. J. Walsh, Rev. Sci. Instrum. **75**, 3986 (2004).

Filamentation Analysis in Large-Mode-Area Fiber Lasers

Introduction

Fiber lasers have developed rapidly in recent years,[1,2] with output powers above the kilowatt level.[3,4] Along with the increasing output power, nonlinear effects become important and can ultimately limit the power scalability in the fiber. Two well-known nonlinear effects that have limited the output power of fiber lasers are stimulated Brillouin scattering (SBS) and stimulated Raman scattering (SRS). Several methods can be used to increase the SBS threshold, including increasing the signal bandwidth to decrease the Brillouin gain,[5] using new fiber designs to decrease the overlap between acoustic and optics modes,[6] varying the temperature along the cavity,[7,8] and using low-numerical-aperture, large-mode-area (LMA) fibers.[9] Spectral filtering and LMA fibers are also used to mitigate SRS. In LMA fibers, the large mode area serves to decrease the optical intensity, therefore increasing the nonlinear threshold.

While many methods are being investigated to suppress SBS and SRS, other nonlinear effects, such as self-focusing, also have an impact. In 1987 Baldeck *et al.*[10] observed the self-focusing effect in the optical fiber with picosecond laser pulses. Self-focusing can lead to beam-quality degradation through a process called filamentation. The physical nature of filamentation arises from self-focusing through the nonlinear refractive index. When the light intensity is strong enough for self-focusing to occur, the beam in the laser cavity is focused narrower and narrower. As a result, the laser beam is limited in a small region in the center of the core. Thus the corresponding population inversion is depleted in the center of the core, but undepleted in other areas of the core, i.e., spatial hole burning. With spontaneous emission occurring throughout the core, it is easy to generate other lasing beams, finally resulting in filamentation. Filamentation has been studied extensively in semiconductor lasers in the past two decades;[11–13] however, little work has been done in fiber lasers.

In this article, a theoretical model for the filamentation effect in LMA fiber lasers is presented. Solving the paraxial wave equation and population rate equation in three dimensions, an expression for the filament gain is derived using a perturbation method. This expression includes both spatial and temporal characteristics, the filament spacing, and oscillation frequency. The filament gain also depends on the physical parameters of the optical fiber, the nonlinear refractive index, and the pump and signal power. This model can predict the output-power thresholds at which the filamentation will occur for a given set of optical-fiber parameters, in particular the core diameter. A simplified threshold expression is also provided. The results are shown to be consistent with previous experiments.

Theoretical Model and Steady-State Solution

Starting with Maxwell's equation in a dielectric medium, a wave equation is obtained, assuming an optical field of the form $\widetilde{A} = A_s(r, \phi, z, t) e^{i(kz - \omega t)}$ and using the slowly varying envelope approximation to neglect the second derivatives of the time t and axial coordinate z. After considering the gain, loss, nonlinear refractive index, and the coupling of the pump and the signal light in the optical fiber, the optical field of the signal light can be found to satisfy the paraxial wave equation

$$\frac{\partial A_s}{\partial z} + \frac{1}{v_g}\frac{\partial A_s}{\partial t} = \frac{i}{2k_s}\nabla_T^2 A_s + \left[\frac{1}{2}g_s' + i\left(2\gamma_p P_p + \gamma_s P_s\right)\right]A_s, \quad (1)$$

where A_s is the slowly varying amplitude of the signal light along z and t, v_g is the group velocity, $k_s = n_{\text{eff}} k_0$ is the mode propagation constant of the signal light, n_{eff} is the effective index of the refraction, and k_0 is the free-space propagation constant. $\nabla_T^2 = (1/r)(\partial/\partial r) + (\partial^2/\partial r^2) + (1/r^2)(\partial^2/\partial \phi^2)$ is the transverse Laplacian operator, representing diffraction. $g_s' = g_s - \alpha_{\text{cav}}$ is the net gain of the signal light, where $g_s = N_2\sigma_s^e - N_1\sigma_s^a$ is the local gain of the signal light. The energy-level system of the excitation ion is assumed to be a two-level system,[16] where N_2, N_1 are the upper- and lower-state population densities, respectively. σ_j^a, σ_j^e are the absorption and emission cross sections at frequency ω_j with $j = p, s$ representing pump and signal light. To analyze the optical fiber laser, the mirror losses are distributed throughout the cavity, $\alpha_{\text{cav}} = \alpha_{\text{int}} - \ln(R_1 R_2)/2L$, where α_{int} is the internal loss, L is the cavity length, and R_1 and R_2 are the reflectivities of the mirrors. For the case of a fiber ampli-

fier, the cavity loss is the same as the internal loss, $\alpha_{\text{cav}} = \alpha_{\text{int}}$. $\gamma_j = \bar{n}_2 k_0 / A_{\text{eff}_j}$ is the nonlinear parameter at frequency ω_j, $\bar{n}_2$ is the Kerr coefficient, and A_{eff_j} is the effective cross-section area at frequency ω_j. The nonlinear parameter γ_j represents self-focusing in optical fibers, for $\gamma_j > 0$; $P_j = |A_j|^2$ is the optical power in the core at frequency ω_j.

With the assumption of a two-level system, the rate equation of the excited state is given by[16]

$$\frac{\partial N_2}{\partial t} = -\frac{N_2}{\tau} - \left(N_2 \sigma_s^e - N_1 \sigma_s^a\right)\phi_s - \left(N_2 \sigma_p^e - N_1 \sigma_p^a\right)\phi_p, \quad (2)$$

where $\phi_j = P_j / \left(A_{\text{eff}_j} h v_j\right)$ is the photon flux at the frequency v_j, τ is the spontaneous lifetime of the excited state, and $N_t = N_1 + N_2$ is the total population density.

Equation (1) is a nonlinear equation without an exact solution. The waveguide mode is first solved in the absence of gain and loss for low-intensity levels (i.e., no nonlinear effects). The solution in the core can be found:[14]

$$\begin{aligned}\widetilde{A} &= A_s \exp\left[i\left(k_s z - \omega_s t\right)\right] \\ &= A_{s_0} J_m\left(p_s r\right) \exp\left(im\phi\right) \exp\left[i\left(k_s z - \omega_s t\right)\right],\end{aligned} \quad (3)$$

where A_{s_0} is a constant, $p_s^2 = n_1^2 k_0^2 - k_s^2$, and n_1 is the refractive index in the core. The index m can take only integer values, with $m = 0$ for the fundamental mode. Therefore, the optical field in Eq. (1) should have the form $A_s = A_{s_1}(z) J_m(p_s r) \exp(im\phi)$. Substituting the Laplacian term with $\nabla_T^2 A_s = -p_s^2 A_s$, Eq. (1) can be rewritten in the steady state as

$$\frac{\partial A_s}{\partial z} = \left[\frac{1}{2}g_s' - \frac{ip_s^2}{2k_s} + i\left(2\gamma_p P_p + \gamma_s P_s\right)\right]A_s. \quad (4)$$

For simplicity, bi-directional pumping is assumed, so the pump power P_p can be regarded as nearly constant along the cavity, which leads to a constant gain along the cavity. When a laser is above threshold, the gain is clamped to the value of cavity loss at threshold. Since the loss is distributed along the cavity in this unfolded cavity model,[13] net gain g_s' is zero and the signal power $P_s = |A_s|^2$ must therefore be independent of $z\left[|A_{s_1}(z)| = A_{s_0}\right]$. Thus, the solution of Eq. (4) has the form $A_s = A_{s_0} J_m(p_s r)\exp(im\phi)\exp(i\Delta k_s z)$, is given by

$$\Delta k_s = \frac{1}{2}g_s' - \frac{ip_s^2}{2k_s} + i\left(2\gamma_p P_p + \gamma_s P_s\right). \quad (5)$$

Equation (5) shows the change for the complex propagation constant due to the gain, loss, nonlinearity, and the waveguide mode.

The modal gain $g_s = \Gamma_s g$ includes the transverse confinement factor $\Gamma_s = A_{\text{eff}s} / A_{\text{core}}$ to account for the fact that excited ions are doped only in the core. Substituting the relation $N_1 = N_t - N_2$ into Eq. (2), the upper-state population can be found in the steady state as

$$N_2 = \frac{N_t\left(\dfrac{\sigma_s^a}{\sigma_s^e + \sigma_s^a}\dfrac{P_s}{P_s^{\text{sat}}} + \dfrac{\sigma_p^a}{\sigma_p^e + \sigma_p^a}\dfrac{P_p}{P_p^{\text{sat}}}\right)}{1 + \dfrac{P_s}{P_s^{\text{sat}}} + \dfrac{P_p}{P_p^{\text{sat}}}}, \quad (6)$$

where $P_j = |A_j|^2$, $P_j^{\text{sat}} = \left(A_{\text{eff}_j} h v_j\right) / \left[\left(\sigma_j^e + \sigma_j^a\right)\tau\right]$ is defined as saturation power with $j = p, s$. For the case of the fiber laser, with the threshold condition of $g_s = \alpha_{\text{cav}}$ and the assumption of constant pump power, the signal power is constant along the z direction in the cavity solved from Eq. (6):

$$\begin{aligned}P_s = &\left\{-\left(N_t \sigma_s^a + \frac{\alpha_{\text{cav}}}{\Gamma_s}\right)\right.\\ &\left.+\left[\frac{N_t\left(\sigma_p^e \sigma_s^a - \sigma_p^a \sigma_s^e\right)}{\sigma_p^e + \sigma_p^a} + \frac{\alpha_{\text{cav}}}{\Gamma_s}\right]\frac{P_p}{P_p^{\text{sat}}}\right\}\frac{\alpha_{\text{cav}}P_s^{\text{sat}}}{\Gamma_s}. \quad (7)\end{aligned}$$

Linear Stability Analysis and Filament Gain

The stability of the single-mode solution against nonlinear spatial perturbations must be asserted to determine under what condition beam filamentation will occur. If small perturbations grow with propagation, then the steady-state solution is unstable and the beam can break up under propagation through the fiber. Small perturbations a and n are introduced in the optical field $A_s = \left[\sqrt{P_s} + a(r,\phi,z,t)\exp(i\Delta k_s z)\right]$ and upper-state population density $N_2' = N_2 + n(r,\phi,z,t)$. Linearizing Eqs. (1) and (2) in a and n, while using the steady-state solutions, leads to two coupled linear equations:

$$\begin{aligned}\frac{\partial a}{\partial z} + \frac{1}{v_g}\frac{\partial a}{\partial t} = &\frac{i}{2k_s}\left(p_s^2 a + \nabla_T^2 a\right) + \frac{1}{2}g_s' a \\ &+ \frac{1}{2}\Gamma_s n\sqrt{P_s}\left(\sigma_s^e + \sigma_s^a\right) + i\gamma_s P_s\left(a + a^*\right), \quad (8)\end{aligned}$$

$$\begin{aligned}-\tau\frac{\partial n}{\partial t} = &n\left(1 + \frac{P_s}{P_s^{\text{sat}}} + \frac{P_p}{P_p^{\text{sat}}}\right) \\ &+ \left(N_2 - N_t\frac{\sigma_s^a}{\sigma_s^e + \sigma_s^a}\right)\frac{\sqrt{P_s}}{P_s^{\text{sat}}}\left(a + a^*\right). \quad (9)\end{aligned}$$

Due to the cylindrical geometry, the perturbation is assumed to have the form of a Bessel function,

$$a = a_1 J_{k_\phi}(pr)\exp\left[i\left(k_\phi\phi + k_z z - \Omega t\right)\right]$$
$$+ a_2 J_{k_\phi}(pr)\exp\left[-i\left(k_\phi\phi + k_z z - \Omega t\right)\right], \quad (10)$$

$$n = n_0 J_{k_\phi}(pr)\exp\left[i\left(k_\phi\phi + k_z z - \Omega t\right)\right]$$
$$+ n_0^* J_{k_\phi}(pr)\exp\left[-i\left(k_\phi\phi + k_z z - \Omega t\right)\right], \quad (11)$$

where p is a Bessel parameter, k_ϕ has integer value, k_z is the propagation constant of the perturbation, Ω is its oscillation frequency, and n_0, a_1, and a_2 are constants. The two field-perturbation parameters originate from the fact that a represents a complex field, which is determined by two independent variables.[17] The perturbation in population density n is a real number, which can be determined by one variable. Substituting Eqs. (10) and (15) into the coupled equations leads to linear equations about a_1 and a_2^*. In the condition that they have nontrivial solutions, k_z needs to satisfy

$$k_z = \frac{\Omega}{v_g} + i\frac{1}{2}\left[G(1 + i\xi) - g_s'\right]$$

$$\pm \sqrt{\frac{p'^2}{2k_s}\left(\frac{p'^2}{2k_s} - 2\gamma_s P_s\right) - \frac{1}{4}\left[G^2(1 + i\xi)^2 + g'^2_s\right]}, \quad (12)$$

where $p'^2 = p^2 - p_s^2$. The factor ξ and the saturated power gain G are defined respectively as

$$\xi = \frac{\Omega\tau}{1 + \dfrac{P_s}{P_s^{sat}} + \dfrac{P_p}{P_p^{sat}}}, \quad (13)$$

$$G = \Gamma_s g_s \frac{\dfrac{P_s}{P_s^{sat}}\left(1 + \dfrac{P_s}{P_s^{sat}} + \dfrac{P_p}{P_p^{sat}}\right)}{\left(1 + \dfrac{P_s}{P_s^{sat}} + \dfrac{P_p}{P_p^{sat}}\right)^2 + (\Omega\tau)^2}. \quad (14)$$

The steady-state solution is stable provided the perturbation gain (which is the imaginary part of the k_z) is less than the cavity loss, a reflection of the growth of the laser field in the cavity. With the relation $g = -2Im(k_z)$, the perturbation gain can be extracted from Eq. (14), where the factor 2 is added to define the power gain:

$$g = \mathrm{Re}\sqrt{\frac{2p'^2}{k_s}\left(2\gamma_s P_s - \frac{p'^2}{2k_s}\right) + \left[G^2(1 + i\xi)^2 + g'^2_s\right]}$$
$$- \left(G - g_s'\right). \quad (15)$$

The negative root from Eq. (12) is selected because the gain needs to be positive for the filamentation to occur. Equation (15) gives a general expression for the filament gain. In a fiber laser, when the population inversion is clamped to the threshold, the net gain g_s' is zero. The filament spacing is defined as $w = \pi/p$, and oscillation frequency $f = |\Omega|/2\pi$.

It is already known that the solution of perturbation must have the form of a Bessel function due to the cylindrical geometry of the fiber. Because the perturbation is also an electromagnetic field, it also needs to satisfy the boundary condition on the interface between the core and cladding, which means for every k_ϕ the Bessel parameter p or filament spacing w has only discrete values. In other words, the perturbation also has mode structure, which is similar to the well-known mode properties of the electromagnetic field in fibers. Equation (15) shows no dependence of k_ϕ to the filament gain, but that does not imply that all the modes can resonate. Mathematically, lower-order modes, especially the fundamental mode of the perturbation, do not have dense enough mode structure for filamentation to occur. Physically, the largest amplitude of the fundamental mode is in the center of the core, where the population is depleted. The amplitudes of higher-order modes are zero at the center and large at the margin where the population is undepleted. Therefore higher-order modes of perturbation are more likely to occur than lower-order modes. The peak-to-peak period of squared higher-order Bessel solutions is approximately equal to π, which accounts for the factor π in the definition of filament spacing.

Spatiotemporal Analysis of Filament Gain in Optical Fiber Lasers

Most high-power fiber lasers are Yb doped, due to high quantum efficiency, high doping density, the absence of excited-state absorption, and a long upper-state lifetime. Therefore the parameters used in this section are for typical Yb-doped fiber lasers and are shown in Table 109.V.

Figure 109.59 shows a 3-D plot of normalized filament gain versus normalized filament spacing and oscillation frequency for the signal peak power $P_s = 10$ kW and core diameter $d_{core} = 100\,\mu$m. The figure is symmetric in frequency space; therefore only positive frequency is plotted. To facilitate understanding of Fig. 109.59, normalized gain $g_{norm} = g/\alpha_{cav}$ and normalized filament spacing $w_{norm} = w/a_{core}$ are used, where a_{core} is the radius of

the fiber core. If perturbation gain is larger than cavity loss ($g_{norm} > 1$), the filament can grow in the cavity; if filament spacing is less than core radius ($w_{norm} < 1$), filament can appear in the core. Both of these conditions need to be satisfied for the filament to occur since the gain exists only within the fiber core. In Fig. 109.59 there is a peak in the spatial dimension, which defines the filament spacing at which the perturbation will grow most rapidly, where $g > \alpha_{cav}$. However, the normalized filament spacing corresponding to

Table 109.V: Parameters for ytterbium-doped optical fiber laser calculations.

Parameter	Value
λ_p	0.976 μm
λ_s	1.053 μm
σ_p^a	2476×10^{-27} m^2
σ_p^e	2483×10^{-27} m^2
σ_s^a	20.65×10^{-27} m^2
σ_s^e	343.0×10^{-27} m^2
N_t	9.4×10^{24} m^{-3}
τ	0.84 ms
Γ_p	0.01
n_{core}	1.46
n_{clad}	1.45562
$\bar{n}_2$	2.6×10^{-20} m^2/W
R_1	1
R_2	0.5
L	0.5 m
α_{int}	0.003 m^{-1}
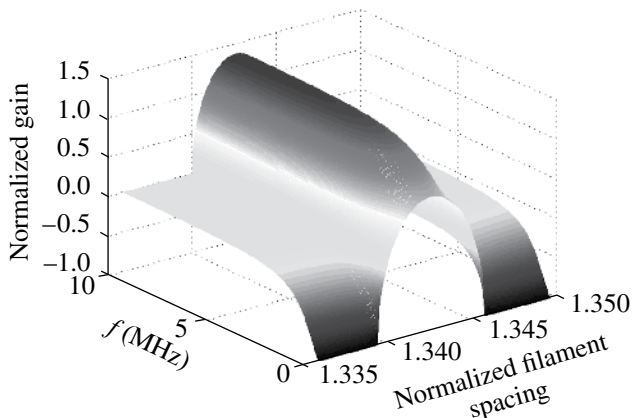
E15023aJR

Figure 109.59
Normalized filament gain versus normalized filament spacing and frequency for $d_{core} = 100$ μm, $P_s = 10$ kW.

the peak region is larger than unity, which means the filament is outside the core, and filamentation cannot occur. In the temporal dimension, the curve is constant with a dip at low frequencies. Since the noise perturbation is dynamic, there is less possibility for the filament to grow statically or in low frequency.

In Fig. 109.60, the signal peak power P_s is increased to 10 MW. The gain peak becomes much larger, and the corresponding filament spacing falls into the core. Because both of the thresholds are reached ($g_{norm} > 1$ and $w_{norm} < 1$), filamentation can occur. There is no observable feature in the temporal dimension. Thus for signal peak power high above the gain threshold, the temporal modulation of the filamentation can occur at any frequency.

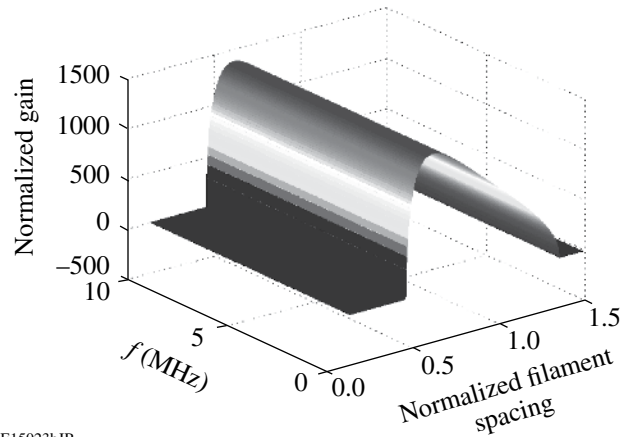E15023bJR

Figure 109.60
Normalized filament gain versus normalized filament spacing and frequency for $d_{core} = 100$ μm, $P_s = 10$ MW.

Figure 109.61 shows normalized filament spacing and normalized filament gain corresponding to the gain peak as functions of signal peak power for the core diameters ranging from 20 μm to 200 μm, when $f = 10$ GHz. With the increase of the signal peak power, the filament gain peak will move toward the small filament spacing and the filament gain will also increase. This agrees with conventional understanding: the higher the power, the denser the filaments and the larger the possibility for filamentation to occur. From Fig. 109.61 the gain threshold for the filamentation to occur ($g = \alpha_{cav}$) can also be observed; it is from a magnitude of 100 W to 10 kW for core diameters ranging from 20 μm to 200 μm. The filament spacing threshold, however, is around a few MW, which then determines the filamentation threshold. Self-focusing, and thus filamentation, is determined only by the peak power (highest power) in fiber lasers, regardless of different average powers. Correspondingly, cw (continuous wave) operation is represented by the same curves in Fig. 109.61.
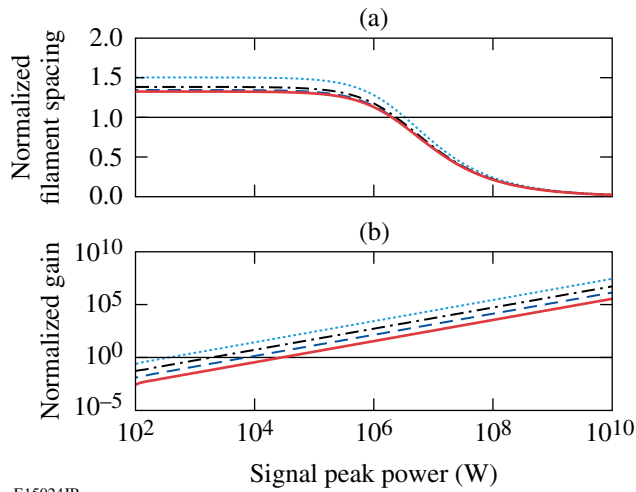
Figure 109.61

(a) Normalized filament spacing and (b) normalized gain as a function of the signal peak power for various core diameters: 20 μm (dotted), 50 μm (dashed–dotted), 100 μm (dashed), and 200 μm (solid) ($f = 10$ GHz).

The gain peak with respect to the normalized filament spacing can be obtained by solving $\partial g/\partial w = 0$. Correspondingly, the filament spacing and signal peak power have the relation $\pi^2/w^2 = 2\gamma_s k_s P_s + p_s^2$. At spatial threshold $w = a_{\text{core}}$, the spatial threshold power is

$$P_{\text{th}}^{\text{spatial}} = \frac{\left(\pi^2/a_{\text{core}}^2\right) - p_s^2}{2\gamma_s k_s}. \tag{16}$$

At high frequency, saturation gain G and factor ξ can be neglected from Eq. (15), and the filament gain can be simplified at the gain peak as $g = 2\gamma_s P_s$. At gain threshold $g = \alpha_{\text{cav}}$, the gain threshold power is

$$p_{\text{th}}^{\text{gain}} = \frac{\alpha_{\text{cav}}}{2\gamma_s}. \tag{17}$$

Figure 109.62 shows the spatial and gain threshold powers as functions of core diameter. As would be expected from an intensity-dependent process, the gain threshold power increases as the core diameter (and thus mode diameter) increases. Conversely, the spatial threshold power decreases with increasing core diameter. For larger modes, the effects of diffraction and waveguiding are weaker; thus the mode becomes more susceptible to filamentation. For all core diameters below 1000 μm, the spatial threshold dominates.

Figure 109.63 shows the normalized and non-normalized filament gains as functions of the signal peak power for three
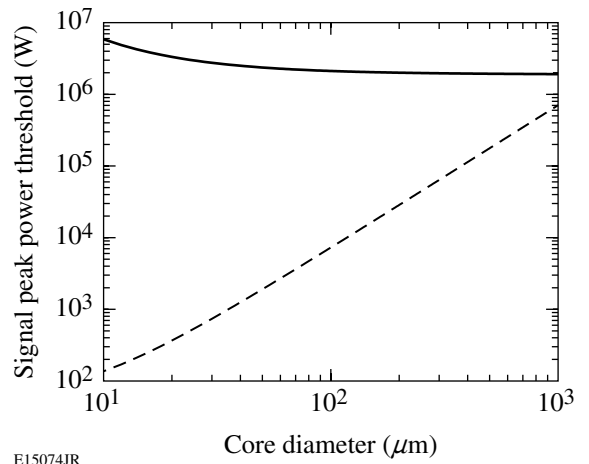
Figure 109.62

Gain threshold power (dashed) and spatial threshold power (solid) as a function of core diameter ($f = 10$ GHz).

cavity lengths, from 0.5 m to 4 m when $d_{\text{core}} = 100$ μm and $f = 10$ GHz. It is instructive to see that the normalized gain changes with cavity length since the cavity length relates to the cavity loss in the unfolded cavity model. The non-normalized gain is not affected by the fiber length since it is dependent only on signal peak power. In the laser cavity, light propagates back and forth, and the optical path is effectively infinitely long.
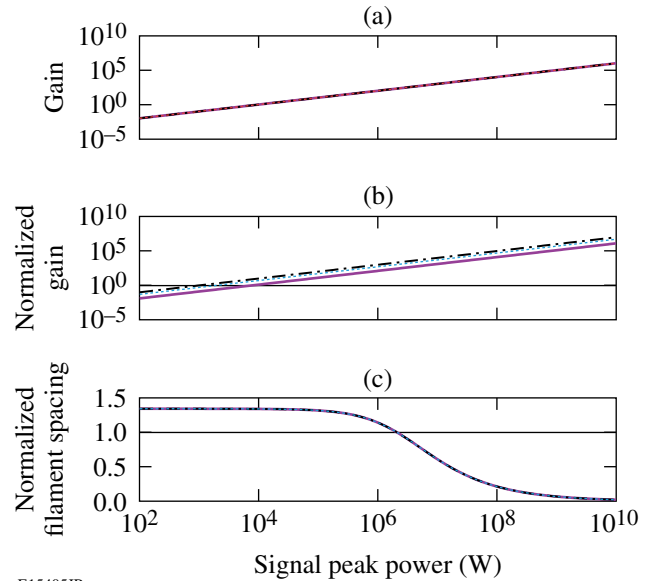
Figure 109.63

(a) Non-normalized filament gain, (b) normalized filament gain, and (c) normalized filament spacing as a function of the signal peak power for three different cavity lengths: 0.5 m (solid), 2 m (dotted), and 4 m (dashed–dotted) ($d_{\text{core}} = 100$ μm, $f = 10$ GHz).

Thus filamentation can occur as long as the filament gain is larger than cavity loss, and it does not depend on cavity length. Figure 109.63(c) shows a plot of the corresponding normalized filament spacing versus signal peak power. The filament spatial properties do not change with cavity length since they have the same transverse spatial structure. Because spatial threshold determines total threshold here, total threshold is independent of cavity length.

Discussion and Conclusion

Only a single experiment reported self-focusing in multi-mode optical fibers.[10] In this work, 25-ps pulses were coupled into multimode fiber, and a mode scrambler was used to distribute pulse energy into every mode. The output beam profile was unchanged for pulse energies less than 1 nJ. When the pulse energy was increased beyond 10 nJ, self-focusing occurred. That is to say, the peak power threshold is between 40 W to 400 W. Considering the use of the mode scrambler, the threshold should be much smaller compared to our model, which assumes an unperturbed starting condition of the fundamental mode. Our model gives a gain threshold of around 1 W and a filament spacing threshold of around 0.5 MW. Starting with a set of modes instead of a single mode will lead to a reduction in the filamentation threshold due to the added spatial variations in the initial condition. More recently, an ultrashort Yb-doped fiber laser system was demonstrated with peak power in the fiber of 15 kW (Ref. 4). Since their peak power is still under the filament spacing threshold (~7 MW from our model), no filamentation occurs.

The thresholds of SBS and SRS are around ~20 W and ~1 kW for short-length cw fiber lasers.[7] For short-pulsed fiber lasers, SBS can be neglected for the broadband spectra; the threshold of SRS can be increased to MW using the LMA fibers. Recently, Cheng[18] has reported a 1.56-MW-peak-power laser system using 80-μm-core, Yb-doped LMA fibers. Given the rapid rate of progress in high-peak-power fiber lasers, self-focusing and filamentation will soon become a problem that will need to be addressed in order to retain high-beam-quality output. It is important to note that since these phenomena effectively increase the spatial frequency of the light in the fiber, bend loss will have a beneficial impact on the filamentation threshold.

In summary, an expression for filament power threshold was derived, using a perturbation method, starting from the paraxial wave equation. The spatial and temporal characteristics of the filament gain were analyzed. Two conditions must be satisfied simultaneously for filamentation to occur: filament gain larger than cavity loss and filament spacing less than the core radius. The filamentation also has the mode characteristics of optical fibers, and its threshold is of the order of a few MW.

REFERENCES

1. B. Ortaç *et al.*, Opt. Lett. **28**, 1305 (2003).

2. J. R. Buckley, F. W. Wise, and F. Ö. Ilday, Opt. Lett. **30**, 1888 (2005).

3. Y.-X. Fan *et al.*, IEEE Photonics Technol. Lett. **15**, 652 (2003).

4. F. Röser *et al.*, Opt. Lett. **30**, 2754 (2005).

5. G. P. Agrawal, *Nonlinear Fiber Optics*, 3rd ed., Optics and Photonics (Academic Press, San Diego, 2001).

6. K. Shiraki, M. Ohashi, and M. Tateda, J. Lightwave Technol. **14**, 549 (1996).

7. J. Toulouse, J. Lightwave Technol. **23**, 3625 (2005).

8. V. I. Kovalev and R. G. Harrison, Opt. Lett. **31**, 161 (2006).

9. C.-H. Liu *et al.*, Electron. Lett. **40**, 1471 (2004).

10. P. L. Baldeck, F. Raccah, and R. R. Alfano, Opt. Lett. **12**, 588 (1987).

11. H. Adachihara *et al.*, J. Opt. Soc. Am. B **10**, 658 (1993).

12. D. J. Bossert, J. R. Marciante, and M. W. Wright, IEEE Photonics Technol. Lett. **7**, 470 (1995).

13. J. R. Marciante and G. P. Agrawal, IEEE J. Quantum Electron. **33**, 1174 (1997).

14. D. Gloge, Appl. Opt. **10**, 2252 (1971).

15. G. P. Agrawal, *Lightwave Technology: Components and Devices* (Wiley, Hoboken, NJ, 2004).

16. P. C. Becker, N. A. Olsson, and J. R. Simpson, *Erbium-Doped Fiber Amplifiers: Fundamentals and Technology* (Academic Press, San Diego, 1999).

17. C.-J. Chen, P. K. A. Wai, and C. R. Menyuk, Opt. Lett. **20**, 350 (1995).

18. M.-Y. Cheng *et al.*, presented at CLEO/QELS 2006, Long Beach, CA, 21–26 May 2006 (Paper CThAA3).

Averaging of Replicated Pulses for Enhanced-Dynamic-Range, Single-Shot Measurement of Nanosecond Optical Pulses

Introduction

Nanosecond-length laser pulses are commonly used in applications such as light detection and ranging (LIDAR) and remote sensing. Accurate measurement of the pulse shape can be critical for specific applications. In particular, laser systems used for inertial confinement fusion (ICF) are required to produce stable, high-contrast pulse shapes to achieve the highest-possible compression of the target.[1,2] While non-linear techniques can measure pulse shapes with a contrast of the order of 10^7 (Refs. 3 and 4), reliable measurement of nanosecond-length pulses can only be achieved with either streak cameras or photodiodes in conjunction with oscilloscopes. Streak cameras offer high-dynamic-range (700:1), multichannel (>8) measurements with 30-ps temporal resolution.[5] However, the relatively slow update rate of single-shot, high-dynamic-range streak cameras (0.1 Hz) precludes their use in applications that require real-time monitoring. Such applications include real-time pulse-shape adjustment or the diagnosis of intermittent problems.

Although oscilloscope sampling rates are continually increasing, the vertical resolution has remained stagnant at 8 bits. Additionally, the effective number of bits (ENOB) is limited to 5 or 6 due to inherent noise floor and digitization effects. Therefore, when using photodiodes with oscilloscopes to measure an optical pulse shape, the oscilloscope becomes the limiting factor of measuring contrast, reducing the measurable dynamic range (DR = 2^{ENOB}) to ~45. Such a contrast is insufficient for the accurate measurement of high-contrast ICF pulse shapes that require measurement of pulses with up to 100:1 shape contrast at a reasonable level of accuracy.

The conventional method for reducing noise on periodic signals is to average temporally sequential events, which has the benefit of reducing the signal-to-noise ratio (SNR) by a factor of $\sqrt{N}$, where N is the number of traces. However, non-repetitive, single-shot events get washed out in the averaging process; this is particularly important when trying to diagnose intermittent failures. Furthermore, the acquisition speed in sequential averaging is reduced by a factor of N.

To capture single-shot events, the pulse can be replicated and averaged with itself to reap the benefits of averaging. In previous work, the pulse of interest was sent through an active fiber loop to produce a replicated pulse train.[6] With gain in the loop, the signal was kept near maximum throughout the pulse train at the expense of amplifier noise added to the signal at every pass. Additionally, the amplitudes of the resultant pulse train followed an exponential decay curve, making it difficult to operate at high repetition rates. In this work, a passive pulse-replication structure is implemented to achieve the series of pulses. The signal is power divided, then recombined with a fixed time delay. Multiple split/recombine stages with digitally increasing delay can yield an arbitrary number of pulses, provided there is sufficient energy in the initial pulse. The replicated pulses are read from a single oscilloscope trace and subsequently averaged in order to achieve increased dynamic range. Similar pulse replication schemes have previously been implemented for increased temporal resolution in measuring picosecond pulses.[7,8]

Experimental Configuration and Measurements

The configuration for passive pulse replication is shown schematically in Fig. 109.64. A series of 2×2 fused-fiber splitters are spliced with $m \times 12.5$-ns-delay fibers between the individual stages. Since successive combinations use splits from previous combinations, the last split is the only place where light is forfeited. It should also be mentioned that since the first splitter has two input ports, two separate pulses can be run simultaneously through this architecture, provided their timing is such that the resultant pulse trains do not overlap in time.

Figure 109.65 shows the resultant 64 pulses from the raw photodiode output as measured on a Tektronix TDS 6154C digital storage oscilloscope, which has a 12-GHz analog bandwidth. The pulses are nominally spaced at 12.5 ns, although precise spacing is not critical to the method.

The trace is acquired from the scope at 25-ps resolution, and the individual pulses are separated by temporal binning. The fine temporal alignment between two pulses $P_i(t)$ and $P_j(t)$

E15367aJR
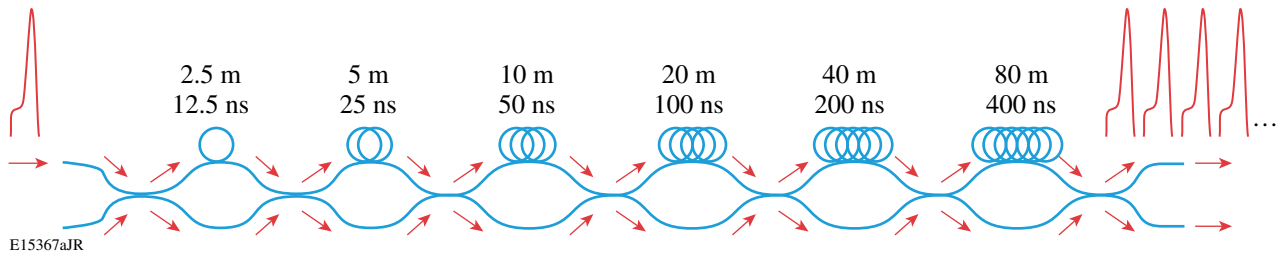
Figure 109.64
Schematic of 64-pulse passive pulse-stacking architecture.

E15367bJR
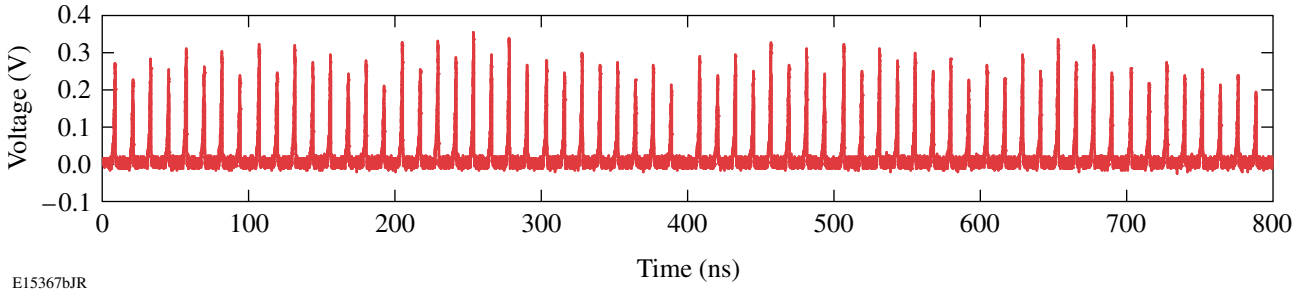
Figure 109.65
Oscilloscope trace showing 64 pulse replicas.

in the pulse train is measured once with a cross-correlation method using the formula

$$X_{ij}(t) = F^{-1}\left\{F[P_i(t)] \times F^*[P_j(t)]\right\}, \tag{1}$$

where F and F^{-1} denote the discrete fast Fourier transform and its inverse and the asterisk denotes the complex conjugate. The temporal offset t_{ij} is the value of t that maximizes the function $X_{ij}(t)$. $P_j(t)$ is offset by this amount before averaging with the other pulses from the pulse train.

Figure 109.66 shows the single-shot, self-averaged pulse together with a multi-shot–averaged pulse (64 averages) and a single pulse (no averaging) for comparison. Similar to the multi-shot average, the single-shot average shows clear performance enhancement compared to the single-shot case. Additionally, due to the jitter inherent in temporal acquisitions, the multi-shot–averaged case has a reduced effective bandwidth compared to the single-shot–averaged trace, as can be seen in the relative sharpness of the leading edges of the corresponding pulses in Fig. 109.66.

The dynamic range of the measurement is defined as the ratio of the peak of the signal to the signal level where the SNR is equal to unity. Figure 109.67 shows the calculated dynamic range for the single-shot and multi-shot averages as a function of the peak signal on the photodiode. In the multi-trace averages, there are 64 temporally displaced copies at different signal amplitudes (as can be seen in Fig. 109.65), each of which is plotted independently. Given that the noise level is identical

E15368aJR

Figure 109.66
Single-shot, single-shot–averaged, and multi-shot–averaged pulse shapes. Arbitrary offsets have been added for clarity.

for all cases, increased signal amplitude corresponds directly to increased dynamic range. For the single-shot–averaging case, the data point is plotted versus the average amplitude of all of the peaks in the 64-pulse train. This plot clearly demonstrates th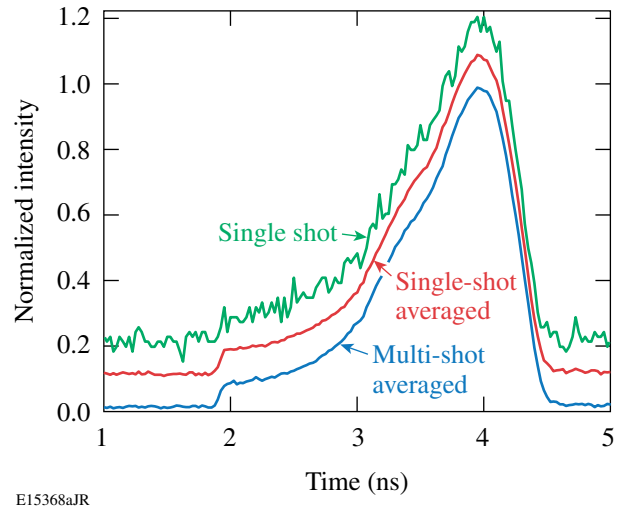at single-shot averaging works just as well as multi-shot averaging without the disadvantages of reduced acquisition time and the loss of single-shot events. For further comparison, the manufacturer's specifications rate the oscilloscope at 5.5 ENOB, corresponding to a maximum dynamic range of 45. The single-shot–averaging technique demonstrates a dynamic range of 312, or an ENOB of 8.3, an improvement of nearly 3 bits over the nominal performance of the oscilloscope. This level of improvement is expected from the averaging function; since the SNR is reduced by $\sqrt{N}$ and the maximum signal remains nearly the same, the dynamic range is improved by the same factor, for which $\sqrt{64} = 2^3$.
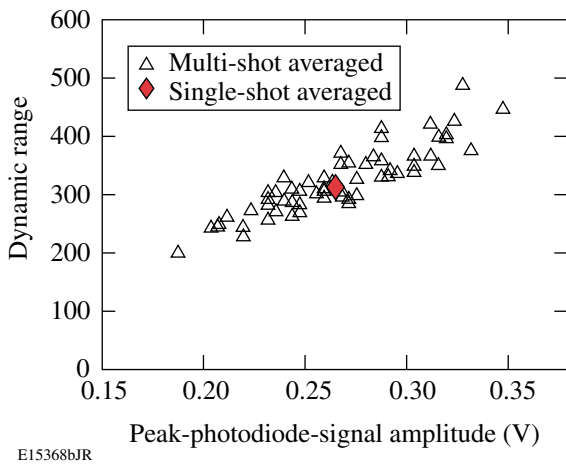

Figure 109.67
Dynamic range of single-shot–averaged and multi-shot–averaged pulses

Discussion and Conclusions

In principle, this method can be extended to a larger number of pulses in the pulse stacker, thereby achieving even better dynamic range and SNR. The ultimate limitation is peak-detected signal power, which is reduced by a factor of 2 every time the number of pulses is doubled. Provided the laser system has sufficient energy to spare for the measurement, the upper limitation on power launched is driven by damage and nonlinear effects in the fiber.

For spectrally narrowband pulses, stimulated Brillouin scattering (SBS) becomes the limiting factor in power launched into the fiber. The conventional threshold equation for the SBS threshold is $g_B P_0 L_{\text{eff}} / A_{\text{eff}} = 21$, where g_B is the Brillouin gain,

P_0 is the threshold peak power, L_{eff} is the effective interaction length, and A_{eff} is the effective mode area.[9] Since the light scattered by SBS is in the reverse propagation direction, the effective length of the interaction is determined by the time of flight of the pulse in the fiber. Using typical numbers for 1053 nm, the SBS energy threshold for a 1-ns pulse is of the order of several microjoules.

Conventional damage thresholds for fibers are near 5 J/cm^2 for a 1-ns pulse, although higher values have been reported.[10] Using the more-conservative value leads to an upper energy limit of the order of a few microjoules for a single-mode fiber at 1053 nm (~6-μm core). Together, damage and SBS considerations limit the maximum launched power to a few microjoules.

The receiver of the system also has its limitations. Generally, detection of low light levels may lead to signal-to-noise issues; therefore, higher light levels are desired. However, the photodiode itself has an upper limit of peak signal power before the pulse becomes distorted by space-charge effects that arise when the extracted charge exceeds more than a few percent of the charge stored in the photodiode. For the Discovery DSC-30 photodiodes that were used, the power was limited to approximately 10 pJ per pulse in the pulse train; reasonably beyond that value, pulse-shape distortion became noticeable.

Together, the fiber launch energy and the photodiode linearity determine the maximum dynamic range of the detected signals. The single-pulse energy after passing through the system is given by $(\eta/2)^N$, where η is the transmission of the coupler and N is the number of stages. Using the energy limitations described above with a conservative 0.6-dB insertion loss for the couplers, a total of 14 stages can be utilized. Thus, this technique can be extended to achieve an increase of 7 bits over the nominal oscilloscope performance.

In conclusion, measuring pulse shapes beyond the dynamic range of oscilloscopes is achieved by passive temporal-pulse stacking. Pulses are averaged with their time-delayed replicas without introducing additional noise or jitter, allowing for high-contrast pulse-shape measurements of single-shot events. A dynamic-range enhancement of 3 bits is demonstrated experimentally, and the technique can be extended to yield an increase of up to 7 bits of additional dynamic range over nominal oscilloscope performance. Moreover, single-shot averaging does not suffer from temporal jitter; therefore it can produce higher bandwidth measurements than conventional multi-shot averaging.

ACKNOWLEDGMENT

REFERENCES

1. J. D. Lindl, *Inertial Confinement Fusion: The Quest for Ignition and Energy Gain Using Indirect Drive* (Springer-Verlag, New York, 1998).

2. P. W. McKenty, V. N. Goncharov, R. P. J. Town, S. Skupsky, R. Betti, and R. L. McCrory, Phys. Plasmas **8**, 2315 (2001).

3. S. Luan *et al.*, Meas. Sci. Technol. **4**, 1426 (1993).

4. A. Jullien *et al.*, Opt. Lett. **30**, 920 (2006).

5. W. R. Donaldson, R. Boni, R. L. Keck, and P. A. Jaanimagi, Rev. Sci. Instrum. **73**, 2606 (2002).

6. A. Jolly, J. F. Gleyze, and J. C. Jolly, Opt. Commun. **264**, 89 (2006).

7. G. C. Vogel, A. Savage, and M. A. Duguay, IEEE J. Quantum Electron. **QE-10**, 642 (1974).

8. K.-L. Deng *et al.*, IEEE Photonics Technol. Lett. **10**, 397 (1998).

9. G. P. Agrawal, *Nonlinear Fiber Optics*, 2nd ed., Optics and Photonics Series (Academic Press, San Diego, 1995), pp. 50–54.

10. A. Galvanauskas, presented at Frontiers in Optics 2006/Laser Science XXII, Rochester, NY 8–12 October 2006 (Paper FWA5).

Laser-Driven Magnetic Flux Compression
for Magneto-Inertial Fusion

Introduction

Direct-drive inertial confinement fusion (ICF) has seen formidable progress in recent years.[1,2] The energy coupling and hydrodynamics of the implosion continue to be the dominant factors in the path to successful conversion of the incident laser energy E_L into thermonuclear burn energy E_{TN} (Ref. 3). For direct-drive implosions, the energy gain $G = E_{TN}/E_L$ depends strongly on the implosion velocity V_i and on the coupling efficiency $\eta_c = \eta_{abs}\eta_h$. The dominant part of this product is the hydrodynamic efficiency η_h, the ratio of the kinetic energy of the implosion to the incident laser energy E_L (a few percent), while the absorption efficiency η_{abs} is of the order of 60% to 80% depending on the laser wavelength. It can be shown[4] that the gain of an ignited target scales as $G \sim \eta_h V_i^{-2}$, while η_h is approximated well with $\eta_h \sim V_i^{-0.75} I_L^{0.25}$, where I_L is the laser intensity. Thus, the thermonuclear gain is roughly inversely proportional to the implosion velocity. On the other hand, successful ignition of the assembled central hot spot (the necessary condition for any gain in ICF) in conventional ICF requires that the hot spot reaches a certain temperature T_{hs} (of the order of 5-keV ion temperature), which requires high implosion velocities. This is confirmed by the scaling relations of Ref. 4, which show that $T_{hs} \sim V_i^{1.4}$. Too slow a compression will not compensate thermal losses and the hot spot will not reach the required temperature, although the areal density of the fuel may attain high values. These restrictions on V_i set limits on both the minimum energy for ignition and the maximum gain in conventional ICF.

In what is called a magneto-inertial fusion (MIF) implosion, an additional thermal insulation of the fuel forming the hot spot is provided by a strong magnetic field in a typical direct-drive ICF target.[5] The hot spot can reach ignition temperatures due to the reduced electron thermal conductivity, and then, when the nuclear burn develops, the alpha particles will also be confined to the burn region, delivering the energy needed to support the burn wave. Considering a hot spot with a characteristic radius $R_h = 40\ \mu$m, a density of ~10 g/cc, and a temperature of 5 keV, an electron–cyclotron frequency ω_{ce} exceeding the collision frequency ν_e is required for magnetic insulation; i.e., $\omega_{ce}\tau_e > 1$,

where $\tau_e = 1/\nu_e$ is the collision time. This corresponds to $B > 10$ MG due to the high densities (small collision times) in the hot spot. The condition for alpha-particle confinement $r_\alpha/R_h < 1$ (where r_α is the gyroradius) requires $B > 95$ MG for the 3.5-MeV fusion alphas in a burning DT plasma. Such strong magnetic fields are very difficult to create externally. The largest macroscopic magnetic fields have so far been generated only by magnetic-flux compression in metallic liners driven by chemical detonation.[6,7] The measured upper limit that we are aware of is of the order of 10 MG (Ref. 8). Flux compression with an ICF-scale laser like OMEGA[9] is a possible way to obtain even stronger fields. The idea is to perform an ICF implosion in which there is a preimposed macroscopic magnetic field, amplified with the compression of the target plasma. Flux compression with a plasma "liner" was discussed by Liberman and Velikovich in Refs. 10 and 11 more than 20 years ago. In Ref. 11 the authors consider a magnetic field that is "frozen" in plasma compressed by a thin cylindrical wall. They show effective compression of the field with low field diffusion losses. Z pinches and laser ablation are mentioned as possible drivers for the hydrodynamic compression of the plasma.

The basic concept of flux compression can be described with the following simple formulas. In cylindrical geometry, neglecting the diffusion of the magnetic field, the conservation of the magnetic flux Φ will yield an increase proportional to the reduction of the encircled area:

$$B_{max} = B_0\left(\frac{r_0}{r_{min}}\right)^2 \frac{\Phi}{\Phi_0} = B_0\left(\frac{r_0}{r_{min}}\right)^2. \qquad (1)$$

In the general case of nonzero flux diffusion out of the confining volume, the flux compression equation is obtained from Eq. (1) by differentiation:

$$\frac{1}{B}\frac{dB}{dt} = \frac{1}{\Phi}\frac{d\Phi}{dt} - \frac{2}{r(t)}\frac{dr(t)}{dt}. \qquad (2)$$

This can be expressed in terms of the implosion velocity $V_i = -dr(t)/dt$ and the speed of resistive field diffusion $V_f = \eta/\mu_0\delta$,

where η is the plasma resistivity, μ_0 is the permeability of vacuum, and δ is a characteristic scale length of the conductor (plasma) shell in question. The ratio $\mathrm{Re}_m V_i / V_f$ is the magnetic Reynolds number, the dimensionless metric that determines the effectiveness of the flux compression scheme. It is the ratio of the convective to the dissipative term in the magnetic flux equation and as such determines the magnetohydrodynamic (MHD) regime (from ideal MHD at $\mathrm{Re}_m \gg 1$ to strictly resistive MHD at $\mathrm{Re}_m < 1$). The speed V_f can be obtained from the time scale[12] of an assumed exponential flux decay through the conductive region interface (with scale length δ), given by the ratio of shell inductance $\mu_0 \pi r^2$ to resistance $\delta/(2\pi r\eta)$ (per unit axial length):

$$\tau = -\left(\frac{\mathrm{d}\ln\Phi}{\mathrm{d}t}\right)^{-1} = \frac{\mu_0 r \delta}{2\eta} = \frac{r}{2V_f}.$$

Expressing (2) in terms of Re_m yields

$$\frac{1}{B}\frac{\mathrm{d}B}{\mathrm{d}t} = -\frac{2V_f}{r(t)} + \frac{2V_i}{r(t)} = -\frac{1}{r(t)}\frac{\mathrm{d}r}{\mathrm{d}t}\left(1 - \frac{1}{\mathrm{Re}_m}\right) \quad (3)$$

and shows that the field will increase only if V_i is much larger than V_f, i.e., $\mathrm{Re}_m \gg 1$. Thus, when the diffusion of flux into the plasma shell due to its finite resistivity is considered, Eq. (1) is modified to

$$B_{\max} = B_0 \left(\frac{r_0}{r_{\min}}\right)^{2\left(1 - \frac{1}{\langle\mathrm{Re}_m\rangle}\right)}, \quad (4)$$

which follows from Eq. (3) for the simple case of Re_m constant in time (or equal to an appropriately chosen average value $\langle\mathrm{Re}_m\rangle$).

The OMEGA laser[9] is an ideal test bed for magnetic-flux-compression experiments in plasmas [Fig. 110.1(a)]. Typical implosion velocities V_i in excess of 10^7 cm/s, coupled with the high conductivity of the hot plasma containing the field, should keep the magnetic Reynolds number large and provide for effective compression of the seed magnetic flux. The seeding of a magnetic field in the target can be accomplished with a coil system driven by a device such as the one shown in Fig. 110.1(b) and described later in this text. In contrast to compression with metallic liners, an ICF-scale, cylindrical-ablator shell (usually plastic) driven by a laser does not by itself trap the enclosed magnetic flux, but delivers kinetic energy to the plasma that contains the field. This is the gas fill that is ionized by the initial hydrodynamic shock to a highly conductive plasma state in which the resident seed magnetic field is captured. At the onset of the laser pulse, the rapid increase in ablation pressure drives this shock through the shell; it breaks out into the gas, filling the capsule, and fully ionizes it, raising the temperature in the gas post-shock region to about 100 eV. It is this region with a high magnetic Reynolds number (a time-averaged value of $\mathrm{Re}_m > 60$ is obtained from the simulations) that traps the magnetic field. The colder and more-resistive shell then provides the mechanical work for compression of this plasma and the field embedded in it. Figure 110.2 shows the simulated electron-temperature
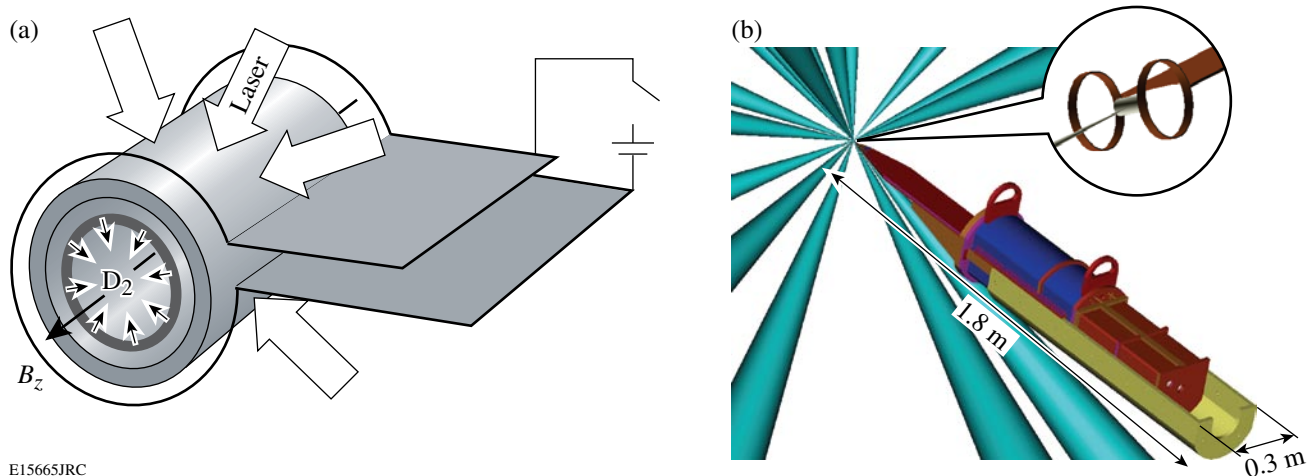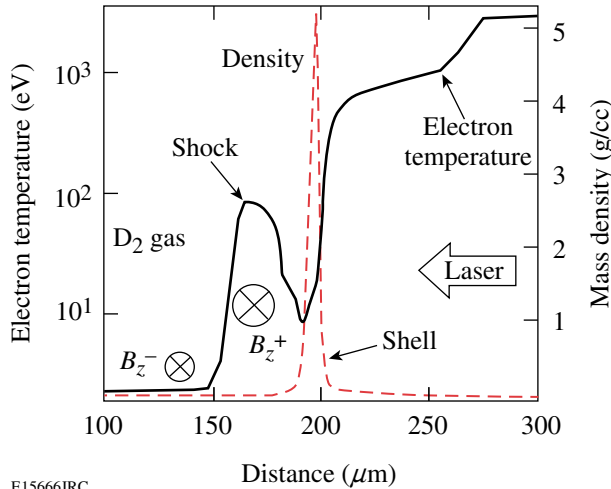

E15665JRC

Figure 110.1
(a) Target-coil geometry for magnetic-flux-compression experiments. The cylindrical target is compressed radially by the laser beams. A single-turn coil delivers the seed magnetic pulse. (b) A compact, capacitive discharge system designed for integration in multibeam OMEGA experiments drives the current in the coils.

Figure 110.2

The imploding shell (peak in dashed curve) compresses the shock-ionized gas fill that has trapped the axial magnetic field in the hot post-shock region.

profile in the D$_2$ gas fill during shock propagation. This is for a 1.5-mm-long, 860-μm-diam, 20-μm-thick cylindrical plastic shell filled with 3 atm of D$_2$. The plastic shell can be identified in the density profile plotted at the same time. It is interesting to note that there is diffusion of magnetic flux out of the post-shock region not only through the shell but also into the unshocked gas inside the target (Fig. 110.2). This is driven by the steep gradient in resistivity and the short scale length of the shock interface, leading to a very large value of the diffusion speed. The simulation confirms it with an increase in the magnetic field ahead of the shock. The shock-front diffusion speed is

$$V_f = \frac{\eta^-}{\mu_0} \frac{1}{B_z^-} \frac{\partial B_z^-}{\partial r}, \tag{5}$$

where the "–" denotes the pre-shock region. For our case, if we consider the good approximation $\eta^- \gg \eta^+ \to 0$, an integration of the induction equation across the shock will yield a jump condition written in the frame of reference of the shock front moving with velocity u_s,

$$u_s B_z^- - \frac{\eta^-}{\mu_0} \frac{\partial B_z^-}{\partial r} = \left(u_s - V_i\right) B_z^+. \tag{6}$$

This can be rewritten as

$$\frac{B_z^+}{B_z^-} = \frac{u_s - V_f}{u_s - V_i}. \tag{7}$$

This ratio shows that field cumulation in the post-shock region (large field ratio) needs large V_i, while V_f acts to reduce the field jump by raising the field ahead of the shock. In contrast, at the ionized gas–shell interface, the resistivity scale length is larger and the shell plasma is a conductor, albeit not as good as the plasma in the post-shock region. This leads to lower outward diffusion of the field and net flux compression due to the high convergence velocity of the shell. The field and density profiles at the center of the target, as simulated by *LILAC*-MHD,[13] are shown in Fig. 110.3 for the time of peak compression. One can see that in the hot spot (in this case the central 20 μm of the target) the magnetic field reaches the values (>95 MG) needed for alpha-particle confinement in a DT fusion target. The result is a six-fold increase in the simulated stagnation ion temperature to >7 keV, when compared to a simulation with no seed field.
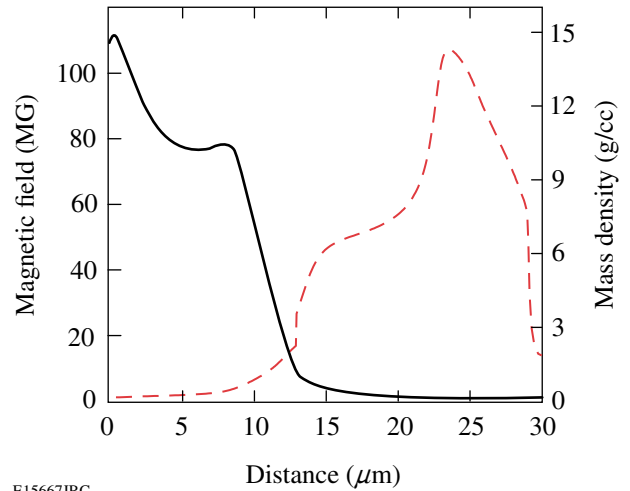
Figure 110.3

LILAC-MHD results for a 3-atm, D$_2$-filled CH capsule at the time of peak compression: field (solid curve) and density (dashed curve) profiles at the target center.

MIFEDS (Magneto-Inertial Fusion Energy Delivery System) Seed-Field Generator

To obtain multi-megagauss fields with the laser-driven flux-compression (LDFC) scheme, it is necessary to start from substantial seed-field values due to the limit in maximum convergence ratio of the compression. For a cylindrical geometry [Fig. 110.1(a)], the convergence ratio is between 10 and 20. Supplying tens of tesla to the target chamber center of OMEGA is nontrivial since the parametric space is restricted on one side by the small physical volume available and on the other by the need of high energy in the magnetic pulse. This is actually a high-power requirement because of the short duration of an

OMEGA implosion (1-ns pulses are used in the experiments). A compact device shown in Fig. 110.4 [see also Fig. 110.1(b)] generating seed magnetic fields of sufficient strength (up to 0.15 MG measured) was built to test the laser-driven magnetic-flux-compression concept. It fits in a diagnostic insertion port on the OMEGA chamber, stores not more than 150 J, and provides magnetic pulses with an intensity of 0.1 to 0.15 MG and ~400-ns duration.
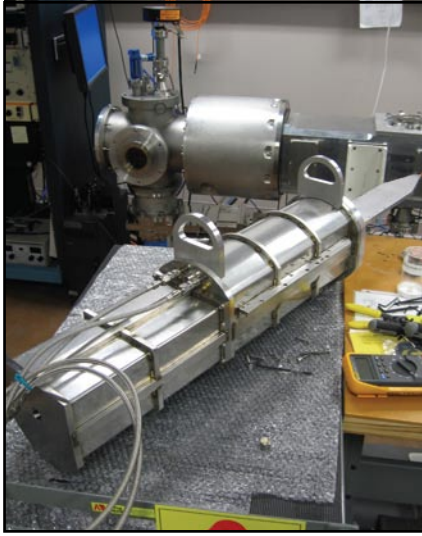
E15668JRC

Figure 110.4
MIFEDS device in the diagnostic TIM (ten-inch manipulator) facility.

The interaction volume in the OMEGA target chamber is characterized by the target size and is thus limited to a linear dimension of a few millimeters. This small volume is in the field of view of an extensive suite of diagnostics, pointed at the target chamber center from various angles and occupying conical space envelopes that should not be broken to prevent beam clipping or conflict/collision with other diagnostics. For the LDFC scheme described above, a magnetic pulse of sufficient strength must be delivered to the target interaction volume within such an envelope, and the field must be created by coils that do not obscure laser beams aimed at the target nor the view of the various diagnostics. Such restrictions point at low-mass, single-turn coils as the best solution. For a cylindrical target configuration, a Helmholtz-type coil provides advantageous geometry since a large number of laser beams can be pointed at the target in between the two coils without obscuration. An optimization of the field-to-coil current ratio

$$B_z/I \approx \mu_0 R^2 \left(R^2 + D^2/4 \right)^{-3/2},$$ (8)

with the incident laser beams taken into account, leads to a choice of radius R for each and separation D between the coils that deviates from the standard Helmholtz coil where $R = D$. In the design suitable for OMEGA experiments, $R = 2.0$ mm and $D = 4.4$ mm. Figure 110.1(b) shows a cylindrical target with a typical diameter of 860 μm as it is placed between coils with the above dimensions. The coils were made from copper-clad Kapton foil with a thickness of 100 μm and an individual coil width of 0.5 mm. The inductance of such a single-turn coil is very low. The calculated value, obtained from both an analytical formula and simulations of the coil's magnetic energy with the magnetostatic code Radia,[14] was ~25 nH, consistent with measurements. To receive most of the energy stored in the charging circuit, the coil inductance must be the dominant portion of the total circuit inductance. If this is observed, the resulting low-inductance circuit will provide the stored energy in a very fast discharge pulse. Since our reference time scale—the duration of the laser-driven implosion—is less than 3 ns, this fast discharge is warranted, reducing the total energy required for the generation and support of the seed magnetic field. A discharge pulse that lasts hundreds of nanoseconds will provide a large time window at peak current/field. A very fast discharge is, in fact, required with this type of low-mass (9-mg total measured mass of the two turns in the base design) coil since the peak current values must be reached before the joule heating destroys the coil and quenches the current rise. The rate of temperature rise, determined from the specific heating rate $j^2\eta$, where j is the current density and η is the resistivity, can be written as $c_p dT/dt = j^2\eta$, with c_p being the specific heat of solid copper, generally a function of temperature. By integrating this relation, we obtain the "fuse" action integral

$$\int_{T_0}^{T_1} \frac{c_p}{\eta} dT = \int_0^{t_p} j^2 dt,$$ (9)

which relates the material properties to the time integral of the current density. At some value of this integral, the coils will melt and the current will be interrupted. Since j is set by the peak field requirement to minimize the action integral, we need to reduce the time of current propagation t_p. Whether this time will be sufficient for the current to reach its peak value is determined by comparing t_p to the time constant $\tau = L/R$ of the discharge. Expressing the joule heating energy deposited from $t = 0$ to t_p, in terms of the peak current I_{max} and the average resistance $\overline{R}(B,T)$, and using the time constant τ, we obtain the ratio of the maximum magnetic energy $E_m(t_p)$ to the heating in the coils, as the ratio of the pulse rise time t_p to the circuit time constant,

$$E_j(t_p) = \int_0^{t_p} R(t)I^2 \, dt \approx \overline{R}(B,T)\frac{I_{max}^2}{2}t_p$$

$$\approx \frac{t_p}{2\tau}LI_{max}^2 = \frac{t_p}{\tau}E_m(t_p). \tag{10}$$

This ratio needs to be minimized for the most-efficient energy transfer. Based on these considerations, we have chosen a capacitor bank consisting of two 100-nF capacitors connected in parallel, with total inductance of ~8 nH. These are S-series[15] plastic case capacitors (Fig. 110.5) from General Atomics, rated for 40 kV, and pulsed currents of 50 kA. Their combined ESR value for the fundamental frequency of the discharge is less than 2.5 mΩ. Charged to their rated voltage, the capacitors can store 160 J but have been used routinely at 30-kV charge voltage, storing 90 J of energy. The same restrictions (as-low-as-possible inductance and resistance) apply to the discharge switch and transmission wiring. In the design, a very-low-inductance, coaxial, laser-triggered spark gap is mounted directly to the capacitors, while the return path consists of two 3-in.-wide copper bars (Fig. 110.5). This compact package can fit in a small vessel that can be placed in an OMEGA TIM (ten-inch manipulator) along with its dedicated charging circuitry. This way, the transmission length is greatly reduced in favor of the desired small overall inductance, and no high-voltage lines are fed into the target chamber.

A CAD drawing of the MIFEDS device as placed in the TIM rolling platform is shown in Fig. 110.6. There are two distinct compartments: In the front is the energy storage and switch block, while the charger and protection circuitry are located in the back. There is a metal barrier between the compartments, with openings only for the trigger beam and the charging cables. This way, the capacitive coupling of noise from the rapid, high-current discharge in the front into the components in the back is reduced. Those components consist of (a) the power supply—a 30-W dc-to-dc converter[16] with a supply voltage of 24-V dc and a rated peak voltage of 40 kV
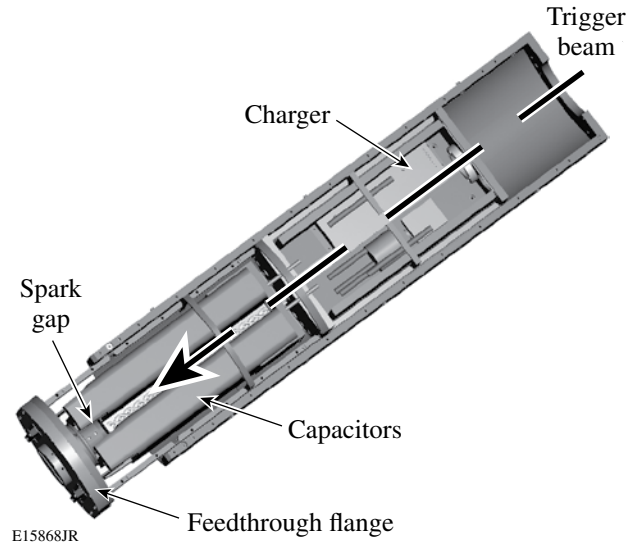

Figure 110.6
CAD drawing of the main MIFEDS components inside the air box that is mounted to the TIM rolling platform.
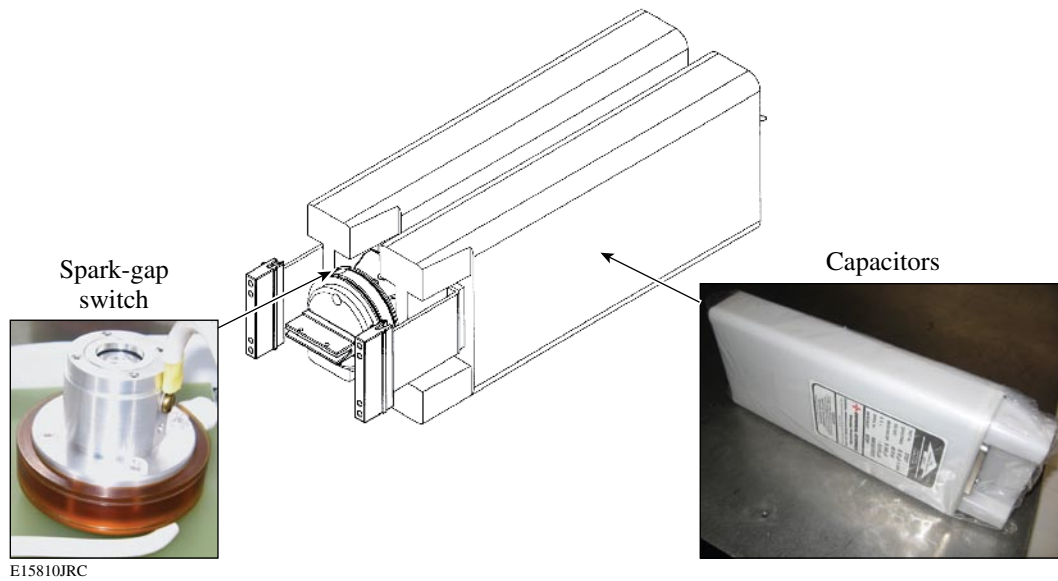

Figure 110.5
Low-inductance assembly of the energy storage capacitors and the laser-triggered spark-gap switch. The actual devices are also shown.

at maximum current of 750 μA; (b) a high-voltage relay, used to dump to ground the residual energy immediately after discharge; and (c) an array of diodes and current-limiting resistors to protect the high-voltage power supply from reverse voltage transients, a pressure sensor, a low-voltage solid-state relay, and an interface board to monitor and control the charge cycle. Careful packaging was necessary to be able to place and safely operate these components at >30 kV. Care was taken to provide a clear optical path for the trigger laser beam along the axis of the air box.
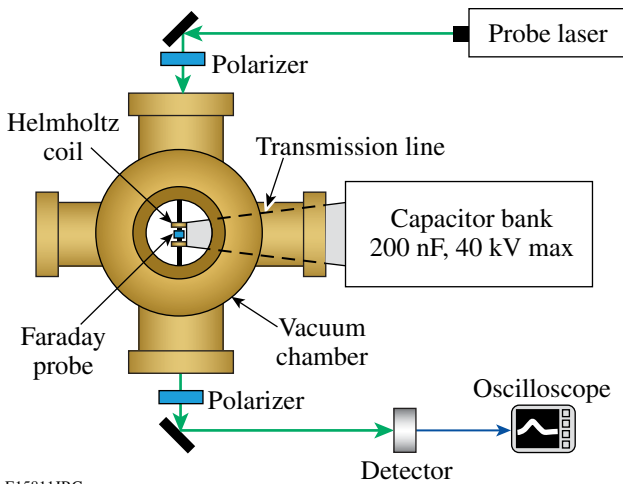
Magnetic-Field Measurements

The main diagnostic method for the seed magnetic field during the development of MIFEDS has been magneto-optical. Faraday rotation (Fig. 110.7) was used to measure the fields generated between the MIFEDS coils when testing coil geometry, transmission line design, and the high-voltage switch. The probe laser was a temperature-stabilized, frequency-doubled, cw Nd-YAG laser providing 50 mW of power at 532-nm wavelength. The probe, placed between the two coils, was a 1-mm-thick, terbium-doped glass disk with a 1.5-mm diameter and Verdet constant $V = 100$ radT^{-1}m^{-1}. Because of the strong fields expected, the two polarizers were coaligned for maximum transmission of the linearly polarized laser light; this is not the highest sensitivity configuration but the easiest to work with, especially when rotation angles larger than 90° are possible. The drop in the signal due to Faraday rotation in the glass sample during the magnetic pulse was then observed and the field determined from the detected light intensity $I_{det}(t)$, $I_{det}(t) = I_0 \cos^2[\theta_{rot}(t)]$, where $\theta_{rot}(t) = V\bar{B}_z(t)d_z$ is the Faraday

rotation angle as a function of the average axial field in the sample and its thickness d_z. Figure 110.8 shows the change in laser intensity triggered by the Faraday rotation and recorded by a fast optical detector connected to an oscilloscope. Three intensity traces show very repetitive magnetic pulses with an average pulsewidth of ~400-ns FWHM and decay time of the order of 1.5 μs. The maximum magnetic field at the center of the coil ranges from 14 to 15.7±0.3 T (10 T = 0.1 MG). These fields correspond to a total coil current of 79.3 kA for a separation $D = 2.4$ mm and a coil radius of 2 mm used in these tests. The magnetostatic Radia simulations,[14] which account for the aspect ratio of the coil, gave a total current of 76 kA for the same peak field.

A simple analytical model was developed to look at the temporal behavior of the coil current. It is based on the equivalent, damped LRC circuit, where the reference damping α was given by an average value of the time-dependent coil resistance. The current from the model,

$$I_{mod}(t) = \frac{\omega_0^2 + \alpha^2}{\sqrt{\omega_0^2 - \alpha^2}} CV_{max} \exp(-\alpha t) \sin\left(\sqrt{\omega_0^2 - \alpha^2}\, t\right), \quad (11)$$

where V_{max} is the charging voltage, C is the capacitance, and ω_0 is the fundamental frequency of the circuit, was then converted to the equivalent Faraday rotation signal, using Eq. (8). The best-fit parameters were sought and the fit is shown in Fig. 110.9. The best-fit parameters are $R_{avg} = 0.21$ Ω, $\omega_0 = 8.78 \times 10^6$ rad/s, and $\alpha = 2.1 \times 10^6$ rad/s. From the fit we then determined a total circuit inductance of 65 nH, which is in line with calculations for the individual components. The agreement between the

E15811JRC

Figure 110.7
Faraday rotation setup for the measurement of the seed magnetic fields on the benchtop.
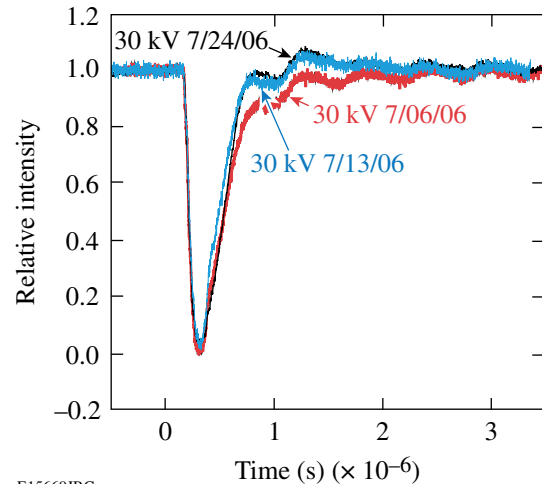
E15669JRC

Figure 110.8
Faraday rotation data over two weeks of MIFEDS discharges. The data show good repeatability with a pulse duration of ~400-ns FWHM and a rise time of ~160 ns.

(a) 30-kV charge — 13 July 2006

◇ Voltage
— Fit

(b)

E15812JRC
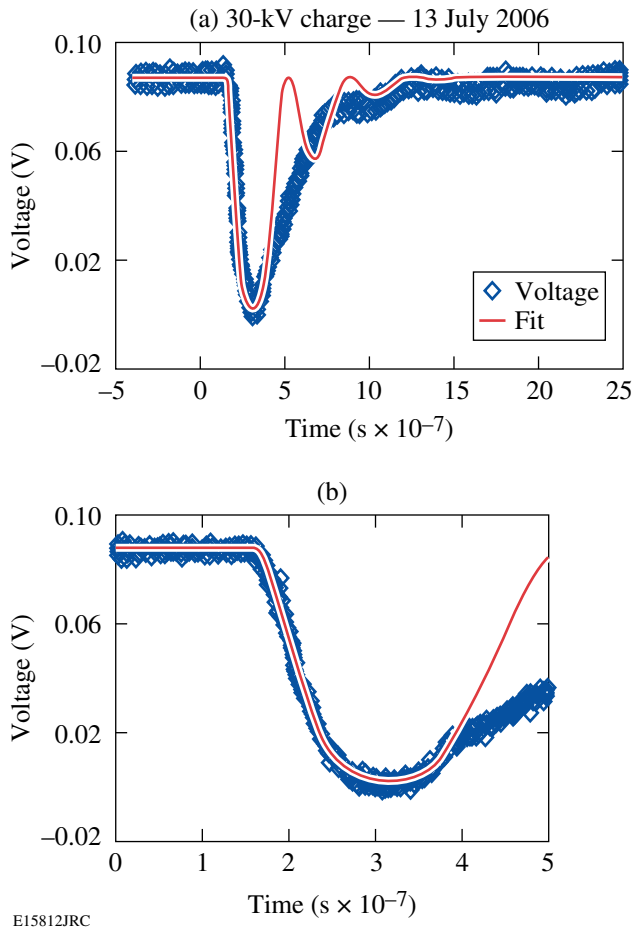
Figure 110.9
A simple analytical model was fit to the data. It matches the experiment very well until after the current peak.

experiment and the analytical model is very good until after the peak of the current pulse. At later times, the experimental data show rapid change in the time-dependent resistance of the circuit, which becomes overdamped. Several possible reasons for that include joule heating in the coil, extinguishing of the streamer in the spark-gap switch, or even change in the contact resistance somewhere in the transmission path. From a design standpoint this is beneficial since we are able to reach the peak current while the load is less resistive. The detrimental voltage reversal, characteristic of underdamped circuits, is avoided with this rapid increase of the circuit resistance.

Initial Experiments on OMEGA

Before testing it on OMEGA, the MIFEDS device was qualified in the diagnostic TIM facility, where a number of discharges were performed to monitor the charge cycle, EMI noise, gas pressure stability, and other parameters. The interfacing of MIFEDS to the diagnostic TIM closely emulated the OMEGA chamber/TIM setup (shown in Fig. 110.10). An optical Faraday rotation setup was arranged and the magnetic field pulses were recorded. The precise time delay from the triggering of a discharge to the time of peak magnetic field was established. The delay was highly repetitive at 310 ns with standard deviation of about 18 ns. One of the concerns was the survival of the cylindrical target during the rise time of the magnetic pulse. The possibility of destroying the target before the laser shot endangers the OMEGA laser components since some of the unterminated beams can back-propagate at full energy. A special safety circuit was implemented to prevent the propagation of OMEGA beams in the case of MIFEDS prefire (Fig. 110.10). It is connected to a pickup coil placed at the spark-gap switch in MIFEDS to detect the current pulse.

E15813JRC

Figure 110.10
Setup of the MIFEDS infrastructure in the OMEGA Target Bay. The three main components are the switching, control and monitoring, and safety circuits.

It was established that the target needs a 100-nm Al overcoat to provide reasonable retention of the gas at 3- to 5-atm pressure. This raised an important question about the time needed by the seed field to diffuse through the aluminum before an OMEGA shot. If the field is excluded from the insi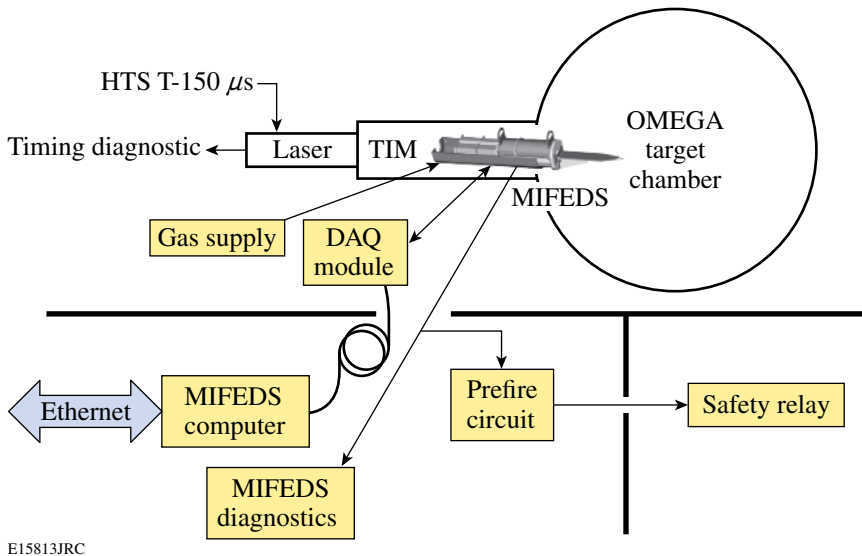de of the target, the consequent flux compression would be impeded. For this purpose we designed a special experiment in the diagnostic TIM facility, using the Faraday rotation setup. An aluminized CH shell with all of the target parameters except for size (its diameter was 1.5 mm to accommodate a Faraday rotator glass sample) was placed between the MIFEDS coils, and several discharges were performed. The difference in the magnetic pulse rise time of these discharges and the earlier experiments with the stand-alone Faraday probe was within a typical time jitter of 16 ns. From this, it was concluded that the Al layer, much thinner than the skin depth of 60 μm at the fundamental frequency of the pulse, was not a barrier for the seed field.

Initial experiments were conducted to integrate MIFEDS into OMEGA and test the experimental geometry, to develop the proton backlighter diagnostic, and to measure the convergence ratio of cylindrical implosions. Forty OMEGA beams were radially incident on the cylindrical target, while the remaining 20 were used to generate 14.7-MeV probe protons in a separate D^3He-filled glass shell for magnetic-field measurement. The technique is a further development of the one described in Ref. 17. Figure 110.11(a) shows a typical configuration with a cylindrical target mounted between the MIFEDS coils and imaged with the OMEGA Target Viewing System. One can also see the outlines of rectangular and circular poly-

imide plugs used in this case, as well as the crossbeam on the target stalk used to correctly orient the axis of the cylinder. The inset shows a time-integrated, x-ray self-emission image of the imploded target. The enhanced emission of x rays with average energy in the 1-keV range is seen from the hot compressed core. The 450-μm-diam glass microballoon used as the proton backlighter is visible in the lower right corner. From these experiments, the time of peak compression was established to within 100 ps. In comparison, the duration of the proton burst is ~150 ps (Ref. 17). The detector medium for the protons is a two-layer package of 1-mm-thick, CR-39 plastic track detectors, shielded by Al filters. The initially chosen filter thickness was not optimal, as can be seen from Fig. 110.11(b) where the proton density map at the surface of the second CR-39 detector is shown. The darker areas have a higher proton density. One can see the deficiency of protons in the area of the compressed core, which is undesirable since these are the particles to be deflected by the compressed fields. Monte Carlo simulations based on the experimental data are ongoing to identify the optimal filter thickness for the next experiment. The goal is to match to the CR-39 detector surface a specific portion of the energy loss versus depth curve (near but before the Bragg peak) of the particles that traverse the compressed core, so that these specific particles are centered in the limited readout energy band with a maximum signal-to-noise ratio. Upcoming experiments will utilize the improved detector geometry.

Conclusions

The concept of laser-driven magnetic-flux compression was briefly introduced with emphasis on its application to the
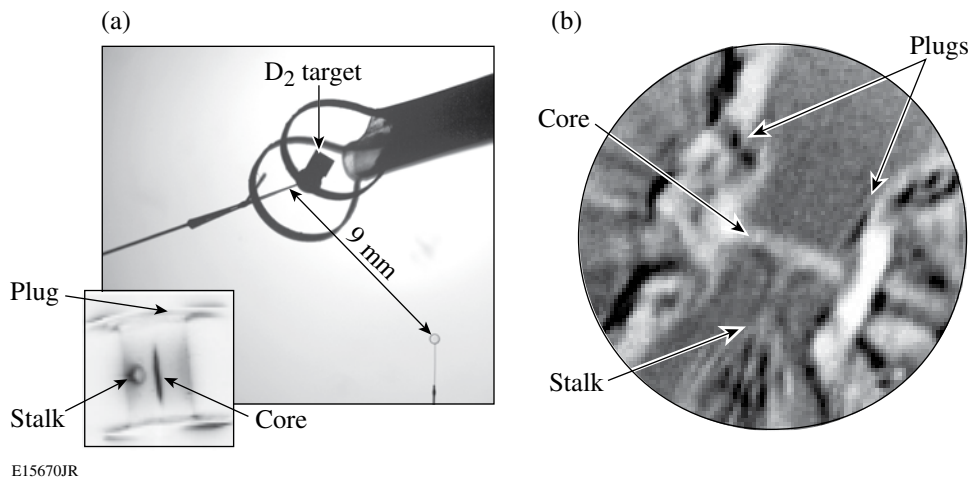
Figure 110.11

(a) D_2-filled shell placed between the MIFEDS coils and imaged with the OMEGA Target Viewing System. The proton backlighter is visible in the lower right. The inset depicts a time-integrated x-ray self-emission image showing the enhanced emission from the compressed hot core. (b) Density map of protons imaging the target near peak compression. The protons passing through the core are slowed down below the detection threshold.

improvement of direct-drive laser fusion. The confinement and amplification of seeded magnetic flux in cylindrical, D_2-filled plastic shells, irradiated by the OMEGA laser, were discussed in this context. A gigawatt seed-field generator that can discharge 100 J of energy in 400 ns was designed and built in a compact package for these experiments. Its spatial and temporal parameters were optimized for the delivery of a strong magnetic pulse in the small (a few tens of mm^3) laser–target interaction volume of OMEGA. Seed magnetic fields larger than 0.15 MG were measured in the center of the low-mass double-coil assembly. A proton deflectrometry technique is being developed for the observation of the flux compression in an optically thick cylindrical target. The initial proton backlighting experiments helped establish the relative timing of the proton pulse with respect to the time of peak convergence of the target. The data aided the matching of the CR-39 detector surface with the appropriate portion of the dose versus depth curve (near but before the Bragg peak) for the protons that are slowed down through the core. These form the basis for future flux-compression experiments, first in cylindrical and later in spherical geometry. Applications of the laser-driven flux compression will not be limited to ICF studies. Work is in progress to use the seed field for OMEGA experiments in the context of laboratory astrophysics experiments, such as magnetized plasma jets. In addition, a scheme that uses moderate flux compression in cylindrical geometry is being evaluated for the confinement of electron–positron plasma[18] generated in an integrated OMEGA/OMEGA EP[19] experiment.

ACKNOWLEDGMENT

REFERENCES

1. S. E. Bodner, D. G. Colombant, J. H. Gardner, R. H. Lehmberg, S. P. Obenschain, L. Phillips, A. J. Schmitt, J. D. Sethian, R. L. McCrory, W. Seka, C. P. Verdon, J. P. Knauer, B. B. Afeyan, and H. T. Powell, Phys. Plasmas **5**, 1901 (1998).

2. R. L. McCrory, D. D. Meyerhofer, S. J. Loucks, S. Skupsky, R. Betti, T. R. Boehly, T. J. B. Collins, R. S. Craxton, J. A. Delettrez, D. H. Edgell, R. Epstein, K. A. Fletcher, C. Freeman, J. A. Frenje, V. Yu. Glebov, V. N. Goncharov, D. R. Harding, I. V. Igumenshchev, R. L. Keck, J. D. Kilkenny, J. P. Knauer, C. K. Li, J. Marciante, J. A. Marozas, F. J. Marshall, A. V. Maximov, P. W. McKenty, S. F. B. Morse, J. Myatt, S. Padalino, R. D. Petrasso, P. B. Radha, S. P. Regan, T. C. Sangster, F. H. Séguin, W. Seka, V. A. Smalyuk, J. M. Soures, C. Stoeckl, B. Yaakobi, and J. D. Zuegel, J. Phys. IV France **133**, 59 (2006).

3. R. Betti, K. Anderson, T. R. Boehly, T. J. B. Collins, R. S. Craxton, J. A. Delettrez, D. H. Edgell, R. Epstein, V. Yu. Glebov, V. N. Goncharov, D. R. Harding, R. L. Keck, J. H. Kelly, J. P. Knauer, S. J. Loucks, J. A. Marozas, F. J. Marshall, A. V. Maximov, D. N. Maywar, R. L. McCrory, P. W. McKenty, D. D. Meyerhofer, J. Myatt, P. B. Radha, S. P. Regan, C. Ren, T. C. Sangster, W. Seka, S. Skupsky, A. A. Solodov, V. A. Smalyuk, J. M. Soures, C. Stoeckl, W. Theobald, B. Yaakobi, C. Zhou, J. D. Zuegel, J. A. Frenje, C. K. Li, R. D. Petrasso, and F. H. Séguin, Plasma Phys. Control. Fusion **48**, B153 (2006).

4. R. Betti and C. Zhou, Phys. Plasmas **12**, 110702 (2005).

5. P. W. McKenty, V. N. Goncharov, R. P. J. Town, S. Skupsky, R. Betti, and R. L. McCrory, Phys. Plasmas **8**, 2315 (2001).

6. C. M. Fowler, W. B. Garn, and R. S. Caird, J. Appl. Phys. **31**, 588 (1960).

7. A. D. Sakharov *et al.*, Sov. Phys. Doklady AN SSSR **165**, 65 (1965).

8. A. I. Bykov *et al.*, Physica B **294–295**, 574 (2001).

9. T. R. Boehly, D. L. Brown, R. S. Craxton, R. L. Keck, J. P. Knauer, J. H. Kelly, T. J. Kessler, S. A. Kumpan, S. J. Loucks, S. A. Letzring, F. J. Marshall, R. L. McCrory, S. F. B. Morse, W. Seka, J. M. Soures, and C. P. Verdon, Opt. Commun. **133**, 495 (1997).

10. M. A. Liberman and A. L. Velikovich, J. Plasma Phys. **31**, 369 (1984).

11. A. L. Velikovich *et al.*, Sov. Phys.-JETP **61**, 261 (1985).

12. F. Herlach, Rep. Prog. Phys. **62**, 859 (1999).

13. N. W. Jang, R. Betti, J. P. Knauer, O. Gotchev, and D. D. Meyerhofer, Bull. Am. Phys. Soc. **51**, 144 (2006).

14. O. Chubar, P. Elleaume, and J. Chavanne, J. Synchrotron Radiat. **5**, 481 (1998).

15. Series S/SS High Voltage Rep-Rate Capacitors, General Atomics Energy Products, General Atomics Electronic Systems, Inc., San Diego, CA 92123, http://www.gaep.com/series-s-ss-capacitors.html (18 June 2007).

16. 40A Series, part no. 40A24N30, Ultravolt, Inc., Ronkonkoma, NY 11779, http://www.ultravolt.com/coa-40aser.htm (18 June 2007).

17. C. K. Li, F. H. Séguin, J. A. Frenje, J. R. Rygg, R. D. Petrasso, R. P. J. Town, P. A. Amendt, S. P. Hatchett, O. L. Landen, A. J. Mackinnon, P. K. Patel, V. Smalyuk, J. P. Knauer, T. C. Sangster, and C. Stoeckl, Rev. Sci. Instrum. **77**, 10E725 (2006).

18. J. Myatt, A. V. Maximov, and R. W. Short, Bull. Am. Phys. Soc. **51**, 25 (2006).

19. L. J. Waxer, D. N. Maywar, J. H. Kelly, T. J. Kessler, B. E. Kruschwitz, S. J. Loucks, R. L. McCrory, D. D. Meyerhofer, S. F. B. Morse, C. Stoeckl, and J. D. Zuegel, Opt. Photonics News **16**, 30 (2005).

Gain Curves and Hydrodynamic Simulations of Ignition and Burn for Direct-Drive Fast-Ignition Fusion Targets

Introduction

In fast-ignition[1] inertial confinement fusion (ICF) a cryogenic shell of deuterium and tritium (DT) is first imploded by a high-energy driver to produce an assembly of thermonuclear fuel with high densities and areal densities. Such a dense core is then ignited by the fast electrons (or protons) accelerated through the interaction of a high-power, ultra-intense laser pulse with either a coronal plasma or a solid, cone-shaped target.[2,3] The fast particles slow down in the cold, dense fuel and deposit their kinetic energy through collisions with the background plasma. In direct-drive fast ignition, the high-energy driver is typically a laser with a wavelength $\lambda_L \approx 0.25, 0.35,$ or 0.53 μm, and the high-intensity laser has a power in the petawatt range with a wavelength of 0.53 or 1.06 μm. The energy gain is defined as the ratio between the thermonuclear energy yield and the laser energy on target. Such a definition does not take into account the energy required to power the lasers. Including the wall-plug efficiency of the lasers is essential to assess the ultimate validity of fast-ignition inertial confinement fusion as an economical energy source but it requires detailed considerations of the laser technology that are beyond the scope of this article. Earlier attempts[4] to determine the gain curves for fast ignition were based on heuristic models of the fuel assembly and thermonuclear yields. The results shown here represent a calculation of the gain curve based on realistic target designs and hydrodynamic simulations of the implosion, as well as simulations of the ignition by a collimated electron beam and burn propagation. The targets are chosen according to the design of Ref. 5, where the laser pulses and target characteristics are optimized to achieve a fuel assembly with a small hot spot, large densities, and areal densities suitable for fast ignition. Here, we consider a high-energy laser as the compression driver and focus on two forms of the thermonuclear gain. The first is the maximum gain $G_M = E_F / E_c$ given by the ratio between the thermonuclear energy E_F and the compression laser energy on target E_c. The second is the total gain $G_T = E_F / E_T$ defined as the ratio between the thermonuclear energy and the total laser energy on target including the petawatt laser energy $E_T = E_c + E_{pw}$. It is shown in this article that the maximum gain G_M is only a function of the compression laser energy and

wavelength $G_M = G_M(E_c, \lambda_L)$, thus leading to the following form of total gain:

$$G_T = \frac{G_M(E_c, \lambda_L)}{1 + E_{pw}/E_c}. \tag{1}$$

The second term in the denominator of Eq. (1) can be neglected for large compression lasers with $E_c \gg E_{pw}$, thus leading to $G_T \simeq G_M$.

It is important to emphasize that the hydrodynamic simulations of fast-ignition (FI) targets reported in this article are meant to address only one aspect of the physics pertaining to fast ignition: the issue of the hydrodynamic fuel assembly and its potential for high energy gains. The complicated physics of the fast-electron beam generation and transport is not considered here. Instead, the e-beam is assigned as an ideal beam, collimated and uniform, with or without a Maxwellian energy spread. Likely, such an ideal beam is very different from the experimental conditions, where the beam may be broken up into filaments and become divergent. Based on the available experimental data, it is currently not possible to predict the e-beam characteristics in a fast-ignition target because most of the experiments on fast-electron generation and transport pertain to the interaction of intense light with solid targets rather than plasmas relevant to fast ignition.[6] Fast-electron transport properties in plasmas are vastly different than in solid targets,[6] and fast-ignition–relevant plasmas are difficult to produce without an implosion facility. However, the next generation of petawatt lasers such as FIREX-I[7] and OMEGA EP[8] will be combined with an implosion facility and integrated experiments will become possible. Such experiments should provide a wealth of experimental data to be used for the characterization of the fast-electron beam produced in the fast-ignition targets. In this article, the injection of an ideal electron beam is simply assumed. All of the difficulties pertaining to hot-electron generation and transport physics are buried in the parameter describing the conversion efficiency of laser light into collimated hot electrons and the hot-electron temperature.

The latter is either assigned or estimated using the widely used ponderomotive scaling formula,[9] derived from particle-in-cell (PIC) simulations of intense light–plasma interaction. Results based on such a formula should be taken with caution since there is no experimental confirmation that the ponderomotive scaling is applicable to fast-ignition targets. It is also worth mentioning that the conversion efficiency used here defines the conversion of laser light into an ideal collimated beam. Departures from the collimated beam configuration would cause deterioration in efficiency. Because of uncertainties in values of conversion efficiency, the results in this article are parameterized as a function of efficiency.

The hydrodynamic simulations of fast-ignition targets[5] reported in this article include one-dimensional (1-D) simulations of the implosion and two-dimensional (2-D) axisymmetric simulations of ignition by a collimated electron beam and burn propagation. In the case of cone-in-shell targets, the final phase of the implosion is simulated in two dimensions assuming that the cone walls are rigid and truncated at a given distance from the center. This idealized, optimistic configuration is used to estimate the deterioration of the gain due to the presence of the cone. The targets are thick shells of wetted-foam $(DT)_6CH$ with an inner DT-ice layer and a thin CH overcoat. Such targets[5] are designed to achieve a massive compressed core with a uniform density and a small hot spot. Because of their low in-flight aspect ratio (IFAR), such targets are not sensitive to the growth of hydrodynamic instabilities during the acceleration phase. Thus, one-dimensional simulations of the implosions provide a reasonably accurate description of the final fuel assembly (unless a cone is present).

A derivation of the gain curves for target densities around $\rho \approx 300$ g/cm^3 is described briefly by the same authors in Ref. 10. There, an analytic gain formula is derived and compared with the results of ignition and burn simulations of imploded targets. In Ref. 10, ignition is triggered by a monoenergetic 1- to 3-MeV electron beam with an energy of 15 kJ. The approach used in this article is similar to the one taken by Atzeni in Ref. 11 to describe the ignition conditions for a uniform-density, spherical DT plasma heated by a collimated electron beam. A major step forward in our work is that the DT plasma core is produced by simulating the implosion of realistic fast-ignition targets. Such targets are designed to produce an optimized fuel assembly for fast ignition featuring high densities, high areal densities, and small hot spots. Furthermore, our simulations of ignition and burn are extended to an entire family of fast-ignition targets, scaled for different compression driver energies, to generate a gain curve for direct-drive fast ignition.

This article presents the details of the simulation results that led to the conclusions of Ref. 10. As in Ref. 10, we use a simple parallel straight-line transport model for the fast electrons, in which the electrons lose their energy in the dense core according to the well-established relativistic slowing-down theory of Refs. 12 and 13. Furthermore, we extend the work of Ref. 10 to include sensitivity studies of ignition and gain deterioration due to the cone. The ignition sensitivity studies are carried out with respect to the electron-beam parameters (spot size, duration, electron energy), injection time, fast-electron temporal distribution, and fast-electron distribution function.

To model the energy spectrum of electrons generated by the ultra-intense laser–plasma interaction, simulations using Maxwellian electrons are performed, having ponderomotive temperature scaling with the laser intensity and the wavelength, and assuming a Gaussian temporal profile of the laser pulse. A minimum laser energy for ignition exceeding 100 kJ is found for the 1.054-μm wavelength. Electrons generated by such laser pulses have energies in the range of several MeV. The stopping distance of such energetic electrons in the DT plasma greatly exceeds the optimal for ignition[11] $\rho R = 0.3$ to 1.2, thus increasing the energy required for ignition. The simulations show that the energy of fast electrons, the stopping distance, and the minimum energy for ignition can be reduced using frequency-doubled laser pulses since the mean energy of fast electrons is proportional to the laser wavelength. This conclusion is in agreement with earlier results by Atzeni *et al.*[14] and Honrubia *et al.*,[15] where the ponderomotive scaling was used to estimate the fast-electron energy.

In this article, the gain of cone-in-shell targets is also estimated through two-dimensional simulations. Gold cones were suggested as a way to keep a plasma-free path for the fast-ignitor pulses and deliver the petawatt pulse energy to the fuel core. While improving the energy transport to the hot spot, cone-focus geometries can complicate the implosion. A simple model of cone-in-shell targets is considered here, where the shell is imploding along a fixed-boundary "rigid" cone with a truncated tip. After the shell departs from the cone tip, the high-pressure shell plasma is free to expand into the hole left by the cone. This last phase of the implosion is simulated with the two-dimensional hydrocode *DRACO*,[16] which is also used to simulate the ignition and burn phases. This is a highly simplified model of cone-in-shell target implosions, and the resulting gains should be viewed as an optimistic estimate. The simulations show that, in spite of the fact that the shell integrity is not preserved and the density profile is modified facing the cone, the minimum energy for ignition (using monoenergetic

electron beams) is only weakly increased by 3 to 4 kJ, while the target gain is reduced by only 20% to 30%.

The following sections (1) present a summary of the high-density and high-ρR target design recently developed for fast ignition; (2) describes the simulations of ignition and burn using monoenergetic (and Maxwellian) electron beams with prescribed parameters and calculation of the gain curve; (3) discuss the effects of a fast-electron Maxwellian distribution, ponderomotive temperature scaling, and Gaussian laser pulses; and (4) present and discuss the results from simulations of pseudo-cone targets.

Review of the Target Designs and Gain Formula

We follow the work of Ref. 5 with regard to the optimization of the target designs for fast ignition. The optimal fuel assembly for fast ignition[5] requires a small-size, low-temperature hot spot surrounded by a massive cold shell of densities in the 300- to 500-g/cm^3 range. A small and relatively cold hot spot is preferred in that most of the driver energy is used to compress the fuel assembly rather than heating the hot spot. The optimum density for ignition is determined based on considerations concerning the fast-electron energy required for ignition and the fast-electron beam radius. It follows from Atzeni's work[11] that the minimum energy for ignition using a monoenergetic electron beam can be approximated by $E_{ig}^{min} = 11\left[400/\rho(g/cm^3)\right]^{1.85}$ and the optimum beam radius by $r_b^{opt} = 16\left[400/\rho(g/cm^3)\right]^{0.97}$, where ρ is the density of the precompressed DT fuel. While lower ignition energies are needed for greater fuel densities, they require a more-focused electron beam. A reference density of 300 g/cm^3 is often used in the literature, for which a reasonable-sized electron beam of about 20-μm radius requires about 20 kJ of electron energy for ignition. Since technological limitations make it difficult to achieve electron-beam radii shorter than 15 to 20 μm, a fuel density of 300 to 500 g/cm^3 can be a reasonable compromise to keep the ignition energy relatively low without imposing severe requirements on the e-beam focus.

In Ref. 5, relations between the in-flight and stagnation hydrodynamic variables of the imploded shells are derived and used to design optimized fast-ignition targets. According to these relations, the maximum density at stagnation scales as $\rho_{max} \sim V_i/\alpha$ and the maximum areal density scales as $\rho R \sim E_c^{0.33}/\alpha^{0.57}$, where V_i is the implosion velocity at the end of the acceleration phase and α is the value of the in-flight adiabat at the inner shell surface. Here the adiabat is defined as the ratio of the plasma pressure to the Fermi pressure of a degenerate electron gas. For a DT plasma, the adiabat can be approximated by $\alpha \approx p(\text{Mbar})/2.2\,\rho(g/cm^3)^{5/3}$. The aspect ratio at stagnation, defined as the ratio of the hot-spot radius to the shell thickness $A_s = R_h/\Delta_s$, scales as $A_s \sim V_i$. Simple formulas for the target gain and the maximum in-flight aspect ratio (IFAR) are also obtained, according to which $G_M \sim V_i^{-1.25}\theta$ and IFAR $\sim V_i^2/\langle\alpha\rangle^{0.6}$, where $\langle\alpha\rangle$ is the average in-flight adiabat and the common expression for the burn fraction $\theta \approx (1 + 7/\rho R)^{-1}$ can be used. The energy gain decreases with the implosion velocity and increases with ρR. For a given driver energy on target, lower implosion velocities require more massive targets, and therefore more fuel available for reactions. Higher ρR's lead to longer confinement time and therefore higher burn fractions. Thus low implosion velocities (i.e., massive targets) and low adiabats (i.e., high ρR) are necessary to achieve high gains. A low implosion velocity also decreases the IFAR, reducing the growth rate of the most-dangerous Rayleigh–Taylor instability modes. The latter are the Rayleigh–Taylor modes with a wave number k such that $k\Delta_{if} \approx 1$, where Δ_{if} represents the in-flight thickness. Furthermore, with a low implosion velocity, the stagnation aspect ratio, and, consequently, the size and energy of the hot spot, decreases.

The scaling law for the maximum density at stagnation suggests that the minimum implosion velocity is set by the adiabat and the density required for ignition. Thus, high-gain fast-ignition implosions require low values of the inner-surface in-flight adiabat. As long as the ratio $V_i/\alpha \sim \rho$ is sufficiently large to achieve the densities required for fast ignition, the implosion velocity can be minimized by driving the shell on the lowest-possible adiabat. However, very low adiabat implosions require long pulse lengths and careful pulse shaping. The long pulse length is due to the slow velocity of the low-adiabat shocks, and the careful shaping is required to prevent spurious shocks from changing the desired adiabat. Furthermore the ratio between the peak power and the power in the foot of the laser pulse (i.e., the power contrast ratio) increases as the adiabat decreases, thus leading to difficult technical issues in calibrating the pulse shape. These constraints on the pulse shape are alleviated by using the relaxation laser-pulse technique.[17] As suggested in Ref. 5, reasonable minimum values of the inner surface adiabat and implosion velocity are $\alpha \approx 0.7$ and $V_i \sim 1.7 \times 10^7$ cm/s, corresponding to an average density of about 400 g/cm^3. An adiabat below unity implies that at shock breakout, the inner portion of the shell is not fully ionized. Reference 5 also shows that a very modest IFAR $\simeq 16$ corresponds to such implosion velocity and adiabat. Since the number of e foldings for the growth of the most-dangerous Rayleigh–Taylor instability modes with wave number $k \simeq 1/\Delta_{if}$ is approximately $0.9\sqrt{\text{IFAR}} \simeq 3.6$, one concludes that the implosion of such capsules is approximately

one dimensional. This is an important consideration since it allows us to make use of the one-dimensional code *LILAC*[18] to simulate the generation of the dense core of the fast-ignition fuel assembly (in the absence of a cone).

It is important to emphasize that the peak values of the density and total areal density occur at different times. As the shell stagnates, the density and areal density grow as a result of the plasma compression induced by the return shock traveling outward from the center. The peak density occurs before the time of peak areal density. Furthermore, a significant amount of relatively low density ($\rho < 200$ g/cm^3), unshocked free-falling plasma surrounds the dense core at the time of peak ρR. Such a low-density plasma carries a significant fraction of the areal density ($\sim$25%), thus preventing the fast particles from fully penetrating the dense core. Hence, it can be beneficial to launch the igniter beam soon after the time of peak ρR when the return shock has propagated farther out and compressed the low-density region. One-dimensional simulations of the implosions indicate that at such a time, the average density of the compressed core is about half its peak value.

Using low-velocity implosions of massive shells for fast-ignition fuel assembly should also improve the performance of cone-in-shell targets where a gold cone is inserted into the shell to keep a plasma-free path for the fast-ignitor pulse.[2,3] Recent experiments and simulations of cone-in-shell target implosions[19] have shown that the integrity of the cone tip is compromised by the large hydrodynamic pressures and that a low-density plasma region develops between the cone tip and the dense core, thus complicating the fast-electron transport. Since the stagnation pressure scales as $\rho \sim V_i^{1.8}$ (Ref. 20), the fuel assemblies from low-velocity implosions can improve the cone target's performance since the resulting dense core has relatively low pressure (due to the low velocity), thus reducing the hydrodynamic forces on the cone tip. Furthermore, since low velocities are obtained by imploding shells with large masses, the resulting core size is large, thus reducing the distance between the tip and the dense core edge.

While the simulations in Ref. 5 consider only implosions driven by a compression laser pulse with a wavelength $\lambda = 0.35$ μm, the wavelength dependence for the stagnation variables is included analytically into the gain formula. After setting the values of the adiabat $\alpha \approx 0.7$ and implosion velocity $V_i \sim 1.7 \times 10^7$ cm/s, the maximum gain becomes a function of the compression laser energy and wavelength (see Ref. 10):

$$G_M \approx \frac{743\, I_{15}^{-0.09}\left(0.35/\lambda_L\right)^{0.66}\left(1 - E_{\mathrm{cut}}/E_c\right)^{\mu}}{1 + 21\left(\lambda_L/0.35\right)^{0.25}\big/\left[\xi E_c^{0.33}\right]}\ , \qquad (2)$$

where E_c is in kilojoules and a weak analytical dependence on the maximum pulse intensity $I_{15} \sim 1$ (in units of 10^{15} W/cm^2) is included. This expression uses fitting parameters μ and ξ, which need to be determined by comparison with ignition and burn simulations. Here ξ represents the fraction of the maximum total areal density available for the burn to be used in $\theta(\rho R)\big[\rho R = \xi(\rho R)_{\max}\big]$. The *ad hoc* term $\left(1 - E_{\mathrm{cut}}/E_c\right)^{\mu}$ has been introduced to account for the yield deterioration of small targets where the burn temperature is below 30 keV and the electron-beam size is of the order of the compressed core size occurring for $E_c \sim E_{\mathrm{cut}} \approx 40$ kJ. The factors μ and ξ are of order unity and are to be determined by a numerical fit to the gain in the ignition and burn simulations reported in the next section.

Simulation of Ignition and Burn by Monoenergetic and Maxwellian Electron Beams

To simulate the burn phase of the fast-ignited capsules, we start from the one-dimensional fuel assembly obtained from the code *LILAC* and simulate the ignition by a collimated electron beam and subsequent burn with the two-dimensional, two-fluid hydrocode *DRACO*.[16] The latter has been recently modified[21] to include the electron-beam-energy deposition into the dense fuel. The effects of electron-beam instabilities such as Weibel and resistive filamentation are not included in this work. An overview of the physics issues related to fast-electron generation and transport problem in fast ignition can be found in Refs. 6 and 22. Here a simple straight-line transport model for fast electrons is chosen, in which fast electrons lose energy due to collisions with thermal electrons and to collective plasma oscillations. We use the slowing-down theory of Ref. 13 that includes the effect of multiple scattering. The value of the Coulomb logarithm in the stopping-power term of Ref. 13 has been modified to account for quantum effects. Burn simulations of several fuel assemblies have been performed, characterized by the implosion parameters mentioned above. The targets used in the simulations (Fig. 110.12 shows three of them) are massive wetted-foam targets with an initial aspect ratio of about 2 (outer radius/thickness) driven by UV laser energies varying from 50 kJ to 2 MJ and $I_{15} \simeq 1$. The relaxation-type[17] laser pulses are shown in Fig. 110.13 with the main pulse length varying from 11.5 ns for the 100-kJ target to 22 ns for the 750-kJ target. In all cases, the fast electrons are injected at about 50 μm from the dense core and close to the time of peak areal density.

The main properties of the ignition and burn propagation are illustrated below for a particular example of the 300-kJ fuel assembly. Figure 110.14 shows the target radial density profiles at consecutive moments of time close to the time of maximum areal density. During this period of time, the target expands and the maximum density drops from about 700 g/cm^3 to 300 g/cm^3. The dense part of the core is surrounded by a relatively low density unshocked region. As the return shock propagates outward, more fuel gets compressed, thus increasing the total ρR available for the burn. Figure 110.15 shows the density (a) as a function of the areal density and (b) as a function of the volume. The areal density of the dense region varies between 1.1 to 1.3 g/cm^2, while the

ρR in the unshocked region decreases from 0.6 to 0.28 g/cm^2 with time. The hot-spot volume [Fig. 110.15(b)] is less than 8% of the compressed volume.

Figure 110.16 shows snapshots of ignition and burn simulations for the 300-kJ fuel assembly. Ignition is triggered by a 2-MeV monoenergetic electron beam with a radius of 20 μm and duration of 10 ps. The cylindrically symmetric, radially uniform electron beam is injected from the right. The beam's temporal distribution is also uniform. Ignition is triggered first in a small plasma volume heated by the electrons [Figs. 110.16(a) and 110.16(b)]; the thermonuclear burn wave then propagates to the remaining fuel [Figs. 110.16(c)–110.16(f)].
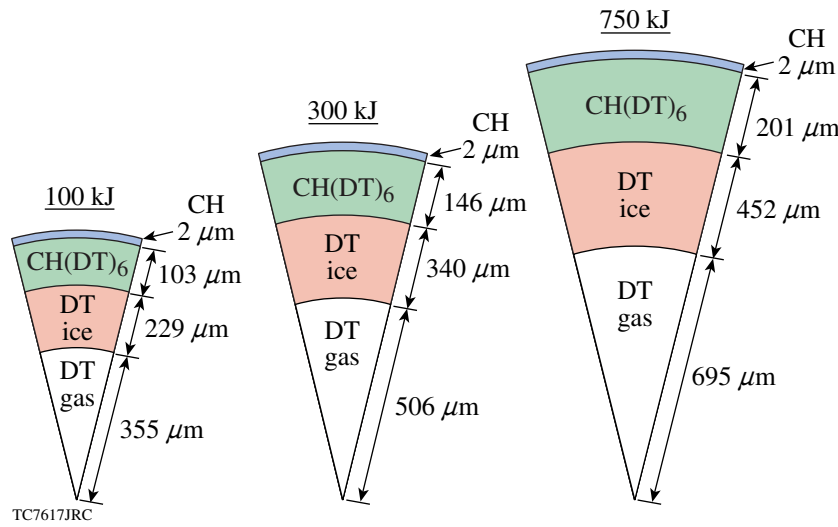
Figure 110.12
100-, 300-, and 750-kJ targets for optimized fast-ignition fuel assembly.
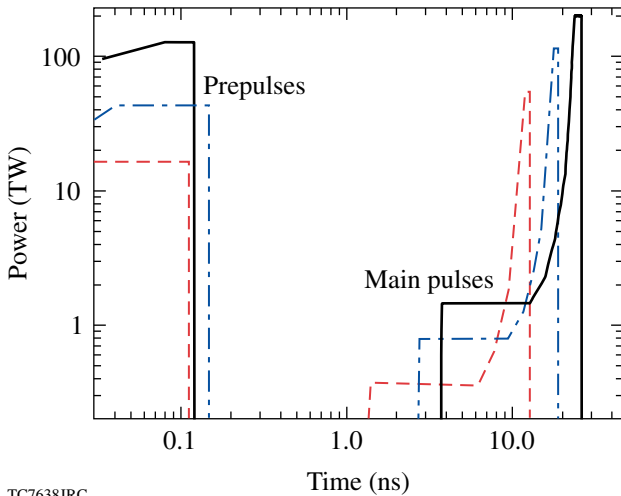
Figure 110.13
Laser pulses (power versus time) for the 100-kJ (dashed lines), 300-kJ (dashed–dotted lines), and 750-kJ (solid lines) targets.
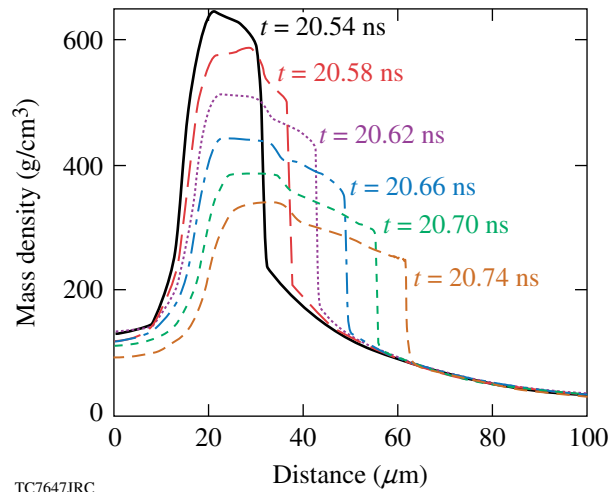
Figure 110.14
Density profiles of the 300-kJ target at different times (about the time of peak ρR) when the fast electrons are injected in the simulations of Fig. 110.17.

TC7731JRC
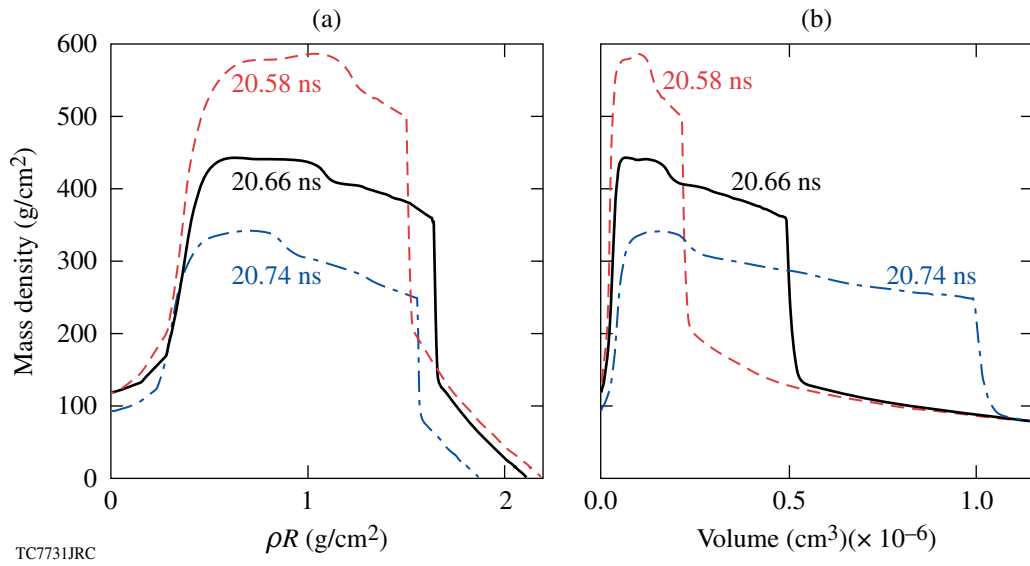
Figure 110.15
Density profiles of the 300-kJ target versus (a) areal density and (b) volume at three times near the time of peak ρR.

TC7722JRC
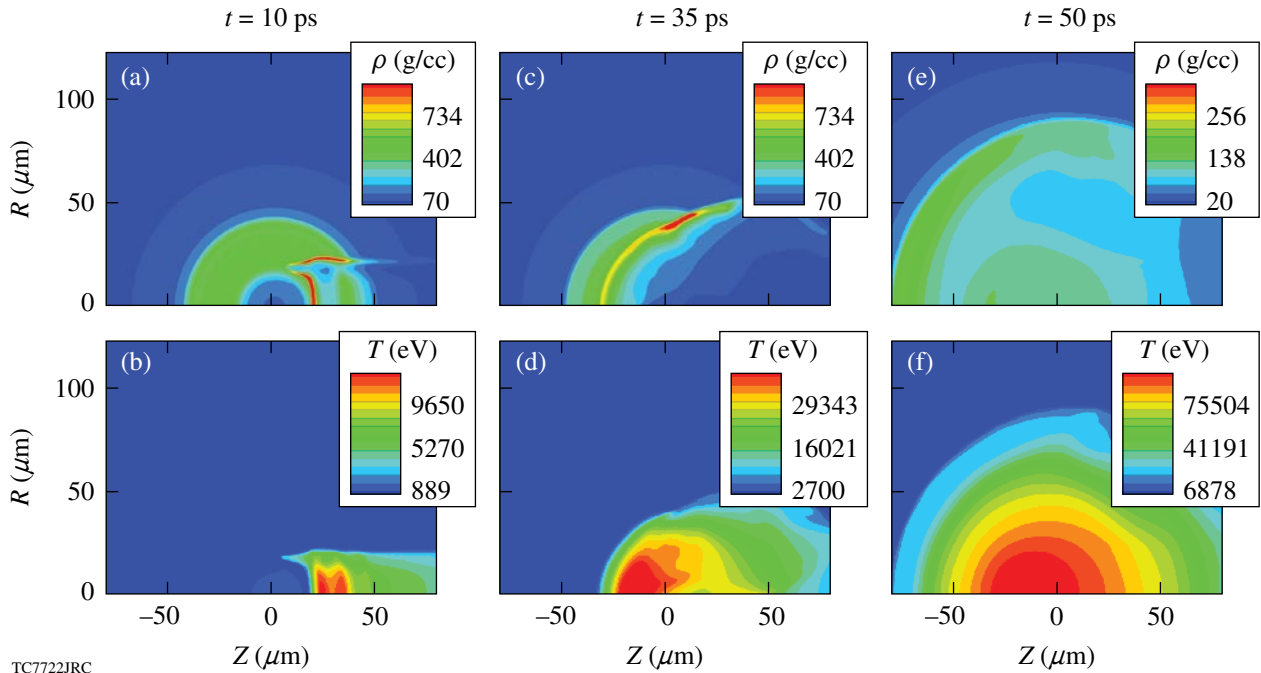
Figure 110.16
Contour plots of the density (ρ) and ion temperature (T) at selected moments of time in the burn simulation induced by ignition by an 18-kJ, 10-ps, 2-MeV monoenergetic electron beam.

We have performed simulations using monoenergetic electron beams to find how the minimum energy for ignition depends on the electron-beam parameters and the injection time. The results for the 300-kJ fuel assembly are shown below. Figure 110.17 shows the dependence of the minimum ignition energy for a 10-ps, 2-MeV monoenergetic electron beam on the beam injection time for three beam radii: 20, 30, and 40 μm. The minimum ignition energy is found with an error $\leq$4% by changing the total electron-beam energy while keeping all the other parameters constant. For a 20-μm electron beam, minimum ignition energy of about 15 kJ is found when the density is maximum for earlier injection times. It increases for late injections when the target density decreases. While focused beams with a radius $\leq$20 μm are preferable for ignition, realistic electron beams may have a larger spot size when entering the fuel core because of their angular spread. For a 30-μm electron beam, the ignition energy reaches its minimum of 26 kJ at the injection time of $t = 20.58$ ns and for a 40-μm beam the minimum ignition energy is 41 kJ at $t = 20.62$ ns.

Atzeni's formula can be attributed to the loss of fast electrons in the low-density unshocked region. Notice that the electron-pulse duration in our simulation is less than the hydrodynamic confinement time of the heated region as required by Atzeni.

Figure 110.18(a) shows the dependence of the minimum ignition energy on the beam radius for a pulse duration of 10 ps and injection time of 20.62 ns. Figure 110.18(b) shows how the minimum ignition energy depends on the electron-pulse duration for a fixed radius of 20 μm and the same injection time. The minimum ignition energy increases with both the electron-beam radius and pulse duration.

Figure 110.19 shows the dependence of the minimum ignition energy on the electron energy. The beam radius is 20 μm, the pulse duration is 10 ps, and the injection time is 20.62 ns.

Figure 110.17
Minimum ignition energy versus injection time for a 10-ps, 2-MeV monoenergetic electron beam and three values of the beam radius: 20, 30, and 40 μm.
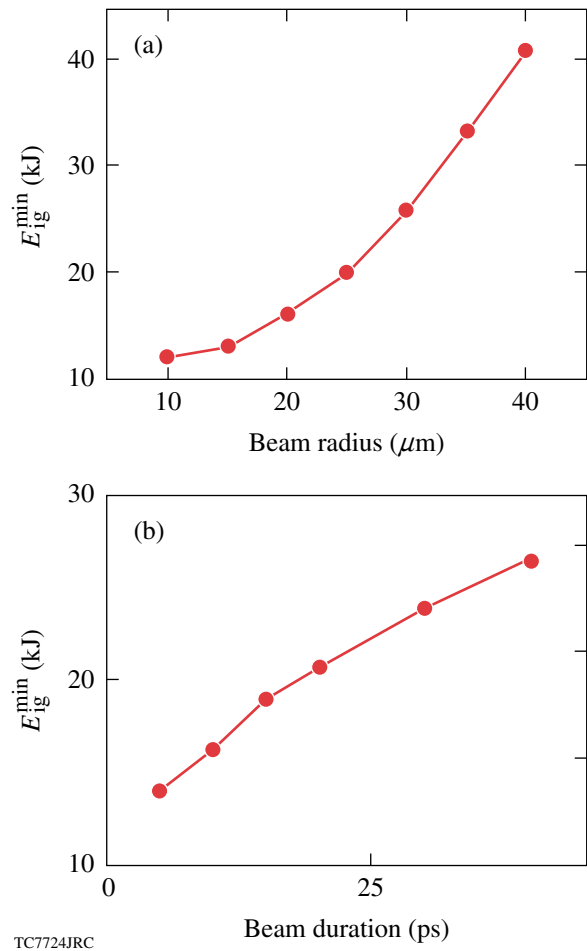
Figure 110.18
Minimum ignition energy versus (a) beam radius and (b) duration for a 2-MeV monoenergetic electron beam. (a) The beam duration is 10 ps and (b) the beam radius is 20 μm.

The minimum energy for ignition found in our simulations is in good agreement with that found by Atzeni.[11] According to Atzeni's formula, the minimum ignition energy of 19.7 kJ is reached for a density of 300 g/cm^3 and a beam radius of 20 μm. Our simulations predict a minimum ignition energy of about 25 kJ for the same beam radius and injection when the density has a similar value in the dense region. The 25% difference in the ignition energy between our simulations and

The results for monoenergetic electrons (solid line) and electrons with an energy spread (dashed line) are shown. In the simulations with an energy spread, a relativistic Maxwellian electron distribution function is used. For monoenergetic electrons, the lowest ignition energy of 16.25 kJ is reached at 2 MeV, while for Maxwellian electrons, 21.5 kJ for the mean energy of 1.25 MeV is reached. The minimum ignition energy is higher for Maxwellian electrons because the energy is deposited over a larger region in the longitudinal direction and is not as localized as for monoenergetic electrons. This is seen from the snapshots for the plasma temperature just after the energy is deposited by fast electrons ($t = 10$ ps) in the simulations with 2-MeV Maxwellian (Fig. 110.20) and monoenergetic electrons (Fig. 110.16). Maxwellian electrons with $E > \langle E \rangle$ transfer more energy than electrons with $E < \langle E \rangle$. This explains why the mean electron energy that minimizes the ignition energy is lower for Maxwellian than for monoenergetic electrons. Figure 110.19 also shows that the minimum ignition energy greatly increases for high-energy multi-MeV electrons. This is because the stopping length of such electrons greatly exceeds the optimal size of the heated region[11] $0.3 < \rho R < 1.2$ g/cm^2, so that a much longer region is heated. Unfortunately, this appears to be the case of realistic laser pulses (see **Simulation of Ignition by Maxwellian Electrons with Ponderomotive Temperature Scaling and Gaussian Laser Pulses**, p. 82).

Our simulations for different targets show that, for a 20-μm beam radius, the minimum energy required for ignition is consistently ≈ 15 kJ using electron beams with a 20-μm radius.

As long as the ignition is triggered, the thermonuclear energy yield is approximately independent of the electron-beam characteristics. The neutron yields for the 100-, 300-, and 750-kJ assemblies are 2.0×10^{18}, 1.2×10^{19}, and 4.2×10^{19}, and the thermonuclear energy yields are 5.6, 34, and 118 MJ, respectively. The results of these simulations are used to determine the fitting parameters $\xi \approx 0.7$ and $\mu \approx 1.1$ in Eq. (2), leading to the following maximum gain formula:

$$G_M = \frac{743\, I_{15}^{-0.09}\left(0.35/\lambda_L\right)^{0.66}\left(1 - E_{\text{cut}}/E_c\right)^{1.1}}{1 + 30\left(\lambda_L/0.35\right)^{0.25}/E_c^{0.33}}, \qquad (3)$$

where E_c is in kilojoules and $E_{\text{cut}} \approx 40$ kJ. Notice that even a modest-sized UV laser driver with an energy of 100 kJ can produce a fuel assembly yielding a maximum gain close to 60. Figure 110.21 shows that Eq. (3) accurately fits all simulation results and can be used to determine the total gain in Eq. (1). Figure 110.22 shows the total gain for three values of the ignition-pulse energy $E_{\text{PW}} = 50$ kJ, 75 kJ, and 150 kJ. Even in the case of $E_{\text{PW}} = 150$ kJ, the target gain from a 100-kJ fuel assembly is still remarkably high ($G_T \simeq 22$).
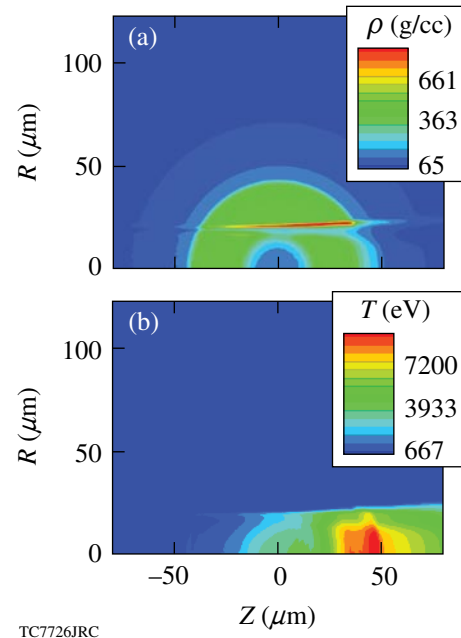

TC7725JRC

Figure 110.19
Minimum ignition energy versus electron energy for 2-MeV monoenergetic (solid line) and Maxwellian (dashed line) electron beams. The beam duration is 10 ps and the radius is 20 μm.

TC7726JRC

Figure 110.20
Contour plots of the density and ion temperature after the 300-kJ target is heated by a 25-kJ, 10-ps, 20-μm, 2-MeV Maxwellian electron beam.
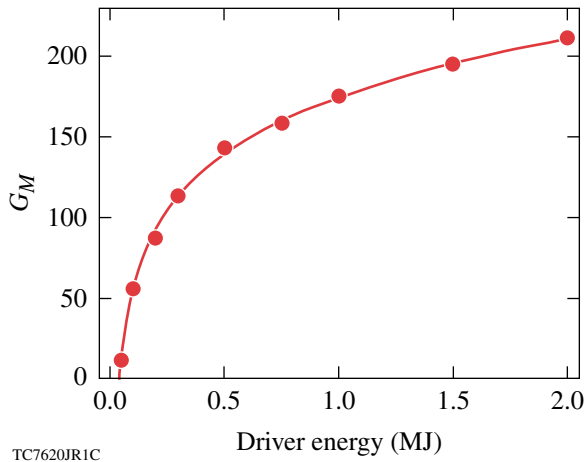
TC7620JR1C

Figure 110.21
Maximum gain (energy yield/compression driver energy) versus compression driver energy from Eq. (3) (curve) and *DRACO* simulations (dots).
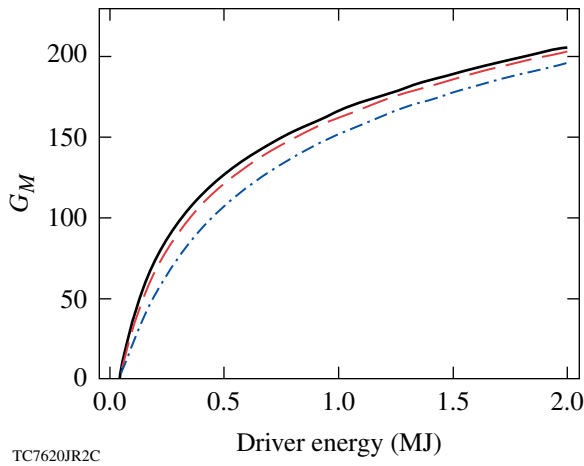

TC7620JR2C

Figure 110.22
Target gain (energy yield/total energy on target) versus compression driver energy for E_{PW} = 50 kJ (solid line), 75 kJ (dashed line), and 150 kJ (dashed–dotted line).

Simulation of Ignition by Maxwellian Electrons with Ponderomotive Temperature Scaling and Gaussian Laser Pulses

Hot electrons in fast ignition are produced during the interaction of ultra-intense laser pulses with either the coronal plasma or a solid target. The spectrum of fast electrons and the energy conversion efficiency from the laser to electrons generally depend on the details of this interaction. An assumption, however, is often used[14,15,23] that the mean energy of hot electrons equals the energy of their oscillation in the laser field $E \sim mc^2 (\gamma - 1)$ (so-called ponderomotive scaling[9]), where

$\gamma = \sqrt{1 + p^2/2}$, $p \sim eA/mc^2$ is the momentum of electrons (normalized to mc) in the linearly polarized laser field with the amplitude of the vector potential A. The experimental data predict different values of the energy conversion efficiency from the laser to electrons in the range $\eta \sim 0.2$ to 0.5 for laser intensities $I > 10^{19}$ W/cm^2 (Refs. 2 and 24). We have performed simulations assuming a Gaussian temporal profile for the laser pulse and a relativistic Maxwellian distribution function for fast electrons with a mean energy following the ponderomotive scaling that can also be rewritten as

$$\langle E \rangle \approx \left[\frac{I(\lambda/1.054 \ \mu\text{m})^2}{10^{19} \ \text{W/cm}^2} \right]^{1/2} \text{MeV}. \qquad (4)$$

According to this scaling, the mean energy is a function of the laser intensity and the wavelength. Notice that for a relativistic Maxwellian distribution function of the form $f(E) \sim \exp[-mc^2(\gamma - 1)/kT](\gamma^2 - 1)^{1/2}\gamma$, the mean energy is $\langle E \rangle = 3kT/2$ in the nonrelativistic and $\langle E \rangle = 3kT$ in the ultra-relativistic limit. Two values of the energy conversion efficiency to fast electrons were used: $\eta = 0.3$ and $\eta = 0.5$. Simulations with different parameters of the laser pulse such as spot size (rectangular beam profile in the radial direction), duration, and wavelengths of 1.054 μm and 0.527 μm were performed for the 300-kJ fuel assembly to find the minimum energy required for ignition. The optimal injection time is found to be close to $t = 20.62$ ns when the averaged density is about 450 g/cm^3. Using a smaller beam radius and pulse duration lead to higher intensities and more-energetic electrons, according to the ponderomotive scaling Eq. (4). However, very energetic (multi-MeV) electrons require a large stopping distance that can even exceed the size of small-to-moderate energy targets. Larger beam radii with $\rho r_b > 0.6$ g/cm^2 lead to a heated volume greater than the optimal value.[11] Also very long laser pulses with durations exceeding the confinement time of the heated region are detrimental and lead to a higher ignition energy. Optimal values of the duration and radius exist for which the laser ignition energy is minimized.

A set of simulations was performed to find such conditions. Tables 110.I and 110.II summarize the results. The optimal laser pulse duration and radius, the mean hot-electron energy (at the time of the Gaussian peak), the electron-beam fuel coupling efficiency, and the minimum ignition energy (of the laser pulse and the electron beam) are provided from simulations carried out with two values of the coupling efficiency and two laser wavelengths ($\lambda = 1.054 \ \mu$m and 0.527 μm). The minimum laser energy for ignition is 235 kJ (with 71 kJ in fast electrons) for

Table 110.I: Summary of the simulations for $\lambda = 1.054$ μm.

η	r_b (μm)	τ_b (ps)	$E_{\text{las.ig}}^{\min}$ (kJ)	$E_{\text{e.ig}}^{\min}$ (kJ)	$\langle E \rangle$ (MeV)	$\eta_{e-\text{pl}}$
0.3	26.3	16.3	235	71	7.7	0.69
0.5	22.5	13.8	105	53	6.3	0.76

Table 110.II: Summary of the simulations for $\lambda = 0.527$ μm.

η	r_b (μm)	τ_b (ps)	$E_{\text{las.ig}}^{\min}$ (kJ)	$E_{\text{e.ig}}^{\min}$ (kJ)	$\langle E \rangle$ (MeV)	$\eta_{e-\text{pl}}$
0.3	19	8	106	32	3.7	0.86
0.5	16.8	7	50	25	3.2	0.92

wavelength $\lambda = 1.054$ μm and conversion efficiency $\eta = 0.3$ (Table 110.I). Figure 110.23 shows snapshots of the plasma density and ion temperature for this simulation at two moments of time: at the end of the laser pulse and at the developed burn stage. Figure 110.23(b) shows that the plasma is heated throughout the core. Electrons are not completely stopped in the core and continue to heat the low-density plasma behind it. Ignition is triggered first in the plasma column heated by the electrons and the burn region then expands radially [Figs. 110.23(c) and 110.23(d)]. The laser intensity at the time of the Gaussian peak is 6.5×10^{20} W/cm^2, and very energetic electrons are

produced with a mean energy of 7.7 MeV (Table 110.I). Only 69% of the total electron energy is deposited into the plasma. Table 110.I also shows that the laser energy required for ignition decreases to 105 kJ (53 kJ in fast electrons) for $\eta = 0.5$. This significant reduction in the ignition energy is due not only to a larger fraction of the laser energy converted into hot electrons but also to the lower electron energies produced with reduced intensities.

It was suggested by Atzeni and Tabak[14] that shorter laser wavelengths can reduce the mean energy of fast electrons [see Eq. (4)], their stopping length, and the energy required for ignition. Indeed, Table 110.II shows that for a frequency-doubled green light ($\lambda = 0.527$ μm), the laser energy required for ignition decreases to 106 kJ (32 kJ in fast electrons) for $\eta = 0.3$ and 50 kJ (25 kJ in fast electrons) for $\eta = 0.5$. The mean hot-electron energy, however, is still high in these simulations (3.7 MeV and 3.2 MeV, respectively), which suggests that even shorter laser wavelengths can be desirable.

While simulations predict that using a green laser light reduces the energy required for ignition, frequency doubling of the red light with high conversion efficiency can present a technologically challenging task. In this context, finding other mechanisms to reduce the energy of hot electrons generated by ultra-intense laser pulses would be very helpful.
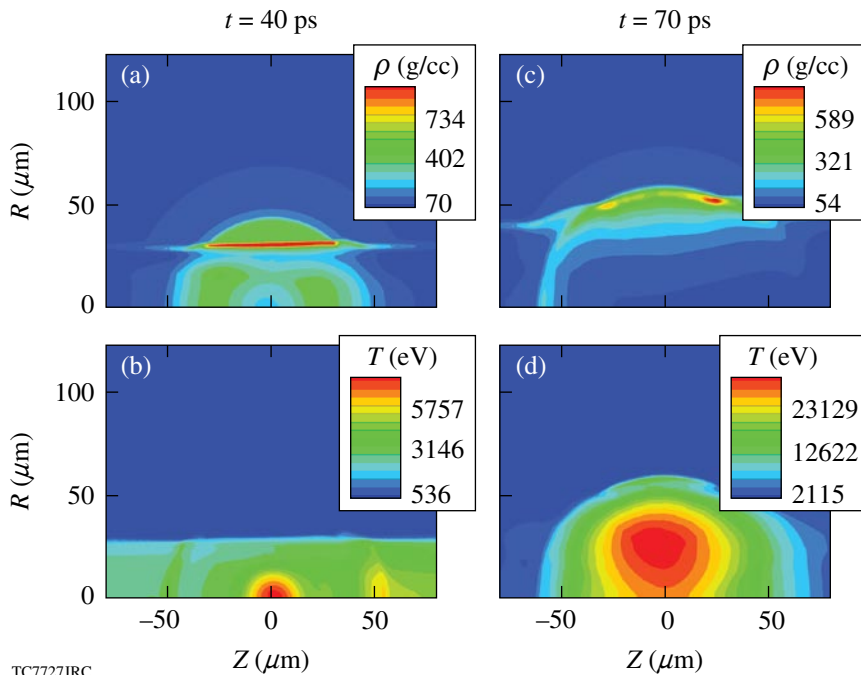

Figure 110.23
Contour plots of the density and ion temperature at selected moments of time in the burn simulation induced by a 235-kJ, 26.3-μm, 16.3-ps laser pulse with an energy conversion efficiency to fast electrons of $\eta = 0.3$.

TC7727JRC

Simulations of Pseudo-Cone Targets

The use of gold cones is currently considered as one of the most promising options to deliver the petawatt-pulse laser energy to the compressed fuel. The cone provides an access path for an ignition laser beam to the fuel, free of the coronal plasma that otherwise can reflect the laser light at the critical plasma surface 1 to 2 mm away from the compressed core. Fast electrons are produced by the interaction of the laser beam with the cone tip located tens to a few hundred microns from target center and then transported toward the core. Cone-focus geometries, while improving the transport of energy to the hot spot, can complicate the implosion. The question arises whether the fuel can still be compressed to the same high densities and areal densities as for spherically symmetric implosions. The compressed core should be significantly modified from the side of the cone where the laser-generated fast electrons enter the core to ignite it. It is important to determine how the minimum energy for ignition and the target gain are affected by the cone.

We have performed simulations of cone-target implosions using a highly simplified model of the cone. We assume that the cone walls are rigid and truncated at a given distance from the center. The pseudo-cone target is schematically shown in Fig. 110.24. The cone walls are directed toward the center of the target and truncated at a distance of about 200 μm from it. The cone opening angle is 90°. A narrow cone tip may exist and go farther toward the center. We use 1-D *LILAC* implo-

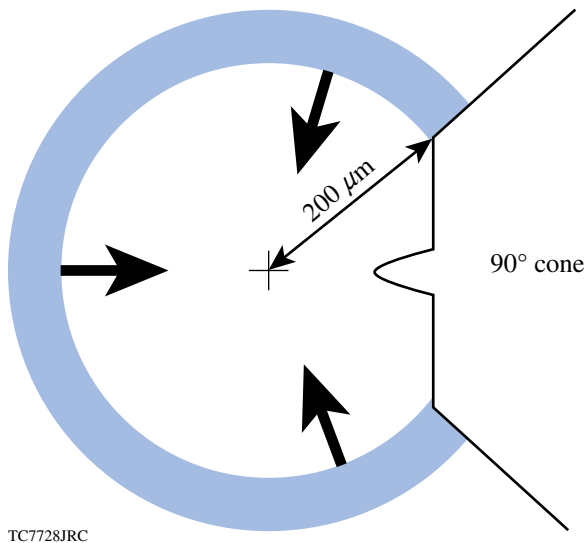sion simulations until the converging shell reaches the cone tip. From this point on, the simulation is continued with the 2-D *DRACO* code. The 1-D *LILAC* outputs are used as initial conditions (time $t = 0$) after removing the section of the shell corresponding to the cone tip. Such a model accounts only for the effect associated with the hole left in the shell after its departure from the cone. Other effects such as shear flow down the sides of the cone and DT contamination by the gold[19,25] or more-complicated cone shapes are not considered here and will be addressed in future work.

We first study how the perturbed shell converges. Figure 110.25 shows snapshots of the fuel density in the *DRACO* simulation for the 300-kJ fuel assembly. The 2-D simulation starts from the spherically symmetric shell with the hole caused by the cone. When the shell approaches the center, the hole does not close and the hot gas flows out from the central region. Figure 110.25(c) shows the density profile at the moment of time ($t = 0.98$ ns) when the maximum density is reached in the simulation without the cone, while Fig. 110.25(d) covers the moment of time ($t = 1.14$ ns) slightly before the maximum areal density. At $t = 0.98$ ns, the density profile on the left side of the target is practically the same as in the 1-D simulation (without the cone) and the maximum density is approximately the same. At $t = 1.14$ ns, the density profile on the left side is still close to that in the 1-D simulation except for the hot spot, which shrinks. The opening in the shell at $t = 1.14$ ns has a radius of about 6 μm and is surrounded by a high-density region. While the compressed core is certainly modified by the cone, these changes do not seem to significantly affect the ignition energy requirements. To verify this, we have performed burn simulations using a 2-MeV monoenergetic electron beam with a radius of 20 μm and a duration of 10 ps, injected at $t = 1.14$ ns in the z direction. It is found that the ignition energy increased by only 4 kJ to 19 kJ with respect to the 1-D implosion without the cone. The maximum gain in the pseudo-cone target simulation is equal to 90 instead of 113 without the cone.

Similar pseudo-cone simulations were performed for other targets driven by laser pulses with energies ranging from 50 kJ to 2 MJ. For all of the targets, the minimum ignition energy ranges from 18 to 20 kJ and is found to be only weakly affected by the cone. Figure 110.26 shows the maximum gain in the pseudo-cone target simulations and the gain predicted by Eq. (3). The maximum gain decreases by 20% to 25% for driver pulse energy between 200 kJ and 2000 kJ and slightly more (up to 30%) for lower-energy drivers. Notice that removing a part of the shell in place of the cone in these simulations reduces the total mass of the thermonuclear fuel by approximately 15%;
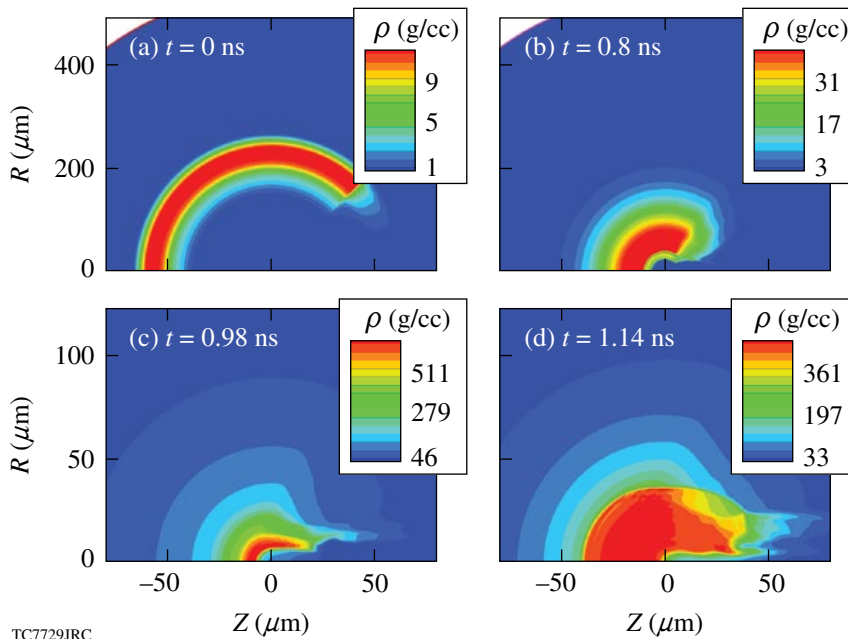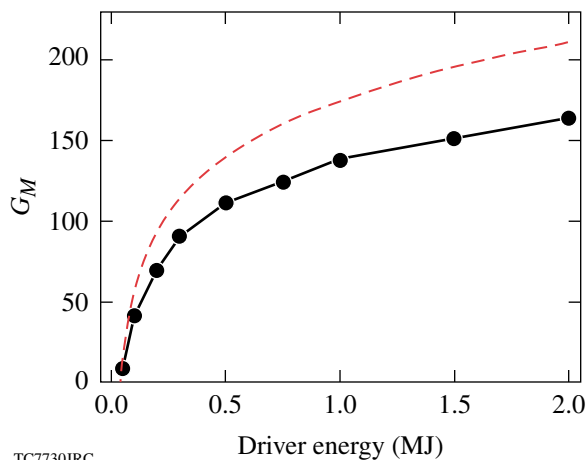

TC7728JRC

Figure 110.24
Pseudo-cone target.

Figure 110.25
Contour plots of the density at different times in the pseudo-cone-target simulation.

Figure 110.26
Maximum gain versus compression driver energy for the pseudo-cone targets (dots connected by a solid line) and for spherically symmetric implosions [Eq. (3)] (dashed line).

however, the maximum gain in the simulation is reduced more than that. This signifies that not all of the remaining fuel can be assembled so effectively as for an unperturbed shell. Nevertheless, the reduced gain in the pseudo-cone target simulations is still remarkably high; in particular, a maximum gain of 70 is still possible with driver-pulse energies of only 200 kJ.

Summary and Discussion

Hydrodynamic simulations of realistic, high-gain, fast-ignition targets, including one-dimensional simulations of the

implosion and two-dimensional simulations of ignition by a collimated electron beam and burn propagation are presented and discussed in this article. The targets' design is based on the fuel assembly theory of Ref. 5. The fast-ignition targets are massive wetted-foam, cryogenic DT shells with an initial aspect ratio close to 2. They are imploded by relaxation-type pulses to form high-density and high-areal-density cores with small hot spots, which are optimal for fast ignition. Due to the large thickness and small in-flight aspect ratio, such targets are practically unperturbed by Rayleigh–Taylor instability, making 1-D hydrocodes suitable to simulate the implosion.

The simulations of ignition and burn have been used to find the minimum energy for ignition and to generate gain curves for direct-drive, fast-ignition inertial confinement fusion based on realistic fast-ignition target designs. A large number of runs for targets driven by UV-laser compression pulses with energies from 50 kJ to 2 MJ have been performed. Fitting parameters in the analytical scaling for the target gain are obtained, accounting for the fraction of the maximum total areal density available for the burn and yield deterioration of small targets. It is found that even modest-sized UV-laser drivers, with an energy of 100 kJ, can produce a fuel assembly yielding a maximum gain (energy yield/compression driver energy) close to 60. Assuming a 100-kJ ignition laser pulse, the total gain (energy yield/total energy on target) can be as high as 30 for a 100-kJ compression pulse and about 60 for a 200-kJ driver. Notice that at 1 MJ, the total gain of the optimized fast-ignition target $G_T = 160$ (for a 100-kJ ignition pulse) is considerably higher than the gain of

direct-drive NIF targets, $G \simeq 50$ (Ref. 26). Although less than earlier heuristic model predictions[4] (which also use different optimizations), Eq. (3) shows that fast ignition can achieve significant gains with relatively small drivers.

In our simulations of ignition and burn, the energy of fast electrons, beam radius (20 μm and larger), and pulse length were varied to find the minimum beam energy for ignition close to 15 kJ for different (25-kJ to 2-MJ driver-pulse energy) fuel assemblies, using monoenergetic electron beams. The dependence of the minimum beam energy for ignition on the electron-beam parameters and injection time has been analyzed in detail. The minimum beam energy for ignition increases up to 20 kJ for electrons with energy spread (relativistic Maxwellian distribution function) and optimal mean energy. Simulations using ponderomotive temperature scaling for fast electrons with the laser intensity and Gaussian (in time) laser pulses have also been performed for the 300-kJ fuel assembly. It is shown that for a laser wavelength of 1.054 μm, the minimum laser pulse energy required for ignition is 235 kJ (with 71 kJ in fast electrons) if the energy conversion efficiency from the laser to fast electrons is 30%. The laser ignition energy decreases to 105 kJ (53 kJ in fast electrons) if the energy conversion efficiency is 50%. Such large laser ignition energies are caused by the high electron energy. Indeed, the hot electrons produced by ultra-intense laser pulses have multi-MeV energies, and their stopping range can greatly exceed the optimal value for fast ignition. A possible solution may be using frequency-doubled ignition pulses, for which the mean energy of fast electrons decreases by a factor of 2 (for the same laser intensity). Simulations for a laser wavelength of 0.527 μm predict a minimum laser pulse energy for ignition of 106 kJ (with 32 kJ in fast electrons) for an energy conversion efficiency of 30% and 50 kJ (25 kJ in fast electrons) for a conversion efficiency of 50%. It has been reported[27] that sharp solid–plasma interface electrons can be produced with energy below the ponderomotive scaling prediction. A strong reduction in energy conversion efficiency to fast electrons, however, simultaneously takes place. Finding mechanisms to reduce the energy of fast electrons without a significant loss of conversion efficiency would be very helpful to avoid a technologically complicated task of resorting to green laser light for high-power lasers.

We have also performed simplified cone-target simulations assuming that the cone walls are rigid and truncated at a certain distance from the center. Such simulations predict a gain deterioration of 20% to 30% and a small increase in the minimum ignition energy with respect to unperturbed targets. More-sophisticated cone models are currently under

implementation in the code *DRACO*[28] and the results from more-realistic cone-in-shell target implosion simulations will be reported in future articles.

ACKNOWLEDGMENT

REFERENCES

1. M. Tabak *et al.*, Phys. Plasmas **1**, 1626 (1994).

2. R. Kodama *et al.*, Nature **412**, 798 (2001).

3. K. A. Tanaka *et al.*, Phys. Plasmas **10**, 1925 (2003); P. A. Norreys, K. L. Lancaster, C. D. Murphy, H. Habara, S. Karsch, R. J. Clarke, J. Collier, R. Heathcote, C. Hernandez-Gomez, S. Hawkes, D. Neely, M. H. R. Hutchinson, R. G. Evans, M. Borchesi, L. Romagnani, M. Zepf, K. Akli, J. A. King, B. Zhang, R. R. Freeman, A. J. MacKinnion, S. P. Hatchett, P. Patel, R. Snavely, M. H. Key, A. Nikroo, R. Stephens, C. Stoeckl, K. A. Tanaka, T. Norimatsu, Y. Toyama, and R. Kodama, Phys. Plasmas **11**, 2746 (2004).

4. M. Tabak *et al.*, Fusion Sci. Technol. **49**, 254 (2006).

5. R. Betti and C. Zhou, Phys. Plasmas **12**, 110702 (2005).

6. R. R. Freeman *et al.*, Fusion Sci. Technol. **49**, 297 (2006); R. R. Freeman, K. Akli, F. Beg, R. Betti, S. Chen, D. J. Clark, P. M. Gu, G. Gregori, S. P. Hatchett, D. Hey, K. Highbarger, J. M. Hill, N. Izumi, M. Key, J. A. King, J. A. Koch, B. Lasinki, B. Langdon, A. J. MacKinnon, D. Meyerhofer, N. Patel, P. Patel, J. Pasley, H. S. Park, C. Ren, R. A. Snavely, R. B. Stephens, C. Stoeckl, M. Tabak, R. Town, L. Van Woerkom, R. Weber, S. C. Wilks, and B. B. Zhang, J. Phys. IV France **133**, 95 (2006); M. Tabak *et al.*, Phys. Plasmas **12**, 057305 (2005); R. B. Stephens, R. P. J. Snavely, Y. Aglitskii, K. U. Akli, F. Amiranoff, C. Andersen, D. Batani, S. D. Baton, T. Cowan, R. R. Freeman, J. S. Green, H. Habara, T. Hall, S. P. Hatchett, D. S. Hey, J. M. Hill, J. L. Kaae, M. H. Key, J. A. King, J. A. Koch, R. Kodama, M. Koenig, K. Krushelnick, K. L. Lancaster, A. J. MacKinnon, E. Martinolli, C. D. Murphy, M. Nakatsutsumi, P. Norreys, E. Perelli-Cippo, M. Rabec Le Gloahec, B. Remington, C. Rousseaux, J. J. Santos, F. Scianitti, C. Stoeckl, M. Tabak, K. A. Tanaka, W. Theobald, R. Town, T. Yabuuchi, and B. Zhang, J. Phys. IV France **133**, 355 (2006).

7. K. Mima, T. Takeda, and FIREX Project Group, Fusion Sci. Technol. **49**, 358 (2006).

8. C. Stoeckl, J. A. Delettrez, J. H. Kelly, T. J. Kessler, B. E. Kruschwitz, S. J. Loucks, R. L. McCrory, D. D. Meyerhofer, D. N. Maywar, S. F. B. Morse, J. Myatt, A. L. Rigatti, L. J. Waxer, J. D. Zuegel, and R. B. Stephens, Fusion Sci. Technol. **49**, 367 (2006).

9. S. C. Wilks *et al.*, Phys. Rev. Lett. **69**, 1383 (1992).

10. R. Betti, A. A. Solodov, J. A. Delettrez, and C. Zhou, Phys. Plasmas **13**, 100703 (2006).

11. S. Atzeni, Phys. Plasmas **6**, 3316 (1999).

12. C. Deutsch *et al.*, Phys. Rev. Lett. **77**, 2483 (1996).

13. C. K. Li and R. D. Petrasso, Phys. Rev. E **70**, 067401 (2004).

14. S. Atzeni and M. Tabak, Plasma Phys. Control. Fusion **47**, B769 (2005).

15. J. J. Honrubia and J. Meyer-ter-Vehn, Nucl. Fusion **46**, L25 (2006).

16. P. B. Radha, T. J. B. Collins, J. A. Delettrez, Y. Elbaz, R. Epstein, V. Yu. Glebov, V. N. Goncharov, R. L. Keck, J. P. Knauer, J. A. Marozas, F. J. Marshall, R. L. McCrory, P. W. McKenty, D. D. Meyerhofer, S. P. Regan, T. C. Sangster, W. Seka, D. Shvarts, S. Skupsky, Y. Srebro, and C. Stoeckl, Phys. Plasmas **12**, 056307 (2005).

17. R. Betti, K. Anderson, J. Knauer, T. J. B. Collins, R. L. McCrory, P. W. McKenty, and S. Skupsky, Phys. Plasmas **12**, 042703 (2005).

18. J. Delettrez, R. Epstein, M. C. Richardson, P. A. Jaanimagi, and B. L. Henke, Phys. Rev. A **36**, 3926 (1987).

19. R. B. Stephens *et al.*, Phys. Rev. Lett. **91**, 185001 (2003); R. B. Stephens, S. P. Hatchett, M. Tabak, C. Stoeckl, H. Shiraga, S. Fujioka, M. Bonino, A. Nikroo, R. Petrasso, T. C. Sangster, J. Smith, and K. A. Tanaka, Phys. Plasmas **12**, 056312 (2005).

20. C. D. Zhou and R. Betti, "Hydrodynamic Relations for Direct-Drive Fast-Ignition and Conventional Inertial Confinement Fusion Implosions," submitted to Physics of Plasmas.

21. J. A. Delettrez, J. Myatt, P. B. Radha, C. Stoeckl, S. Skupsky, and D. D. Meyerhofer, Plasma Phys. Control. Fusion **47**, B791 (2005).

22. Y. Sentoku *et al.*, Fusion Sci. Technol. **49**, 278 (2006).

23. R. P. J. Town *et al.*, Nucl. Instrum. Methods Phys. Res. A **544**, 61 (2005); R. J. Mason, Phys. Rev. Lett. **96**, 035001 (2006).

24. M. H. Key *et al.*, Phys. Plasmas **5**, 1966 (1998); R. Kodama *et al.*, Nature **418**, 933 (2002); K. Yasuike *et al.*, Rev. Sci. Instrum. **72**, 1236 (2001); M. H. Key, M. D. Cable, T. E. Cowan, K. G. Estabrook, B. A. Hammel, S. P. Hatchett, E. A. Henry, D. E. Hinkel, J. D. Kilkenny, J. A. Koch, W. L. Kruer, A. B. Langdon, B. F. Lasinski, R. W. Lee, B. J. MacGowan, A. MacKinnon, J. D. Moody, M. J. Moran, A. A. Offenberger, D. M. Pennington, M. D. Perry, T. J. Phillips, T. C. Sangster, M. S. Singh, M. A. Stoyer, M. Tabak, G. L. Tietbohl, M. Tsukamoto, K. Wharton, and S. C. Wilks, Phys. Plasmas **5**, 1966 (1998).

25. S. P. Hatchett, D. Clark, M. Tabak, R. E. Turner, C. Stoeckl, R. B. Stephens, H. Shiraga, and K. Tanaka, Fusion Sci. Technol. **49**, 327 (2006).

26. P. W. McKenty, V. N. Goncharov, R. P. J. Town, S. Skupsky, R. Betti, and R. L. McCrory, Phys. Plasmas **8**, 2315 (2001).

27. S. C. Wilks and W. L. Kruer, IEEE J. Quantum Electron. **33**, 1954 (1997).

28. K. S. Anderson, R. Betti, P. W. McKenty, P. B. Radha, and M. M. Marinak, Bull. Am. Phys. Soc. **51**, 32 (2006).

Femtosecond Optical Generation and Detection of Coherent Acoustic Phonons in GaN Single Crystals

Introduction

Coherent acoustic phonons (CAP's) excited by ultrafast laser pulses have been investigated using optical pump/probe spectroscopy in GaN systems, including GaN thin films, $In_xGa_{1-x}N/$ GaN heterostructures, and multiple quantum wells.[1–5] A common feature of such structures is the existence of a significant lattice mismatch, which results in highly strained interfaces. Since GaN and its alloys are piezoelectric semiconductors with large piezoelectric constants, the presence of strain at the interface gives rise to a strong, of-the-order-of-several-MV/cm,[5] built-in piezoelectric field. When a pump-laser pulse excites electron-hole pairs, the strain-induced piezoelectric field spatially separates the electrons and holes and, in turn, leads to a stress that serves as the source of CAP generation.

In addition to the piezoelectric effect, two other CAP-generation mechanisms have been reported in the literature:[6,7] the deformation-potential–coupled electronic stress and the heat-induced thermal stress. Both of these stresses originate in the transient photoexcitation of electron-hole pairs in the material. In one case, the transition of electrons from the valence band to the conduction band breaks the lattice equilibrium and results in a deformation of the lattice. Such deformation, in turn, alters the semiconductor band structure and induces the electronic stress coupled to the conduction-band free carriers through the deformation potential. In the other case, the photoexcited carriers simply transfer their excess energy to the lattice via electron–phonon scattering, as they relax down toward the band edge. The fast cooling process of hot carriers produces a sharp increase in the lattice temperature, leading to thermal stress.

Among the above-mentioned mechanisms of CAP generation, the piezoelectric effect always makes the dominant contribution in the strained systems, studied in Refs. 1–5, while the other two typically play only a very weak role, as discussed in Ref. 5. However, in bulk semiconductor single crystals (GaN, in our case), there is obviously no lattice-mismatch–induced strain and the piezoelectric field cannot be built. Thus, the CAP generation can only be due to either the electronic or thermal stress, or both, depending on the photon excitation energy and the studied material's properties.

In recent work,[8] we have demonstrated that in bulk GaN crystals the stress-induced CAP's are very long lived and propagate macroscopic distances without losing their coherence. We utilized far-above-bandgap, ultraviolet (UV) femtosecond pump pulses to excite the CAP's at the sample surface and detected them by measuring the transient differential reflectivity ($\Delta R/R$) signal of a time-delayed, near-infrared (NIR) probe pulse. We observed the CAP oscillations (superimposed on the exponentially decaying $\Delta R/R$ electronic transient) with the amplitude of the order of 10^{-5} to 10^{-6} and the frequency linearly dependent (no dispersion) on the probe-beam wave number. We have also made an early prediction that the electronic stress was the dominant factor in CAP generation in bulk GaN crystals.

In this work, we report our systematic experimental and detailed theoretical modeling studies on all-optical generation and detection of CAP's in bulk GaN crystals with the two-color (UV/blue–NIR), time-resolved, femtosecond pump/probe technique. Our theoretical modeling is based on the one-dimensional elastic wave equation and diffusion effects and predicts that the electronic stress is the dominant factor in CAP generation in GaN single crystals. For a CAP-detection mechanism, we have derived an analytic expression for the time-dependent, probe-beam reflectivity change caused by the propagating CAP's. Experimentally, we have varied the energy of the pump excitation pulses from far above the GaN bandgap, through near bandgap, up to just below bandgap (band-tail states). In all cases, we were able to produce easily measurable CAP oscillations, and, by careful investigation of their amplitude changes as a function of the energy (wavelength) of the pump photons, we confirmed that indeed the CAP excitation origin was due to the electronic stress, generated by the femtosecond pump at the sample surface region. By using, in all of our tests, probe beams with photon energies far below

the GaN bandgap (corresponding wavelengths were around 800 nm), we took advantage of a very small, $\sim$50-cm^{-1} absorption coefficient (very weak attenuation) of probe light in GaN crystals[8,9] and were able to demonstrate that the CAP pulses propagated deeply into the GaN crystal volume without any measurable loss of coherence/attenuation.

Another advantage of our two-color pump/probe configuration was that the NIR probe was not sensitive to the details of the band-gap structure, nor to any interband absorption.[10] The possibility of the two-photon–absorption process was also negligible because the total energy of two $\sim$800-nm probe photons was still considerably lower than the GaN bandgap energy. Thus, the UV–NIR, two-color femtosecond spectroscopy allowed us to avoid any undesired effects and made our phonon dynamics studies in GaN very clear to interpret.

In the next section we present our theoretical approach to the phenomenon of acoustic phonon generation and their coherent propagation in bulk semiconducting single crystals, stressing the need to include both electronic and thermal stresses in the phonon-generation mechanism. We also demonstrate that under our experimental conditions, for GaN, the amplitude of the CAP's depends only on the energy/wavelength of pump photons, while their oscillation frequency is probe dependent only in the simplest-possible dispersionless manner. The last two sections (1) briefly review our GaN crystal growth, describe the two-color femtosecond spectroscopy setup used in our measurements, and present detailed experimental results and their interpretation; and (2) present our conclusions and underline the applicability of our theoretical model for CAP studies in any high-quality single-crystal semiconducting materials.

Theoretical Modeling

Following the approach presented by Thomsen *et al.*,[7] we have developed a theoretical model of the generation, propagation, and detection of CAP's in bulk GaN crystals, studied using a femtosecond, two-color pump/probe technique. In our scheme, an intense, femtosecond laser pump pulse with photon energy above the material bandgap excites both the electronic and thermal stresses at the sample surface. These two stresses act as the driving terms in the elastic wave equation that describes generation and propagation of CAP's. The propagating CAP's modulate optical properties of the GaN dielectric function, which is represented as disturbance of a dielectric permittivity in Maxwell's equations. By solving the Maxwell equations, we obtained an analytical expression for the time-dependent modulation of the $\Delta R/R$ transient caused by the

traveling CAP waves, which, in turn, could be directly measured in our experiments, using below-bandgap probe pulses.

We stress that the Thomsen model was developed to explain generation and detection of CAP's in $\alpha - As_2Te_3$ and similar compounds with a picosecond, one-color pump/probe method.[7] In such a case, the CAP generation was assumed to be solely due to the thermal stress, and the detection was limited in a near-surface region. In the model presented here, we will consider both the electronic- and thermal-stress generation mechanisms. Since GaN exhibits relatively large deformation potential and different coefficients in ambipolar and thermal diffusion, the contribution of the electronic stress to the CAP's amplitude and shape is different from that of the thermal stress. Our theoretical calculations show that in GaN, CAP's generated by electronic stress have actually an-order-of-magnitude-larger strength than that generated by the thermal stress.

In the experimental CAP detection, we use far-below-bandgap femtosecond probe-beam pulses. For bulk samples, surface-generated CAP's propagate forward into the material with no reflections toward the surface. Thus, the surface (one-color scheme) detection scheme that was used by Thomsen *et al.*[7] to detect the echo of a CAP pulse is not appropriate in our case. In contrast, by using a far-below-bandgap probe beam, we were able to detect the CAP perturbation propagating deeply inside the material, taking advantage of the very long penetration depth (very low absorption) of our NIR probe photons.

1. CAP Pulse Generation

We consider a femtosecond UV pump pulse with photon energy higher than the GaN bandgap that is incident on the surface of a bulk GaN crystal. Given that the diameter of the irradiated area is much larger than the UV pulse absorption depth, both the electronic and thermal stresses generated by the pump pulse can be assumed to depend only on the z axis, which is defined to be perpendicular to the sample surface and pointing into the sample. Therefore, the lattice displacement has a nonzero component only in the z direction, and, in our case, the CAP generation is reduced to a one-dimensional (1-D) problem.

The 1-D elastic (nondissipative) wave equation describing generation and propagation of CAP's is given by

$$\frac{\partial^2 \eta_{zz}(z,t)}{\partial t^2} - v_s^2 \frac{\partial^2 \eta_{zz}(z,t)}{\partial z^2} = \frac{1}{\rho} \frac{\partial}{\partial z} \left(\sigma_{zz}^{\text{th}} + \sigma_{zz}^e \right), \qquad (1)$$

where $\eta_{zz}(z,t) = \partial u(z,t)/\partial z$ represents the acoustic phonon field with $u(z,t)$ defined as the lattice displacement, v_s is the longitudinal sound velocity in GaN, ρ is the mass density of GaN, and σ_{zz}^{th} and σ_{zz}^{e} are the thermal and electronic stresses, respectively. Both σ_{zz}^{th} and σ_{zz}^{e} are functions of z and time t and can be expressed as

$$\sigma_{zz}^{\text{th}}(z,t) = -3B\beta\Delta T(z,t), \tag{2}$$

$$\sigma_{zz}^{e}(z,t) = d_c n_e(z,t) - d_v n_h(z,t), \tag{3}$$

where B is the bulk modulus, β is the linear thermal expansion coefficient, $\Delta T(z,t)$ is the lattice temperature rise, d_c and d_v are the conduction-electron and valence-hole deformation potentials, respectively, and, finally, $n_e(z,t)$ and $n_h(z,t)$ are the photoexcited electron and hole densities, respectively. In general, $n_e(z,t)$ and $n_h(z,t)$ have different spatiotemporal evolutions, but, since in our case they are initially excited in equal numbers by the same pump pulse, we are going to ignore this difference and assume that $n_e(z,t) \approx n_h(z,t) = n(z,t)$, and, hence, Eq. (3) becomes

$$\sigma_{zz}^{e}(z,t) = (d_c - d_v)n(z,t). \tag{4}$$

Assuming that both the carrier motion and heat conduction have a diffusive character, we utilize a simple transport model to describe the evolution of $n(z,t)$ and $\Delta T(z,t)$:

$$\frac{\partial n(z,t)}{\partial t} - D\frac{\partial^2 n(z,t)}{\partial z^2} = 0, \tag{5}$$

$$\frac{\partial \Delta T(z,t)}{\partial t} - \chi\frac{\partial^2 \Delta T(z,t)}{\partial z^2} = 0, \tag{6}$$

with the initial conditions

$$n(z,0) = \frac{\alpha_{\text{pump}}(1 - R_{\text{pump}})Q}{E_{\text{pump}}}\exp(-\alpha_{\text{pump}}z), \tag{7}$$

$$\Delta T(z,0) = \frac{\alpha_{\text{pump}}(1 - R_{\text{pump}})Q}{E_{\text{pump}}} \\ \times \frac{E_{\text{pump}} - E_g}{C_V}\exp(-\alpha_{\text{pump}}z), \tag{8}$$

and boundary conditions

$$D\frac{\partial n(0,t)}{\partial z} = 0, \tag{9}$$

$$\chi\frac{\partial \Delta T(0,t)}{\partial z} = 0, \tag{10}$$

where D is the ambipolar diffusion coefficient of the GaN electron-hole plasma; χ is the thermal diffusivity; $R_{\text{pump}}, Q, \alpha_{\text{pump}}$, and E_{pump} are the reflectance, fluence, absorption coefficient, and photon energy of the pump beam; and E_g and C_V are the GaN bandgap energy and the specific heat per unit volume, respectively. We have also assumed above that during the duration of our ~150-fs-wide pump pulses, the photoexcitation is instantaneous and the plasma diffusion is negligible.

Knowing the $n(z,t)$ and $\Delta T(z,t)$ distributions, we can readily solve the wave equation [Eq. (1)], subject to the initial, $t = 0$, and elastic boundary, $z = 0$, conditions:

$$\eta_{zz}(z,0) = 0, \tag{11}$$

$$\eta_{zz}(0,t) = \frac{1}{\rho V_s^2}\left[3B\beta\Delta T(0,t) - (d_c - d_v)n(0,t)\right]. \tag{12}$$

In our analysis of CAP generation, the two trigger mechanisms, namely, the electronic and thermal stresses, are completely decoupled. Thus, the CAP fields excited by each mechanism can be treated separately, and the total CAP field is just the simple sum of both the electronic and thermal components. Figure 110.27 presents examples of numerically computed profiles of CAP transients, generated by the electronic stress, the thermal stress, and the sum of both, respectively. The CAP pulses plotted in Fig. 110.27(a) were calculated for the far-above-bandgap pump-photon excitation (photon energy of 4.59 eV; corresponding wavelength 270 nm), while those shown in Fig. 110.27(b) correspond to the excitation using just-above-bandgap pump photons (energy of 3.54 eV; wavelength 350 nm). In both cases, Q was kept constant and equal to 0.08 mJ/cm^2/pulse, the value actually implemented in our pump/probe experiments, while the α_{pump} values were taken to be 2.07×10^5 and 1.29×10^5 cm^{-1}, corresponding to the pump-photon energies of 4.59 eV and 3.54 eV, respectively.[9] The other GaN material parameters used in our calculations can be found in Table 110.III.
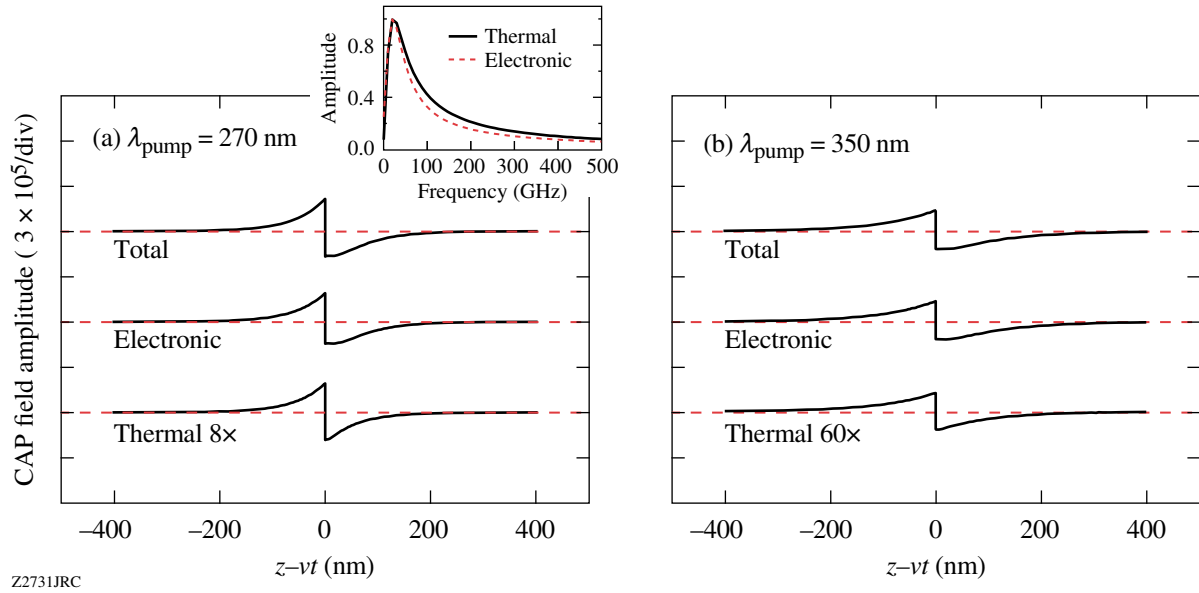
Figure 110.27

Simulation of spatial-time profiles of propagating CAP transients generated by the electronic stress, thermal stress, and the sum of both, respectively. The CAP pulses shown in (a) and (b) were excited by the pump photons with photon energies of 4.59 eV and 3.54 eV (wavelengths 270 nm and 350 nm), respectively. The inset shows the frequency spectra of the electronically (solid line) and thermally induced (dashed line) CAP.

Table 110.III. Material parameters for wurtzite GaN.

Parameter	GaN
Longitudinal sound velocity v_s (m/s)	8020[11]
Mass density ρ (g/cm³)	6.15[12]
Bulk modulus B (GPa)	207[13]
Linear thermal expansion coefficient β (K⁻¹)	3.17×10^{-6}[14]
Electron deformation potential d_c (eV)	−4.08[15]
Hole deformation potential d_v = D1 + D3 (eV)	2.1[16]
Ambipolar diffusion coefficient D (cm²/s)	2.1[17]
Thermal diffusivity χ (cm² s⁻¹)	0.43[12]
Band gap E_g (eV)	3.4[18]
Specific heat per unit volume C_V (J cm⁻³°C⁻¹)	3.01[12]

As seen in Fig. 110.27, CAP pulses have a strength of the order of 10^{-5} and a spatial width of approximately twice the pump-beam penetration depth $\left(\xi_{pump} = 1/\alpha_{pump} \right)$. We note, however, that our simulations predict that the electronic stress contribution is the major, dominant contribution in CAP generation, as compared to the thermal-stress contribution, in both the far-above- and just-above-bandgap excitations [Figs. 110.27(a) and 110.27(b), respectively], with the strength ratio between the electronic- and thermal-induced CAP's equal to about 8 and 60 for the 4.59- and 3.54-eV pump photons, respectively. The electronically induced strength of CAP's decreases only slightly when the pump photon energy decreases from 4.59 eV to 3.54 eV, while the thermal one drops by about an order of magnitude. Thus, the change of the total CAP strength is small [see Figs. 110.27(a) and 110.27(b), bottom curves], as it is electronically dominated. The CAP amplitude is determined mainly by α_{pump}, which changes only a little in the studied above-bandgap, pump-energy region.

The shapes of all CAP pulses presented in Fig. 110.27 are asymmetrically bipolar with a slight broadening at their trailing sides. This broadening is caused by the diffusion effects[7] and is much more pronounced in the electronically induced CAP's because the electron-hole diffusion is about five times faster than the thermal diffusion. The diffusion effects not only broaden the CAP pulse, but they also narrow its frequency

spectrum [inset in Fig.110.27(a)], where the spectra of the electronically and thermally induced CAP's are shown.

2. CAP Pulse Detection

In the discussed GaN sample geometry, the surface-generated CAP pulses propagate into the crystal along the z axis, causing a spatiotemporal modulation of the material's dielectric function. This modulation can be detected through the change in the reflectivity R of a time-delayed probe beam. The R dependence in the presence of a generalized disturbance of the dielectric function can be obtained by solving the Maxwell equations inside the GaN sample and was derived by Thomsen *et al.*[7] as

$$R = \left| r_0 + \Delta r \right|^2, \qquad (13)$$

where

$$r_0 = \frac{1 - n - i\kappa}{1 + n + i\kappa} \qquad (14)$$

is the reflection coefficient at the sample surface and represents that part of the probe beam's electric field reflected from the free surface, while

$$\Delta r = \frac{2i\omega}{c(1 + n + i\kappa)^2} \int_0^\infty dz' e^{2i(n + i\kappa)k_0 z'} \Delta\varepsilon(z,t) \qquad (15)$$

corresponds to the probe beam's electric field reflected from the CAP pulse. In Eqs. (14) and (15), n and κ are the real and imaginary parts of the refractive index, respectively; ω, c, and k_0 are the angular frequency of the probe light, the light speed, and the wave vector of the probe beam in vacuum, respectively; and $\Delta\varepsilon(z,t)$ is the change in dielectric function, which, under assumption that the disturbance is caused only by the propagating CAP pulse, can be expressed as

$$\Delta\varepsilon(z,t) = 2(n + i\kappa)\left(\frac{dn}{d\eta_{zz}} + i\frac{d\kappa}{d\eta_{zz}}\right)\eta_{zz}(z,t). \qquad (16)$$

Finally, we note that κ is related to the probe-beam absorption coefficient α_{probe} or, equivalently, the penetration depth ζ_{probe} through $\kappa = \alpha_{probe}\lambda/4\pi = \lambda/4\pi\zeta_{probe}$, where λ is the probe-beam wavelength.

Since our experiments measure the probe's $\Delta R/R$ signal, Eq. (13) must be rewritten in the form

$$\Delta R/R = \frac{\left| r_0 + \Delta r \right|^2 - \left| r_0 \right|^2}{\left| r_0 \right|^2}. \qquad (17)$$

The analytic expression of $\Delta R/R$ can be obtained if $n_{zz}(z,t)$, which we have only in a numerical form presented in Fig. 110.27, is substituted in Eq. (16) by an analytic expression:

$$\eta_{zz}(z,t) = -Ae^{-\alpha_{pump}\left| z - v_s t \right|}\mathrm{sgn}(z - v_s t), \qquad (18)$$

which fits our stress pulses very well and neglects only the electron-hole and thermal diffusion effects in the CAP generation, and A is the strength of the CAP pulse given by

$$A = \frac{\alpha_{pump}(1 - R_{pump})Q}{2E_{pump}\rho v_s^2}$$

$$\times \left[-(d_c + d_v) + \frac{3B\beta}{C_V}(E_{pump} - E_g)\right]. \qquad (19)$$

Combining the above formulas and considering that for our two-color pump/probe technique the condition $\alpha_{pump} \gg \alpha_{probe}$ holds, we find an analytic expression for $\Delta\varepsilon(z,t)$ and, finally, obtain the closed-form formula for $\Delta R/R$, correct to the first order in $n_{zz}(z,t)$:

$$\Delta R/R = \sqrt{\left(\frac{dn}{d\eta_{zz}}\right)^2 + \left(\frac{d\kappa}{d\eta_{zz}}\right)^2}\, AF_1$$

$$\times \left[\sin\left(\frac{4\pi n v_s t}{\lambda} - \phi\right)e^{-v_s t/\zeta_{probe}} + F_2 e^{-v_s t/\zeta_{pump}}\right], \qquad (20)$$

where

$$F_1 = \frac{\sqrt{n^2(n^2 + \kappa^2 - 1)^2 + \kappa^2(n^2 + \kappa^2 + 1)^2}}{n(n^2 + \kappa^2 + 1)^2 - 4n^3} \qquad (21)$$

is the probe-beam–related amplitude,

$$\phi = \arctan\left[\frac{\kappa(n^2 + \kappa^2 + 1)}{n(n^2 + \kappa^2 - 1)}\right]\arctan\left[\frac{dn/d\eta_{zz}}{d\kappa/d\eta_{zz}}\right] \qquad (22)$$

is the phase, and

$$F_2 = \frac{8\pi^2 n^2 \sin\phi - 2\pi n\lambda \alpha_{\text{pump}} \cos\phi}{16\pi^2 n^2 + \lambda^2 \alpha_{\text{pump}}^2}. \qquad (23)$$

Equation (20) allows us to directly compare our theoretical modeling with the experiments, facilitating data analysis and making our results more explicit. We can, however, simplify Eq. (20) somewhat further by noting that under our experimental conditions, ζ_{pump} is of the order of several tens of nanometers; thus, for the GaN sound speed $v_s = 8020$ m/s, the second term in the square bracket in Eq. (20) rapidly damps out within several picoseconds and can be neglected, as in our experiments we study CAP's within at least a few-hundred-ps-wide time delay window. The simplified expression of $\Delta R/R$ can be written as

$$\Delta R/R = \sqrt{\left(\frac{\mathrm{d}n}{\mathrm{d}\eta_{zz}}\right)^2 + \left(\frac{\mathrm{d}\kappa}{\mathrm{d}\eta_{zz}}\right)^2}$$

$$\times AF_1 \sin\left(\frac{4\pi n v_s t}{\lambda} - \phi\right) e^{-v_s t/\zeta_{\text{probe}}}. \qquad (24)$$

The temporal dependence of $\Delta R/R$ is represented in Eq. (24) as a simple damped-sinusoidal function and it follows Eq. (48) in Ref. 7, but now we also have an expression for the $\Delta R/R$ amplitude, as the product of A, F_1, and $\sqrt{(\mathrm{d}n/\mathrm{d}\eta_{zz})^2 + (\mathrm{d}\kappa/\mathrm{d}\eta_{zz})^2}$. The probe-related F_1 [see Eq. (21)] can be considered as a constant since for far-below-bandgap NIR light, n and κ in high-quality GaN crystals remain almost unchanged. The $\mathrm{d}n/\mathrm{d}\eta_{zz}$ and $\mathrm{d}\kappa/\mathrm{d}\eta_{zz}$ terms are the photoelastic constants and are related only to n and κ; thus, $\sqrt{(\mathrm{d}n/\mathrm{d}\eta_{zz})^2 + (\mathrm{d}\kappa/\mathrm{d}\eta_{zz})^2}$ also contributes a constant term in the total $\Delta R/R$ amplitude. Finally, following Eq. (19), the term A (strength of the CAP pulse) is only pump light related. We note that A experiences a dramatic change when the pump energy is tuned across the band edge because of the step-like change of α_{pump} near E_g. Experimentally it means that the total $\Delta R/R$ amplitude measured using the two-color pump/probe technique should change with the pump-beam energy, following the same functional dependence as A, namely the spectral characteristics of α_{pump}. Furthermore, this theoretical prediction indicates that we should be able to undeniably determine which stress contribution—electronic or thermal—is the dominant factor for triggering the CAP's in our bulk GaN crystals. If the electronic stress is dominant, as we saw in **CAP Pulse Generation** (p. 89), the experimentally observed $\Delta R/R$ amplitude should exhibit only a slight decrease when the pump energy changes from far above to just above bandgap. On the

other hand, when the thermal stress is dominant, the oscillation amplitude should experience an-order-of-magnitude drop in the same pump-energy range. Independently, when the pump beam energy is tuned across band edge, the amplitude of the experimental $\Delta R/R$ signal should almost abruptly decrease to zero, due to the rapid decrease of α_{pump}.

In agreement with the Thomsen model,[7] the $\Delta R/R$ damping constant in Eq. (21) is determined by the ζ_{probe}/v_s ratio. For the ~800-nm-wavelength (energy far below the GaN bandgap) probe light used in our two-color measurements, ζ_{probe} is ~200 μm,[8,9] which gives a damping time of ~25 ns. Thus, we should observe CAP's propagating deeply into the GaN crystal, actually, in full agreement with our early studies.[8]

Following again Eq. (24), the frequency of the $\Delta R/R$ oscillations is given by

$$f = 2nv_s/\lambda = \frac{nv_s}{\pi}k_0 \qquad (25)$$

and is related only to the probe beam. For a constant n, expected under our experimental conditions, f is proportional to k_0, which indicates a linear dispersion relation for CAP's with the slope corresponding to the fixed v_s. Finally, ϕ [see Eq. (22)] is, in our case, predicted to be a constant.

Experimental Procedures and Results
1. Sample Fabrication and Experimental Setup
Our GaN single crystals were grown with a high-pressure, solution-growth (HPSG) method.[19] The growth process was carried out at an external nitrogen gas pressure of 8 to 14 kbar and temperatures of 1350°C to 1600°C because of the high solubility of GaN in Ga at high temperatures. Nitrogen was first compressed to a 10- to 15-kbar level with a two-step pressure compressor and intensifier and then transported into the metallic Ga melt with a temperature gradient of 5°C to 50°C cm⁻¹. GaN single crystals formed at the cooler zone of the HPSG chamber. They grew up to 1-mm-thick platelets with typical sizes of up to 3×4 mm². These crystals exhibited an excellent wurtzite crystalline structure according to x-ray diffraction measurements, while their morphology depended on the growth process pressure, temperature range, and nitrogen supersaturation. In our experiments, we have studied a 2.5×2.5-mm², transparent (slightly brownish) GaN crystal piece that was ~0.4 mm thick.

Two-color, femtosecond pump/probe spectroscopy experiments were performed in a reflection mode using a commercial mode-locked Ti:sapphire laser with a pulse duration

of ~100 fs and repetition rate of 76 MHz. Our experimental setup is schematically shown in Fig. 110.28. In our study, two arrangements were used to generate the pump beam with desired photon energy. One optical path (see Fig. 110.28) was designed to deliver photons with energies in the range of 3.1 to 3.54 eV (wavelength of 400 to 350 nm) in the vicinity of a GaN bandgap of 3.4 eV and was based on frequency doubling of the fundamental Ti:sapphire pulse train. The other included our homemade third-harmonic generator and allowed us to generate pump photons with energies ranging from 4.13 eV to 4.64 eV (wavelength of 300 to 267 nm), far above the GaN bandgap. The pump beam was focused onto the surface of the GaN crystal with a spot diameter of ~20 μm at an incident angle of ~30°. The incident fluence was ~0.08 mJ/cm^2 per pulse and was kept constant while varying the pump-photon energy. Probe pulses were directly generated by the Ti:sapphire laser and had photon energies varying from 1.38 eV to 1.77 eV (wavelengths from 900 nm to 700 nm) far below the GaN gap; their fluence was always much lower (at least by a factor of 10) than that of the pump. The probe beam was delayed with respect to the pump and near-normally incident on the same area on the sample surface with a spot diameter of ~10 μm, and its reflection from the sample surface was filtered from any scattered pump photons and collected by a photodetector connected to a lock-in amplifier. The lock-in amplifier was synchronized with a mechanical chopper that modulated the pump beam at a frequency of ~2 KHz. The lock-in output was sent to a computer for data processing. The magnitude of $\Delta R/R$ that we measured was in the range of 10^{-3} to 10^{-6}.

2. Experimental Results

Typical time-resolved $\Delta R/R$ probe signals from our GaN crystal excited with far-above-bandgap (wavelength of 283 nm) and just-above-bandgap (wavelength of 350 nm) pump photons

are shown in Figs. 110.29(a) and 110.29(b), respectively. The corresponding probe wavelengths are 850 nm in Fig. 110.29(a) and 720 nm in Fig. 110.29(b). As we can see, although the two presented $\Delta R/R$ waveforms exhibit different electronic relaxation features, observed during the initial few picoseconds of relaxation and associated with the conduction band inter- and intra-valley electron scattering,[10] both are characterized by the same, few-hundred-ps-long exponential decay, associated
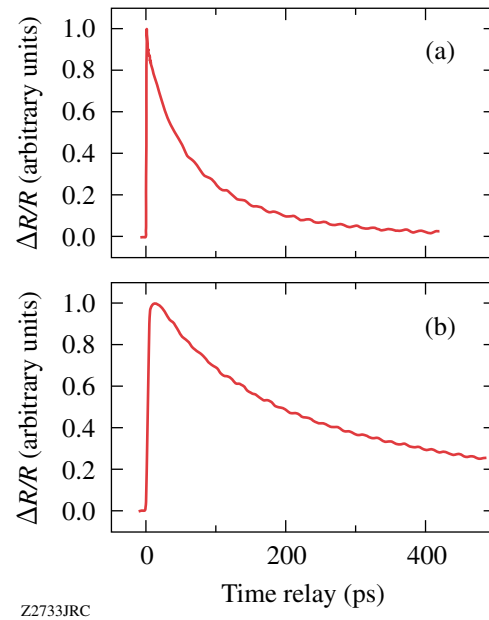
Figure 110.29
Time-resolved normalized $\Delta R/R$ waveforms as a function of the pump/probe delay time, measured in GaN single crystals for (a) the pump/probe wavelength of 283 nm/850 nm; (b) pump/probe wavelength of 360 nm/720 nm. The case (a) corresponds to the far-above-bandgap optical excitation, while case (b) corresponds to just-above-bandgap excitation.
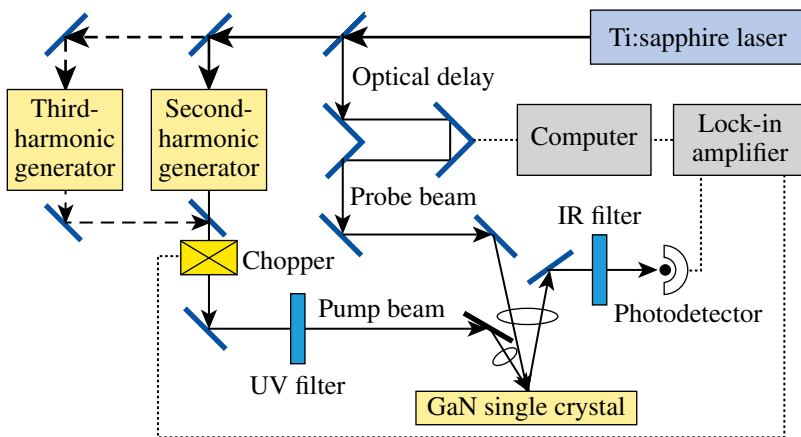

Figure 110.28
Experimental setup for the two-color, femtosecond pump/probe spectroscopy.

with the electron-hole recombination, with pronounced regular oscillations on top of it.

In this work, we focus only on this latter oscillatory feature, which we identify as propagation of the CAP transient inside the crystal.[8] Thus, in order to get a clearer view, we have subtracted numerically the electronic relaxation background from all of our collected raw data. Figure 110.30(a) shows the oscillatory component of the measured $\Delta R/R$ signal for four experimental examples, representative of our measurement cases. The presented traces correspond to the three different experimental conditions for CAP excitation, namely, far-above-bandgap excitation (trace 283 nm/850 nm), just-above-bandgap excitation (traces 350 nm/700 nm and 360 nm/720 nm), and band-tail-state excitation (trace 370 nm/740 nm), respectively. In all cases, no attenuation of the oscillations is observed within our experimental ~450-ps-wide time-delay window, which is consistent with Eq. (24), predicting that in our experiments the CAP oscillation damping constant is limited by the ζ_{probe}/v_s ratio and for $\zeta_{\text{probe}}/v_s \approx 25$ ns is much longer than our experimental time window.

Figure 110.30(b) presents four $\Delta R/R$ CAP-related transients calculated using Eq. (24) and corresponding directly to the four experimental transients shown in Fig. 110.30(a). In our theoretical calculations, the refractive index $n = 2.3$ and the probe absorption coefficient $\alpha_{\text{probe}} = 50$ cm^{-1} are assumed to remain unchanged for all of the studied probe wavelengths. The pump reflectance R_{pump} was set to be 0.2 and the constants $dn/d\eta_{zz}$ and $d\kappa/d\eta_{zz}$ entering into Eqs. (21) and (22) were set to be

1.2 and 0.5, respectively, in order to keep the CAP amplitude term F_1 and phase ϕ consistent with our experimental values. We note that there is extremely good agreement between the corresponding experimental [Fig. 110.30(a)] and theoretical [Fig. 110.30(b)] traces, in terms of both the oscillation amplitude and frequency.

Comparing the traces 283 nm/850 nm, 350 nm/700 nm, and 360 nm/720 nm, we observe only a slight amplitude decrease as we move from the far-above- to just-above-bandgap excitation. On the other hand, the 370-nm/740-nm trace, collected for the pump-photon energy corresponding to GaN band-tail states, has a much smaller amplitude than the other three, but the oscillatory feature is still observable. The above observations experimentally confirm our theoretical prediction that the driving mechanism for CAP generation in bulk GaN crystals is the electronic stress associated with the deformation potential. The rapid drop in CAP amplitude that occurs when we move the energy of our excitation photons across the GaN bandgap (compare traces 360 nm/720 nm and 370 nm/740 nm in Fig. 110.30) is caused by the dramatic change of the α_{pump} coefficient at the band edge. The latter is clearly illustrated in Fig. 110.31, where we plot the experimental CAP oscillation amplitude dependence on the pump-photon wavelength (energy) for the whole pump tuning range. The solid line shows the theoretical $\Delta R/R$ amplitude dependence on the pump-photon energy, using Eq. (24) [see also Eq. (19)]. We used the values listed in Ref. 9 for the α_{pump} spectral dependence in GaN crystals. The solid squares, circles, and triangles represent our experimental data corresponding to the far-above-bandgap, just-above-bandgap,
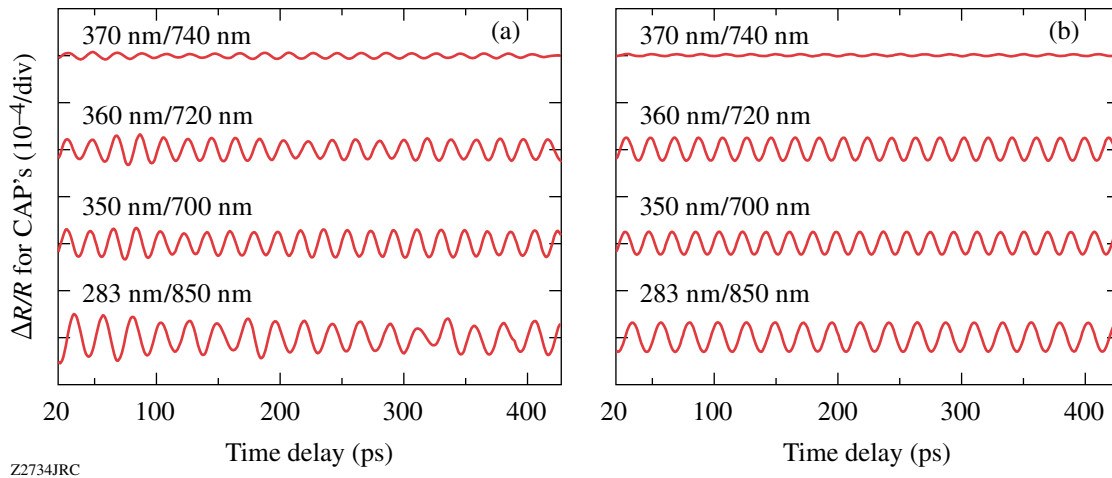

Figure 110.30
The oscillatory components of the $\Delta R/R$ signals as a function of the pump/probe delay time for several pump/probe wavelength configurations: 370 nm/740 nm, 360 nm/720 nm, 350 nm/700 nm, and 283 nm/850 nm. Panels (a) and (b) show the experimental and theoretical results, respectively.
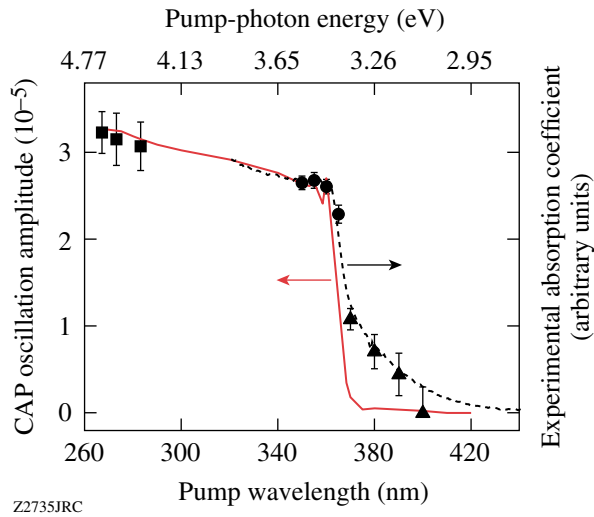
Figure 110.31
The amplitude of the CAP oscillations versus the pump-beam wavelength (energy–top axis). The solid line is the theoretical curve, while the solid squares, circles, and triangles are our experimental data points corresponding to the far-above-bandgap, just-above-bandgap, and band-tail-state pump excitations, respectively. The dashed line (right axis) is the experimental GaN absorption coefficient spectrum, extracted from the transmission and reflection data obtained for our actual GaN single crystal.

and band-tail-state pump excitations, respectively. We see very good overall agreement between our experimental points and the modeling. Only in the case of the pump photons exciting the band-tail states (solid triangles in Fig. 110.31), the decrease of the CAP amplitudes with the pump-wavelength increase is slower than the theoretical prediction. The latter discrepancy, however, is clearly a consequence that in our theoretical calculations we used the values of α_{pump} from Ref. 9 and not α_{pump} directly measured for our GaN samples. The dashed line in Fig. 110.31 corresponds to the GaN absorption coefficient spectrum extracted from the transmission and reflection data of our actual GaN single crystal, experimentally measured using a Perkin-Elmer Lambda 900 spectrophotometer. We note that in this case the agreement is excellent.

For all of the traces plotted in Fig. 110.30, the CAP oscillation phase was essentially constant and equal to ~1.2, as shown in Fig. 110.32, which presents ϕ as a function of the probe-photon wavelength (energy) for our entire experimental tuning range. The constant ϕ is very consistent with our theoretical prediction based on Eq. (22) and the fact that n, κ, $dn/d\eta_{zz}$, and $d\kappa/d\eta_{zz}$ can be assumed constant for our NIR probe photons. The solid line in Fig. 110.32 was obtained by fitting Eq. (20) with $\left(dn/d\eta_{zz}\right)/\left(d\kappa/d\eta_{zz}\right) = 2.5$ as the best fit.

Finally, Fig. 110.33 demonstrates the dispersion relation of the CAP oscillation frequency on the probe beam's wave number. For the entire probe-beam tuning range from 700 nm to 850 nm, we observe a linear (dispersionless) relationship between f and k_0, as predicted by Eq. (25). The slope of the data (solid line in Fig. 110.33) gives $\nu_s = 8002 \pm 22$ m/s. The
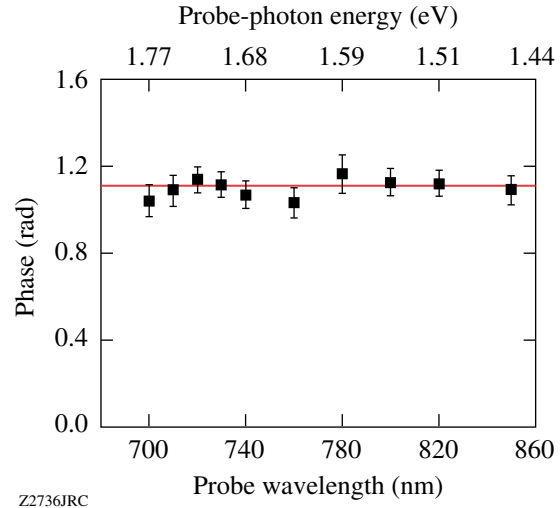
Figure 110.32
The phase of the CAP oscillation versus the probe–beam wavelength (energy–top axis). The solid line shows the theoretical fit based on Eq. (22) with $\left(dn/d\eta_{zz}\right)/\left(d\kappa/d\eta_{zz}\right) = 2.5$.
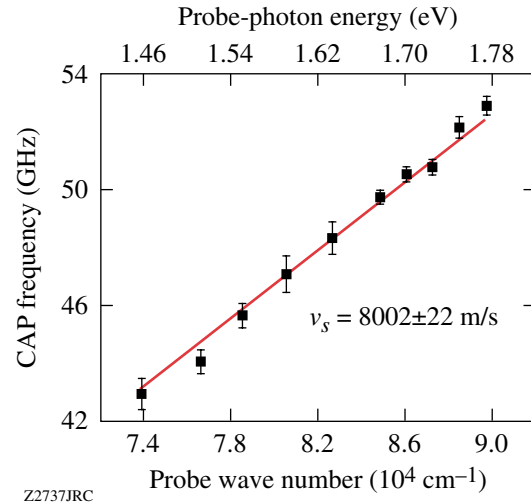
Figure 110.33
The CAP oscillation frequency dependence on the probe beam's wave number (energy–top axis). The solid squares are the peak values of the CAP oscillations Fourier spectra, while the solid line shows the linear fit, intercepting the plot origin, based on Eq. (25).

latter result is very close to our earlier finding,[8] as well as to the values of 8160 m/s and 8020 m/s reported in literature.[1,11]

Conclusions

We have presented our comprehensive studies of CAP generation and detection in a bulk GaN single crystal, using a time-resolved, femtosecond, two-color pump/probe technique. We theoretically predicted and experimentally confirmed that the CAP transients, in our case, were initiated by electronic stress induced at the GaN crystal surface by generation of free carriers, photoexcited by ~100-fs pump UV pulses. Using far-below-bandgap, ~100-fs-wide probe pulses with a very long penetration depth into the GaN crystal, we monitored the CAP propagation that manifested itself as regular, single-frequency oscillations superimposed on the probe $\Delta R/R$ signal. The amplitude of the oscillations was of the order of 10^{-5} to 10^{-6}, and within our ~450-ps time window, we observed no signal attenuation. We also found that the CAP oscillation amplitude was dependent only on the pump-photon energy and, in general, followed the spectral dependence of the GaN optical absorption coefficient, as was predicted by our theoretical model. For the entire tuning range of our NIR probe photons, the phase of the CAP oscillations was constant and the CAP frequency was dispersionless (proportional to the probe k_0) with the slope corresponding to $v_s = 8002\pm22$ m/s, the speed of sound in GaN. Very good agreement between our theoretical modeling and experimental results demonstrates that our theoretical approach, which is a generalization of the Thomsen model,[7] comprehensively describes the dynamics of CAP's in bulk materials, generated by the strong, above-the-bandgap optical excitation and synchronously probed using almost nonattenuated probe pulses. Thus, our above-bandgap pump and far-below-bandgap probe experimental approach makes it possible to successfully generate nanoscale acoustic waves at the surface of bulk semiconductors and, simultaneously, to nondestructively probe the material's structure deeply under its surface. The two-color femtosecond spectroscopy technique, implemented here for the studies of GaN, should be very promising in producing and detecting CAP waves in a large variety of bulk semiconducting materials.

REFERENCES

1. Y.-K. Huang *et al.*, Appl. Phys. Lett. **79**, 3361 (2001).

2. R. L. Liu *et al.*, Phys. Rev. B **72**, 195335 (2007).

3. C.-K. Sun, J.-C. Liang, and X-Y. Yu, Phys. Rev. Lett. **84**, 179 (2000).

4. Ü. Özgür, C.-W. Lee, and H. O. Everitt, Phys. Status Solidi B **228**, 85 (2001).

5. G. D. Sanders and C. J. Stanton, Phys. Rev. B **64**, 235316 (2001).

6. O. Matsuda *et al.*, Phys. Rev. B **71**, 115330 (2005).

7. C. Thomsen *et al.*, Phys. Rev. B **34**, 4129 (1986).

8. S. Wu, P. Geiser, J. Jun, J. Karpinski, J.-R. Park, and R. Sobolewski, Appl. Phys. Lett. **88**, 041917 (2006).

9. G. Yu *et al.*, Appl. Phys. Lett. **70**, 3209 (1997).

10. S. Wu, P. Geiser, J. Jun, J. Karpinski, D. Wang, and R. Sobolewski, J. Appl. Phys. **101**, 043701 (2007).

11. C. Deger *et al.*, Appl. Phys. Lett. **72**, 2400 (1998).

12. V. Bougrov *et al.*, in *Properties of Advanced Semiconductor Materials: GaN, AIN, InN, BN, SiC, SiGe*, edited by M. E. Levinshtein, S. L. Rumyantsev, and M. Shur (Wiley, New York, 2001), Chap. 1, pp. 1–30.

13. M. Leszczynski *et al.*, J. Phys. D: Appl. Phys. **28**, A149 (1995).

14. W. Qian, M. Skowronski, and G. S. Rohrer, in *III-Nitride, SiC, and Diamond Materials for Electronic Devices*, edited by D. K. Gaskill, C. D. Brandt, and R. J. Nemanich, Mat. Res. Soc. Symp. Proc. Vol. 423 (Materials Research Society, Pittsburgh, PA, 1996), pp. 475–486.

15. S. L. Chuang and C. S. Chang, Phys. Rev. B **54**, 2491 (1996).

16. G. Tamulaitis *et al.*, Phys. Status Solidi C **3**, 1923 (2006).

17. S. N. Nakamura and G. Fasol, *The Blue Laser Diode: GaN Based Light Emitters and Lasers* (Springer, Berlin, 1997).

18. J. Karpiński, J. Jun, and S. Porowski, J. Cryst. Growth **66**, 1 (1984).

Subsurface Damage and Microstructure Development in Precision Microground Hard Ceramics Using MRF Spots

Introduction

Chemical vapor–deposited (CVD) silicon carbide (Si_4C/SiC), polycrystalline alumina (Al_2O_3/PCA), and aluminum oxynitride ($Al_{23}O_{27}N_5$/ALON) polycrystalline ceramics display a great potential for advanced optical applications in severe environments that require high hardness, high toughness, and excellent thermal properties. These materials are nominally fully dense; therefore, there is growing interest in grinding and ultimately polishing them to nanometer levels of surface microroughness.

Grinding of ceramic materials usually involves the use of metal- or resin-bonded diamond abrasive wheels.[1] The material-removal mechanism can be described by indentation fracture mechanics, where removal is caused by multiple indentation events.[2,3] Two crack systems extend from the plastic deformation zone induced by the indentation: median/radial and lateral cracks.[2] For a given process, lateral cracks control the extent of material removal,[4,5] while the extensions of median/radial cracks are commonly associated with subsurface damage (SSD),[6] which contributes to the degradation of the materials' strength.[2]

For optical applications, SSD can be the source of component instability (e.g., surface stress) and contamination. Polishing abrasives embedded in cracks can lead to laser-induced damage, and thermal cycling can result in component fracture.[7–9] Therefore, determination of SSD depth is critical for high-quality optics. Unfortunately, SSD from grinding is often masked by a deformed surface layer that is smoothed or smeared over the part surface.[9–11] For polycrystalline ceramics, this layer may also consist of pulverized grains or powder. The thickness of this deformed layer varies along the ground surface because of the nonhomogeneity of the composite and the nonuniform distribution of diamond abrasives on the grinding wheel.[12] Therefore, it is valuable to develop new analytical techniques for understanding the damaged surface left from grinding and how it extends into the subsurface for these optical ceramics.[9,10]

Different techniques for estimating SSD depth induced by grinding have been pursued. Randi et al.[13] reviewed both nondestructive and destructive techniques to evaluate SSD in brittle materials. Nondestructive methods include transverse electron microscopy, x-ray diffractometry, Raman spectroscopy, optical microscopy, photoluminescence, and the use of ultrasound for ground ceramic materials. Destructive techniques include taper polishing, cleavage, sectioning, ball dimpling, and spotting with magnetorheological finishing (MRF). These destructive techniques are ultimately followed by microscopy or diffractive-based techniques to observe and measure SSD depth.

One recent example of a nondestructive technique is light scattering, as described by Fine et al.,[7] whose results were confirmed by the sectioning technique. Another recent study by Wang et al.[8] showed how the measurement of the quasi-Brewster angle (qBAT) as a function of wavelength could be used to estimate SSD depth for polished CaF_2 (111) surfaces. The MRF spot technique, as described by Randi et al.,[13] was used by Wang et al.[8] to validate their results.

Examples of sectioning techniques include the work by Xu et al.[14] done on polycrystalline alumina scratched by a single diamond, or Kanematsu,[10] who visualized the morphology of SSD induced by grinding on silicon nitride. His approach included a combination of taper-polishing and plasma-etching techniques, finally observing SSD using scanning electron microscopy (SEM). In addition, dye impregnation was used to identify the crack morphology of previously ground samples that were subsequently broken using a flexure test.[10] Miller et al.[9] and Menapace et al.[5,15] utilized MRF computer numerically controlled (CNC) machines with raster polishing capabilities to study the distribution of SSD in larger, polished fused-silica parts by fabricating a wedge.

SSD depth can also be estimated by correlating SSD depth to the grinding-induced surface microroughness, or by correlating SSD depth to the size of grinding or polishing abrasives. Preston[16] showed that surface microroughness was three to four

times the SSD depth, by comparing polished and ground glass microscope slides in the early 1920s. In the 1950s Aleinikov[17] expressed the proportionality factor to be ~4 for optical glasses and ceramics. Hed *et al.*[18] extended Aleinikov's work using bound-abrasive tools (diamond and boron carbide), finding that the ratio between SSD depth and peak-to-valley (p–v) surface microroughness (measured using a contact profilometer) for Zerodur, fused silica, and BK-7 glass was ~6.5, a much higher value than previous results. For a large variety of optical glasses ground with bound-abrasive diamond tools, Lambropoulos *et al.*[19] estimated SSD depth to be less than two times the p–v surface microroughness (from areal measurements using a white-light interferometer). In more recent work, Randi *et al.*[13] found the ratio between p–v microroughness (from areal measurements using a white-light interferometer) and SSD to be 1.4 for some optical single crystals ground with diamond-bonded tools, where SSD was measured directly by combining MRF spotting and microscopy techniques. Using the MRF-based technique described here, we demonstrated that, for nonmagnetic nickel-based tungsten carbides (WC-Ni—a challenging composite for optical applications), there is a strong positive correlation between p–v surface microroughness (from areal measurements using a white-light interferometer) and SSD depth for rough-ground surfaces.[20] The application of this technique to magnetic cobalt-based tungsten carbides (WC-Co) was also successful.[21] In all work cited above, it is critical to be aware of the instruments used to characterize surface roughness since different instruments produce different surface-roughness values, due to their different lateral scale-length capabilities.

SSD was also found to be a function of abrasive size used in the controlled grinding stages for fabrication of precision optics, as discussed by Lambropoulos[22] for a variety of optical glasses and glass ceramics. In practice, by reducing the abrasive size with each grinding cycle, the plastically deformed material is removed, reducing the residual stresses associated with the indentation events, and subsequently reducing the initiation of cracks within the plastic zone.[4] This suggests that, by gradually reducing abrasive size, SSD can be minimized with every subsequent grinding step.

We present here a procedure for estimating SSD depth induced by deterministic microgrinding of hard polycrystalline optical ceramics with diamond-bonded tools. This estimate comes from tracking the evolution of surface microroughness (measured using a white-light interferometer) with the amount of material removed by multiple MRF spots (measured using a contact profilometer) of increasing depth into the surface. In addition to extending our p–v microroughness/SSD correlation to hard ceramics, this technique also reveals information about the specimen microstructure (i.e., grain size), mechanical properties (i.e., hardness and fracture toughness), and the grinding conditions (i.e., abrasive size used), from extended spotting with the MRF process.

Experimental Procedure

1. Materials

Samples were obtained from the following sources: three ALON (Surmet Corp., MA, Lot 1472, April 2006) disks (40 mm in diameter × 15 mm thick), two PCA (commercial manufacturer) disks (40 mm in diameter × 2.5 mm thick), and three CVD SiC (Rohm and Haas Company, Advanced Materials, MA) disks (76 mm in diameter × 11.5 mm thick). Grain-size ranges were 150 to 250 μm for ALON, submicron size for PCA, and 5 to 10 μm for CVD SiC.

2. Mechanical Properties (Hardness and Fracture Toughness)

Hardness measurements were taken on a Tukon microindenter equipped with a Vickers diamond indenter and a built-in microscope (×50 objective). A constant dwell time of 15 s was used, with a nominal indentation load of 1 kgf (9.8 N). Averaging was performed on the diagonals of five to ten random indents on the surface.

In the case of ALON, individual grains were easily distinguished, allowing placement of indentations in the middle of individual grains. There were no grain boundaries observable for CVD SiC and PCA using the microscope. For all of the materials tested, indentations were randomly placed on specimen surfaces, avoiding large pores and/or inclusions.

Fracture toughness K_c values were calculated from the observed radial cracks produced at the indentation corners using the Evans correlation.[23] The relevant physical and mechanical properties are listed in Table 110.IV.

3. Grinding Experiments

All samples were processed under the same conditions using deterministic microgrinding. The first set of grinding experiments was performed on a CNC grinding machine[25] using a contour-tool grinding configuration for flat surfaces [see Fig. 110.34(a)], with three different diamond tools: rough, medium, and fine (40-μm, 10- to 20-μm, and 2- to 4-μm grit size, respectively). Both the rough and medium tools had a bronze matrix while the fine tool matrix was resin. To avoid tak-

ing the part off the machine between operations, the tools were trued and dressed in advance using Al_2O_3 dressing sticks that were 320 or 800 grit (29- to 32-μm and 9- to 12-μm grit size, respectively). Table 110.V lists the grinding conditions used.

For PCA an additional grinding experiment was performed because of the large form error on the part surface from grind-

ing using the previous contour configuration. These experiments were completed on a CNC grinding machine[26] using a ring-tool grinding configuration for flat surfaces [see Fig. 110.34(b)]. Grinding was done using rough and medium diamond tools (65-μm and 10- to 20-μm grit size, respectively). Both tools had a bronze matrix, and dressing procedures were performed as discussed above. Table 110.V lists the grinding conditions used.

Table 110.IV: Physical and mechanical properties of hard ceramics listed by increasing Vickers hardness and fracture toughness.[a]

Material ID	Density ρ (g/cm^3)	Grain size (μm)	Young's modulus E (GPa)	Vickers hardness H_V (GPa)	Fracture toughness K_c (MPa$\sqrt{m}$)[b]
ALON ($Al_{23}O_{27}N_5$)	3.69[c]	150 to 250	334	15.4±0.3[d]	2.7±0.2
PCA (Al_2O_3)	3.99[e]	<1	400[f]	21.6±0.3[g]	3.3±0.1
CVD SiC (Si_4C)	3.21	5 to 10	466	25.0±0.1[g]	5.1±0.3

[a] Catalog values, unless otherwise specified.
[b] Calculated using the Evans correlation.[23]
[c] Density may vary slightly depending on the stoichiometry.
[d] Averaging ten Vickers indentations at 1 kgf.
[e] Using Archimedes' water immersion principles.[24]
[f] Calculated from measurement using ultrasonic tests and density values. Data were averaged for two PCA disks (~30 mm in diameter × ~1 mm thick) polished on both sides.
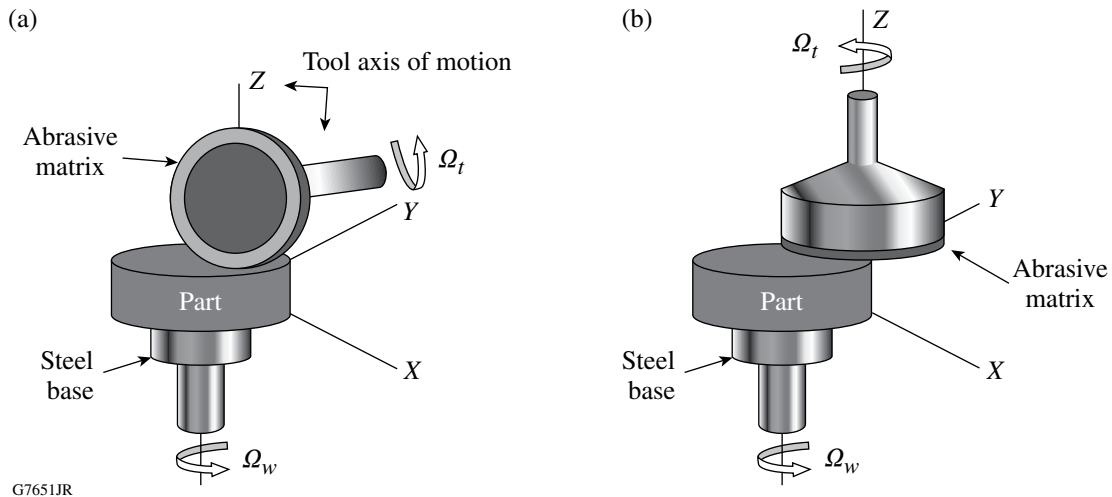[g] Averaging five Vickers indentations at 1 kgf.

Figure 110.34
Schematics of the two grinding configurations used in our experiments: (a) contour and (b) ring-tool configurations.

Table 110.V: Grinding conditions used in a single pass.[a]

Tool grit size (μm)	Depth of cut (μm)	In-feed (z axis) (mm/min)	Duration of single pass	Cross-feed (x axis) (mm/min)	Duration of single pass (min)
Contour tool grinding configuration.[25]					
40[b]	100	0.5	12 (s)	1.0	30 to 40
10 to 20[b]	20	0.5	2.4 (s)	1.0	30 to 40
2 to 4[c]	5	0.5	0.6 (s)	5.0	6 to 8
Ring tool grinding configuration.[26]					
65[b]	100	0.1	~20 (min)	NA	NA
10 to 20[b]	30	0.01	~45 (min)	NA	NA

[a] The following parameters remained constant: Wheel speed, Ω_t = 6800 rpm for contour tool grinding; Ω_t = 3000 rpm for ring tool grinding; work spindle speed, Ω_w = 100 rpm in both cases.
[b] Bronze bonded, 75 diamond concentration.
[c] Resin bonded, 75 diamond concentration.

Before all grinding experiments, each workpiece was attached to a steel base with hot wax and then placed in the grinding machine parallel to the tool axis of rotation. Water–oil emulsion coolant[27] was delivered to the tool/workpiece interface to avoid burnout and thermal damage. In the case of the contour grinding configuration, grinding was done with two passes for each tool; i.e., the total material removed per tool was 200, 40, and 10 μm (rough, medium, and fine tools, respectively). No subsequent "spark-out " passes were performed. For example, the fine grinding was done only after the part had gone through two-pass cycles with the rough and medium tools. Finally, the workpieces were cleaned using acetone. For ring-tool grinding, multiple tool passes were performed until material was evenly removed from the surface.

4. Spotting of Ground Surfaces

Magnetorheological finishing (MRF)[28,29] is a commercial polishing process for the manufacturing of precision optics. We used MRF spotting, with a commercial CNC machine,[30] in our experiment to estimate the depth of subsurface damage induced by grinding. For all of our experiments, MRF spots were polished onto the ground surface of a nonrotating part, by lowering the part surface into contact with a rotating magnetic fluid ribbon. The MRF fluid used was a commercial product[31] that consisted of an aqueous mixture of nonmagnetic nanodiamond abrasives, magnetic carbonyl iron, water, and stabilizers. Machine parameters such as the magnetic-field strength (~2 to 3 kG), wheel speed (250 rpm), pump speed (125 rpm), ribbon height (1.6 mm), and depth of the part penetrating into the ribbon (0.3 mm) were kept constant and the spotting time

was varied. Spotting was done on previously rough-ground, medium-ground, and fine-ground surfaces of each material. Multiple spots with time durations of 1 to 8, 12, and 16 min were taken on subsets of the ground surfaces of ALON and CVD SiC, whereas in the case of the PCA, multiple spots with time durations of 6, 12, 24, 48, and 96 min were taken as described in **Surface Evaluation from the Spotting Experiments** (p. 103).

5. Microscopy of Processed Surfaces

Surfaces were studied using a contact profilometer, a white-light interferometer, a scanning electron microscope (SEM), and an atomic force microscope (AFM). Before the surfaces were analyzed, the samples were ultrasonically cleaned in acetone (30 min at room temperature), then rinsed with alcohol, and finally dried using a nitrogen gun.

Metrology was conducted as follows:

• A stylus profilometer[32] was used to perform 3-D scans of the MRF spots, which were then used to extract the spots' physical dimensions, i.e., spot volume, peak removal depth, and spot profile. The stylus tip is a cone with a 60° angle and a 2-μm spherical tip radius of curvature. The instrument has a 12-nm vertical resolution, and the lateral resolution is about the size of the tip.

• Average microroughness data [peak-to-valley (p–v) and root mean square (rms)] were obtained with a noncontacting white-light interferometer[33] over five 350×250-μm^2 areas

randomly distributed across ground areas and within MRF spots as described in **Surface Evaluation from the Spotting Experiments** (p. 103). This instrument has a lateral resolution of ~1 μm and a vertical resolution of ~0.3 nm. The motorized XY stage and field-of-view stitching software allow this instrument to be programmed to measure a large area at high resolution.

- The morphologies of the processed surfaces following grinding, and for selected MRF spots, were analyzed using a field emission SEM.[34] The preferred imaging configuration was a mix signal of the in-lens and in-chamber secondary electron detectors. Surfaces of ground and spotted CVD SiC material were not etched or coated prior to SEM. Imaging of the nonconductive materials (i.e., PCA and ALON) was also performed without etching or application of a conductive coating, using a low beam voltage (1.5 to 0.7 kV), at an ~3-mm working distance.

- Additional surface scans for selected spots were taken on the AFM[35] over three 10×10-μm^2 areas randomly distributed within spots where the deepest point of fluid penetration (ddp) occurred, as discussed in **Surface Evaluation from the Spotting Experiments** (p. 103). Silicon tips with tip radii of approximately 10 nm were used. The lateral image resolution can be as small as the tip radius (5 to 15 nm) and the instrument vertical noise resolution is less than 0.5 Å.

Experimental Results

1. Surface Microroughness and Surface Morphology from Grinding

Surface microroughness data for all materials after each grinding stage were taken using the white-light interferometer. As expected, surface microroughness decreased with decreasing diamond abrasive size. Using the light microscope[36] we observed pitting on the ground surfaces, with no traces of grain boundaries for all the materials tested, as seen in Fig. 110.35. The p–v surface microroughness varied from ~14.5 μm (ALON) to ~3.7 μm [CVD SiC; see Fig. 110.35(a)] after grinding with the rough tool (40-μm grit size), from ~12 μm (ALON) to ~3.5 μm (CVD SiC) for the medium tool (10- to 20-μm grit size), and from ~4 μm [ALON; see Fig. 110.35(b)] to ~0.4 μm [CVD SiC; see Fig. 110.35(c)] for the fine tool (2- to 4-μm grit size). Surface microroughness for PCA was ~9 μm [see Fig. 110.35(d)] with the medium ring tool (10- to 20-μm grit size).

(a)

(b)

(c)

(d)

25 μm
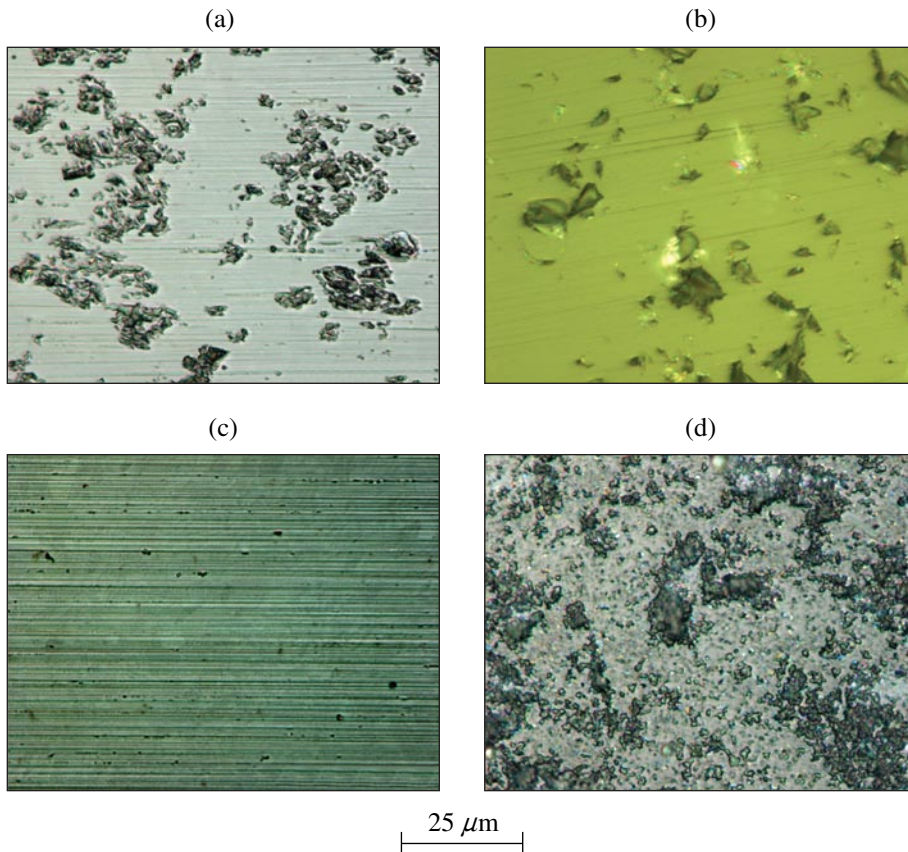
Figure 110.35
Light microscope images of ground surfaces: (a) rough-ground CVD SiC (5- to 10-μm grain size, 40-μm tool grit size with contour configuration, ~4-μm p–v); (b) fine-ground ALON (150- to 300-μm grain size, 2- to 4-μm tool grit size with contour configuration, ~4-μm p–v); (c) fine-ground CVD SiC (5- to 10-μm grain size, 2- to 4-μm tool grit size with contour configuration, ~0.4-μm p–v); (d) medium-ground PCA (submicron grain size, 10- to 20-μm tool grit size with ring configuration, ~8.5-μm p–v).

G7652JRC

By using the SEM's high-magnification capabilities we examined the morphologies of the ground surfaces with greater detail. Figure 110.36(a) shows the morphology of the rough-ground ALON, where the material microstructures, i.e., grain boundaries, are not visible. By using high magnification, Fig. 110.36(b) shows that the removal mechanism involved fracture. Figure 110.36(c) shows that for CVD SiC, the rough-ground surface is pitted, with the surrounding surface relatively smooth. Using higher magnification, Fig. 110.36(d) shows that the pit lengths, approximately 5 μm long, are comparable to the average grain size (5 to 10 μm) of this CVD SiC material.

Examination of the PCA surface in Fig. 110.36(e) shows that the deformed layer induced by grinding covers/masks the grains and any SSD, for PCA. Using higher magnification, Fig. 110.36(f) shows the exposed PCA subsurface where it appears that single grains pulled out, leaving craters of the order of 0.2 to 0.4 μm wide.

2. Surface Evaluation from the Spotting Experiments

MRF spots of increasing time duration were taken on all ground surfaces. Figure 110.37(a) shows a typical 3-D map generated with a profilometer for an 8-min MRF polishing spot taken on a rough-ground CVD SiC surface. After using the software to remove form figure errors (e.g., tilt and curvature), we calculated the physical properties such as volume and maximum amount of material removed by the MRF spot (i.e., spot depth). The volumetric removal rates for ALON, CVD SiC, and PCA using the MRF operating conditions described previously were found to be 0.020, 0.006, and 0.002 mm^3/min, respectively, from averaging the results of four spots.

The area enclosed by the white ellipse in Fig. 110.37(a) constitutes the region of maximum removal within the spot, where the depth of deepest penetration (ddp) into the subsurface

(a)

Leading edge   ddp region   Trailing edge

(b)

MRF flow direction

G7654JRC
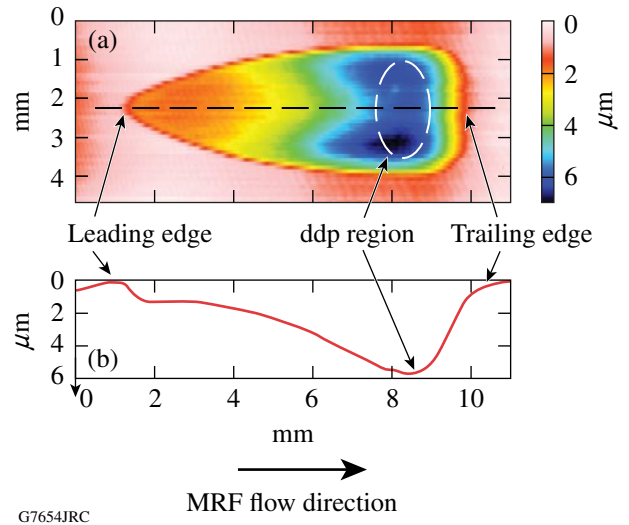
Figure 110.37
(a) 3-D image of an MRF spot taken with a contact stylus profilometer on rough-ground CVD SiC for 8 min. Arrows indicate the spot's leading edge (where an MRF ribbon first contacts the material), the spot's ddp region, identified by an ellipse (deepest point of part penetration into the MRF fluid ribbon), and the spot's trailing edge. The fluid flow direction is from left to right. (b) Spot profile extracted from a line scan through the center of the 3-D map (indicated by a dashed line). The distance between the trailing edge and the ddp region is ~2 mm in the horizontal direction. The spot depth reaches ~6 μm in the region sampled with the line scan.

G7653JR
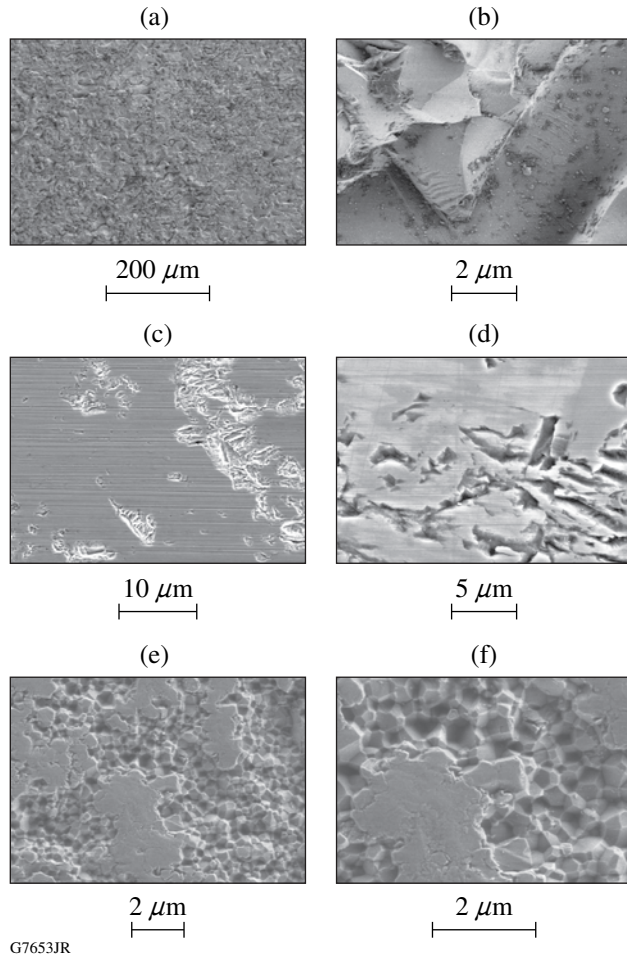
Figure 110.36
Morphology of the as-ground surfaces using SEM with different magnifications: (a),(b) ALON ground with contour configuration, 40-μm tool grit size, and ~14.5-μm p–v, low and high magnification, respectively, taken using low beam voltage (1 kV), at a 5-mm working distance; (c),(d) CVD SiC ground with contour configuration, 40-μm tool grit size, ~4-μm p–v, low and high magnification, respectively, taken using nominal beam voltage (10 kV), at a 10-mm working distance; and (e),(f) PCA ground with ring configuration, 10- to 20-μm tool grit size, ~8.5-μm p–v, low and high magnification, respectively, taken using low beam voltage (1.5 kV), at a 3-mm working distance.

occurs. The ddp in Fig. 110.37(a) has some asymmetry with respect to the spot center profile line [shown in Fig. 110.37(b)], in this case exhibiting a variation of ±0.6 μm. This feature is typically encountered for many of the longer-time-duration spots examined in this work. It could be due, in part, to subtle misalignments of the plane of a part surface with respect to the MRF ribbon. Figure 110.37(b) illustrates how we extract the spot center profile from the 3-D map to establish the location of the ddp region relative to the trailing edge for roughness measurements.

Figure 110.38(a) shows a 3-D map of a different spot taken on a rough-ground CVD SiC surface transverse to the MRF flow direction (as indicated by an arrow in the figure), with the white-light interferometer in stitching mode. Figures 110.38(b) and 110.38(c) give 3-D maps (0.3×0.3 mm^2) of the rough-ground surface and within the ddp, extracted from the map of Fig. 110.38(a), respectively. Figures 110.38(d) and 110.38(e) show line scans, or 2-D profiles, extracted from Figs. 110.38(b) and 110.38(c) (as indicated by the arrows), respectively. These line scans show the significant roughness reduction from ~1.4-μm p–v [~100-nm rms; Fig. 110.38(d)] for the ground surface to ~95-nm p–v [~18-nm rms; Fig. 110.38(e)] achieved inside the MRF spot, in agreement with the areal microroughness values, which vary from ~3.2-μm p–v [~99-nm rms; Fig. 110.38(b)] on the ground surface and ~170-nm p–v [~19-nm rms; Fig. 110.38(c)] within the spot ddp. Note that the discrepancy between the line scans and the areal data
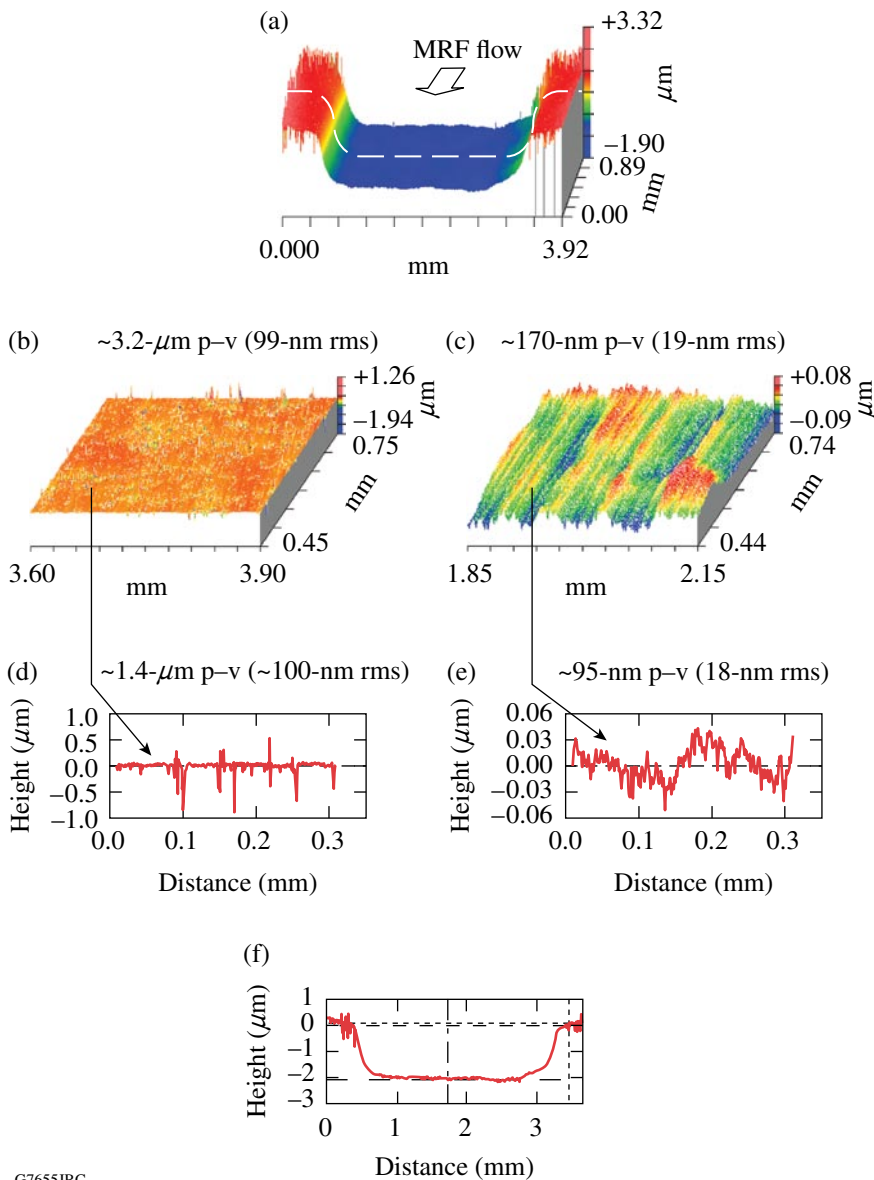
Figure 110.38
Scans taken on rough-ground CVD SiC, spotted for 3 min: (a) 3-D map done with the white-light interferometer in stitching mode, transverse to the MRF flow (see arrow indicating the MRF flow direction); (b),(c) areal maps (0.3×0.3 mm^2) of microroughness on the ground surface and within the spot ddp, respectively; (d) line scan of the ground surface, taken from the center of (b); (e) line scans within the ddp region transverse to the MRF flow direction, taken from the center of (c) (as indicated by the arrows); and (f) line scan of the spot-width profile (indicated by a dashed white line in the 3-D map) in (a).

G7655JRC

comes from the larger areas sampled with the latter method. Another discrepancy between the 3-D map and line scans in Fig. 110.38 is associated with the spot depth. The vertical scale in Fig. 110.38(a) indicates the overall areal p–v roughness variations of ~5.2 μm, which artificially indicates a spot depth of that scale because it includes the highest peaks on the rough surface. However, when we examine single line scans of the spot width profile [represented by a dashed line in Fig. 110.38(a)], the spot depth is shown to be ~2 μm [see Fig. 110.38(f)].

After the location of a given spot's ddp was identified [as described in Fig. 110.37(b)], areal surface microroughness measurements were taken using the white-light interferometer at five random locations within the ddp region over areas of 0.35×0.26 mm^2 as seen schematically in Fig. 110.39(a). In

(a)

(b)

G7656JRC

Figure 110.39
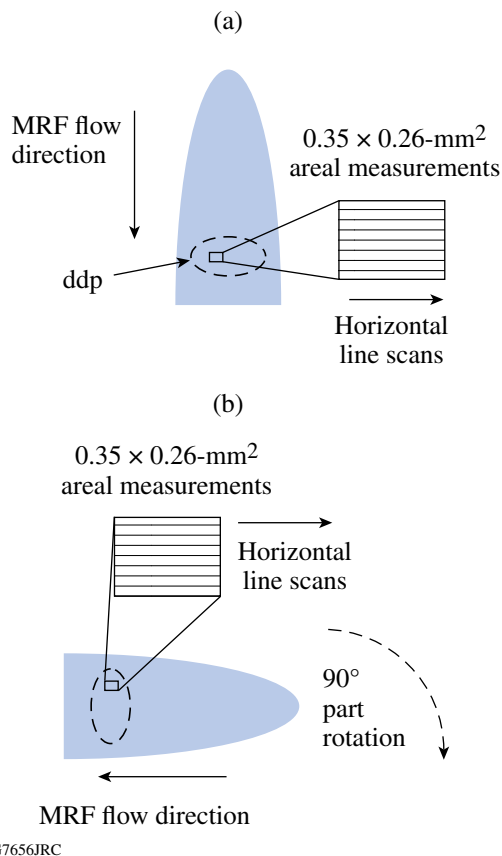Schematic diagram of the procedure used for surface microroughness measurements within MRF spots. The dashed ellipse represents the ddp region. The rectangle within the ddp represents one of five random sites over which surface roughness was measured. (a) First orientation of the spot for generating line scans perpendicular ($\perp$) to the MR fluid flow direction, and (b) after rotating the part 90° to generate line scans parallel (||) to the MR fluid flow direction.

addition, horizontal line scans were taken perpendicular ($\perp$) to the MRF flow direction. Then, the part was rotated by 90° and remeasured so that horizontal line scans parallel (||) to the MRF flow direction were also obtained, as seen in Fig. 110.39(b). This procedure is necessary because the interferometer analog camera creates images with a horizontal raster pattern.

Surface microroughness data taken on initial ground surfaces and in ddp areas for long-time-duration spots are listed in Tables 110.VI(a)–110.VI(c). The areal data represent averages of 5 random measurements, while the values for the line scans ($\perp$ and ||) represent averages of 50 line scans. The amount of material removed in each spot, or the spot maximum depth, is reported for measurements done using the contact profilometer, as described in the text that discusses Fig. 110.37(a).

Tables 110.VI(a)–110.VI(c) summarize the results of grinding and spotting experiments (the complete set of experimental data can be found elsewhere[37]). The evolution of microroughness with the amount of material removed by the MRF spot indicates that by removing an optimal amount of material from the as-ground surface, p–v surface microroughness was significantly reduced. This observation is valid for all initial surface conditions: rough, medium, and fine ground. For example, in the case of ALON, the initial surface microroughness values were ~14.5-μm p–v (~1.5-μm rms), while after removing ~11 μm with the MRF process, surface microroughness decreased to ~1.2-μm p–v (~0.09-μm rms). When an additional ~13 μm of material were removed, surface microroughness decreased to ~1.1 μm (~0.07-μm rms). In addition, we found differences in microroughness values between areal and line scans, either in a direction perpendicular ($\perp$) or parallel (||) to the MRF flow. For example, in the case of CVD SiC, the initial rough-ground surface microroughness values were ~3.7-μm p–v (~0.11-μm rms), whereas using line scans, surface microroughness values were ~1.5-μm p–v (~0.1-μm rms). [Note that there is no preferred directionality to the ground surface.] After removing ~1.7 μm with the MRF process, surface microroughness decreased to ~0.11-μm p–v (~0.02-μm rms) in a direction perpendicular ($\perp$) to the flow, compared to ~0.06-μm p–v (~0.01-μm rms) measured parallel (||) to the flow direction. Similar observations can be made in the case of PCA.

Discussion
In this work MRF spots were placed on previously ground hard optical ceramics, exposing the subsurface without introducing new damage. By removing several microns of material (proportional to the initial p–v microroughness in the as-ground state), surface roughness was significantly reduced. With the

removal of additional material (i.e., using longer MRF spotting time), we observed that roughness continued to decrease or to slightly increase.

These results suggest that, after examining the evolution of surface roughness within the spots as a function of the amount of material removed (see Fig. 110.40), two stages can be identified: a stage where removal of the initial grinding damage occurs, and a stage where removal shows the development of a texture relating to the interaction between MRF and the material surface. In the first stage, surface roughness resulting from deformation and fracture by grinding is removed, starting with the initial surface condition and ending when the surface

roughness reaches a low value after spotting with MRF. Here the improvement in surface condition is best characterized by the drop in areal p–v roughness, a measurement that captures all features over a reasonably large area.

As seen in Fig. 110.40, the areal p–v for the initially rough-ground ALON [Fig. 110.40(a)], rough-ground CVD SiC [Fig. 110.40(b)], and medium-ground PCA [Fig. 110.40(c)] falls from ~14.5, ~3.7, and ~9 μm to ~1.2, ~0.20, and ~0.25 μm, with ~11, ~1.7, and ~9 μm removed in the first stage, respectively. Beyond this point, differences become apparent in the second stage, depending on how the surface roughness is examined.

Table 110.VI(a): Selected summary of results for grinding and spotting experiments. Surface microroughness measurements were taken at five random locations within a spot ddp with the white-light interferometer. The amount of material removed by MRF (spot maximum depth) was extracted from the 3-D profilometer scans.

Material		ALON Processed with Contour Tool		
		Rough ground		
MRF Material Removal (μm)		0 (as ground)	10.93±0.23	23.83±0.12
Areal (μm)	p–v	14.52±1.04	1.2±0.4	1.1±0.2
	rms	1.45±0.02	0.09±0.01	0.07±0.02
Perpendicular ($\perp$) (μm)	p–v	8.12±0.49	0.40±0.04	0.30±0.06
	rms	1.41±0.05	0.09±0.00	0.07±0.02
Parallel (‖) (μm)	p–v	8.12±0.49	0.39±0.05	0.23±0.10
	rms	1.41±0.05	0.07±0.02	0.06±0.03
		Medium Ground		
MRF Material Removal (μm)		0 (as ground)	9.12±0.11	21.57±0.51
Areal (μm)	p–v	11.72±0.00	0.56±0.16	0.65±0.17
	rms	0.72±0.02	0.09±0.02	0.12±0.03
Perpendicular ($\perp$) (μm)	p–v	4.84±0.42	0.39±0.09	0.47±0.11
	rms	0.70±0.03	0.09±0.02	0.12±0.03
Parallel (‖) (μm)	p–v	4.84±0.42	0.23±0.06	0.18±0.03
	rms	0.70±0.03	0.05±0.01	0.04±0.01
		Fine Ground		
MRF Material Removal (μm)		0 (as ground)	5.98±0.31	21.50±0.10
Areal (μm)	p–v	4.24±1.44	0.51±0.09	1.05±0.06
	rms	0.10±0.05	0.08±0.01	0.16±0.04
Perpendicular ($\perp$) (μm)	p–v	0.67±0.50	0.33±0.03	0.72±0.16
	rms	0.07±0.03	0.07±0.00	0.16±0.04
Parallel (‖) (μm)	p–v	0.67±0.50	0.22±0.04	0.19±0.09
	rms	0.07±0.03	0.05±0.01	0.05±0.03

Table 110.VI(b): Selected summary of results for grinding and spotting experiments. Surface microroughness measurements were taken at five random locations within a spot ddp with the white-light interferometer. The amount of material removed by MRF (spot maximum depth) was extracted from the 3-D profilometer scans.

Material		CVD SiC Processed with Contour Tool		
		Rough Ground		
MRF Material Removal (μm)		0 (as ground)	1.70±0.060	9.41±0.012
Areal (μm)	p–v	3.680±0.228	0.193±0.042	0.126±0.013
	rms	0.108±0.006	0.021±0.004	0.018±0.004
Perpendicular ($\perp$) (μm)	p–v	1.453±0.200	0.107±0.014	0.080±0.016
	rms	0.10±0.005	0.020±0.004	0.017±0.004
Parallel (‖) (μm)	p–v	1.453±0.200	0.061±0.008	0.056±0.007
	rms	0.10±0.005	0.013±0.002	0.012±0.001
		Medium Ground		
MRF Material Removal (μm)		0 (as ground)	1.61±0.020	8.64±0.03
Areal (μm)	p–v	3.464±0.177	0.169±0.041	0.140±0.025
	rms	0.077±0.009	0.021±0.007	0.020±0.004
Perpendicular ($\perp$) (μm)	p–v	1.184±0.066	0.105±0.031	0.080±0.039
	rms	0.070±0.004	0.020±0.007	0.030±0.021
Parallel (‖) (μm)	p–v	1.184±0.066	0.054±0.010	0.047±0.007
	rms	0.070±0.004	0.011±0.002	0.010±0.002
		Fine Ground		
MRF Material Removal (μm)		0 (as ground)	1.86±0.090	10.23±0.120
Areal (μm)	p–v	0.424±0.069	0.141±0.054	0.136±0.025
	rms	0.018±0.002	0.013±0.001	0.019±0.003
Perpendicular ($\perp$) (μm)	p–v	0.011±0.005	0.073±0.009	0.091±0.012
	rms	0.018±0.001	0.012±0.001	0.019±0.003
Parallel (‖) (μm)	p–v	0.011±0.005	0.060±0.006	0.043±0.006
	rms	0.018±0.001	0.012±0.001	0.009±0.002

Table 110.VI(c): Selected summary of results for grinding and spotting experiments. Surface microroughness measurements were taken at five random locations within a spot ddp with the white-light interferometer. The amount of material removed by MRF (spot maximum depth) was extracted from the 3-D profilometer scans.

Material		PCA Processed with Ring Tool		
		Medium Ground		
MRF Material Removal (μm)		0 (as ground)	8.84±0.07	15.9±0.06
Areal (μm)	p–v	8.942±1.067	0.247±0.031	0.276±0.045
	rms	0.569±0.076	0.033±0.006	0.044±0.008
Perpendicular ($\perp$) (μm)	p–v	3.613±0.401	0.177±0.0028	0.220±0.039
	rms	0.460±0.082	0.033±0.006	0.043±0.008
Parallel (‖) (μm)	p–v	3.613±0.401	0.128±0.008	0.101±0.008
	rms	0.460±0.082	0.030±0.002	0.022±0.002

For orthogonal line scans, the initial ground p–v rough-ness is similar, as the ground surface shows no processing-related directional features {~8.1-, ~1.4-, ~3.6-μm p–v, for ALON [see Fig. 110.40(a)], CVD SiC [see Fig. 110.40(b)], and PCA [see Fig. 110.40(c)], respectively}. In the case of ALON [Fig. 110.40(a)], for both line-scan orientations ($\perp$ and $\parallel$) with respect to the direction of MRF fluid flow over the surface, p–v surface roughness is seen to drop from ~400 nm to ~300 ($\perp$) and ~230 nm ($\parallel$), respectively, in the second stage as the diamonds in the MR fluid continue to polish the surface, removing a total of ~24 μm of material. In the case of CVD SiC [Fig. 110.40(b)], p–v surface roughness ($\perp$) is seen to drop from 107 to 80 nm, whereas p–v surface roughness ($\parallel$) drops slightly from 61 to 56 nm, as the diamonds in the MR fluid continue to polish the surface, removing a total of ~9.4 μm of material. In the case of PCA, p–v surface roughness ($\parallel$) is seen to drop from ~0.13 to 0.1 μm, as the diamonds in the MR fluid continue to polish the surface, removing a total of 16 μm of material. Although not described here, it is possible to study the microstructure of the material with this sampling technique,

one example being decoration of grain boundaries.[38] However, as in the case of PCA [Fig. 110.40(c)], p–v roughness (areal and $\perp$) is seen to increase with additional material removed beyond ~9 μm in the second stage. This increase is real, and is due to a texture or grooving impressed on the polished, damage-free surface by the abrasives in the MR fluid. These grooves come from a lack of part rotation during long-duration spotting.

An interesting observation can be made for both ALON and CVD SiC: In the second stage, where the interaction between the MR fluid abrasives and the surface is strong, there is a gradual increase in p–v roughness as shown with all three measurement protocols ending with an abrupt drop in the p–v roughness; after this, the roughness either increases or slightly decreases. For both ALON and CVD SiC, this phenomenon takes place when the amount of material removed by the MRF reaches a depth comparable to the material grain size {~12 and 4 μm for ALON [see Fig. 110.40(a)] and CVD SiC [see Fig. 110.40(b)], respectively}. This phenomenon is not present in the case of PCA [Fig. 110.40(c)], suggesting that, as grain
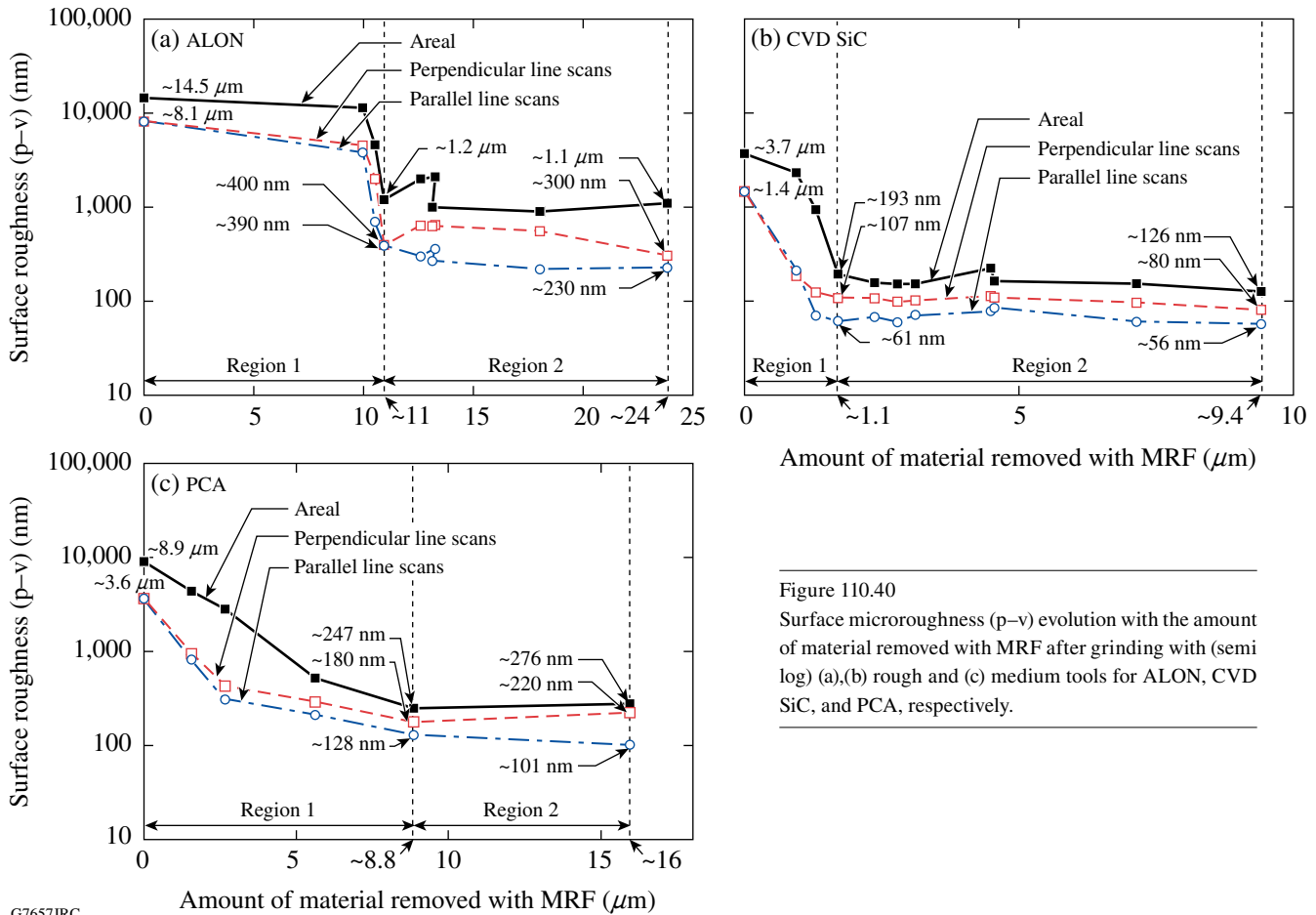

Figure 110.40
Surface microroughness (p–v) evolution with the amount of material removed with MRF after grinding with (semi log) (a),(b) rough and (c) medium tools for ALON, CVD SiC, and PCA, respectively.

G7657JRC

size increases, the interaction between a material's grains and the polishing abrasives contributes to surface roughening, or "grain decoration."

SEM analysis within polishing spots confirms that MRF exposes and removes fractured material in both stages 1 and 2, without creating additional damage. Figure 110.41 shows the evolution of surface texture in spots taken on previously medium-ground PCA. Figures 110.41(a) and 110.41(b) represent spot depths of ~2 to 3 μm, where MRF processing exposed voids and pulverized powder regime beneath the deformed layer. Longer spotting times to remove up to a total of 16 μm of material [see Figs. 110.41(c)–110.41(e)] verify that MRF eliminated all pitting and hidden damage, with the subsequent development of a grooved texture.
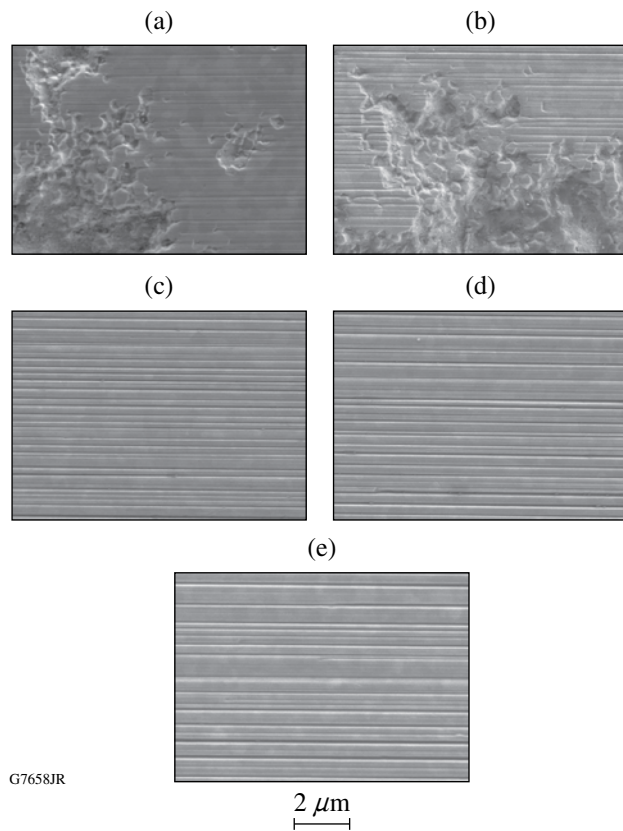

(a)   (b)

(c)   (d)

(e)

G7658JR

2 μm

Figure 110.41
SEM images inside MRF spots taken on PCA that was previously medium ground (10- to 20-μm grit size) to an initial roughness of 3.6-μm p–v. (a)–(e) ~1.6-, 2.6-, 5.6-, 9-, and 16-μm spot depths (MRF material removed), respectively. The initial deformation layer as seen in Figs. 110.36(e) and 110.36(f) is completely removed. Long spot dwell times [(d), (e)] enhanced the intrinsic directionality of the MRF process.

1. Use of Power Spectrum to Quantify Surface Topography

In addition to the conventional p–v and rms values that define surface roughness, the interaction between the MR fluid and the material surface is discussed in terms of the power spectral density (PSD). This analysis results in a unique signature,[39] in which surface texture parallel (∥) and perpendicular (⊥) to the MR fluid flow direction may be observed and studied to obtain information on the surface and its microstructure.

For a given surface profile $z(x)$, the rms roughness is defined as

$$\text{rms} = \sqrt{\frac{1}{N} \cdot \sum_{i=1}^{N} z_i^2} \quad (m) \qquad (1)$$

and the 1-D PSD at spatial frequency $f_j = j\Delta f$ is[40]

$$PSD_{\text{1-D}}(f_j) \approx \frac{\Delta x}{N} \left| \sum_{k=1}^{N} z_k \exp\left[(2\pi i)jk/N\right] \right|^2,$$

$$j = 1, 2, \ldots N/2, \qquad (2)$$

where $\Delta f = 1/(N\Delta x) = 1/L$, with L being the scan length. PSD is a statistical function that allows a breakdown of the surface roughness over a range of spatial frequencies. Furthermore, the area under a 1-D PSD curve (between two spatial-frequency limits) is a measure of the rms surface roughness in this spatial range:[41]

$$\text{rms}_{\text{1-D}}^2 = \int_{f_{\text{min}}}^{f_{\text{max}}} PSD_{\text{1-D}}(f)\,df. \qquad (3)$$

After removing the low-frequency terms (tilt, curvature, etc.) from the roughness data for part surfaces discussed in **Experimental Results** (p. 102), horizontal 1-D PSD plots were generated from areal measurements (0.35 × 0.26 mm^2) taken with a white-light interferometer over spatial frequencies extending from 2.0×10^{-6} nm^{-1} to 2.0×10^{-2} nm^{-1} by using multiple line scans in a direction perpendicular (⊥) to the MRF flow, as seen in Fig. 110.39(a). Removing the low-frequency terms resulted in an improved PSD spectrum.[42]

Because the white-light interferometer has a lateral resolution limit of 1 μm, additional 1-D PSD plots were generated from AFM scans with a lateral resolution in the nanometer range. These scans were also done within spot ddp regions.

A consideration of PSD data generated from profiles perpendicular ($\perp$) to the MRF flow direction allows us to study the residual grooving pattern of the MR fluid flow that represents the abrasive/surface interactions.

2. MRF Signature on Hard Materials

Figure 110.42 shows the PSD curves in ddp regions for two spots of increasing time duration taken on the surface of initially rough-ground ALON. The curves represent the evolution of surface texture with the amount of material removed by the MRF spot, from ~10.5 μm to ~24 μm (corresponding to 3- and 16-min spot dwell times, respectively). The interferometer PSD curves (i.e., at lower spatial frequencies) show an amplitude reduction from the short- to the long-dwell-time spots, due to surface smoothing of roughness contributions of the MRF process. The material's microstructure dominates the curve in

the spatial frequency range of 7×10^{-5} to 3×10^{-4} nm^{-1}, corresponding to features of the order of ~50 to 100 μm (comparable to the ALON grain size).

AFM measurements were taken and evaluated to examine the PSD across the surface of a single grain in the spatial frequency range of 1×10^{-4} to 1×10^{-2} nm^{-1} (corresponding to features of the order of 10 to 0.1 μm; see scale at top of Fig. 110.42). When compared to the interferometer results, the AFM measurements show a reversal. PSD values for the 16-min-duration spot have higher amplitudes across all relevant spatial frequencies due to the grooving effect of the MRF process on the surface of a single grain. The morphology of the grooving pattern represents the "MRF signature on hard materials." Figures 110.43(a) and 110.43(b) show the surface morphologies within these spots detected by the AFM. Profiles
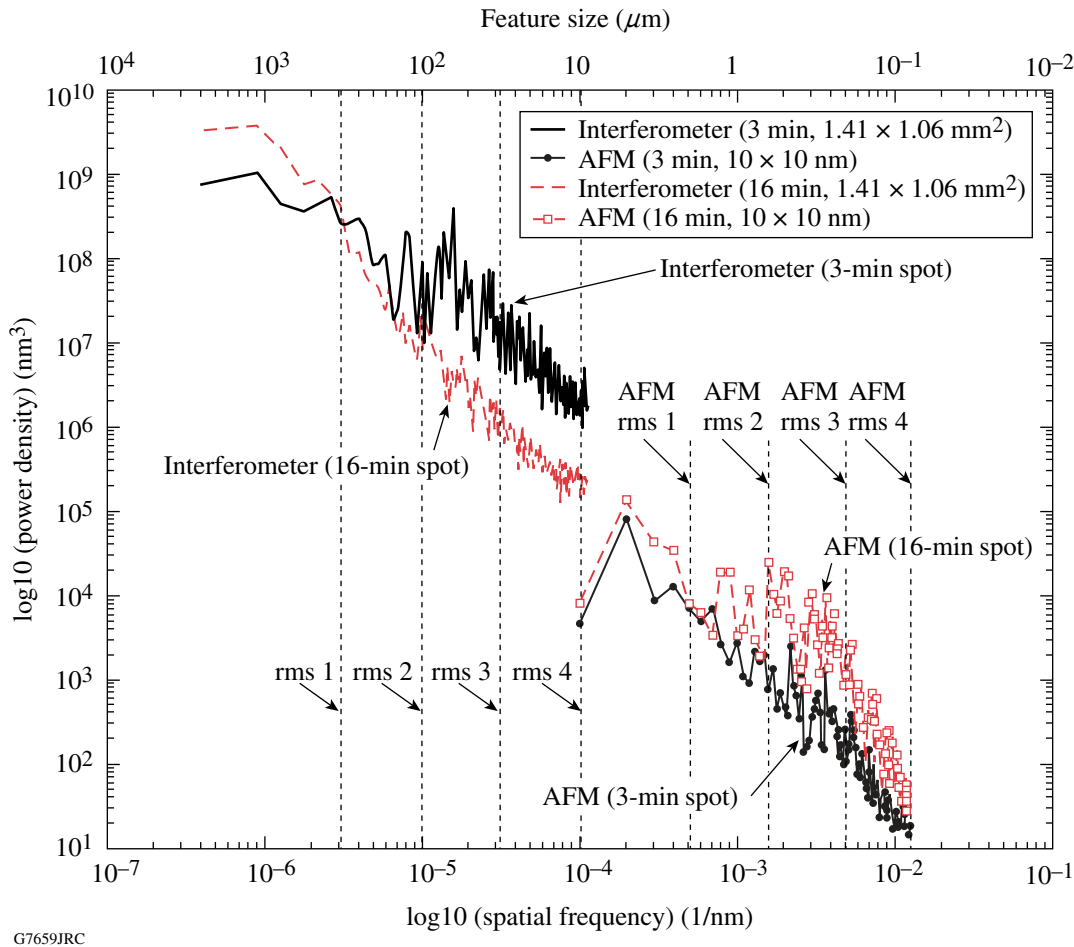

Figure 110.42

PSD (log–log) for MRF spotting done on initially rough-ground (40-μm grit size) ALON. White-light interferometer measurements were taken using a 2.5 objective using a 2× magnification (1.41 × 1.06 mm^2).

of these scans taken across the image diagonal represented by a white line are shown in Fig. 110.43(c) and 110.43(d). The images and accompanying profiles agree well with the PSD function. For example, when we calculate the number of features ($\sim$40) across the diagonal ($\sim$15 μm) of Fig. 110.43(b), formed by the long-dwell-time MRF spot, the number corresponds to a feature size of the order of 0.5 μm at 2×10^{-3} nm^{-1} spatial frequency, which corresponds to the peak in that frequency, as seen in Fig. 110.42. The markers in Fig. 110.43(c) extend over vertical heights in the range of $\sim$11 to 14 nm, for the short-dwell-time spot, whereas the markers in Fig. 110.43(d) for the long-dwell-time spot extend over vertical heights in the range of $\sim$19 to 30 nm.

The calculated rms values from the PSD curves of Fig. 110.42, designated as rms 1, rms 2, etc., on the figure, are plotted in Fig. 110.44. The left-hand side of Fig. 110.44 shows the calculated rms values for ALON, corresponding to the spatial frequency of the interferometer PSD curves in Fig. 110.42, and the calculated rms values from the PSD curves for CVD SiC and PCA where we used a 20$\times$ objective and a $\sim$350-μm spatial scan length (511 data points) in the spatial-frequency range of 0.2×10^{-5} to 0.9×10^{-3} nm^{-1} (corresponding to features of the order of $\sim$100 to 1 μm) on the interferometer. As seen in Fig. 110.42, we notice a decrease in rms surface roughness from the short- to the long-dwell-time spots for ALON (see arrow 1). [The roughness increase for the 16-min spot at

low frequencies is due to surface figure errors from grinding.] In the case of CVD SiC there is an increase in the PSD from the short to the long MRF spot dwell time (see arrow 2). This increase represents an increase in surface roughness on the part surface due to decoration of grain boundaries within the spatial-frequency range of 10^{-4} to 10^{-3} nm^{-1}, representing features of the order of 1 to 10 μm, comparable to the material grain size. [The increase in the curve amplitude for CVD SiC (16-min spot) in the low-frequency range is also attributed to surface figure error as mentioned above for ALON.] In the case of PCA, we see a large reduction in roughness values for the long- compared to the short-dwell-time spots (see arrow 3). This can be attributed to surface smoothing of roughness contributions in this interval, in the spatial-frequency range of 3.2×10^{-5} to 10^{-4} nm^{-1}. There is almost no change in the spatial-frequency range of 3.2×10^{-4} to 10^{-3} nm^{-1}, corresponding to a feature size of the order of 3.3 to 1 μm. This represents features that are much larger than the nominal grain size, possibly due to grain clusters.

The right-hand side of Fig. 110.44 shows the calculated rms values for PSD curves done in the spatial-frequency range of 0.0002 to 0.02 nm^{-1} (corresponding to features of the order of 1 to 0.05 μm) using the AFM. These results are within the boundaries of a single grain for ALON, whereas for both CVD SiC (5- to 10-μm grain size) and PCA (submicron-range grain size), these results span at least one grain boundary. Notice

(a)   (b)   (c)   (d)

G7660JRC
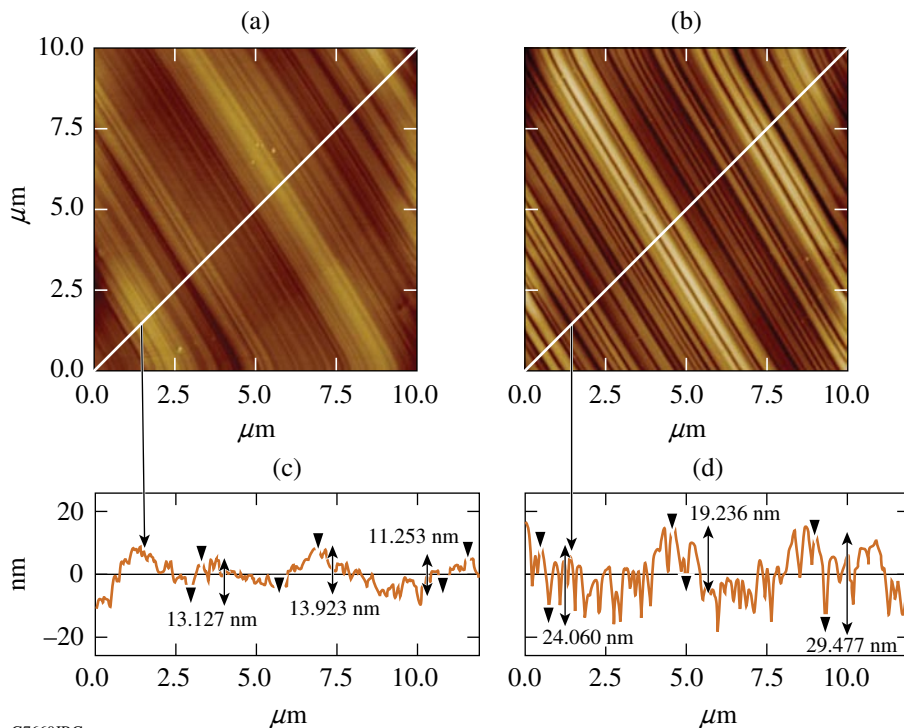
Figure 110.43
AFM scans taken at spots' ddp of initially rough-ground ALON: (a) short- and (b) long-dwell-time spots (3 and 16 min, respectively); (c),(d) profiles taken across the diagonal of scans, represented by the white lines in (a) and (b), respectively. The markers in (c) and (d) represent vertical heights in a range of $\sim$11 to 14 nm and $\sim$19 to 30 nm for the short- and long-dwell-time spot, respectively. The grain size is 50 to 100 μm.
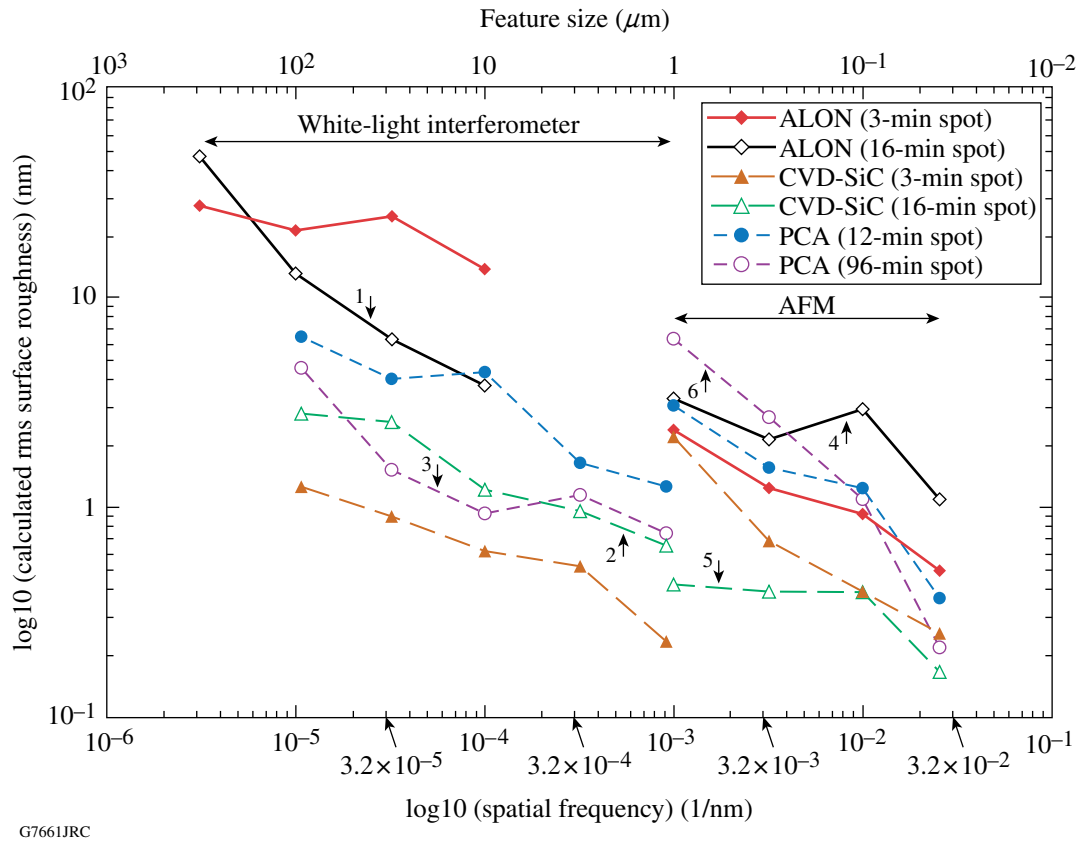
Figure 110.44

Calculated rms (nm) surface roughness from PSD plots generated from the interferometer and AFM measurements (log–log). Data points represent the averaged rms values for a specific spatial-frequency bandwidth, indicated as rms 1, rms 2, etc., in Fig. 110.42.

the increase in the roughness values for ALON at the spatial frequency 10^{-2} nm^{-1} (see arrow 4), indicating the presence of MRF signature, as discussed for Figs. 110.42 and 110.43. There is almost no change in surface roughness at the spatial frequency 10^{-2} nm^{-1} for both CVD SiC and PCA, corresponding to the MRF signature. Beyond this frequency we notice a reduction in roughness for all three materials: In the case of CVD SiC, there is a decrease in surface roughness from the short- to the long-dwell-time spot (see arrow 5). In the case of PCA, an increase in surface roughness from the short- to the long-dwell-time spot (see arrow 6) in a spatial-frequency range of 10^{-3} to 3.2×10^{-3} nm^{-1}, corresponding to features of the order of 1000 to 300 nm (comparable to the PCA grain size), is due to grain boundary highlighting by the MRF process, i.e., grain decoration.[43]

Conclusions

The response of three hard optical ceramics to deterministic microgrinding has been studied. Grinding experiments showed that grinding-induced surface roughness decreased with a decreasing size in the diamond abrasive used. Microgrinding with a rough tool involved fracture, leading to p–v surface roughness in the range of 14.5 to 4 μm (1.4- to 0.1-μm rms). Using high-magnification SEM images, we found that the deformed layer induced by grinding covered the actual damage depth/SSD.

We have demonstrated that an MRF spot can be placed on ground surfaces of hard ceramics without introducing additional damage, and that the spot can be used to estimate the induced SSD depth from microgrinding. For initially rough and medium surfaces, SSD depth is ~11 μm (ALON), ~1.7 μm (CVD SiC), and ~9 μm (PCA), corresponding to initial p–v surface roughness values of ~14.5 μm, ~3.7 μm, and ~9 μm, respectively. The evolution of surface roughness with the amount of material removed by the MRF process, as measured within the spot's deepest point of penetration (least roughness), can be divided into two stages: In the first stage the induced damaged layer and associated SSD from microgrinding are removed, reaching a low surface-roughness value. In the

second stage we observe interaction between the MRF process and the material's microstructure as MRF exposed the subsurface without introducing new damage. We showed that SSD depth can be estimated by using an optical profilometer–based measurement of the areal p–v surface microroughness of the as-ground surface. This provides an upper bound to the SSD value. SEM images confirmed these observations.

We also showed the development of the "MRF signature" on hard ceramics by computing PSD curves within the resolution capabilities of the interferometer and the AFM. By considering PSD data generated from profiles perpendicular to the MRF flow direction, we studied the residual grooving pattern of the MR fluid flow that represents the abrasive/surface interactions. Additional work is still needed, however, to characterize MR fluid particles/surface (i.e., materials' microstructure) interactions parallel to the MR fluid flow direction.

The spotting technique is intended only as a diagnostic tool, by removing material from rough surfaces to expose the subsurface damage. It does not reflect on the true polishing capabilities with MRF technology for hard ceramics.

REFERENCES

1. L. Yin *et al.*, Wear **256**, 197 (2004).

2. S. Malkin and T. W. Hwang, CIRP Ann. **45**, 569 (1996).

3. B. Lin *et al.*, Key Eng. Mater. **202/203**, 121 (2001).

4. A. G. Evans and D. B. Marshall, in *Fundamentals of Friction and Wear of Materials*, edited by D. A. Rigney (American Society for Metals, Metals Park, OH, 1981), pp. 439–452.

5. J. A. Menapace *et al.*, in *Laser-Induced Damage in Optical Materials: 2005*, edited by G. J. Exarhos *et al.* (SPIE, Bellingham, WA, 2006), Vol. 5991, p. 599102.

6. J. C. Lambropoulos, S. D. Jacobs, and J. Ruckman, in *Finishing of Advanced Ceramics and Glasses*, edited by R. Sabia, V. A. Greenhut, and C. G. Pantano, Ceramic Transactions, Vol. 102 (The American Ceramic Society, Westerville, OH, 1999), pp. 113–128.

7. K. R. Fine *et al.*, in *Modeling, Simulation, and Verification of Space-Based Systems II*, edited by P. Motaghedi (SPIE, Bellingham, WA, 2005), Vol. 5799, pp. 105–110.

8. J. Wang and R. L. Maier, Appl. Opt. **45**, 5621 (2006).

9. P. E. Miller *et al.*, in *Laser-Induced Damage Optical Materials: 2005*, edited by G. J. Exarhos *et al.* (SPIE, Bellingham, WA, 2006), Vol. 5991, p. 599101.

10. W. Kanematsu, J. Am. Ceram. Soc. **89**, 2564 (2006).

11. B. Zhang and T. Howes, CIRP Ann. **43**, 305 (1994).

12. B. Zhang and T. D. Howes, CIRP Ann. **44**, 263 (1995).

13. J. A. Randi, J. C. Lambropoulos, and S. D. Jacobs, Appl. Opt. **44**, 2241 (2005).

14. H. H. K. Xu, S. Jahanmir, and Y. Wang, J. Am. Ceram. Soc. **78**, 881 (1995).

15. J. A. Menapace *et al.*, in *Laser-Induced Damage in Optical Materials: 2005*, edited by G. J. Exarhos *et al.* (SPIE, Bellingham, WA, 2006), Vol. 5991, p. 599103.

16. F. W. Preston, Trans. Opt. Soc. **XXIII**, 141 (1921–22).

17. F. K. Aleinikov, Sov. Phys.-Tech. Phys. **2**, 505 (1957).

18. P. P. Hed and D. F. Edwards, Appl. Opt. **26**, 4677 (1987).

19. J. C. Lambropoulos, Y. Li, P. D. Funkenbusch, and J. L. Ruckman, in *Optical Manufacturing and Testing III*, edited by H. P. Stahl (SPIE, Bellingham, WA, 1999), Vol. 3782, pp. 41–50.

20. S. N. Shafrir, J. Lambropoulos, and S. D. Jacobs, Precision Engineering **31**, 83 (2007).

21. S. N. Shafrir, J. C. Lambropoulos, and S. D. Jacobs, "Technical Note: Toward Magnetorheological Finishing of Magnetic Materials," to be published in the Journal of Manufacturing Science and Engineering.

22. J. C. Lambropoulos, in *Optical Fabrication and Testing*, Vol. 42, 2000 OSA Technical Digest Series (Optical Society of America, Washington, DC, 2000), pp. 17–18.

23. A. G. Evans, in *Fracture Mechanics Applied to Brittle Materials*, edited by S. W. Freiman (American Society for Testing and Materials, Philadelphia, 1979), Vol. ASTM STP 678, Part 2, pp. 112–135.

24. D. Halliday, R. Resnick, and J. Walker, *Fundamentals of Physics*, 5th ed. (Wiley, New York, 1997).

25. SX 50 CNC deterministic microgrinding machine, OptiPro Systems, Ontario, NY 14519.

26. SX 150 CNC deterministic microgrinding machine, OptiPro Systems, Ontario, NY 14519.

27. Opticut GPM 5% in water, pH 9-10, Lighthouse Lubricant Solutions, LLC, Overland Park, KS 66282.

28. S. D. Jacobs, H. M. Pollicove, W. I. Kordonski, and D. Golini, in *International Conference on Precision Engineering*, ICPE '97 (ICPE, Taipei, Taiwan, 1997), pp. 685–690.

29. A. B. Shorey, S. D. Jacobs, W. I. Kordonski, and R. F. Gans, Appl. Opt. **40**, 20 (2001).

30. Q22-Y, QED Technologies, LLC, Rochester, NY 14607.

31. D10 MR fluid, QED Technologies, LLC, Rochester, NY 14607.

32. TalySurf 2 PGI profilometer, Taylor Hobson, Inc., Rolling Meadows, IL 60008-4231.

33. NewView™ 5000 noncontact profilometer, Zygo Corporation, Middlefield, CT 06455.

34. LEO 982 FE SEM, Nano Technology Systems Division, Carl Zeiss NTS GmbH, A Carl Zeiss SMT AG Company, 73447 Oberkochen, Germany.

35. Dimension 3100S-1 AFM, Digital Instruments/Veeco Metrology Dimension 3100S-1 Atomic Force Microscope, Veeco Instruments, Inc., Woodbury, NY 11797-2902.

36. Light Microscope, Leica Microsystems Inc., Bannockburn, IL 60015.

37. S. N. Shafrir, "Surface Finish and Subsurface Damage in Polycrystalline Optical Materials," Ph.D. thesis, University of Rochester, 2007.

38. S. R. Arrasmith, I. A. Kozhinova, L. L. Gregg, A. B. Shorey, H. J. Romanofsky, S. D. Jacobs, D. Golini, W. I. Kordonski, S. J. Hogan, and P. Dumas, in *Optical Manufacturing and Testing III*, edited by H. P. Stahl (SPIE, Bellingham, WA, 1999), Vol. 3782, pp. 92–100.

39. J. E. DeGroote, A. E. Marino, K. E. Spencer, and S. D. Jacobs, in *Optifab 2005* (SPIE, Bellingham, WA, 2005), Vol. TD03, pp. 134–138.

40. E. Marx *et al.*, J. Vac. Sci. Technol. B **20**, 31 (2002).

41. A. Duparré *et al.*, Appl. Opt. **41**, 154 (2002).

42. C. J. Walsh, A. J. Leistner, and B. F. Oreb, Appl. Opt. **38**, 4790 (1999).

43. L. L. Gregg, A. E. Marino, J. C. Hayes, and S. D. Jacobs, in *Optical Manufacturing and Testing V*, edited by H. P. Stahl (SPIE, Bellingham, WA, 2004), Vol. 5180, pp. 47–54.

Spectral Filtering in a Diode-Pumped Nd:YLF Regenerative Amplifier Using a Volume Bragg Grating

Introduction

Holographic volume Bragg gratings (VBG's) represent a new class of robust, highly efficient, and spectrally selective optical elements that are recorded in photo-thermo-refractive glass.[1] VBG's have extremely high spectral and angular dispersions that are higher than any dispersive elements previously used. VBG's are stable at elevated temperatures, have a high optical-damage threshold similar to that of bulk glass materials, and have high diffraction efficiency and low losses, allowing their use in laser resonators.

VBG's are widely used in laser devices for spectrum and beam profile control. Employing VBG's in an external resonator of laser diodes makes it possible to produce high-brightness, near-diffraction–limited beams and coherently combine them.[2] A high-brightness spectral-beam combination of two vertical-external-cavity, surface-emitting lasers has been demonstrated with the aid of a VBG.[3] VBG's have also been used as spectrally selective elements for laser wavelength tuning[4] as well as line narrowing in lasers[5,6] and optical parametric oscillators.[7] Chirped VBG's have been employed for ultrashort-pulse stretching and compression.[8]

Generating high-energy optical pulses in laser amplifiers requires high gain that inherently produces amplified spontaneous emission (ASE) with bandwidths of the order of the amplification bandwidth of the laser system, which can be detrimental to the temporal quality, energy extraction, and stability of laser amplifiers.[9] Amplification of optical pulses usually requires low ASE levels. For example, the temporal contrast of high-energy, short optical pulses amplified by the optical parametric chirped-pulse–amplification (OPCPA) system can be degraded by ASE-induced noise on the pump pulse.[10]

In this article we demonstrate for the first time that employing a VBG as a spectrally selective reflective element in a regenerative amplifier resonator significantly improves the spectral quality of the regenerative amplifier output by suppressing out-of-band amplified spontaneous emission. This spectrally filtered regenerative amplifier should be very beneficial for applications where high spectral quality of pulsed radiation is required, such as pump lasers for high-contrast OPCPA systems.[11]

Experimental Setup

The Nd:YLF diode-pumped regenerative amplifier (DPRA) shown in Fig. 110.45 is identical to the one described in Ref. 12, the only difference being that it has a longer cavity length. It has a folded linear cavity with a round-trip time of 21 ns that allows amplification of pulses as long as 13-ns FWHM in duration. The Nd:YLF active element is oriented for a 1053-nm operational wavelength and is pumped by a 150-W, fiber-coupled laser diode (Apollo Instruments, Irvine, CA), which is operated in a pulsed mode producing a 1-ms pump pulse at 805 nm with a 5-Hz repetition rate. The DPRA intracavity Pockels cell driven by fast electrical circuitry allows the injection and cavity dumping of the amplified pulse. The injected pulse is mode matched to the DPRA resonator and, after a certain number of round-trips, reaches its maximum energy and is dumped from the DPRA cavity (inset in Fig. 110.45). Two DPRA resonator configurations have been compared: (1) with a flat end mirror having 99.9% reflectivity and (2) with a combination of AR-coated VBG (OptiGrate, Orlando, FL) having 99.4% diffraction efficiency and the same flat end mirror. The VBG has a bandwidth of 230 pm (FWHM) centered at ~1053 nm with an ~7° angle of incidence.

Spectral filtering in a regenerative amplifier cavity benefits from the large number of passes on the filtering element. Assuming a single-pass filtering spectral transmission $T(\omega)$, the spectral filter after N round-trips in the cavity is $T(\omega)^N$, or $T(\omega)^{2N}$ if the filter is seen twice per round-trip, which is the case in this implementation. Figure 110.46(a) displays the spectral reflection of a Gaussian filter with a 230-pm (FWHM) bandwidth centered at 1053 nm and the spectral reflection after 50 round-trips in a cavity with two passes on the filter per round-trip. The effective filtering function has a bandwidth of 23 pm (FWHM). Filtering of the ASE can be performed as long as the bandwidth reduction in the amplifier does not degrade the temporal pulse shape of the output pulse. Figure 110.46(b)
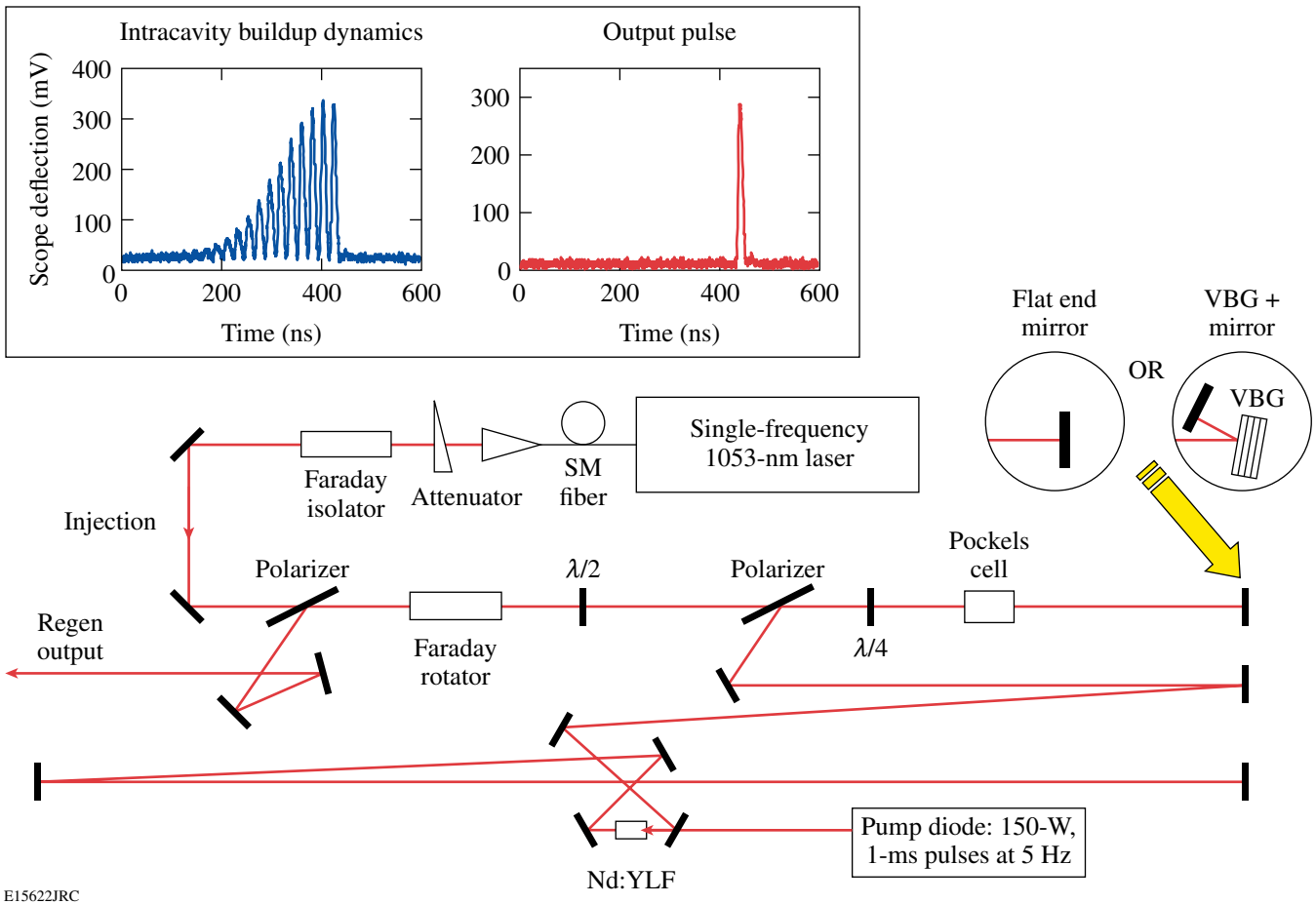
Figure 110.45
A volume Bragg grating (VBG) is used in a folded-linear-cavity regenerative amplifier as one of the mirrors for spectral filtering. DPRA cavity dumping occurs when intracavity buildup reaches its maximum (inset).
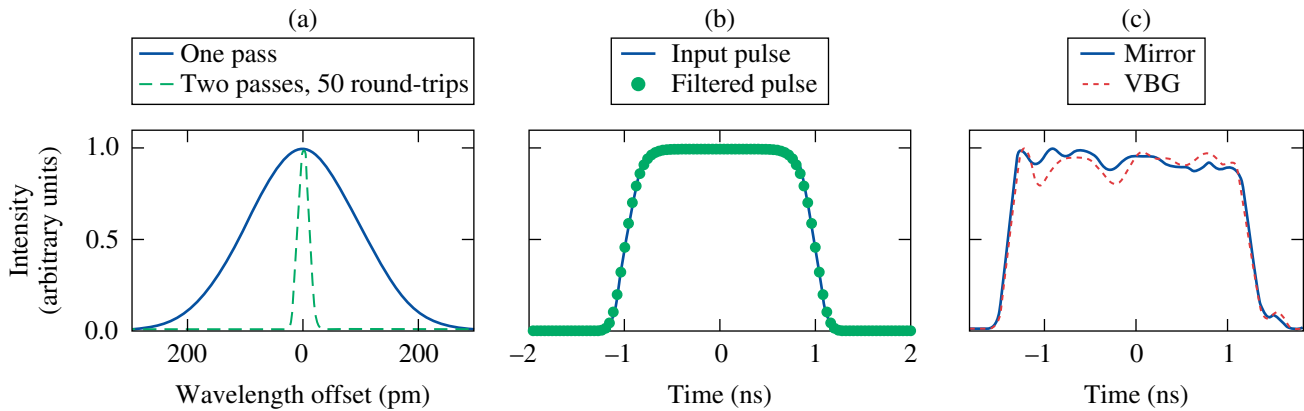
Figure 110.46
(a) VBG with a Gaussian filter function using a 230-pm FWHM, one-pass bandwidth (solid line) produces a filter function with an effective bandwidth of 23-pm FWHM after 50 round-trips in the DPRA with a VBG two-pass configuration (dashed line); (b) 2-ns-FWHM, super-Gaussian pulse before (solid line) and after (white circles) bandwidth narrowing using a 23-pm-FWHM filter (simulation); (c) measured 2.4-ns-FWHM pulse shape after the DPRA with further amplification and doubling for the DPRA with mirror (solid line) and VBG (dotted line).

shows a 2-ns (FWHM), 20th-order super-Gaussian pulse before and after filtering by a 23-pm (at –3-dB level) filtering function. The choice of the 2-ns-FWHM pulse duration corresponds to the typical pulse widths used to pump OPCPA systems.[11] In this simulation, no significant change in the temporal intensity is observed, showing that an even narrower filter could be used. While different round-trips in the cavity correspond to a different effective bandwidth of the filter, ASE is expected mostly from the source seeding the regenerative amplifier and the first few round-trips in the amplifier (when the pulse energy is low), which correspond to the narrowest effective filtering function. Figure 110.46(c) displays the pulse shape measured after amplification in the DPRA and a four-pass ring power amplifier and after second-harmonic generation, for use as the pump pulse in an OPCPA system. No significant change in the output square pulse, including the fast rising and falling edges, is observed when the mirror in the DPRA is replaced with the VBG + mirror combination.

In our experiment the DPRA is injected with a 13-ns-FWHM, Gaussian-like pulse that is sliced out of a 150-ns-FWHM pulse produced by a diode-pumped, single-frequency, Q-switched Nd:YLF laser.[13] The bandwidth of this pulse is obviously narrower than that of the 2-ns-FWHM, super-Gaussian pulse; therefore, no output-pulse distortion due to VBG spectral filtering is expected. The DPRA output energy, beam profile, and spectra have been recorded for both DPRA resonator configurations (with a mirror and a VBG + mirror combination).

Experimental Results and Discussion

The beam profiles shown in Fig. 110.47 correspond to the TEM$_{00}$ mode for both DPRA configurations (mirror and VBG). These beam profiles have been taken at a DPRA operational output-pulse energy of 4 mJ.
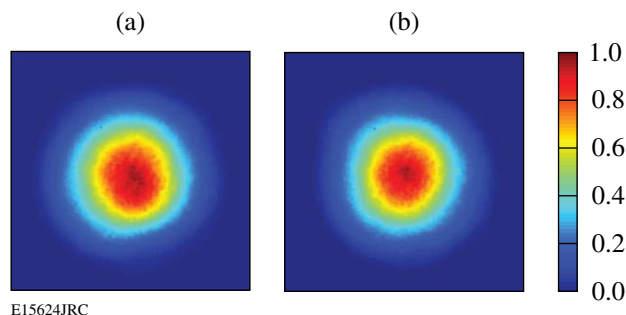
Figure 110.47
Output beam profile corresponds to TEM$_{00}$ mode for both DPRA configurations with (a) a mirror and (b) VBG. DPRA output energy is 4 mJ.

The maximum energy produced by the DPRA with a mirror is 18 mJ. After introducing the VBG into the DPRA cavity, the maximum output energy drops to 14 mJ, which is consistent with introducing ~1.2% of additional losses per round-trip by VBG with 99.4% diffraction efficiency. The output-beam profile corresponds to a TEM$_{00}$ mode over the whole range of output energy when using the VBG.

We recorded an output spectra using an ANDO AQ6317B (Yokogawa Corp. of America, GA) optical spectrum analyzer (OSA) for an injected DPRA and a DPRA without injection with the same number of round-trips (21). In each case the pump diode current has been adjusted to achieve cavity dumping at the maximum of the intracavity pulse-buildup dynamics. An unseeded DPRA with a mirror produces the gain-narrowed ASE spectrum shown in Fig. 110.48 (solid line) with an ASE
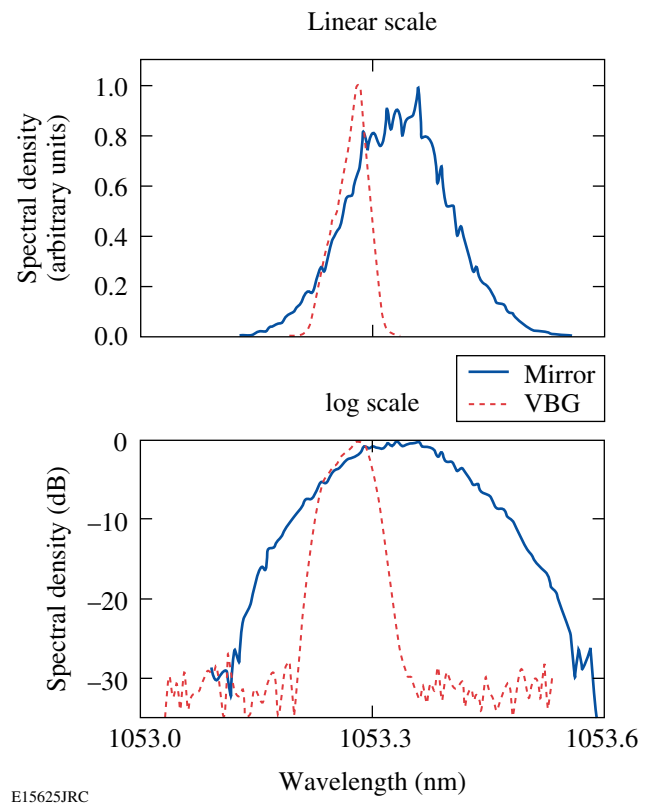
Figure 110.48
Output spectra for the DPRA without injection: the DPRA with a mirror produces a gain-narrowed ASE spectrum with 150-pm FWHM (solid line); the DPRA with the VBG spectrum is narrowed to 43-pm FWHM (dashed line). In the latter case, the spectrum width and shape are defined by the common action of the VBG reflection curve and Nd:YLF gain profile. In both cases DPRA performance has been optimized for cavity dumping after 21 cavity roundtrips.

bandwidth of 150 pm (FWHM). In contrast, the unseeded DPRA using the VBG shown in Fig. 110.48 (dashed line) provides a much narrower spectrum with a width (43-pm FWHM) and shape defined by the common action of the VBG reflection curve and Nd:YLF gain profile. The position of the output spectrum is defined by the VBG angular alignment. The VBG in the DPRA cavity is aligned using an injection laser in cw mode as an alignment beam, i.e., the VBG position provides the best DPRA cavity alignment (maximum VBG reflectivity) for the wavelength that is going to be injected. This injection wavelength is not exactly at the peak of the DPRA gain curve, leading to the asymmetric spectrum shape when using the VBG in a DPRA without injection.

Observing the VBG spectral-filtering effect is limited by an instrument spectral resolution and dynamic range of 20 pm and 40 dB, respectively. We have simulated the DPRA spectral behavior as it will be seen by the OSA to determine experimental conditions for reliable observation of the VBG spec-

tral-filtering effect. Our simulations show that DPRA injection energy must be about equal to ASE energy. The injected pulse energy in this case is $\sim$0.0025 pJ, which corresponds to a gross gain of greater than 10^{12}. The simulated output spectrum of the DPRA with the mirror is shown in Fig. 110.49(a); the simulated output spectrum consists of an injected line on top of an ASE pedestal, which is reliably recorded by the OSA. The measured output spectra are shown in Fig. 110.49(b) and agree very well with the simulated results. The number of round-trips for both simulated and experimental results is 21. In the DPRA with the VBG + mirror combination (even at this very low injection level), the ASE in the output spectrum [shown in Fig. 110.49(b) (dashed line)] is suppressed to the instrument's 40-dB dynamic range. The OSA spectral resolution does not allow us to make the spectra comparison at higher levels of DPRA injection; however, it is obvious that spectral contrast will be even better when the injection level is increased due to domination of the injected pulse over ASE even on initial cavity round-trips.
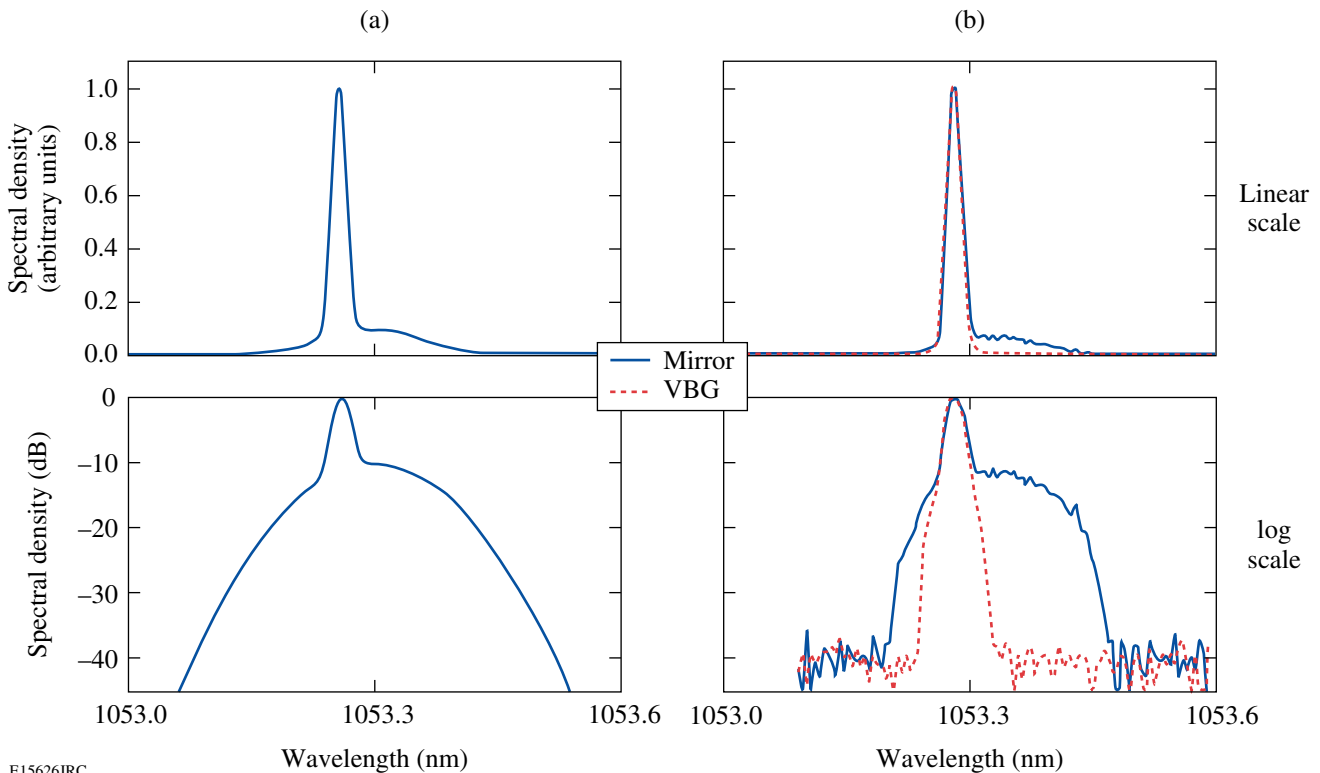
Figure 110.49
(a) Simulations show that for a reliable OSA recording of ASE filtering effect, the injected energy must be about equal to the DPRA ASE (in this case E_{ASE} = 0.7 E_{in}). (b) Output spectra for the DPRA with injected pulse energy of 0.0025 pJ, comparable to DPRA ASE: with the mirror (solid line) a significant ASE pedestal is observed; with the VBG (dashed line), the spectrum does not show any presence of ASE. The number of round-trips (21) is the same for all cases.

Conclusion

We have demonstrated a VBG spectrally filtered DPRA operation for the first time. Using VBG as the DPRA resonator spectrally selective element allows out-of-band ASE suppression even for a very low DPRA injection level. Using DPRA with VBG spectral filtering can be beneficial in high-energy laser amplifiers.

REFERENCES

1. L. B. Glebov *et al.*, in *Laser Weapons Technology III*, edited by W. E. Thompson and P. H. Merritt (SPIE, Bellingham, WA, 2002), Vol. 4724, pp. 101–109.

2. G. B. Venus *et al.*, Opt. Lett. **31**, 1453 (2006).

3. Y. Kaneda *et al.*, IEEE Photonics Technol. Lett. **18**, 1795 (2006).

4. B. Jacobsson, V. Pasiskevicius, and F. Laurell, Opt. Lett. **31**, 1663 (2006).

5. A. Dergachev *et al.*, in *Conference on Lasers and Electro-Optics/ Photonic Applications, Systems and Technologies Conference (CLEO/ PhAST 2004)*, OSA Technical Digest (Optical Society of America, Washington, DC, 2004), p. CThZ3.

6. T. Chung *et al.*, Opt. Lett. **31**, 229 (2006).

7. B. Jacobsson *et al.*, Opt. Lett. **30**, 2281 (2005).

8. K.-H. Liao *et al.*, Opt. Express **15**, 4876 (2007).

9. W. Koechner, *Solid-State Laser Engineering*, 4th rev. ed., Springer Series in Optical Sciences, Vol. 1 (Springer, Berlin, 1996), p. 182.

10. N. Forget *et al.*, Opt. Lett. **30**, 2921 (2005).

11. V. Bagnoud, M. J. Guardalben, J. Puth, J. D. Zuegel, T. Mooney, and P. Dumas, Appl. Opt. **44**, 282 (2005).

12. A. V. Okishev and J. D. Zuegel, Appl. Opt. **43**, 6180 (2004).

13. A. V. Okishev, M. D. Skeldon, and W. Seka, in *Advanced Solid-State Lasers*, edited by M. M. Fejer, H. Injeyan, and U. Keller, OSA TOPS, Vol. 26 (Optical Society of America, Washington, DC, 1999), pp. 228–235.

Impact of Transverse Spatial-Hole Burning on Beam Quality in Large-Mode-Area Yb-Doped Fibers

Introduction

In recent years fiber lasers and amplifiers have been widely used in high-power applications such as material processing and industrial manufacturing. Their main advantages are heat-dissipation capability, broad gain bandwidth, compactness, robustness, and high efficiency. The primary limitation in their power scaling is the onset of nonlinear effects, including stimulated Brillouin scattering (SBS) and stimulated Raman scattering (SRS).[1] This limitation can be significantly mitigated by the adoption of large-mode-area (LMA) fibers due to the resulting reduction in intensity. The damage threshold is also increased for LMA fibers. However, increasing the mode area in traditional step-index fibers will introduce higher-order transverse modes and therefore degrade the beam quality. The optimization of the beam quality in LMA fibers has been a subject of intense research.[2–9]

Many designs of LMA fibers for high-power applications have been developed for beam-quality control. Design aspects have included internal structure designs such as photonic crystal fibers and helical-core fibers;[2–4] external structure designs such as coiled multimode fibers;[5] refractive-index designs such as low-numerical-aperture (NA), single-mode fibers and ring-shaped index fibers;[6,7] and gain dopant designs in multimode fibers.[8,9]

The impact, however, of transverse spatial-hole burning (TSHB) on beam quality has often been ignored. When a multimode optical beam with nonuniform transverse intensity is propagating in the fiber, the gain becomes more saturated where the intensity is highest. As the gain seen by each transverse mode changes, the net beam profile, and thus the beam quality, changes. At high powers, this effect becomes pronounced due to heavily saturated population inversion. To our knowledge, TSHB in LMA fibers has not yet been modeled.

In this article, the beam-quality factor is measured for an amplified spontaneous emission (ASE) source based on an ytterbium-doped LMA multimode fiber as a function of pump power. A localized multimode model is presented with spatially resolved gain and a modal decomposition of the optical field. Numerical simulations are performed with this localized multimode model as well as a simplified model and compared to experimental results. The comparison validates the localized model and demonstrates the impact of TSHB on beam quality.

In the following sections, (1) the experimental setup and measured results are presented; (2) a localized multimode model is introduced and the equations to calculate beam-quality factor are presented; (3) the results of numerical simulations based on this model are compared to experimental results and extrapolated to higher power; (4) the validity of a simplified model that does not include TSHB is discussed; and (5) the theoretical models are further applied to fiber amplifiers. The main conclusions are presented in the last section.

Experiment Configuration and Results

The experimental arrangement used for this work is shown schematically in Fig. 110.50. A fiber-coupled diode laser provided a maximum continuous-wave (cw) pump power of 9 W at 915 nm. The ytterbium-doped, dual-clad (YDDC) fiber was 7 m long with a core diameter of 30 μm, an inner cladding diameter of 300 μm, a core NA of 0.06, and an absorption rate of approximately 4 dB/m at 915 nm. While the back end of the fiber was angle cleaved to prevent reflection of the forward ASE, a dichroic mirror was set between two aspheric lenses to extract the backward ASE output light. A beam splitter in the output beam made it possible for the output power and the beam-quality factor (M^2 parameter) to be measured simultaneously. The ASE output power was measured by a power meter, and the beam widths (defined as the second moment) were measured by a charge-coupled-device (CCD) camera placed at different distances.[10] Using a least-squares-fitting method,[11] the beam-quality factor in the x or y direction was calculated by fitting the beam widths and distances to a polynomial:[10]

$$W^2(z) = W_0^2 + M^4 \left(\frac{\lambda}{\pi W_0} \right)^2 (z - z_0)^2, \qquad (1)$$
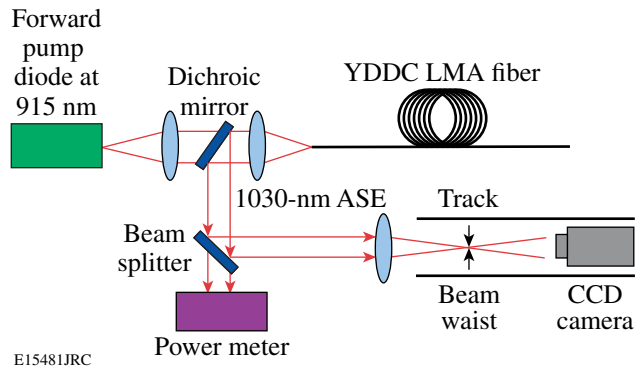
Figure 110.50
Experimental configuration of the multimode-fiber ASE source.

where $W(z)$ is the beam width at distances z, W_0 and z_0 are the respective beam width and distance at the beam waist where the beam width has a minimum, and λ is wavelength.

The ASE output power is plotted as a function of pump power in Fig. 110.51. The figure shows that output power increases exponentially and quasi-linearly when the pump power is below and above ~7 W, respectively, which means the saturation effect becomes apparent at 7-W pump power. We define this "soft" threshold as the pump threshold for saturation.

The beam-quality factor is plotted as a function of pump power in Fig. 110.52. It is instructive to note that the beam-quality factors are identical within experimental error in the x and y directions, as expected from symmetrical circular geometry. Compared with Fig. 110.51, Fig. 110.52 shows that the beam quality improves with pump power below the pump
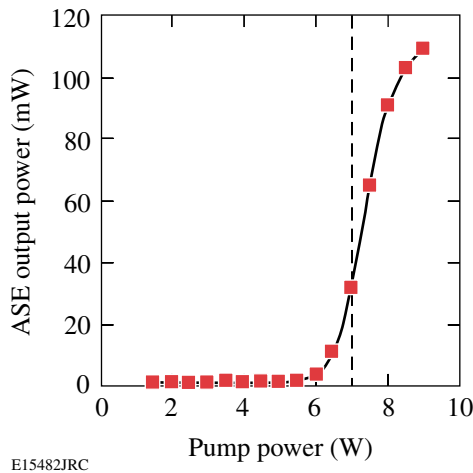
Figure 110.51
Output power versus pump power from the ASE source. The dashed vertical line is the pump threshold for saturation.
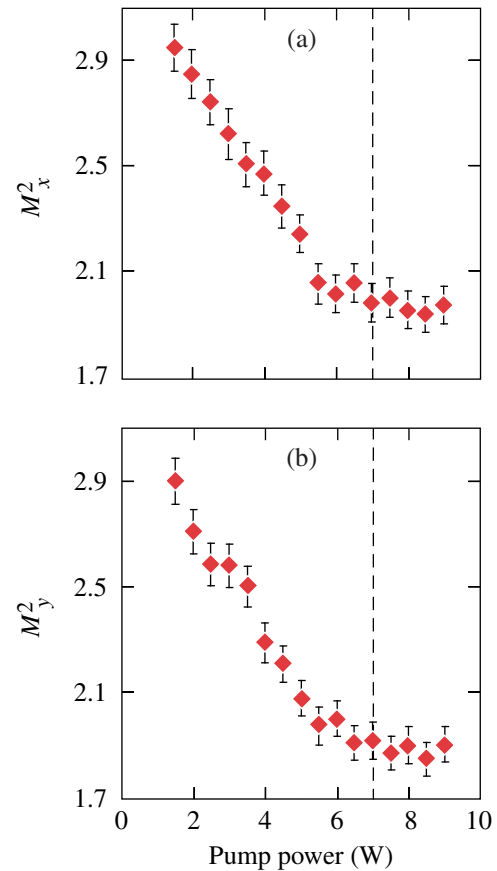
Figure 110.52
The beam-quality factor of ASE source versus pump power in the (a) x direction and (b) y direction. The dashed vertical lines are the pump thresholds for saturation.

threshold for saturation and is nearly steady as the gain medium saturates. To fully understand the physics behind this beam-quality behavior, numerical simulations based on theoretical modeling have been developed.

Localized Model and Beam-Quality Factor Calculation Method

Since the beam quality is related to the modal properties of the output beam, a model that can treat multiple transverse modes is required. A multimode model has been developed for dealing with multiple spectral modes in single-spatial-mode, rare-earth–doped fibers.[12] In this work, the model is extended to multi-transverse-spatial modes in multimode fibers for the first time.

The optical power is quantized into the transverse modes of the fiber, while the population inversion retains spatial dependence. In this way, TSHB can be accounted for while retaining

the simplicity and transparency of a mode-based picture. A similar treatment has also been developed for modeling vertical-cavity, surface-emitting lasers.[13]

The two-level rate equations are given by

$$
\frac{dn_2(r,\phi,z)}{dt} = \sum_k \frac{P_k(z)i_k(r,\phi)\sigma_{ak}}{hv_k} n_1(r,\phi,z)
$$

$$
- \sum_k \frac{P_k(z)i_k(r,\phi)\sigma_{ek}}{hv_k} n_2(r,\phi,z)
$$

$$
- \frac{n_2(r,\phi,z)}{\tau} , \tag{2}
$$

$$
n_t(r,\phi,z) = n_1(r,\phi,z) + n_2(r,\phi,z) , \tag{3}
$$

where the mode order k denotes any combination of beam propagation direction (+, –), wavelength (λ), transverse-mode order (vm), and orientation (even, odd); n_1, n_2, and n_t are ground-level, upper-level, and total ytterbium ion density, respectively, as a function of time and spatial coordinates; σ_a and σ_e are the absorption and emission cross sections of ytterbium ions, respectively; and τ is the upper-state lifetime.

$P_k(z)$, the power of the kth mode at position z in the fiber, is the integration of the light-intensity distribution $I_k(r,\phi,z)$ over the radial and azimuthal coordinates:

$$
P_k(z) = \int_0^{2\pi} \int_0^{\infty} I_k(r,\phi,z) r dr d\phi . \tag{4}
$$

The normalized modal-intensity distribution $i_k(r,\phi)$ is defined as

$$
i_k(r,\phi) = I_k(r,\phi,z) / P_k(z) \tag{5}
$$

and is determined by the spatial shape of the mode and therefore independent of z.

The terms on the right side of Eq. (2) describe the effects of absorption, stimulated emission, and spontaneous emission, respectively. Note that the interference terms are neglected in this model. This assumption is correct for transverse modes of

ASE because they do not interfere with each other due to their lack of coherence. For a coherent multimode beam, this model could be modified by adding the interference terms. Mode coupling and scattering in the fiber are not considered.

In the steady-state case, the time derivative in Eq. (2) is set to zero and the inversion is solved as

$$
n_2(r,\phi,z) = n_t \frac{\displaystyle\sum_k \frac{P_k(z)i_k(r,\phi)\sigma_{ak}}{hv_k}}{\displaystyle\frac{1}{\tau} + \sum_k \frac{P_k(z)i_k(r,\phi)(\sigma_{ak}+\sigma_{ek})}{hv_k}} . \tag{6}
$$

The numerator accounts for small signal gain and the summation in the denominator accounts for TSHB.

The propagation equations are given by

$$
\frac{dP_k(z)}{dz} = u_k \sigma_{ek} \left[P_k(z) + mh \frac{c^2}{\lambda_k^3} \Delta\lambda_k \right]
$$

$$
\times \int_0^{2\pi} \int_0^a i_k(r,\phi) n_2(r,\phi,z) r dr d\phi
$$

$$
- u_k \sigma_{ak} P_k(z) \int_0^{2\pi} \int_0^a i_k(r,\phi) n_1(r,\phi,z)
$$

$$
\times r dr d\phi - u_k \alpha P_k(z) . \tag{7}
$$

where $u_k = 1$ for the modes traveling in the forward direction or $u_k = -1$ in the backward direction, m is the number of polarizations of each mode, $\Delta\lambda_k$ is the bandwidth, and α is the fiber-loss term. The terms on the right side of Eq. (7) describe the effects of stimulated emission, spontaneous emission, absorption, and scattering loss, respectively.

The ASE and pump have different optical properties. The modes of ASE propagate in the fiber in both directions, but the pump propagates only in the forward direction. The bandwidth of ASE is relatively narrow, so the ASE is simplified as a single spectral mode. The pump light is considered to be a single spectral mode with $\Delta\lambda_k = 0$ (no spontaneous emission at the pump wavelength).

Under the weakly guided approximation, the transverse modes of ASE can be represented by linearly polarized (LP) modes.[14] For the LP$_{\nu m}$ mode, the normalized optical intensity $i_{\nu m}(r,\phi)$ and the normalized electrical field distribution $E_{\nu m}(r,\phi)$ can be written as

$$i_{\nu m}(r,\phi) = E_{\nu m}^2(r,\phi),\qquad(8)$$

$$E_{\nu m}(r,\phi) = \begin{cases} bJ_\nu(\kappa_{\nu m}r)f_\nu(\phi) & r < a_{\text{core}} \\[2ex] b\dfrac{J_\nu(\kappa_{\nu m}a_{\text{core}})K_\nu(\gamma_{\nu m}r)f_\nu(\phi)}{K_\nu(\gamma_{\nu m}a_{\text{core}})} & r \geq a_{\text{core}} \end{cases},\qquad(9)$$

where ν and m are the azimuthal and radial mode numbers, respectively; J_ν and K_ν are the Bessel function of the first kind and modified Bessel function of the second kind, respectively; a_{core} is the radius of the core; and b is the normalization coefficient of the electrical field.

The transverse attenuation coefficient of the mode in the inner cladding $\gamma_{\nu m}$ and the transverse wave vector $\kappa_{\nu m}$ are solutions of the following system of equations:[15]

$$\kappa_{\nu m}\frac{J_{\nu-1}(\kappa_{\nu m}a_{\text{core}})}{J_\nu(\kappa_{\nu m}a_{\text{core}})} = -\gamma_{\nu m}\frac{K_{\nu-1}(\gamma_{\nu m}a_{\text{core}})}{K_\nu(\gamma_{\nu m}a_{\text{core}})},\qquad(10)$$

$$\kappa_{\nu m}^2 + \gamma_{\nu m}^2 = V^2/a_{\text{core}}^2.\qquad(11)$$

The V number and NA are defined as

$$V = \frac{2\pi}{\lambda}a_{\text{core}}\text{NA},\qquad(12)$$

$$\text{NA} = \sqrt{n_{\text{core}}^2 - n_{\text{clad}}^2},\qquad(13)$$

where λ is the wavelength and n_{core} and n_{clad} are the refractive indexes in the core and cladding, respectively.

The azimuthal component $f_\nu(\phi)$ is equal to 1 for those transverse modes with zero azimuthal mode number and is given by

$$f_\nu(\phi) = \begin{cases} \cos(\nu\phi) & \text{even} \\[2ex] \sin(\nu\phi) & \text{odd} \end{cases}\qquad(14)$$

for the other transverse modes with even or odd orientation.

Since the area of the inner cladding is much larger than the core, the highly multimode pump light can be simplified as one transverse mode effectively being uniformly distributed across the inner cladding and the core, which means the intensity distribution of pump I_{pump} and normalized intensity distribution of pump i_{pump} can be considered independent of radial and azimuthal coordinates. The normalized intensity distribution of the pump in inner cladding and core is then obtained from Eqs. (4) and (5) by

$$i_{\text{pump}} = \frac{1}{\pi a_{\text{clad}}^2},\qquad(15)$$

where a_{clad} is the radius of inner cladding.

The output power is the sum of the backward output power contained in each mode and is given by

$$P_{\text{output}} = \sum_{\nu,m} P_{\nu m}^-(0).\qquad(16)$$

The output-fraction factor $\alpha_{\nu m}$ of LP$_{\nu m}$ mode is defined as

$$\alpha_{\nu m} = P_{\nu m}^-\big/P_{\text{output}}.\qquad(17)$$

The transverse modes with the same mode numbers but different orientations will have the same fraction factor for ASE due to symmetry.

The beam-quality factor of an optical beam can be calculated given the electrical field distribution.[16] Since the electrical field of ASE is real and symmetric at the output end and without inference, many terms in the equations to calculate the beam-quality factors vanish. The equations can then be simplified as

$$M_x^2 = 2\left[\left(\iint \sum_{\nu,m}\alpha_{\nu m}\left|\frac{\partial E_{\nu m}(r,\phi)}{\partial x}\right|^2 r\,dr\,d\phi\right)\right.$$
$$\left.\times\left(\iint x^2\sum_{\nu,m}\alpha_{\nu m}\left|E_{\nu m}(r,\phi)\right|^2 r\,dr\,d\phi\right)\right]^{1/2},\qquad(18)$$

$$M_y^2 = 2 \left[\left(\iint \sum_{v,m} \alpha_{vm} \left| \frac{\partial E_{vm}(r,\phi)}{\partial y} \right|^2 r \, dr \, d\phi \right) \right.$$

$$\left. \times \left(\iint y^2 \sum_{v,m} \alpha_{vm} \left| E_{vm}(r,\phi) \right|^2 r \, dr \, d\phi \right) \right]^{1/2}. \quad (19)$$

Numerical Simulations and Discussions

Initial boundary conditions are needed to solve the propagation Eq. (7) and are specified at $z = 0$ and $z = L$ as

$$P_{pump}^+(0) = P_0,$$

$$P_{pump}^-(L) = 0,$$

$$\quad (20)$$

$$P_{vm}^+(0) = 0,$$

$$P_{vm}^-(L) = 0,$$

where P_0 is the forward pump power injected into the fiber and L is the length of the fiber. For ASE sources, the input signal is zero.

The parameters used in numerical simulation are listed in Table 110.VII. The emission and absorption cross sections for the fiber used in the experiment are unknown and therefore cited from another fiber with similar parameters.[17] Although the value of the bandwidth of ASE $\Delta\lambda_{ASE}$ does not affect the simulation result significantly, it is set to make the output power from simulation match that from experiment.

Given the initial boundary conditions, the propagation Eq. (7) is resolved by standard numerical integration techniques. The ASE output power and the output-fraction factors are obtained by Eqs. (16) and (17), and then the beam-quality factor is calculated by Eqs. (18) and (19). The ASE output power, the output-fraction factors, and the beam-quality factor as functions of pump power up to 25 W are calculated and plotted in Figs. 110.53, 110.54, and 110.55, respectively.

Compared with Fig. 110.51, Fig. 110.53 shows that the calculated output power has the same behavior as that from the experiment with a slightly larger value, which may result from the discrepancy between the cross sections used in simulation and experiment or over-estimation of pump power since coupling efficiency is not included in the model. The

pump threshold for saturation is about 7.5 W, close to experimental results.

Figure 110.54 shows that all of the transverse modes have nearly the same output-fraction factors at very low pump power. The output-fraction factors of lower-order modes (LP_{01} and LP_{11} in this case) increase with pump power while those of higher-order modes (LP_{01}, LP_{11}, and LP_{31} in this case)

Table 110.VII: Parameters used in simulations.

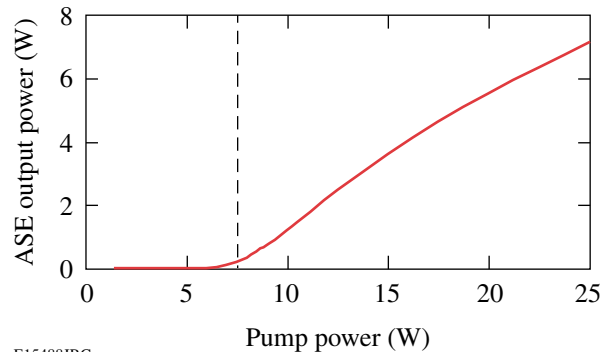| Parameter	Value
n_t	1.45×10^{26} m^{-3}
λ_{ASE}	1030 nm
λ_{pump}	915 nm
$\sigma_{a\,ASE}$	4.88×10^{-26} m^2
$\sigma_{e\,ASE}$	6.24×10^{-25} m^2
$\sigma_{a\,pump}$	8.21×10^{-25} m^2
$\sigma_{e\,pump}$	3.04×10^{-26} m^2
τ	0.84 ms
$\Delta\lambda_{ASE}$	5 nm
m	2
L	7 m
a_{core}	15 μm
a_{clad}	150 μm
NA	0.06
α	0.003 m^{-1}

E15488JRC

Figure 110.53
ASE output power versus pump power from the localized model. The dashed vertical line is the pump threshold for saturation.

decrease. Most importantly, the lower-order modes maximize near the pump threshold for saturation, while the higher-order modes minimize.

From Eqs. (18) and (19), it is obvious that the output-fraction factors determine the beam-quality factor since the beam-quality factor of each LP transverse mode is fixed. Generally speaking, lower-order modes have a smaller beam-quality factor, while the higher-order modes have a larger beam-quality factor.[16] So the beam-quality factor decreases, minimizes, and increases when the output fractions of lower-order modes increase, maximize, and decrease, respectively.

This behavior is manifest in Fig. 110.55, which shows that the beam-quality factor decreases with increasing pump power below pump threshold for saturation as shown experimentally in Fig. 110.52. The calculation further shows that the nearly

steady part near pump threshold for saturation in Fig. 110.52 is a minimum. The behavior of the beam-quality factor follows directly from the behavior of output-fraction factors as shown in Fig. 110.55. The output-fraction factors, and thus the beam-quality factor, are determined by how much gain is experienced by each transverse mode, which depends on the overlap of mode field distribution and population inversion distribution.

The upper-level dopant distribution across the injection fiber end for various pump powers is plotted in Fig. 110.56. When 5-W pump power is below the pump threshold for saturation, the population inversion is nearly uniform across the core, so the modal gain is nearly proportional to the fraction of the mode in the core. Since the fields of lower-order modes are more confined in the core, the lower-order modes have larger gain than the higher-order modes, as shown in Table 110.VIII. In this small-signal regime, the power in the modes with larger gain increases faster than in the modes with smaller gain. Therefore, the output-fraction factors of lower-order modes increase and the beam quality improves.

Figure 110.54
Output-fraction factors of LP fiber modes versus pump power from the localized model. The dashed vertical line is the pump threshold for saturation.
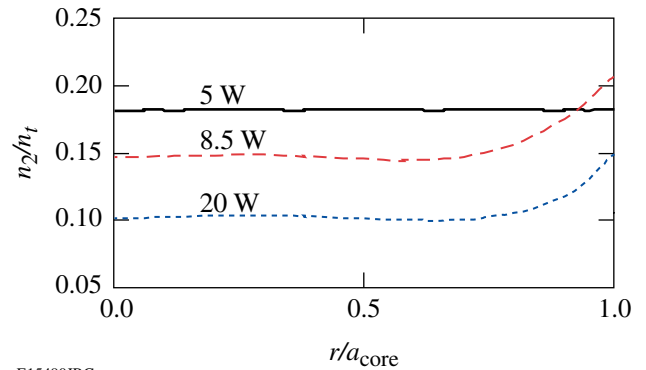
Figure 110.56
Upper-level dopant distributions with various pump powers across the injection fiber end.

Figure 110.55
Beam-quality factor versus pump power from the localized model. The dashed vertical line is the pump threshold for saturation.

Table 110.VIII: The ratio of the gain seen by other transverse modes to the gain seen by the fundamental mode with 5-W pump power.

Mode	$g_{\mathrm{LP}_{vm}}/g_{\mathrm{LP}_{01}}$
LP_{11}	95.6%
LP_{21}	89.8%
LP_{02}	85.4%
LP_{31}	78.0%

Above the pump threshold for saturation, TSHB is shown in the upper-level dopant distribution with 8.5- and 20-W pump power in Fig. 110.56, where the gain profile is much more saturated in the center of the core than on the edge. Since lower-order modes are more concentrated in the center of the core, the gain of lower-order modes decreases relative to the gain of higher-order modes. In the saturation region, the faster the gain in the modes decreases, the slower the power in the modes increases. So under the impact of TSHB the output-fraction factors of lower-order modes decrease and the beam quality degrades.

The Validity of a Simplified Model

The rate and propagation equations are often simplified by replacing transverse space integrals with overlap integrals, especially in single-mode fibers.[18] The validity of such simplification in multimode fibers is discussed below.

The rate equations of such a simplified model are given by

$$\frac{dn_2(z)}{dt} = \sum_k \frac{P_k(z)\Gamma_k\sigma_{ak}}{h\nu_k A} n_1(z)$$

$$- \sum_k \frac{P_k(z)\Gamma_k\sigma_{ek}}{h\nu_k A} n_2(z) - \frac{n_2(z)}{\tau} , \qquad (21)$$

$$n_t(z) = n_1(z) + n_2(z), \qquad (22)$$

where n_1 and n_2 represent average ground-level and upper-level ytterbium ion density across the fiber cross section, respectively, A is the area of the core cross section, and Γ_k is the overlap integral between the mode and dopants.

The overlap integral of ASE modes is given by

$$\Gamma_{vm} = \frac{\int_0^{2\pi}\int_0^{\infty} i_{vm}(r,\phi)n_t(r,\phi,z)rdrd\phi}{\int_0^{2\pi}\int_0^{\infty} n_t(r,\phi,z)rdrd\phi} . \qquad (23)$$

If the dopant is distributing uniformly in the fiber core, Γ_{vm} depends only on the mode field and can be simplified as

$$\Gamma_{vm} = \int_0^{2\pi}\int_0^{a_{core}} i_{vm}(r,\phi)rdrd\phi . \qquad (24)$$

The overlap integral of pump is given by

$$\Gamma_{\mathrm{pump}} = a_{\mathrm{core}}^2 \big/ a_{\mathrm{clad}}^2 . \qquad (25)$$

In the steady-state case, n_2 is solved as

$$n_2(z) = n_t \frac{\displaystyle\sum_k \frac{P_k(z)\Gamma_k\sigma_{ak}}{h\nu_k A}}{\displaystyle\frac{1}{\tau} + \sum_k \frac{P_k(z)\Gamma_k(\sigma_{ak}+\sigma_{ek})}{h\nu_k A}} . \qquad (26)$$

Since the upper-level dopant distribution depends only on the longitudinal coordinate z and is independent of radial and azimuthal coordinates, TSHB is not included in the simplified model. The saturation effect is included as an averaged level across the core.

The simplified propagation equation is given by

$$\frac{dP_k(z)}{dz} = u_k\sigma_{ek}\left[P_k(z) + mh\frac{c^2}{\lambda_k^3}\Delta\lambda_k\right]\Gamma_k n_2(z)$$

$$- u_k\sigma_{ak}P_k(z)\Gamma_k n_1(z) - u_k\alpha P_k(z). \qquad (27)$$

Given the same initial boundary conditions as Eq. (20), the propagation equation (27) is resolved. The output power as a function of pump power is the same in the simplified model as the localized model; however, the modal properties are significantly different. The output-fraction factors and beam-quality factor as functions of pump power up to 25 W in the simplified model compared to the localized model are shown in Figs. 110.57 and 110.58.

Figure 110.57 shows that the output-fraction factors in the simplified model are the same as those in the localized model when the pump power is below the pump threshold for saturation. However, the output-fraction factors of lower-order modes in the simplified model keep increasing beyond the pump threshold for saturation, becoming constant after 15 W. Similarly, Fig. 110.58 shows that the beam-quality factor in the

simplified model is the same as that in the localized model at pump power below pump threshold for saturation. Above the pump threshold for saturation, however, the beam-quality factor in the simplified model keeps decreasing until 15 W and then becomes constant.

The behaviors of output-fraction factors and beam-quality factor are consistent and can be explained as follows: In the simplified model, the gain seen by each transverse mode is always proportional to the fraction of the mode in the core, so the simplified model gives the same simulation results as the localized model below the pump threshold of saturation. Above the pump threshold for saturation, the gain of each mode decreases at the same rate, so the power in each mode increases

at the same rate. Therefore, the output-fraction factor of each mode becomes constant, as does the beam-quality factor.

The beam-quality factors from simulation results of both models and the experimental results near pump threshold for saturation are compared in Fig. 110.59. Figure 110.59 shows that the beam-quality factor of the simplified model does not plateau like the experiment data, but the localized model predicts this behavior. The failure to show the minimum of beam-quality factor near pump threshold for saturation proves that the simplified model is not valid and TSHB is required to model LMA multimode fibers when dealing with beam quality.

Fiber Amplifiers

Fiber amplifiers are more important than ASE sources in high-power applications of LMA fibers. As mentioned in **Localized Model and Beam-Quality Factor Calculation Method** (p. 121), the localized model assumes no interference, which is true for an optical beam from incoherent sources like ASE, but not for coherent sources like fiber amplifiers. While the equations could be easily modified to include the interference terms, the relative phases between modes create a large additional parameter space that would require exploration. The calculations that follow neglect these interference terms since the additional complication does not aid in underscoring the importance of TSHB.

E15493JRC
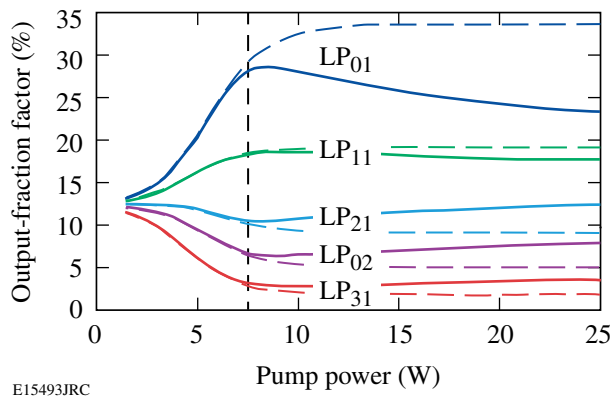
Figure 110.57
Output-fraction factors of LP fiber modes versus pump power from localized (solid) and simplified (dashed) models. The dashed vertical line is the pump threshold for saturation.

E15493JR2C

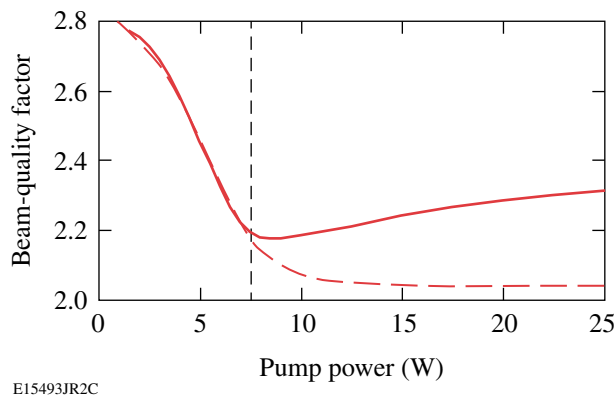Figure 110.58
Beam-quality factor versus pump power from localized (solid) and simplified (dashed) models. The dashed vertical line is the pump threshold for saturation.
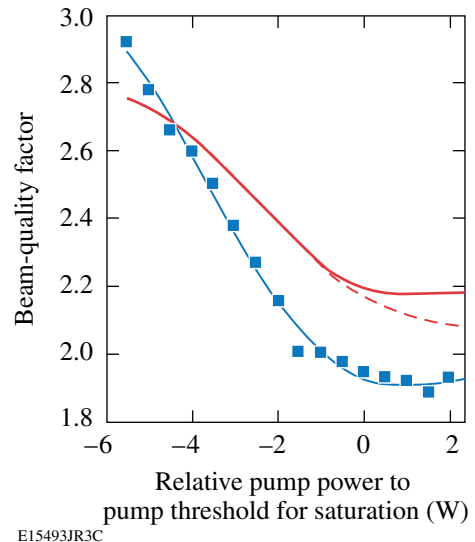

E15493JR3C

Figure 110.59
Beam-quality factor versus relative pump power to pump threshold for saturation from localized (solid) and simplified (dashed) models as well as experimental measurements (squares with solid-line fit).

For the purpose of simplicity, only the LP_{01} and LP_{11} modes are assumed to be coupled into the fiber amplifier. The power contained in the LP_{11} mode is assumed to be evenly distributed in two orientations.

The initial boundary conditions are changed to

$$P_{\text{pump}}^{+}(0) = P_0,$$

$$P_{\text{pump}}^{-}(L) = 0,$$

$$P_{01}^{+}(0) = P_s \chi,$$

$$P_{11}^{+}(0) = P_s(1-\chi),$$ (28)

$$P_{vm}^{+}(0) = 0, \text{otherwise}$$

$$P_{vm}^{-}(L) = 0,$$

where P_s is the total signal power and χ is the input-fraction factor of the LP_{01} mode.

The normalized electrical field distribution of the output beam can be written as

$$E(r,\phi) = \sum_{v,m} \sqrt{\alpha_{vm}} E_{vm}(r,\phi) e^{-i\beta_{vm}L},$$ (29)

where the propagation coefficient β_{vm} is given by[15]

$$\beta_{vm}^2 = \left(\frac{2\pi}{\lambda}\right)^2 n_{\text{core}}^2 - \kappa_{vm}^2.$$ (30)

In this form, modal dispersion is included. No initial phase difference is considered between the modes since the two modes are assumed to be excited by a single-mode input beam (for example, by misalignment).

Since the output beam is real and symmetrical, the equations to calculate the beam-quality factors in Ref. 16 can be simplified as

$$M_x^2 = 2\sqrt{\left[\iint \left|\frac{\partial E(r,\phi)}{\partial x}\right|^2\right]\left[\iint x^2 |E(r,\phi)|^2 rdrd\phi\right]},$$ (31)

$$M_y^2 = 2\sqrt{\left[\iint \left|\frac{\partial E(r,\phi)}{\partial y}\right|^2\right]\left[\iint y^2 |E(r,\phi)|^2 rdrd\phi\right]}.$$ (32)

The new parameters used in the simulation and those that differ from Table 110.VII are listed in Table 110.IX: λ_s is the wavelength of the signal, $\Delta\lambda_{\text{ASE}}$ is set to be the same as the bandwidth of the signal, and P_0 is set far above the pump threshold for saturation, which is true in most high-power applications.

Table 110.IX: New and changed parameters used in simulations.

Parameter	Value
λ_S	1030 nm
P_s	10 W
n_{core}	1.5
$\Delta\lambda_{\text{ASE}}$	0.1 nm
P_0	1.5 kW

The calculations show that the output power is nearly the same in both models and does not change as the input-fraction factor. For both models, the output-fraction factor of the fundamental mode and the beam-quality factor are calculated as a function of the input-fraction factor of the LP_{01} mode from 0.5 to 1 (shown in Figs. 110.60 and 110.61).

Figure 110.60 shows that the output-fraction factor of the fundamental mode in the localized model is smaller than the corresponding input-fraction factor, while the output-fraction factor of the fundamental mode in the simplified model is larger. These behaviors can be explained as follows: The pump power used in the simulations is well above pump threshold for saturation. In the localized model, the gain of fundamental mode is less than that of the LP_{11} mode due to the effect of TSHB. Therefore, the fundamental mode is amplified less than the LP_{11} mode, leading to a smaller output-fraction factor of the fundamental mode. In the simplified model, however, TSHB is ignored and the gain of fundamental mode is always larger than that of the LP_{11} mode. In this case, the fundamental mode is always amplified more than the LP_{11} mode, leading to a larger output-fraction factor of the fundamental mode.

Figure 110.61 shows that the beam-quality factor in the simplified model is underestimated by as much as 15% compared to the localized model due to underestimation of the output-fraction factor of the fundamental mode. This significant difference underscores the importance of TSHB on beam quality in LMA fiber amplifiers for high-power applications.
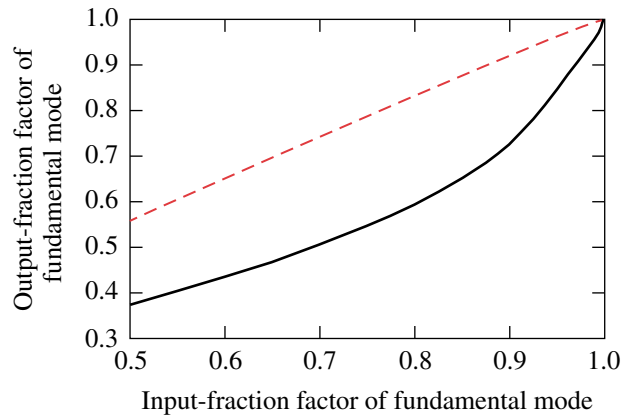
E15696JRC

Figure 110.60

Output-fraction factors of the fundamental mode versus input-fraction factors of the fundamental mode from localized (solid) and simplified (dashed) models.

E15697JRC

Figure 110.61

Beam-quality factors versus pump power from localized (solid) and simplified (dashed) models.

Conclusions

In conclusion, the importance of TSHB on the beam quality of LMA multimode fibers was revealed through measurements and simulations. The measured beam-quality factor decreases until the gain beco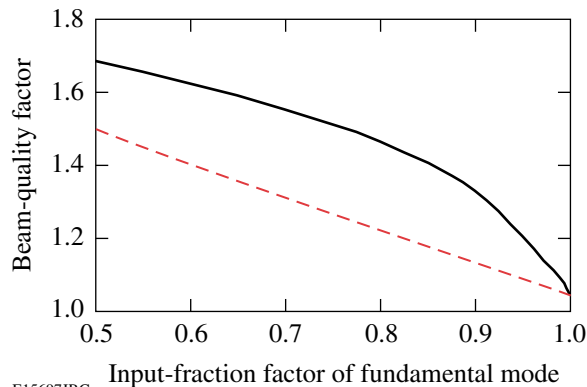mes saturated in an ASE source based on an ytterbium-doped, large-mode-area, multimode fiber. Numerical simulation trends based on a model using spatially resolved gain and transverse-mode decomposition of the optical field

agree with the experimental results. A simplified model without TSHB is shown not fit to predict the observed behavior of beam quality in LMA fibers, especially at high powers. A comparison of both models shows that TSHB is also critical for properly modeling beam quality in LMA fiber amplifiers.

REFERENCES

1. G. P. Agrawal, *Nonlinear Fiber Optics* (Academic Press, Boston, 1989).

2. T. A. Birks, J. C. Knight, and P. St. J. Russell, Opt. Lett. **22**, 961 (1997).

3. P. Wang *et al.*, Opt. Lett. **31**, 226 (2006).

4. Z. Jiang and J. R. Marciante, J. Opt. Soc. Am. B **23**, 2051 (2006).

5. P. Koplow, D. A. V. Kliner, and L. Goldberg, Opt. Lett. **25**, 442 (2000).

6. D. Taverner *et al.*, Opt. Lett. **22**, 378 (1997).

7. H. L. Offerhaus *et al.*, Opt. Lett. **23**, 1683 (1998).

8. J. M. Sousa and O. G. Okhotnikov, Appl. Phys. Lett. **74**, 1528 (1999).

9. J. R. Marciante, presented at ASSP 2007, Vancouver, Canada, 28–31 January 2007.

10. A. E. Siegman, in *Diode Pumped Solid State Lasers: Applications and Issues*, edited by M. W. Dowley, OSA TOPS, Vol. 17 (Optical Society of America, Washington, DC, 1998), pp. 184–199.

11. P. R. Bevington, *Data Reduction and Error Analysis for the Physical Sciences* (McGraw-Hill, New York, 1969), pp. 135–155.

12. C. R. Giles and E. Desurvire, J. Lightwave Technol. **9**, 271 (1991).

13. J. Y. Law, IEEE Photonics Technol. Lett. **9**, 437 (1997).

14. D. Gloge, Appl. Opt. **10**, 2252 (1971).

15. C. R. Pollock, *Fundamentals of Optoelectronics* (Irwin, Chicago, 1995).

16. H. Yoda *et al.*, J. Lightwave Technol. **24**, 1350 (2006).

17. J. R. Marciante and J. D. Zuegel, Appl. Opt. **45**, 6798 (2006).

18. Hardy, J. Lightwave Technol. **16**, 1865 (1998).

Time-Dependent Nuclear Measurements of Mix in Inertial Confinement Fusion

Ignition and high gain in inertial confinement fusion (ICF)[1,2] are critically dependent on mitigation of the Rayleigh–Taylor (RT) instability. ICF capsules typically consist of a spherical shell filled with a gaseous fuel and are imploded using lasers (direct drive) or x rays (indirect drive) to rapidly deposit energy and ablate the capsule surface. The RT instability, which is the growth of nonuniformities at a density interface when a low-density material accelerates a high-density material, occurs during two distinct intervals in ICF implosions. During the acceleration phase, the low-density ablating plasma accelerates the solid shell inward, and perturbations seeded by energy deposition nonuniformities or initial capsule surface roughness feed through to the inner fuel–shell surface. During the deceleration phase, shortly before the time of maximum capsule compression, growth of the RT instability at the fuel–shell interface quickly saturates, resulting in small-scale, turbulent eddies that lead to atomic-scale mixing of the fuel and shell.[3] RT growth and the resulting mixing processes disrupt the formation of a hot spot in the fuel, lowering its temperature and reducing its volume, which may prevent the capsule from igniting. Understanding the nature and timing of RT growth and mix under different conditions is an important step toward mitigating their adverse effects.

Substantial and sustained efforts to understand RT instability and mix have been ongoing for many decades.[4] This article presents the first time-dependent nuclear burn measurements of the mix region in ICF implosions. Although it has been previously demonstrated that there is no mix in the burn region at shock bang time,[5,6] it was unknown how long after shock collapse it takes for atomic mixing to occur. Other relevant work on the mix region in ICF implosions includes time-integrated nuclear yield measurements in both direct-drive[6–10] and indirect-drive[11] configurations, as well as time-dependent x-ray measurements of capsules doped with tracer elements.[12] In addition, time-dependent nuclear measurements obtained from implosions of CD-shell capsules filled with nearly pure tritium have recently been reported.[13]

This article reports results from direct-drive experiments conducted with the OMEGA Laser System,[14] with 60 fully smoothed,[15] UV ($\lambda = 351$ nm) beams in a 1-ns flat-top pulse and a total energy of 23 kJ. The on-target illumination uniformity was typically $\leq 2\%$ rms. The spherical plastic target capsules had diameters between 860 and 880 μm, a total shell thickness of 20 μm, and a 0.1-μm-rms outer surface roughness. "CH" capsules had plastic (CH) shells and a gaseous fill of deuterium and helium-3 (D_2 and ^{3}He, equimolar by atom). "CD" capsules had gaseous fills of pure ^{3}He and a shell made mostly of CH, except for a 1-μm layer of deuterated plastic (CD) on the inner surface (Fig. 110.62). The fill pressures of the D^3He and the pure ^{3}He mixtures in CH and CD capsules were chosen to give equal initial fill mass densities ρ_0 at values of 0.5 or 2.5 mg/cm^3. Because fully ionized D and ^{3}He have the same value of $(1+Z)/A$, mixtures with the same mass density have the same total particle density when fully ionized and can be considered hydrodynamically equivalent.[16]

Implosions of CH and CD capsules were observed using simultaneous measurements of products from two distinct primary nuclear reactions to study the nature and timing of mix. The D-^{3}He reaction, $D + {}^3He \rightarrow {}^4He + p$, and the DD-$n$ reaction, $D + D \rightarrow {}^3He + n$, have dramatically different composition and temperature sensitivities,[16] which are used herein to constrain possible mix scenarios. The D-^{3}He reaction depends much more strongly on temperature due to the doubly charged ^{3}He reactant, and when the reactant species are initially separated, such as in CD capsules, they must be mixed before nuclear production will occur.[17]

Possible scenarios of atomic mix are constrained using spectral measurements of nascent 14.7-MeV D^{3}He protons. D^{3}He protons experience energy loss from their birth energy as they pass through the compressed shell plasma on their way out of the capsule. The proton-emission, path-averaged capsule areal density ρL is inferred using the mean-energy downshift of measured proton spectra.[18] For implosions with the same

mean radial areal density ρR, the value of ρL depends on the spatial distribution of the proton source and shell mass.[18] A larger correction factor is needed as the mean source radius approaches the mean shell radius, as protons traverse longer paths through the shell. For example, a quasi-one-dimensional scenario of atomic mix that consists of a spherical mixing layer just inside a compressed spherical shell will require a much larger correction factor than a three-dimensional scenario involving turbulent mix induced at the tips of RT spikes driven into the hot core.

The dynamics of RT growth are of essential importance for any mix scenario. These dynamics are studied using temporal measurements of the emission of D^3He protons, obtained using the proton temporal diagnostic (PTD).[19,20] The PTD primarily consists of a 1-mm-thick BC-422 scintillator, an optical transport system, and a fast streak camera. Optical fiducial pulses simultaneously recorded by the streak camera give an absolute timing accuracy of ~25 ps. The time history of the proton arrival at the scintillator is obtained by deconvolution of the detector response from the streak camera image. D^3He proton spectral measurements[18] are then used to infer the D-^3He reaction rate history from the proton current at the scintillator. Additional details on PTD instrumentation and data processing can be found in Frenje et al.[19]

Temporal measurements of 2.45-MeV neutrons from the DD-n nuclear reaction were obtained using the neutron temporal diagnostic (NTD),[21] which works on the same principle as the PTD, but is optimized for neutron detection. Although the D-D reaction rate in CD capsule implosions is below the noise floor of the NTD, integrated D-D yields were readily obtained using time-of-flight neutron detectors.[22]

Implosions of CH capsules with D^3He fuel characteristically emit D^3He protons at two distinct times (Fig. 110.62). The shock burn is induced by the collapse of an ingoing spherical shock and occurs before the imploding shell starts to decelerate. About 250 ps later, during the deceleration phase, the compression burn occurs as the imploding capsule compresses and reheats the fuel. In contrast to the two stages of proton emission observed in CH capsule implosions with D^3He fills, CD capsules emit protons only during the later phase (Fig. 110.62), confirming the hypothesis that there is no mix at the time of shock collapse,[23] first presented by Petrasso et al.[5]

Measurements of time-integrated nuclear yields demonstrate that capsules with lower ρ_0 have an increased susceptibility to mix.[6,9] Yields increased with lower ρ_0 for CD capsule implosions, even though low ρ_0 is less favorable for nuclear production in the capsule core, as seen through the decrease
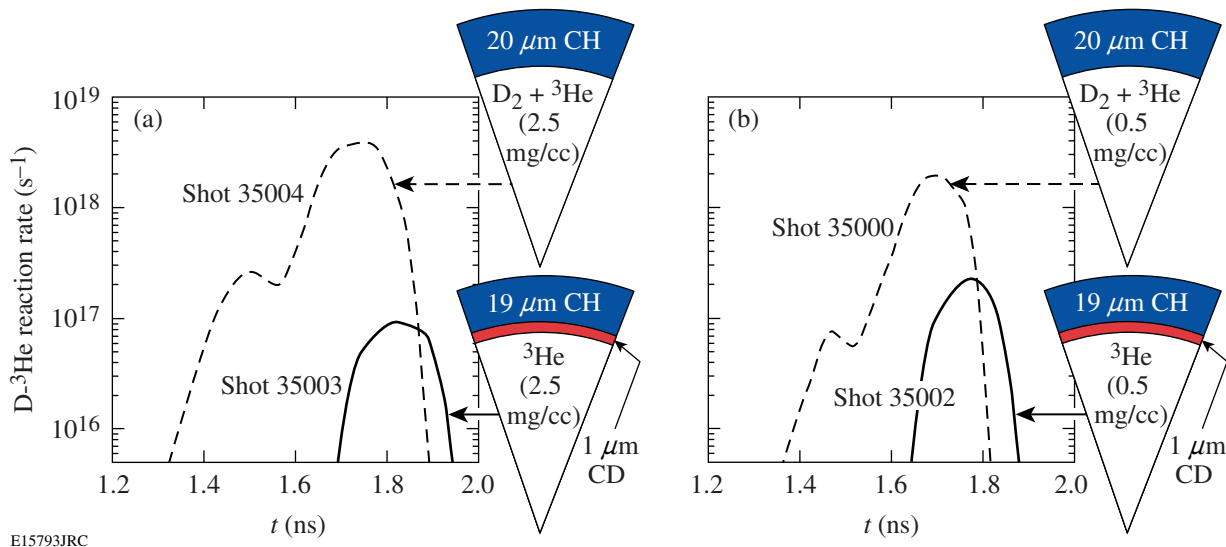
Figure 110.62
Measurements of the D-^3He nuclear reaction history from implosions of spherical plastic (CH) shells filled with an equimolar D_2-^3He mixture, and of equivalent CD-layer capsules filled with pure ^3He. The gaseous fuel was filled to initial densities of (a) 2.5 mg/cm^3 and (b) 0.5 mg/cm^3. The CH capsule histories show distinct times of D-^3He nuclear production corresponding to the shock (at ~1.5 ns) and compression (~1.75 ns) burns. CD capsule implosions require mixing of the fuel and shell on the atomic scale for D-^3He production, and the histories show that no such mix has occurred at shock-bang time. The time necessary for hydro-instabilities to induce fuel–shell mix results in a typical 75±30-ps delay in the peak D-^3He reaction rate in CD capsules compared to equivalent CH capsules. In addition, nuclear production in CD implosions continues even after the compression burn ends in CH capsules, staying well above the typical noise level of 3×10^{15}/s for an additional 50 ps.

in yields for CH capsules (see Fig. 110.62 and Table 110.X). The increase in yields for lower ρ_0 cannot be attributed to a difference in the temperature profile because both DD-n and D-^{3}He yields increased by about the same factor of 1.8, despite markedly different composition and temperature dependence. Additional mix of ^{3}He with the CD shell in low-ρ_0 implosions must be invoked to explain the yield trends.[24]

The time necessary for RT growth to induce turbulent, atomic-scale mixing of the fuel and shell results in a delay in the bang time (defined as the time of peak D-^{3}He reaction rate) of CD capsules compared to equivalent CH capsules of 83±37 ps and 69±21 ps for high and low ρ_0 (Fig. 110.63 and Table 110.X), respectively; this is equal to about half the typical 150-ps burn duration (defined as the full temporal width above half peak reaction rate). The delay is calculated as the difference between the ensemble averages of CD and CH capsule bang times, and the error is calculated as the quadrature sum of the standard errors of the mean for each ensemble average.

Measurements of DD-n bang time in CH capsules closely match the observed D-^{3}He bang time (Fig. 110.63); however, the D-D reaction rate in CD capsules was too low for robust timing measurements.

The observed bang-time delay is not an artifact of limitations of the diagnostics or experimental setup. The timing jitter of the PTD is the same for CH and CD implosions and is less than 20 ps, while bang-time errors of only 10 ps are introduced in the deconvolution process by proton energy spectrum uncertainties. A small systematic difference in shell thickness between CH and CD capsules was corrected using a 13-ps adjustment to the bang-time delay,[25] and it has been demonstrated that bang time does not depend on potential differences in implosion dynamics between capsules with pure ^{3}He fuel and capsules with D_2-^{3}He mixtures.[16]

The observed delay of the peak reaction rate for CD capsules is likely due to the difference in how mix affects nuclear production in CH and CD capsules. Whereas mix tends to quench nuclear production in CH capsules through dilution and cooling of the hot fuel, in CD capsules mix enhances nuclear production by the addition and heating of the D reactant from the shell. Nuclear production in CD capsules does not occur until later in the deceleration phase, when the growth of the RT instability has had time to induce turbulent mixing. Enhancement of reactant densities in CD capsules by continued mix in the later stages of compression, combined with the larger total
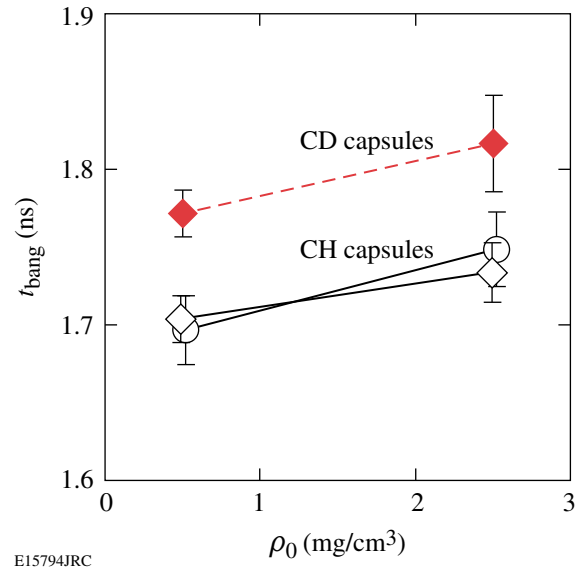
Figure 110.63
Mean and standard error of D^{3}He (diamonds) and DD-n (circles) compression-bang times from CH (open markers) and CD (solid markers) capsule implosions as a function of initial fill density. In CD capsules, D^{3}He bang time consistently occurs ~75 ps later than in CH capsules.

Table 110.X: The number of shots in different ensembles of implosions of D^{3}He-filled CH capsules and ^{3}He-filled CD capsules with two values of initial fill density ρ_0 is shown, along with ensemble averages and standard errors of the mean for several experimental observables: bang time and burn duration for DD-n and D-^{3}He nuclear reaction histories, time-integrated DD-n and D-^{3}He yields (Y_n and Y_p), and areal density ρL. Standard errors are quoted in the same units as the averages, except for the yields, which are expressed as a percent. Only the compression component is included for Y_p and ρL in CH capsules.

Type	ρ_0 (mg/cm^3)	N shots	DD bang (ps)	DD burn (ps)	D^{3}He bang (ps)	D^{3}He burn (ps)	Y_n ($\times 10^8$)	Err (%)	Y_p ($\times 10^7$)	Err (%)	ρL (mg/cm^2)
CH	2.5	8	1749±24	157±10	1734±19	155±11	129	6	61	10	54±2
CH	0.5	8	1697±22	148±11	1704±15	123±12	29	9	30	16	61±2
CD	2.5	7	—	—	1817±31	154±15	5.1	9	1.7	11	64±4
CD	0.5	5	—	—	1772±15	153±13	9.4	7	3.0	13	66±4

mass of fuel in such capsules, is enough to prolong nuclear production even after production would have been quenched in a CH implosion (Fig. 110.62).

Furthermore, systematically later nuclear production in CD capsule implosions leads to higher expected ρL. The mean radial areal density ρR increases throughout the deceleration phase as the shell continues to compress, so protons will selectively sample higher ρR (and ρL) if they are emitted later in time. This effect is in addition to the potentially higher ρL for CD capsules from geometric effects due to a noncentralized proton source profile, described above.

As seen in Fig. 110.64 and Table 110.X, ρL is 9% and 18% higher for implosions of CD capsules than for equivalent CH capsules with low and high ρ_0, respectively.[26] These values are not much higher, suggesting that one or both of the effects described above might not be as significant as expected. On this basis we conjecture that the source of protons in CD capsules may be dominated by atomic mixing at the tips of RT

E15795JRC

Figure 110.64
Mean and standard error of proton-emission-path–averaged areal densities (ρL) for CH (open markers) and CD (solid markers) implosions as a function of initial fill density. D^{3}He proton spectral measurements are used to infer this compression-burn averaged ρL, where the shock component of CH implosion spectra has been excluded. For CH capsules, the radial areal density (ρR) can be obtained from ρL using a small correction ($\rho R \sim 0.93 \, \rho L$), which depends on the shell aspect ratio. The relation between ρR and ρL for CD capsules sensitively depends on the source profile as the mean source radius approaches the mean shell radius; that ρL is not much higher than in CH capsules suggests that the source profile is still centrally peaked.

spikes from the shell that drive into the hot core, which would result in a more central proton emission profile and a smaller increase in ρL.

In summary, temporal measurements of D^{3}He protons emitted from ICF implosions of CD-shell, ^{3}He-filled capsules offer new and valuable insights into the dynamics of turbulent mixing induced by saturation of the Rayleigh–Taylor instability. The first such measurements have demonstrated that bang time is substantially delayed as RT growth saturates to produce mix. The 83±37-ps bang-time delay of CD implosions compared to D^{3}He-filled, CH implosions for high initial fill densities (ρ_0) is equal to half the burn duration. Reducing ρ_0 by a factor of 5 increases the susceptibility of the implosion to mix and does not significantly affect the bang-time delay, observed to be 69±21 ps. Continued mixing of the fill gas and shell prolongs nuclear production in CD capsules even after it is quenched in equivalent CH capsules. Finally, the relatively small increase in areal density ρL of CD compared to CH capsules, despite the later bang time, suggests that nuclear production is dominated by mixing induced at the tips of RT spikes driven into the hot core.

REFERENCES

1. J. Nuckolls *et al.*, Nature **239**, 139 (1972).

2. S. Atzeni and J. Meyer-ter-Vehn, *The Physics of Inertial Fusion: Beam Plasma Interaction, Hydrodynamics, Hot Dense Matter*, International Series of Monographs on Physics (Clarendon Press, Oxford, 2004).

3. P. E. Dimotakis, Annu. Rev. Fluid Mech. **37**, 329 (2005).

4. See, for example, Sec. 8.9 of Ref. 2 for a review of the literature.

5. R. D. Petrasso, J. A. Frenje, C. K. Li, F. H. Séguin, J. R. Rygg, B. E. Schwartz, S. Kurebayashi, P. B. Radha, C. Stoeckl, J. M. Soures, J. Delettrez, V. Yu. Glebov, D. D. Meyerhofer, and T. C. Sangster, Phys. Rev. Lett. **90**, 095002 (2003).

6. J. R. Rygg, J. A. Frenje, C. K. Li, F. H. Séguin, R. D. Petrasso, J. A. Delettrez, V. Yu. Glebov, V. N. Goncharov, D. D. Meyerhofer, P. B. Radha, S. P. Regan, and T. C. Sangster, Phys. Plasmas **14**, 056306 (2007).

7. D. D. Meyerhofer, J. A. Delettrez, R. Epstein, V. Yu. Glebov, V. N. Goncharov, R. L. Keck, R. L. McCrory, P. W. McKenty, F. J. Marshall, P. B. Radha, S. P. Regan, S. Roberts, W. Seka, S. Skupsky, V. A. Smalyuk, C. Sorce, C. Stoeckl, J. M. Soures, R. P. J. Town, B. Yaakobi, J. D. Zuegel, J. Frenje, C. K. Li, R. D. Petrasso, D. G. Hicks, F. H. Séguin, K. Fletcher, S. Padalino, C. Freeman, N. Izumi, R. Lerche, T. W. Phillips, and T. C. Sangster, Phys. Plasmas **8**, 2251 (2001).

8. P. B. Radha, J. Delettrez, R. Epstein, V. Yu. Glebov, R. Keck, R. L. McCrory, P. McKenty, D. D. Meyerhofer, F. Marshall, S. P. Regan, S. Roberts, T. C. Sangster, W. Seka, S. Skupsky, V. Smalyuk, C. Sorce, C. Stoeckl, J. Soures, R. P. J. Town, B. Yaakobi, J. Frenje, C. K. Li, R. Petrasso, F. Séguin, K. Fletcher, S. Padalino, C. Freeman, N. Izumi, R. Lerche, and T. W. Phillips, Phys. Plasmas **9**, 2208 (2002).

9. C. K. Li, F. H. Séguin, J. A. Frenje, S. Kurebayashi, R. D. Petrasso, D. D. Meyerhofer, J. M. Soures, J. A. Delettrez, V. Yu. Glebov, P. B. Radha, F. J. Marshall, S. P. Regan, S. Roberts, T. C. Sangster, and C. Stoeckl, Phys. Rev. Lett. **89**, 165002 (2002).

10. D. C. Wilson, C. W. Cranfill, C. Christensen, R. A. Forster, R. R. Peterson, H. M. Hoffman, G. D. Pollak, C. K. Li, F. H. Séguin, J. A. Frenje, R. D. Petrasso, P. W. McKenty, F. J. Marshall, V. Yu. Glebov, C. Stoeckl, G. J. Schmid, N. Izumi, and P. Amendt, Phys. Plasmas **11**, 2723 (2004).

11. R. E. Chrien *et al.*, Phys. Plasmas **5**, 768 (1998).

12. S. P. Regan, J. A. Delettrez, F. J. Marshall, J. M. Soures, V. A. Smalyuk, B. Yaakobi, V. Yu. Glebov, P. A. Jaanimagi, D. D. Meyerhofer, P. B. Radha, W. Seka, S. Skupsky, C. Stoeckl, R. P. J. Town, D. A. Haynes, Jr., I. E. Golovkin, C. F. Hooper, Jr., J. A. Frenje, C. K. Li, R. D. Petrasso, and F. H. Séguin, Phys. Rev. Lett. **89**, 085003 (2002).

13. D. C. Wilson, P. S. Ebey, A. Nobile, Jr., J. H. Cooley, T. C. Sangster, W. T. Shmayda, M. J. Bonino, D. Harding, V. Yu. Glebov, F. J. Marshall, and R. A. Lerche, Bull. Am. Phys. Soc. **51**, 295 (2006).

14. T. R. Boehly, D. L. Brown, R. S. Craxton, R. L. Keck, J. P. Knauer, J. H. Kelly, T. J. Kessler, S. A. Kumpan, S. J. Loucks, S. A. Letzring, F. J. Marshall, R. L. McCrory, S. F. B. Morse, W. Seka, J. M. Soures, and C. P. Verdon, Opt. Commun. **133**, 495 (1997).

15. S. Skupsky and R. S. Craxton, Phys. Plasmas **6**, 2157 (1999).

16. J. R. Rygg, J. A. Frenje, C. K. Li, F. H. Séguin, R. D. Petrasso, J. A. Delettrez, V. Yu. Glebov, V. N. Goncharov, D. D. Meyerhofer, S. P. Regan, T. C. Sangster, and C. Stoeckl, Phys. Plasmas **13**, 052702 (2006).

17. Non-atomic mix scenarios fail to produce significant yield since thermal ^{3}He ions cannot penetrate far enough into the CD layer. For example, to give D^{3}He yields comparable to those observed, it can be shown that all ^{3}He ions in the fuel ($\sim 2 \times 10^{17}$) would have to be launched into the CD layer at energies of 50 keV, grossly higher than the typical fuel ion temperature of 4 keV.

18. F. H. Séguin, J. A. Frenje, C. K. Li, D. G. Hicks, S. Kurebayashi, J. R. Rygg, B.-E. Schwartz, R. D. Petrasso, S. Roberts, J. M. Soures, D. D. Meyerhofer, T. C. Sangster, J. P. Knauer, C. Sorce, V. Yu. Glebov, C. Stoeckl, T. W. Phillips, R. J. Leeper, K. Fletcher, and S. Padalino, Rev. Sci. Instrum. **74**, 975 (2003).

19. *LLE Review Quarterly Report* **96**, 230, Laboratory for Laser Energetics, University of Rochester, Rochester, NY, LLE Document No. DOE/SF/19460-509, NTIS Order No. PB2006-106668 (2003).

20. J. A. Frenje, C. K. Li, F. H. Séguin, J. Deciantis, S. Kurebayashi, J. R. Rygg, R. D. Petrasso, J. Delettrez, V. Yu. Glebov, C. Stoeckl, F. J. Marshall, D. D. Meyerhofer, T. C. Sangster, V. A. Smalyuk, and J. M. Soures, Phys. Plasmas **11**, 2798 (2003).

21. R. A. Lerche, D. W. Phillion, and G. L. Tietbohl, Rev. Sci. Instrum. **66**, 933 (1995).

22. R. A. Lerche and T. J. Murphy, Rev. Sci. Instrum. **63**, 4880 (1992).

23. Or that such mix, if present, has been insufficiently heated to give nuclear production.

24. For example, if it is assumed that the DD-*n* yield increase is due only to an increase in the temperature of the mix region, then the fraction of ^{3}He fuel contained in the mix region must be three times greater for low ρ_0 to produce the observed D-^{3}He yield increase.

25. The 13-ps reduction in the delay corrects for a $1/3$-μm systematic difference in the total thickness of the CH and CD shells, where the timing of each burn history was adjusted by (40 ps) $\times$ (20 Δ), where Δ is the capsule thickness in μm. The 40-ps/μm correction factor was obtained by a linear fit of CH capsule bang times over a range of thicknesses from 15 to 27 μm.

26. The slightly higher (<2%) initial shell mass in CD capsules due to the high density of the 1-μm-thick CD layer and the systematic thickness difference has a minimal impact on ρL (<1%).

Pump-Induced Temporal Contrast Degradation in Optical Parametric Chirped-Pulse Amplification: Analysis and Experiment

Introduction

Laser–matter interactions in new regimes have occurred due to the generation of high-intensity optical pulses using large-scale laser systems.[1] The interaction regime of a laser pulse with a target is basically set by the peak intensity of the pulse, which is fundamentally proportional to the ratio of the pulse energy to the duration of the pulse and surface of the focal spot. Intensities of the order of 10^{22} W/cm^2 have been claimed,[2] and facilities delivering high-energy, high-intensity laser pulses are under operation or construction.[3] The interaction can be detrimentally impacted by light present before the main pulse since absorbed light can lead to physical modification of the target.[4] The temporal contrast of a laser pulse is the ratio of the peak power of the main pulse to the power of the light in some predetermined temporal range before the main pulse. The contrast can be reduced significantly during the generation and amplification of laser pulses, and contrast degradation manifests itself as isolated prepulses or as a slowly varying pedestal. Incoherent laser and parametric fluorescence can significantly impact the contrast of laser pulses and can lead to a long-range pedestal on the recompressed pulse.[4,5] This contrast degradation is fundamental since fluorescence is always present for classical optical amplifiers. The contrast of optical parametric chirped-pulse amplifiers, however, is also detrimentally impacted by temporal variations of the intensity of the pump pulse that induce spectral variations on the stretched amplified signal via the instantaneous parametric gain. This is a practical limitation that can be eliminated or reduced by proper design of the pump pulse and the optical parametric chirped-pulse amplification (OPCPA) system.

The parametric gain induced by a pump pulse in a non-linear crystal is an efficient process for large-bandwidth, high-energy amplification of chirped optical pulses.[6–8] It is used in stand-alone systems[9–16] or as the front end of large-scale laser facilities.[17] The impact of temporal fluctuations on the contrast of the recompressed signal in an OPCPA system was first identified by Forget *et al.*[18] Simulations of the effect of pump-pulse amplified spontaneous emission (ASE) on an OPCPA system have linked the ASE coherence time to the

temporal extent of the induced pedestal.[19] These publications offer a physical explanation of pump-induced contrast degradation, but an analytical treatment is necessary to quantify the impact of this phenomenon, improve the contrast of existing systems, and design new high-contrast OPCPA systems. This article quantifies the impact of incoherent pump-pulse ASE using an analytic formalism for pump-induced temporal contrast degradation in OPCPA systems and presents an experimental solution to reduce this impact. The impact of incoherent pump ASE is analytically quantified as a function of the operating regime of the OPCPA system. The following sections (1) present the necessary formalism and derive general equations describing the pump-induced contrast degradation in OPCPA systems; (2) compare these analytical derivations with simulations, bringing to light the magnitude of these effects in a typical OPCPA system; and (3) describe an LLE experiment that demonstrates the reduction of pump-induced temporal contrast degradation by filtering the pump pulse with a volume Bragg grating (VBG) in a regenerative amplifier.

Analysis of Pump-Induced Contrast Degradation in an OPCPA System

1. General Approach

The derivations presented in this section assume a one-dimensional representation of the electric field of the signal and pump as a function of time (and equivalently optical frequency), without spatial resolution. Such a model is sufficient to introduce the various aspects of contrast degradation in OPCPA systems. Some of these systems use flattop pumps and signals, in which case the temporal contrast is mostly limited by the contrast obtained in the constant-intensity portion of the beam. For high energy extraction, efficient phase matching, and optimal beam quality, OPCPA systems are usually run in configurations where spatial walk-off and diffraction are not significant. An instantaneous transfer function between the intensity of the pump, the intensity of the input signal, and the intensity of the output signal is used to describe the parametric amplifier. This applies to an amplifier where temporal walk-off and dispersion-induced changes in the intensity of the interacting waves are small compared to the time scales of the

temporal variations of the signal and pump. This also applies to a sequence of amplifiers where scaled versions of the same pump are used in each amplifier with an identical relative delay between the signal being amplified and the pump. Figure 111.1 presents a schematic of an OPCPA system. The short input signal is stretched by a stretcher, amplified by the pump pulse in an optical parametric amplifier (one or several nonlinear crystals properly phase matched), and recompressed. As identified in Refs. 18 and 19, the variations of the parametric gain due to variations in the pump intensity lead to modulations of the temporal intensity of the amplified stretched pulse, which are equivalent to modulations of the spectrum of this pulse. These modulations lead to contrast-reducing temporal features after recompression.
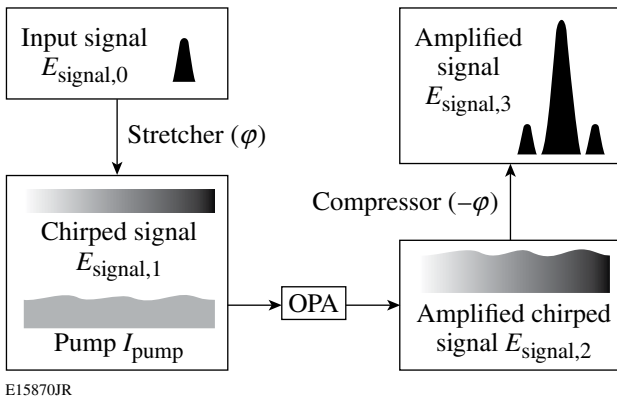

E15870JR

Figure 111.1
Schematic of an OPCPA system. Pump-intensity modulation gets transferred onto the spectrum of the chirped signal in an optical parametric amplifier (OPA). The modulation of the spectrum of the recompressed signal induces contrast-reducing temporal features on the recompressed signal.

2. Contrast Degradation of an OPCPA System in the Presence of Pump Noise

In this article, E and $\tilde{E}$ relate to the temporal and spectral representations of the analytic signal of an electric field, and I and $\tilde{I}$ relate to the corresponding intensities. The initial signal is described by the spectral field $\tilde{E}_{\mathrm{signal},0}(\omega)$. After stretching with second-order dispersion φ, the stretched pulse is described in the time domain by

$$E_{\mathrm{signal},1}(t) = \left(1/\sqrt{\varphi}\right)\tilde{E}_{\mathrm{signal},0}(t/\varphi)\exp\left(-it^2/2\varphi\right)$$

up to some multiplicative constants. The quadratic phase describes the one-to-one correspondence between time and optical frequency in the highly stretched pulse, which is symbolically written as $t = \varphi\omega$. The temporal intensity of the signal after parametric amplification is a function of the temporal

intensity of the stretched signal $I_{\mathrm{signal},1}(t) = (1/\varphi)\tilde{I}_{\mathrm{signal},0}(t/\varphi)$ and the temporal intensity of the pump $I_{\mathrm{pump}}(t)$, which can be written as

$$I_{\mathrm{signal},2}(t) = f\left[I_{\mathrm{signal},1}(t), I_{\mathrm{pump}}(t)\right]. \tag{1}$$

The function f depends on the parametric amplifier length and nonlinear coefficient.

Figure 111.2 displays two examples of behavior of the function f for a given input signal intensity, namely the relation between the output signal intensity and the pump intensity. In Fig. 111.2(a), the amplifier is unsaturated, and there is a linear relation between variations of the pump intensity and variations of the amplified signal intensity around point A. In Fig. 111.2(b), the amplifier is saturated. The output signal intensity reaches a local maximum, and there is a quadratic relation between variations of the pump intensity and variations of the amplified signal intensity around point B. Assuming that the intensity modulation of the pump does not significantly modify the instantaneous frequency of the chirped signal, the intensity of a spectral component of the amplified signal at the optical frequency ω is

$$f\left[I_{\mathrm{signal},1}(\varphi\omega), I_{\mathrm{pump}}(\varphi\omega)\right] = f\left[\tilde{I}_{\mathrm{signal},0}(\omega)/\varphi, I_{\mathrm{pump}}(\varphi\omega)\right].$$

The pump-intensity noise $\delta I_{\mathrm{pump}}(t)$ is introduced by writing the intensity as $I_{\mathrm{pump}}(t) = I_{\mathrm{pump}}^{(0)}(t) + \delta I_{\mathrm{pump}}(t)$. Assuming the amplifier is not saturated [Fig. 111.2(a)], the function f is developed to first order around the operating point set by $I_{\mathrm{pump}}^{(0)}$ as

$$f\left[\tilde{I}_{\mathrm{signal},0}(\omega)/\varphi, I_{\mathrm{pump}}(\varphi\omega)\right]$$

$$= f\left[\tilde{I}_{\mathrm{signal},0}(\omega)/\varphi, I_{\mathrm{pump}}^{0}(\varphi\omega)\right]$$

$$+ \delta I_{\mathrm{pump}}(\varphi\omega)\frac{\partial f}{\partial I_{\mathrm{pump}}}\left[\tilde{I}_{\mathrm{signal},0}(\omega)/\varphi, I_{\mathrm{pump}}^{0}(\varphi\omega)\right]. \tag{2}$$

The spectral intensity of the amplified recompressed signal is

$$\tilde{I}_{\mathrm{signal},3}(\omega) = \varphi f\left[\tilde{I}_{\mathrm{signal},0}(\omega)/\varphi, I_{\mathrm{pump}}(\varphi\omega)\right].$$
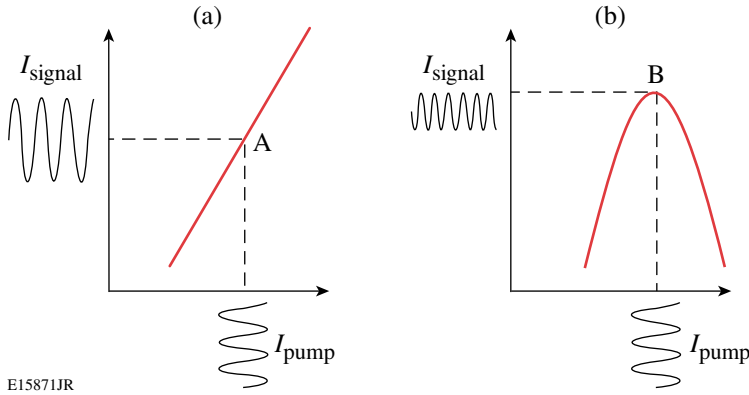
Figure 111.2
Representation of the transfer function between output signal intensity and pump intensity around the operating point of a parametric amplifier in the (a) unsaturated and (b) saturated regimes. At point A, there is a linear relation between pump-intensity modulation and amplified-signal-intensity modulation. At point B, there is a quadratic relation between pump-intensity modulation and amplified-signal-intensity modulation.

E15871JR

and one can define

$$\tilde{I}^{(0)}_{\text{signal},3}(\omega) = \varphi f\left[\tilde{I}_{\text{signal},0}(\omega)\big/\varphi, I^0_{\text{pump}}(\varphi\omega)\right]$$

as the spectral intensity of the signal amplified by a noiseless pump. The partial derivative of f with respect to the pump intensity is assumed to be independent of the signal intensity, and one defines the constant

$$f_{(1)} = \frac{\partial f}{\partial I_{\text{pump}}}\left[\tilde{I}_{\text{signal},0}(\omega)\big/\varphi, I^0_{\text{pump}}(\varphi\omega)\right].$$

For a compressor matched to the stretcher up to a residual spectral phase $\varphi_{\text{residual}}(\omega)$, the electric field of the recompressed signal is simply

$$\tilde{E}_{\text{signal},3}(\omega) = \sqrt{\tilde{I}^{(0)}_{\text{signal},3}(\omega) + \varphi f_{(1)}\delta I_{\text{pump}}(\varphi\omega)}$$

$$\times \exp\left[i\varphi_{\text{residual}}(\omega)\right]. \qquad (3)$$

A first-order development of Eq. (3) gives a spectral representation of the signal:

$$\tilde{E}_{\text{signal},3}(\omega) = \sqrt{\tilde{I}^{(0)}_{\text{signal},3}(\omega)}\,\exp\left[i\varphi_{\text{residual}}(\omega)\right]$$

$$\times \left[1 + \frac{\varphi f_{(1)}\delta I_{\text{pump}}(\varphi\omega)}{2\tilde{I}^{(0)}_{\text{signal},3}(\omega)}\right]. \qquad (4)$$

One can define

$$\tilde{E}^{(0)}_{\text{signal},3}(\omega) = \sqrt{\tilde{I}^{(0)}_{\text{signal},3}(\omega)}\,\exp\left[i\varphi_{\text{residual}}(\omega)\right]$$

as the electric field of the recompressed signal in the absence of noise. In the OPCPA process, the spectral density of the amplified signal is usually approximately constant (or slowly varying) because of saturation effects, so that $\tilde{I}^{(0)}_{\text{signal},3}(\omega)$ is replaced by $\varphi I_{\text{signal},2}$ in the denominator of Eq. (4). This leads to

$$\tilde{E}_{\text{signal},3}(\omega) = \tilde{E}^{(0)}_{\text{signal},3}(\omega)\left[1 + \frac{f_{(1)}\delta I_{\text{pump}}(\varphi\omega)}{2 I_{\text{signal},2}}\right]. \qquad (5)$$

The Fourier transform of Eq. (5) gives the electric field in the temporal domain:

$$E_{\text{signal},3}(t) = E^{(0)}_{\text{signal},3}(t) + \frac{f_{(1)}}{2 I_{\text{signal},2}\varphi}$$

$$\times E^{(0)}_{\text{signal},3}(t) \otimes \delta\tilde{I}_{\text{pump}}(t/\varphi). \qquad (6)$$

Further simplification stems from defining

$$f_{(1,N)} = f_{(1)} I^{(0)}_{\text{pump}}\big/ I_{\text{signal},2},$$

which is the change in intensity of the amplified signal normalized to the intensity of the amplified signal for a change in the pump intensity normalized to the pump intensity. The field of

the recompressed signal is

$$
E_{\text{signal},3}(t) = E_{\text{signal},3}^{(0)}(t) + \frac{f_{(1,N)}}{2\varphi I_{\text{pump}}^{(0)}}
$$

$$
\times E_{\text{signal},3}^{(0)}(t) \otimes \delta \tilde{I}_{\text{pump}}(t/\varphi), \qquad (7)
$$

and the intensity of the compressed signal is

$$
I_{\text{signal},3}(t) = I_{\text{signal},3}^{(0)}(t) + \frac{f_{(1,N)}^2}{4\left[\varphi I_{\text{pump}}^{(0)}\right]^2}
$$

$$
\times \left| E_{\text{signal},3}^{(0)}(t) \otimes \delta \tilde{I}_{\text{pump}}(t/\varphi) \right|^2, \qquad (8)
$$

using the fact that the first term in the right-hand side of Eq. (7) is a short pulse while the second term describes the contrast reduction over a large temporal range.

When the amplifier is saturated [Fig. 111.2(b)], $f_{(1)} = 0$ and Eq. (2) must be replaced by the second-order decomposition of f, which is

$$
f\left[\tilde{I}_{\text{signal},0}(\omega)\big/\varphi, I_{\text{pump}}(\varphi\omega)\right]
$$

$$
= f\left[\tilde{I}_{\text{signal},0}(\omega)\big/\varphi, I_{\text{pump}}^{(0)}(\varphi\omega)\right]
$$

$$
+ \frac{1}{2}\left[\delta I_{\text{pump}}(\varphi\omega)\right]^2
$$

$$
\times \frac{\partial^2 f}{\partial I_{\text{pump}}^2}\left[\tilde{I}_{\text{signal},0}(\omega)\big/\varphi, I_{\text{pump}}^{(0)}(\varphi\omega)\right]. \qquad (9)
$$

Assuming that the second-order derivative of f with respect to the pump intensity does not depend on the signal intensity, one defines

$$
f_{(2)} = \partial^2 f \big/ \partial I_{\text{pump}}^2\left[\tilde{I}_{\text{signal},0}(\omega)\big/\varphi, I_{\text{pump}}^{(0)}(\varphi\omega)\right].
$$

Replacing $\tilde{I}_{\text{signal},3}^{(0)}(\omega)$ by $\varphi I_{\text{signal},2}$, one obtains

$$
\tilde{E}_{\text{signal},3}(\omega) = \tilde{E}_{\text{signal},3}^{(0)}(\omega)\left[1 + \frac{f_{(2)}\delta I_{\text{pump}}^2(\varphi\omega)}{4 I_{\text{signal},2}}\right]. \qquad (10)
$$

The Fourier transform of Eq. (10) gives the temporal field of the recompressed signal:

$$
E_{\text{signal},3}(t) = E_{\text{signal},3}^{(0)}(t) + \frac{f_{(2,N)}}{4\left[\varphi I_{\text{pump}}^{(0)}\right]^2}E_{\text{signal},3}^{(0)}(t)
$$

$$
\otimes \delta \tilde{I}_{\text{pump}}(t/\varphi) \otimes \delta \tilde{I}_{\text{pump}}(t/\varphi), \qquad (11)
$$

where $f_{(2,N)} = f_{(2)}\left[I_{\text{pump}}^{(0)}\right]^2\big/I_{\text{signal},2}$ is the normalized change in the amplified signal intensity for a normalized change in the pump intensity. Finally, the intensity of the recompressed signal is

$$
I_{\text{signal},3}(t) = I_{\text{signal},3}^{(0)}(t) + \frac{f_{(2,N)}^2}{16\left[\varphi I_{\text{pump}}^{(0)}\right]^4}
$$

$$
\times \left| E_{\text{signal},3}(t) \otimes \delta \tilde{I}_{\text{pump}}(t/\varphi) \otimes \delta \tilde{I}_{\text{pump}}(t/\varphi) \right|^2. \qquad (12)
$$

Equations (8) and (12) are general expressions linking the variations in pump intensity to the intensity of the recompressed pulse in the two practically relevant cases: $f_{(1)} \neq 0$ describes the linear modulation regime, with a linear relation between the pump intensity and the amplified stretched signal intensity around the operating point; $f_{(1)} = 0, f_{(2)} \neq 0$ describe the quadratic modulation regime, with a quadratic relation between the pump intensity and the amplified stretched signal intensity around the operating point. In the next two subsections these general expressions are evaluated when ASE is present on the pump pulse.

3. Contrast Degradation of an OPCPA System in the Linear-Modulation Regime due to the Pump-Pulse ASE

The pump-pulse ASE is described as an additive stationary process E_{ASE}, and the field of the pump pulse is

$$
E_{\text{pump}}(t) = E_{\text{pump}}^{(0)}(t) + E_{\text{ASE}}(t). \qquad (13)
$$

One has at first order

$$I_{pump}(t) = I_{pump}^{(0)}(t) + E_{pump}^{(0)}(t) E_{ASE}^{*}(t)$$
$$+ E_{pump}^{(0)*}(t) E_{ASE}(t),$$

which allows one to identify

$$\delta I_{pump}(t) = E_{pump}^{(0)}(t) E_{ASE}^{*}(t) + E_{pump}^{(0)*}(t) E_{ASE}(t).$$

One can use the simplification

$$E_{pump}^{(0)}(t) = E_{pump}^{(0)*}(t) = \sqrt{I_{pump}^{(0)}}$$

over the interval $[0,T]$, where the pump has significant intensity, and set the ASE electric field to 0 outside the interval $[0,T]$. The electric field of one realization of the ASE restricted to the interval $[0,T]$ and its Fourier transform are noted $E_{ASE,T}$ and $\tilde{E}_{ASE,T}$, respectively. One obtains

$$\delta \tilde{I}_{pump}(\omega) = \sqrt{I_{pump}^{(0)}} \left[\tilde{E}_{ASE,T}(\omega) + \tilde{E}_{ASE,T}^{*}(-\omega) \right]. \quad (14)$$

In the linear modulation regime, the calculation of the intensity of the recompressed pulse using this expression and Eq. (8) leads to

$$I_{signal,3}(t) = I_{signal,3}^{(0)}(t) + \frac{f_{(1,N)}^2}{4\varepsilon_{pump}} \int I_{signal,3}^{(0)}(t - \varphi \omega')$$
$$\times \left[\tilde{I}_{ASE,T}(\omega') + \tilde{I}_{ASE,T}(-\omega') \right] d\omega', \quad (15)$$

where ε_{pump} is the energy of the pump pulse. The pump-induced pedestal is therefore given by a convolution of the symmetrized spectrum of the ASE present on the pump pulse with the recompressed pulse intensity. The intensity of the pedestal is proportional to $f_{(1,N)}^2$. Proper spectral filtering of the pump pulse reduces the temporal extent of the induced pedestal. In the usual case where the recompressed pulse is significantly shorter than the temporal variations of the induced pedestal, Eq. (15) can be simplified as

$$I_{signal,3}(t) = I_{signal,3}^{(0)}(t) + \frac{f_{(1,N)}^2 \varepsilon_{signal}^{(0)}}{4\varphi \varepsilon_{pump}}$$
$$\times \left[\tilde{I}_{ASE,T}(t/\varphi) + \tilde{I}_{ASE,T}(-t/\varphi) \right]. \quad (16)$$

The pedestal due to the ASE present on the pump pulse is therefore directly given by a symmetrized version of the spectrum of the ASE present on the pump pulse. The symmetrized spectrum of the ASE is spread in time proportionally to the second-order dispersion of the chirped pulse. Integration of Eq. (15) gives

$$\varepsilon_{signal} = \varepsilon_{signal}^{(0)} \left[1 + f_{(1,N)}^2 \varepsilon_{ASE,T} / 2\varepsilon_{pump} \right],$$

which allows the energy in the pedestal $\varepsilon_{pedestal}$ normalized to the energy of the signal $\varepsilon_{signal}^{(0)}$ to be expressed as

$$\frac{\varepsilon_{pedestal}}{\varepsilon_{signal}^{(0)}} = \frac{f_{(1,N)}^2}{2} \frac{\varepsilon_{ASE,T}}{\varepsilon_{pump}}. \quad (17)$$

The ratio of the pedestal energy to the signal energy,

$$\varepsilon_{pedestal} / \varepsilon_{signal}^{(0)},$$

is directly proportional to the ratio of the energy of the ASE in the temporal range defined by the pump to the energy of the pump. The ratio $\varepsilon_{ASE,T} / \varepsilon_{pump}$ is called "fractional ASE energy" in the remainder of this article.

4. Contrast Degradation of an OPCPA System in the Quadratic-Modulation Regime due to the Pump ASE

The intensity of the recompressed pulse for an OPCPA system in the quadratic-modulation regime with ASE present on the pump can be calculated using Eqs. (12) and (14):

$$I_{signal,3}(t) = I_{signal,3}^{(0)}(t) + \frac{f_{(2,N)}^2}{8(\varphi \varepsilon_{pump})^2} I_{signal,3}^{(0)}(t)$$
$$\otimes \left[\tilde{I}_{ASE,T}(t/\varphi) + \tilde{I}_{ASE,T}(-t/\varphi) \right]$$
$$\otimes \left[\tilde{I}_{ASE,T}(t/\varphi) + \tilde{I}_{ASE,T}(-t/\varphi) \right]. \quad (18)$$

Equation (18) shows that the pedestal is given by the double convolution of the symmetrized spectrum of the pump ASE

with the recompressed signal in the absence of pump ASE. The convolution of the symmetrized spectrum of ASE with itself is broader than the spectrum of ASE (e.g., by a factor $\sqrt{2}$ for a Gaussian spectrum). Therefore, the temporal extent of the pedestal is larger than in the linear-modulation regime. In the case where the intensity of the recompressed signal is short compared to the temporal variations of the pedestal, Eq. (18) can be simplified into

$$I_{\text{signal}, 3}(t) = I_{\text{signal}, 3}^{(0)}(t) + \frac{f_{(2,N)}^2 \varepsilon_{\text{signal}}^{(0)}}{8\varphi^2 \varepsilon_{\text{pump}}^2}$$

$$\times \left[\tilde{I}_{\text{ASE}, T}(t/\varphi) + \tilde{I}_{\text{ASE}, T}(-t/\varphi) \right]$$

$$\otimes \left[\tilde{I}_{\text{ASE}, T}(t/\varphi) + \tilde{I}_{\text{ASE}, T}(-t/\varphi) \right]. \quad (19)$$

Finally, integrating Eq. (18) leads to the energy in the pedestal,

$$\frac{\varepsilon_{\text{pedestal}}}{\varepsilon_{\text{signal}}^{(0)}} = \frac{f_{(2,N)}^2 \varepsilon_{\text{ASE}, T}^2}{2\varepsilon_{\text{pump}}^2}. \quad (20)$$

In the quadratic-modulation regime, the ratio of the energy of the pedestal to the energy of the signal is proportional to the square of the fractional ASE energy. Comparing Eq. (20) with Eq. (17) leads to the conclusion that if $\varepsilon_{\text{ASE}, T}/\varepsilon_{\text{pump}} < \left[f_{(1,N)}/f_{(2,N)} \right]^2$, there is less energy in the pedestal when the amplifier is run in the quadratic-modulation regime. Operating the OPCPA in the saturation regime locally decreases the modulation of the output intensity and reduces the total energy of the associated temporal pedestal, provided that the previous inequality is verified.

Simulations of Pump-Induced Contrast Degradation

1. Model Description

Simulations of an OPCPA system with parameters similar to those of the OPCPA preamplifier of LLE's Multi-Terawatt laser[10] and the front end of the OMEGA EP Laser Facility[17] have been performed. The signal has a central wavelength equal to 1053 nm. The case of a flat spectral density has been simulated since it corresponds closely to the derivations performed in the previous section. The case of a Gaussian spectral density with a full width at half maximum (FWHM) equal to 6 nm has also been simulated since it is closer to the actual experimental conditions. The stretcher introduces a dispersion equal to 300 ps/nm, i.e., $\varphi = 1.76 \times 10^{22}$ s². The preamplifier

has two lithium triborate (LBO) crystals cut for type-I phase matching at 1053 nm and 526.5 nm in collinear interaction, i.e., $\varphi_{\text{LBO}} = 11.8°$ and $\theta_{\text{LBO}} = 90°$, with a total length of 59.5 mm. The OPCPA pump at 526.5 nm is obtained by doubling a pump pulse at 1053 nm in an 11-mm LBO crystal. The pump at 1053 nm is a 20th-order super-Gaussian, with a FWHM equal to 2.6 ns. The intensity of the up-converted pump has been obtained using a Runge–Kutta resolution of the corresponding nonlinear equations. Figure 111.3 displays the normalized intensity of the pump and stretched signal in the OPCPA crystal. The operation of the preamplifier was simulated by solving the system of three equations describing the parametric interaction of the electric field of the signal, idler, and pump using the Runge–Kutta method. No spatial resolution or temporal effects have been introduced, for the reasons expressed at the beginning of the previous section. It is straightforward (although computationally more intensive) to introduce these effects. The phase mismatch between the interacting waves was chosen equal to zero. Figure 111.4 displays the amplified stretched signal intensity as a function of the pump intensity for an input stretched signal intensity of 0.1 W/cm², i.e., the function $I_{\text{signal}, 2} = f\left[I_{\text{signal}, 1}, I_{\text{pump}} \right]$ used in the previous section for $I_{\text{signal},1} = 0.1$ W/cm². Points A and B correspond to the linear- and quadratic-modulation regimes, respectively. A fit of the curve plotted in Fig. 111.4 around these two points leads to the values $f_{(1,N)} = 8$ and $f_{(2,N)} = 66$. The next two subsections present the contrast degradation results for a pump with ASE and a signal with constant spectral density followed by results for a pump with ASE and a signal with a Gaussian spectral density. For the sake of clarity, the intensity of the recompressed signal is plotted only at negative times (i.e., before the peak of the signal), bearing in mind that the pump-induced contrast degradation is symmetric.
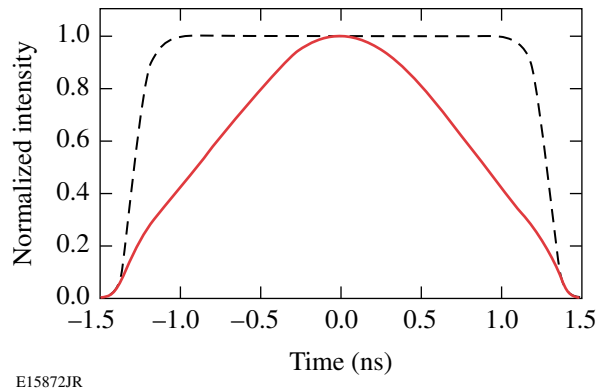

E15872JR

Figure 111.3
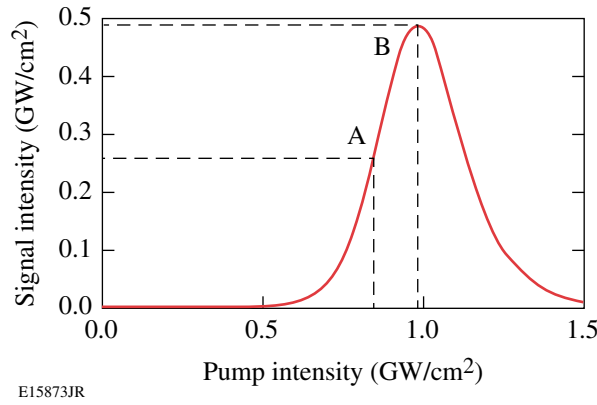Normalized intensity of the chirped Gaussian signal (solid curve) and pump (dashed curve) in the OPCPA system.

Figure 111.4
Transfer function of the OPCPA preamplifier for a signal intensity equal to 0.1 W/cm^2. Points A and B identify the linear and quadratic regimes of operation, respectively.

2. Pump with ASE and Signal with Flat Spectral Density

In this section, the stretched signal has a flat spectral density and an intensity of 0.1 W/cm^2. The pump ASE spectrum is assumed Gaussian and centered at the wavelength of the pump pulse. The FWHM of the spectrum is chosen equal to either 0.14 nm (which was experimentally measured on the Nd:YLF regenerative amplifier used to generate the pump pulse) or 0.03 nm (which corresponds to a hypothetical pump spectral bandpass filtering). Figure 111.5 displays close-ups of the simulated intensity of the pump for an ASE bandwidth of 0.14 nm and 0.03 nm at various fractional ASE energies $\varepsilon_{ASE,T}/\varepsilon_{pump}$. The homodyne beating of the electric field of the ASE with the electric field of the pump leads to significant pump intensity modulation even at low ASE energy levels. Figure 111.6 displays a comparison of the results of the simulation with the analytical results for the 0.14-nm bandwidth. The OPCPA is run either in the linear modulation regime [Figs. 111.6(a)–111.6(c)] or in the quadratic-modulation regime [Figs. 111.6(d)–111.6(f)]. The fractional ASE energy is specified as 10^{-5}, 10^{-4}, and 10^{-3}. Significant pedestal levels are observed, even for relatively low pump intensity modulation, indicating that such contrast degradation can severely limit OPCPA systems, or laser systems that include an OPCPA as one of their amplifiers. Good agreement of the simulations with the analytical predictions is obtained. Discrepancy in the quadratic modulation regime at low fractional ASE energies is attributed to the leading and the falling edge of the pump, for which the amplification process is in the linear regime. The pedestal due to the pump ASE extends at longer times in the case of quadratic modulation, as expected from the double convolution of Eq. (18). The pedestal is typically more intense at short times in the linear regime, and it can also be seen that the total energy in the
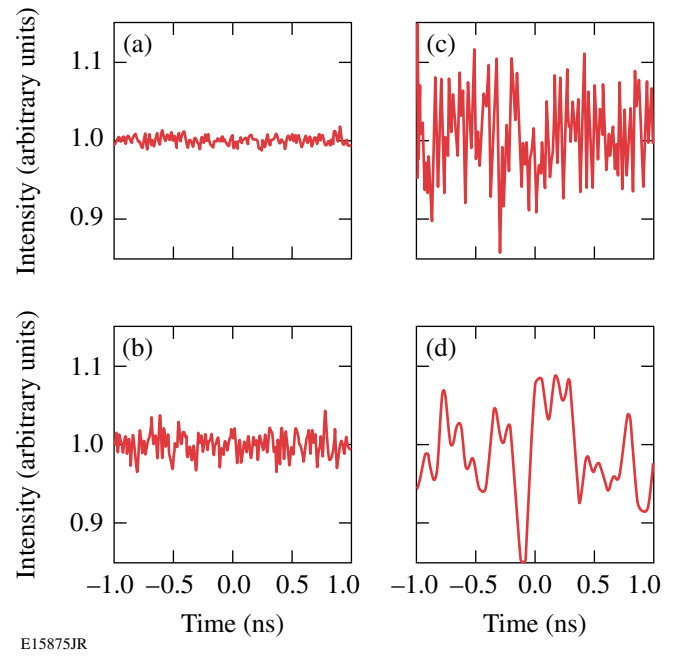

Figure 111.5
Close-ups of the temporal intensity of the pump for ASE with a Gaussian spectrum with a FWHM equal to 0.14 nm and a fractional energy equal to (a) 10^{-5}, (b) 10^{-4}, and (c) 10^{-3}, and (d) for ASE with a Gaussian spectrum with a FWHM equal to 0.03 nm and a fractional energy equal to 10^{-3}.

pedestal is smaller in the quadratic modulation regime than in the linear modulation regime {in agreement with the relation $\varepsilon_{ASE,T}/\varepsilon_{pump} < \left[f_{(1,N)}/f_{(2,N)}\right]^2$, with $\left[f_{(1,N)}/f_{(2,N)}\right]^2 = 0.014$}. It should be noted, however, that the two modulation regimes lead to similar pedestal levels around –100 ps. Figures 111.7(a) and 111.7(d) display the intensity of the recompressed signal for an ASE bandwidth of 0.03 nm and a fractional ASE energy equal to 10^{-3}, which can be compared to the intensity plotted in Figs. 111.6(c) and 111.6(f). Reduction of the bandwidth of the pump ASE leads to a drastic improvement of the signal temporal contrast. This result shows that a significant increase in the contrast of OPCPA systems can be obtained via proper spectral filtering of the pump pulse, as is discussed in **Experimental Demonstration of Temporal Contrast Improvement of an OPCPA System by Pump Spectral Filtering** (p. 144). While this was expressed previously in terms of the coherence time of the pump ASE,[19] the temporal contrast away from the peak of the signal is influenced mostly by the spectral density of the ASE at optical frequencies significantly different from the central frequency of the pump. A non-zero spectral density at these optical frequencies leads to a finite extinction ratio for the pulse. The coherence time of the ASE describes the variations of the temporal electric field of the ASE due to interference between different optical frequencies in the ASE spectrum.

Figure 111.6
Intensity of the recompressed signal for an input signal with a flat spectral density and an ASE Gaussian spectrum with a FWHM equal to 0.14 nm. (a)–(c) correspond to an amplifier run in the linear-modulation regime when the fractional ASE energy is equal to (a) 10^{-5}, (b) 10^{-4}, and (c) 10^{-3}. (d)–(f) correspond to an amplifier run in the quadratic-modulation regime when the fractional ASE energy is equal to (d) 10^{-5}, (e) 10^{-4}, and (f) 10^{-3}. In each case, the simulated intensity is plotted with a continuous line, and the intensity predicted analytically is plotted with solid circles.

Figure 111.7
Intensity of the recompressed signal for an input signal with a flat spectral density, ASE with various Gaussian spectra, and fractional ASE energy equal to 10^{-3}. (a) and (d) correspond to a FWHM equal to 0.03 nm in the linear and quadratic modulation regimes, respectively. (b) and (e) correspond to a FWHM equal to 0.14 nm filtered by a 0.20-nm FWHM, 20th-order super-Gaussian filter in the linear and quadratic modulation regimes, respectively. (c) and (f) correspond to a FWHM equal to 0.14 nm centered 0.07 nm away from the central wavelength of the pump in the linear and quadratic modulation regimes. In each case, the simulated intensity is plotted with a continuous line, and the intensity predicted analytically is plotted with solid circles.

However, the modulations of pump intensity are mostly due to the interference between optical frequencies of the noiseless pump pulse and optical frequencies of the pump ASE. Figure 111.7 presents simulations and analytic predictions for two different ASE spectra that have a FWHM equal to 0.14 nm, i.e., the same coherence time, for a fractional ASE energy equal to 10^{-3}. In the first case [Figs. 111.7(b) and 111.7(e)], a 20th-order super-Gaussian filter with 0.20-nm FWHM has been used to filter the ASE. A large decrease in the level of the pedestal is observed away from the peak of the pulse, although the pedestal conserved its value closer to the peak, as expected from the dependence of the pedestal to the spectrum of the ASE. In the second case [Figs. 111.7(c) and 111.7(f)], the ASE has a Gaussian spectrum with 0.14-nm FWHM centered 0.07 nm away from the central wavelength of the pump. The contrast is significantly degraded compared to Figs. 111.6(c) and 111.6(f), and an increase of the pedestal intensity by approximately 20 dB is observed. Optimization of the contrast can be performed by proper spectral filtering of the pump. A narrow filter on the pump pulse increases the contrast of the recompressed signal and is not detrimental to the operation of the OPCPA system as long as the pump pulse is not temporally distorted by the spectral filter. Generally speaking, the pedestal shape, extent, and intensity vary significantly with the energy of the ASE, its spectrum, and the regime of operation of the amplifier.

3. Pump with ASE and Signal with Gaussian Spectral Density

In this section, the spectral density of the signal is assumed Gaussian, and the intensity of the stretched signal varies significantly as a function of time, taking its maximal value

of 0.1 W/cm^2 at the peak of the pulse. The condition that the first-order derivative or second-order derivative of the function f as a function of the intensity of the signal is independent of the signal intensity is not strictly verified. Some temporal components (i.e., spectral components) of the signal have an optical intensity placing them in the quadratic-modulation regime for the OPCPA process, but other components have an optical intensity placing them in the linear-modulation regime. The contrast of the recompressed signal is generally linked in a nontrivial manner to the noise of the pump pulse. Figure 111.8 displays the transfer function between pump intensity and output signal intensity for a signal input intensity equal to 0.1 W/cm^2 and 0.05 W/cm^2. While the pump intensity corresponding to point B ensures that the output signal intensity is approximately the same for these two input signal intensities (i.e., the spectral density of the amplified pulse does not depend on the wavelength at first order), it allows operation only in the quadratic-modulation regime for the highest signal intensity. Figure 111.9 presents the intensities simulated with ASE parameters identical to those of Fig. 111.6. The analytical results plotted on this figure correspond to the stretched signal pulse with a constant intensity of 0.1 W/cm^2. For the linear- and quadratic-modulation regimes, no significant difference between the two sets of simulations is observed, and the analytical derivation is still in good agreement with the simulations. In the linear regime for the peak intensity of the stretched pulse, all of the optical frequencies in the pulse are in a similar linear regime, and the resulting contrast is equivalent to the contrast obtained for a constant spectral density. The discrepancy observed for low ASE energy in the quadratic regime is more prevalent in this case, which indicates that additional contribution to the

E15878JR

Figure 111.8

Transfer function of the parametric preamplifier for a signal intensity equal to 0.1 W/cm^2 (solid curve) and 0.05 W/cm^2 (dashed curve). Points A and B represent the linear- and quadratic-modulation regimes for the OPCPA system for a stretched signal intensity of 0.1 W/cm^2. (a) Full transfer function; (b) close-up around point B.
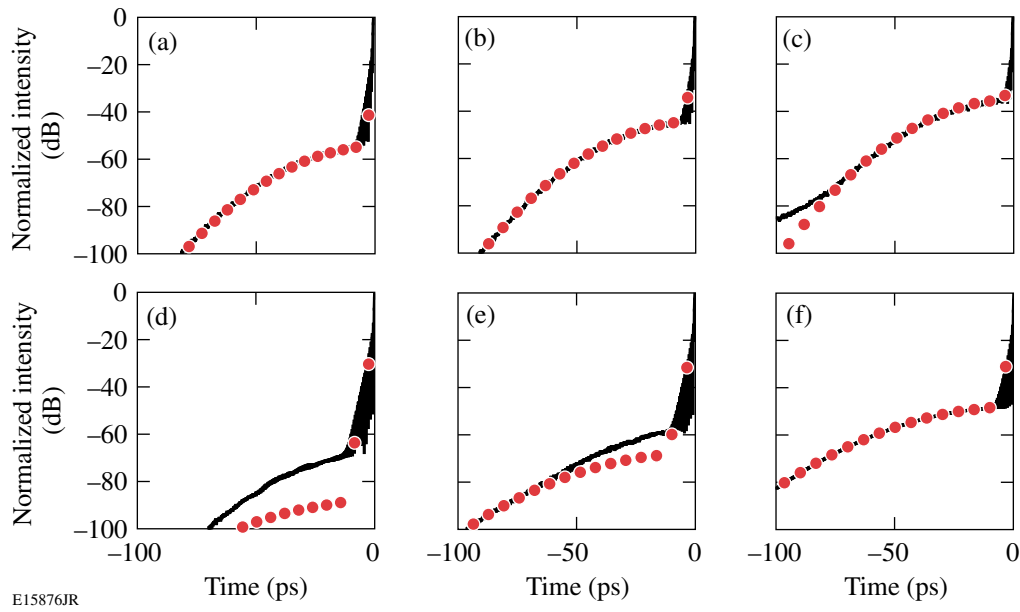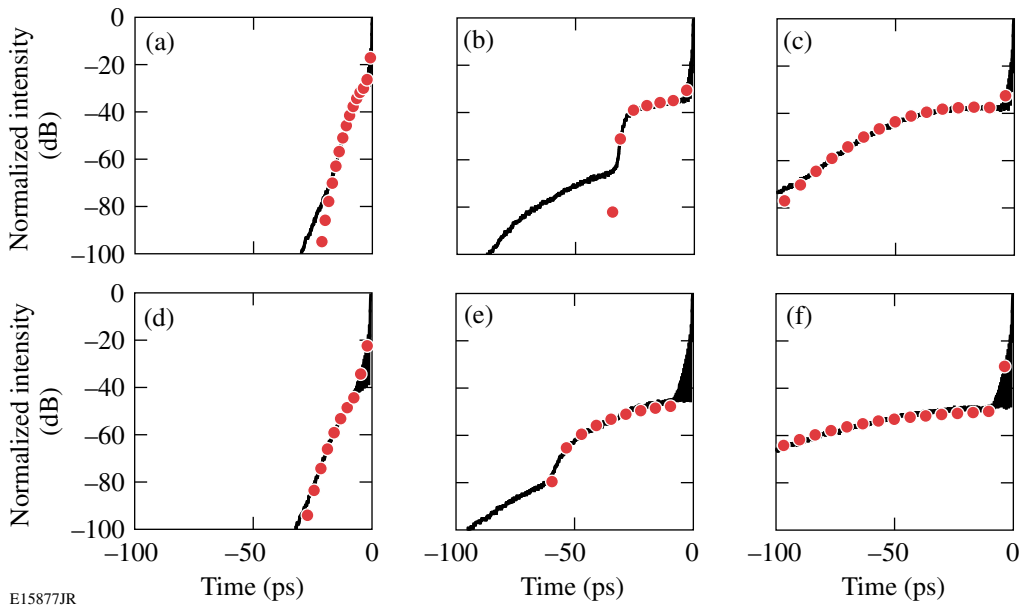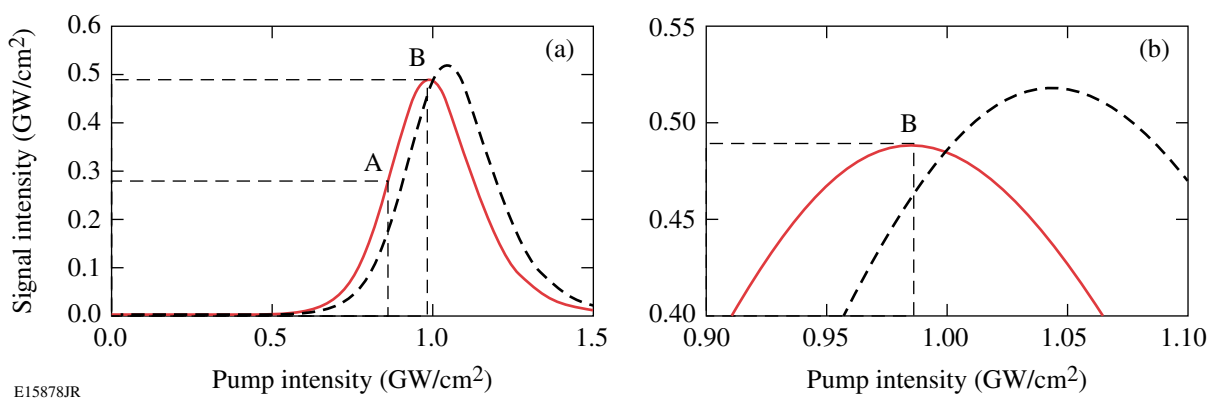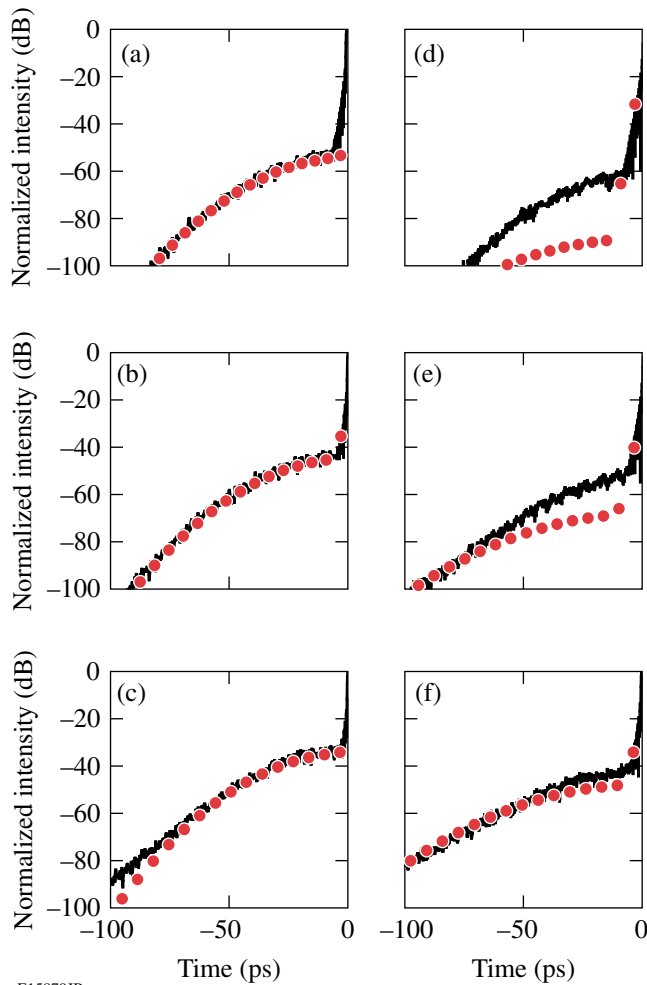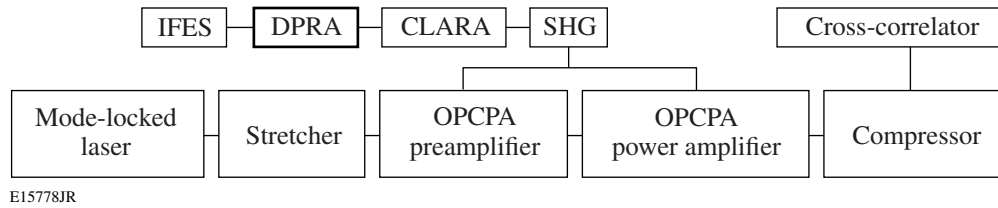
Figure 111.9

Intensity of the recompressed signal for an input signal with a Gaussian spectral density and ASE with a Gaussian spectrum with a FWHM equal to 0.14 nm. (a)–(c) correspond to an amplifier run in the linear-modulation regime when the fractional ASE energy is equal to (a) 10^{-5}, (b) 10^{-4}, and (c) 10^{-3}. (d)–(f) correspond to an amplifier run in the quadratic-modulation regime when the fractional ASE energy is equal to (d) 10^{-5}, (e) 10^{-4}, and (f) 10^{-3}. In each case, the simulated intensity is plotted with a continuous line, and the intensity predicted analytically is plotted with solid circles.

pedestal is present due to some components of the signal in the linear-modulation regime. The coupling between pump intensity and amplified signal intensity for these wavelengths is smaller than at point A of Fig. 111.4. A fit of the dashed curve of Fig. 111.8 at its intersection with the vertical dashed line representing the pump intensity for these simulations leads to $f_{(1,N)} = 4$, which implies a smaller impact of the pump intensity modulation. These results demonstrate that, in the general case, both linear- and quadratic-modulation regimes influence the induced pedestal on an OPCPA system.

Experimental Demonstration of Temporal Contrast Improvement of an OPCPA System by Pump Spectral Filtering

1. Experimental Setup

A general approach to significantly improve the contrast of OPCPA systems by spectrally filtering the pump pulse has been experimentally demonstrated. Simple and efficient filtering of the pump pulse is performed in a regenerative amplifier using a VBG, and the bandwidth of the filtering is narrowed significantly by the large number of round-trips in the cavity. Contrast improvement by regenerative spectral filtering was performed on the prototype front end of the OMEGA EP Laser Facility (Fig. 111.10).[10,17] The pump pulse is generated by a fiber integrated front-end source (IFES), where a 2.4-ns pulse around 1053 nm is temporally shaped to precompensate the square-pulse distortion during amplification. This pulse is amplified at 5 Hz from 100 pJ to 4 mJ in a diode-pumped regenerative amplifier (DPRA).[20] One of the flat end-cavity mirrors of the DPRA is replaced by the VBG and a flat mirror, so that the mirror acts as the DPRA end-cavity mirror and the beam is reflected twice per round-trip on the VBG. The incidence angle on the VBG, designed for high reflection at 1057.5 nm at normal incidence, is approximately 7° to provide maximum reflection at 1053 nm. The VBG is a bulk piece of photothermo-refractive glass, where a grating is permanently written by UV illumination followed by thermal development.[21] The damage threshold of similar VBG's has been found to be higher than 10 J/cm^2 in the nanosecond regime. With sol-gel antireflection coating, the VBG has a single-pass reflectivity of 99.4% at 1053 nm, and the slight increase in the DPRA build-up time due to the additional losses was compensated by increasing the diode-pump current. No change in the output beam spatial profile was observed. Without active temperature control of the VBG, the DPRA operated for several days in a temperature-controlled room with no variation in performance. (Additional characterization can be found in Ref. 22.) The bandwidth of the VBG reflectivity around 1057.5 nm is 230 pm, which, assuming a Gaussian shape, should provide a 23-pm bandwidth after 50 round-trips in the DPRA, with two reflections on the VBG per round-trip. With the intracavity VBG, the unseeded DPRA output spectrum shows a reduction of the bandwidth of the DPRA from 146 pm to 41 pm, but is broad enough to amplify the pump pulse without distortion (Fig. 111.11). Subsequent amplification to 2 J is performed by four passes in a crystal large-aperture ring amplifier containing two flash-lamp–pumped Nd:YLF rods, after apodization of the DPRA beam.[23] Frequency conversion to 526.5 nm occurs in an 11-mm LBO crystal with an efficiency of 70%. Filtering in the DPRA decreases the amount of ASE from the IFES and

Figure 111.10

Schematic of the laser system. IFES: integrated front-end source; DPRA: diode-pumped regenerative amplifier; CLARA: crystal large-aperture ring amplifier; SHG: sum-harmonic generation. Filtering of the pump pulse is performed in the DPRA (shown above in bold).
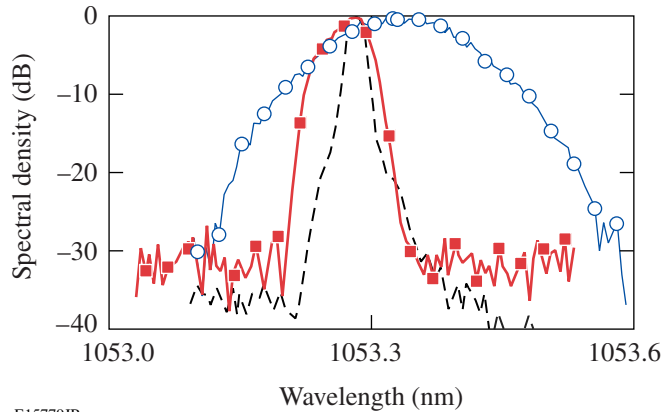
Figure 111.11

Optical spectrum of the unseeded DPRA measured with a mirror in the cavity (thin solid curve with open circles) and with the VBG in the cavity (solid curve with solid squares). The optical spectrum of the signal amplified by the DPRA (dashed curve) is limited by the resolution of the optical spectrum analyzer and is significantly narrower than the unseeded DPRA with the intracavity VBG.

from the DPRA itself (these two high-gain stages having the largest contribution to the pump ASE) and benefits from the large number of reflections on the filter.

The OPCPA system is composed of a mode-locked laser operating at 1053 nm, an Öffner-triplet stretcher providing a dispersion of 300 ps/nm, a preamplifier with two 29.75-mm LBO crystals in a walk-off compensating geometry, a power amplifier with one 16.5-mm LBO crystal, and a two-grating compressor in a double-pass configuration. The pump pulse is split to pump the preamplifier and power amplifier. Amplification of the signal to 250 mJ is achieved, and a portion of the amplified pulse is sent to the diagnostic compressor.

2. Experimental Results

The temporal contrast was measured using a scanning third-order cross-correlator (Sequoia, Amplitude Technologies).

The dynamic range of the diagnostics is 10^{11} but is limited to 10^8 by the parametric fluorescence from the OPCPA system. Postpulses are due to multiple reflections in the cross-correlator and are of no practical concern. Figure 111.12 displays the cross-correlations measured (a) when the preamplifier and power amplifier are operated at full energy, (b) when only the preamplifier is operated at saturation, and (c) when only the preamplifier is operated at half its nominal output power. The prepulse contrast is consistently improved with the intracavity VBG. The pump-induced contrast degradation is particularly important in the preamplifier, even when it is run at saturation, and a contrast improvement of the order of 20 dB is observed. When the preamplifier is run at half output power, a larger coupling between the pump intensity and the amplified signal intensity magnifies the impact of the pump noise on the contrast. These two operating points correspond to the linear- and quadratic-modulation regimes for the preamplifier, as identified by points A and B in Fig. 111.4. The choice of the crystals and pump intensities in this system reduces the spatial-intensity modulations in the amplified signal. This decreases the temporal-intensity modulations in the amplified signal and reduces the impact of the pump-intensity variations on the contrast of the recompressed pulse. Most OPCPA systems are not designed with these considerations in mind, and the contrast improvement is expected to be significant for these systems.

The optical signal-to-noise ratio (OSNR) of the OPCPA pump pulse was reduced by decreasing the average power of the monochromatic source in the IFES from its nominal value of 10 mW to 2 mW, 0.4 mW, and 0.1 mW, and compensating the reduced output energy by increasing the DPRA diode pump current. The reduced OSNR is due to the reduced seed level in both the IFES fiber amplifier and the DPRA. Figure 111.13 displays the cross-correlations measured when the preamplifier and power amplifier are operated in nominal conditions [the cross-correlations measured for the nominal value of 10 mW can be seen in Fig. 111.12(a)]. Without spectral filtering, a large increase in the temporal pedestal is observed, and the contrast
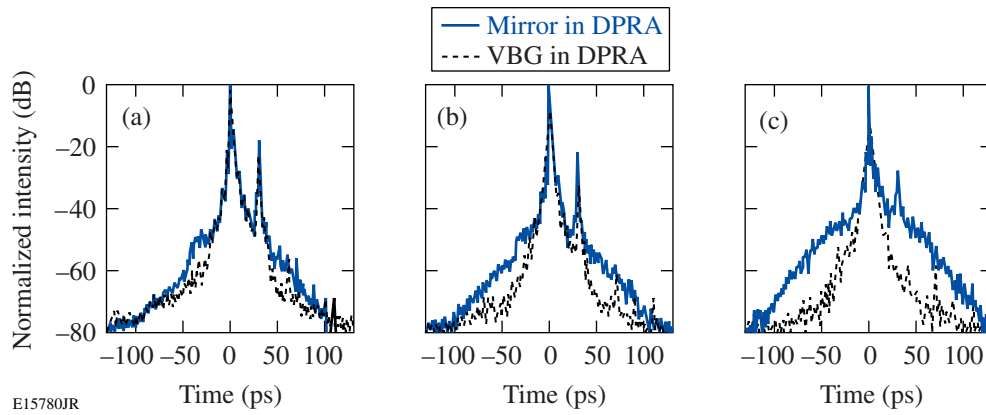
Figure 111.12
Third-order scanning cross-correlation of the OPCPA output pulse (a) when the preamplifier and power amplifier are operated at full energy, (b) when only the preamplifier is operated at saturation, and (c) when only the preamplifier is operated at half its nominal output power. In each case, the cross-correlation measured with the mirror in the DPRA is plotted with a solid line, and the cross-correlation measured with the VBG in the DPRA is plotted with a dashed line.

50 ps before the peak of the pulse is 54 dB, 46 dB, and 35 dB, respectively, for a 2-mW, 0.4-mW, and 0.1-mW average power. No contrast degradation is observed with the filtered DPRA, and the contrast 50 ps before the peak of the pulse is consistently equal to 68 dB.
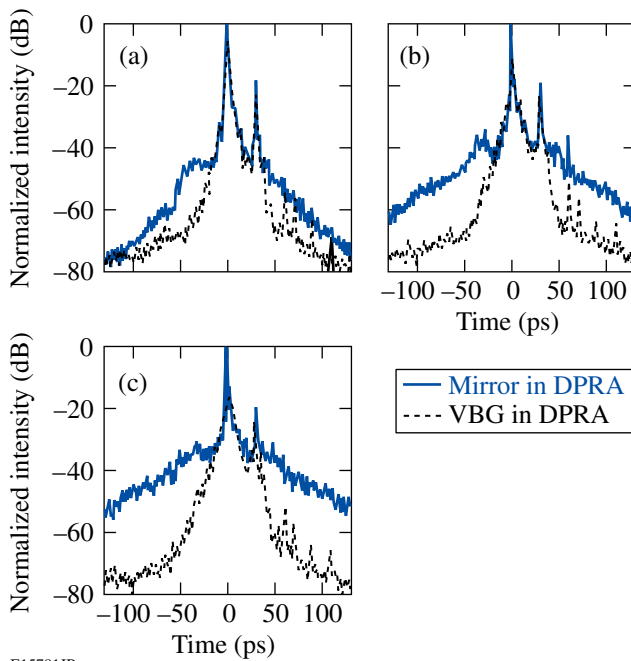
Figure 111.13
Third-order scanning cross-correlation of the OPCPA output pulse when the average power of the monochromatic laser of IFES is reduced from 10 mW to (a) 2 mW, (b) 0.4 mW, and (c) 0.1 mW. In each case, the cross-correlation measured with the mirror in the DPRA is plotted with a solid line, and the cross-correlation measured with the VBG in the DPRA is plotted with a dashed line.

Conclusions

An analysis of pump-induced contrast degradation in an OPCPA system has been performed. The general link between pump modulation and the contrast of the recompressed pulse has been derived in the two cases of practical interest, for which pump-intensity modulation couples either linearly or quadratically to the amplified signal intensity during the parametric process. Analytical expressions linking the spectrum of the ASE present on the pump pulse to the temporal pedestal of the signal amplified in the OPCPA system have been derived and compared to simulations. Significant reduction of the induced temporal pedestal was experimentally demonstrated in an OPCPA system by filtering the pump pulse during its amplification in a regenerative amplifier. The general expressions of the contrast degradation should prove useful for understanding the contrast limitation of current OPCPA systems and predicting the performance of future systems. The demonstrated solution is simple to implement and is applicable to most OPCPA systems.

REFERENCES

1. D. Umstadter, Phys. Plasmas **8**, 1774 (2001).

2. S.-W. Bahk *et al.*, Opt. Lett. **29**, 2837 (2004).

3. J. D. Zuegel, S. Borneis, C. Barty, B. LeGarrec, C. Danson, N. Miyanaga, P. K. Rambo, C. LeBlanc, T. J. Kessler, A. W. Schmid,

L. J. Waxer, J. H. Kelly, B. Kruschwitz, R. Jungquist, E. Moses, J. Britten, I. Jovanovic, J. Dawson, and N. Blanchot, Fusion Sci. Technol. **49**, 453 (2006).

4. M. Nantel *et al.*, IEEE J. Sel. Top. Quantum Electron. **4**, 449 (1998).

5. V. Bagnoud, J. D. Zuegel, N. Forget, and C. Le Blanc, Opt. Express **15**, 5504 (2007).

6. A. Dubietis, G. Jonusauskas, and A. Piskarskas, Opt. Commun. **88**, 437 (1992).

7. I. N. Ross *et al.*, Opt. Commun. **144**, 125 (1997).

8. A. Dubietis, R. Butkus, and A. P. Piskarskas, IEEE J. Sel. Top. Quantum Electron. **12**, 163 (2006).

9. H. Yoshida *et al.*, Opt. Lett. **28**, 257 (2003).

10. V. Bagnoud, I. A. Begishev, M. J. Guardalben, J. Puth, and J. D. Zuegel, Opt. Lett. **30**, 1843 (2005).

11. N. Ishii *et al.*, Opt. Lett. **30**, 567 (2005).

12. I. Jovanovic *et al.*, Opt. Lett. **30**, 1036 (2005).

13. S. Witte *et al.*, Opt. Express **13**, 4903 (2005).

14. V. V. Lozhkarev *et al.*, Opt. Express **14**, 446 (2006).

15. O. V. Chekhlov *et al.*, Opt. Lett. **31**, 3665 (2006).

16. D. Kraemer *et al.*, J. Opt. Soc. Am. B **24**, 813 (2007).

17. J. H. Kelly, L. J. Waxer, V. Bagnoud, I. A. Begishev, J. Bromage, B. E. Kruschwitz, T. J. Kessler, S. J. Loucks, D. N. Maywar, R. L. McCrory, D. D. Meyerhofer, S. F. B. Morse, J. B. Oliver, A. L. Rigatti, A. W. Schmid, C. Stoeckl, S. Dalton, L. Folnsbee, M. J. Guardalben, R. Jungquist, J. Puth, M. J. Shoup III, D. Weiner, and J. D. Zuegel, J. Phys. IV France **133**, 75 (2006).

18. N. Forget *et al.*, Opt. Lett. **30**, 2921 (2005).

19. I. N. Ross, G. H. C. New, and P. K. Bates, Opt. Commun. **273**, 510 (2007).

20. A. V. Okishev and J. D. Zuegel, Appl. Opt. **43**, 6180 (2004).

21. L. B. Glebov *et al.*, in *Laser Weapons Technology III*, edited by W. E. Thompson and P. H. Merritt (SPIE, Bellingham, WA, 2002), Vol. 4724, pp. 101–109.

22. A. V. Okishev, C. Dorrer, V. I. Smirnov, L. B. Glebov, and J. D. Zuegel, Opt. Express **15**, 8197 (2007).

23. V. Bagnoud, M. J. Guardalben, J. Puth, J. D. Zuegel, T. Mooney, and P. Dumas, Appl. Opt. **44**, 282 (2005).

Dual Nuclear Product Observations of Shock Collapse in Inertial Confinement Fusion

The speed and heating of convergent shocks are of fundamental importance for the design of high-gain implosions in inertial confinement fusion (ICF).[1,2] Strong, spherically convergent shocks are formed by the rapid deposition of energy in the form of lasers (direct drive) or x rays (indirect drive) on the surface of a spherical capsule. Current ICF ignition designs include a sequence of up to four convergent shocks that must be precisely timed to coalesce at the inner shell surface in order to obtain maximal shell compression,[3,4] a necessity for high fusion gain. All shocks formed after the first must propagate through hot, already-shocked material, which introduces uncertainty into the shock speed and strength. A thorough understanding of shock speeds in cold and heated material, and in planar and convergent geometries, will be vital for satisfactory ICF implosion performance.

Previous studies of shock propagation relevant to ICF have focused largely on planar geometry.[5,6] The planar approximation works well for the propagation of converging shocks in the shell at early times, but it breaks down as the shock approaches the center of collapse. Nuclear measurements of some aspects of shock collapse using a single nuclear product have also recently been reported.[7,8]

This article presents the first results of temporal and spectral measurements of products from two nuclear reaction types induced by the central collapse of convergent shocks. Observations of these products provide information about the speed and heating of the shocks, as well as the state of the imploding capsule at the time of shock collapse, which, in the experiments discussed here, occurs immediately before the onset of the deceleration phase and the final stages of compression. The dual nuclear reaction measurements act as a powerful constraint and verification of observable and inferred values of shock collapse.

Direct-drive implosions were conducted on the OMEGA laser[9] with 60 beams of ultraviolet (351 nm) light in a 1-ns flattop pulse, a total energy of 23 kJ, and full single-beam smoothing.[10] The spherical capsules had diameters between 860 and 880 μm, plastic (CH) shell thicknesses of 20, 24, or 27 μm, and a flash coating of 0.1 μm of aluminum. The capsules were filled with an equimolar (by atom) mixture of D_2 and ^{3}He gas with a total fill pressure (P_0) of 3.6 or 18 atm at 293 K, corresponding to initial fill mass densities of 0.5 and 2.5 mg/cm^3, respectively.

Three distinct primary nuclear reactions proceed during capsule implosions with D_2 and ^{3}He fuel: $D + D \rightarrow {}^3He + n$; $D + D \rightarrow T + p$; and $D + {}^3He \rightarrow {}^4He + p$. The neutron and proton branches of the D-D reaction have nearly equal probabilities over temperatures of interest. The D-^{3}He reaction depends much more strongly on temperature due to the doubly charged ^{3}He reactant.[11]

Nuclear products were observed by using the proton and neutron temporal diagnostics (PTD and NTD)[8,12] to measure the D-^{3}He and DD-n reaction histories; multiple wedged-range-filter (WRF) proton spectrometers[13] to measure the D-^{3}He proton yield and spectrum; and a magnet-based charged-particle spectrometer[13] to measure D-D protons emitted at shock-bang time. The birth energies of D-^{3}He and D-D protons are 14.7 and 3.0 MeV, respectively.

Experimental results were compared with numerical simulations performed using *LILAC*,[14] a one-dimensional (1-D) Lagrangian hydrodynamic code, which includes laser-beam ray-tracing, a tabular equation of state, and multigroup diffusion radiation transport. The electron thermal energy is transported using a flux-limited diffusion model in which the effective energy flux is defined as the minimum of the diffusion flux and a fraction f of the free-streaming flux. The flux limiter $f = 0.06$ unless otherwise specified.

The D-^{3}He reaction rate history shows two distinct times of nuclear production [Fig. 111.14(a)]: "shock burn" begins shortly after shock collapse and ends near the beginning of the deceleration phase; "compression burn" begins near the onset of the deceleration phase and lasts approximately until stagnation of the imploding shell. For ordinary D^{3}He mixtures, the DD-n

reaction rate during the shock burn is below the diagnostic detection threshold.

The shock and compression components can often be distinguished in D^{3}He proton spectra [Fig. 111.14(b)].[7] The protons emitted at shock-bang time experience relatively little downshift (~0.4 MeV) due to the low total capsule areal density (ρR) at that time. The shell continues to compress after shock burn ends, and by compression-bang time the ρR has increased enough to downshift the D^{3}He protons by several MeV.

The ρR during the shock burn is low enough to also allow nascent 3.0-MeV DD protons to escape the capsule [Fig. 111.14(c)]. Measurement of DD protons emitted during shock burn provides a valuable and sole measurement of the D-D shock yield when the reaction rate is below the NTD threshold. Measurement of their downshift can also provide a double check on the ρR at shock-bang time inferred using the D^{3}He proton spectra, or the sole measurement in cases where the shock component of the D^{3}He proton spectrum cannot be separated from the compression component.

Observed and simulated shock-bang times and D-^{3}He and DD-p shock yields are shown in Fig. 111.15 as functions of shell thickness for implosions of capsules with different P_0. The shock-bang time is the time of peak D-^{3}He nuclear production during the shock-burn phase, the D-^{3}He shock yield includes only the contribution from the higher-energy "shock" component of the D^{3}He-proton spectrum, and the DD-p shock yield includes only that part of the spectrum above the high-energy cutoff of ablator protons[15] [seen at 0.8 MeV in Fig. 111.14(c)].

The figure plots the mean and the standard error of the mean for shot ensembles of each capsule configuration. Summaries of experimental results are included in Tables 111.I and 111.II.

Experiments show that shock-bang time is linearly delayed with increasing shell thickness [Fig. 111.15(a)], corresponding to a shock speed of ~30 km/s in the shell. No difference in shock-bang time was observed for capsules with different P_0. Simulations predict shock-bang time to occur much later than is consistent with experiments,[16] as well as a strong dependence on fill pressure.

Observations show that both D-^{3}He and D-D shock yields decrease for implosions of targets with thicker shells and lower P_0. The reduction factor for lower fill pressures has a lower value (3 to 5), however, than that expected (25) due only to the density dependence of the nuclear fusion rate; the lower density also results in less-efficient thermal coupling between ions and electrons, so that the ion temperature, and consequently the nuclear fusion rate, stays higher.

The average ion temperature at shock-bang time $\langle T_i \rangle_{sh}$ can be inferred using the measured yields of the two different nuclear reactions, based on the ratio of their respective thermal reactivities.[17] Figure 111.16 demonstrates the anticipated higher $\langle T_i \rangle_{sh}$ for 3.6-atm implosions. The shock temperature of 5.4±0.4 keV for 24-μm-thick, 18-atm implosions compares favorably with the value of 6±1 keV obtained by a fit to the shock line width, assuming only thermal broadening, reported by Petrasso *et al.*[7]
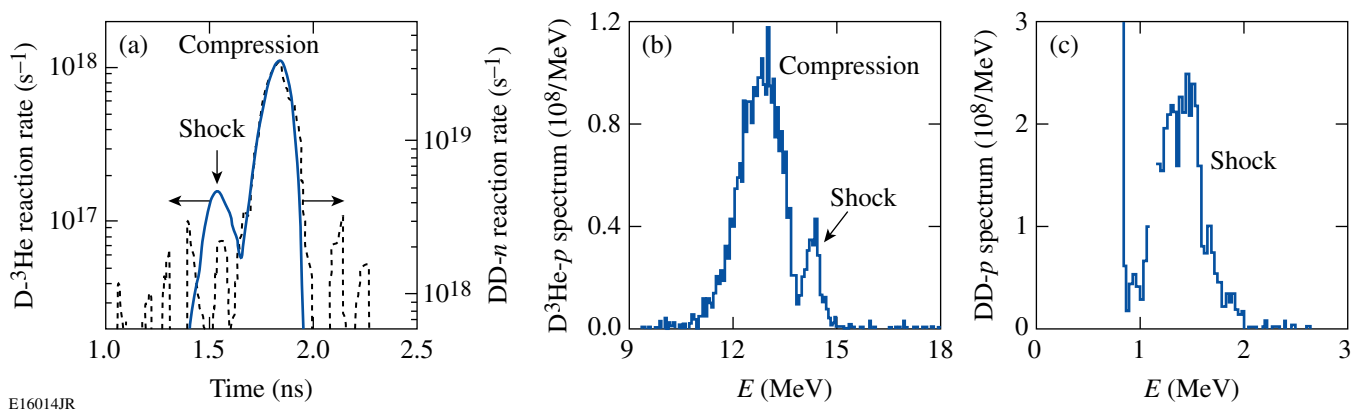

E16014JR

Figure 111.14
Representative experimental observations of D-D and D-^{3}He nuclear products emitted at shock- and compression-bang time from an implosion of a 24-μm-thick CH capsule shell filled with 18 atm of D^{3}He gas (OMEGA shot 38525). (a) D-^{3}He (solid) and DD-n (dashed) reaction rate histories; (b) D^{3}He-proton spectrum; (c) DD-proton spectrum.

E16015JR
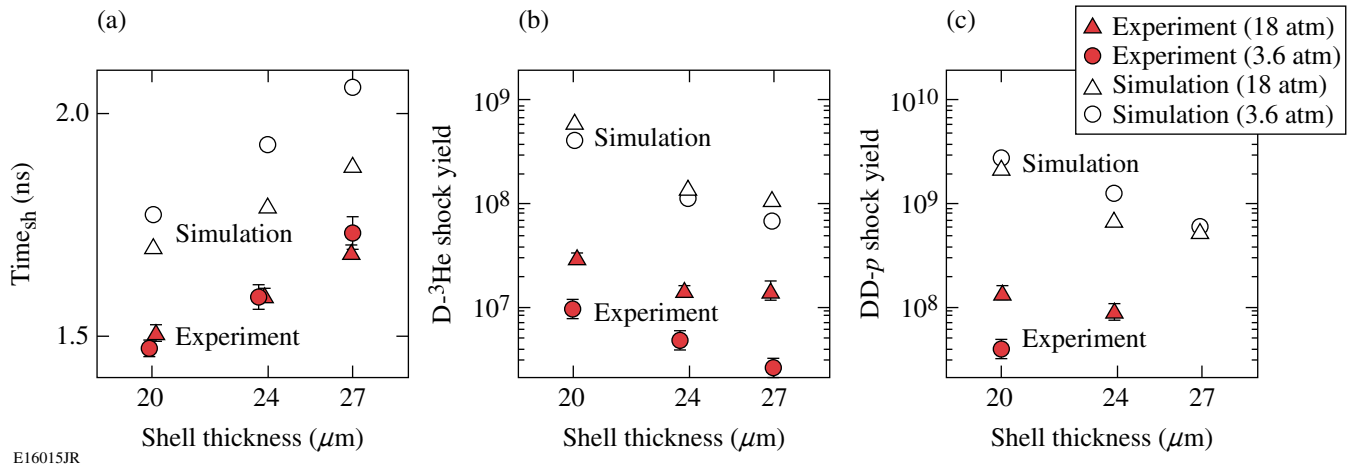
Figure 111.15
Experimental observations (solid) and 1-D simulations (open) of (a) shock-bang time, (b) D-^{3}He shock yield, and (c) DD-p shock yield as a function of capsule shell thickness for ensembles of capsules filled with 18 atm (triangles) or 3.6 atm (circles) of D^{3}He gas.

Table 111.I: Mean and error of measured values of shock-bang time, D-^{3}He shock yield, and ρR at shock time for implosions with different shell thicknesses and fill pressures. The D-^{3}He shock yield is shown as both an absolute yield and a percentage of the total D-^{3}He yield.

P (atm)	ΔR (μm)	N	t_{sh} (ps)	$Y_{p\text{-}s}$ ($\times 10^7$)	err (%)	$Y_{p\text{-}s}$ (% Y_p)	ρR (mg/cm^2)
3.6	19.9	8	1470±16	—	—	—	—
3.6	23.7	6	1585±27	0.48	9	10.6±0.9	9.8±0.4
3.6	27.0	4	1731±39	0.25	20	12.2±1.7	12.0±0.9
18	20.1	8	1506±16	3.09	7	6.2±0.5	8.2±1.0
18	23.9	9	1591±12	1.45	9	9.3±0.6	8.9±0.7
18	26.9	6	1690±11	1.44	18	19.8±2.5	9.4±1.2

Table 111.II: Mean and error of measured values of DD-p shock yield, shock T_i, and ρR at shock time inferred from the downshift of DD-p, for implosions with different shell thicknesses and 18-atm fill pressure. The DD-p shock yield is shown as both an absolute yield and a percentage of the total DD-n yield.

P (atm)	ΔR (μm)	N	$\langle T_i \rangle_{sh}$ (keV)	$Y_{DD\text{-}s}$ ($\times 10^7$)	err (%)	$Y_{DD\text{-}s}$ (% Y_n)	ρR (mg/cm^2)
3.6	19.9	5	7.9±0.9	4.2	10	1.5±0.2	8.3±0.7
18	20.2	3	5.9±0.4	14.1	13	1.2±0.2	9.3±0.6
18	23.9	3	5.4±0.4	9.2	20	1.9±0.3	10.0±0.7
18	27.1	2	—	—	—	—	11.1±1.0

Figure 111.16
Shock-burn–averaged ion temperature, calculated using the ratio of the DD-p to D-^{3}He shock yields from experiments (solid) and from 1-D simulations (open) for capsules filled with 18 atm (triangles) and 3.6 atm (circles) of D^{3}He gas.

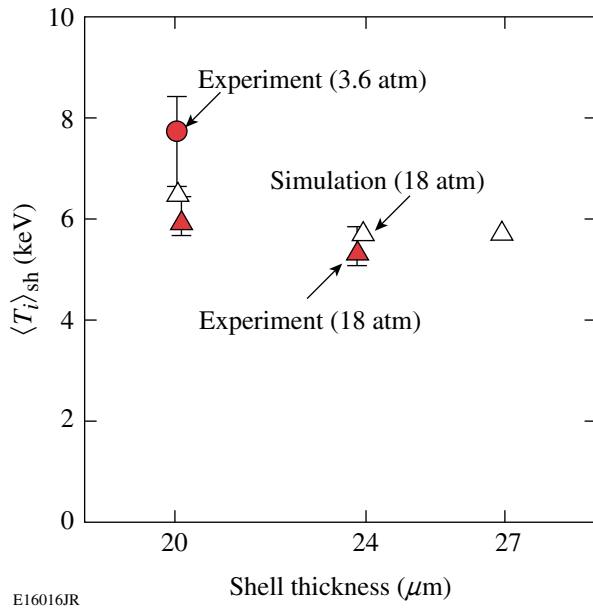Figure 111.17
Shock ρR's for 18-atm (triangles) and 3.6-atm (circles) D^{3}He fills of capsules as functions of shell thickness. The experimental ρR_{sh} is inferred from the downshift of nascent (a) 14.7-MeV D^{3}He protons and (b) 3-MeV DD protons from their birth energy. Markers show mean and standard error. The simulated ρR [open markers in (a)] is the ρR of the implosion weighted by the D-^{3}He reaction rate over the shock burn.

One-dimensional simulations grossly overestimate the experimentally observed D-^{3}He and DD-p shock yields. The experimental yield over the calculated yield (YOC) is 3%–4% for 3.6-atm fills and 5%–15% for 18-atm fills. These higher predicted yields combined with only slightly higher values of $\langle T_i \rangle_{sh}$ indicate that simulations calculate that, compared to experiment, capsules at shock-bang time are more highly compressed.

The compression of the capsule at shock-bang time can be quantified by the shock-burn–averaged areal density, ρR_{sh}. Experimentally, ρR_{sh} is inferred from the measured mean energy downshift from the birth energy of DD protons or D^{3}He protons in the shock line, using a theoretical formalism to relate their energy loss to plasma parameters.[13,18] The inferred ρR_{sh} value is insensitive to the exact values assumed, particularly when using the downshift of 14.7-MeV protons; a CH plasma density of 3 g/cm^3 and a temperature of 0.3 keV were used to derive the quoted ρR_{sh} values. The simulated ρR_{sh} is calculated as the ρR weighted by the D-^{3}He reaction rate over the shock burn.

Excellent agreement is observed between ρR_{sh} inferred from spectral results obtained using both DD and D^{3}He protons, as shown in Fig. 111.17 and Tables 111.I and 111.II. Compared to

experiments, 1-D simulations predict much higher ρR_{sh} and show an opposing trend of ρR_{sh} as a function of shell thickness and a very strong dependence of ρR_{sh} on P_0. A higher predicted ρR_{sh} is consistent with the expectation of higher compression discussed above.

On the basis of physical principles, ρR_{sh} should be nearly independent of P_0 since the trajectory of the shell will not be affected by the fill gas until the deceleration phase, well after shock-bang time. Scrutiny of the simulated reaction rate histo-

ries for low-P_0 implosions reveals additional nuclear production caused by a reflection of the outgoing shock from the imploding shell. This shock reverberation explains the larger discrepancy for the yields, shock-bang times, and ρR_{sh}'s seen for low-P_0 simulations; however, no evidence of heating due to the shock reverberation is seen in the observed reaction rates.

Several competing shell-thickness–dependent effects could alter ρR_{sh}. For the same laser drive, the same amount of shell mass gets ablated, which for thicker shells results in more remaining mass (which tends to increase ρR_{sh}) and lower implosion velocity (which tends to decrease ρR_{sh}). The opposing trends of ρR_{sh} with shell thickness for experiments and simulations demonstrate that the simulations are improperly treating these competing effects.

The overprediction of shock yields, ρR_{sh}'s, and time until shock collapse by 1-D simulations might at first indicate the need for 2-D or 3-D simulations to capture the complete physics of collapsing shocks. Indeed, theoretical analysis suggests that converging shocks are weakly unstable to initial asymmetries;[19] however, experiments have demonstrated that the observables are highly robust to drive asymmetries[20] and that the growth of asymmetries due to hydrodynamic instabilities is insufficient to mix the shell with the fill gas at shock collapse time.[21] The collapse and resulting nuclear production of converging shocks can thus be well approximated as a 1-D situation; more computationally intensive 2-D or 3-D simulations are unnecessary.

One-dimensional simulations can be adjusted to match experimental timing by increasing the flux limiter *f*; however, increasing *f* will also push the shock yield and ρR into further disagreement with experiments. No value of the flux limiter can match both the shock timing and yield simultaneously, suggesting a limitation of handling shock collapse using only a hydrodynamic treatment. The fuel plasma during the shock burn is hotter and sparser than it is during the compression burn, which results in lower collision frequency and ion mean free paths that are comparable to the size of the plasma. Comparison of hydrodynamic and kinetic simulations[22] shows that the kinetic treatment results in a weaker reflected shock and a nuclear production substantially lower during the shock burn.

In summary, nuclear production induced by the collapse of strong, spherically convergent shocks was observed using temporal and spectral measurements of products from two distinct nuclear reactions. The dual nuclear observations create a comprehensive description of the state of the implosion at shock-collapse time, which, temporal measurements show, occurs immediately before the onset of the deceleration phase. Measuring both DD and D^{3}He nuclear products acts as a powerful constraint and verification of data reliability; observations of their yields and spectra are used to infer temperatures and areal densities at shock-bang time near 6 keV and 10 mg/cm^2, respectively. Comparison of the experimental results to predictions made by 1-D hydrodynamic simulations revealed numerous differences, including earlier time of shock collapse, lower nuclear production and fill-gas temperature, and lower capsule compression at shock-bang time. Given the importance of shock timing and heating to the success of ignition in ICF, it is worthwhile to re-examine the treatment of shocks in current hydrodynamic codes; the constraints imposed by this compelling set of dual nuclear shock-burn measurements make it possible for efficient and insightful alterations to be selectively made in ICF simulations at a level hitherto unavailable.

REFERENCES

1. J. Nuckolls *et al.*, Nature **239**, 139 (1972).

2. S. Atzeni and J. Meyer-ter-Vehn, *The Physics of Inertial Fusion: Beam Plasma Interaction, Hydrodynamics, Hot Dense Matter*, International Series of Monographs on Physics (Clarendon Press, Oxford, 2004).

3. D. H. Munro *et al.*, Phys. Plasmas **8**, 2245 (2001).

4. R. L. McCrory, R. E. Bahr, R. Betti, T. R. Boehly, T. J. B. Collins, R. S. Craxton, J. A. Delettrez, W. R. Donaldson, R. Epstein, J. Frenje, V. Yu. Glebov, V. N. Goncharov, O. Gotchev, R. Q. Gram, D. R. Harding, D. G. Hicks, P. A. Jaanimagi, R. L. Keck, J. Kelly, J. P. Knauer, C. K. Li, S. J. Loucks, L. D. Lund, F. J. Marshall, P. W. McKenty, D. D. Meyerhofer, S. F. B. Morse, R. D. Petrasso, P. B. Radha, S. P. Regan, S. Roberts, F. Séguin, W. Seka, S. Skupsky, V. Smalyuk, C. Sorce, J. M. Soures, C. Stoeckl, R. P. J. Town, M. D. Wittman, B. Yaakobi, and J. D. Zuegel, Nucl. Fusion **41**, 1413 (2001).

5. T. R. Boehly, E. Vianello, J. E. Miller, R. S. Craxton, T. J. B. Collins, V. N. Goncharov, I. V. Igumenshchev, D. D. Meyerhofer, D. G. Hicks, P. M. Celliers, and G. W. Collins, Phys. Plasmas **13**, 056303 (2006).

6. V. N. Goncharov, O. V. Gotchev, E. Vianello, T. R. Boehly, J. P. Knauer, P. W. McKenty, P. B. Radha, S. P. Regan, T. C. Sangster, S. Skupsky, V. A. Smalyuk, R. Betti, R. L. McCrory, D. D. Meyerhofer, and C. Cherfils-Clérouin, Phys. Plasmas **13**, 012702 (2006).

7. R. D. Petrasso, J. A. Frenje, C. K. Li, F. H. Séguin, J. R. Rygg, B. E. Schwartz, S. Kurebayashi, P. B. Radha, C. Stoeckl, J. M. Soures, J. Delettrez, V. Yu. Glebov, D. D. Meyerhofer, and T. C. Sangster, Phys. Rev. Lett. **90**, 095002 (2003).

8. J. A. Frenje, C. K. Li, F. H. Séguin, J. Deciantis, S. Kurebayashi, J. R. Rygg, R. D. Petrasso, J. Delettrez, V. Yu. Glebov, C. Stoeckl, F. J. Marshall, D. D. Meyerhofer, T. C. Sangster, V. A. Smalyuk, and J. M. Soures, Phys. Plasmas **11**, 2798 (2003).

9. T. R. Boehly, D. L. Brown, R. S. Craxton, R. L. Keck, J. P. Knauer, J. H. Kelly, T. J. Kessler, S. A. Kumpan, S. J. Loucks, S. A. Letzring, F. J. Marshall, R. L. McCrory, S. F. B. Morse, W. Seka, J. M. Soures, and C. P. Verdon, Opt. Commun. **133**, 495 (1997).

10. S. Skupsky and R. S. Craxton, Phys. Plasmas **6**, 2157 (1999).

11. H.-S. Bosch and G. M. Hale, Nucl. Fusion **32**, 611 (1992).

12. R. A. Lerche, D. W. Phillion, and G. L. Tietbohl, Rev. Sci. Instrum. **66**, 933 (1995).

13. F. H. Séguin, J. A. Frenje, C. K. Li, D. G. Hicks, S. Kurebayashi, J. R. Rygg, B.-E. Schwartz, R. D. Petrasso, S. Roberts, J. M. Soures, D. D. Meyerhofer, T. C. Sangster, J. P. Knauer, C. Sorce, V. Yu. Glebov, C. Stoeckl, T. W. Phillips, R. J. Leeper, K. Fletcher, and S. Padalino, Rev. Sci. Instrum. **74**, 975 (2003).

14. J. Delettrez, R. Epstein, M. C. Richardson, P. A. Jaanimagi, and B. L. Henke, Phys. Rev. A **36**, 3926 (1987).

15. Protons from the shell (ablator) material are accelerated by electrostatic fields while the laser pulse illuminates the capsule. These fields have decayed well before the time of nuclear production, several 100 ps after the end of the pulse, so they do not affect nuclear product spectra. See also D. G. Hicks, C. K. Li, F. H. Séguin, J. D. Schnittman, A. K. Ram, J. A. Frenje, R. D. Petrasso, J. M. Soures, D. D. Meyerhofer, S. Roberts, C. Sorce, C. Stoeckl, T. C. Sangster, and T. W. Phillips, Phys. Plasmas **8**, 606 (2001).

16. Comparison of absolute shock-bang times, which is timing with respect to the onset of the laser drive pulse, is quoted here. Comparison of the relative shock-bang times, with respect to the initial rise of compression burn, reveals that simulations predict shock-bang time to occur 12±15 ps early for 18-atm fills and 65±15 ps late for 3.6-atm fills.

17. C. K. Li, D. G. Hicks, F. H. Séguin, J. A. Frenje, R. D. Petrasso, J. M. Soures, P. B. Radha, V. Yu. Glebov, C. Stoeckl, D. R. Harding, J. P. Knauer, R. L. Kremens, F. J. Marshall, D. D. Meyerhofer, S. Skupsky, S. Roberts, C. Sorce, T. C. Sangster, T. W. Phillips, M. D. Cable, and R. J. Leeper, Phys. Plasmas **7**, 2578 (2000).

18. C. K. Li and R. D. Petrasso, Phys. Rev. Lett. **70**, 3059 (1993).

19. J. H. Gardner, D. L. Book, and I. B. Bernstein, J. Fluid Mech. **114**, 41 (1982).

20. J. R. Rygg, J. A. Frenje, C. K. Li, F. H. Séguin, R. D. Petrasso, F. J. Marshall, J. A. Delettrez, J. P. Knauer, D. D. Meyerhofer, and C. Stoeckl, "Observations of the Collapse of Asymmetrically Driven Convergent Spherical Shocks," manuscript in preparation (2007).

21. J. R. Rygg, J. A. Frenje, C. K. Li, F. H. Séguin, R. D. Petrasso, V. Yu. Glebov, D. D. Meyerhofer, T. C. Sangster, and C. Stoeckl, Phys. Rev. Lett. **98**, 215002 (2007).

22. O. Larroche, Eur. Phys. J. D **27**, 131 (2003).

Equation-of-State Measurements in Ta$_2$O$_5$ Aerogel

Introduction

In the last 15 years, there has been considerable interest in experiments that use laser-driven shock waves to measure high-energy-density equation-of-state (HED-EOS) data.[1–5] During this time, the generation of laser-driven shock waves has been refined, and the accuracy of the techniques employed has been improved significantly. Highly accurate optical studies of SiO$_2$ with laser-driven shock waves have shown strong agreement with experimental results obtained with other established drivers;[6] these measurements have extended the available data to many millions of atmospheres and identified new mechanisms that affect the material's HED-EOS.[7] Many HED-EOS experiments use standards or reference materials to which the behavior of the studied material is compared. These impedance-matching experiments are particularly important in laser-driven shock-wave experiments where nonreferenced HED-EOS measurements are complex.[8,9] The measurements on SiO$_2$ and the consistent structure of quartz lend themselves to the establishment of quartz as a standard material, as will be demonstrated in this study.

While shock waves in a material in its standard state can produce a wide range of pressures (depending upon the strength of the shock wave), the density and temperature states attainable are limited to the locus of solutions for the hydrodynamic equations commonly known as the principal Hugoniot of the material. One method to expand the attainable states from shock waves is to alter the initial density of the study material.[10] Experiments on these porous materials then enable the researcher to attain measurements of the material's HED-EOS over a broad range of conditions. Additionally, experiments on porous materials have also been used to understand the exotic shock phenomenon of supersonic, radiative transport.[11]

In supersonic radiative transport, the radiative flux from a shock front exceeds the material flux, indicating that the radiation front advances faster than the material shock front.[12] The experimental study in Ref. 11 used tantalum pentoxide (Ta$_2$O$_5$) aerogels as a host material for the study of radiative transport.

These low-density aerogels were shocked to pressures over a million atmospheres, and both the radiation and hydrodynamics were tracked experimentally. However, to fully understand this experiment and future experiments with this material, reliable radiation-hydrodynamic (RadHydro) simulations are needed, which requires an understanding of the HED-EOS of the study material. To date, there were no HED-EOS measurements to provide guidance for the development of theoretical models of this high-porosity material.

This study provides accurate EOS measurements on Ta$_2$O$_5$ aerogel material to support model development. It uses the accumulated developments in laser-driven shock waves and their diagnosis to obtain compression and temperature data at pressures up to 3 Mbar ($\sim 3 \times 10^6$ atm). At these pressures, the Ta$_2$O$_5$ aerogels compress over four times their initial density and achieve temperatures ≥ 5 eV ($\geq 60{,}000$ K). The aerogel densities used in this study are 0.1, 0.15, and 0.25 g/cm^3, far smaller than the solid-state density of this material, 8.2 g/cm^3. Twelve beamlines of the OMEGA Laser System[13] generated experimental pressures up to 1.25 Mbar in the 0.1-g/cm^3 aerogel and up to 3 Mbar in the 0.25-g/cm^3 aerogel. Since the material is transparent, the shock velocity was diagnosed with Doppler interferometry,[14] and the temperature was diagnosed with a streaked optical pyrometer.[15] Impedance-matching experiments were performed using two reference standards: aluminum (a legacy standard) and alpha quartz.

The shock-wave driver, diagnostics, and experimental materials necessary for this study will be discussed in the next section. The remaining sections (1) give important experimental observations, including the physical properties of the Ta$_2$O$_5$ aerogel samples (refractive index and density as well as the manufacturing residuals present), the measurements that justify the use of quartz as a reference material, and the EOS measurements (density, temperature, and pressure) of the HED Ta$_2$O$_5$; (2) discuss the EOS measurements with respect to the available qEOS model; (3) address a diagnostic modification that could benefit future studies of this type; and (4) present conclusions.

Experimental Technique

This experimental study used laser-driven shock waves to achieve the desired states required for HED-EOS model refinement. The OMEGA laser[13] is the driver for the experiments; the diagnostics were the velocity interferometer system for any reflector (VISAR)[14] and the streaked optical pyrometer (SOP).[15] Using these two diagnostics, it is possible to completely determine the EOS of a material using the impedance-matching technique. These diagnostics operate on a subnanosecond time scale so that they can fully capture the material response over the entire multinanosecond OMEGA laser pulse. The millimeter-scale targets of this study were precision manufactured, machined, and assembled through a collaboration between technicians in the LLE Target Fabrication Group and chemists at the Lawrence Livermore National Laboratory Target Fabrication Group.

OMEGA is a 60-beam, 351-nm, third-harmonic Nd:glass laser system designed for spherical illumination of imploding spherical targets.[13] To produce shocks in these planar EOS targets, up to 12 of the OMEGA beamlines irradiate the target package. Six of these beams have an angle of incidence of 23° with respect to the target normal; the other six are incident at 48°. All of the beams are focused (at $f/6.7$) to the same spot on the target. Each beam was outfitted with a distributed phase plate[16] that produces a super-Gaussian intensity distribution at the target with a full width at half maximum (FWHM) of approximately 800 μm. A 3.7-ns, flattop pulse shape was used to maximize the steadiness of the shock-wave front while minimizing the coronal temperature for the desired experimental conditions. The total energy per beamline was ~240 J of 351-nm radiation, yielding irradiances in the range of 15 to 80 TW/cm^2, depending on the number of beams and their incidence angle.

The primary diagnostics used during this experimental campaign were the VISAR[14] and the SOP.[15] Due to the fact that the shocked states are very hot ($\gtrsim 1$ eV), the shocked material has a significant population of free electrons and readily emits in the near-infrared, optical, and ultraviolet portions of the spectrum. The VISAR records the time evolution of the Doppler shift of a probe laser that results from the advancing reflective shock-wave front. With the measurement of the shock-wave velocity in the reference material (or witness) and the target, the pressure and density of the shocked material can be determined with the impedance-matching technique. The SOP records the time evolution of the shock emission, which can then be related to a Planck radiation source to determine the temperature of the shock front. Using these diagnostics it is possible to fully capture the EOS of a shocked material.

The VISAR and the SOP share a common telescope located on the experimental axis directly opposite the OMEGA beams used to launch the shock wave into the sample (see Fig. 111.18). The telescope includes a mechanical assembly that allows the *in-situ* pointing and focusing of the diagnostics on the experimental package. The probe beam and the self-emission from the shock are relayed from the target, and a dichroic beam splitter separates the VISAR probe beam from the rest of the self-emission. Both the VISAR probe beam and the self-emission are relayed to the front of streak cameras that provide two-dimensional records. One dimension corresponds to a slit view of the relayed image, and the second dimension corresponds to a time sweep of that slit view. The spatial information from the slit allows the records from these diagnostics to be used to obtain shock evolution on complex targets with more than one region of interest.
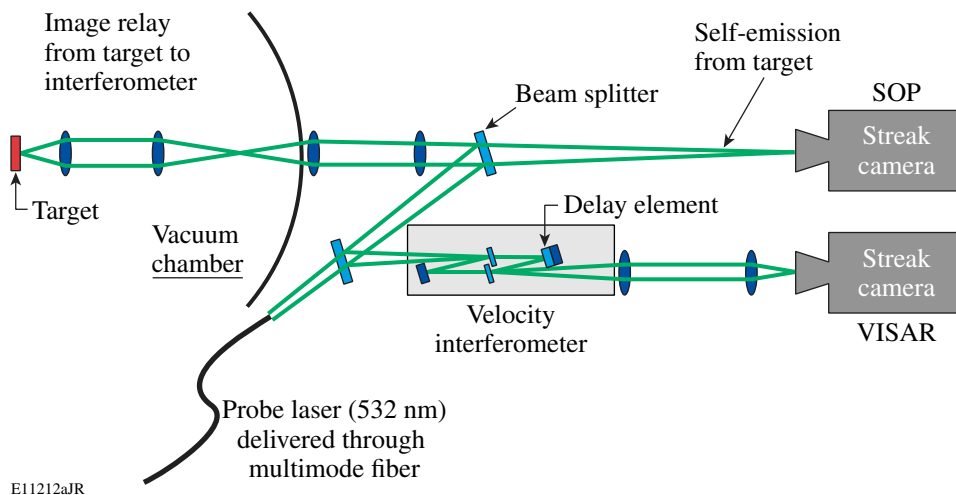

Figure 111.18
Basic configuration of the VISAR/SOP system on OMEGA. VISAR: velocity interferometer system for any reflector; SOP: streaked optical pyrometer.

E11212aJR

Figure 111.19 shows side-by-side VISAR and SOP records that are representative of the data taken for this study. In the case of this experiment, OMEGA shot 37190, experimental records from an optically transparent, quartz/Ta$_2$O$_5$ aerogel target (image in Fig. 111.20) are shown. The two diagnostic records are displayed as two-dimensional, gray-scale density plots with the brightest regions being darkest. Time zero is the point at which the OMEGA drive beams begin to irradiate the target. Variations in the gray scale are related to shock evolution, showing that the material reflectivity (VISAR record) and the brightness (SOP record) are not constant. The two main contributors to this behavior are shock strength and the local material properties. The shock strength affects the quantity and energy of the free electrons, and the material properties dictate the scattering of light. The relative location of the fringes on the VISAR record corresponds to the shock velocity. The shock brightness temperature corresponds to the intensity of the SOP record.

The targets used in this study consist of a pusher assembly (a plastic ablator and an aluminum or quartz reference) that transmits a shock wave into a low-density aerogel sample (silica or Ta$_2$O$_5$) that is under study. These targets are generally 3-mm square, and the aerogel targets are transparent to optical wavelengths (Fig. 111.20). The targets are mounted on stalks and oriented such that the OMEGA beams are incident symmetrically about the target normal and the two principal diagnostics (VISAR and SOP).

The reference assembly has two components: a plastic ablator and a reference material. The plastic ablator is a 20-μm-thick foil of polystyrene (CH) that is irradiated by the laser.

E15902JR
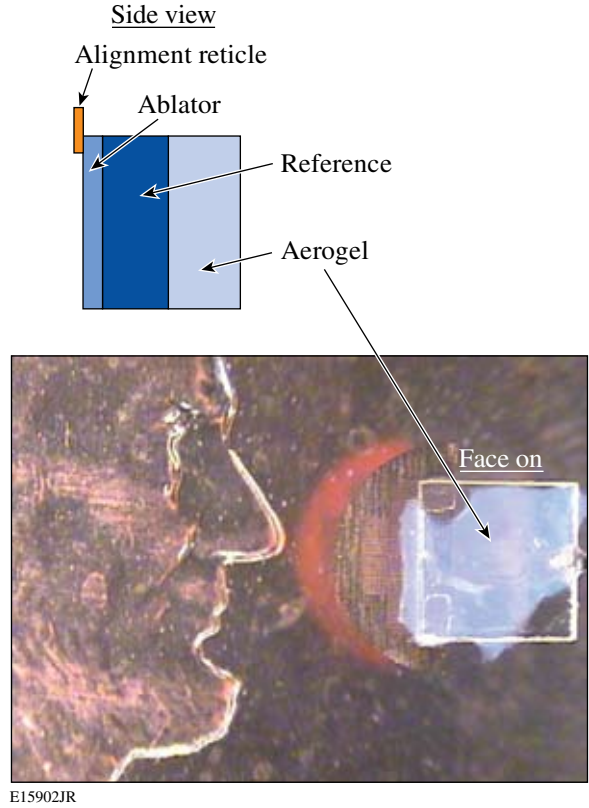
Figure 111.20
A typical Ta$_2$O$_5$ aerogel, planar target with a plastic ablator and quartz reference shown relative to a penny. These targets are generally 3 × 3-mm slides attached to a mounting stalk. This view shows the target as seen from the diagnostics (VISAR and SOP). The backing is a combination of a plastic ablator and a quartz slide, and the light amorphous material is the aerogel. Target alignment reticles, the grid to the left of the sample, are used to aid in pointing, rotation, and focusing during the experiment.

E15893JR
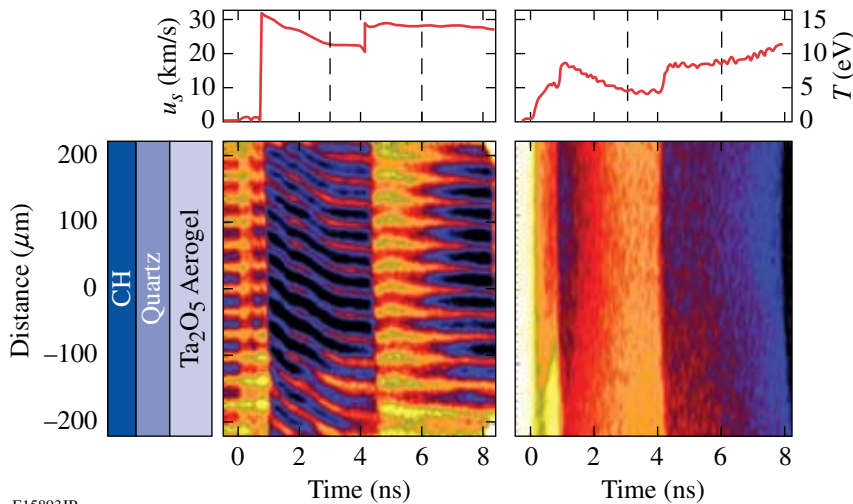
Figure 111.19
The target cross-section is depicted on the left. The VISAR (left plot) and SOP (right plot) records for OMEGA shot 37190 give simultaneous records of the evolution of shock velocity and shock temperature along with the associated inferred velocity and temperature profiles for a 12-beam, 1.9-TW/cm^2 shot on a quartz reference Ta$_2$O$_5$ aerogel target. Each lineout is taken at position zero in the records, which corresponds to the same point on the target.

Polystyrene is commonly used as the ablator due to its low atomic number [which reduces the production of high-energy (>2 keV) x rays] and its ease of handling and machining. Lower-energy x rays are more easily absorbed in the dense, highly ionized, shocked ablator, keeping x rays away from the reference and the target and minimizing the preheat of the materials before the shock arrives. The ablator thickness is chosen to be about twice the ablation depth of the laser to ensure that none of the higher-atomic-number reference material is heated by the laser while minimizing the amount of time the shock propagates through the ablator. The ablator is attached to the reference material using a UV-cured epoxy.

The two reference materials used in this study were aluminum and *z*-cut alpha quartz. The aluminum pushers were approximately 70 μm thick while the alpha-quartz thicknesses were 100 μm thick to compensate for the slightly lower x-ray absorption in the quartz. The aerogels were mounted to the aluminum reference by bonding a freestanding aerogel sample onto an aluminum foil. To ensure that the glue did not wick into the aerogel, the samples were glued only at the edges, again with the UV-cured epoxy. The consequence of gluing the aerogel to the aluminum was that gaps, owing to the surface roughness of the aerogel, were present between the reference and the target. These gaps increase the uncertainty in the selection of the proper isentrope (initial state) for the release wave. With the alpha-quartz pushers the aerogel was grown directly onto the pusher, eliminating the gaps at the contact surface. This manufacturing technique was possible because, while the aluminum would disintegrate in the environment of the aerogel manufacturing process, the alpha quartz was unaffected.

Tantalum pentoxide, in its standard state, is a white to creamy-white solid with a density of ~8.2 g/cm^3. The material has a relatively large band gap of ~4.2 eV, a high index of refraction (~2.1 at 532 nm), low absorption of optical and IR wavelengths (300 nm to 2 mm), and a low melting point (~1800 K, as compared to pure Ta, ~2700 K). The Ta₂O₅ aerogel in this study had three mean densities: 0.1, 0.15, and 0.25 g/cm^3. Since the aerogel grains are of the order of 2- to 50-nm scale, much less than the wavelength of light, a significant amount of Rayleigh scattering occurs within these aerogels. This limits the maximum sample thickness that can be probed with optical diagnostics to a few-hundred micrometers for 0.1-g/cm^3 aerogel and approximately 100 μm for the 0.25-g/cm^3 aerogel.

The Ta₂O₅ aerogels were produced by the Target Fabrication Group at Lawrence Livermore National Laboratory via a sol-gel process that entails the hydrolysis of tantalum ethoxide [Ta(OC₂H₅)₅] in an ethanol solution.[17] The targets are grown by dip-coating quartz slides in the gelatinous solution. They are then placed in a casting vessel for supercritical extraction of the ethanol. While in the solution and during the extraction of the ethanol solvent, the tantalum atoms bond with oxygen atoms, forming primarily Ta₂O₅ molecules. Unbonded surface oxygen atoms may terminate in either a hydroxol or an alkynol (typically methanol) group. If the aerogel is sintered after the drying process, the alkyl groups will be released, leaving only hydroxyl groups, which greatly increases the water absorptivity of the aerogel. Samples studied with an aluminum reference are then removed from the quartz and bonded to the reference assembly. Quartz-referenced targets merely require affixing the plastic ablator on the quartz slide.

Porous aerogels are hydrophilic, readily absorbing atmospheric moisture, which is physiosorbed (held by Van der Waals forces). The high polarizability of the hydroxyl groups as compared to an alkyl group makes the sintered materials especially hydrophilic, making it difficult to remove all of the moisture from the sample. Most experiments with a Ta₂O₅ aerogel (including this study) use unsintered samples, so that these aerogels have residual alkyl groups that are weakly chemically bound, or chemisorbed, to the surfaces of the aerogel structures. Combustion analysis puts the mass percentage of carbon at 1% or less, which is interpreted as a chemically absorbed contaminant that is present during all unsintered studies with this material.

The aerogel targets used in this study were produced by creating a "vat" of the catalyzed tantalum ethoxide/ethanol solution as described above. The samples were formed on quartz slides by coating them with the gelatin and placing the slide in a casting vessel. The manufacturer casts a much larger witness from the same vat that is machined and weighed for density estimates. These growth techniques are expected to be highly reproducible with manufacturer-quoted density errors of less than 10%. A systematic densification of the samples (compared to the witness) is possibly due to an increase in the importance of capillary effects for the large-aspect-ratio targets.

Experimental Observations

In this section, the series of measurements required to determine the EOS of the Ta₂O₅ aerogel will be discussed. The measurements can be subdivided into two categories: (1) characterization of the targets and the reference and (2) the actual target experiments.

The characterization measurements provide input so that the target experiments can be evaluated. They include the refractive-index characterization (needed to determine shock velocity), the density characterization (needed for the impedance-matching technique), and the quantification of manufacturing residuals (needed to verify the manufacturer's estimate). The refractive index was measured as an input to the shock-velocity measurements, and this value helped evaluate density measurements. To determine the amount of absorbed contaminants removed prior to an experiment, a series of experiments were performed that exposed aerogel samples to heat and vacuum to determine the quantity and type of contaminants for comparison with the manufacturer's estimates.

With the characterization of the target and the reference materials established, the necessary inputs are available for interpreting experimental observations of the EOS of Ta_2O_5. The observations include kinematic properties, which can be determined by measuring the shock velocities with VISAR, and the thermal properties, which can be determined by measuring the shock brightness with the SOP.

1. Refractive-Index Measurements of the Ta_2O_5 Aerogel

The refractive index n of the sample material affects the VISAR sensitivity,[14] and due to the highly porous nature of aerogels, the optical properties of an aerogel material differ greatly from its standard amorphous state. For these aerogels, the real part of the refractive index is near unity and the imaginary part is negligible.[18] Due to this near-unity refractive index and the thinness of these aerogel samples, it was necessary to use an optical technique based on white-light interferometry to measure the refractive index of the targets.[19] This technique uses the short coherence length of white light to identify the apparent depth of a reflective surface that is viewed through a refractive medium of thickness d, as shown in Fig. 111.21(a). This depth adjustment ΔL achieves a total optical path length (OPL*) through the sample that is equal to the OPL from the reflective surface through air. Using these two positions to eliminate the unknown distance between the image plane and the surface of the refractive medium, a relationship among these quantities is obtained:

$$OPL - \Delta L - d = OPL^* - nd , \qquad (1)$$

and after solving for n, the simple relation

$$n = 1 + \Delta L / d \qquad (2)$$

is found, where n is the real part of the index of refraction.

A ZYGO NewView 5000 white-light interferometer,[20] was used to measure both the depth adjustment ΔL due to the refractive property of the aerogels and the thickness of the aerogels. The objective numerical aperture (N.A.) for the ΔL measurement was 0.075 to keep the incident rays as normal to the aerogel surface as possible. The thicknesses d of the aerogel targets were measured in the manner shown in Fig. 111.21(b). Because the refractive index for these aerogels is close to that of air and the surface of the aerogel has a surface roughness of the order of a few microns, the thickness measurements required the use of an objective with a N.A. of 0.33 to achieve a small depth of focus. The use of this relatively large N.A. limited the overall depth of field to about a millimeter. Through multiple measurements around the edge, a reasonable surface profile was obtained. The uncertainty in the ΔL measurement was dominated by the need to use a small N.A. objective that had a depth of focus of about 0.1 μm, resulting in an uncertainty of ΔL at about 4%, while the uncertainty in identifying the thickness d of the target was approximately 3%. The refractive indices of the Ta_2O_5 aerogel targets were measured to be 1.0206±0.0010, 1.0297±0.0017, and 1.0471±0.0024 for the 0.1-, 0.15-, and 0.25-g/cm³ aerogel targets, respectively.

E14135JR
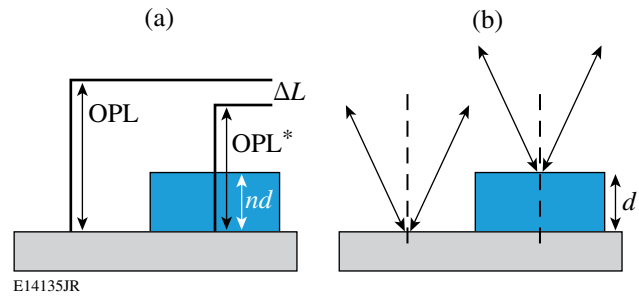
Figure 111.21
The measurement technique that determined the refractive index included two steps: First, the change in stage position, ΔL, required that the base of the sample be kept at an equal optical path length (OPL) through air and the target (a). Second, the thickness of the sample was measured by the difference d in stage position for the target's upper surface in focus position and the base in focus position (b). Because the measurement (a) is through the sample, a small N.A. is desirable, whereas a large N.A. works best for the surface measurement of (b).

2. Density Measurements of an Ta_2O_5 Aerogel

The nominal initial density values of 0.1, 0.15, and 0.25 g/cm³ supplied by the manufacturer were estimates based on a witness sample rather than the actual sample itself. To determine if the target densified more than the witness during the drying process, it was deemed necessary to validate the provided estimates. These microscopic samples were validated by relating the density to the refractive index of the target.

The Claussius–Mossotti relation[21] applied to a highly porous material shows that the refractive index *n* less unity is proportional to the density ρ of the porous material:

$$n - 1 = \alpha\rho, \qquad (3)$$

where α is a proportionality constant associated with the strength of the dipole oscillators.[18] Knowing this proportionality constant and the refractive measurements discussed in **Refractive-Index Measurements of the Ta_2O_5 Aerogel** (p. 158), the density of the actual target materials can then be determined. To ascertain the proportionality constant, the manufacturer machined a witness sample of known density to approximately 100 μm thick. At this thickness, the technique described on p. 158 was used to determine the refractive index. Based on such measurements, the proportionality constant was determined to be 0.188±0.013. Using this result, it was found that the densification of the targets compared to the witness sample is less than the combined uncertainties of the measurements of the refractive index and the proportionality constant; thus, the density of the witness accurately reflects that of the target. This equality provides no information on the purity of the samples, or what contaminants, such as water or alkyls, are present in a target. To resolve the amount of the residuals, another set of measurements was required to quantify the amount of contaminants absorbed and the nature of their bonding mechanisms.

A series of three tests were run on samples from the same batch of Ta_2O_5 aerogel in ambient laboratory air having 30% to 40% relative humidity. The samples were approximately 0.5 cm in diameter, roughly 2 cm in height, and weighed approximately 100 mg prior to testing. The first test determined the total amount of residuals by heating the sample in a dry nitrogen atmosphere utilizing a Computrac moisture analyzer.[22] The samples were heated to 450 K over approximately 5 min based on the analyzer's termination criteria, then removed from the analyzer and transferred to a scale capable of 0.1-mg-accuracy measurements. The mass of the sample and absorbed moisture was tracked as a function of time after its initial exposure to air. Because of the need to transfer from the test apparatus to a scale, the measurement began ~15 s after initial exposure. Figure 111.22 shows the measured time-dependent aerogel and absorbed contaminant mass after exposure to atmosphere. Extrapolating these results to time zero, the mass of the target without any contaminants was inferred to be 100.8±0.1 mg. The measured initial mass (prior to heat exposure), 104.7±0.1 mg, was then normalized to this extrapolated value to determine the mass percentage of
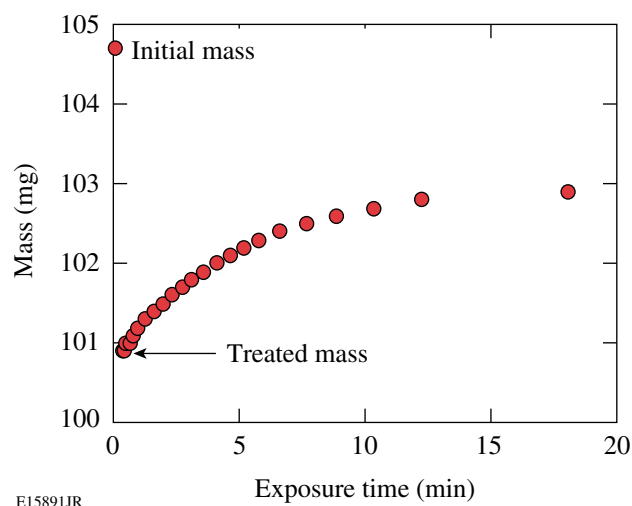

Figure 111.22
A characteristic plot of the total mass of a sample with absorbed water as a function of time after removal from the heat-addition test. Three such tests were performed: this first test was performed to measure the full chemically and physically absorbed contaminants, a second to determine the amount of physically absorbed contaminants, and a third to determine the amount of physically absorbed contaminants removed in an OMEGA shot cycle.

contaminants, which constitutes about 4% of the mass of the sample as it came from the manufacturer. The second sample was exposed to a vacuum (~10^{-4} Torr), however, with no heat addition. This sample remained in a vacuum environment for a week and was then removed and measured in the same manner as previously described. After normalization, it was found that approximately 3% of the as-manufactured mass is due to absorbed contaminants that can be removed by vacuum alone. To determine if the normal OMEGA shot cycle, which is approximately 20 min of vacuum exposure, achieves the same result, a third sample was placed in an equivalent vacuum for a period of 20 min and then removed and measured in time. The extrapolation of this sample again showed that the mass percentage of physiosorbed contaminants removed was 3% of the total as-manufactured mass.

These measurements indicate that approximately 1% of the as-manufactured mass fraction is from chemisorbed contaminants (contaminants that require heat addition to break bonds), while the remaining 3% is physiosorbed and sufficient for vacuum removal. Correlating these results with the manufacturer's carbon estimates based on combustion analysis experiments, it is expected that the chemisorbed contaminants are the alkyls and that the primary physiosorbed contaminant is absorbed water. The importance of these measurements is that the contaminants that can be removed by vacuum are removed

in times less than the OMEGA shot cycle; however, a small amount of the residual alkyl groups are present in experiments using this aerogel.

3. Kinematic Properties of Ta$_2$O$_5$ Aerogel

The kinematic properties of the Ta$_2$O$_5$ aerogel samples were studied using both aluminum and alpha quartz as reference materials. The shock velocity in the aluminum reference was inferred from a quartz witness adjacent to the aerogel sample, as shown in Fig. 111.23, following the high-precision method proposed by Hicks *et al.*[6] In this study, the linear relationship, reported by Hicks *et al.*, between the measured shock velocity in a quartz witness and the shock velocity in aluminum, $u_s^{Al} = B_0 + B_1\left(u_s^Q - \overline{u_s^Q}\right)$, where $\overline{u_s^Q} = 20.57\ \mu m/ns$, $B_0 = 21.14 \pm 0.12\ \mu m/ns$, and $B_1 = 0.91 \pm 0.03$, was used to determine the aluminum shock velocity. The shock velocities in both the quartz and aerogel portions of the sample were determined with VISAR and are tabulated in Table 111.III along with the other kinematic parameters determined from the impedance-matching analysis using the SESAME-3700 equation-of-state model for aluminum.

Although aluminum is a proven reference material, the difficulties of affixing these aerogels to the aluminum contact surface without gaps proved to be challenging and had a low success rate; consequently, the target design was switched to the quartz reference similar to that shown in Fig. 111.24 with Ta$_2$O$_5$ aerogel across the entire target. With the aerogel grown directly on the reference, the interface between the two materials was gapless, leading to a perfect shot success rate. With the quartz pushers and transparent aerogels, the shock velocity was continuously measured through the quartz pusher and into the aerogel. Table 111.IV lists the 19 experimental results, u_s^Q and $u_s^{Ta_2O_5}$, for the aerogels of the three nominal densities along with the particle velocity and pressure inferred from the impedance-matching technique using the Kerley-7360 model.

Figure 111.25 shows the results for the shock-velocity dependence on the particle velocity for the three different densities of Ta$_2$O$_5$ aerogel (the initial densities 0.1-, 0.15-, and 0.25-g/cm^3 targets are solid diamond, open ellipses; solid diamond, gray ellipses; and open diamond, solid ellipses, respectively). Experiments with the 0.25-g/cm^3 aerogels were performed with both aluminum and alpha-quartz pushers. In Fig. 111.26, these points are translated into the pressure-density equation-of-state plane, with the same designations. Also shown in Fig. 111.26 are the *a priori* predictions by the qEOS model for this material (shown with the open, gray, and solid curves correlating to 0.1, 0.15, and 0.25 g/cm^3 as with the measurements). Figure 111.26
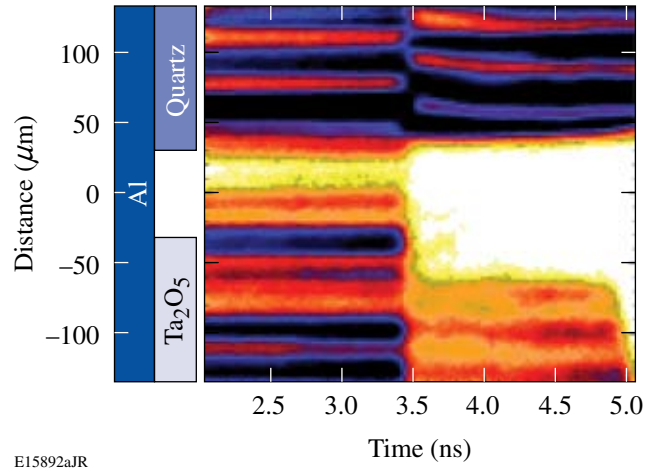
E15892aJR

Figure 111.23
The experimental package used when the reference material is aluminum includes a quartz witness material in addition to the aerogel. The interferogram shows the shock within the aerogel (lower half) and within the quartz (upper half). Before 3.5 ns, the shock is within the aluminum reference. After 3.5 ns, the shock reaches the material interface where it breaks out of the aluminum. The quartz and aerogel shock velocities are both determined within 1 ns of the breakout.
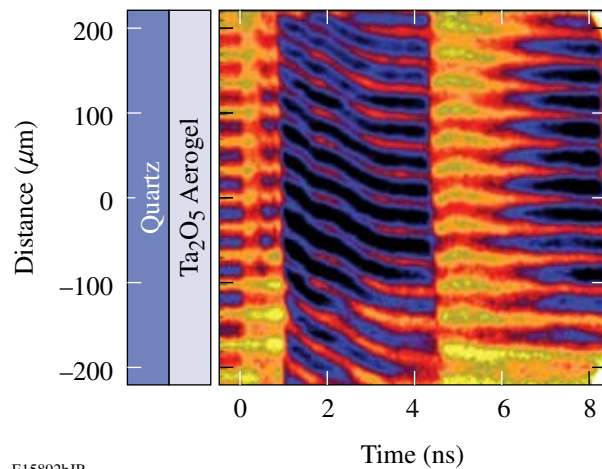
E15892bJR

Figure 111.24
The target and VISAR data with a quartz pusher are shown. The interferogram from an experimental record shows the shock evolution as it propagates through the target. At $t = 0$, OMEGA begins irradiating the surface of the target. At approximately 1 ns, the shock exits the plastic ablator and enters the quartz with a reflected shock going back into the ablator. Due to the expansion of the critical surface, the coupling between the laser and the target decreases, resulting in a decay in the strength of the shock as evidenced by the fringe movement. At $t = 3.5$ ns, the shock is strengthened by the arrival of a compression wave due to the arrival of the reflected shock at the vacuum interface. This causes the shock wave to become steady as it approaches the interface. The shock reaches the interface at 4.5 ns. In this example, the shock velocity for the quartz is determined between 3 to 4.5 ns and for the aerogel between 4.5 to 6 ns.

Table 111.III: Ta$_2$O$_5$ aerogel-aluminum impedance matching.

Shot number	$\rho_0^{Ta_2O_5}$ (g/cm^3)	u_s^{Al} (μm/ns)	P^{Al} (Mbar)	$u_s^{Ta_2O_5}$ (μm/ns)	u_p μm/ns	$P^{Ta_2O_5}$ (Mbar)	$\rho^{Ta_2O_5}$ (g/cm^3)
34136	0.25±0.025	24.6±0.3	10.1±0.3	30.6±0.5	25.3±0.7	1.94±0.18	1.46±0.24
34138	0.25±0.025	19.1±0.3	5.5±0.2	21.7±0.5	18.3±0.6	0.99±0.11	1.58±0.38
34141	0.25±0.025	25.5±0.3	11.0±0.3	32.2±0.5	26.5±0.7	2.13±0.19	1.40±0.22
34143	0.25±0.025	24.1±0.3	9.6±0.3	30.0±0.5	24.7±0.6	1.85±0.17	1.41±0.23
34915	0.25±0.025	27.1±0.3	12.6±0.3	35.1±0.5	28.4±0.7	2.50±0.22	1.32±0.18
34917	0.25±0.025	22.0±0.3	7.8±0.25	26.5±0.5	22.0±0.6	1.46±0.14	1.48±0.26
35152	0.25±0.025	26.3±0.3	11.7±0.3	33.5±0.5	27.4±0.7	2.30±0.21	1.38±0.21
35153	0.25±0.025	25.9±0.3	11.4±0.3	32.4±0.5	27.0±0.7	2.19±0.20	1.51±0.25
34136	0.25±0.025	24.6±0.3	10.1±0.3	30.6±0.5	25.3±0.7	1.94±0.18	1.46±0.24

Shot data and inferred EOS parameters of Ta$_2$O$_5$ aerogel. The columns correspond to the OMEGA shot archive number, the initial density of the aerogel, the inferred shock velocity within the aluminum, the final shock strength prior to the wave decomposition, the shock velocity measured within the aerogel, the particle velocity that conserves mass and momentum for the wave decomposition, the strength of the shock within the aerogel, and the density of the shocked compressed aerogel.
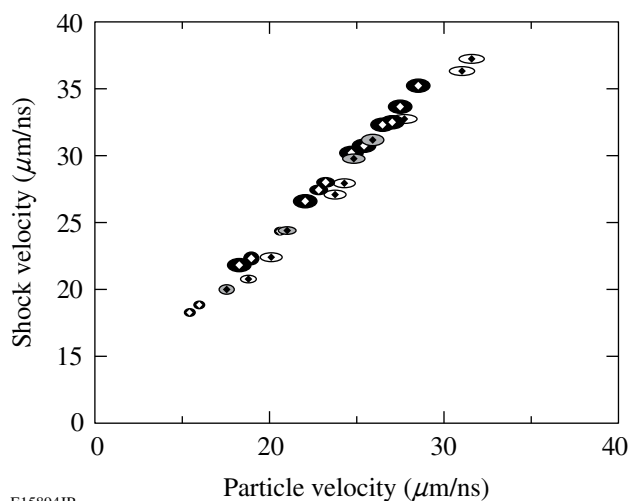
E15894JR

Figure 111.25
The shock-velocity dependence on the particle velocity for the three densities of this study. The points with the open error ellipses and gray error ellipses are from the 0.1- and 0.15-g/cm^3 aerogels, respectively. Experiments in 0.25-g/cm^3 aerogels (solid ellipses) used aluminum references and quartz references. The uncertainty of the velocity measurements was dramatically reduced with the quartz reference as evidenced by the relative area of the error ellipses.
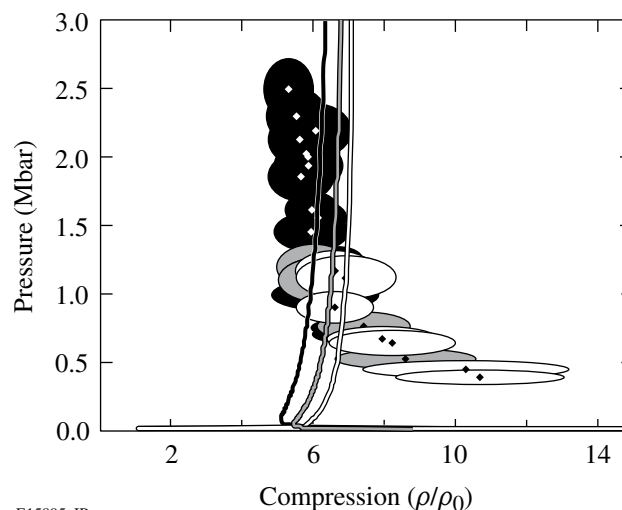
E15895aJR

Figure 111.26
The translation of the u_s–u_p plane to the shock strength versus the compressed-density plane for the three densities: 0.1, 0.15, and 0.25 g/cm^3 (open, gray, and solid, respectively). In addition to the measurements, the qEOS model's predicted dependence for the three densities is shown as the solid lines. As can be seen, below 1 Mbar the measured compressed density is significantly higher than that predicted; however, above 1 Mbar, the qEOS model appears to adequately predict the material behavior.

Table 111.IV: Ta_2O_5 aerogel-quartz impedance matching.

Shot number	$\rho_0^{Ta_2O_5}$ (g/cm^3)	u_s^Q (μm/ns)	P^Q (Mbar)	$u_s^{Ta_2O_5}$ (μm/ns)	u_p (μm/ns)	$P^{Ta_2O_5}$ (Mbar)	$\rho^{Ta_2O_5}$ (g/cm^3)
37190	0.10±0.01	21.2±0.2	7.4±0.15	27.0±0.3	23.7±0.6	0.64±0.09	0.82±0.18
37729	0.10±0.01	26.8±0.2	12.4±0.2	37.1±0.3	31.5±0.7	1.17±0.15	0.66±0.11
37730	0.10±0.01	18.5±0.2	5.5±0.1	22.3±0.2	20.1±0.5	0.45±0.06	1.03±0.29
37731	0.10±0.01	17.6±0.1	4.9±0.1	20.7±0.2	18.8±0.3	0.39±0.05	1.07±0.24
37732	0.10±0.01	21.6±0.2	7.7±0.2	27.8±0.3	24.3±0.6	0.68±0.09	0.79±0.16
37734	0.10±0.01	24.1±0.2	9.8±0.2	32.6±0.2	27.7±0.6	0.90±0.12	0.66±0.11
38790	0.10±0.01	26.4±0.3	12.0±0.3	36.2±0.3	31.0±0.8	1.12±0.15	0.69±0.14
38127	0.15±0.015	17.3±0.1	4.7±0.1	19.9±0.3	17.6±0.4	0.53±0.07	1.29±0.30
38129	0.15±0.015	19.9±0.2	6.4±0.1	24.3±0.2	21.0±0.5	0.77±0.10	1.11±0.20
38793	0.15±0.015	23.6±0.2	9.4±0.2	31.0±0.4	25.8±0.6	1.20±0.16	0.90±0.16
38794	0.15±0.015	22.8±0.2	8.7±0.2	29.7±0.3	24.8±0.6	1.10±0.15	0.90±0.15
36542	0.25±0.025	19.2±0.2	6.0±0.1	22.2±0.4	19.0±0.4	1.05±0.09	1.72±0.31
36545	0.25±0.025	24.8±0.2	10.5±0.2	31.1±0.4	25.8±0.5	2.00±0.16	1.46±0.19
36546	0.25±0.025	22.7±0.2	8.6±0.2	27.9±0.3	23.2±0.5	1.62±0.13	1.48±0.19
42092	0.25±0.025	16.5±0.1	4.2±0.1	18.2±0.2	15.5±0.3	0.71±0.06	1.70±0.22
42094	0.25±0.025	16.9±0.1	4.4±0.1	18.8±0.2	16.0±0.3	0.75±0.06	1.70±0.22
42097	0.25±0.025	24.9±0.1	10.6±0.1	31.3±0.2	25.9±0.3	2.03±0.14	1.44±0.13
42098	0.25±0.025	20.6±0.1	6.9±0.1	24.3±0.2	20.7±0.3	1.26±0.09	1.67±0.18
42099	0.25±0.025	22.4±0.2	8.4±0.2	27.3±0.3	22.8±0.4	1.56±0.13	1.53±0.20
37190	0.10±0.01	21.2±0.2	7.4±0.15	27.0±0.3	23.7±0.6	0.64±0.09	0.82±0.18

Shot data and inferred EOS parameters of Ta_2O_5 aerogel. The columns are arranged as in Table 111.III.

shows that the model predicts the observed local asymptote at approximately six-fold compression for a strong shock. A disagreement exists at the lower pressures (≲Mbar) where the experiments exhibit higher compression than predicted by the model. The model's region of high compression, occurring at ~0.10 Mbar, is at much lower shock strength than that found in these experiments.

The shock velocities across the contact surface are used with the impedance-matching technique to derive the kinematic properties of the shock. This procedure is shown in Fig. 111.27 for OMEGA shot 37190. The shock velocity in the quartz just prior to the shock arrival at the contact surface is 21.2 μm/ns with an uncertainty of ~1% because the contact surface is free of gaps. This yields a Rayleigh line with a slight slope uncertainty. The intersection of the Rayleigh line and its uncertainty lines with the reference Hugoniot (in this case quartz) identifies the release shock state P_0 with its associated uncertainty. The isentropes from P_0 and its uncertainty are calculated for the reflected wave. These isentropes are matched to the Rayleigh line for the aerogel, the product of 0.1 g/cm^3 and 27 μm/ns, with the associated uncertainty in this slope, ~10%. The uncertainties in the final kinematic parameters reported in this study were reported as the larger of the uncertainties in the matched
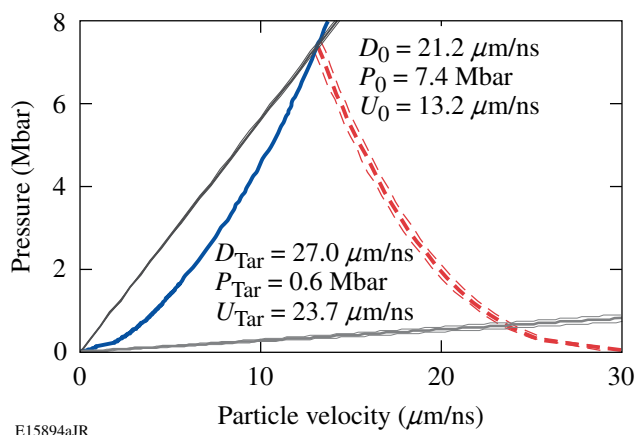
Figure 111.27
Uncertainties in the slopes of the Rayleigh lines were used to determine the uncertainties in the kinematic properties for shot 37190. The uncertainty in the measurement of the shock velocity of the reference standard produces uncertainties in the isentrope (dashed curves), which combines with the uncertainties in the density of the aerogel and shock velocity in the aerogel (thin, light gray curves).
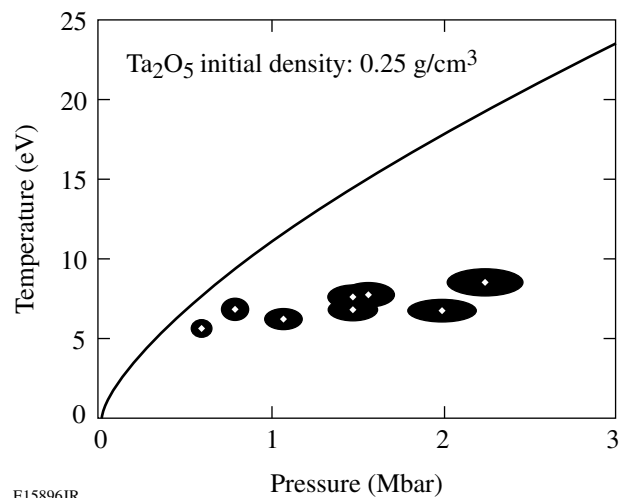

Figure 111.28
The temperature dependence on the shock strength for the 0.25-g/cm^3 aerogel shows that the predicted temperature for qEOS is significantly different than that observed. Above 0.1 Mbar the rise in predicted temperature as the shock strength increases is about three times greater than the observed temperature dependence on shock strength.

values, i.e., $\delta u_p = \max\left[\left\{\delta u_{p_-}, \delta u_{p_+}\right\}\right]$, $\delta P = \max\left[\left\{\delta P_-, \delta P_+\right\}\right]$.

4. Thermal Properties of Ta$_2$O$_5$ Aerogel

The streaked optical pyrometer was used to infer the brightness temperature of the shock front. These measurements involved the simultaneous measurement of the shock velocity and its brightness just prior to the shock's arrival at the rear surface. Brightness measurements are acquired just before shock breakout to eliminate uncertainties in the shock-front brightness that might occur due to the scattering or absorption of light within the unshocked target ahead of the shock. The dependence of brightness and shock-velocity measurements are translated to temperature dependence on shock pressure using the NIST-traceable calibration of the SOP[15] and the kinematic measurements discussed in **Kinematic Properties of Ta$_2$O$_5$ Aerogel** (p. 160), respectively. The results for the 0.25-g/cm^3, Ta$_2$O$_5$ aerogel are shown in Fig. 111.28 along with the prediction by qEOS (solid line). As can be seen in this figure, the qEOS model overpredicts the temperature of the shock front. In the strong-shock limit [temperature (T) $\propto$ shock strength (P)], the slope of the locus of points, $(\Delta T/\Delta P)_{\text{Hug}}$, is a few times greater than that of the measured values.

Discussion

The measurements of the EOS of the Ta$_2$O$_5$ showed marked differences to the *a priori* qEOS model that has been built for the material. It was shown that the qEOS model exhibits very different behavior in the sub-Mbar regime than the measurements. In this shock-strength regime, the qEOS model behavior is much stiffer (small compression for given shock strength) than that observed experimentally. High temperatures with only translational degrees of freedom available would restrict the final compression to this extent, so it is necessary to look at the Ta$_2$O$_5$ molecule to see if there may be neglected degrees of freedom to account for this deviation. While the temperature measurements could be consistent with the higher compressions in experiment (as opposed to those found with qEOS), the temperature's very weak dependence on shock strength suggests consideration of other potential reasons.

In **qEOS Kinematic Agreement** (p. 164), the Ta$_2$O$_5$ aerogel measurements will be compared with SiO$_2$ aerogel measurements conducted at multiple laboratories. The silica aerogels have a comparable final density to the Ta$_2$O$_5$ aerogels; however, they exhibit marked differences in some of their fundamental properties, namely the binding energy. Due to the finite time required for ionization, the possibility of nonequilibrium between the free electrons and the ions will be considered in **qEOS Thermal Properties** (p. 164). While this nonequilibrium would adversely affect thermal measurements that rely on the local electron temperature near the critical surface of the SOP, it would not affect the kinematic measurements, which

rely on an equilibrium wave that is much less localized.

1. qEOS Kinematic Agreement

The shock-strength dependence of the compression for silica aerogel and Ta_2O_5 is shown in Fig. 111.29. Based on the Ta_2O_5 response, the Thomas-Fermi–based qEOS model [lines in Fig. 111.29(b)] is in good agreement with the high-pressure, kinematic behavior of Ta_2O_5. This agreement begins approximately between 0.75 and 1 Mbar for the three studied aerogel sample densities. The agreement at higher pressure means that sufficient ionization exists to allow the free electrons in the
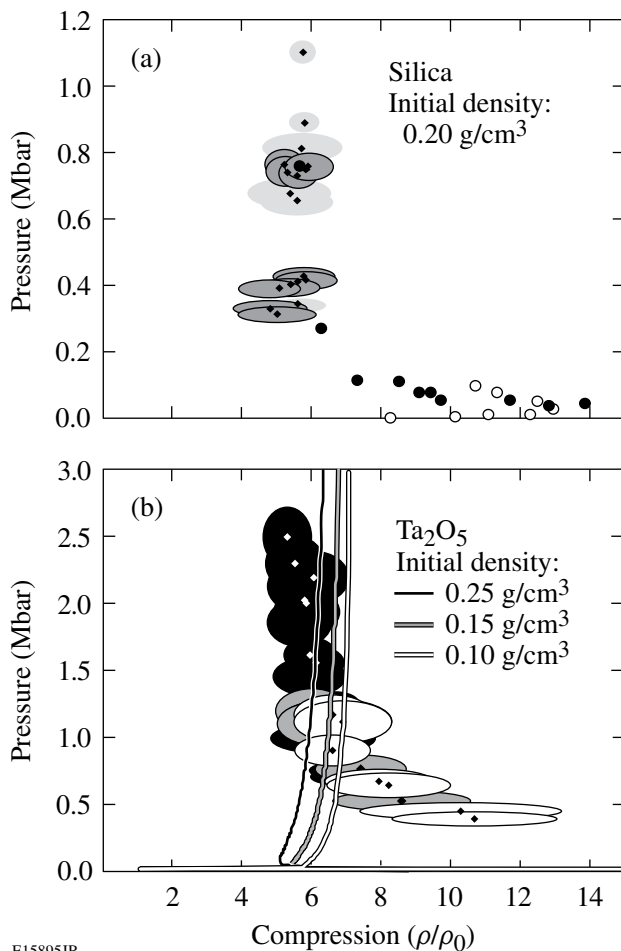

Figure 111.29
These two graphs show the shock-strength dependence of the compression for (a) silica aerogel and (b) the Ta_2O_5 aerogel. The data and curves in both (a) and (b) exhibit high compressions at low pressures due to molecular contributions to the material compressibility. The molecular contributions become negligible at about 0.3 Mbar in the silica aerogel and at about 0.1 Mbar in the Ta_2O_5 aerogel. Above these threshold values, the compression is essentially independent of shock strength. The silica data are from Boehly *et al.* (light gray ellipses), Knudson *et al.* (dark gray ellipses), Trunin and Simakov (solid circles), and Vildanov *et al.* (open circles).[13,23–26]

plasma to dominate the kinematic behavior of the background molecules/ions. At low pressure, the difference between the predicted and observed response is large, with predicted compression ratios far lower than those experimentally observed. This behavior indicates that the qEOS model is probably handling the dissociation of the material incorrectly. This is consistent with a reduction in the observed temperature.

When comparing the Ta_2O_5 aerogel to the silica aerogel, it is clear that there is precedent for this increased compressibility relative to qEOS predictions for these two materials, which are of comparable final density. The main difference between this Ta_2O_5 study and the studies in the silica aerogel is that the pressure at which the Ta_2O_5 aerogels exhibit compression independence is about three times higher than that in the silica aerogel. Ta_2O_5 has a total sublimation/dissociation energy[26] of

$$Ta_2O_5(s) \rightarrow 2\ Ta(g) + 5\ O(g);$$
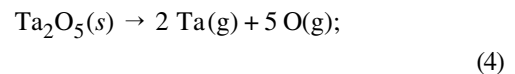
$$\Delta H_0 = 1157\ kcal/mol, \tag{4}$$

which is approximately three times larger than that of SiO_2 (Ref. 27):

$$SiO_2(s) \rightarrow Si(g) + 2\ O(g);$$
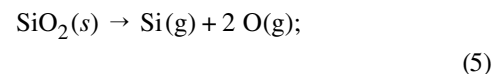
$$\Delta H_0 = 443\ kcal/mol. \tag{5}$$

This difference appears to account for the delayed onset of Thomas–Fermi behavior. The Ta_2O_5 remains more compressible because these molecular structures provide an increased compressibility through the additional degrees of freedom and higher energy consumption to break the bonds.

2. qEOS Thermal Properties

The disagreement between the qEOS model and the temperature measurements in **Thermal Properties of Ta_2O_5 Aerogel** (p. 163) is pronounced. The kinematic results indicate that the Ta_2O_5 material can absorb more energy than predicted by the qEOS model. The apparent independence of the measured temperature on the pressure suggests that local, nonequilibrium processes may also be important. Studies of other material have indicated that at sufficiently high pressures the brightness/temperature measurements in alkali halides (NaCl, KCl, and KBr) approached a similar plateau where the observed temperature became nearly constant with shock strength.[28] An explanation for these observations based on a lack of equilibrium between electrons and the atoms just behind

the shock front was provided by Zeldovich.[29] Zeldovich argued that the energy of a shock wave is carried by the atoms and transferred (via collisions) to the electrons; thus, full equilibrium depends on the rate of electron–ion collisions. In most crystalline materials, the collision frequency is sufficiently high that equilibration occurs on a subpicosecond time scale. If the shock speed is sufficiently high and the collision rates are moderate, then equilibration can lag significantly behind the shock-wave front. This would result in the electron temperature being lower than the ion temperature until deep into the shock front. As the electron temperature is equilibrating, ionization is taking place, resulting in an increase in electron density as a function of position within the shock. Consequently, if the critical surface of a pyrometer channel is closer to the observer than the equilibrium temperature, then the brightness temperature, which is predominantly related to bound-free and free-free electronic transitions, would be artificially low.

To determine if these aerogels exhibit this nonequilibrium behavior, a simulation of the experiment was performed using the one-dimensional hydrodynamics code HYDRA.[30] In this simulation, a 0.1-g/cm^3 sample of Yb$_2$O$_5$ was shocked by a quartz pusher in the same configuration as shown in Fig. 111.24. It should be noted that ytterbium (Yb) was used as a surrogate for Ta because opacity tables for Ta were unavailable at the time of the simulation. The simulated drive environment was identical to that used in OMEGA shot 37190. Figure 111.30(a) shows the predicted electron density $\left(n_e/n_c\right)$ as a function of the one-dimensional spatial coordinate in the simulation. The density is normalized to the critical density for the band of the SOP centered at 1.84 eV. Figure 111.30(b) shows the temperature of the electrons (dotted) and the ions (solid) as a function of the one-dimensional spatial coordinate in the simulation. As with density, the temperature is normalized to the electron temperature at the critical surface for the SOP measurement wavelength. These snapshots are from 7 ns after the laser pulse began and spatially referenced to the front surface of the ablator. In the density plot looking from left to right, the high-density shocked region, at positions less than 141 μm, is the advancing quartz pusher. The density gradient between 141 and 142 μm is due to the release of the high-density quartz into the lower-density, shocked aerogel. The measured shock-wave front is at approximately 145 μm and is a little over 500 nm thick. Ahead of the shock wave is a region where the radiation from the shock is ionizing some of the atoms in the unshocked material to ~4% of the equilibrium electron density of the shocked material. In the temperature plot, one can see the corresponding features behind the shock front. As one approaches the shock front, significant deviations
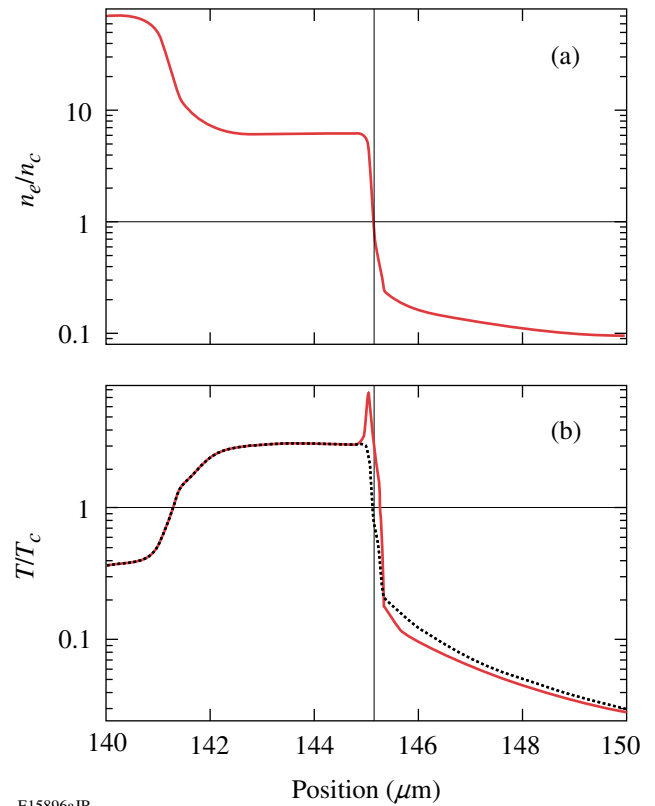
Figure 111.30

The electron density in the vicinity of the shock front (a) normalized to the critical density of the pyrometer's band center, 670 nm, and (b) the temperature of the electrons (dotted) and the ions (solid) in the vicinity of the shock front normalized to the electron temperature at the SOP's critical surface. In the position coordinate, up to 141 μm, the material is quartz, while from 142 μm and beyond, the material is the Yb$_2$O$_5$ aerogel. Between 141 and 142 μm, the quartz is releasing into the less-dense aerogel. From about 145 μm and beyond, the shock wave has not yet arrived; however, radiation from the shock front is ionizing and heating the nearby material in advance of the arrival of the shock. The actual shock front arrives at about 145 μm and rapidly heats the ions. The electrons come into equilibrium with the ions at about 0.5 μm behind the shock front.

occur between the electron and ion temperatures. The leading edge of the shock front transfers energy to the ions by ion–ion collisions, heating them very rapidly to a level above the final equilibrium value. The electron–ion collision cross section is much smaller; therefore the energy transfer to the electrons is much slower and lags behind the shock front.

The simulation indicates that the critical electron density for the measurement wavelength is achieved at a point ahead of where the electrons and the ions come into full equilibrium. Therefore, the measurement would exhibit lower temperatures than that produced by the shock wave. The most reasonable method to overcome this skin-depth issue is to observe the

shock at shorter wavelengths (i.e., at higher critical frequencies). For example, this simulation indicates that a 200-nm pyrometer would likely make an accurate measurement of the shock temperature.

Conclusions

This study provided experimental EOS data of highly porous Ta$_2$O$_5$ aerogels. Using the OMEGA Laser System, aerogel samples were compressed from their initial densities of 0.1, 0.15, and 0.25 g/cm^3 by shock waves with strengths between 0.3 and 3 Mbar. Under these shock loads, the materials were compressed to densities between 5 and 15 times their initial density and to temperatures $\geq$50,000 K. The shocked states as diagnosed with the VISAR and the SOP show strong deviations from the available qEOS model for this material. When the compression measurements are compared to qEOS, it is found that the model underestimates the level of compression achieved by shock loading below 1 Mbar but reproduces the material behavior above 1 Mbar. This observation indicates that there are material degrees of freedom below 1 Mbar that are not fully captured by the qEOS model. The thermal measurements indicate that this might be due to less-significant heating; however, the weak dependence of temperature on shock strength could indicate that nonequilibrium effects require more attention when considering aerogel materials.

REFERENCES

1. R. Cauble *et al.*, Astrophys. J. Suppl. Ser. **127**, 267 (2000).

2. G. W. Collins *et al.*, Science **281**, 1178 (1998).

3. M. Koenig *et al.*, Appl. Phys. Lett. **72**, 1033 (1998).

4. P. M. Celliers *et al.*, Phys. Plasmas **11**, L41 (2004).

5. D. K. Bradley *et al.*, Phys. Rev. Lett. **93**, 195506 (2004).

6. D. G. Hicks, T. R. Boehly, P. M. Celliers, J. H. Eggert, E. Vianello, D. D. Meyerhofer, and G. W. Collins, Phys. Plasmas **12**, 082702 (2005).

7. D. G. Hicks, T. R. Boehly, J. H. Eggert, J. E. Miller, P. M. Celliers, and G. W. Collins, Phys. Rev. Lett. **97**, 025502 (2006).

8. R. Cauble *et al.*, Phys. Rev. Lett. **80**, 1248 (1998).

9. M. D. Knudson *et al.*, Phys. Rev. Lett. **87**, 225501 (2001).

10. L. V. Al'tshuler, Sov. Phys.-Usp. **8**, 52 (1965).

11. C. A. Back *et al.*, Phys. Plasmas **7**, 2126 (2000).

12. R. P. Drake, *High-Energy-Density Physics: Fundamentals, Inertial Fusion, and Experimental Astrophysics*, Shock Wave and High Pressure Phenomena (Springer, Berlin, 2006).

13. T. R. Boehly, R. S. Craxton, T. H. Hinterman, J. H. Kelly, T. J. Kessler, S. A. Kumpan, S. A. Letzring, R. L. McCrory, S. F. B. Morse, W. Seka, S. Skupsky, J. M. Soures, and C. P. Verdon, Rev. Sci. Instrum. **66**, 508 (1995).

14. P. M. Celliers, D. K. Bradley, G. W. Collins, D. G. Hicks, T. R. Boehly, and W. J. Armstrong, Rev. Sci. Instrum. **75**, 4916 (2004).

15. J. E. Miller, T. R. Boehly, A. Melchior, D. D. Meyerhofer, P. M. Celliers, J. H. Eggert, D. G. Hicks, C. M. Sorce, J. A. Oertel, and P. M. Emmel, Rev. Sci. Instrum. **78**, 034903 (2007).

16. Y. Lin, T. J. Kessler, and G. N. Lawrence, Opt. Lett. **20**, 764 (1995).

17. T. F. Baumann *et al.*, in *Handbook of Porous Solids*, edited by F. Schüth, K. S. W. Sing, and J. Weitkamp (Wiley-VCH, Weinheim, Germany, 2002), p. 2014.

18. P. Wang *et al.*, J. Phys. D: Appl. Phys. **27**, 414 (1994).

19. A. G. Van Engen, S. A. Diddams, and T. S. Clement, Appl. Opt. **37**, 5679 (1998).

20. Zygo NewView™ 5000, Zygo Corporation, Middlefield, CT 06455.

21. E. Hecht, *Optics*, 4th ed. (Addison-Wesley, Reading, MA, 2002).

22. Computrac Max-1000 moisture analyzer, Arizona Instruments, Phoenix, AZ 85040-1941.

23. T. R. Boehly, J. E. Miller, D. D. Meyerhofer, J. G. Eggert, P. M. Celliers, D. G. Hicks, and G. W. Collins, "Measurement of Release of Alpha Quartz: A New Standard for Impedance-Matching Experiments," submitted to the Proceedings of the APS.

24. M. D. Knudson, J. R. Asay, and C. Deeney, J. Appl. Phys. **97**, 073514 (2005).

25. G. V. Simakov and R. F. Trunin, Izv. Akad. Nauk SSSR Fiz. Zemli (11), 72 (1990).

26. V. G. Vildanov *et al.*, in *Shock Compression of Condensed Matter '95, AIP Conference Proceedings 370*, edited by S. C. Schmidt and W. C. Teo (American Institute of Physics, Melville, NY, 1996), pp. 121–124.

27. M. G. Inghram, W. A. Chupka, and J. Berkowitz, J. Chem. Phys. **27**, 569 (1957).

28. J. D. Cox, D. D. Wagman, and V. A. Medvedev, *CODATA Key Values for Thermodynamics* (Hemisphere, New York, 1989).

29. S. B. Kormer, Sov. Phys.-Usp. **11**, 229 (1968).

30. S. B. Kormer, M. V. Sinitsyn, and A. I. Kuryapin, Sov. Phys.-JETP **28**, 852 (1969); Ya. B. Zel'dovich, S. B. Kormer, and V. D. Urlin, Sov. Phys.-JETP **28**, 855 (1969).

EXAFS Measurements of Quasi-Isentropically Compressed Vanadium Targets on the OMEGA Laser

Introduction

The response of materials to shocks and other high-strain-rate deformation is the subject of intense research.[1] There is particular interest in developing and testing constitutive models that allow continuum hydrodynamic computer codes to simulate plastic flow in the solid state. Such models are important for the study of material strength under high-strain and high-strain-rate conditions. To test such models, the conditions within the compressed samples (such as compression and temperature) must be measured on a nanosecond time scale. We describe experiments on the OMEGA[2] laser where vanadium (V) is compressed quasi-isentropically to a pressure of ~0.75 Mbar and its compression and temperature are measured by Extended X-Ray Absorption Fine Structure (EXAFS).[3] Isentropic compression (where the entropy is kept constant) enables us to reach high compressions at relatively low temperatures. This is important for the study of highly compressed metals at temperatures well below the melting point. Additionally, significant EXAFS modulations can be obtained only at sufficiently low temperatures. The study of deformations and crystal phase transformations of compressed metals requires that the temperature be kept below melting. This limits the pressure that can be applied in shock compression. Examining the Hugoniot curve that describes the trajectory of shocks in parameter space shows that vanadium will melt[4] at a pressure of ~2.4 Mbar (and a temperature of ~8000 K), precluding solid-state studies at higher pressures. However, quasi-isentropic compression experiments (ICE), involving a slower-rising compression, can access much higher pressures and still stay below the melting curve. Laser-driven quasi-isentropic compression can be achieved by a two-stage target design[5] where a laser of a few-nanosecond pulse irradiates a "reservoir" layer. When the laser-generated shock wave reaches the back of the reservoir, the material releases and flows across a vacuum gap and stagnates against the sample ("plasma impact"), causing its pressure to rise over a period of a few tens of nanoseconds. This configuration has been previously studied and pressures of up to 2 Mbar demonstrated.[6–8] The main diagnostic in those experiments was the interferometric measurement of the back target surface, which, when back-integrated (in time and space), can yield the

pressure on the front surface as a function of time. EXAFS has the unique advantage of yielding information on the sample temperature. This is particularly important to measure because the stagnating reservoir material causes severe heating of the front sample surface, unless protected by a heat shield. The ability to measure temperatures of the order of 10^3 K is unique to EXAFS, as is the ability to *directly* measure compression and temperature within the sample. The EXAFS results show details not seen in the VISAR results: without the use of a heat shield, the heating of the target leads to a lower compression. Also, higher laser intensities can lead to nonuniformities due probably to hydrodynamic instability.

The use of *in-situ* EXAFS for characterizing nanosecond laser–shocked vanadium, titanium, and iron has been recently demonstrated.[9,10] Additionally, the observed EXAFS was shown to indicate crystal phase transformation due to shock compression: the α-to-ω transformation in titanium[9] and the body-centered-cubic (bcc) to hexagonal-closely-packed (hcp) phase transformation in iron.[10] We show here that EXAFS can likewise be applied to the case of laser-driven, quasi-isentropic compression experiments (ICE).

EXAFS modulations above an absorption edge are due to the interference of the ejected photoelectron wave with the reflected wave from neighboring atoms.[3] This interference translates into modulations in the cross section for photon absorption above the K edge, the measured quantity. The frequency of these modulations relates to the interparticle distance, hence the density of the compressed material. The decay rate of the modulation with increasing photoelectron energy yields the mean-square relative displacement (σ) of the crystal atoms and serves as a temperature diagnostic. The basic theory of EXAFS[3] yields an expression for the relative absorption $\chi(k) = \mu(k)/\mu_0(k) - 1$, where $\mu(k)$ is the absorption coefficient and $\mu_0(k)$ is the absorption of the isolated atom. The wave number k of the ejected photoelectron is given by the de Broglie relation $\hbar^2 k^2/2m = E - E_K$, where E is the absorbed photon energy and E_K is the energy of the K edge. The measured spectrum yields the absorption $\mu(E)$, which is converted

to $\chi(k)$. The derived $\chi(k)$ is analyzed with the FEFF *ab initio* EXAFS software package.[11] The basic EXAFS formula for a single reflection in the plane-wave approximation is[3]

$$\chi(k) = \sum_j N_j S_0^2 F_j(k) \exp\left[-2\sigma^2 k^2 - 2R_j/\lambda(k)\right]$$

$$\times \sin\left[2kR_j + \phi_j(k)\right]/kR_j^2, \qquad (1)$$

where N_j is the number of atoms in the *j*-th shell, that is, the number of atoms surrounding the absorbing atom at a distance R_j, and $\lambda(k)$ is the mean free path for collisions. FEFF uses the scattering potential to calculate the amplitude and phase shift of the photoelectron waves scattered from several shells of neighboring atoms including multiple scattering paths. The total $\chi(k)$ is constructed in the curved-wave approximation (i.e., the assumption of plane wave is removed) and iteratively fitted to the experimental $\chi(k)$. The main fitting parameters are the nearest-neighbor distance R and the vibration amplitude σ^2 appearing in the Debye–Waller term. R yields the density or compression; since R is the frequency of the modulations in k space, a compression results in the lengthening of the period of EXAFS modulations (a similar lengthening will also be evident in the photon-energy space, i.e., in the original spectrum). As a function of temperature, σ^2 was calculated using the Debye model[12] for the phonon density of states, including correlation, and it also depends on the density through the Debye temperature. Using the density dependence[13] of the Debye temperature for V and the result for σ^2 from the FEFF fitting, the temperature can be derived. As the temperature increases, the EXAFS oscillations decay faster with increasing photon energy (or increasing electron wave number).

The use of EXAFS for diagnosing compressed metals places a severe restriction on the temperature since at higher temperatures the damping of the EXAFS modulations (because of an increase in σ^2) may preclude reliable measurement. A useful general criterion for the observation of significant EXAFS modulations is the requirement for σ^2 to not exceed ~0.015 Å^2. The averaged square vibration amplitude σ^2 increases with the temperature, but compression mitigates this increase because the Debye temperature increases with density. At normal density the temperature T_0 of vanadium at which $\sigma^2 = 0.015$ Å^2 is $T_0 \sim 500$ K, whereas at a compression of 1.5 that temperature increases to $T_0 \sim 1800$ K. Thus, compression extends the range of temperatures where EXAFS can be observed. This compression, when achieved by a shock [at a pressure of ~1.8 Mbar (Ref. 14)], will result in a temperature of ~5000 K, much higher

than T_0. Thus, in spite of the compression, significant EXAFS modulations would not be visible in that case. On the other hand, an examination of the equation of state of vanadium[15] shows that in a purely isentropic compression, the temperature corresponding to 1.8 Mbar will rise to only ~530 K. Thus, in future ICE experiments, even if not purely isentropic, EXAFS could be measured at pressures of several Mbar and possibly higher.

The drive (i.e., the pressure as a function of time at the front surface of the sample) is calibrated by substituting aluminum for the vanadium; this pressure is independent of the material of the sample. The drive pressure is deduced, for various laser intensities, by interferometrically measuring the velocity of the back target surface (VISAR[16]) as a function of time and then integrating it backward in time and space to obtain the drive.[17] Aluminum is used because its equation of state is well known, and LiF is used because it is transparent to the VISAR laser and its acoustical impedance is well matched to that of aluminum, minimizing reflections at the interface. The behavior of the total target (reservoir, vacuum gap, and sample) is simulated by the hydrodynamic code *LASNEX*.[18] The code results are compared with both the measured back-surface velocity as well as the drive pressure obtained as explained above. Good agreement validates the use of such simulations for the case of the vanadium sample. The *LASNEX*-simulated compression and temperature within the vanadium can be compared with the EXAFS results.

In addition to the inevitable heating due to the compression, there are three sources of extraneous heating (called here preheat): (a) radiation from the imploding target (the radiation source, or the backlighter), (b) radiation from the laser-drive absorption region, and (c) heat generated from the plasma impact upon stagnation and conducted into the sample. The first preheating occurs during the EXAFS probing, whereas the other two occur before the onset of sample compression. Ways to measure as well as to minimize these heating sources are described below.

The present work demonstrates the feasibility and finds the limitations of laser-driven quasi-isentropic compression experiments, rather than carrying out a systematic parameter study. Typical results will highlight these limitations.

The following sections of this article (1) explain the experimental setup and procedures; (2) present the VISAR results and their analysis; (3) present the special case of high-irradiance, which leads to nonuniform compression; (4) analyze the role of the heat shield; (5) discuss the measurement of preheat;

and (6) present the EXAFS measurements of compression and heating.

Experimental

Figure 111.31 shows a schematic of the experimental configuration used to measure K-edge EXAFS absorption spectra. The target consisted of two parts: a reservoir and a sample (V or Al), separated by a vacuum gap of either 300 or 400 μm. The reservoir includes an undoped, 125-μm-thick polyimide layer and a 50-μm-thick CH layer, doped with 2% (by number of atoms) of bromine. The bromine minimizes the sample heating by radiation from the laser-absorption region. The doping is limited to only the back of the reservoir to prevent laser heating of the doped layer, which would have increased the emitted radiation, and thus the preheating. The doping concentration is limited to minimize the absorption of source radiation within the reservoir, which reduces the intensity available for the EXAFS measurement. The sample (10-μm-thick polycrystalline V) was coated on the laser side with 8 μm of a low-conduction parylene-N heat shield. Its role is to protect the sample from heat conducted from its surface, where the reservoir plasma impact occurs. On some of the shots the heat shield was absent in order to demonstrate its effect. The V sample was backed by a 500-μm-thick C_2H_4 substrate, which served to minimize sample heating by the soft radiation from the imploding EXAFS source. This radiation shield also prevents rarefaction of the sample when the pressure wave arrives at its rear surface. The thickness of the radiation shield was chosen to heavily absorb the radiation below the vanadium K edge (5.463 keV) while absorbing only slightly the radiation above

the K edge, where the EXAFS modulations occur. To further minimize this preheat, the target–backlighter distance (19 mm) was the largest possible on OMEGA. As explained before, in the VISAR drive-calibration shots, the V was replaced by Al and the radiation shield was changed to LiF. The rest of the targets were identical to that with the vanadium sample. For the calibration shots there is no backlighter and the VISAR laser travels from the right in Fig. 111.31.

Eleven driving laser beams, 3-ns square pulse each, were fired simultaneously and focused to an ~3-mm focal spot, yielding an irradiance of ~17 TW/cm^2 (some results for different irradiances are mentioned below). The x-ray spectrum is obtained when a fan of rays originating at the backlighter fall on the flat crystal at different Bragg angles, reflecting a slightly different wavelength at each point. The spectral range of the EXAFS spectrum (~5.5 to 6 keV) subtends a distance of ~0.5 mm at the target. A 3-mm-focal-spot size was chosen so that the EXAFS rays probe a small central region of the focal spot. This necessitates working without distributed phase plates (DPP's),[19] which create intensity nonuniformity in the focal spot. Some of this nonuniformity is smoothed out when the reservoir material flows across the vacuum gap (as will be shown in Fig. 111.33) for the uniformity of the back-surface motion. Specially designed phase plates for an ~3-mm focal-spot size could improve the quality of these experiments. The spectral resolution (limited by the size of the imploded back-lighter core) is ~10 eV, much smaller than a typical EXAFS modulation period.

E15766JR
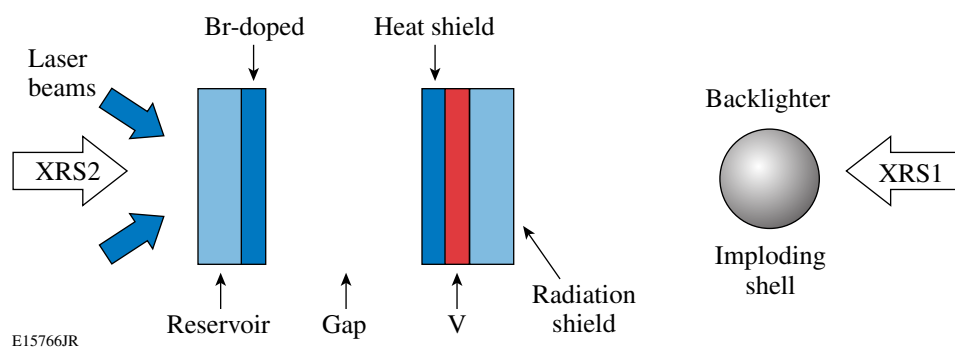
Figure 111.31

Schematic of the experimental configuration for EXAFS measurement of ICE targets. For calibrating the drive, the V is replaced by Al and the radiation shield by LiF, the backlighter is removed, and the VISAR laser travels from right to left. XRS1 and XRS2 are x-ray spectrometers that measure, respectively, the incident and transmitted spectra. The Br doping reduces heating due to radiation from the laser-deposition region, the heat shield reduces heating due to the impact of reservoir material on the sample, and the radiation shield reduces heating due to the backlighter.

The backlighter is formed by focusing 40 of the OMEGA beams on a CH shell of ~16-μm thickness and ~850-μm outer diameter, filled with 0.1 atm of argon, using a 1-ns square pulse. At peak compression the compressed core of the target (<100 μm in size) emits an intense continuum that is spectrally smooth [see Fig. 111.32(a)]; this is a requisite for measuring the inherently weak modulations in the absorption spectrum. Two cross-calibrated, flat-crystal spectrometers equipped with a Ge (1,1,1) crystal were placed at the extreme right and left positions in Fig. 111.31. The first was used to measure the inci-

dent spectrum (I_0) and the second to measure the transmitted spectrum (I). The absorption as a function of photon energy E is defined as $\mu(E) = \ln\left[I_0(E)/I(E)\right]$. I_0 has to be corrected for the (known) absorption of backlighter radiation in the radiation shield. Absorption of the transmitted radiation (I) in the reservoir is small, and, additionally, at the time of EXAFS probing, most of the reservoir material has been ablated away. The measured intensity also includes radiation from the laser-deposition region, which is subtracted. To measure this contribution (typically, ~10% of the total), we fire the drive beams without irradiating the backlighter. A final adjustment of I_0/I can be done far above the K edge, where EXAFS modulations are heavily damped and the absorption $\mu_0(E)$ is well known. The delay time of the drive beams with respect to the back-lighter beams was varied so that the EXAFS could probe the vanadium at different times during the compression. Although the spectrometers used in the EXAFS measurement are time integrated, a meaningful shock diagnosis can be obtained without streaking the spectrum in time because the x-ray pulse width [Fig. 111.32(b)] is only ~120 ps, much shorter than the compression-wave transit time through the metal (~20 ns).

Results and Analysis

1. VISAR Results

Figure 111.33 shows a typical VISAR record for the case of an ICE target without a heat shield, driven at 17 TW/cm². The time refers to the delay with respect to firing the drive-laser beams; a timing fiducial is shown above the VISAR record. The
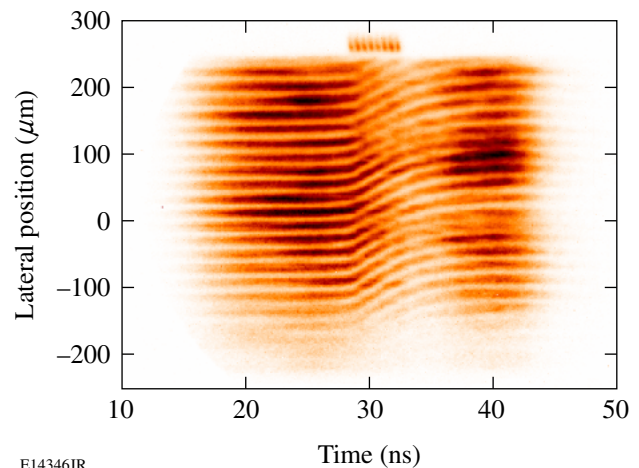

Figure 111.32
(a) Typical spectrum emitted by the backlighter, used as a source for the measurement of absorption above the vanadium K-shell edge at 5.46 keV. The use of imploding CH shells creates a continuum without spectral lines, essential for reliable EXAFS measurements. (b) Streaked x-ray emission from the imploding backlighter target. Radiation above ~3 keV is emitted during peak compression (earlier emission is negligibly small), ensuring a short x-ray probing pulse.

Figure 111.33
VISAR record for the case of an ICE target without a heat shield, driven at 17 TW/cm². The time refers to the delay with respect to firing the drive-laser beams; a timing fiducial is shown above the VISAR record. The fringe motion tracks the Al particle motion at the reflective Al–LiF interface. The smooth, gradual fringe shift with time is indicative of shockless, quasi-isentropic compression.

fringes are produced by the interference of the VISAR laser with the beam reflected from the back surface of the target. The vertical displacement of fringes is proportional to the Al particle velocity at the Al–LiF interface. The velocity results reported here refer to a spatial average over the 150-μm central portion of the field of view. The smooth, gradual fringe shift with time indicates shockless, quasi-isentropic compression. The relative uniformity (or planarity) of the drive is evidenced by the quasi-simultaneous arrival of the pressure wave (at ~30 ns) and the small variations (±10%) in the slope of the fringes (i.e., the acceleration). This uniformity is achieved even though no smoothing was applied to the incident laser beams; nonuniformities in the laser irradiation are smoothed during the propagation through the target vacuum gap, leading to a more-uniform back-surface velocity.

The analysis of VISAR records, such as that in Fig. 111.33, proceeds in two directions: by back-integrating the VISAR-measured velocity and by comparing with 1-D simulations of the *LASNEX* code. Normally, the back-surface velocity is used to derive the front-surface pressure, which is then used as input to a hydrodynamic code. The code then simulates the forward propagation whose end result is the back-surface velocity. This derived velocity is, in turn, compared with the measured velocity. This procedure cannot yield any information on the heating due to the three preheat sources mentioned above. *LASNEX* is used to simulate the entire experiment, starting with the laser interaction, the reservoir expansion, and the sample compression. Because of the resulting complexity, the application of *LASNEX* requires some adjustments to fit the data. This is thought to be due to 2-D effects that are neglected in these 1-D runs (primarily related to the nonuniformities of the unsmoothed beams) as well as uncertainties in the equation of state of the expanding reservoir plasma. Our confidence in the validity of the simulations depends on their agreement with both the measured back-surface velocity as well as the deduced front-surface pressure. Additionally, the code simulations are compared with the EXAFS results.

A sample of such an analysis of VISAR results (Fig. 111.34) shows the rear-surface velocity (upper frames) and the drive pressure (lower frames) for three different cases: irradiance of (a) 17 TW/cm², (b) 17 TW/cm² with no Br in the ablator, and (c) 10 TW/cm². In (a) and (c) the reservoir contained a brominated layer; in (b) the brominated layer was replaced with an equal-thickness CH layer. The vacuum gap was 400 μm. The solid curves show simulation results by the *LASNEX* code; the dashed curves show experimental results. The dashed velocity curves are directly from the VISAR-measured results; the
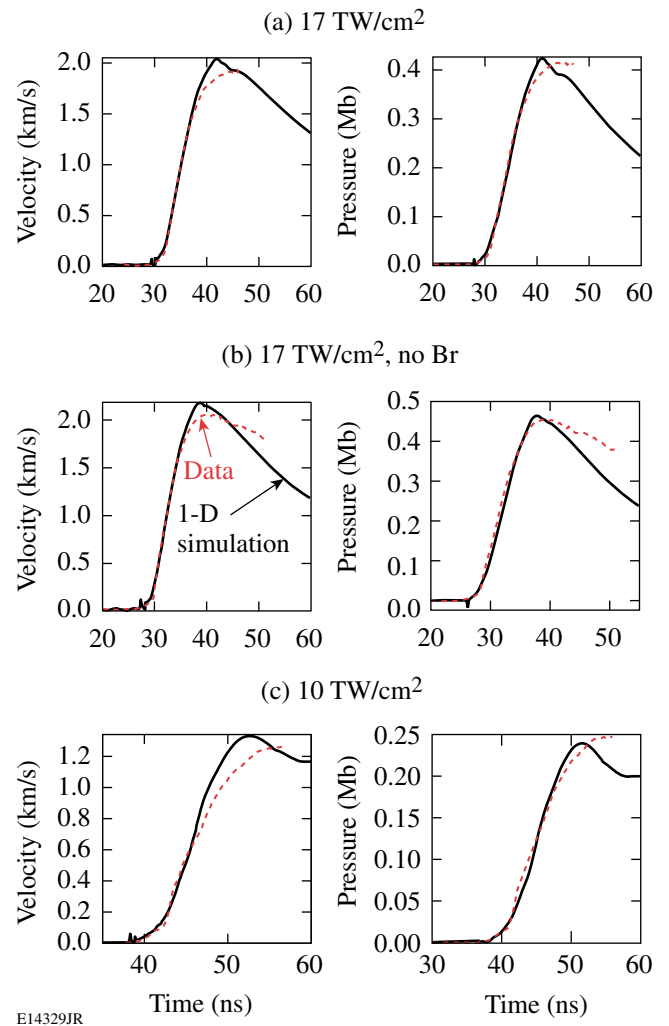
Figure 111.34

Rear-surface velocity (left column) and drive pressure (right column) for three different cases: irradiance of (a) 17 TW/cm², (b) 17 TW/cm² (no Br), and (c) 10 TW/cm². The solid curves show simulation results by the *LASNEX* code. The dashed velocity curves (upper) show the VISAR-measured results; the dashed pressure curves (lower) are obtained from the measured velocity curves by back-integration. The rise in velocity and pressure is seen to be slow and smooth, characteristic of shockless compression.

dashed pressure curves are obtained from the measured velocity curves by back-integration.[17] A heat shield was not used in any of these cases. The rise in velocity and pressure is seen to be slow and smooth, characteristic of shockless compression. The small differences between the code and experimental results around peak compression and later are not well understood; similar disagreements with 1-D simulations were also observed in ICE results reported in Fig. 7(b) of Ref. 5. To obtain the velocity fits in Fig. 111.34, two small adjustments had to be introduced in the *LASNEX* runs (no additional adjustments

had to be made to fit the pressure curves): (a) the assumed laser power had to be reduced by ~30% from the measured values to fit the magnitude of the velocity curve; this is due to the reduction in absorption due to the oblique incidence of the laser beams, and (b) the time scale had to be shifted by a few nanoseconds to fit the time of peak velocity. Nevertheless, the code simulations provide strong support for the VISAR measurements of velocity and pressure as well as the compression and temperature measurements by EXAFS. This is because the main interest here is understanding the sample compression, whereas the interaction of the laser with the reservoir is of secondary importance. Figure 111.34 shows that the inclusion of Br doping slightly reduces the pressure achieved. Examination of the simulations shows that this is caused by the weakening of the compression pressure: the shock traveling within the reservoir weakens when passing from the polyimide to the less-dense CH(Br) layer, then further weakens when traveling through the latter layer. Thus, the total weakening is higher for a thicker CH(Br) layer.

2. High-Irradiance Target Experiments

The laser irradiance for most of the target experiments described in this article was 17 TW/cm^2 for which the achieved pressure was ~0.4 Mbar (see Fig. 111.34). At the higher irradiance of 25 TW/cm^2, the VISAR results indicate a pressure of 0.75 Mbar. However, significant target nonuniformities are indicated in the EXAFS record, at irradiances above ~22 TW/cm^2. This precludes meaningful EXAFS analysis. Figure 111.35(a) shows the VISAR-measured velocity and the deduced pressure evolution for a 400-μm-vacuum-gap target, without a heat shield, and a laser irradiance of 25 TW/cm^2. Figure 111.35(b) shows the EXAFS record for a target experiment at the same conditions. The horizontal axis corresponds to the dispersed photon energies (the K edge is seen at 5.46 keV), whereas the vertical axis corresponds to a one-dimensional image (or face-on radiograph) of the vanadium layer. The energy range shown (~5.4 to 5.8 keV) is where the EXAFS modulations are normally seen. The horizontal axis also corresponds to a face-on radiograph of the vanadium sample, except that at each horizontal position, a different photon energy contributes to the image. Thus, Fig. 111.35(b) is a quasi-2-D face-on radiograph of the vanadium. The relative modulation depth of the structures is ~15% (corresponding to vanadium thickness modulation of ± 0.5 μm), considerably higher than the modulation depth of the expected EXAFS (<5%), making the reliable measurement of EXAFS impossible. It should be noted that the EXAFS modulations [appearing as vertical lines in records like that in Fig. 111.35(b)] are due to modulations in the absorption as functions of photon energy, whereas the 2-D structure modulations
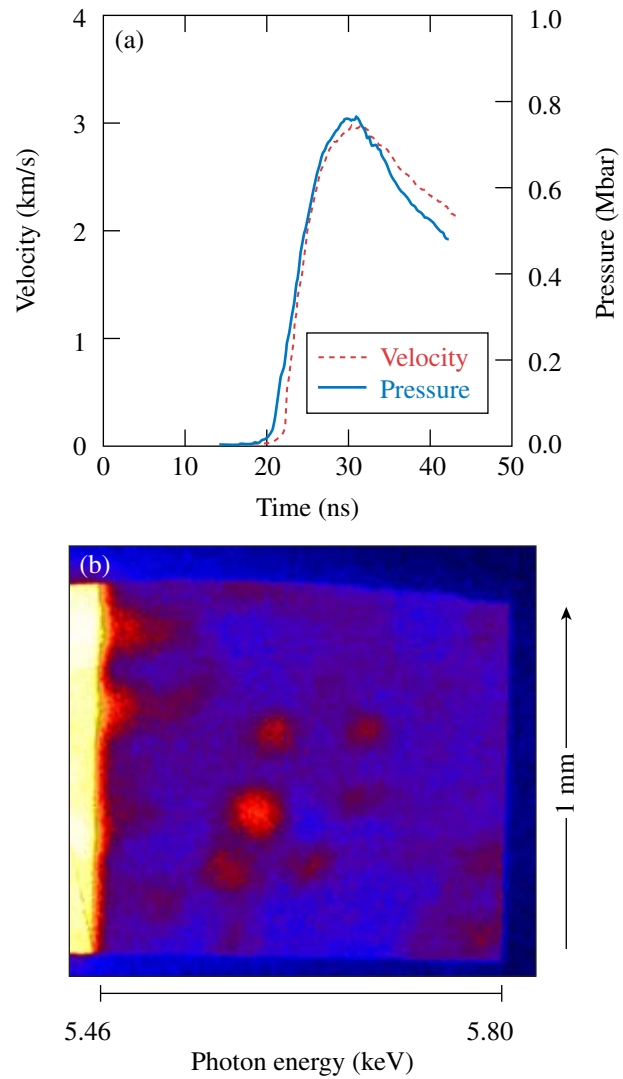
Figure 111.35
(a) High pressure achieved with high laser irradiance: VISAR-measured back-surface velocity and derived pressure for an irradiance of 25 TW/cm^2 (400-μm-vacuum-gap target, without a heat shield). (b) EXAFS record for a target shot at this irradiance showing nonuniformities believed to be due to the instability of the rarefaction wave following the unloading of the laser-launched shock at the rear surface of the reservoir. (The EXAFS record is effectively a 2-D radiograph of the target, and the intensity modulations are due to modulations in the thickness of the vanadium layer.)

in Fig. 111.35(b) must be due to modulations in the thickness of the vanadium layer. Similar behavior was seen for targets with or without a heat shield. A possible explanation for this observed modulation is related to the instability occurring when the laser-launched shock arrives at the back surface of the reservoir, leading to a rarefaction wave moving in the opposite direction.[20] Modulations in the density of the expanding reservoir material grow linearly with time, at a rate proportional to

the shock speed and the perturbation wave number (see Fig. 5 in Ref. 20). These modulations result in modulations in the strength of impact on the target and, therefore, to modulations in the latter's compression. The instability appears for targets with or without a heat shield. The only common characteristic of the unstable cases is the high laser irradiance. This can be explained by the higher shock speed at higher laser intensities, leading to a higher growth rate. It is noteworthy that these nonuniformities do not seem to affect the VISAR signal [Fig. 111.35(a)]. The remainder of this article shows only results at irradiances lower than 20 TW/cm^2, where the nonuniformities discussed here were not observed.

3. The Heat Shield

Simulations described below show that without a heat shield, the front surface of the sample heats up substantially ($>10^4$ K for 17 TW/cm^2) and the heat flow into the sample creates a temperature gradient. The inclusion of a heat shield greatly reduces this heating and creates a quasi-uniform temperature profile of the order of 10^2 K. This heating has a dramatic effect on the EXAFS spectra, as seen when comparing EXAFS results for the two cases of targets with and without a heat shield. As explained above, EXAFS is sensitive to the temperature because of the Debye–Waller term in Eq. (1). The back-surface velocity (both measured and simulated) is affected very little by this heating. This is related to the fact that the pressure in the sample is determined mainly by the reservoir plasma at stagnation and the effect of target preheat is mainly to lower the density; in the relevant part of parameter space a very large increase in temperature at a constant pressure causes only a small decrease in density. Therefore, to achieve maximum compression and uniform, low temperature in laser ICE experiments, it is necessary to use targets with a heat shield.

The effect of the heat shield on the target behavior was studied with 1-D runs of the *LASNEX* code. Figure 111.36(a) shows the evolution of pressure on the front surface of the vanadium sample, with and without a heat shield, for otherwise identical conditions. Dashed curves refer to targets with a heat shield; solid curves refer to targets without a heat shield. In Fig. 111.36(b), the curves that rise later correspond to the 400-μm vacuum gaps. The smaller vacuum gap yields a higher pressure. The introduction of a heat shield creates a weak shock, as evidenced by the sharp initial rise in pressure. Some reverberation is due to shock reflections, but when the pressure increases further, its behavior is almost the same as when the heat shield is absent. The predicted effect of the heat shield on the rear-surface velocity is seen in the experiment (Fig. 111.33 compared with Fig. 111.37 below). Figure 111.36(b) shows the
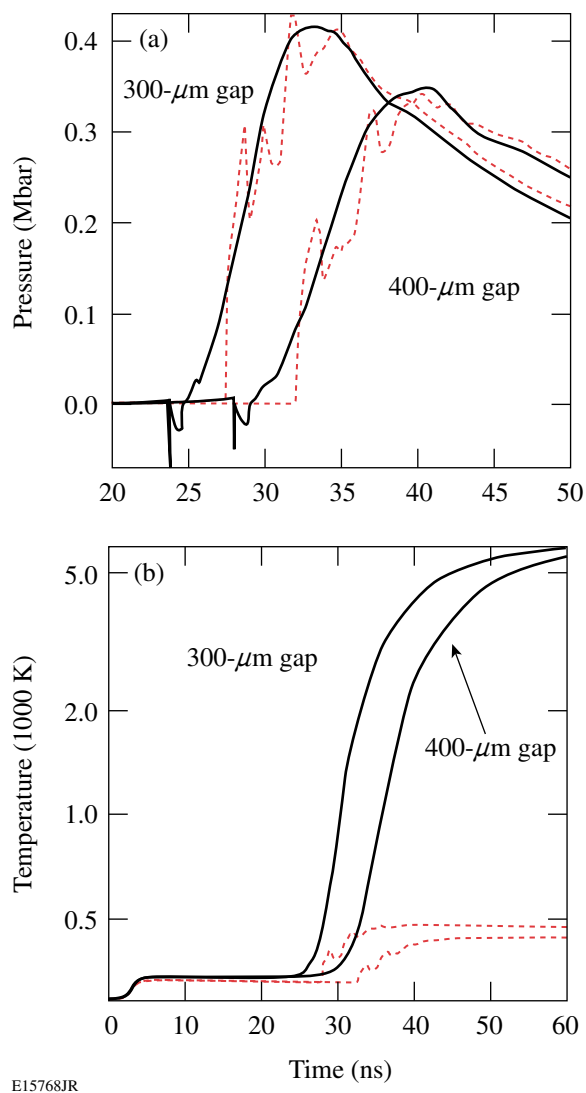
Figure 111.36
LASNEX simulation for targets of two different vacuum gaps, with and without a heat shield: (a) the evolution of pressure on the front surface of the vanadium sample, and (b) the evolution of temperature in the middle of the vanadium sample. Dashed curves: with a heat shield; solid curves: without a heat shield. The heat shield is seen to effectively block the heating from reaching the sample. It has a much greater effect on the temperature than on the pressure. The results in (a) are borne out by the VISAR results and those in (b) by the EXAFS results.

evolution of temperature in the middle of the vanadium sample with and without a heat shield. The heat shield effectively eliminates the heat flow from the front surface. More simulation examples, as will be shown in Figs. 111.42 and 111.43, can be summarized as follows (for 17 TW/cm^2 at times $\geq$35 ns): (a) With a heat shield the temperature is quasi-uniform and low (~10^2 K) and the compression is 15%. (b) Without a heat shield the temperature falls sharply from a very high surface value

($>10^4$ K) and toward the back surface approaches ~500 K. The compression, ~8%, is much smaller than with a heat shield. These simulation results are borne out by the EXAFS measurements (as will be shown in Fig. 111.43).

Figure 111.37 shows the VISAR-measured rear-surface velocity of an ICE target of 300-μm vacuum gap, with a heat shield, irradiated at 20 TW/cm^2. In close agreement with Fig. 111.36, the heat shield introduces a sharp initial rise in the velocity due to a shock, but later the velocity approaches a curve characteristic of a shockless compression. Thus, the employment of a heat shield results in a significant improvement in target performance, with only a small perturbation. The thickness of the heat shield (8 μm) was chosen to be sufficiently large to protect the sample from heating but not large enough to cause steepening of the compression wave into a strong shock. With Be, where both the density and the sound speed are higher than for CH, a thicker heat shield could be used without causing such steepening.
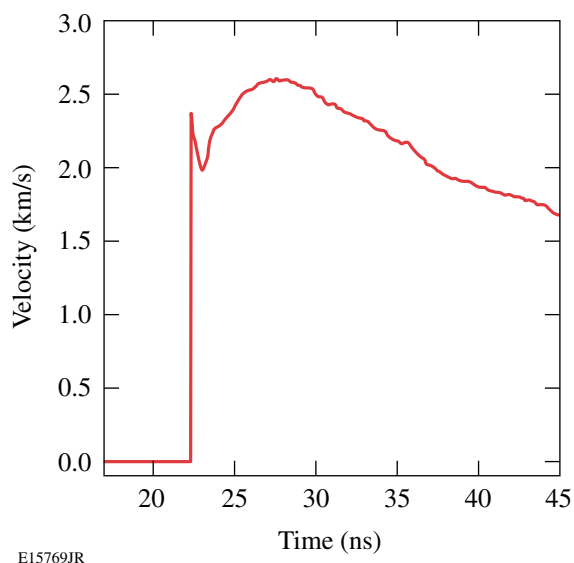

E15769JR

Figure 111.37
VISAR-measured rear-surface velocity of an ICE target of 300-μm vacuum gap, with a heat shield, irradiated at 20 TW/cm^2. In close agreement with Fig. 111.36, the heat shield introduces a sharp initial rise in the velocity due to a shock, but later the velocity approaches the shape of the velocity curve obtained with no heat shield.

4. Measurements of Preheat

To measure the temperature rise due to backlighter radiation, the EXAFS spectrum is obtained when irradiating the backlighter but without firing the drive beams. The temperature rise deduced from the EXAFS spectrum is then solely due to the backlighter radiation. The temperature is deduced from a

fit of the EXAFS spectrum calculated by the FEFF code to the experimental spectrum. As explained in the **Introduction** (p. 167), the parameters R (nearest-neighbor distance) and σ (mean atomic vibration amplitude) in the FEFF code are varied to yield the best fit. The resulting values of R and σ yield the temperature and compression. A typical result is shown in Fig. 111.38. Here the best fit of the FEFF code corresponds to a compression of 1 (i.e., the normal density of vanadium, 6.11 g/cm^3) and a temperature rise from room temperature of $\Delta T \sim 200$ K. The precision of temperature determination[8] is 10% to 15%.

To measure the preheat by radiation from the laser-deposition region, the target is probed at ~20 ns after firing the driving beams, i.e., before the impact of the expanding reservoir on the vanadium sample. The FEFF fit shown in Fig. 111.39 yields a temperature of 630 K (and normal density). Of this, a rise of ~200 K is shown in Fig. 111.38 to be due to the backlighter radiation. Thus, the temperature rise due to radiation from the laser-deposition region is ~130 K. The corresponding calculated preheat can be read off Fig. 111.36(b) at times <30 ns (preheat due to the backlighter is not included in the simulations). The result is ~90 K; the discrepancy could be due to shot irreproducibility (since two target experiments are required to make this determination). It should be noted that heating due to radiation from the laser-deposition region in the case of shock compression[8,9] is negligible because in that case

E14661JR

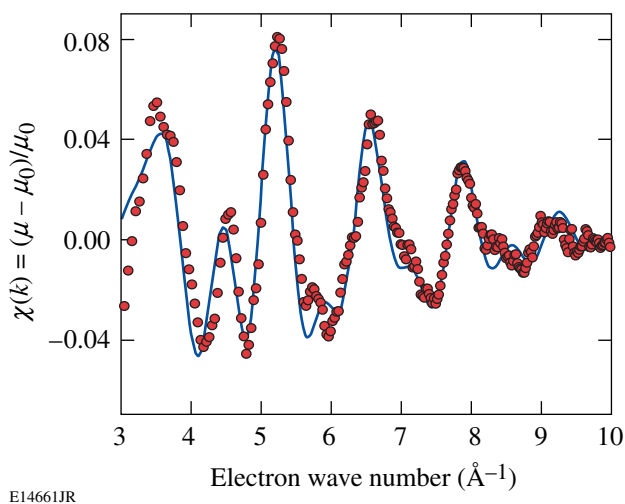Figure 111.38
Fitting spectra calculated by the FEFF code to the measured EXAFS for the case where the drive beams were not shot. The temperature of the best-fit spectrum corresponds to an increase above room temperature of $\Delta T \sim 200$ K. This heating is due to radiation from the imploding spherical target. The density of the best-fit spectrum corresponds to the normal density of vanadium.
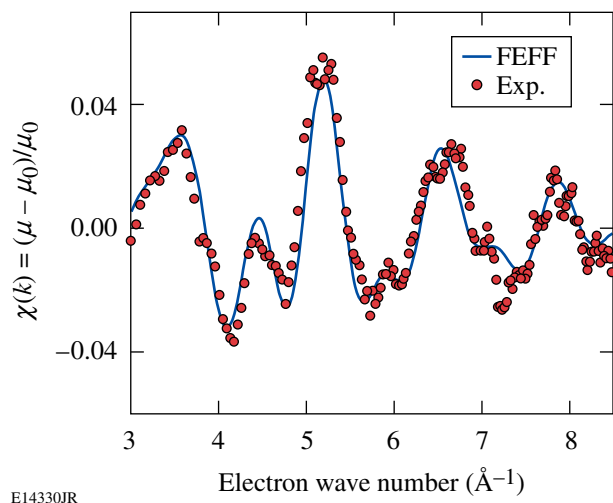
E14330JR

Figure 111.39
Fitting FEFF spectra to the measured EXAFS of a driven target at 20 ns (i.e., before the impact of the expanding reservoir on the vanadium sample). This serves to determine the preheat due to radiation from the laser-deposition region, 130 K in this case.

the laser intensity required for achieving the same pressure is about ten times smaller than in the case of ICE. Nevertheless, the heating due to compression alone is considerably lower in the case of ICE.

5. EXAFS Measurement of Compression and Temperature

EXAFS measurements of the vanadium were made around peak compression. Figure 111.40 shows the raw measured spectra for undriven and driven ICE vanadium targets [(before extracting the $\chi(k)$ function]. In the undriven case only the backlighter target was irradiated; the driven case refers to a target with a heat shield, a 300-μm vacuum gap, irradiated at 17 TW/cm^2. Comparison of the EXAFS modulations above the vanadium K edge for the two spectra clearly shows the effect of compression: (a) a higher density, as evidenced by the lengthening of the EXAFS modulation period, and (b) heating, as evidenced by the faster damping of the oscillations with increasing photon energy. The driven spectrum of Fig. 111.40 was analyzed with the FEFF EXAFS code. The best fit, shown in Fig. 111.41, yields the conditions within the vanadium at the time 39 ns (with respect to firing the drive-laser beams). The best fit corresponds to a compression of 15% (i.e., a density of 7 g/cm^3) and a temperature of 720 K.

As explained in the **Introduction** (p. 167), the FEFF fit yields the parameters R and σ^2; R (the nearest-neighbor distance) yields the density, whereas the temperature is derived

E15770JR
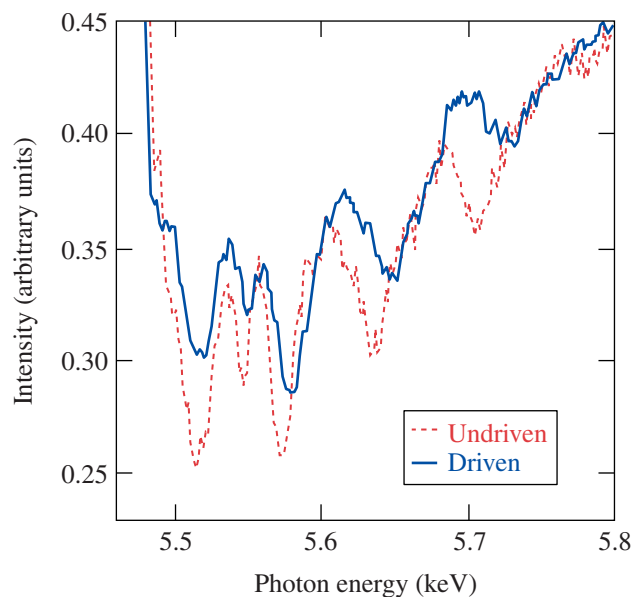
Figure 111.40
Measured spectra for undriven and driven ICE vanadium targets (before extracting the χ function). Comparison of the EXAFS modulations above the vanadium K edge for the two spectra clearly shows the effect of compression, namely, the lengthening of the modulation period, and the effect of heating, namely, the faster damping with increasing photon energy.

E14660JR
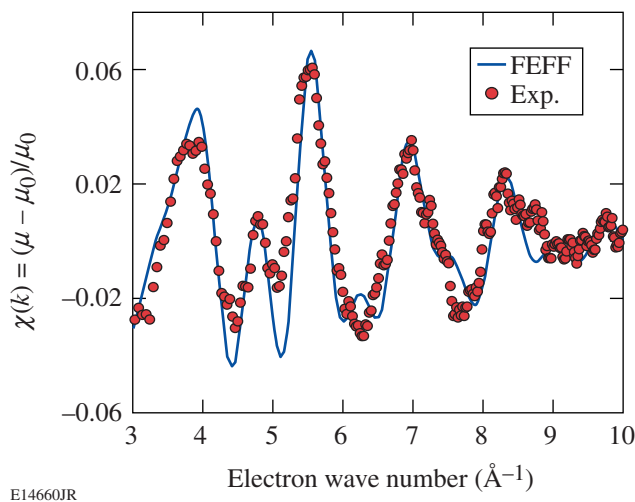
Figure 111.41
EXAFS measurement of ICE compression: fitting FEFF spectrum to the measured EXAFS for the case of an ICE target irradiation at ~17 TW/cm^2. The fitting parameters yield a compression of 15% and a temperature of 720 K. Only ~90 K is the increase due to compression; the rest is preheat. This is a demonstration that laser-driven ICE can achieve a similar compression at a lower temperature than in shock compression.

from σ^2 and the density. The corresponding *LASNEX* simulation of the vanadium density for a 300-μm-vacuum-gap target, with heat shield, at 39 ns is shown in Fig. 111.42, showing a uniform profile. The time 39 ns [which is slightly past peak compression, see Fig. 111.36(a)] was chosen because then the compression profile becomes uniform. The measured compression value is in excellent agreement with *LASNEX*. As seen above, of the total temperature rise from room temperature, $\Delta T \sim 200$ K is the increase due to radiation from the backlighter and $\Delta T \sim 130$ K is the increase due to radiation from the laser-absorption region. Thus, only ~90 K is the increase due to compression. This result can be compared with the EXAFS measurement of shock compression of vanadium,[8] where the same compression was accompanied by a temperature rise of $\Delta T = 770$ K. Thus, *laser-driven ICE can achieve a similar compression at a lower temperature than in shock compression*. At higher drive pressures this advantage of ICE will increase because although preheat by radiation from the laser-absorption region will be higher, the main preheat (due to the backlighter) need not increase.
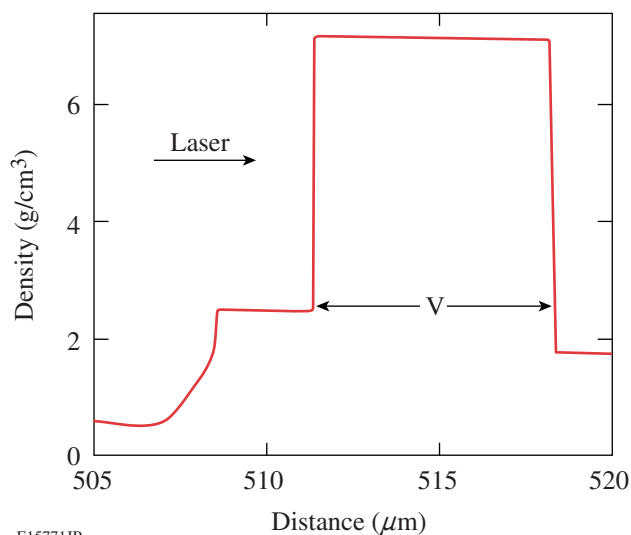
E15771JR

Figure 111.42
LASNEX simulation of the vanadium (V) density for a target with a heat shield, 300-μm vacuum gap, at 39 ns. By the time the pressure starts to fall the density becomes uniform. The density (~7 g/cm^3) corresponds to a compression of 1.15, in very good agreement with the measured value (Fig. 111.4l).

We turn now to the case of an ICE target without a heat shield. As discussed above, the severe heating of the vanadium front surface creates a strong temperature gradient that makes the EXAFS analysis more complicated and less reliable. The value of such target shots is mostly in demonstrating that without a heat shield such severe heating indeed takes place. Fig-

ure 111.43 shows the relevant *LASNEX*-simulated temperature and density profiles for a 400-μm-vacuum-gap target without a heat shield, at 37 ns. Heating from the plasma impact is seen to be severe. The density profile shows, as explained above, a lower density than in the case of a target with a heat shield (Fig. 111.42): ~6.5 g/cm^3 (compression of 8%) as compared with ~7 g/cm^3 (compression of 15%). We use these profiles to calculate the expected EXAFS spectra, shown in Fig. 111.44(a). For various depths within the vanadium, EXAFS spectra are calculated by the FEFF code, using the local density and temperature values given by *LASNEX*. Three examples of such spectra are shown, as well as the spatial average. The
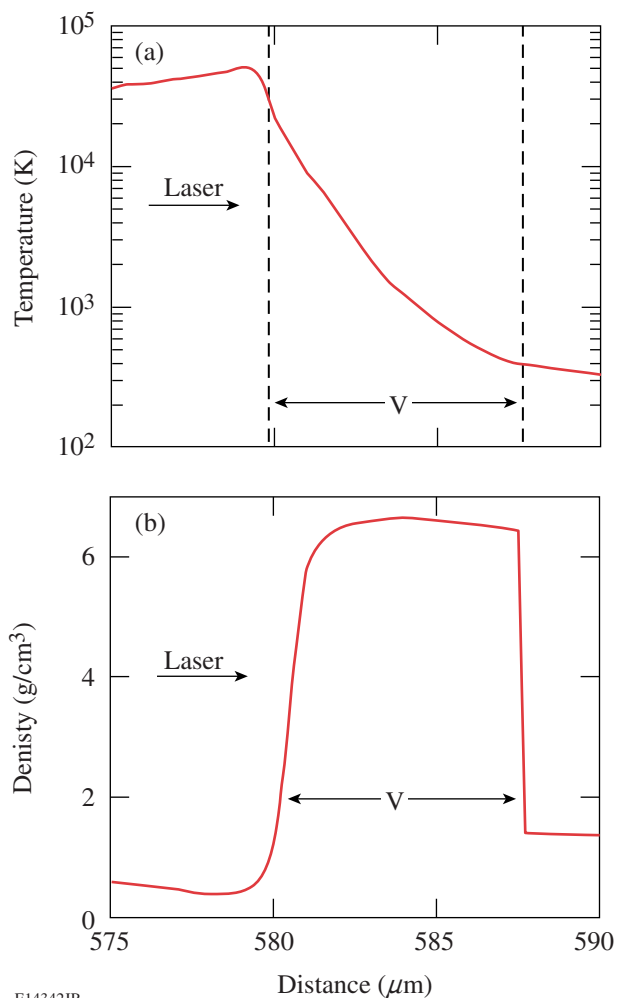
E14342JR

Figure 111.43
LASNEX-simulated temperature (a) and density (b) profiles for a 400-μm-vacuum-gap target without a heat shield, at 37 ns. Heating from the plasma impact is seen to be severe, resulting in a lower density (or compression). The profiles are used to calculate the expected EXAFS spectrum [Fig. 111.44(a)] by averaging over the spatially resolved EXAFS spectra.

regions of higher temperatures contribute very little to the average. Effectively, the average is over the region where the temperature is less than ~1000 K. The main effect of the high temperature is to lower the amplitude of the average spectrum. This is because the secular absorption $\mu_0(k)$, appearing in the denominator of $\chi(k)$, is independent of temperature and thus corresponds to absorption throughout the vanadium thickness. Since the amplitude of the average spectrum in Fig. 111.44(a) is smaller than that in Fig. 111.41 (the case with a heat shield) by a factor of ~2.5, the front ~60% of the vanadium thickness has temperatures much higher than ~1000 K; this agrees with the computed temperature profile in Fig. 111.43(a). Thus, *the impact heating and its suppression by the heat shield is demonstrated*. Figure 111.44(b) shows a comparison of the average spectrum from (a) and the corresponding experimental spectrum. Unlike in Figs. 111.38, 111.39, and 111.41 where FEFF profiles were adjusted to fit the data, here the FEFF profiles are fixed by the *LASNEX*-calculated parameters.

However, some adjustment had to be made in the frequency of the calculated EXAFS (adding 4% compression) to fit the data, but, even so, the fit is poor. This is due to the difficulty in correctly simulating EXAFS in a steep temperature gradient. Nevertheless, the main goal of such target shots was realized: the low amplitude of the spectrum in Fig. 111.44(b) as compared with that in Fig. 111.41 is clear evidence of significant sample heating when a heat shield is not used.

Conclusions

In summary, EXAFS measurements in isentropic compression experiments show details not accessible by VISAR measurements. In particular, the sample temperature has been measured. To determine the temperature rise due to the compression, the preheat was determined separately and subtracted out. This preheat is due to three sources: radiation from the laser-deposition region, radiation from the backlighter, and heat conduction from the front surface of the target. In the present experiment the preheat was higher than the heating due to the compression. In future experiments at higher compressions, however, the reverse may be true. The experiments showed that when a heat shield is not present, significant heating occurs within a few microns of the surface. The shock generated by the heat shield has only a small effect on the main compression wave; a heat shield made of a material of high sound speed (such as diamond) may greatly reduce this shock. The experiments also showed that a nonuniform compression occurs at irradiances higher than ~20 TW/cm^2 (or pressures higher than ~0.6 Mbar); the more-uniform irradiation of a hohlraum excited by the laser beams may reduce this effect.
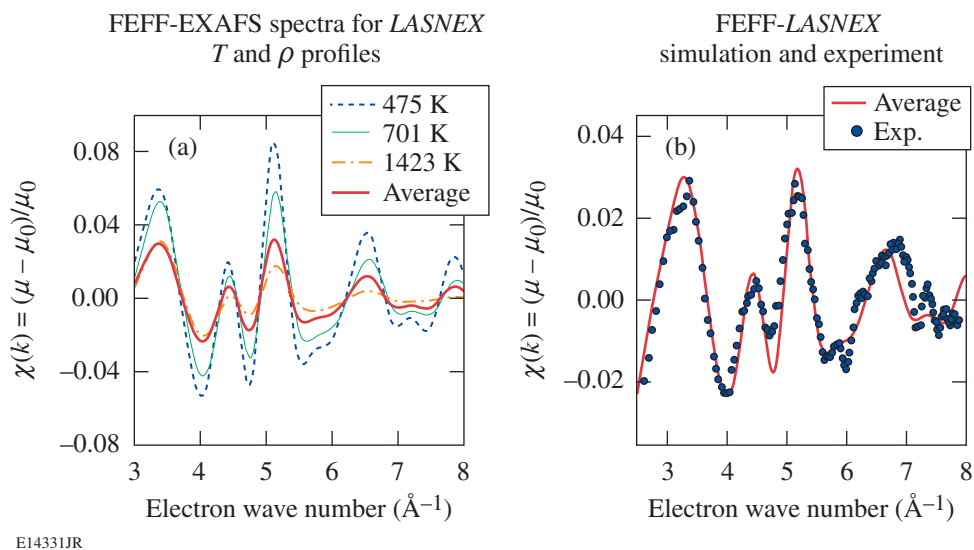
Figure 111.44
EXAFS analysis for the nonuniform case of an ICE target without a heat shield. (a) For various depths within the vanadium, EXAFS spectra are calculated by the FEFF code, for the density and temperature values given by *LASNEX* (Fig. 111.43). Three examples of such spectra are shown, as well as the spatial average. (b) Comparison of the average spectrum from (a), with slight adjustments, and the corresponding experimental spectrum. The low amplitude of the spectrum in Fig. 111.44(b) as compared with that in Fig. 111.41 is evidence for significant sample heating when a heat shield is not used.

REFERENCES

1. B. A. Remington, G. Bazan, J. Belak, E. Bringa, M. Caturla, J. D. Colvin, M. J. Edwards, S. G. Glendinning, D. S. Ivanov, B. Kad, D. H. Kalantar, M. Kumar, B. F. Lasinski, K. T. Lorenz, J. M. McNaney, D. D. Meyerhofer, M. A. Meyers, S. M. Pollaine, D. Rowley, M. Schneider, J. S. Stölken, J. S. Wark, S. V. Weber, W. G. Wolfer, B. Yaakobi, and L. V. Zhigilei, Metall. Mater. Trans. A **35A**, 2587 (2004).

2. T. R. Boehly, R. S. Craxton, T. H. Hinterman, J. H. Kelly, T. J. Kessler, S. A. Kumpan, S. A. Letzring, R. L. McCrory, S. F. B. Morse, W. Seka, S. Skupsky, J. M. Soures, and C. P. Verdon, Rev. Sci. Instrum. **66**, 508 (1995).

3. P. A. Lee *et al.*, Rev. Mod. Phys. **53**, 769 (1981).

4. C. Dai *et al.*, J. Phys. D: Appl. Phys. **34**, 3064 (2001).

5. J. Edwards *et al.*, Phys. Rev. Lett. **92**, 075002 (2004).

6. K. T. Lorenz *et al.*, Phys. Plasmas **12**, 056309 (2005).

7. K. T. Lorenz *et al.*, High Energy Density Phys. **2**, 113 (2006).

8. R. F. Smith *et al.*, Astrophys. Space Sci. **307**, 269 (2007).

9. B. Yaakobi, D. D. Meyerhofer, T. R. Boehly, J. J. Rehr, B. A. Remington, P. G. Allen, S. M. Pollaine, and R. C. Albers, Phys. Plasmas **11**, 2688 (2004).

10. B. Yaakobi, T. R. Boehly, D. D. Meyerhofer, T. J. B. Collins, B. A. Remington, P. G. Allen, S. M. Pollaine, H. E. Lorenzana, and J. H. Eggert, Phys. Plasmas **12**, 092703 (2005).

11. J. J. Rehr, R. C. Albers, and S. I. Zabinsky, Phys. Rev. Lett. **69**, 3397 (1992).

12. E. Sevillano, H. Meuth, and J. J. Rehr, Phys. Rev. B **20**, 4908 (1979).

13. R. M. More *et al.*, Phys. Fluids **31**, 3059 (1988).

14. G. R. Gathers, J. Appl. Phys. **59**, 3291 (1986).

15. G. J. Streletz and L. H. MacFarland, in *Shock Compression of Condensed Matter–1999*, edited by M. D. Furnish, L. C. Chhabildas, and R. S. Hixson, AIP Conf. Proc. 505 (American Institute of Physics, New York, 2000), pp. 201–204.

16. P. M. Celliers *et al.*, Appl. Phys. Lett. **73**, 1320 (1998).

17. D. B. Hayes, Sandia National Laboratory, Albuquerque, NM, SAND2001-1440, NTIS Order No. DE2001-783087 (2001); D. B. Hayes *et al.*, J. Appl. Phys. **96**, 5520 (2004).

18. G. B. Zimmerman and W. L. Kruer, Comments Plasma Phys. Control. Fusion **2**, 51 (1975).

19. T. J. Kessler, Y. Lin, J. J. Armstrong, and B. Velazquez, in *Laser Coherence Control: Technology and Applications*, edited by H. T. Powell and T. J. Kessler (SPIE, Bellingham, WA, 1993), Vol. 1870, pp. 95–104.

20. J. G. Wouchuk and R. Carretero, Phys. Plasmas **10**, 4237 (2003).

The Effect of Resonance Absorption in OMEGA Direct-Drive Designs and Experiments

Introduction

Ignition of thermonuclear fuel (DT mixture) requires a fuel areal density $\gtrsim 0.3$ g/cm^2 and a hot-spot temperature $\gtrsim 10$ keV (Refs. 1 and 2). Such conditions are predicted to be achieved in direct-drive inertial confinement fusion (ICF) designs, in which a cryogenic spherical DT-ice-shell target is imploded using direct illumination by intense laser beams.[3–7] High energy gain in direct-drive ICF designs is achieved by optimizing the laser pulse shape and target dimensions.[1,8,9]

Physical understanding of laser–plasma coupling is required for accurate numerical modeling of high-gain, direct-drive ICF designs. These designs are based on precise timing of laser-driven shocks, which determine the target adiabat (defined as a ratio of the fuel pressure to the Fermi-degenerate pressure).[10,11] The shock strength depends crucially on mechanisms of laser light absorption. A theoretical and experimental investigation of laser absorption, focusing on the effect of resonance absorption for typical conditions in the direct-drive experiments on the OMEGA Laser System,[12] is the subject of this article.

Resonance absorption of electromagnetic waves in an unmagnetized, inhomogeneous plasma has been of considerable interest for a long time.[13–25] In this process, a p-polarized electromagnetic wave, i.e., a wave that has a nonzero electric field component along the electron-density gradient ∇n_0, propagates from low to high densities and approaches the critical surface with an electron density $n_0 = n_{cr}$, where the laser frequency ω matches the local electron plasma frequency $\omega_{pe} = 4\pi n_0 e^2 / m_e$. Here, e and m_e are the electron charge and mass, respectively. During this propagation, the wave is partially reflected from the turning point, defined by the condition $\omega_{pe} = \omega \cdot \cos\theta$, where θ is the angle between the vacuum wave vector $\mathbf{k}$ and the density gradient, and the small part of the wave energy tunnels to the critical density and excites the resonance plasma oscillations. These oscillations can be damped by various mechanisms, including electron–ion collisional damping and excitation of Langmuir waves. A one-dimensional model of resonance absorption in linear density profiles has been the subject of numerous analytical and numerical investigations.

Forslund et al.[19] solved numerically the wave equation for the electric field $\mathbf{E}$ and found the absorption fraction of electromagnetic waves as a function of $q \equiv (kL)^{2/3} / \sin^2\theta$, where L is the density scale length. This result was confirmed later by the simulations of Pert[21] and Means et al.,[22] who employed different methods. All of these numerical results agree well with analytic results obtained by Omel'chenko and Stepanov,[16] Speziale and Catto,[20] and Tang[17] for limited ranges of q. An analytic expression for the absorption fraction in the whole range of q was obtained by Hinkel–Lipsker et al.[23] in the limit of small thermal and collisional effects. Later, the same authors[24] found analytic solutions of the problem in the case of parabolic density profiles. In our current numerical study, we do not restrict ourselves by linear or parabolic density profiles using density profiles obtained in hydrodynamic simulations. A recent study by Xu et al.[25] concentrated on modifications in resonance absorption caused by the relativistic effect and pondermotive force.

Direct-drive experiments conducted on OMEGA are routinely simulated using the 1-D hydrodynamic code *LILAC*.[26] The standard laser-absorption algorithm in *LILAC* is the ray-trace algorithm with ion–electron collisional absorption (inverse bremsstrahlung). An optional semi-analytic model of resonance absorption[27] can be used in conjunction with the ray-trace algorithm. An advantage of this semi-analytic model is its simplicity, whereas a disadvantage is its insufficient accuracy: it typically overestimates the resonance absorption by a factor of ~2 (Ref. 27). In this study, to more accurately investigate resonance absorption, the ray-trace algorithm of laser absorption in *LILAC* is replaced by a new algorithm based on the numerical solution of a wave equation in planar geometry.

This article addresses the following issues: (1) The wave equation describing the steady-state structure of electromagnetic and Langmuir wave components in inhomogeneous plasma is presented, and the numerical method in the planar geometry is described. (2) The results of numerical simulations of the resonance absorption in OMEGA plasmas are presented in the case of both planar and spherical geometries. (3) The

results of planar reflection light experiments on OMEGA are presented and compared with simulations, and a design of planar shock-timing experiments is considered. (4) The main results are discussed and summarized in the final section.

Resonance Absorption in the Fluid Approximation

We consider an electromagnetic wave of frequency ω propagated in vacuum, which obliquely irradiates a slab of warm, unmagnetized plasma. Properties of the slab are assumed to vary with a characteristic scale length $\gg c/\omega$. Neglecting ion and low-frequency electron motions, one can describe a high-frequency electron motion caused by the electromagnetic wave using the linearized momentum equation

$$\frac{\partial \mathbf{u}_e}{\partial t} = -\frac{1}{m_e n_0} \nabla P_e - \frac{e}{m_e} \mathbf{E} - \nu \mathbf{u}_e, \tag{1}$$

where $\mathbf{u}_e$ is the velocity and P_e is the pressure of electrons, $\mathbf{E}$ is the electric field, and ν is the damping rate. Assuming a polytropic equation of state (e.g., Ref. 28), $P_e \propto n^3$, where n is the electron density, and a time variation of all perturbed quantities $\propto e^{-i\omega t}$, and combining Eq. (1) with the Poisson equation $\nabla \cdot \mathbf{E} = -4\pi e n$, we derive the expression for the current density

$$\mathbf{j} = -e n_0 \mathbf{u}_e = i \frac{\omega_{pe}^2 \mathbf{E}}{4\pi(\omega + i\nu_{em})} - i \frac{3 v_e^2 \nabla(\nabla \cdot \mathbf{E})}{4\pi(\omega + i\nu_w)}, \tag{2}$$

where $v_e^2 = T_e/m_e$ is the electron thermal velocity square and T_e is the electron temperature. In Eq. (2), two different damping rates ν_{em} and ν_w have been introduced instead of the single damping rate ν in Eq. (1) (see Ref. 19). The rate ν_{em} corresponds to the electromagnetic and ν_w to the Langmuir wave components represented by the first and second terms on the right-hand side of Eq. (2), respectively. The electric field $\mathbf{E}$ obeys Maxwell's equations, which can be reduced to the steady-state wave equation

$$\nabla^2 \mathbf{E} - \nabla(\nabla \cdot \mathbf{E}) + \frac{\omega^2}{c^2}\left(\mathbf{E} + i\frac{4\pi}{\omega}\mathbf{j}\right) = 0, \tag{3}$$

where $\mathbf{j}$ is defined by Eq. (2). Solving Eq. (3) with respect to $\mathbf{E}$, one can calculate the laser-absorption rate $Q = \mathbf{j} \cdot \mathbf{E}$. With the help of Eq. (2), Q can be expressed in the following form:

$$Q = Q_{em} + Q_w$$

$$= \nu_{em}\frac{\omega_{pe}^2}{\omega^2 + \nu_{em}^2}\frac{\mathbf{E}^2}{8\pi} + \nu_w\frac{3v_e^2}{\omega^2 + \nu_w^2}\frac{(\nabla \cdot \mathbf{E})^2}{8\pi}. \tag{4}$$

This form allows one to distinguish the different contributions to laser absorption: the electromagnetic Q_{em} and Langmuir wave Q_w components. The damping rate ν_{em} is determined by the collisional damping, $\nu_{em} = \nu_{ei}$ (Ref. 2). The damping rate ν_w, in addition to collisional damping, must include damping due to kinetic effects, which describe dissipation of Langmuir waves at $k\lambda_D \gtrsim 1$, where k is the wave number and λ_D is the Debye length. This gives $\nu_w = \nu_{ei} + \nu_L$, where

$$\nu_L = \left(\frac{27\pi}{8}\right)^{1/2}\frac{\omega_{pe}^2\omega^2}{\left(\omega^2 - \omega_{pe}^2\right)^{3/2}}e^{-\frac{3}{2}\frac{\omega^2}{\omega^2 - \omega_{pe}^2}} \tag{5}$$

is the Landau damping rate.[29]

We consider planar geometry and introduce the cartesian coordinates (x, y, z) with the z axis perpendicular to the plane of the plasma slab. The slab is uniform in the x and y directions and nonuniform in the z direction. The vacuum wave vector $\mathbf{k}$ of the incident plane electromagnetic wave is located in the y–z plane and inclined at an angle θ with the z axis. In these coordinates, the s-polarized electromagnetic wave is described by a solution E_x of the x component of Eq. (3). This solution is completely independent of a solution for the p-polarized wave described by E_y and E_z, which obey the coupled y and z components of Eq. (3). Assuming an independence of the field of the x coordinate and periodic dependence on the y coordinate, $\propto e^{ik_y y}$, where $k_y = (\omega/c)\sin\theta$, the corresponding components of Eq. (3) can be reduced to second-order ordinary differential equations in the following form: for the s-polarized wave,

$$\frac{d^2 E_x}{dz^2} + \frac{\omega^2}{c^2}(\epsilon - \sin^2\theta)E_x = 0, \tag{6}$$

and for the p-polarized wave,

$$\frac{d^2 E_y}{dz^2} - ik_y(1-\eta)\frac{dE_z}{dz} + \frac{\omega^2}{c^2}(\epsilon - \eta\sin^2\theta)E_y = 0, \tag{7}$$

$$\eta \frac{\mathrm{d}^2 E_z}{\mathrm{d}z^2} - ik_y(1-\eta)\frac{\mathrm{d}E_y}{\mathrm{d}z} + \frac{\omega^2}{c^2}\left(\epsilon - \sin^2\theta\right)E_z = 0, \qquad (8)$$

where we use the notations

$$\epsilon = 1 - \frac{\omega_{\mathrm{pe}}^2}{\omega(\omega + i\nu_{\mathrm{em}})} \ \ \text{and} \ \ \eta = \frac{3v_e^2}{\omega(\omega + i\nu_w)}\frac{\omega^2}{c^2}.$$

These differential equations are solved using the standard finite-difference numerical technique, which requires the solution of linear matrix equations. The matrix equations have a band diagonal form and can be efficiently solved by the LU decomposition method.[30] We assume vacuum boundary conditions for the incident and reflected electromagnetic waves at the outer edge of the plasma corona. For example, these conditions for the s-polarized wave are derived by using a vacuum solution in the form $E_x = Ae^{ik_zz} + Be^{-ik_zz}$, where $k_z = (\omega/c)\cos\theta$, and the complex coefficients A and B to be determined matching this solution and its first derivative with the corresponding numerical solution at the outer edge. Similarly, other solutions of the electric field, E_y and E_z, are considered in the case of the p-polarized wave. Knowing the field components, one can calculate the laser-absorption rate using Eq. (4) as the energy source in a 1-D hydrodynamic code.

Resonance Absorption in Typical OMEGA Plasmas

The 60-beam, 30-kJ OMEGA Laser System[12] is used to study the physics of implosions by conducting spherical and planar experiments with millimeter-scale targets. OMEGA operates at a laser wavelength of $\lambda = 351$ nm and peak intensities varying from 10^{14} to 10^{15} W/cm^2 with a typical pulse rise time ~100 ps and a pulse duration ~1 to 3 ns. The pulse can be shaped to optimize target performance.[10,11]

In this section we investigate numerically the effects of resonance absorption for plasma conditions relevant to direct-drive OMEGA experiments. Currently, plastic (CH) material is used as an ablator in most applications;[7] therefore, we concentrate our analysis on CH plasma. All numerical results reported hereafter are obtained by employing the flux-limited Spitzer–Härm thermal-conduction model.[26,31] If not explicitly mentioned, simulations assume a flux-limiter value $f_{\mathrm{lim}} = 0.06$, and all of our numerical results include the Langdon effect.[32] Note that other more-sophisticated thermal-conduction models can be used, including the models based on the solution of the Fokker–Planck equation[33] and different nonlocal electron transport treatments.[34,35] We found, however, that the effect

of resonance absorption is not very sensitive to the particular choice of the thermal-conduction model.

The method of laser-absorption simulation described in the previous section was developed in planar geometry, where the incident light can be properly separated on the s- and p-polarized components. In spherical geometry, such a separation is not possible and the exact solution of the problem is more complicated. Instead of exactly solving the problem in spherical geometry, an approximate approach can be used to estimate laser absorption with the resonance effect. In the following two subsections we consider first the case of planar geometry, in which the effect of resonance absorption is calculated using the exact method; we then consider the case of spherical geometry, applying the planar-geometry approximation.

1. Planar Geometry

Figure 111.45 shows an example of a simulated electric field in a plasma developed during irradiation of a thick CH foil by a single p-polarized OMEGA laser beam with an angle of incidence $\theta = 23.2°$. This angle is typically used in planar OMEGA experiments and close to the angle at which resonance absorption is most effective (see the definition of this angle below). The drive laser pulse [Fig. 111.45(a)] is taken from the actual experiment and has a square shape with about 1-ns duration, an average intensity $I \approx 5 \times 10^{14}$ W/cm^2, and an initial rise time ≈ 100 ps. The intensity modulation seen in Fig. 111.45(a) is due to the effect of smoothing by spectral dispersion.[36] The solutions shown in Fig. 111.45(b) correspond to the time when the pulse intensity reaches the average value at $t = t_0$. The distribution of electron density n_0 [shown by the thick line in Fig. 111.45(b)] is obtained using a *LILAC* simulation. The incident laser light propagates from right to left. The electron temperature $T_e \approx 1$ keV at the critical surface, which is defined by the condition

$$n_0 = n_{\mathrm{cr}} \equiv \frac{m_e\omega^2}{4\pi e^2} \approx 9 \times 10^{21}\left(\frac{351\,\mathrm{nm}}{\lambda}\right)^2 \mathrm{cm}^{-3}. \qquad (9)$$

The value of T_e varies insignificantly on the spatial interval displayed in Fig. 111.45(b). The solution shown by the thin solid line is obtained including all terms in Eq. (1). This solution shows some increase in the electric field near the critical surface and, at the same time, shows a resonant excitation of Langmuir waves. These waves can be clearly seen in Fig. 111.45(b) as the short-wavelength structures at $z \approx 64$ μm, whereas the long-wavelength structures at $z > 64$ μm correspond to electromagnetic waves. The Langmuir
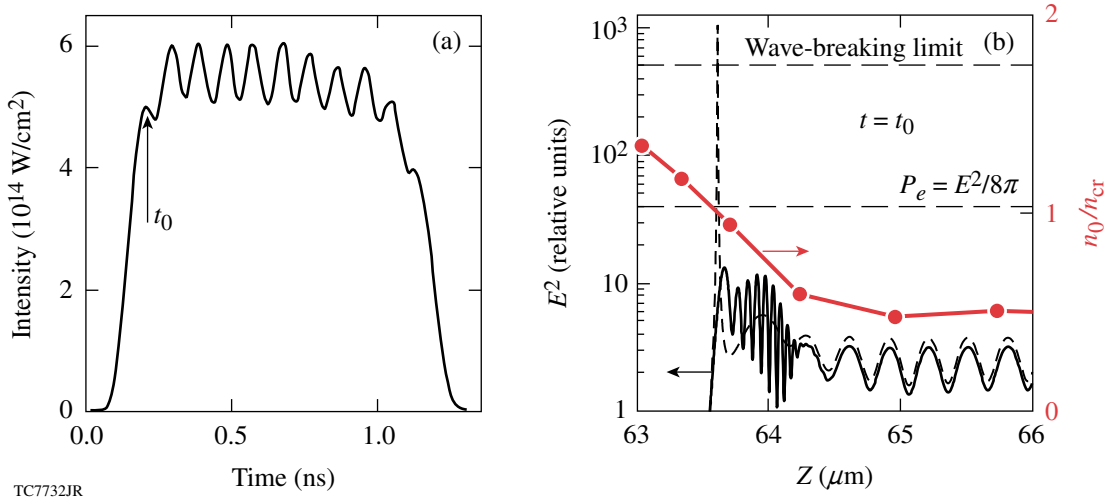
TC7732JR

Figure 111.45

Example distribution of the electric field in a CH plasma near the critical surface, $n_0 = n_{cr}$. (a) The drive laser pulse irradiated a thick planar CH target at $\theta = 23.2°$; the vertical arrow shows time t_0 and laser intensity for solutions presented in plot (b). (b) Distributions of the electron density n_0 and squared amplitude of the electric field $E^2 = E_y^2 + E_z^2$. Laser light with p-polarization propagates from right to left. The distribution of n_0 (thick solid line) is obtained using a 1-D *LILAC* simulation. The electron temperature near the critical surface is ≈ 1 keV. The thin solid and short-dashed lines show the distribution of E^2 obtained with and without the pressure term in Eq. (1), respectively. The two horizontal dashed lines represent the estimates of the wave-breaking and thermal pressure limits for E^2.

waves propagate from the critical surface to the right, toward the lower electron density, and decay due to Landau damping at $n_0 \lesssim 0.6\, n_{cr}$ (the "wave-decay" region). Landau damping results in a conversion of the energy stored in Langmuir waves into hot electrons with $T_h \approx 5$ keV, where the latter temperature is estimated using the phase velocity of Langmuir waves in the wave-decay region. Heating of the plasma [see Eq. (4)] occurs due to both collisional and Landau damping and is localized mainly between the critical surface and the wave-decay region. A typical electron temperature in the hot corona is about 1 to 2 keV, which is 2 to 5 times lower than our estimate of T_h. This could result in a deviation of the electron distribution function from Maxwellian and nonlocal effects in the energy deposition. In our simulations, however, we neglect such nonlocal effects and assume only the local energy deposition into thermal electrons. For comparison, the solution without excitation of Langmuir waves is shown by the short-dashed line in Fig. 111.45(b). This solution, obtained using Eq. (1) without the pressure term (the cold plasma limit), has a distinctive resonance peak in the electric field at the critical surface. Note that the resonant field in the latter case exceeds the limits for the field corresponding to the electron pressure P_e and wave-breaking threshold[37] [represented by the lower and upper horizontal dashed lines in Fig. 111.45(b), respectively].

Two important conclusions regarding plasma conditions in direct-drive OMEGA experiments result from the considered example: First, the resonant electric field in a typical OMEGA plasma is significantly below the wave-breaking limit. Second, the electromagnetic pressure corresponding to this field is typically below the electron pressure, which means that the pondermotive force is weak and can be neglected. These conclusions justify the omission of the nonlinear convection term $(\mathbf{u}_e \nabla)\mathbf{u}_e$ in Eq. (1).

Next, we study the time evolution of the resonance absorption and its dependence on laser intensity and incident angle. The resonance absorption in a simulation can be quantified by comparing the absorption rates for s- and p-polarized laser beams (Q^s and Q^p, respectively) since Q^p includes the effect of resonance absorption and Q^s does not. Figure 111.46 compares these absorption rates and also presents Q_w^p, which is the contribution to the absorption rate due to the resonant excitation of Langmuir waves [see Eq. (4)], calculated for the case of thick (>200 μm) CH foils irradiated by a 1-ns square pulse at $\theta = 23.2°$. Three different average beam intensities have been considered: 10^{14}, 5×10^{14}, and 10^{15} W/cm². Figure 111.46(a) shows the laser pulse shape and absorption rates Q^s for these three cases. Figure 111.46(b) shows the relative difference $(Q^p - Q^s)/Q^s$ (solid lines), which characterizes the contribu-
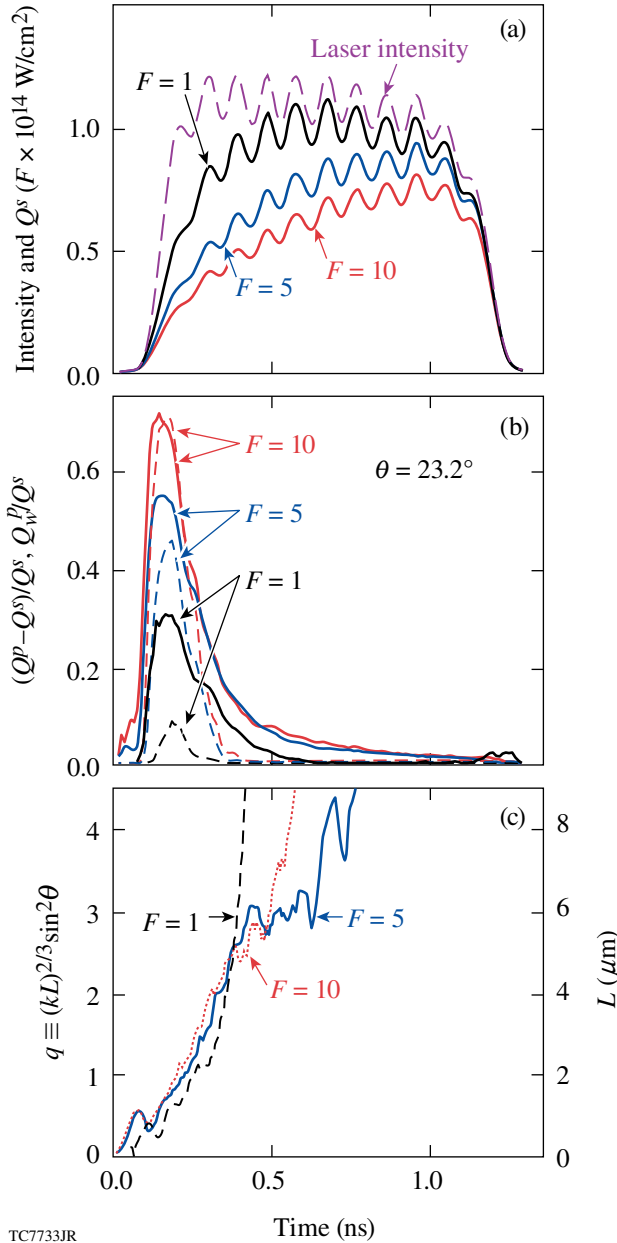
TC7733JR

Figure 111.46
Simulated evolution of the laser-absorption rate for single, s- and p-polarized, 1-ns OMEGA laser beams irradiating a thick planar CH target at $\theta = 23.2°$. Three different average laser intensities are considered: 10^{14}, 5×10^{14}, and 10^{15} W/cm^2, which are indicated by the corresponding values of the scaling factor $F = 1$, 5, and 10, respectively. (a) Drive-laser pulse (long-dashed line) and absorption rates Q^s (solid lines) for the s-polarized beams. These rates do not include the effect of resonance absorption. (b) The relative differences between the absorption rates for p- and s-polarized beams $(Q^p - Q^s)/Q^s$ (solid lines), which demonstrate the effect of resonance absorption in the p-polarized beams, and the relative absorption rates Q_w^p/Q^s due to the resonant excitation of Langmuir waves (dashed lines). (c) Evolution of $q \equiv (kL)^{2/3} \sin^2\theta$ and the density scale length L at the critical surface. The resonance absorption is important as soon as $0.1 < q < 2$ (Ref. 19).

tion of resonance absorption to the total laser absorption, and the ratio Q_w^p/Q^s (dashed lines). The results show that the effect of resonance absorption is important only in the initial 200- to 300-ps period of the laser pulse. This time dependence can be explained by the inverse dependence of resonance absorption on the density scale length L near the critical surface. Figure 111.46(c) shows the evolution of L and the dimensionless quantity $q \equiv (kL)^{2/3} \sin^2\theta$, where k is the vacuum wave number of laser light. The resonance absorption can be efficient if $0.1 \lesssim q \lesssim 2$ (Ref. 19). The density scale length is relatively short, $L \approx 1$ to 2 μm (so $q < 2$), during the rise of laser power. At a later time, at maximum laser power, the length becomes long enough, $L > 5$ μm ($q > 2$), to quench the resonance absorption. Another effect seen in Fig. 111.46(b) is that the resonance absorption, including absorption via Langmuir waves, is more significant for higher laser intensities. In particular, the resonance mechanism dominates over inverse bremsstrahlung at the beginning of the laser pulse for pulses with peak intensity $\gtrsim 5 \times 10^{14}$ W/cm^2. The dependence of resonance absorption on the intensity can be attributed to increased temperature near the critical surface in the case of higher laser intensities.[19]

The angular dependence of resonance absorption is demonstrated in Fig. 111.47, where the results of simulations are shown for a 100-ps laser pulse. For such a short pulse, the contribution of resonance absorption to the total absorption is more prominent and can be more easily measured experimentally (see Fig. 111.46). A laser pulse with a peak intensity of 5×10^{14} W/cm^2 is shown by the long-dashed line in Fig. 111.47(a). In the same figure, example absorption rates in the case of p- and s-polarized laser beams (thick and thin lines, respectively) and resonant excitation of Langmuir waves in the p-polarized beam (short-dashed line) are shown for $\theta = 17°$. Figure 111.47(b) plots the angular dependence of absorption fractions in the case of p- and s-polarized beams and resonant excitation of Langmuir waves, using the same notations as in Fig. 111.47(a). Here, the absorption fraction is defined as the ratio of the corresponding time-integrated absorption rate per unit surface to the time-integrated laser intensity on target. The difference between the absorption fractions for p- and s-polarized beams illustrates the relative effect of resonance absorption. This effect peaks at $\theta \approx 17°$ and corresponds to about a 30% increase in total absorption in comparison with the case of s-polarized beams. The energy absorbed due to the resonant excitation of Langmuir waves also peaks at $\theta \approx 17°$, where the contribution of this energy to the total absorption energy is about 50%.
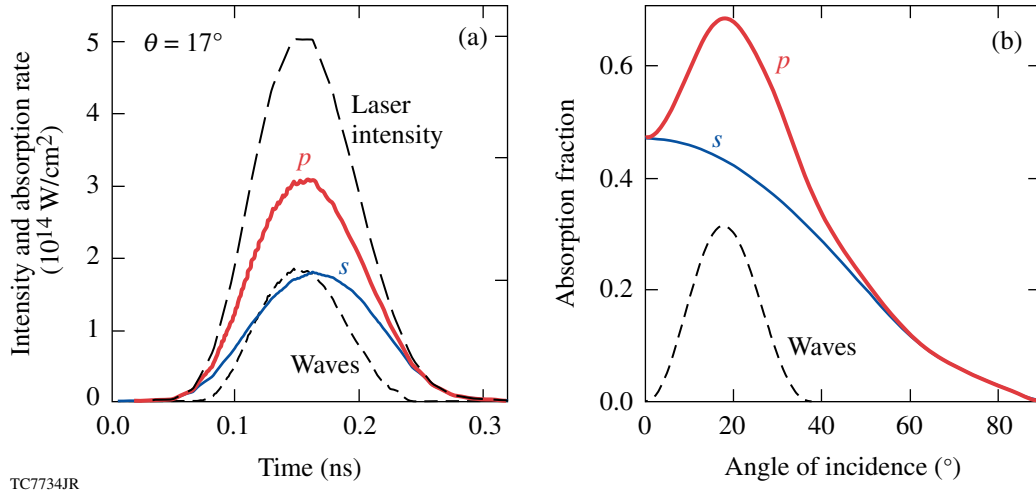
TC7734JR

Figure 111.47
Simulated absorption rate and angular dependence of absorption fraction for single, s- or p-polarized, 100-ps OMEGA laser beams irradiating a thick planar CH target. (a) Drive-laser pulse with a peak intensity of 5×10^{14} W/cm^2 (long-dashed line); the absorption rate for the p- and s-polarized beams (thick and thin solid lines, respectively), and the absorption rate due to the resonant excitation of Langmuir waves (short-dashed line). All of these rates are calculated assuming $\theta = 17°$. (b) Time-integrated absorption fractions as functions of θ in the same cases considered in (a). The effect of resonance absorption is represented by the difference in absorption rates and absorption fractions for the p- and s-polarized beams. This effect produces the maximum absorption fraction at $\theta \approx 17°$.

2. Spherical Geometry

In this section, we use an approximate approach to estimate the laser absorption, including the resonance effect, in spherical implosions. We apply the planar method to a small surface element of a spherical target. Such an element is irradiated by the laser light distributed over a range of incident angles θ from 0° to 90°. The total absorption rate for a target can be estimated by integrating the absorption rates for a given surface element over θ from all angles in the hemisphere that cover the surface element and integrating the result over the entire target surface. This approach can be justified if the thickness of the absorption region is much smaller than the target radius. Such a condition typically occurs during the first few hundred picoseconds in direct-drive OMEGA implosions.

The intensity profile $I(r)$ across an individual OMEGA laser beam can be approximated by the super-Gaussian[38] $I(r) = I_0 e^{-(r/r_0)^n}$, where I_0 is the center beam intensity, r is the distance from the beam's central axis, r_0 is the beam radius, and n is the super-Gaussian index. Assuming spherically symmetric illumination of a target of radius R, it is straightforward to obtain the angular-dependent laser intensity at each point of the target surface, $I(\theta) = I_0 e^{-(\sin\theta \cdot R/r_0)^n}$. Then, the intensity on target is

$$\bar{I} = 2\pi \int_0^{\pi/2} I(\theta) \cos\theta \sin\theta \, d\theta. \tag{10}$$

The angular distribution $I(\theta)$ is used in the modified planar method in *LILAC* to numerically estimate the laser-absorption rate Q in spherical implosions. To account for a mixed polarization of laser light from many randomly polarized OMEGA laser beams (up to 13 beams can irradiate a given small surface element), the method assumes an equal mixture of s- and p-polarized lights. The corresponding absorption rate is denoted as $Q^{s,p}$. The absorption rate calculated using only the s-polarized light, Q^s, does not include the effect of resonance absorption and is used for comparison. Note that, with respect to the assumed laser-absorption mechanisms, Q^s is similar to the absorption rate calculated using the spherical ray-trace method.[26]

Figure 111.48 shows an example of simulated laser-absorption rates in the spherical implosion of a CH target driven by a 12.4-kJ, 1-ns square OMEGA laser pulse. In this example, the target radius $R = 430$ μm, and the beam parameters $r_0 = 352$ μm and $n = 4.12$. The drive-laser pulse (long-dashed line) and calculated evolution of the absorption rates Q^s (solid lines) and $Q^{s,p}$ (short-dashed lines) for two values of the flux limiter $f_{\lim} = 0.06$ and 0.1 are shown in Fig. 111.48(a). The reduced values of Q^s and $Q^{s,p}$ for smaller $f_{\lim}$ can be explained by an increased coronal temperature and, as a result, the less-efficient inverse bremsstrahlung absorption. Figure 111.48(b) shows the evolution of the relative difference $(Q^{s,p} - Q^s)/Q^s$ (solid lines),
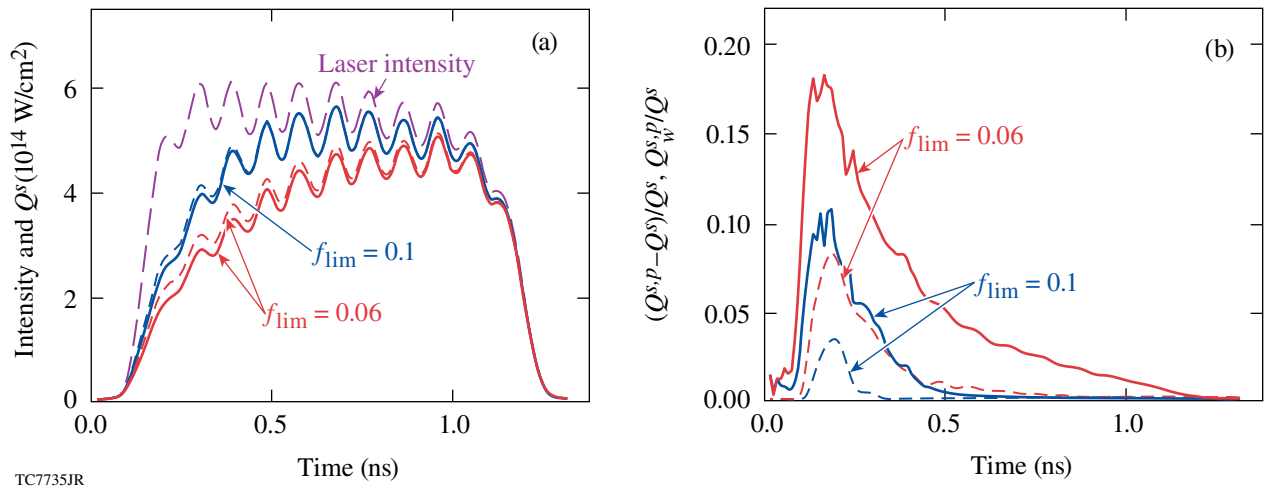
Figure 111.48
Simulated laser-absorption rates for two values of the flux limiter f_{lim} in the spherical implosion of a CH target driven by a 12.4-kJ, 1-ns OMEGA laser pulse. The approximate method to simulate the laser absorption in spherical implosions is discussed in the text. (a) Drive-laser pulse (long-dashed line) and absorption rates Q^s (solid lines) and $Q^{s,p}$ (short-dashed lines), for the s-polarized and mix-polarized (s and p) lights, respectively. The rate Q^s does not include the effect of resonant absorption, but $Q^{s,p}$ does. (b) The relative difference of absorption rates $\left(Q^{s,p} - Q^s\right)/Q^s$ (solid lines) and the relative absorption rates $Q_w^{s,p}/Q^s$ due to the resonant excitation of Langmuir waves (dashed lines).

which represents the relative effect of resonance absorption, and the ratio $Q_w^{s,p}/Q^s$ (dashed lines), where $Q_w^{s,p}$ represents a part of $Q^{s,p}$ due to the resonant excitation of Langmuir waves. Similar to the planar case (see Fig. 111.46), resonance absorption in spherical targets has a maximum effect at the beginning of the laser pulse, during the first 200 to 400 ps. Also, the resonantly excited Langmuir waves give a noticeable contribution to the total absorption only at the beginning of the laser pulse. The resonance absorption is reduced with an increase in f_{lim}. This reduction can be explained by an increase in the density scale length near the critical surface with an increase in f_{lim}. Based on the numerical results presented in Fig. 111.48(a), the effect of resonance absorption can be modeled with the standard laser ray-trace absorption method[26] by adjusting the flux limiter to a higher value (e.g., from the typical $f_{lim} = 0.06$ to 0.08) during the first ~200 ps of the pulse.

The dependence of resonance absorption on laser intensity in spherical implosions is demonstrated in Fig. 111.49 in the case of a 100-ps laser pulse. The pulse shape with a peak intensity of 5×10^{14} W/cm^2 (long-dashed line) and calculated absorption rates $Q^{s,p}$, Q^s, and $Q_w^{s,p}$ (thick solid, thin solid, and short-dashed lines, respectively) are shown in Fig. 111.49(a). The total absorption fractions calculated using these rates, integrated over the pulse duration, are shown in Fig. 111.49(b) [using the same notations as in Fig. 111.49(a)] as functions of the peak laser intensity. Note that the relative effect of resonant

absorption has a weak dependence on the intensity. Specifically, this effect varies from about 13% to 20% for an intensity varied from 10^{14} to 10^{15} W/cm^2. The contribution of Langmuir waves to the total laser absorption varies from about 2% to 15% for the same range of intensity. Example absorption fractions in spherical implosion experiments on OMEGA employed ~100-ps drive pulses are shown in Fig. 111.49(b) by solid circles.

Planar Experiments

Two series of planar direct-drive experiments on OMEGA have been proposed to verify the model of resonance absorption presented in **Resonance Absorption in the Fluid Approximation** (p. 180): reflection-light experiments and shock-timing experiments. Both series are based on similar experimental designs employing a single OMEGA laser beam, either s- or p-polarized, which irradiates a CH foil. The experiments are designed for beams with $\theta = 23.2°$, which is one of the allowed values of θ, determined by the construction of the OMEGA target chamber, and close to the angle of the maximum effect of resonance absorption in OMEGA plasmas (see Fig. 111.47). The goal of these experiments is to demonstrate the relative effect of a resonance absorption mechanism by comparing reflection light and shock timing for the case of s- and p-polarized laser beams. In this section, the results of the reflection-light experiments are presented and compared with simulations, and the effect of resonance absorption in the proposed shock-timing experimental design is discussed.
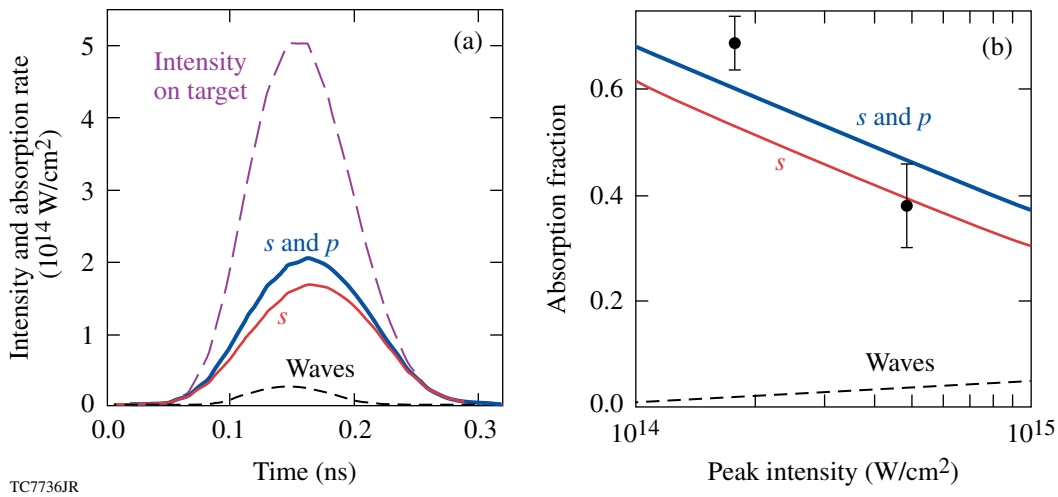
TC7736JR

Figure 111.49

Simulated absorption rates and dependence of absorption fractions on the peak laser intensity in spherical implosions of a CH target driven by a 100-ps OMEGA laser pulse. The approximate method to simulate the laser absorption in spherical implosions is discussed in the text. (a) Drive-laser pulse (long-dashed curve); absorption rates calculated using an equal mixture of s- and p-polarized lights (thick solid line), and using only the s-polarized light (thin solid line); absorption rate due to the resonant excitation of Langmuir waves (short-dashed line). (b) Absorption fraction as a function of peak laser intensity for the same cases considered in (a) and in implosion experiments (solid circles), which include a mixture of s- and p-polarized lights. The effect of resonance absorption is represented by the difference in absorption rates and absorption fractions for the lights with mixed polarization and s-polarization.

The setup for the reflection-light experiments is shown schematically in Fig. 111.50. In these experiments, a 200-ps laser beam with an energy of 55 J ($\pm 5\%$) is propagated from port 23 [see Figs. 111.50(a) and 111.50(b)] toward a target and focused into a spot ~500 μm in diameter, resulting in an intensity $\approx 1.2 \times 10^{14}$ W/cm^2. The beam is smoothed in space and time by the spectral dispersion technique[39] and distributed phase plates.[40] The light reflected and scattered from the target is collected by three calorimeters located in ports 25, 17, and 30. The calorimeter in port 25 collects the specularly reflected light, whereas the other two calorimeters, in ports 17 and 30, collect the scattered light at about 23° from the direction to port 25. The calorimeter in port 17 is located on the target normal.

Table 111.V shows the beam energy along with the energy collected by the three calorimeters in two experiments with single s- and p-polarized OMEGA laser beams. In agreement with theory, which predicts smaller light reflection from the p-polarized beam, the energy reflected from the s-polarized beam exceeds the energy reflected from the p-polarized beam (both energies collected in port 25). Quantitatively, the experiments show a larger difference in these energies: the corresponding energy ratio is 2.5 versus 1.8 obtained in simulations. Figure 111.51 shows time-resolved reflected power in the experiments and simulations, where the simulation data (thin solid lines) are given in W/cm^2 and the experimental data
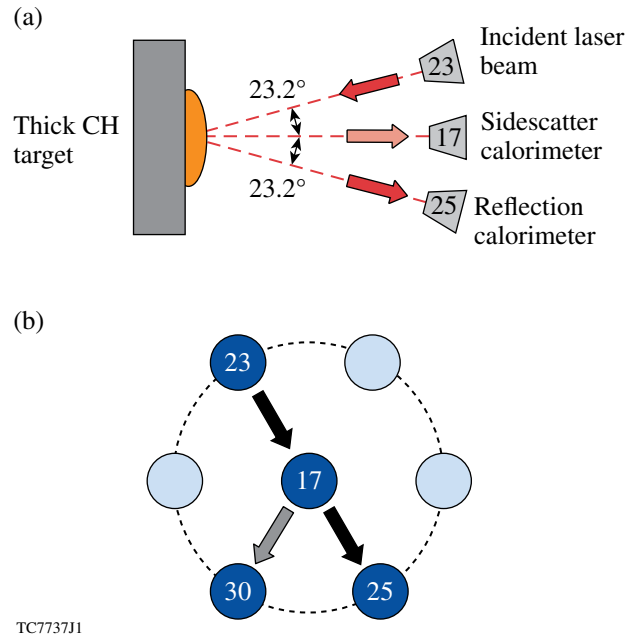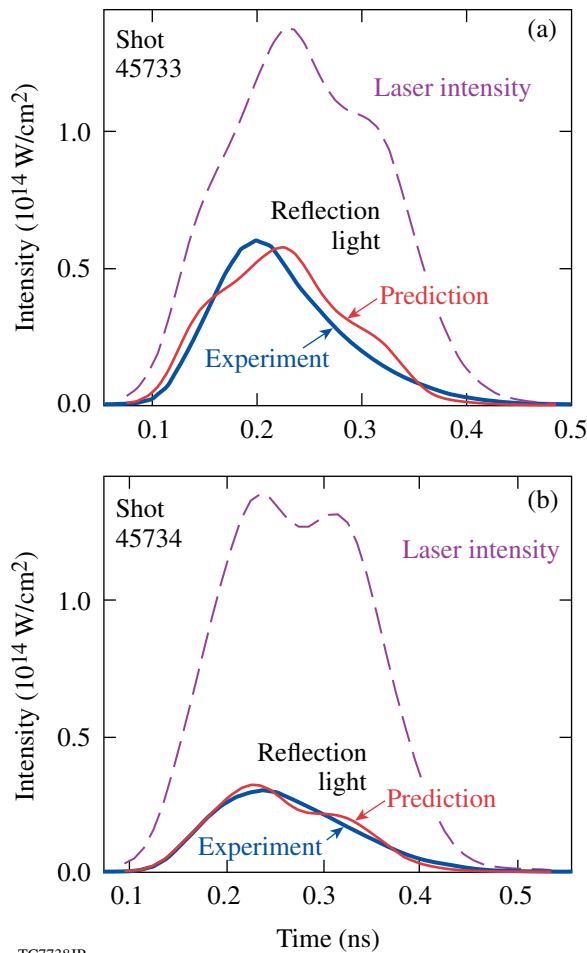

TC7737J1

Figure 111.50

(a) Experimental setup for the reflection-light measurements, using single laser beams of s- or p-polarization. Port 17 is on the direction of target normal. (b) View of the OMEGA ports used in the experiment. Port 30 is not depicted in (a).

Table 111.V: Reflection- and scattered-light measurements. The experimental setup is illustrated in Fig. 111.50.

Beam polarization	Beam energy (J)	Collected Energy (J)		
		Port 25	Port 30	Port 17
s	52.5	1.59	0.15	0.14
p	57.1	0.63	0.17	0.22

Shot 45733 (a)

Laser intensity

Reflection light

Prediction

Experiment

Shot 45734 (b)

Laser intensity

Reflection light

Prediction

Experiment

TC7738JR

Figure 111.51

Time-resolved measured (thick solid lines) and simulated (thin solid lines) intensities of reflection light in the experiments illustrated in Fig. 111.50. The cases of (a) s-polarized and (b) p-polarized beams are shown. The incident laser intensities (in W/cm^2) are shown by the dashed lines. The simulated reflection data are presented in W/cm^2, whereas the experimental data are given in arbitrary normalizations.

(thick solid lines) use arbitrary normalizations. Note a good agreement of time profiles of the experimental and simulated energy fluxes in both cases of s- and p-polarized beams.

The reflection experiments revealed significant sidescatter of laser light in both cases of s- and p-polarized beams. Due to this scatter, the measured reflection energies are about an order of magnitude smaller than the values predicted in simulations. An estimate using the amount of energy scattered in ports 17 and 30 (see Table 111.V) and assuming a uniform scatter suggests that the total scattered energy exceeds the reflection energy by at least a factor of 20. A possible explanation for this scatter is the development of laser-induced perturbations of the reflection surface in plasma corona. These perturbations, or nonuniformities, can have spatial scales comparable to the laser wavelength and cause significant sidescatter of laser light if the amplitude of perturbations is large enough. The 1-D model of resonance absorption used in this article cannot consider perturbations in the transverse directions to the target normal and, therefore, cannot simulate such a scatter.

The early-time enhancement of laser absorption due to the resonance mechanism can affect the velocities of shocks originating at initial stages of implosions. A change in these velocities can be important for high-gain, direct-drive implosion designs that utilize adiabat-shaping techniques.[10,11] Shock-timing experiments, somewhat analogous to the shock-compressibility experiments,[41] can be suitable for the study of the effect of resonance absorption on shock properties.

The shock-timing experimental design uses a setup similar to that used in the reflection-light experiments (see Fig. 111.50). The measured quantity in this design is the velocity of shocks driven by the laser beams with different polarization. The effect of resonance absorption is estimated by comparing the shock-breakout times in finite-thickness targets in experiments with s- and p-polarized beams. On OMEGA, the shock-breakout time can be measured to an accuracy of about 50 ps by using two independent techniques: one that employs a velocity interferometer system for any reflector (VISAR),[42,43] and another that utilizes temporal records of the shock-front self-emission (600 to 1000 nm) acquired using an imaging streak camera.[44]

Figure 111.52 shows simulated time-dependent travel distances for two shocks driven by s- and p-polarized laser beams in thick CH targets. The simulations assume a 100-ps laser pulse, similar to one shown in Fig. 111.47(a), but with a peak intensity of 10^{14} W/cm^2. For a fixed travel distance, which corresponds to an assumed target thickness in experiments, the
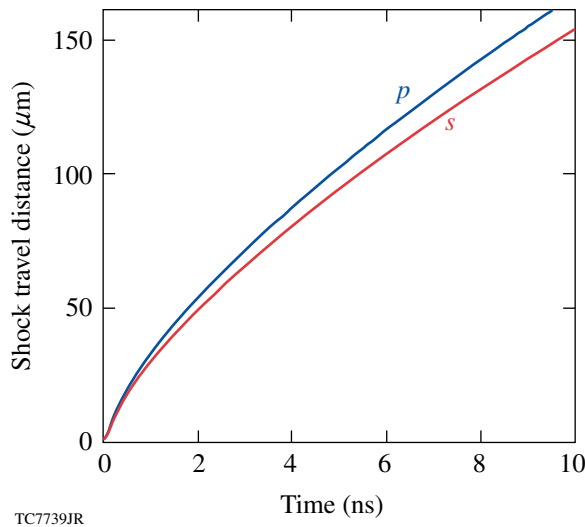
TC7739JR

Figure 111.52
Simulated time dependence of the travel distance of shocks driven by single 100-ps OMEGA laser beams of different polarizations in thick CH foils. The beams have a peak intensity of 10^{14} W/cm^2 and $\theta = 23.2°$. Two cases of s- and p-polarized beams (marked by "s" and "p", respectively) are considered.

difference Δt between the propagation time of the two shocks corresponds to the difference of experimentally measured breakout time in the case of s- and p-polarized beams. The value Δt exceeds the experimental accuracy limit of 50 ps for targets thicker than 30 μm, and Δt is in the well-detectable range of several hundred picoseconds for target thicknesses $\gtrsim 100$ μm. Specifically, one gets $\Delta t \approx 800$ ps for a 125-μm-thick target.

Discussion and Conclusions

The effect of resonance absorption in a CH plasma has been investigated theoretically and experimentally for the physical conditions relevant to direct-drive ICF experiments with a 351-nm laser and intensities in the range of 10^{14} to 10^{15} W/cm^2. It has been shown that nonlinear effects, such as pondermotive force and wave breaking, are not important; therefore, the linear theory of resonance absorption has been used in the 1-D hydrodynamic code *LILAC* to construct numerical models. The resonant excitation of Langmuir waves at the critical surface is an important mechanism that contributes to resonance absorption and dominates inverse bremsstrahlung absorption in the case of laser intensities $\gtrsim 5 \times 10^{14}$ W/cm^2 and angles of incidence of laser beams in the optimum range, $10° \lesssim \theta \lesssim 30°$. The decay of Langmuir waves caused by Landau damping results in a release of wave energy in the form of hot electrons with temperature ≈ 5 keV, which is larger by a factor

of 2 to 5 than the electron temperature in hot corona, where $T_e \approx 1$ to 2 keV. This could lead to a deviation of the electron distribution function from Maxwellian in hot corona if the energy released in hot electrons is relatively large. In implosion experiments on OMEGA, however, this energy is predicted to be relatively low [less than 15% of the total absorbed energy (see the short-dashed lines in Fig. 111.49)], so that the coronal plasma there is expected to be nearly Maxwellian.

On OMEGA, resonance absorption has a maximum effect during a rapid increase in laser power, typically ~100 ps. Simulations show that the resonance absorption in a 1-ns square laser pulse can be important only during the first 200 to 300 ps. At this initial period, the density scale length in plasma near the critical surface is relatively short, ~1 to 2 μm, resulting in enhanced resonance absorption. At later times, when the laser power reaches its maximum, the density scale length increases to more than 5 μm, causing significant reduction in resonance absorption. In short laser pulses, or pickets, ~100 ps, the resonance absorption has a maximum relative effect, the value of which depends on the intensity and angle of incidence of the laser. In the case of spherical implosions, the predicted relative effect of resonance absorption varies from about 13% to 20% for intensities between 10^{14} and 10^{15} W/cm^2.

We suggest, based on our numerical results, that the resonance absorption in spherical implosions can be modeled with the standard laser ray-trace method,[26] using a time-variable flux limiter, the value of which is increased by ~30% during the first ~200 ps of the laser pulse.

Planar reflection-light experiments have been conducted on OMEGA to verify the theoretical predictions of resonance absorption. These experiments used CH foils irradiated by single s- and p-polarized laser beams with an angle of incidence $\theta = 23.2°$ and showed the reflection energy's clear dependence on polarization, in good quantitative agreement with simulation results. The experiments also revealed significant sidescatter of laser light, which reduces the amount of reflection energy by about an order of magnitude in comparison with simulations. This sidescatter, affecting both s- and p-polarized lights, can be explained by laser-induced perturbations in the reflection surface of plasma corona. The effect of these perturbations cannot be accounted for in the simplified 1-D approach used in this study. We expect that the surface perturbations could reduce the difference between reflected s- and p-polarized laser lights predicted in simulations because of the introduction of additional polarization components (mixed s- and p-polarized lights) in the incident laser beams.

Another OMEGA planar, direct-drive experiment that could demonstrate the effect of resonance absorption in laser-driven shocks has been designed and simulated. This design employs CH foils irradiated by single *s*- or *p*-polarized laser beams that initiate shocks with different velocities. The effect of resonance absorption is inferred by comparing the shock-breakout time at the target's rear surface in the case of *s*- and *p*-polarized beams. Assuming a 100-ps laser pulse with a peak intensity of 10^{14} W/cm^2, the simulations predict a time difference of shock breakout in the well-detectable range of several hundred picoseconds for a target thickness of about 100 μm.

ACKNOWLEDGMENT

REFERENCES

1. J. D. Lindl, *Inertial Confinement Fusion: The Quest for Ignition and Energy Gain Using Indirect Drive* (Springer-Verlag, New York, 1998), pp. 39–52.

2. S. Atzeni and J. Meyer-ter-Vehn, *The Physics of Inertial Fusion: Beam Plasma Interaction, Hydrodynamics, Hot Dense Matter*, International Series of Monographs on Physics (Clarendon Press, Oxford, 2004), pp. 38–41 and 366.

3. R. L. McCrory, J. M. Soures, C. P. Verdon, F. J. Marshall, S. A. Letzring, S. Skupsky, T. J. Kessler, R. L. Kremens, J. P. Knauer, H. Kim, J. Delettrez, R. L. Keck, and D. K. Bradley, Nature **335**, 225 (1988).

4. S. E. Bodner, D. G. Colombant, J. H. Gardner, R. H. Lehmberg, S. P. Obenschain, L. Phillips, A. J. Schmitt, J. D. Sethian, R. L. McCrory, W. Seka, C. P. Verdon, J. P. Knauer, B. B. Afeyan, and H. T. Powell, Phys. Plasmas **5**, 1901 (1998).

5. P. W. McKenty, V. N. Goncharov, R. P. J. Town, S. Skupsky, R. Betti, and R. L. McCrory, Phys. Plasmas **8**, 2315 (2001).

6. P. W. McKenty, T. C. Sangster, M. Alexander, R. Betti, R. S. Craxton, J. A. Delettrez, L. Elasky, R. Epstein, A. Frank, V. Yu. Glebov, V. N. Goncharov, D. R. Harding, S. Jin, J. P. Knauer, R. L. Keck, S. J. Loucks, L. D. Lund, R. L. McCrory, F. J. Marshall, D. D. Meyerhofer, S. P. Regan, P. B. Radha, S. Roberts, W. Seka, S. Skupsky, V. A. Smalyuk, J. M. Soures, K. A. Thorp, M. Wozniak, J. A. Frenje, C. K. Li, R. D. Petrasso, F. H. Séguin, K. A. Fletcher, S. Padalino, C. Freeman, N. Izumi, J. A. Koch, R. A. Lerche, M. J. Moran, T. W. Phillips, G. J. Schmid, and C. Sorce, Phys. Plasmas **11**, 2790 (2004).

7. R. L. McCrory, S. P. Regan, S. J. Loucks, D. D. Meyerhofer, S. Skupsky, R. Betti, T. R. Boehly, R. S. Craxton, T. J. B. Collins, J. A. Delettrez, D. Edgell, R. Epstein, K. A. Fletcher, C. Freeman, J. A. Frenje, V. Yu. Glebov, V. N. Goncharov, D. R. Harding, I. V. Igumenshchev, R. L. Keck, J. D. Kilkenny, J. P. Knauer, C. K. Li, J. Marciante, J. A. Marozas, F. J. Marshall, A. V. Maximov, P. W. McKenty, J. Myatt, S. Padalino, R. D. Petrasso, P. B. Radha, T. C. Sangster, F. H. Séguin, W. Seka, V. A.

Smalyuk, J. M. Soures, C. Stoeckl, B. Yaakobi, and J. D. Zuegel, Nucl. Fusion **45**, S283 (2005).

8. M. C. Herrmann, M. Tabak, and J. D. Lindl, Nucl. Fusion **41**, 99 (2001).

9. R. Betti, K. Anderson, V. N. Goncharov, R. L. McCrory, D. D. Meyerhofer, S. Skupsky, and R. P. J. Town, Phys. Plasmas **9**, 2277 (2002).

10. V. N. Goncharov, J. P. Knauer, P. W. McKenty, P. B. Radha, T. C. Sangster, S. Skupsky, R. Betti, R. L. McCrory, and D. D. Meyerhofer, Phys. Plasmas **10**, 1906 (2003).

11. K. Anderson and R. Betti, Phys. Plasmas **10**, 4448 (2003).

12. T. R. Boehly, D. L. Brown, R. S. Craxton, R. L. Keck, J. P. Knauer, J. H. Kelly, T. J. Kessler, S. A. Kumpan, S. J. Loucks, S. A. Letzring, F. J. Marshall, R. L. McCrory, S. F. B. Morse, W. Seka, J. M. Soures, and C. P. Verdon, Opt. Commun. **133**, 495 (1997).

13. N. G. Denisov, Sov. Phys.-JETP **4**, 544 (1957).

14. P. Hirsch and J. Shmoys, Radio Sci. J. Res. NBS/USNC–URSI **69D**, 521 (1965).

15. A. D. Piliya, Sov. Phys.-Tech. Phys. **11**, 609 (1966).

16. A. Ya. Omel'chenko and K. N. Stepanov, Ukr. Fiz. Zh. **12**, 1396 (1967).

17. T. Tang, Radio Sci. **5**, 111 (1970).

18. V. L. Ginzburg, *The Propagation of Electromagnetic Waves in Plasmas* (Pergamon Press, New York, 1970), pp. 319–438.

19. D. W. Forslund *et al.*, Phys. Rev. A **11**, 679 (1975).

20. T. Speziale and P. J. Catto, Phys. Fluids **20**, 990 (1977).

21. G. J. Pert, Phys. Plasmas **20**, 175 (1978).

22. R. W. Means *et al.*, Phys. Fluids **24**, 2197 (1981).

23. D. E. Hinkel-Lipsker, B. D. Fried, and G. J. Morales, Phys. Fluids B **4**, 559 (1992).

24. D. E. Hinkel-Lipsker, B. D. Fried, and G. J. Morales, Phys. Fluids B **4**, 1772 (1992); D. E. Hinkel-Lipsker, B. D. Fried, and G. J. Morales, Phys. Fluids B **5**, 1746 (1993).

25. H. Xu *et al.*, Phys. Plasmas **13**, 123301 (2006).

26. J. Delettrez, R. Epstein, M. C. Richardson, P. A. Jaanimagi, and B. L. Henke, Phys. Rev. A **36**, 3926 (1987); J. Delettrez, Can. J. Phys. **64**, 932 (1986).

27. W. L. Kruer, *The Physics of Laser–Plasma Interactions*, Frontiers in Physics, Vol. 73, edited by D. Pines (Addison-Wesley, Redwood City, CA, 1988), Chap. 4, pp. 39–43.

28. F. F. Chen, *Introduction to Plasma Physics and Controlled Fusion*, 2nd ed., Vol. 1 (Plenum Press, New York, 1984), p. 87.

29. E. M. Lifshitz and L. P. Pitaevskifi, *Physical Kinetics*, 1st ed., Course of Theoretical Physics, Vol. 10 (Pergamon Press, Oxford, 1981), pp. 124–127.

30. W. H. Press *et al.*, *Numerical Recipes in FORTRAN: The Art of Scientific Computing*, 2nd ed. (Cambridge University Press, Cambridge, England, 1992), pp. 34–38.

31. L. Spitzer, Jr. and R. Härm, Phys. Rev. **89**, 977 (1953).

32. A. B. Langdon, Phys. Rev. Lett. **44**, 575 (1980).

33. A. Sunahara, J. A. Delettrez, C. Stoeckl, R. W. Short, and S. Skupsky, Phys. Rev. Lett. **91**, 095003 (2003).

34. G. P. Schurtz, Ph. D. Nicolaï, and M. Busquet, Phys. Plasmas **7**, 4238 (2000).

35. V. N. Goncharov, O. V. Gotchev, E. Vianello, T. R. Boehly, J. P. Knauer, P. W. McKenty, P. B. Radha, S. P. Regan, T. C. Sangster, S. Skupsky, V. A. Smalyuk, R. Betti, R. L. McCrory, D. D. Meyerhofer, and C. Cherfils-Clérouin, Phys. Plasmas **13**, 012702 (2006).

36. S. Skupsky, R. W. Short, T. Kessler, R. S. Craxton, S. Letzring, and J. M. Soures, J. Appl. Phys. **66**, 3456 (1989).

37. T. P. Coffey, Phys. Fluids **14**, 1402 (1971).

38. S. P. Regan, J. A. Marozas, R. S. Craxton, J. H. Kelly, W. R. Donaldson, P. A. Jaanimagi, D. Jacobs-Perkins, R. L. Keck, T. J. Kessler, D. D. Meyerhofer, T. C. Sangster, W. Seka, V. A. Smalyuk, S. Skupsky, and J. D. Zuegel, J. Opt. Soc. Am. B **22**, 998 (2005).

39. S. Skupsky and R. S. Craxton, Phys. Plasmas **6**, 2157 (1999).

40. Y. Lin, T. J. Kessler, and G. N. Lawrence, Opt. Lett. **21**, 1703 (1996).

41. T. R. Boehly, E. Vianello, J. E. Miller, R. S. Craxton, T. J. B. Collins, V. N. Goncharov, I. V. Igumenshchev, D. D. Meyerhofer, D. G. Hicks, P. M. Celliers, and G. W. Collins, Phys. Plasmas **13**, 056303 (2006).

42. L. M. Barker and R. E. Hollenbach, J. Appl. Phys. **43**, 4669 (1972).

43. P. M. Celliers, D. K. Bradley, G. W. Collins, D. G. Hicks, T. R. Boehly, and W. J. Armstrong, Rev. Sci. Instrum. **75**, 4916 (2004).

44. J. E. Miller, T. R. Boehly, E. Vianello, W. J. Armstrong, C. Sorce, W. Theobald, D. D. Meyerhofer, D. G. Hicks, J. H. Eggert, and P. M. Celliers, Bull. Am. Phys. Soc. **50**, 60 (2005); J. A. Oertel *et al.*, Rev. Sci. Instrum. **70**, 803 (1999).

Diagnosing Direct-Drive, Shock-Heated, and Compressed Plastic Planar Foils with Noncollective Spectrally Resolved X-Ray Scattering

Introduction

The achievement of energy gain with a direct-drive inertial confinement fusion (ICF) ignition target requires an accurate prediction of the shock-heated and compressed conditions in the main fuel layer.[1] A direct-drive ICF target for hot-spot ignition consists of a spherical cryogenic main fuel layer of deuterium and tritium surrounded by a thin plastic layer.[1–3] Intense laser beams uniformly irradiate the target and launch a shock wave through the main fuel layer. The pressure in the shock-heated shell determines the implosion performance of the target. The laser pulse for a direct-drive implosion consists of a low-intensity foot and high-intensity main drive. The low-intensity foot launches a relatively weak shock to isentropically compress the target, and the main drive sends a compression wave that implodes the target to form a central hot spot with sufficient fuel areal density and temperature to ignite the target. The entropy of the main fuel layer or shell adiabat α is defined as the ratio of the pressure in the main fuel layer to the Fermi-degenerate pressure. It is a critical parameter in ICF because it is related to the minimum laser drive energy needed for ignition and the growth rate of the Rayleigh–Taylor (RT) hydrodynamic instability.[4,5] The RT instability distorts the uniformity of the implosion, reduces the target compression, and could prevent hot-spot formation.[6] Therefore, the successful target design for a stable, high-performance ICF implosion creates an adiabat in the shell that strikes a balance between the target stability and the laser-energy requirements.

The shock-heated shell in direct-drive ICF is predicted to have plasma conditions in the warm dense matter (WDM) regime.[7] The coupling parameter[8] Γ and ratio of Fermi temperature to electron temperature Θ characterize plasmas in T_e–n_e space. The electron–electron coupling parameter Γ_{ee} is the ratio of Coulomb potential between free electrons to the average kinetic energy of the free electrons:

$$\Gamma_{ee} = \frac{e^2}{d k_B T_e},\qquad(1)$$

where $d = (3/4\pi n_e)^{1/3}$ is the average interparticle spacing. When a plasma is strongly coupled ($\Gamma_{ee} \gg 1$), the Coulomb interac-

tions between particles determine the physical properties of the plasma. When $\Gamma_{ee} \ll 1$, plasma behaves as an ideal gas and the interparticle coupling is insignificant. Similar considerations can be made with regards to the electron–ion and ion–ion coupling parameters.[8] In an ICF implosion, the shock-heated shell becomes a partially or fully degenerate plasma. The degree of degeneracy is described as

$$\Theta = T_F / T_e,\qquad(2)$$

where T_F is the Fermi temperature [$T_F = \hbar^2(3\pi^2 n_e)^{2/3}/2m_e k_B$, k_B is the Boltzmann constant]. In degenerate plasmas, the electron energy depends only on n_e, and the coupling constant is defined as the ratio between the potential and Fermi energy $\left(\Gamma_{ee} = e^2/d E_F\right)$. Figure 111.53 shows T_e–n_e space characterized by the electron coupling parameter, Γ_{ee}; the ratio of the T_e and T_F, $\Theta\left(T_F/T_e\right)$; the average interparticle spacing $d\left[= (3/4\pi n_e)^{1/3}\right]$; and the Debye length λ_D. The plane is divided by the lines $\Theta = 1$, $\Gamma_{ee} = 1$, and $d = \lambda_D$ into regions where Fermi-degenerate, strongly coupled, Fermi-degenerate and strongly coupled, weakly coupled, and ideal plasmas exist. As shown in Fig. 111.53, the predicted conditions for the direct-drive experiments (see triangle symbols) lie in the WDM regime on the boundary between Fermi-degenerate, strongly coupled, and weakly coupled plasmas.

Diagnosing WDM is challenging because the temperature of the plasma is too low (~10 eV) for it to emit x rays and dense plasmas above the critical density cannot be probed with optical lasers for Thomson-scattering measurements.[9] Two viable techniques exist to diagnose these plasmas: spectrally resolved x-ray scattering[10] and time-resolved x-ray absorption spectroscopy.[11] X-ray absorption spectroscopy measurements provide time-resolved local measurements of the plasma conditions in the shock-heated foil; they require, however, a buried mid-Z tracer layer such as Al. The Al $1s$–$2p$ absorption spectroscopy was used to diagnose similar plasma conditions in a direct-drive, shock-heated CH planar foil by using a point-source Sm backlighter.[12] The spectrally resolved x-ray scattering does not require a tracer layer; it requires, however, a large volume of shock-heated matter to scatter a sufficient number of x rays,
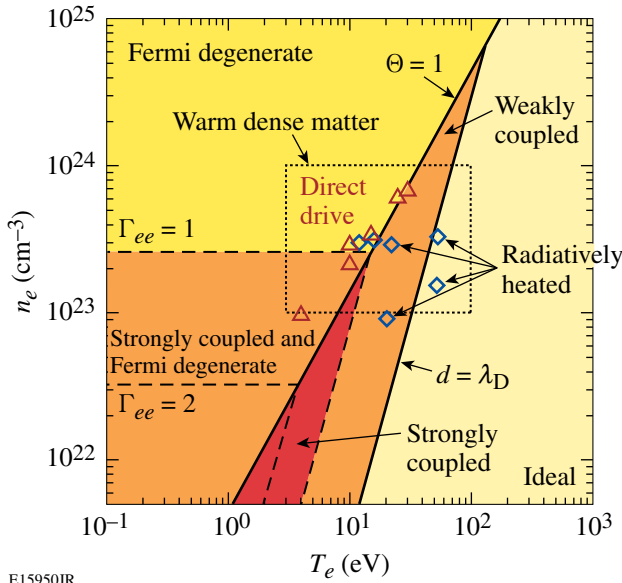
E15950JR

Figure 111.53

T_e–n_e space characterized by the electron coupling parameter Γ_{ee}; the ratio of the Fermi temperature T_F and the electron temperature T_e, $\Theta(=T_F/T_e)$; the average interparticle spacing $d\left[=(3/4\pi n_e)^{1/3}\right]$; and Debye length λ_D. The plane is divided by the lines $\Theta = 1$, $\Gamma_{ee} = 1$, and $d = \lambda_D$ into regions where Fermi-degenerate, strongly coupled, Fermi-degenerate and strongly coupled, weakly coupled, and ideal plasmas exist. Predicted conditions of direct-drive, shock-heated experiments are shown as triangle symbols. Plasma conditions of radiatively heated targets inferred with noncollective and collective spectrally resolved x-ray scattering are shown as diamond symbols.

limiting its spatial resolution. Noncollective spectrally resolved x-ray scattering experiments reported in the literature have characterized the plasma conditions of an isochorically heated Be cylinder, a carbon foam, and a CH gas bag.[13] Recently, collective scattering was observed from an isochorically heated Be cylinder and was used to infer the electron density.[14] In principle, when collective scattering is used in conjunction with noncollective scattering, the spatially averaged quantities of electron density, electron temperature, and ionization can be diagnosed. The radiatively heated plasmas conditions are shown as the diamond symbols in Fig. 111.53.

Diagnosing plasmas that have conditions comparable to those in the shock-heated main fuel layer of a direct-drive ICF ignition target is the central focus of this article. For the first time, noncollective, spectrally resolved x-ray scattering is used to probe the plasma conditions in direct-drive, shock-heated planar plastic foils. Compared to x-ray scattering measurements from isochorically heated targets, direct-drive targets present new experimental challenges associated with the smaller physical dimensions of the target and gradients in the plasma conditions, as well as target compression and acceleration during the

scattering measurements. The scattering volumes and hence the scattered x-ray signal level of direct-drive targets are at least an order of magnitude smaller compared to the radiatively heated targets. Some direct-drive scenarios shape the adiabat in the target, which would require a spatially resolved and spectrally resolved x-ray scattering diagnostic. The direct-drive coronal plasma is in close proximity to the scattering volume and creates a major source of unwanted background x-ray continuum, which must be shielded from the detector. However, the target trajectory moves the coronal plasma into the field of view of the detector during the scattering measurement. Plastic foils are surrogates for cryogenic fuel layers. These results, required for ICF ignition, provided an opportunity to study the shell conditions of a direct-drive ICF imploded target without the cost and complexity of cryogenic hardware. The spectral line shapes of the elastic Rayleigh and the inelastic Compton components are fit to infer the electron temperature T_e and ionization Z: the Doppler-broadened Compton feature is sensitive to T_e for T_e greater than the Fermi temperature T_F, and the ratio of the Rayleigh and the Compton components is sensitive to Z.

The following sections of this article (1) describe spectrally resolved x-ray scattering; (2) present the experimental setup and simulations from the 1-D hydrodynamics code; (3) present the experimental results and compare them with the predicted plasma conditions; and (4) discuss the future use of spectrally resolved x-ray scattering to infer the plasma conditions in the main fuel layer of a direct-drive inertial confinement fusion target.

Spectrally Resolved X-Ray Scattering

Scattering processes are classified as collective or noncollective based on the scattering parameter, defined as

$$\alpha_{scatter} = \frac{1}{k\lambda_D} = \frac{1.08 \times 10^{-4} \cdot \lambda_0 (cm)}{\sin(\theta/2)} \left[\frac{n_e(cm^{-3})}{T_{eff}(eV)}\right]^{1/2}, \quad (3)$$

where θ is the scattering angle, k is the wave number of scattered x rays $\left[k = 4\pi/\lambda_0 \cdot \sin(\theta/2)\right]$, λ_0 is the probe wavelength, and λ_D is the Debye length calculated with the effective temperature[15] T_{eff}, which is defined as $T_{eff} = \sqrt{T_e^2 + T_q^2}$, where $T_q = T_F/(1.33 - 0.18\sqrt{r_s})$ with $r_s = d/a_B$ (a_B is the Bohr radius).[16] The characteristic plasma length in the scattering parameter, λ_D, in Eq. (3) is replaced by the Thomas–Fermi screening length

$$\lambda_{TF}\left(= \sqrt{2\varepsilon_0 E_F/3n_e e^2}\right)$$

for Fermi-degenerate plasma, and by the interparticle spacing d for strongly coupled plasma. With the use of the effective

temperature, the scattering parameter between ideal, strongly coupled, and Fermi-degenerate regimes is smoothly interpolated. For noncollective scattering ($\alpha_{scatter} < 1$), x rays are scattered by individual electrons. As a result, the red wing of the Compton component in the scattered spectrum reflects the free electron velocity distribution function,[17] and the Doppler-broadened spectrum is sensitive to T_e for $T_e > T_F$. When $T_e < T_F$, the electron distribution becomes a Fermi distribution and its spectral shape is only weakly sensitive to the electron density. All of the scattering investigated in this article is noncollective. In the case of $\alpha_{scatter} > 1$, the incident x-ray photons interact with a collective electron cloud; in particular, collective scattering is of interest for electron-density measurements.[14,18]

Detailed calculations of the modeled x-ray scattering spectra presented here can be found in Refs. 13, 19, 20, and 21. A brief description of the model is given in this section. Spectrally resolved x-ray scattering can be modeled with the total dynamic structure factor in the differential scattering cross section. As derived by Chihara,[22,23] the total dynamic structure factor and the free-electron correlation function are written as

$$S(k,\omega) = \left| f_1(k) + q(k) \right|^2 S_{ii}(k,\omega) + Z_f S_{ee}^0(k,\omega)$$

$$+ Z_b \int \tilde{s}_{ce}(k, \omega - \omega') S_s(k, \omega') d\omega', \tag{4}$$

$$S_{ee}^0(k,\omega) = -\frac{\hbar}{1 - \exp\left(-\hbar\omega / k_B T_e\right)} \frac{\varepsilon_0 k^2}{\pi e^2 n_e} \, \mathrm{Im}\left[\frac{1}{\varepsilon(k,\omega)}\right]. \tag{5}$$

Although Eq. (4) is valid only for a single-ion component plasma, the model for the experiment under consideration includes the scattering contribution from all ion species as well as their mutual correlations as described by Gregori *et al.*[13] The first term on the right-hand side of Eq. (4) corresponds to the elastic Rayleigh-scattering component. $f_I(k)$ is the ionic form factor for bound electrons and $q(k)$ is the Fourier transform of the free-electron cloud surrounding the ion. $S_{ii}(k,\omega)$ is the ion–ion dynamic structure factor, which describes the degree of ion–ion correlations.

In Eq. (4) Z_f and Z_b are the number of free (or valence) electrons and bound electrons, respectively. The number of electrons associated with each atom, Z_A, is the sum of Z_f and Z_b. Z_f represents electrons that are not bound to any single atom or ion including valence, delocalized, or conduction electrons. These electrons are all described in terms of plane-wave or Bloch wave functions. From a hydrodynamic perspective the useful

quantity to compare with numerical modeling is the number of free electrons or the average ionization Z, not Z_f. From the discussion above, Z_f differs from Z because it includes valence states together with kinematically free electrons. For the case of cold (undriven) plastic foil targets, Z_f is just the number of valence electrons and has no relation to Z. On the other hand, as soon as the temperature in the plastic foil is raised by the laser interaction, atomic bonds are broken and the underlying lattice responsible for the formation of the valence band is destroyed. In this case Z_f can be identified with Z and direct comparison with simulations is possible. The second term in Eq. (4) thus represents scatterings from either free or valence electrons that move independently from the ions. As shown in Eq. (5), their corresponding electron–electron correlation function $S_{ee}^0(k,\omega)$ can be obtained through the fluctuation-dissipation theorem[24] in terms of the electron dielectric response function derived using the random phase approximation (RPA).[25,26] The RPA is accurate without any local field corrections in our noncollective scattering experiment. While the RPA is rigorously valid for kinematically free electrons, valence electrons can also be described in a similar way.[27] Extension to a finite band gap is also possible, but its effect is small for the conditions of this experiment.[19] The last term of Eq. (4) contributes to inelastic scattering from core electrons. Differently from valence and free electrons, electrons bound to localized levels in the L or K shells are treated as hydrogenic states in terms of a modified impulse approximation,[28] which was shown to reproduce well experimental x-ray scattering data from shock-compressed Al plasmas;[29] these are the bound electrons included in Z_b. This term becomes important when L-shell bound electrons are involved in the scattering process, which is the case for a carbon-hydrogen plasma, created by the laser-induced ionization of a CH (C_8H_8) planar target. The average number of free (or valence) electrons for CH is given by

$$Z_f = \frac{Z_C + Z_H}{2} = \frac{(6 - Z_b)_C + (1 - Z_b)_H}{2}, \tag{6}$$

where Z_C and Z_H are the number of delocalized electrons in carbon and hydrogen, respectively. Figure 111.54 shows the modeled scattered spectra for CH foils using Eq. (4). Figure 111.54(a) shows the calculated total spectra including free electrons, weakly bound electrons, and tightly bound electrons. Figure 111.54(b) shows the contributions of inelastic scatterings from free electrons and weakly bound electrons to the Compton component. All spectra are calculated with an x-ray probe of 9.0-keV Zn He$_\alpha$, a 130° scattering angle, and a Compton downshifted energy of 260 eV. The Compton down-
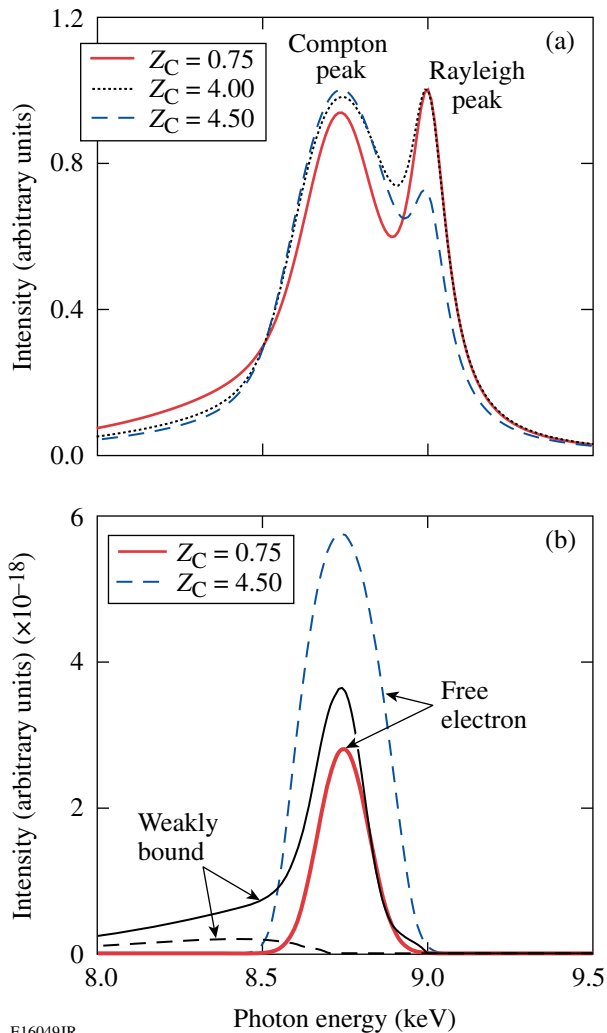
Figure 111.54

(a) Calculated total scattered spectra including ion, free-electron, and bound-free components for $Z_C = 0.75$, $Z_C = 4$, and $Z_C = 4.5$. All spectra are normalized to the larger of either the Rayleigh or Compton peak. (b) Contributions of inelastic scatterings from free electrons and weakly bound electrons to the Compton component for $Z_C = 0.75$ and $Z_C = 4.5$. The T_e and ρ are fixed to be 10 eV and 4.96 g/cm^3.

shifted energy is consistent with a 130° scattering angle, which is within the experimental tolerance of the 120° design. The calculated spectra, including all three terms in Eq. (4) for $Z_C = 0.75$, $Z_C = 4.0$, and $Z_C = 4.5$, are shown in Fig. 111.54(a). In all cases discussed here $Z_H = 1$ is set. The ratio of the Compton and Rayleigh peaks are comparable for $Z_C = 0.75$ and $Z_C = 4.0$. This is because of the contribution of the scatterings from weakly bound electrons to the Compton component at low Z_C. Figure 111.54(b) shows that the contributions from the free and weakly bound electrons to the Compton component for $Z_C =$

0.75 and $Z_C = 4.5$, with $T_e = 10$ eV and $\rho = 4.96$ g/cm^3. For $Z_C = 0.75$, the contribution of the scattering from weakly bound electrons is slightly higher than that from the free electrons and the total intensity of the Compton peak is comparable to the Rayleigh, as shown in Fig. 111.54(a). As Z_C is increased, the Compton component is dominated by the scattering from free electrons while the ratio of the two peaks is comparable for $Z_C = 4$. Therefore, low ionizations of shocked CH foils (i.e., $Z < 2$) cannot be accurately diagnosed with this technique. Once a carbon K-shell electron is ionized ($Z_C > 4$), the ratio of the Compton and Rayleigh peak significantly changes for CH, as shown in Fig. 111.54(a).

Experiment

Spectrally resolved x-ray scattering experiments were performed with 90° and 120° scattering angles. The error in the exact determination of the scattering angle is estimated as ±10°. The experimental configuration for the 120° scattering geometry is shown in Fig. 111.55(a), with a photograph of the target shown in Fig. 111.55(b). The target consists of a large Au/Fe light shield, a Zn backlighter foil, a CH drive foil, and a Ta pinhole substrate. Up to six overlapped beams smoothed with phase plates (SG8)[30] were used to drive a 125-μm-thick planar CH target with a uniform intensity in an ~0.5-mm laser spot of 1×10^{14} W/cm^2. Eighteen additional tightly focused beams (~100-μm spot) irradiated the Zn foil with an overlapped intensity of ~10^{16} W/cm^2 and generated a point-source back-lighter of Zn He$_\alpha$ emission at 9.0 keV. The 0.5-mm-thick CH foil positioned between the Zn foil and the Ta pinhole substrate blocked x rays with photon energies less than ~4 keV with minimal attenuation to the Zn K-shell emission. This prevented the Zn backlighter from radiatively heating the target. The Ta pinhole substrate with a 400-μm-diam aperture restricted the backlighter illumination of the CH drive foil to the portion of the target that was uniformly shock heated. The scattering angle was reduced to 90° by adjusting the locations of the aperture and the focal position of the backlighter beams.

Most of the Zn He$_\alpha$ emission propagates through the drive foil; however, a small fraction of the x rays are scattered. X rays scattered at 90° or 120° were dispersed with a Bragg crystal spectrometer and recorded with an x-ray framing camera[31] outfitted with a charge-coupled-device (CCD) camera. A highly oriented pyrolytic graphite (HOPG)[32] crystal with a 2d spacing of 6.7 Å was used in the mosaic focusing mode[33] to provide high reflectivity of the scattered x-ray spectrum.[34] The Au/Fe shields reduced the measured background x-ray continuum levels by blocking the direct lines of sight to the Zn and CH coronal plasmas.
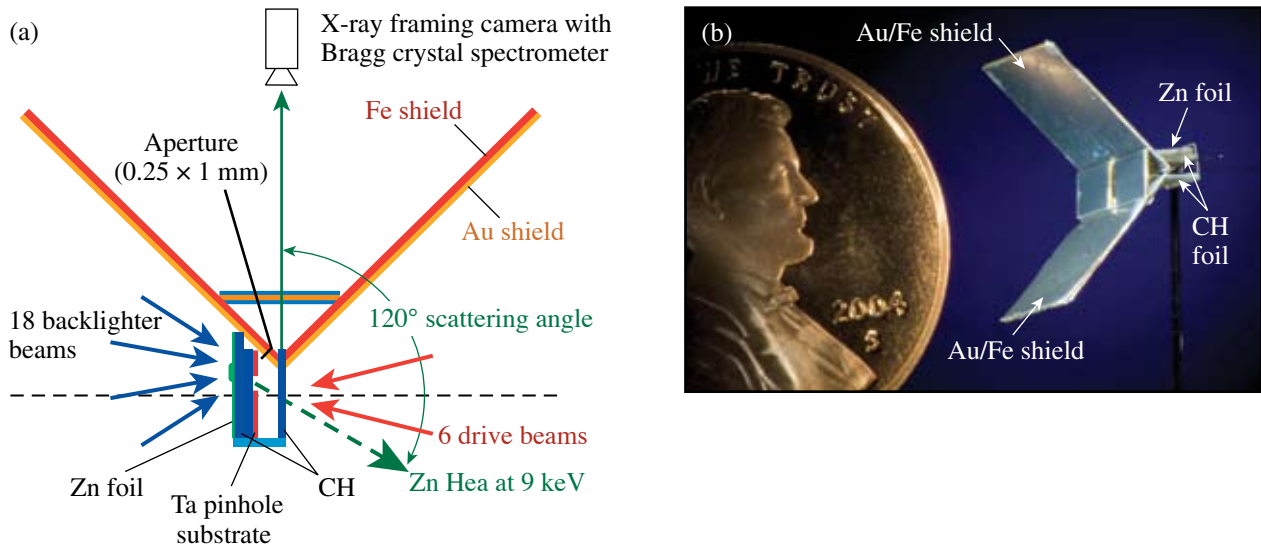
E15952JR

Figure 111.55

(a) Target design of the noncollective spectrally resolved x-ray scattering experiment on OMEGA using a 120° scattering geometry; (b) a photograph of an x-ray scattering target compared in size to a penny.

The strategy of the experiment was to drive a shock wave through the CH foil and to scatter the Zn He$_\alpha$ x rays from the uniformly compressed portion of the shock-heated CH around the time that the shock breaks out of the rear side of the target (i.e., the side opposite the laser-irradiated side). Two drive conditions were examined: undriven (i.e., cold, uncompressed CH foil) and an $\alpha = 3$ drive. The measured time history of the laser power for the $\alpha = 3$ drive is presented in Fig. 111.56. The plasma conditions of directly driven CH foils were simulated with the 1-D hydrodynamics code *LILAC*. A detailed description of *LILAC* can be found elsewhere[35] with the main features of the code described in this section. Laser absorption is calculated using a ray-trace algorithm that models inverse bremsstrahlung. Transport of radiation is modeled through multigroup diffusion with the Los Alamos National Laboratory Astrophysical Tables[36] or an average ion model providing the opacities. The *SESAME* tables are used to model the equation of state. *LILAC* uses a flux-limited[37] Spitzer–Härm[38] electron thermal-conduction model. This drive is predicted to create a 15-Mbar shock-wave pressure. Figure 111.57 shows the spatial profile of the predicted plasma conditions created with an $\alpha = 3$ drive around the time the shock breaks out the rear side of the target. A single shock is launched by the $\alpha = 3$ drive and breaks out the rear side of the target at 2.7 ns. The measurement was made around the shock-breakout time. The plasma conditions in the CH at the time of shock breakout are predicted to be fairly uniform. For the $\alpha = 3$ drive, the foil is predicted to be heated to $T_e = 12$ eV with an average ionization
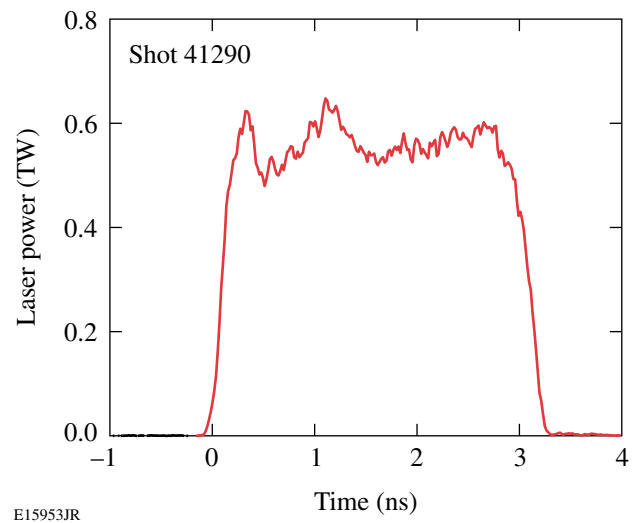
E15953JR

Figure 111.56

The measured laser pulse for the $\alpha = 3$ drive (shot 41290).

$Z = 0.95$. As shown in Fig. 111.58, there is little difference in the predicted x-ray scattered spectra from the CH foil targets for undriven and $\alpha = 3$ drive cases. The plasma condition for an undriven case is $T_e = 0.1$ eV and $Z_C = 0.1$. The ion temperature is predicted to be equal to the electron temperature for all of the drive cases under consideration. The spatially integrated, time-resolved spectra were collected over a 500-ps integration time, which is short compared to the hydrodynamic time scales of the experiment.
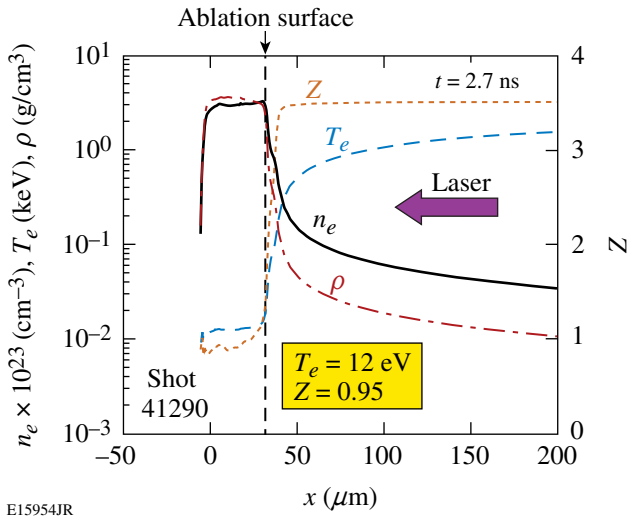
E15954JR

Figure 111.57

Predictions from the 1-D hydrodynamics code *LILAC* of the spatial profiles of electron temperature (T_e), electron density (n_e), average ionization (Z), and mass density (ρ) for laser-irradiated CH foil targets with $\alpha = 3$ drive.
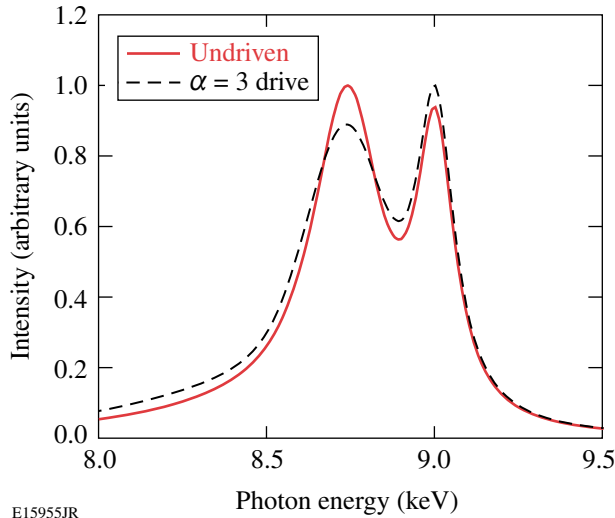

E15955JR

Figure 111.58

Predicted x-ray scattered spectra for undriven and $\alpha = 3$ driven CH foils.

The total number of the detected photons per nanosecond, N_{det}, was estimated for the x-ray scattering experiment. It is given by

$$N_{det} = \left(\frac{E_L}{h\nu} \eta_L \frac{1}{\tau_L} \right) \left(\frac{\Omega_{pinhole}}{4\pi} \right) \eta_{CH}$$

$$\times \left[\frac{n_e \sigma_T x}{(1 + \alpha_{scatter})^2} \right] \left(\frac{\Omega_{detector}}{4\pi} R_{crystal} \eta_d \right), \qquad (7)$$

where E_L is the laser energy, τ_L is the laser pulse duration, η_L is the conversion efficiency from the laser energy into the 9.0-keV x rays, η_{CH} is the attenuation due to 500 μm of CH, n_e is the electron density, x is the thickness of the compressed target, $\Omega_{pinhole}$ and $\Omega_{detector}$ are the solid angles limited by the pinhole diameter and crystal size, $R_{crystal}$ is the integrated reflectivity of the crystal, and η_{CH} is the efficiency inside the detector, including the MCP efficiency and filter transmission. Using $E_L = 280$ J $\times$ 18 beams in the 3-ns pulse, $h\nu = 9.0$ keV, η_L is assumed to be ~0.1%, $\Omega_{pinhole}/4\pi = 0.04$, $\eta_{CH} = 85\%$, $n_e = 1.5 \times 10^{23}$ cm^{-3}, $x = 40$ μm for a shock-compressed target with the $\alpha = 3$ drive, $\alpha_{scatter} = 0.2$ for the 120° scattering geometry, $\Omega_{detector}/4\pi = 5.7 \times 10^{-3}$, $R_{crystal} = 2 \times 10^{-3}$, and $\eta_d = 1\%$. Using Eq. (7), N_{det} is estimated to be ~1500 photons/ns. Since the integration time was 500 ps and the spectrum was dispersed over the ~90 spectrally resolved bins (~10 eV/bin), the estimated ratio of the signal due to photon statistics is 8.2, which is consistent with the measured signal-to-noise ratio of 8.

Results and Discussion

X-ray spectra detected at 90° and 120° scattering angles were recorded for an undriven CH foil. Figure 111.59(a) shows the measured spectra from undriven CH foils in 90° and 120° scattering geometries, as well as the signal from a control target whose drive foil has a 1-mm-diam thru-hole in the center of the foil. Figure 111.59(b) shows a microscope image of the control target. The purpose of the control shot was to experimentally confirm that the measured x rays were scattered from the intended target. The lack of signal measured for this shot indicates that x rays are scattering from the intended portion of the nominal drive foil (i.e., without a thru-hole), and scattering from other unintended sources is negligible. The Compton peaks of measured spectra with 90° and 120° scattering angles are consistent with the calculated Compton downshifted energies of $E_C = \hbar^2 k^2 / 2m_e = 158$ eV and 238 eV, respectively. In this article, all of the x-ray scattering measurements from the driven foils were taken with the 120° scattering angle; however, measurements from two different scattering angles would be beneficial to determine the accuracy of the experimentally determined values of T_e and Z_f.

The spectra of x rays detected at a 120° scattering angle are presented in Fig. 111.60(a) for the CH targets and in Fig. 111.60(b) for the Br-doped CH targets for the two drive conditions under consideration (i.e., undriven and $\alpha = 3$ drive). The Br-dopant concentration level in the CH foil was 2% atomic in the bulk of the target, but no Br was in the ablator portion of the target. All of the spectra in Fig. 111.60 are normalized to the larger peak of the Rayleigh or Compton feature. The location
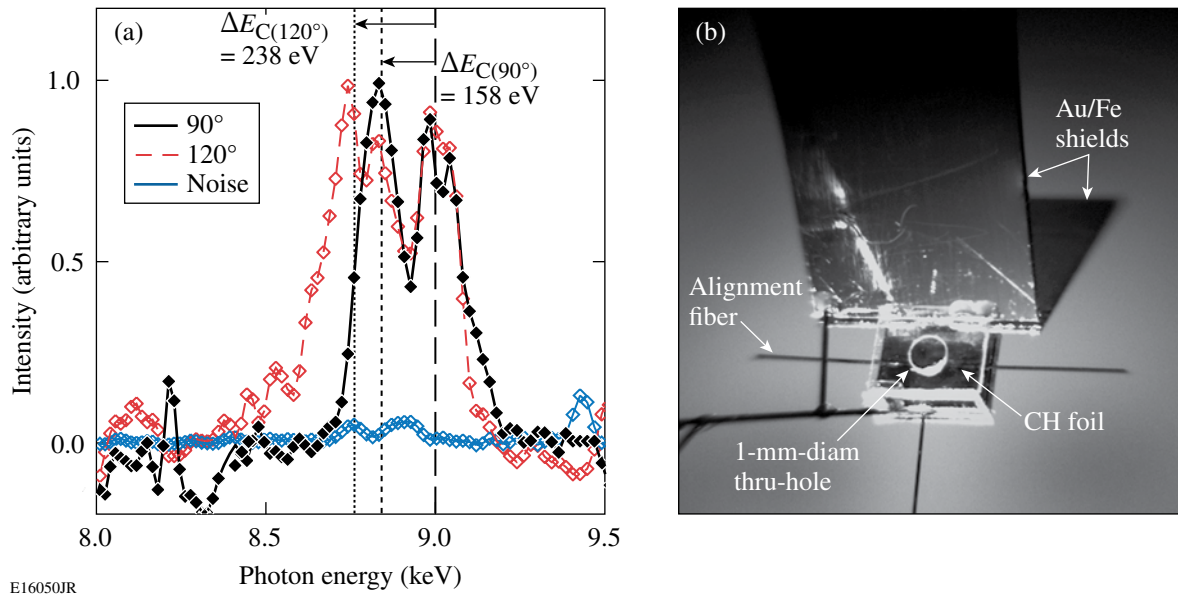
Figure 111.59

(a) Measured x-ray spectra scattered from undriven CH targets with 90° and 120° scattering geometries are compared with the noise level. The dotted and dashed vertical lines show the Compton downshifted energy of 158 eV/238 eV for the 90°/120° scattering angles. (b) A microscope image of the control target with a 1-mm-diam thru-hole in the center of the CH foil.

of line emissions of Zn He$_\alpha$ at 9.0 keV and Zn Ly$_\alpha$ at 9.3 keV is indicated with vertical dotted lines in the figure. A comparison of the spectra scattered from the CH targets shows little difference between the driven and undriven targets. A detailed analysis of the measured spectra with models is presented in Figs. 111.61(a) and 111.61(b). A similar comparison for the x-ray spectra from the Br-doped CH shows significant changes in the heights of the Compton feature. Zn Ly$_\alpha$ line emission contributes to the blue wings of the measured Rayleigh features. For the quantitative analysis, the measured spectra were fit with models to infer T_e and Z_b for each ion in the plasma as described in Eq. (6). The modeled spectra were calculated as described in **Spectrally Resolved X-Ray Scattering** (p. 192), and a best fit to the measured spectra was obtained using a least-squares-fitting routine that varied T_e and the Z_b's.

The experimental scattered spectrum from the cold, undriven target is compared with three modeled spectra in Fig. 111.61(a). All of the modeled spectra have solid densities ($\rho = 1.24$ g/cm^3) and low electron temperatures ($T_e = 0.1$ eV) to indicate that no ionization in CH has occurred, but the Z_C is varied from 0.1 to 4. The lowest Z_C agrees with the experimental result as expected in cold CH; however, the models are not very sensitive to Z_C for $Z_C < 2$, suggesting that valence electrons in cold CH could scatter x rays like free electrons. In order to investigate the T_e sensitivity in the case of driven CH,

Z_f was set to 2.5 (corresponding to $Z_C = 4$ and $Z_H = 1$ delocalized electrons) shown in Fig. 111.61(b). As mentioned before, in this case all of the carbon bonds are destroyed and Z_f does indeed represent the average ionization state in the plasma. In addition to scattering from valence electrons, scattering from the remaining bound electrons into L and K shells must be included, with the respective ionization levels corrected for continuum lowering.[39] In Fig. 111.61(b), the measured spectrum of the CH foil for the $\alpha = 3$ drive is compared with the modeled spectra for three electron temperatures: $T_e = 1$, 10, and 20 eV with $Z_C = 4$. The mass density used in the models is four times solid density ($\rho = 4.96$ g/cm^3), as suggested by *LILAC* simulations. Since the measured spectrum from the driven CH is bounded by the models with $T_e = 1$ eV and $T_e = 20$ eV, an upper limit of $T_e = 20$ eV is inferred for the $\alpha = 3$ drive. As described in Fig. 111.54(b), the ratios of the Compton and Rayleigh peaks are comparable when $Z_C < 4$ in a driven CH. Therefore, the inferred Z in this experiment is an upper limit of $Z \sim 2$. The predicted spectra show that the width of the Compton peak is not very sensitive to the electron temperature because T_e is comparable to the Fermi temperature $T_F = 16$ eV from the hydro calculation ($n_e \sim 3 \times 10^{23}$ cm^{-3} and $Z \sim 1$). It is also noted that for the compressed case with $\alpha = 3$, the electron density is $n_e \sim 3 \times 10^{23}$ cm^{-3}, which lowers the continuum by ~20 eV (Ref. 20); thus a fraction of the L-shell electrons should be indeed delocalized.

Trace amounts of Br in the CH foil (i.e., 2% atomic concentration) increase the sensitivity of the spectrally resolved x-ray spectra to changes in the electron temperature. The experimental spectra scattered from CHBr targets are presented in Fig. 111.62 for the two drives under consideration, along with the fitted spectra. A comparison of the scattered x-ray spectra from the undriven CHBr target [see Fig. 111.62(a)] with the undriven CH target [see Fig. 111.61(a)] reveals that the Br dopant enhances the ratio of the Rayleigh peak to the Compton peak. This is a consequence of the increased number of tightly bound electrons in the CHBr foil. The models for scattered spectra of CHBr foils include the scattering contributions from all ionic species as
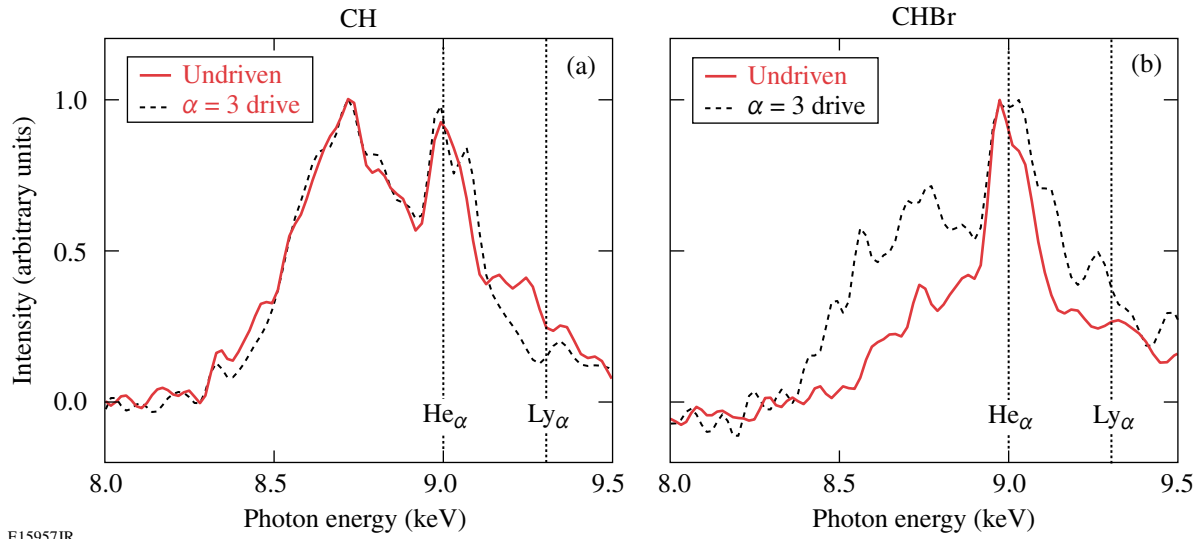
Figure 111.60
(a) Measured x-ray spectra scattered from (a) CH and (b) CHBr targets with the following drive conditions: undriven and $\alpha = 3$ drive. Spectra are normalized at the Rayleigh peak. The spectral location of Zn He$_\alpha$ at 9.0 keV and Zn Ly$_\alpha$ at 9.3 keV is indicated with vertical dotted lines.

Figure 111.61
(a) Measured spectrum from the undriven CH target compared with modeled spectra for $Z_C = 0.1$, $Z_C = 2$, and $Z_C = 4$ with $T_e = 0.1$ eV. (b) Measured spectrum for the $\alpha = 3$ drive compared with modeled spectra of $T_e = 1$, 10, and 20 eV, and $Z_C = 4$.
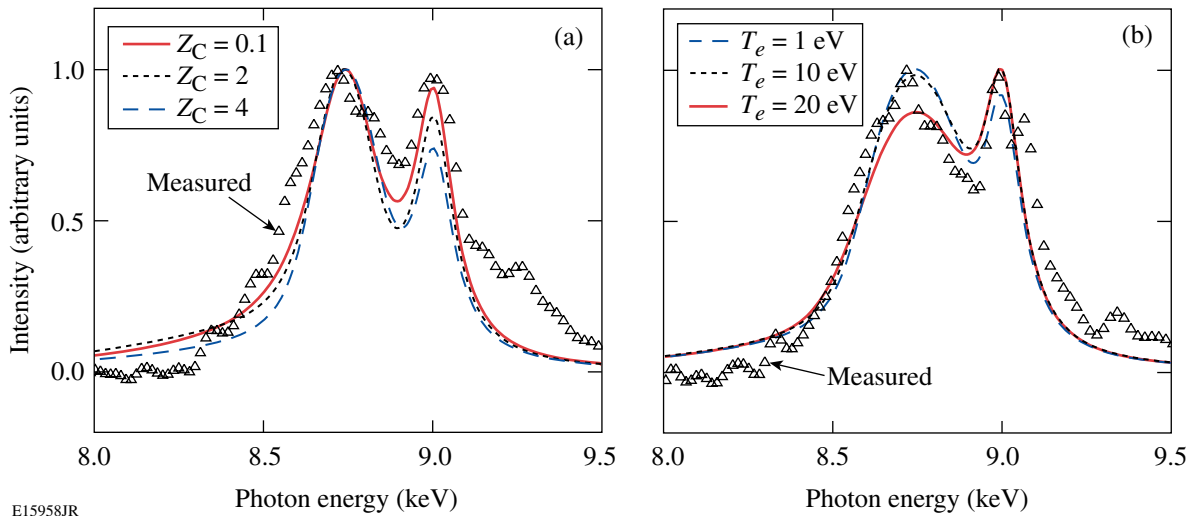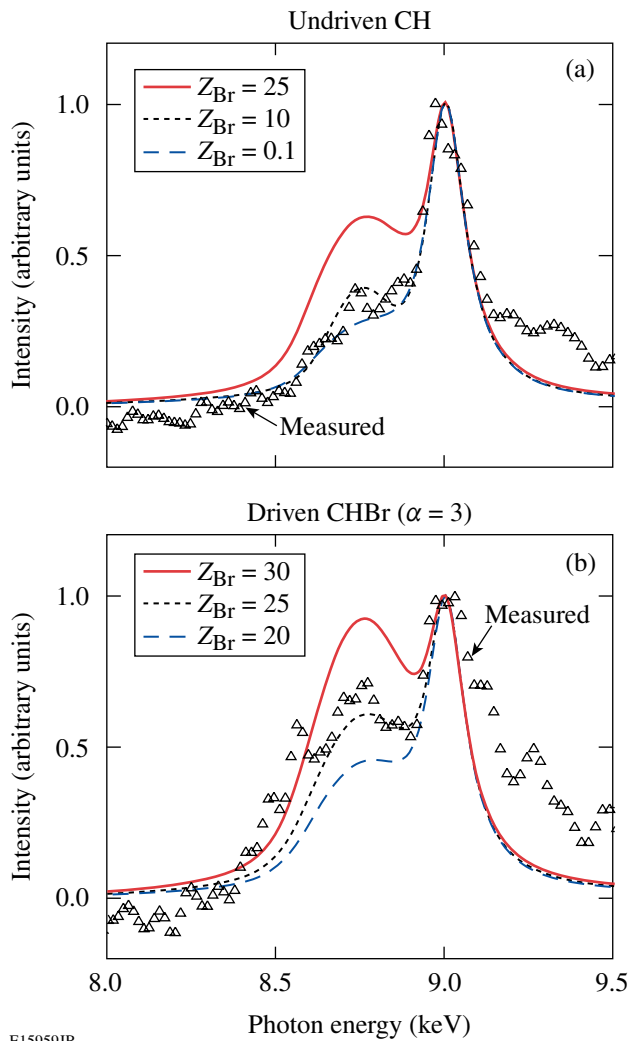
Figure 111.62
Measured x-ray spectra scattered from CHBr targets for (a) undriven and (b) $\alpha = 3$ drive are compared with modeled spectra varying Z_{Br}. The inferred parameters are $T_e = 0.1$ eV and $Z_f = 2.6$ for undriven and $T_e = 10$ eV and $Z_f = 2.9$ for the $\alpha = 3$ drive. $Z_C = 4$ was set for both undriven and driven cases.

well as their mutual correlations. In addition, the attenuation of the scattered x rays due to the path length in the CHBr foil is included in the modeled scattered spectra. The electron temperatures inferred from the spectral fitting for the undriven and $\alpha = 3$ drive are $T_e = 0.1$ eV and $T_e = 10$ eV, respectively, which are similar to the observations for the pure CH foils. Adding the Br dopant increases the sensitivity of the x-ray scattering to changes in Z. As shown in Fig. 111.60(b), the height of the Compton feature is increased for the driven target, in contrast to the results with the CH target shown in Fig. 111.60(a). The density is assumed to be solid density for undriven and four

times solid density for $\alpha = 3$ drive. The undriven case has $Z_{Br} = 10$, $Z_C = 4$, and $Z_H = 1$; the $\alpha = 3$ drive has $Z_{Br} = 25$, $Z_C = 4$, and $Z_H = 1$. The ratio of the Rayleigh peak to the Compton peak is primarily dependent on Z_{Br}. It is observed that Z_{Br} increases for the driven CHBr foil, while Z_C is not very sensitive to the $\alpha = 3$ drive. For the undriven case, little differences are seen between $Z_{Br} = 0.1$ and $Z_{Br} = 10$, while Z_{Br} needs to be increased close to $Z_{Br} = 25$ to match the model to data for the driven case. Since the binding energy of 257 eV for a 3-s M-shell electron of a neutral bromine atom is comparable to the Compton downshifted energy of ~240 eV, electrons of a bromine ion in the M and N shell (25 electrons) can be ionized with the Zn He$_\alpha$ x rays. Due to the high electron densities in the compressed plasma, continuum lowering is likely to be responsible for the large number of delocalized electrons in bromine. Those electrons belong to extended M and N shells for which electron bonding to the ion core may be heavily screened in the dense plasma. The values of Z_f inferred from the spectral fitting are $Z_f = 2.6$ and $Z_f = 2.9$ for the undriven and $\alpha = 3$ drive, respectively.

The electron temperatures predicted with *LILAC* for the shocked CH and CHBr targets ($T_e = 12$ eV) are comparable with the measured results ($T_e = 10$ to 20 eV) for a drive intensity of 1×10^{14} W/cm^2; however, an experimental accuracy for T_e of 10% to 20% is needed to validate the simulations from the hydrodynamics codes. Attempts were made to increase the electron temperature in the direct-drive target by increasing the laser drive intensity to ~10^{15} W/cm^2. However, the x-ray background levels measured for higher drive intensities were found to overwhelm the scattered x-ray spectrum.

Future Application

The main objective of this research is to develop techniques to probe the plasma conditions in the DT shell of a direct-drive implosion target during the laser irradiation to diagnose the shell adiabat. X-ray scattering is an attractive option for this application since it is noninvasive. The experimental results presented here demonstrate that it is possible to infer the spatially averaged electron temperature of a nearly Fermi-degenerate, direct-drive, shock-heated, and compressed CH foil. The complications arising from the L-shell electrons of carbon associated to a structural phase transition from the solid state to plasma will not be present in the fully ionized hydrogen isotope plasma comprising the shell of the ICF target. Consequently, a straightforward interpretation of the spatially averaged quantities of electron temperature and average ionization in the shell of a DT ICF implosion target is expected from the noncollective x-ray scattering. Predicted x-ray-scattering spectra from

an imploding cryogenic capsule in hohlraum are discussed in Ref. 40. The recent observations of plasmons in warm dense matter[14] show that it is possible to infer the electron density from the collective, forward x-ray scattering. Therefore, a combination of collective and noncollective x-ray scattering should provide the capability to diagnose the spatially averaged quantities of electron density, electron temperature, and the average ionization of a direct-drive DT cryogenic implosion target.

Conclusion

The electron temperature (T_e) and average ionization (Z) of nearly Fermi-degenerate, direct-drive, shock-heated, and compressed CH planar foils were investigated for the first time using noncollective spectrally resolved x-ray scattering on the OMEGA Laser System. CH and Br-doped CH foils were driven with six beams, having an overlapped intensity of 1×10^{14} W/cm^2 and generating 15-Mbar pressure in the foil. An examination of the scattered x-ray spectra reveals an upper limit of $Z \sim 2$, and $T_e = 20$ eV is inferred from the spectral line shapes of the elastic Rayleigh and inelastic Compton components. The electron temperatures predicted with *LILAC* ($T_e = 12$ eV) were found to be comparable with the measured results ($T_e = 10$ to 20 eV). Low average ionizations (i.e., $Z < 2$) cannot be accurately diagnosed in this experiment due to the difficulties in distinguishing delocalized valence or free electrons. Trace amounts of Br in the CH foil (i.e., 2% atomic concentration) were shown to increase the sensitivity of the noncollective, spectrally resolved x-ray scattering to changes in the average ionization. A combination of noncollective and collective spectrally resolved x-ray scattering looks like a promising diagnostic technique to probe the spatially averaged plasma conditions in the DT shell of a direct-drive implosion target during the laser irradiation to diagnose the shell adiabat.

REFERENCES

1. J. Nuckolls *et al.*, Nature **239**, 139 (1972); J. D. Lindl, R. L. McCrory, and E. M. Campbell, Phys. Today **45**, 32 (1992); R. L. McCrory, J. M. Soures, C. P. Verdon, F. J. Marshall, S. A. Letzring, S. Skupsky, T. J. Kessler, R. L. Kremens, J. P. Knauer, H. Kim, J. Delettrez, R. L. Keck, and D. K. Bradley, Nature **335**, 225 (1988); R. L. McCrory, S. P. Regan, S. J. Loucks, D. D. Meyerhofer, S. Skupsky, R. Betti, T. R. Boehly, R. S. Craxton, T. J. B. Collins, J. A. Delettrez, D. Edgell, R. Epstein, K. A. Fletcher, C. Freeman, J. A. Frenje, V. Yu. Glebov, V. N. Goncharov, D. R. Harding, I. V. Igumenshchev, R. L. Keck, J. D. Kilkenny, J. P. Knauer, C. K. Li, J. Marciante, J. A. Marozas, F. J. Marshall, A. V. Maximov, P. W. McKenty, J. Myatt, S. Padalino, R. D. Petrasso, P. B. Radha, T. C. Sangster, F. H. Séguin, W. Seka, V. A. Smalyuk, J. M. Soures, C. Stoeckl, B. Yaakobi, and J. D. Zuegel, Nucl. Fusion **45**, S283 (2005).

2. P. W. McKenty, V. N. Goncharov, R. P. J. Town, S. Skupsky, R. Betti, and R. L. McCrory, Phys. Plasmas **8**, 2315 (2001).

3. P. W. McKenty, T. C. Sangster, M. Alexander, R. Betti, R. S. Craxton, J. A. Delettrez, L. Elasky, R. Epstein, A. Frank, V. Yu. Glebov, V. N. Goncharov, D. R. Harding, S. Jin, J. P. Knauer, R. L. Keck, S. J. Loucks, L. D. Lund, R. L. McCrory, F. J. Marshall, D. D. Meyerhofer, S. P. Regan, P. B. Radha, S. Roberts, W. Seka, S. Skupsky, V. A. Smalyuk, J. M. Soures, K. A. Thorp, M. Wozniak, J. A. Frenje, C. K. Li, R. D. Petrasso, F. H. Séguin, K. A. Fletcher, S. Padalino, C. Freeman, N. Izumi, J. A. Koch, R. A. Lerche, M. J. Moran, T. W. Phillips, G. J. Schmid, and C. Sorce, Phys. Plasmas **11**, 2790 (2004).

4. M. C. Herrmann, M. Tabak, and J. D. Lindl, Phys. Plasmas **8**, 2296 (2001).

5. R. Betti, K. Anderson, V. N. Goncharov, R. L. McCrory, D. D. Meyerhofer, S. Skupsky, and R. P. J. Town, Phys. Plasmas **9**, 2277 (2002).

6. S. P. Regan, J. A. Delettrez, V. N. Goncharov, F. J. Marshall, J. M. Soures, V. A. Smalyuk, P. B. Radha, B. Yaakobi, R. Epstein, V. Yu. Glebov, P. A. Jaanimagi, D. D. Meyerhofer, T. C. Sangster, W. Seka, S. Skupsky, C. Stoeckl, D. A. Haynes, Jr., J. A. Frenje, C. K. Li, R. D. Petrasso, and F. H. Séguin, Phys. Rev. Lett. **92**, 185002 (2004).

7. National Research Council (U.S.) Committee on High Energy Density Plasma Physics, *Frontiers in High Energy Density Physics: The X-Games of Contemporary Science* (National Academies Press, Washington, DC, 2003).

8. S. Ichimaru, Rev. Mod. Phys. **54**, 1017 (1982).

9. S. H. Glenzer *et al.*, Phys. Plasmas **6**, 2117 (1999).

10. S. H. Glenzer *et al.*, Phys. Rev. Lett. **90**, 175002 (2003); O. L. Landen *et al.*, J. Quant. Spectrosc. Radiat. Transf. **71**, 465 (2001).

11. T. R. Boehly, J. A. Delettrez, J. P. Knauer, D. D. Meyerhofer, B. Yaakobi, R. P. J. Town, and D. Hoarty, Phys. Rev. Lett. **87**, 145003 (2001); D. J. Hoarty *et al.*, J. Quant. Spectrosc. Radiat. Transf. **99**, 283 (2006).

12. H. Sawada, S. P. Regan, R. Epstein, D. Li, V. Goncharov, P. B. Radha, D. D. Meyerhofer, T. R. Boehly, V. A. Smalyuk, T. C. Sangster, B. Yaakobi, and R. C. Mancini, "Investigation of Direct-Drive Shock-Heating Using X-Ray Absorption Spectroscopy," to be submitted to Physics of Plasmas.

13. G. Gregori, S. H. Glenzer, H. K. Chung, D. H. Froula, R. W. Lee, N. B. Meezan, J. D. Moody, C. Niemann, O. L. Landen, B. Holst, R. Redmer, S. P. Regan, and H. Sawada, J. Quant. Spectrosc. Radiat. Transf. **99**, 225 (2006).

14. S. H. Glenzer *et al.*, Phys. Rev. Lett. **98**, 065002 (2007).

15. M. W. C. Dharma-wardana and F. Perrot, Phys. Rev. Lett. **84**, 959 (2000).

16. F. Perrot and M. W. C. Dharma-wardana, Phys. Rev. B **62**, 16,536 (2000).

17. J. Sheffield, *Plasma Scattering of Electromagnetic Radiation* (Academic Press, New York, 1975).

18. M. K. Urry *et al.*, J. Quant. Spectrosc. Radiat. Transf. **99**, 636 (2006).

19. G. Gregori, S. H. Glenzer, and O. L. Landen, Phys. Rev. E **74**, 026402 (2006).

20. G. Gregori *et al.*, Phys. Plasmas **11**, 2754 (2004).

21. G. Gregori, S. H. Glenzer, and O. L. Landen, J. Phys. A, Math. Gen. **36**, 5971 (2003).

22. J. Chihara, J. Phys. F, Met. Phys. **17**, 295 (1987).

23. J. Chihara, J. Phys., Condens. Matter **12**, 231 (2000).

24. R. Kubo, J. Phys. Soc. Jpn. **12**, 570 (1957).

25. D. Pines and D. Bohm, Phys. Rev. **85**, 338 (1952).

26. D. Pines and P. Nozieres, *Theory of Quantum Liquids*, Advanced Book Classics (Addison-Wesley, Reading, MA, 1989).

27. P. Nozières and D. Pines, Phys. Rev. **113**, 1254 (1959).

28. M. Schumacher, F. Smend, and I. Borchert, J. Phys. B, At. Mol. Phys. **8**, 1428 (1975).

29. D. Riley *et al.*, Laser Part. Beams **25**, 1 (2007).

30. S. P. Regan, J. A. Marozas, J. H. Kelly, T. R. Boehly, W. R. Donaldson, P. A. Jaanimagi, R. L. Keck, T. J. Kessler, D. D. Meyerhofer, W. Seka, S. Skupsky, and V. A. Smalyuk, J. Opt. Soc. Am. B **17**, 1483 (2000).

31. C. J. Pawley and A. V. Deniz, Rev. Sci. Instrum. **71**, 1286 (2000); R. E. Turner *et al.*, Rev. Sci. Instrum. **72**, 706 (2001).

32. A. Pak *et al.*, Rev. Sci. Instrum. **75**, 3747 (2004).

33. B. Yaakobi and A. J. Burek, IEEE J. Quantum Electron. **QE-19**, 1841 (1983).

34. F. J. Marshall and J. A. Oertel, Rev. Sci. Instrum. **68**, 735 (1997).

35. J. Delettrez, R. Epstein, M. C. Richardson, P. A. Jaanimagi, and B. L. Henke, Phys. Rev. A **36**, 3926 (1987); J. Delettrez, Can. J. Phys. **64**, 932 (1986).

36. W. F. Huebner *et al.*, Los Alamos National Laboratory, Los Alamos, NM, Report LA-6760-M (1977).

37. R. C. Malone, R. L. McCrory, and R. L. Morse, Phys. Rev. Lett. **34**, 721 (1975).

38. L. Spitzer, Jr. and R. Härm, Phys. Rev. **89**, 977 (1953).

39. J. A. Bearden and A. F. Burr, Rev. Mod. Phys. **39**, 125 (1967).

40. A. L. Kritcher *et al.*, High Energy Density Phys. **3**, 156 (2007).

Aperture Tolerances for Neutron-Imaging Systems in Inertial Confinement Fusion

Introduction

The inertial confinement fusion (ICF) approach to fusion ignition relies on inertia to compress the fuel to ignition conditions. A major goal of ICF research is the generation of net energy by imploding targets containing deuterium–tritium (DT) fuel, using lasers, x rays generated by lasers, pulsed power, or ion beams.[1] To achieve ignition, it is necessary for the target irradiation to be as symmetric as possible, minimizing hydrodynamic instabilities that reduce the implosion efficiency. To validate simulations of the implosions, one must measure or infer the density and temperature distribution of the fuel at peak compression.[2] This requires a number of target diagnostics that typically utilize x rays and fusion-reaction products emitted from the core.[3–5]

For example, an x-ray image of an ICF core provides information about the spatial structure of several complex processes within the target that are directly related to the fusion reactions. The x-ray image depends on the spatial and temporal profiles of plasma density and electron temperature. Diagnostics based on neutron emission provide a direct measure of the fusion burn region. These diagnostics are used to infer the fuel areal density, neutron yield, fuel ion temperature, and bang time.[2] The spatial distribution of the burning fuel can be directly determined by imaging the primary and scattered neutron emission from the core[6] (in this context, primary neutron images are based on the thermally broadened 14-MeV neutron emission from D-T fusion reactions in the core, while scattered neutron images are based on primary neutrons that scatter from the dense fuel to energies well below the 14-MeV line emission; these neutrons provide an image of the cold-fuel distribution in a non-igniting implosion). A neutron image is obtained by placing an appropriate aperture in front of a spatially sensitive neutron detector. These apertures typically code the spatial distribution from the source by differentially attenuating the neutron flux. The reconstruction of the core image requires precise knowledge of the aperture geometry.[7] Neutron imaging would be used to identify ignition-failure mechanisms such as poor implosion symmetry or inadequate convergence/areal density. Neutron imaging is

used on the OMEGA[7] laser to measure the core symmetry of gas-filled plastic shells and energy-scaled, ignition-relevant cryogenic target implosions.[8]

A spatially sensitive neutron detector can be based on an array of scintillators or on a bubble chamber.[9] For a required image resolution, the system design considerations include magnification, the signal-to-noise (S/N) ratio, aperture-alignment accuracy, aperture-fabrication tolerances, neutron energy, neutron yield, field of view, and the detector spatial resolution. Here the S/N ratio refers to unwanted neutron signals from scattering sites near the imaging line of sight. This noise typically scales with the signal (primary yield) and can be reduced by shielding the detector. The impact of this noise can be further reduced by acquiring a flat-field (i.e., no aperture) image in a high-field implosion. For the work presented here, no attempt was made to include a neutron noise component in the simulations. For ICF experiments on laser facilities such as OMEGA[7] and the National Ignition Facility (NIF),[10] optimization of the system design is a complex process and understanding the effects and trade-offs of component tolerances requires simulations and image analysis. This article will discuss system design considerations and will focus on the resolution limitations introduced by the aperture alignment and fabrication tolerances.

Design Considerations for Neutron Imaging for ICF

Neutron-imaging (NI) systems use extended pinholes or penumbral apertures (with annular apertures as a particular case of the second) to generate images on the detector plane.[6] A full system consists of a neutron source, an aperture, an alignment system, and a neutron-sensitive detector (Fig. 112.1). When the neutrons pass from the source through the aperture, their spatial intensity at the detector plane is modulated according to the shape of the aperture. The alignment and type of aperture define the image size, shape, and resolution on the detector plane. The aperture's three-dimensional shape is described by a two-variable point-spread function (PSF). The magnification M of the system is the ratio of source-detector distance L divided by the source-aperture distance ℓ.
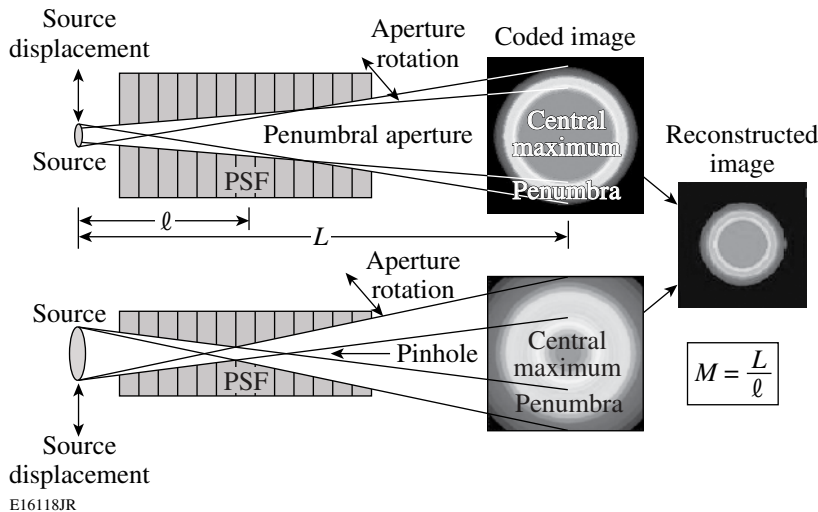
Figure 112.1
Schematic diagrams of penumbral and pinhole-imaging devices. The functional information for source-image reconstruction comes from the penumbral area of the image on the detector plane (except for the case when the pinhole is much smaller than the source). The magnification of the system M is the ratio of the source-detector distance L divided by the source-aperture distance ℓ.

1. Pinhole Imaging

Neutron-based pinhole imaging works on the same principle as an optical pinhole camera, with the source image directly displayed on the detector. Additional processing is required for a pinhole diameter comparable to or larger than the desired resolution. Due to the finite neutron range inside the materials, the pinhole is extended radially and not limited to a single plane along the observation axis. The image on the detector plane consists of a central maximum surrounded by a large penumbra. The small diameter (typically of the order of $10\,\mu$m) of the aperture makes it difficult to produce with the required precision and constitutes one of the main sources of error in the measured/reconstructed image. Relative to a thin aperture (e.g., an optical pinhole), it is more difficult to obtain a clear image due to the finite depth of focus of a neutron aperture (a neutron aperture simply attenuates the neutron flux rather than blocking it from reaching the detector). The image may directly represent the source, as it does for an optical pinhole camera, but it is formed from only those neutrons passing through a small aperture, limiting the resolution and S/N ratio for low-yield (for example, $\leq 10^{14}$) implosions.[11]

2. Penumbral Imaging

Penumbral imaging with an aperture larger than the source size is a coded-aperture-imaging technique (i.e., the image seen on the detector's plane is not the exact representation of the source but is defined by the PSF of the aperture).[5] With a penumbral aperture, the image consists of a uniform, bright central region surrounded by a partially illuminated penumbra. The source image is encoded in the penumbra of the detected image (the bright central region receives signals from the entire source area and does not provide spatial information). The diameter of a penumbral aperture is typically larger than

the source and, therefore, for a comparable resolution, should be easier to fabricate, characterize, and align than a pinhole. Due to the larger solid angle, the image is formed from many more neutrons than for a pinhole; therefore, for a given yield, it typically has an intrinsically higher S/N ratio.[12]

The coded image must be deconvolved to produce an image of the neutron source. This process requires precise knowledge of the aperture point-spread function and the flat-field response of the imaging detector.[6] Therefore, a penumbral aperture is designed to be as isoplanatic as possible. This means that the aperture PSF is independent of the source point in the field of view. In practice, this is difficult to do and is the primary reason for the study of alignment sensitivity.

For both types of apertures, uncertainties in the exact shape (due to finite fabrication tolerances) lead to errors in the reconstructed image due to uncertainties in the calculated PSF. For brighter neutron sources (neutrons per source element), the S/N ratio improves faster for pinholes than for penumbral apertures, making pinholes the preferred aperture type of very high yield (for example, $\geq 10^{16}$) ICF imaging.[10]

Reconstruction of the Detector-Plane Image

Nyquist's theorem states that in order to accurately reconstruct a signal based on periodic sampling, the sampling frequency must be at least twice the maximum frequency of the signal. This limits the maximum resolution of a pixelated imaging system to $2\delta(\text{pixel})/M$, where M is the magnification of the system and $\delta(\text{pixel})$ represents the pixel resolution on the image plane.[13] To diminish the effect of image aliasing (i.e., pixelation of image), various anti-aliasing techniques can be

applied. The numerical noise in the signal (in this case the noise is associated with the image reconstruction) is typically given by Poisson statistics, and its reduction requires low-bandpass filtration; i.e., the signal has a frequency higher than a conveniently chosen cutoff value.[14]

In the neutron-detection measurements associated with imaging, random errors arise from various sources, such as misalignment, detector noise, etc. In most of the cases, a Gaussian distribution, or other similar type, can be used to characterize the random errors encountered. The standard deviation of the distribution is used as a measure of the uncertainty. For a neutron image, the relevant sources of error are due to the detector noise (typically associated with flat-field statistics), aperture alignment, pixel resolution of the detector, and the recoil distances of the nuclei in the detector. Therefore, the overall measurement uncertainty is given by[14]

$$\sigma_s = \sqrt{\sigma_{noise}^2 + \sigma_{align}^2 + \sigma_{pixel}^2 + \sigma_{rec}^2} \, , \qquad (1)$$

where the indices *noise*, *align*, *pixel*, and *rec* represent the errors induced by noise, alignment, pixel, and recoil distance. The resolution of the system (i.e., the scale of the smallest resolvable point in the source under ideal conditions) can be written based on similar assumptions. Because the error given by Poisson statistics is inversely proportional to the cutoff frequency k_c (at which point the noise starts to dominate), the resolution of the imaging system can be written as[14]

$$\delta_s = \sqrt{\frac{1}{k_c^2} + \delta_{align}^2 + \left(\frac{2\delta_{pixel}}{M}\right)^2 + \left(\frac{\delta_{rec}}{M}\right)} \, , \qquad (2)$$

where M is the magnification of the system and δ_{align}, δ_{pixel}, and δ_{rec} are the resolution components given by alignment error, the finite pixelation of the detector, and the particle recoil distance from the interaction of the neutrons with the detector medium. A neutron imaging system could, in principle, achieve an improved resolution by using a high magnification, but a higher value for M increases the sensitivity to alignment errors. Keeping the other parameters fixed, a large target-aperture distance provides a better resolution as M increases in Eq. (2). Higher neutron yields increase the value of k_c in Eq. (2) and decrease the resolution limit of the instrument.

A coded penumbral image and, in most cases, a coded pinhole image on the detector plane can be deconvolved using an inverse Fourier transform.[5] By considering the magnified image

of the source without any penumbral blurring as a function of coordinates $f(x,y)$ and the image created by a point source (or the PSF) as $g(x,y)$, an image on the detector plane $h(x,y)$ is created through the convolution of the first two functions:

$$h(x,y) = f(x,y) \circ g(x,y)$$
$$= \iint f(x',y')g(x-x',y-y')dx'\,dy'. \qquad (3)$$

A deconvolution of the source image can be obtained by using the convolution theorem of the Fourier transform. Since $H(k,l) = F(k,l)\,G(k,l)$, with H, F, G the Fourier transforms of h, f, g,

$$F(k,l) = \frac{H(k,l)}{G(k,l)} \, , \qquad (4)$$

and the source image becomes

$$f(x,y) = F^{-1}\left[\frac{H(k,l)}{G(k,l)}\right] = F^{-1}\left\{\frac{F[h(x,y)]}{F[g(x,y)]}\right\}, \qquad (5)$$

where F and F^{-1} are the Fourier and inverse Fourier transforms. A Wiener filter[12] can be used to reduce the noise levels by replacing

$$G(k,l) = F[g(x,y)] = \frac{|H(k,l)|}{|H(k,l)|^2 + \gamma} \, , \qquad (6)$$

where γ is an arbitrary correction factor (always positive) chosen to minimize the noise on the reconstructed image.

Neutron-Imaging Design Tool

To investigate the influences of various parameters of a NI system on the quality of the reconstructed image, a design tool has been developed. The code was written in PV Wave [http://www.vni.com], and Eqs. (5) and (6) have been used to reconstruct the encoded image. The source and detector plane are described by arrays that define the maximum theoretical system resolution. Various source distributions and intensity profiles can be generated. Noise can be added to simulate neutron background, but for the work presented here no neutron-related noise was added (any such noise can be subtracted from the image recorded on the detector plane). The aperture is described as a succession of thin layers with fixed openings along the particle-flux direction, and the resulting image on the detector plane is created by summing the neutron attenuations of the individual layers. A PSF for the aperture is generated by

ray tracing between the array elements of source and detector. The rays are treated as optical, to precisely define the thin-layered edges of each aperture. In this way, a variety of apertures can be simulated (pinholes and penumbral, cylindrical, biconic, or annular). The only limitation for the simulations is the available computational power. Fabrication and alignment tolerances can be determined by direct simulation using realistic source distributions and detector responses.

The simulations consist of defining a source distribution (shape and brightness) using an array of small source elements (the pixel size in the source is smaller than the system resolution) and calculating the PSF using ray tracing between the source elements and the detector elements (pixels). The pixelation of the detector is typical for existing neutron-imaging systems. The shapes of the reconstructed images can then be compared with the original source to determine if features associated with the aperture shape and alignment would be measurable in an actual imaging system.

For any NI system, several factors determine the characteristics of the image on the detector plane and those of the reconstructed image: The magnification determines the size of the image on the detector plane. If a large magnification is achieved by increasing the source-to-detector distance, a larger detector for a given source size or field of view is required. The aperture regulates the neutron flux on the detector. Its size determines, as much as the magnification, the dimension of the image on the detector plane for penumbral imaging systems. The aperture thickness and material determine its leakage to neutrons, and its shape controls the characteristics of the coded image and, therefore, the accuracy of the deconvolution process. The aperture is also sensitive to misalignment and

can also be simulated. Another factor is the sensitivity of the recording medium. Apart from any intrinsic pixel resolution imposed by the detector dimensions, the detector resolution is ultimately limited by the recoil length of the elastically scattered nuclei at the detector material (e.g., protons in a CH-based scintillator). The last two factors to be taken into consideration are the neutron-scattering sources near the imaging line of sight and the field of view (limits resolution via the PSF).

Specific Examples

This design tool has been tested against simple cases having analytical solutions. Good agreement between the analytic calculations and numerical simulations suggests that the technique can be applied to complex aperture assemblies. For a point source, a perfect fit was obtained between the reconstructed and the analytically calculated image. For a circular flat source (constant brightness), the relative difference between the reconstructed and the analytically calculated image was in the range of 1% (due to the fact that the circular source was approximated by an array and its element centers were either outside or inside the source radius, changing the calculated values of the inverse Fourier transform), as shown in Fig. 112.2.

Data images from implosions generated by OMEGA shots were reconstructed using the technique described above [Fig. 112.3(a)] and compared with the results obtained by using the method described in Ref. 14 (filtered autocorrelation) and shown in Fig. 112.3(b). The biconic aperture used had a 200-μm field of view (FOV), a thickness of 100 mm, and a central diameter of 2 mm. The measured diameter of the neutron source size was ~50 μm, the source–aperture distance was 26 cm, and the source–detector distance was 800 cm, yielding a magnification of 30.8. The DT neutron yield was 8.5×10^{12}.
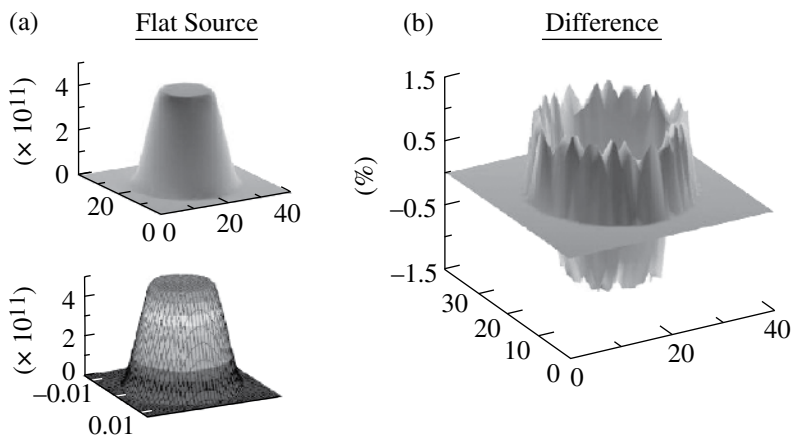
Figure 112.2
Comparison between the analytical solution and numerical simulations for a circular flat source. Graph (b) shows the relative difference between these two cases.
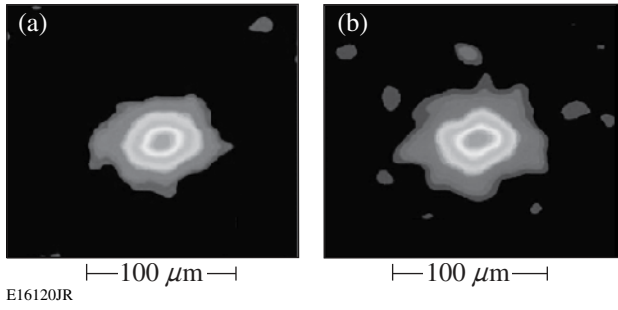
E16119JR

Figure 112.3
Image data (shot 35988, DT[10] CH[20], $Y_n = 8.5 \times 10^{12}$) deconvolved (a) with our code and (b) using filtered autocorrelation.[15]

Aperture Simulations

To test the sensitivity of the reconstructed images to aperture misalignment and fabrication errors, cases similar to the experimental setup described in Ref. 6 (and above) were simulated with the design code for a flat, circular source (Fig. 112.4). A biconic penumbral aperture with a central diameter of 2 mm and a pinhole with a central diameter of 10 μm were used to simulate a flat source 50 μm in diameter. In both cases, the FOV was 200 μm, the source–aperture distance was 26 cm, and the source–detector distance was 800 cm, with a magnification of 30.8. The aperture thickness was 10 cm. The maximum theoretical resolution of the simulated system for the deconvolved images was 4 μm [obtained from Eq. (2) with the assumption of a perfect alignment, and where k_c and δ_{rec} had a cumulative contribution of less than 0.1 μm]. Based on the discussion in **Reconstruction of the Detector-Plane Image** (p. 204), the tolerances for aperture fabrication and alignment can be set by the need to identify certain scale features in the reconstructed image. For this study, based on 50-μm cores on OMEGA, features of 10 μm were considered important. By incrementally moving the source relative to the system axis, an aperture misalignment was simulated. In a second phase, the aperture shape was elliptically distorted (with the eccentricity

e defined in Fig. 112.4). In both cases, the error introduced in the deconvolved image was precisely defined.

1. Penumbral Apertures

The penumbral aperture's sensitivity to misalignment has been examined based on a set of simulations for apertures misaligned up to 2.36 mrad (corresponding to an offset of 250 μm relative to the primary axis). As the source is displaced, the reconstructed image appears more and more distorted (Fig. 112.5), i.e., the ratio between the horizontal and vertical dimensions increases. Image distortions within the range of the 10-μm feature limit were detectable for a misalignment angle as small as 0.4 mrad.

Aperture-fabrication defects were also analyzed for the penumbral aperture. Deviations from the circular conical shape were induced, and the coded image was transformed into an
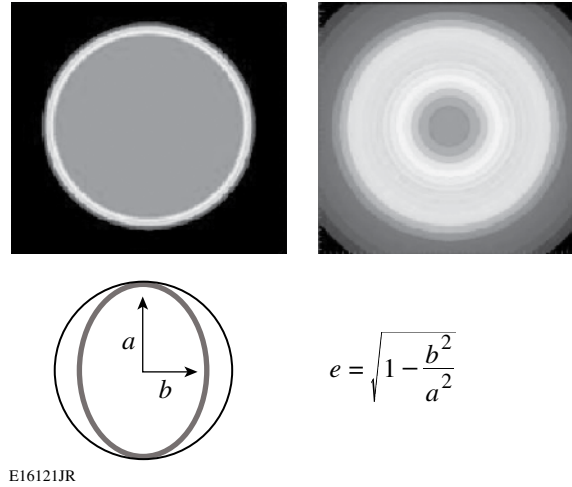

Figure 112.4
Examples of simulated raw images for a penumbral aperture (left) and a pinhole (center) seen at the detector plane level. Right: the aperture cross section and the distortion direction.
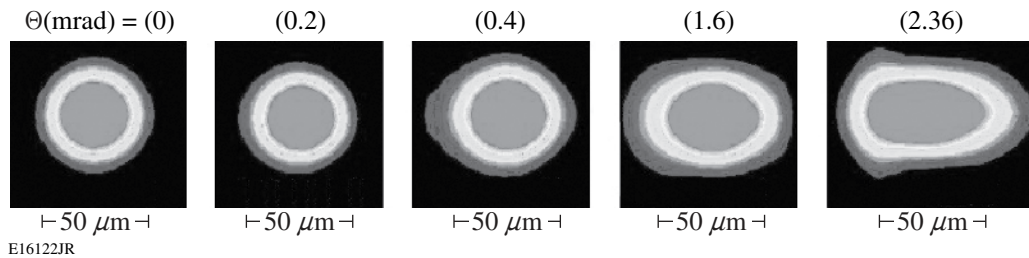

Figure 112.5
Reconstructed images of a penumbral aperture for various angles of misalignment (mrad) simulated by a source displacement.

ellipse. As the ellipse eccentricity (e) increased, the images became more and more distorted, as shown in Fig. 112.6. The subsequent modifications suggested that the aperture defects are as important as alignment for a penumbral imaging system (Fig. 112.6) and were detectable within the feature limit at an eccentricity of 0.15 or a 1.2% difference between the a and b axis parameters (this corresponds to a 24-μm out-of-round error for a 2-mm-diam aperture).

2. Pinhole Apertures

The pinhole sensitivity to misalignment has also been determined based on a set of simulations with progressively misaligned sources, in a geometry identical to the previous case. The same method has been used, first to verify the alignment tolerances (Fig. 112.7) and then to examine the influences of the fabrication defects (Fig. 112.8).
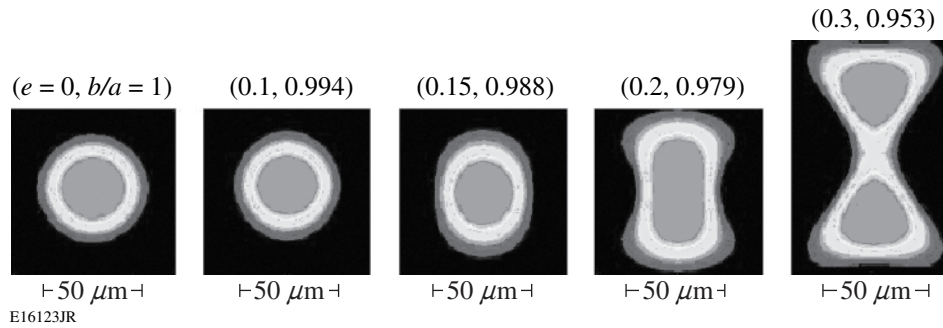

Figure 112.6
Reconstructed images of a penumbral aperture for various degrees of deformation.
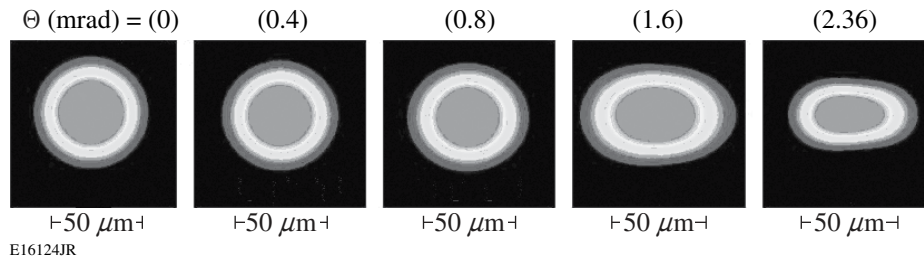

Figure 112.7
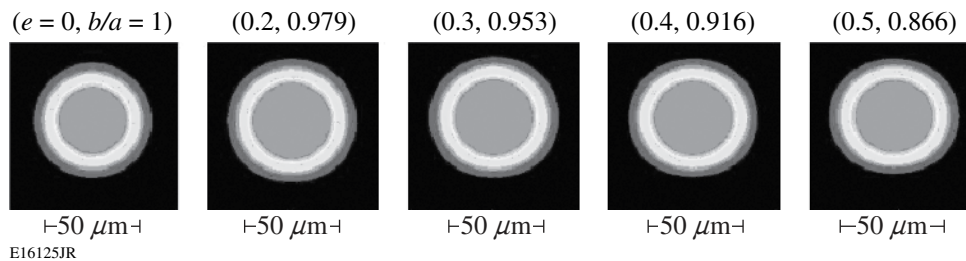Reconstructed images of a pinhole for various angles of misalignment (mrad).

Figure 112.8
Reconstructed images of a pinhole for various degrees of deformation.

Aperture-fabrication defects were further analyzed for the pinhole. Deviations from the circular conical shape were induced and the coded image was transformed into an ellipse. As the ellipse eccentricity (*e*) increased, the images became more and more distorted, as shown in Fig. 112.8. Detectable distortions were observed at 0.8 mrad for the misalignment and for an eccentricity of 0.5 for the fabrication errors (a *b/a* ratio of 0.87 or an out-of-round tolerance of 1.4 μm for a 10-μm pinhole).

For both penumbral and pinhole apertures, the misalignment and fabrication errors can induce measurable false features in the deconvolution process. To minimize these features, alignment and fabrication tolerances can be determined from simulations such as those described above. For the imaging system previously described (and typical for a facility such as OMEGA), the requirements for a NI system designed to observe 10-μm features are summarized in Table 112.I. One can see that penumbral apertures are more sensitive to misalignment, while pinholes are more sensitive to fabrication errors.

Quantitative Analysis for the Errors Induced by Apertures

The distortions induced by the aperture-fabrication error or misalignment can be estimated by measuring the ratio between the reconstructed image axes for a flat disk neutron source. The values for angular misalignments and aperture deformations are detailed in Table 112.II.

The errors in the reconstructed image tend to increase approximately linearly with the alignment or deformation of the aperture (penumbral or pinhole).

Requirements for NI at the National Ignition Facility (NIF)

The NIF facility will use 192 laser beams for ICF with a total power of 1.8 MJ. A directly driven deuterium–tritium shell will have a diameter of 3 mm with a final compressed hot spot of about 80 μm. The geometric and energy constraints will not allow the NI imaging aperture to be placed closer than 50 cm from the source, implying, for a magnification similar to OMEGA, a much longer source–detector distance.

Simulations for penumbral and pinhole apertures similar to those used on OMEGA have been performed for the NIF case. The source–aperture distance was set to 52 cm and the source–detector distance was set to 16 m with a magnification value of $M = 30.8$, similar to the OMEGA simulation previously described. The FOV was maintained at the same value of 150 μm (with the apertures rescaled for the new geometry). The theoretical calculated resolution of the system was also 4 μm (calculated in the same way as for the OMEGA simulation from the previous section). The NIF requirements for a NI system can be summarized in Table 112.I.

Based on Table 112.I and the large source–aperture distance at the NIF, the limits obtained with the design tool suggest that penumbral apertures are slightly more sensitive to fabrication

Table 112.I: Tolerances for a NI system with a 10-μm resolution for the geometric configuration of OMEGA (upper) and the NIF (lower).

Penumbral Apertures (OMEGA)	Pinhole Apertures (OMEGA)
Misalignment of 0.4 mrad or source position off-center by 100 μm	Misalignment of 0.8 mrad or source position off-center by 200 μm
Fabrication eccentricity of 0.15 (i.e., 1.2% difference between the ellipse axes) or an absolute fabrication error of 24 μm	Fabrication eccentricity of 0.5 (i.e., ~14% difference between the ellipse axes) or an absolute fabrication error of 1.4 μm

Penumbral Apertures (NIF)	Pinhole Apertures (NIF)
Misalignment of 0.4 mrad	Misalignment of 0.4 mrad
Source position off-center by 200 μm	Source position off-center by 200 μm
Fabrication eccentricity of 0.15 (i.e., 1.1% difference between the ellipse axes) or an absolute fabrication error of 22 μm	Fabrication eccentricity of 0.4 (i.e., 8.3% difference between the ellipse axes) or an absolute fabrication error of 0.83 μm

Table 112.II: Angular misalignment versus axial deformation (upper). Deformation versus axial deformation (lower) of the reconstructed image for penumbral apertures and pinholes.

Angular Misalignment (mrad)	b/a (penumbral aperture)	Angular Misalignment (mrad)	b/a (pinhole)
0	1	0	1
0.2	1.007	0.2	1.045
0.4	1.195	0.4	1.13
1.6	1.375	1.6	1.53
2.36	1.785	2.36	1.79

Deformation (Eccentricity) for a Penumbral Aperture	b/a (penumbral)	Deformation (Eccentricity) for a Pinhole	b/a (pinhole)
1	1	1	1
1.006	1.025	1.021	1.055
1.012	1.2025	1.049	1.056
1.021	1.8875	1.092	1.098
1.049	5.428	1.154	1.16

errors (from 24 μm to 10 μm) with the angular sensitivity about the same, while pinholes become twice as sensitive to alignment (from 0.8 mrad to 0.4 mrad), with the same sensitivity to the relative fabrication error (1.4 μm).

Conclusions

A neutron-imaging (NI) design tool has been used to quantify the effects of aperture fabrication and alignment on reconstructed images. The simulations indicate that alignment tolerances of less than 1 mrad (current precision on OMEGA[8]) introduce measurable features in a reconstructed neutron image. Penumbral apertures are several times less sensitive to fabrication errors than pinhole apertures (as displayed in Tables 112.I and 112.II). A forthcoming publication will describe a NI bubble chamber that is being developed for high-resolution neutron imaging.

REFERENCES

1. T. C. Sangster, R. L. McCrory, V. N. Goncharov, D. R. Harding, S. J. Loucks, P. W. McKenty, D. D. Meyerhofer, S. Skupsky, B. Yaakobi, B. J. MacGowan, L. J. Atherton, B. A. Hammel, J. D. Lindl, E. I. Moses, J. L. Porter, M. E. Cuneo, M. K. Matzen, C. W. Barnes, J. C. Fernandez, D. C. Wilson, J. D. Kilkenny, T. P. Bernat, A. Nikroo, B. G. Logan, S. Yu, R. D. Petrasso, J. D. Sethian and S. Obenschain, Nucl. Fusion **47** S686–S695 (2007).

2. J. D. Lindl, Phys. Plasmas **2**, 3933 (1995).

3. J. D. Kilkenny, M. D. Cable, C. A. Clower, B. A. Hammer, V. P. Karpenko, R. L. Kauffman, H. N. Kornblum, B. J. MacGowan, W. Olson, T. J. Orzechowski, D. W. Phillion, G. L. Tietbohl, J. E. Trebes, B. Chrien, B. Failor, A. Hauer, R. Hockaday, J. Oertel, R. Watt, C. Ruiz, G. Cooper, D. Hebron, L. Leeper, J. Porter, and J. Knauer, Rev. Sci. Instrum. **66**, 288 (1995).

4. R. J. Leeper, G. A. Chandler, G. W. Cooper, M. S. Derzon, D. L. Fehl, D. L. Hebron, A. R. Moats, D. D. Noack, J. L. Porter, L. E. Ruggles, J. A. Torres, M. D. Cable, P. M. Bell, C. A. Clower, B. A. Hammel, D. H. Kalantar, V. P. Karpenko, R. L. Kauffman, J. D. Kilkenny, F. D. Lee, R. A. Lerche, B. J. MacGowan, M. J. Moran, M. B. Nelson, W. Olson, T. J. Orzechowski, T. W. Phillips, D. Ress, G. L. Tietbohl, J. E. Trebes, R. J. Bartlett, R. Berggren, S. E. Caldwell, R. E. Chrien, B. H. Failor, J. C. Fernández, A. Hauer, G. Idzorek, R. G. Hockaday, T. J. Murphy, J. Oertel, R. Watt, M. Wilke, D. K. Bradley, J. Knauer, R. D. Petrasso, and C. K. Li, Rev. Sci. Instrum. **68**, 868 (1997).

5. T. J. Murphy, C. W. Barnes, R. R. Berggren, P. Bradley, S. E. Caldwell, R. E. Chrien, J. R. Faulkner, P. L. Gobby, N. M. Hoffman, J. L. Jimerson, K. A. Klare, C. L. Lee, J. M. Mack, G. L. Morgan, J. A. Oertel, F. J. Swenson, P. J. Walsh, R. B. Walton, R. G. Watt, M. D. Wilke, D. C. Wilson, C. S. Young, S. W. Haan, R. A. Lerche, M. J. Moran, T. W. Phillips, T. C. Sangster, R. J. Leeper, C. L. Ruiz, G. W. Cooper, L. Disdier, A. Rouyer, A. Fedotoff, V. Yu. Glebov, D. D. Meyerhofer, J. M. Soures, C. Stoeckl, J. A. Frenje, D. G. Hicks, C. K. Li, R. D. Petrasso, F. H. Séguin, K. Fletcher, S. Padalino, and R. K. Fisher, Rev. Sci. Instrum. **72**, 773 (2001).

6. D. Ress *et al.*, Science **241**, 956 (1988).

7. T. R. Boehly, R. S. Craxton, T. H. Hinterman, J. H. Kelly, T. J. Kessler, S. A. Kumpan, S. A. Letzring, R. L. McCrory, S. F. B. Morse, W. Seka, S. Skupsky, J. M. Soures, and C. P. Verdon, Rev. Sci. Instrum. **66**, 508 (1995).

8. L. Disdier, A. Rouyer, I. Lantuéjoul, O. Landoas, J. L. Bourgade, T. C. Sangster, V. Yu. Glebov, and R. A. Lerche, Phys. Plasmas **13**, 056317 (2006).

9. R. K. Fisher, R. B. Stephens, L. Disdier, J. L. Bourgade, A. Rouyer, P. A. Jaanimagi, T. C. Sangster, R. A. Lerche, and N. Izumi, Phys. Plasmas **9**, 2182 (2002).

10. W. J. Hogan, E. I. Moses, B. E. Warner, M. S. Sorem, and J. M. Soures, Nucl. Fusion **41**, 567 (2001).

11. G. L. Morgan *et al.*, Rev. Sci. Instrum. **72**, 865 (2001).

12. R. K. Fisher *et al.*, Rev. Sci. Instrum. **72**, 796 (2001).

13. G. F. Knoll, *Radiation Detection and Measurement*, 3rd ed. (Wiley, New York, 2000).

14. L. Disdier, A. Rouyer, D. C. Wilson, A. Fedotoff, C. Stoeckl, J. L. Bourgade, V. Yu. Glebov, J.-P. Garçonnet, and W. Seka, Nucl. Instrum. Methods Phys. Res. A **489**, 496 (2002).

15. A. Rouyer, Rev. Sci. Instrum. **74**, 1234 (2003).

Hohlraum Energetics and Implosion Symmetry with Elliptical Phase Plates Using a Multicone Beam Geometry on OMEGA

Introduction

The overall coupling efficiency of laser energy to the implosion capsule is an important parameter for inertial confinement fusion (ICF). Indirect-drive-ignition designs planned for the National Ignition Facility (NIF) have predicted coupling efficiencies of about 10% (Ref. 1). The use of phase plates for indirect-drive implosions affects the laser-scattering losses and is a central focus of this article. Laser-beam smoothing with phase plates was shown to reduce stimulated Brillouin scattering (SBS) and stimulated Raman scattering (SRS) of gas-filled hohlraums and to increase the peak radiation temperature on Nova.[2] Phase plates reduce laser–plasma instabilities by controlling the on-target laser-intensity distribution and the speckle modal power spectrum. These experiments extend the previous work[2] to a multicone beam geometry using 40 beams compared with 10 beams configured in a single cone. An experimental platform on the OMEGA Laser System[3] for the National Ignition Campaign drives hohlraums with three cones of beams smoothed with elliptical phase plates. The 60 beams of OMEGA are symmetrically arranged around the spherical target chamber, so only 40 beams can be used to drive a hohlraum: The cones have angles of incidence 21.4° (cone 1 with 5 beams), 42.0° (cone 2 with 5 beams), and 58.8° (cone 3 with 10 beams) to the hohlraum axis. A multicone beam geometry improves the x-ray-drive symmetry of indirect-drive implosions and will be used on the NIF.[1] The new phase plates were designed to provide favorable coupling of laser energy to x-ray drive for a wide variety of indirect-drive experiments on OMEGA. The coupling of laser energy to x-ray drive for gas-filled hohlraums was significantly improved when phase plates were added. The improved coupling correlates with reduced, cone-dependent losses from SRS and SBS. A high-Z dopant in the gas-filled hohlraum[4] is shown to reduce hard-x-ray production and SRS and increase the peak radiation temperature. Indirect-drive implosion symmetry[5] of vacuum and gas-filled hohlraums was investigated for the first time with a multicone laser drive smoothed with phase plates. A shift in symmetry was observed between vacuum and gas-filled hohlraums having identical beam pointing.

Elliptical Phase Plates

The elliptical phase plates can be used to drive hohlraums on OMEGA that have a laser entrance hole (LEH) diameter greater than 800 μm. Elliptical phase plates maximize the beam clearance, while minimizing the peak intensity at the LEH. This is illustrated in the upper row of Fig. 112.9, where the black circle represents the LEH having an 800-μm diameter and the gray spot indicates the size of the beam including the intensity contour, which is 1% of the peak intensity. Each column represents a beam incident on the LEH with the minor axis of the ellipse lying in the plane of incidence for each of the cones. The elliptical laser spot at normal incidence projects to a circular spot at the plane of the LEH when the angle of incidence is 42°. As seen in the upper row of Fig. 112.9, ideal clearance between the edge of the beam and the extent of the LEH is achieved for the cone-2 beam with the elliptical phase plate. The cone-1 and cone-3 beams are slightly elliptical in the plane of the LEH; however, they still have good beam clearance. A single ellipticity was chosen to streamline configuration operations on OMEGA. In contrast to the elliptical far-field laser spot, the lower row of Fig. 112.9 illustrates the limitation of the circular laser spot. To prevent the high-angle, cone-3 beams from clipping the LEH wall, the diameter of the circular laser spot must be reduced to the white circle in Fig. 112.9, which increases the peak intensity of the beam at the LEH. The phase plate is designed to produce an elliptical far field at normal incidence with a super-Gaussian power $n = 5$, a $1/e$ half-width minor radius $\delta_{min} = 103$ μm, and $1/e$ half-width major radius $\delta_{maj} = 146$ μm. The single-beam average (I_{50}) and peak (I_{95}) intensities generated with the phase plate and a 500-J, 1-ns square laser pulse are designed to be $I_{50} = 1.3 \times 10^{15}$ W/cm^2 and $I_{95} = 4.5 \times 10^{15}$ W/cm^2, respectively. The far-field intensity distribution produced with the phase plate was characterized on OMEGA using the ultraviolet equivalent-target-plane diagnostic.[6] The portion of the measured envelope having intensities greater than 10% of the peak intensity was modeled with a super-Gaussian profile having $n = 4.1$, $\delta_{min} = 106$ μm, and $\delta_{maj} = 145$ μm. Analysis of the single-beam intensity shows the E-IDI-300 phase plate generates an average intensity of $I_{50} =$

1.0×10^{15} and a peak intensity of $I_{95} = 3.8 \times 10^{15}$ W/cm^2 with a 500-J, 1-ns square laser pulse drive. Similar measurements performed for 9 of the 43 phase plates were found to be close to the design specifications with $I_{50} = 1.0 \pm 0.05 \times 10^{15}$ W/cm^2, $I_{95} = 3.7 \pm 0.2 \times 10^{15}$ W/cm^2, $n = 4.3 \pm 0.3$, $\delta_{min} = 106 \pm 1.4$ μm, and $\delta_{maj} = 144 \pm 2.7$ μm.

Hohlraum Energetics and Indirect-Drive-Implosion Symmetry Experiments

Hohlraum energetics experiments were conducted using thin-walled (5 μm Au), scale 1, vacuum and gas-filled (0.9 atm C$_5$H$_{12}$) Au halfraums irradiated with the shaped laser pulse PS26. The halfraums have an equal length and diameter of 1.6 mm and an LEH diameter of 1.07 mm. The fully ionized n_e of the hohlraum plasma for the gas-filled targets is 9×10^{20} cm^{-3}. The gas fill is contained with a 0.6-μm-thick polyimide window over the LEH. Time-resolved, absolute levels of the x-ray flux were recorded with the DANTE diagnostic.[7] Time-integrated levels of SRS and SBS that scattered back through the OMEGA focus lens were recorded with the full-aperture backscatter station (FABS), and light scattered just outside the lens was recorded with the near-backscatter imaging (NBI) diagnostic.[8] The coupling of laser energy to x-ray drive is significantly improved for gas-filled halfraums

with phase plates, consistent with earlier work.[2] The targets were irradiated with an ~7-kJ PS26 laser pulse using 20 beams. As shown in Fig. 112.10(a), the peak radiation temperature T_r inferred from the measured levels of the x-ray flux increased by 17 eV when the laser beams were smoothed with phase plates, corresponding to a 44% increase in the peak x-ray flux. The improved coupling is correlated with reduced laser-scattering losses. A shot-by-shot scan was performed to measure the cone-dependent laser-scattering losses. It was assumed that the laser-scattering losses were caused by single-beam interactions; consequently, all of the heater beams had phase plates. Shots were taken with and without phase plates in the interaction beam to complete the shot matrix. As shown in Figs. 112.10(b) and 112.10(c), laser-beam smoothing with phase plates reduces the cone-dependent FABS SRS and FABS SBS signals. The most energetically significant reductions occur for FABS SRS in cone 1 (23% to 10%) and cone 2 (17% to 4%). The total FABS scattering levels are higher for SRS than SBS (11% versus 5% without phase plates and 4% versus 2% with phase plates). The NBI SBS signal was 2% without phase plates and was negligible with phase plates. NBI SRS signals are not available. The scattering losses measured with FABS SRS, FABS SBS, and NBI SBS were reduced by nearly a factor of 3 with phase plates (18% without phase plates and 6% with phase plates).

Figure 112.9
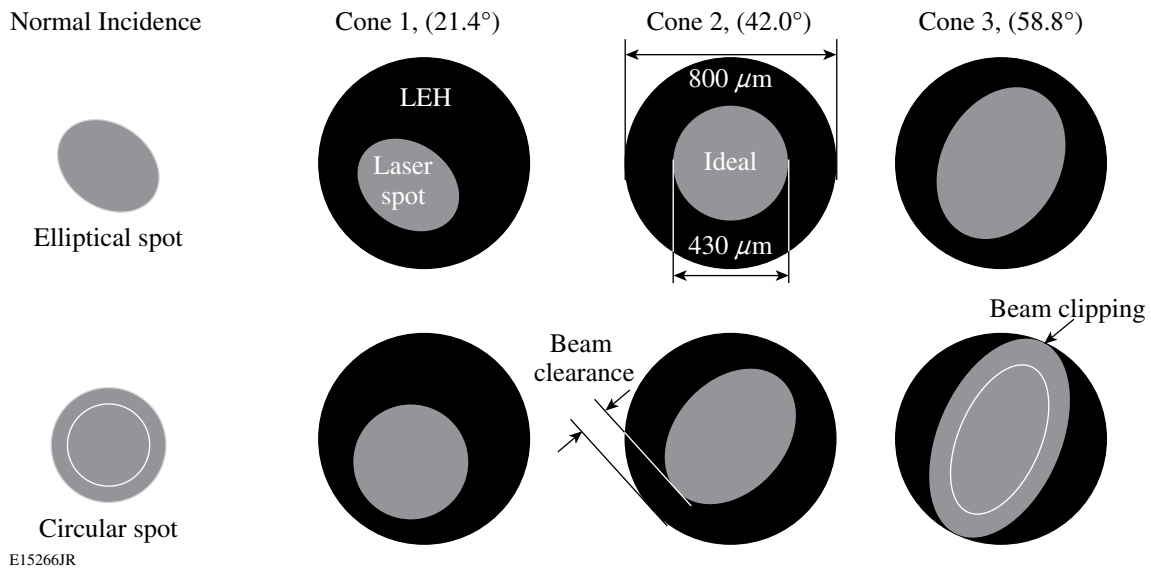
Beam clearance for each of the three cones for an elliptical beam (upper trace) and a circular beam (lower trace). The black circle represents the LEH having an 800-μm diameter; the gray spot indicates the size of the beam including the intensity contour, which is 1% of the peak intensity. The circular spot needs to be reduced to the white circle to prevent beam clipping on the LEH wall.
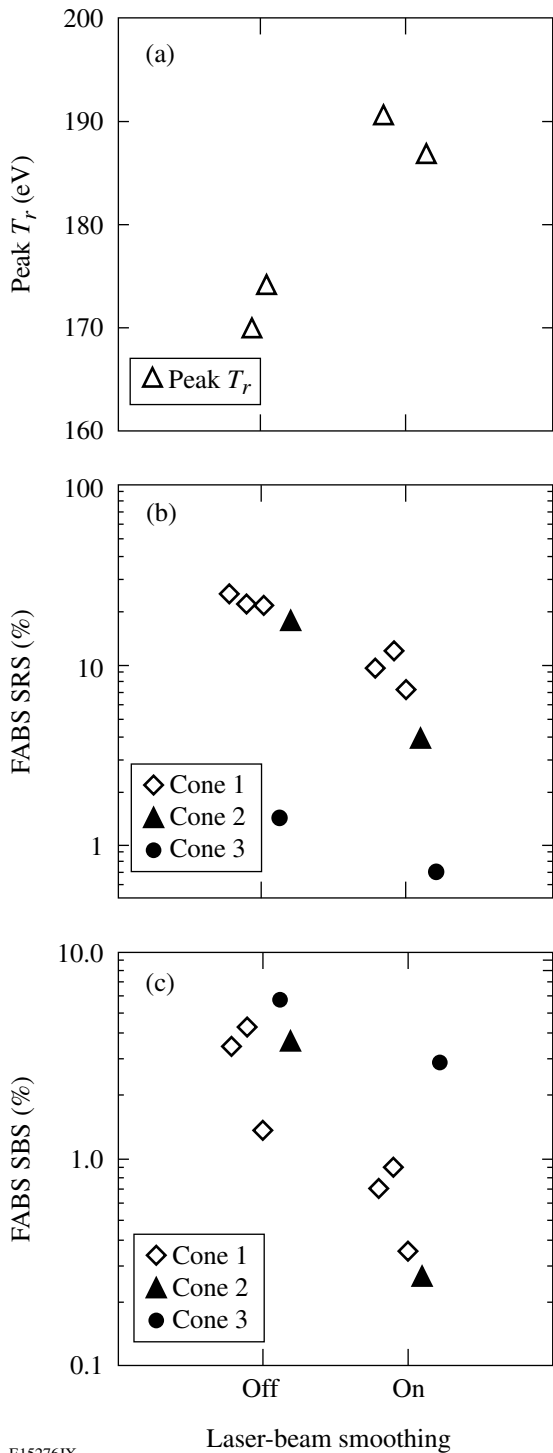
Figure 112.10
(a) The peak T_r with and without laser-beam smoothing with phase plates for gas-filled halfraums. Percent of incident beam energy detected by (b) FABS SRS and (c) FABS SBS for each beam cone.

The symmetry of imploding gas-filled (D_2 doped with Ar) plastic capsules driven with gas-filled, scale-1, Au hohlraums having lengths of 2.3 and 2.5 mm was measured on OMEGA using phase plates in the drive beams. Axial and radial gated-x-ray images of the implosion around the time of peak compression were recorded. Figure 112.11 shows that a shift of 150 μm in symmetry was observed between vacuum and gas-filled (0.9 atm CH_4) hohlraums having identical beam pointing. The fully ionized n_e of the hohlraum plasma for the gas-filled targets is 2.2×10^{20} cm^{-3}. The ratio of x-ray drive at the poles of the capsule relative to the waist increased for the gas-filled hohlraum. As shown above, the inner cone beams (cone 1) have the highest level of SRS. The differential laser-scattering levels between the cones, which is more pronounced for the gas-filled hohlraum, could affect the indirect-drive-implosion symmetry and is the most likely cause for the observed symmetry shift seen in Fig. 112.11.

Figure 112.11
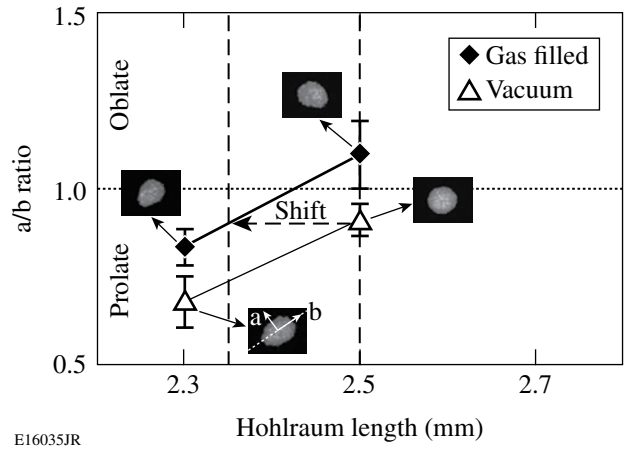Symmetry of indirect-drive implosion quantified from gated-x-ray images ($h\nu > 3$ keV) of implosions taken along a radial view [hohlraum radial and axial directions are (a) and (b), respectively]. A 150-μm symmetry shift was observed between vacuum and gas-filled hohlraums having identical beam pointing.

In conclusion, elliptical phase plates are benefiting indirect-drive experiments on OMEGA.

REFERENCES

1. J. D. Lindl *et al.*, Phys. Plasmas **11**, 339 (2004).

2. S. H. Glenzer *et al.*, Phys. Rev. Lett. **80**, 2845 (1998).

3. T. R. Boehly, D. L. Brown, R. S. Craxton, R. L. Keck, J. P. Knauer, J. H. Kelly, T. J. Kessler, S. A. Kumpan, S. J. Loucks, S. A. Letzring, F. J. Marshall, R. L. McCrory, S. F. B. Morse, W. Seka, J. M. Soures, and C. P. Verdon, Opt. Commun. **133**, 495 (1997).

4. R. M. Stevenson *et al.*, Phys. Plasmas **11**, 2709 (2004).

5. N. D. Delamater *et al.*, Phys. Plasmas **7**, 1609 (2000).

6. S. P. Regan, J. A. Marozas, J. H. Kelly, T. R. Boehly, W. R. Donaldson, P. A. Jaanimagi, R. L. Keck, T. J. Kessler, D. D. Meyerhofer, W. Seka, S. Skupsky, and V. A. Smalyuk, J. Opt. Soc. Am. B **17**, 1483 (2000).

7. C. Sorce *et al.*, Rev. Sci. Instrum. **77**, 10E518 (2006).

8. S. P. Regan, D. K. Bradley, A. V. Chirokikh, R. S. Craxton, D. D. Meyerhofer, W. Seka, R. W. Short, A. Simon, R. P. J. Town, B. Yaakobi, J. J. Carroll III, and R. P. Drake, Phys. Plasmas **6**, 2072 (1999).

Improved Measurement of Preheat in Cryogenic Targets

Introduction

Preheat by fast electrons in cryogenic target implosions is thought to be a crucial parameter in determining target performance, primarily the achieved areal density. To quantitatively relate the achieved areal density to the fuel preheat, the preheat measurement has to be sufficiently reliable and precise. In addition, the validity of the assumptions used in the data analysis and the resulting uncertainty have to be determined. To that end this article presents a reformulated and more consistent analysis of preheat measurements and discusses the sensitivity of the results to the assumptions made in the analysis. The results are applied to both cryogenic and CH targets.

Details of the method of analysis are described in Ref. 1. The preheat is determined from the hard x-ray (HXR) bremsstrahlung radiation; the HXR detector is calibrated by using a CH-coated molybdenum (Mo) solid sphere where the preheat is determined using the Mo K_α line. The resulting calculated curves for both cryogenic and CH targets directly relate the HXR signal to the preheat. The curves are plotted as a function of fast-electron temperature, which is also measured by the HXR detectors.

The main improvement with respect to previous results[1] is the folding of the HXR sensitivity curve[2] into the calculation of emitted radiation. The total bremsstrahlung radiation for a given electron energy is taken from the NIST tables,[3] but the folding also requires the spectrum of the radiation. That spectrum is a function of the photon energy E_p and the electron energy E_e ($E_p < E_e$); the spectrum is usually plotted as a function of $R = E_p/E_e$ but still depends separately on E_e. The folding with detector sensitivity has to be done for each electron energy. Also, because the electron energy distribution changes due to the transport through the target, the folding is done at each target location. The bremsstrahlung spectra were tabulated in papers by Seltzer *et al.*[4] and Pratt *et al.*,[5] on which the NIST tables are based. *Thus, the calibration of the HXR detector is not a stand-alone number but is intertwined with the radiation spectrum and thus with the electron energy distribution.* The detector measures only the absorbed radiation,

and the derivation of incident radiation is model dependent. The radiation spectrum is calculated from the electron energy distribution but the latter has to be assumed.

A simplified, generic formulation of bremsstrahlung radiation given by Jackson[6] is often used. Figure 112.12 compares the total radiation emitted by an electron traveling in Mo, calculated using Eq. (15.30) in Ref. 6 and as given by the NIST tables. Jackson's formula is insufficient for precise calculations of preheat.

E16356JR
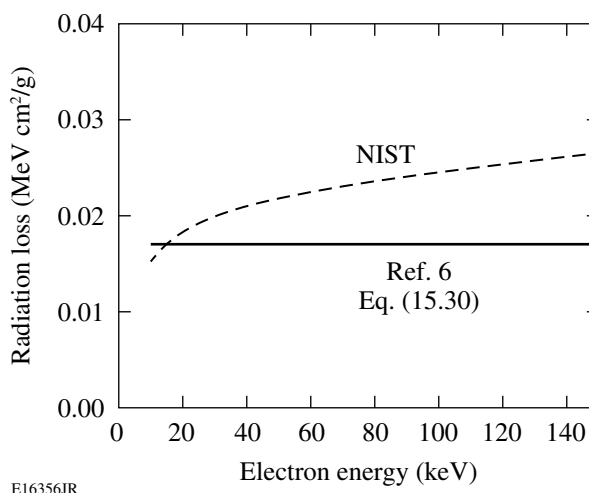
Figure 112.12

Comparison of the total radiation emitted by an electron traveling in Mo, as a function of its energy. The upper curve is given by the NIST tables;[3] the lower curve is calculated by Jackson [Eq. (15.30) in Ref. 6]. Jackson's formula is insufficient for precise calculations of preheat.

Effective Detector Sensitivity

The folding of detector sensitivity described here was done for the three cases of Mo, CH, and cryogenic D_2 (or DT) targets. The relative sensitivity of the HXR detector $S(E_p)$ as a function of photon energy is given in Ref. 2. $S(E_p)$ is the fraction of radiation absorbed in the detector. The fraction of the radiation energy emitted by an electron of energy E_e that is absorbed by the detector is given by

$$S_{\text{eff}}(E_e) = \frac{\int \text{bremss}(E_e, E_p) S(E_p) dE_p}{\int \text{bremss}(E_e, E_p) dE_p}, \qquad (1)$$

where "bremss" is the bremsstrahlung spectrum (from Refs. 4 and 5). Figure 112.13 shows the calculated S_{eff} for a few materials. As seen, the effective sensitivity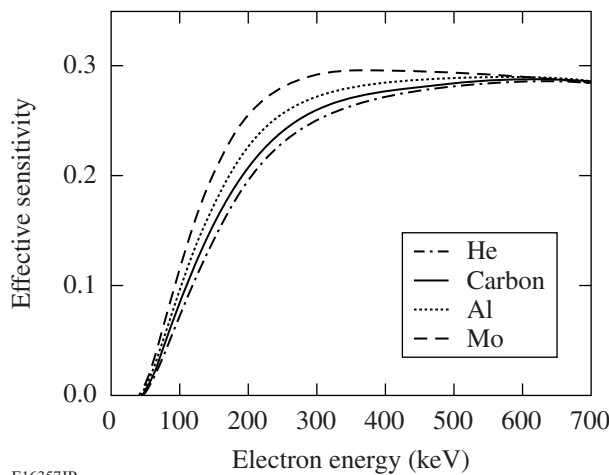 depends weakly on the material. The total energy radiated by an electron of energy E_e that is absorbed in the detector is given by

$$E_{\text{abs}}(E_e) = S_{\text{eff}}(E_e) \times \text{NIST}_{\text{bremss}}(E_e), \qquad (2)$$

where $\text{NIST}_{\text{bremss}}$ is the total radiation emitted by an electron of energy E_e, per cm traveled, and is given by the NIST tables.[3] In the transport calculations described below, the results of Eq. (2), using curves like those in Fig. 112.13, are summed over the electron energy distribution $D(E_e)$ at each target location. Summing over the target volume yields the total radiation energy absorbed in the detector for a given energy in the fast electrons. The calibration to be described below relates the energy absorbed in the detector to the detector reading (in pC). The initial distribution $D(E_e)$ is guessed and is then modified by the transport through the target. Three initial shapes for $D(E_e)$ were tested:

(a) exponential: $D(E_e) = \exp(-E_e/T_e)$

(b) Maxwellian: $D(E_e) = E_e^{1/2} \exp(-E_e/T_e)$ (3)

(c) truncated: $D(E_e) = \begin{cases} \exp(-E_e/T_e), \\ 0 \text{ for } E_e > 3T_e \end{cases}$

Distributions (b) and (c) can be thought of as two extremes of (a): in (b) the low-energy part of $D(E_e)$ is reduced, whereas in

Figure 112.13
Effective sensitivity: the fraction of the radiation emitted by an electron of energy E_e that is absorbed in the detector (HXR2), using Eq. (1). These curves, summed over the assumed electron-energy distribution (for the known temperature), relate the radiation energy absorbed in the detector to the energy in fast electrons.

E16357JR

(c) the high-energy part of $D(E_e)$ is reduced. Since low-energy electrons are more efficient in collisions whereas high-energy electrons are more efficient in radiation, the ratio of preheat to radiation, as expected, is found to increase in going from (b) to (a) to (c).

The Mo Target Calibration Experiment

The preheat energy in any target experiment is determined from the HXR signal. To calibrate the HXR detector in absolute units, we used an ~0.9-mm-diam molybdenum solid sphere, coated with a 20-μm-thick CH layer. The target was irradiated with the 60 OMEGA beams at an intensity of ~1×10^{15} W/cm^2 and a 1-ns square pulse.[1] The preheat was determined from the Mo K_α line and related to the HXR signal. The measured Mo K_α energy was 9.4 mJ (per total solid angle). The HXR2 channel (used to determine the total radiation) measured a signal of 1200 pC, and comparison of channels 2, 3, and 4 yielded a fast-electron temperature of $T_e = 65$ keV.

A 1-D multi-energy transport code was used to transport fast electrons of varying temperatures for each of the three chosen shapes [Eq. (3)]. The calculations using a stationary target are time integrated over the pulse, as are the measurements of K_α and HXR energies. In 1-D calculation, only radial trajectories are considered. For the Mo target this is justified because *LILAC* simulations show that at the end of the pulse the quarter-critical density is ~100 μm away from the target surface, a distance much smaller than the target diameter. At the end of the pulse (when most of the fast electrons are generated) the thickness of the unablated CH layer is ~10 μm. Therefore, in the calculations we assumed a cold, 10-μm-thick CH layer. When the calculations were repeated for a 15-μm CH thickness, the resulting calibration was hardly changed. The transport code calculates the slowing down of electrons, the production and transport of K_α energy, and the production of HXR continuum. For the slowing down and the HXR production, the NIST tables are used; for the K_α production a semi-empirical cross section[7] is used. The transport code shows that more than 99% of the HXR comes from the Mo; however, some of the electron energy (~10%) is deposited in the CH and must be subtracted from the total deposited energy. Two ratios are computed: PH/K_α = (preheat energy)/(K_α energy) and

PH/HXR-abs = (preheat energy)/(energy absorbed in HXR2), both as a function of T_e. The K_α energy refers to the energy exiting the target after absorption within the molybdenum. Here, we need only the results for the case of the Mo experiment (T_e = 65 keV), which we quote in Table 112.III. The absorption of the K_α line within the target increases with electron temperature because higher-energy electrons penetrate deeper; for T_e = 65 keV that absorption is only ~30%.

Table 112.III shows the Mo target analysis results for the three electron distributions considered. Row 1 shows the ratio of preheat to emergent K_α energy. For the measured K_α energy of 9.4 mJ, row 2 shows the preheat energy within the molybdenum. Row 3 shows the ratio of preheat energy to HXR energy absorbed in the detector. Dividing row 2 by row 3 yields the total energy absorbed in the HXR2 detector. Finally, dividing the measured HXR2 signal of 1200 pC by row 4 yields detector absolute calibration, namely the signal in HXR2 (in pC) per radiation energy absorbed in HXR2 (in mJ).

As explained above, the ratio PH/HXR-abs increases in going from (b) to (a) to (c) because the relative number of low-energy electrons in the distribution increases. This is also true for the ratio PH/K_α, but here the change is very small (~6%). This can be shown to be due to the differences in the cross sections for producing K_α and bremsstrahlung radiation. The calibration factor is seen to change appreciably with the change in assumed distribution shape. However, as shown below, in calculating preheat in cryogenic or CH targets, the differences between the three distribution shapes become considerably smaller. This is because the ratio PH/HXR in CH or cryogenic targets is also dependent on the distribution shape, and when applying the corresponding calibration factor from Table 112.III, these differences partly cancel out.

Preheat in CH Targets

The ratio of preheat to the HXR2 signal for CH targets was calculated as a function of temperature of the fast electrons,

for each of the three electron distribution shapes of Eq. (3). As in the case of Mo, the NIST tables are used for both the slowing down (collisions) and the bremsstrahlung radiation. The corresponding calibration numbers of Table 112.III were used to convert radiation energy absorbed in the detector to the signal in pC. We assumed that the shape of the electron distribution is the same in the Mo experiment as in CH target experiments. This assumption is reasonable since in both cases (as well as in the cryogenic targets discussed below) the laser interacts with a CH layer. Thus, for each of the three distribution shapes, we used the corresponding calibration factor from Table 112.III. The results for a 10-μm-thick CH target are shown in Fig. 112.14. The variation around the average for all temperatures is ±25%. This represents the range of uncertainties in the preheat determination. To illustrate how the results depend on the target thickness, we show in Fig. 112.15 the ratio for a Maxwellian electron distribution, for three different thicknesses. The ratio of preheat to the HXR2 signal is almost independent of the target thickness. For electrons of a single

E16358JR
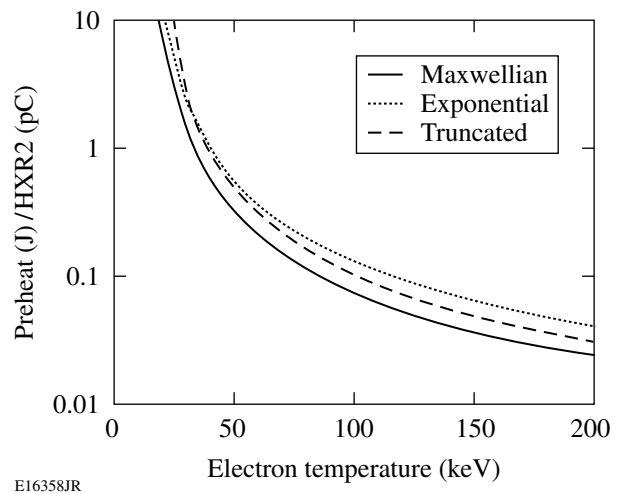
Figure 112.14
The ratio of preheat energy deposited by fast electrons in a 10-μm-thick CH target to the HXR2 reading (pC) for three assumed distributions of electron energies.

Table 112.III: Calculated quantities involved in determining the HXR detector calibration from the Mo experiment, for three electron-energy distribution shapes

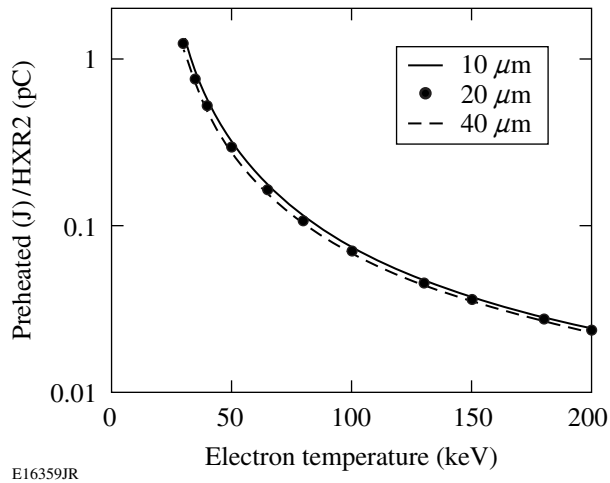|	Quantity Calculated	(a) Exponential	(b) Maxwellian	(c) Truncated
1	Preheat/K_α	1058	996	1063
2	Mo preheat	9.945 J	9.36 J	10.0 J
3	Preheat/HXR-abs	1704	1355	2503
4	HXR-abs	5.83 mJ	6.9 mJ	4.0 mJ
5	Calibration (pC/mJ)	205	174	300

E16359JR

Figure 112.15
Ratio of preheat energy deposited by fast electrons in CH to HXR2 reading (pC) for three thicknesses of the CH target. A Maxwellian distribution of electron energies was assumed.

energy E_e, the ratio increases with thickness (until the thickness exceeds the range corresponding to E_e) because a thicker target yields slower electrons, for which the preheat increases (as $\sim 1/E$) whereas the radiation decreases (see Fig. 112.12). However, for the case of continuous distribution of energies, the shift of the distribution to lower energies is equivalent to lowering the distribution, which does not affect the ratio of the two plotted quantities.

Preheat in Cryogenic Targets

To calculate the preheat and x-ray emission from cryogenic targets we use again a 1-D, multi-energy transport code. However, unlike the case of the CH-coated Mo target, the fraction of radiation emitted by the CH shell is not negligible and its calculation requires a multidimensional treatment of the fast-electron transport. This is because when the fast electrons are generated, the quarter-critical surface is far enough from the target to enable many trajectories that miss the cold-fuel shell. Thus, before applying the preheat results derived here, that fraction has to be determined separately. Using the measured radiation that is emitted by the fuel leads to the determination of the preheat within the fuel alone. The deposition of electron energy within the CH shell is irrelevant to the determination of fuel preheat, but it affects the preheat results marginally since it changes the energy distribution of the electrons entering the fuel. As will be shown below, the results are weakly dependent on that distribution. For the calculation of radiation we again use the NIST tables. However, for the collisional transport (preheat) we must use the formula for slowing down

in a plasma since the fuel is fully ionized even with no preheat. We use Eq. (1) of Ref. 1:

$$(-dE/dx) = \left(2\pi e^4 N_e / E\right) \ln\left(1.52\, E / \hbar\, \omega_p\right) \qquad (4)$$

in terms of the electron density and the plasma frequency. This equation is essentially identical to Eq. (13.88) given by Jackson in Ref. 6. We used the plasma density profile calculated by *LILAC* at the end of the laser pulse (when most of the $2\omega_p$ electrons were found to be generated); however, the results are shown to be insensitive to this choice.

For transport in un-ionized material, the dependence on electron density of the ratio preheat/radiation cancels out. However, because of the appearance of the plasma frequency in the Coulomb logarithm in Eq. (4), we must consider the density profile of a particular case. We used the plasma density profile calculated by *LILAC* for a typical D_2 cryogenic target shot at an irradiance of 5×10^{14} W/cm^2, at the end of the laser pulse. Figure 112.16 shows curves for the ratio of preheat to energy absorbed in the detector for the three distribution shapes; Fig. 112.17 shows the curves after applying the calibration from Table 112.III. The total relative span of the three curves around an average is $\sim 20\%$. To test the sensitivity of the results to the density profile, Fig. 112.18 shows the effect of multiplying or dividing the density profile everywhere by a factor of 4. The preheat deduced from the HXR detector is seen to be weakly dependent on the density (or the areal density) of the fuel. Thus,
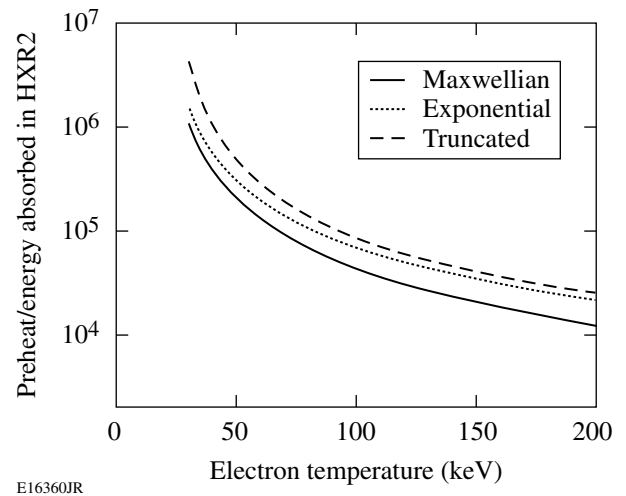

E16360JR

Figure 112.16
Ratio of energy deposited in D_2 by fast electrons to energy absorbed in HXR2 for three different distributions of fast-electron energies. Much of the variation between the three curves disappears when converting the absorbed x-ray energy to a detector signal (Fig. 112.17).

the validity of the preheat curves for CH (Fig. 112.14) and D_2 (Fig. 112.16) is quite general with a precision of ~25%. The uncertainty in the experimentally determined temperature adds an additional uncertainty. The curves for D_2 apply equally to a DT fuel since the loss rate dE/dx due to either collisions or radiation is independent of the atomic mass. The NIST tables

are actually given in terms of $(1/\rho)$dE/dx; this is inconsequential for Mo or CH since only the ratio of the two losses is used. However, for the cryogenic targets, we use the NIST tables only for the collision rate; thus, the tables (which are for hydrogen) had to be restated in terms of dE/dx, for which case they are the same for either D_2 or DT.

The *LILAC*-calculated density profile shows a sharp, well-defined cold shell of ~4-g/cm^3 density. Since the preheating of this cold shell is particularly relevant to target-performance degradation, we calculated the fraction of energy deposited within this shell, assuming the electrons move radially. For all temperatures above ~50 keV, this fraction is about constant at ~0.8 and drops at lower temperatures. This is an upper limit on the fraction of energy deposited in the cold shell, as 2-D effects will lower it. It should be noted that the HXR signal in the ordinates of Figs. 112.16 and 112.17 apply only to the x-ray emission from the fuel, not the CH. Thus, before applying these figures to a particular cryogenic experiment, the fraction of the measured x-ray signal emitted by the fuel has to be determined by a code allowing for the 2-D trajectories of the electrons. No such complication arises in the case of CH-only targets. For these targets, the measured HXR signal yields the total energy absorbed as preheat in the target (integrated over time and space), with no need for 2-D calculation of the electron trajectories. This is also shown in Fig. 112.15 by the independence of the ratio x ray/preheat on the target thickness.
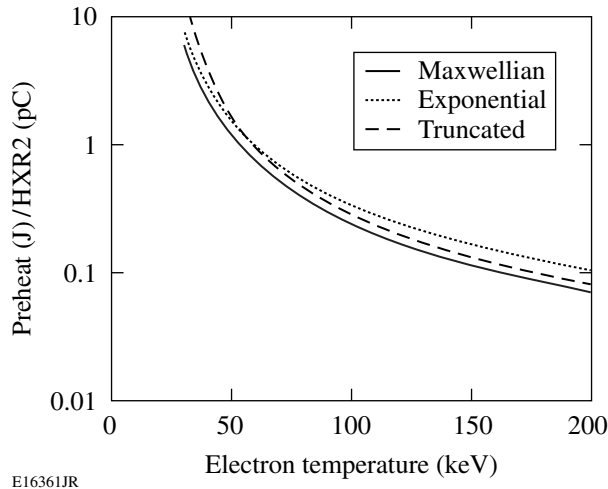

Figure 112.17
Ratio of energy deposited by fast electrons in D_2 to HXR2 reading (in pC) for three different distributions of fast-electron energies. The preheat deduced from the HXR detector is seen to be weakly dependent on the assumed electron distribution.
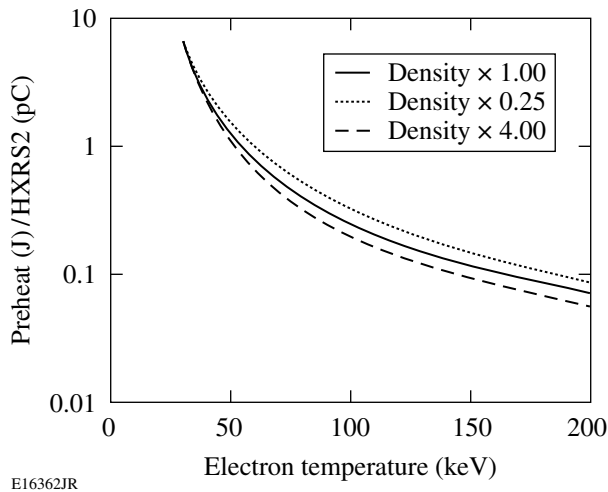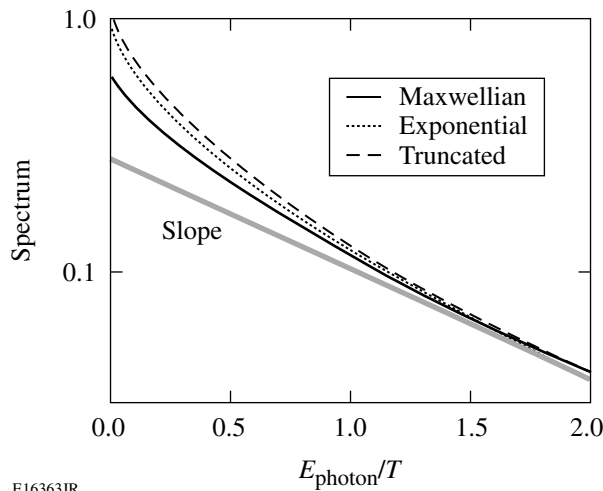
An important result derived from these calculations relates to the determination of the temperature from the measured signals in three of the four HXR channels. The shape of the bremsstrahlung spectrum in these determinations[2] is customarily assumed to be exponential [$\sim\exp(-E/T)$]. However, calculating the x-ray spectrum for a variety of assumed electron-energy distributions shows that the x-ray spectrum deviates from an exponential. Figure 112.19 shows the calculated bremsstrahlung spectrum for three different electron distribution functions plotted versus photon energy normalized to the fast-electron temperature. They are obtained by averaging the spectrum from a single-electron energy[1] over the electron-energy distribution. We see that even for an assumed exponential distribution for the electrons, the distribution for the photons is not exponential, except for high E/T. The curve marked "slope" represents the exponential spectrum assumed in the derivation of the temperature from the HXR signals. Therefore, the HXR data have to be fitted with one of the curves shown in Fig. 112.19. The HXR channels are dominated by radiation in the range ~50 to 80 keV determined by the channel filters. Thus, for temperatures higher than ~80 keV, relevant values of E/T are smaller than 1 and the

Figure 112.18
Ratio of energy deposited by fast electrons in D_2 to HXR2 reading (in pC) for a Maxwellian distribution of fast-electron energies and three different multipliers of the *LILAC*-simulated density profile. The preheat deduced from the HXR detector is seen to be weakly dependent on the density (or the areal density) of the fuel.

E16363JR

Figure 112.19
Bremsstrahlung spectrum calculated using tabulated values from Seltzer and Berger,[4] on which NIST slowing-down tables are based. The spectra for each electron energy were averaged over three different electron-distribution functions and plotted versus photon energy normalized to the fast-electron temperature.

derived temperature would be lower than the true temperature (given by the curve marked "slope"). The correction increases with temperature. For a measured value of $T = 100$ keV, the correct temperature is estimated to be ~130 keV. The corrected temperature would reduce the determined preheat for a given measured HXR signal. Using Fig. 112.17 we estimate that the derived preheat for fast-electron temperatures in the range of 100 to 200 keV would drop by ~50%. This indicates that even for high values of laser irradiance, the preheat by fast electrons may not be an important factor in explaining the degradation in compression.

In summary, an improved procedure for calculating preheat from the measured hard x-ray signal is described. The numerically calculated bremsstrahlung spectrum as a function of electron energy (E) is averaged over an assumed electron-energy distribution and folded with the HXR detector sensitivity. This is done for each value of E and each target location within a multi-group, 1-D electron-transport code. The results relate the measured HXR signal and fast-electron temperature to the preheat. A 2-D transport code has to be used to determine the fraction of the measured x-ray signal coming from the fuel for cryogenic experiments because of the two-material target composition. Additionally, the shape of the measured x-ray spectrum has been calculated; this shape has to be used in the fitting of the HXR channels data. This correct procedure will yield a higher fast-electron temperature than when assuming an exponential x-ray spectrum and, therefore, a lower preheat for a given HXR signal.

ACKNOWLEDGMENT

REFERENCES

1. B. Yaakobi, C. Stoeckl, W. Seka, J. A. Delettrez, T. C. Sangster, and D. D. Meyerhofer, Phys. Plasmas **12**, 062703 (2005).

2. C. Stoeckl, V. Yu. Glebov, D. D. Meyerhofer, W. Seka, B. Yaakobi, R. P. J. Town, and J. D. Zuegel, Rev. Sci. Instrum. **72**, 1197 (2001).

3. M. J. Berger, J. S. Coursey, and M. A. Zucker, *ESTAR*, *PSTAR*, and *ASTAR*: Computer Programs for Calculating Stopping-Power and Range Tables for Electrons, Protons, and Helium Ions (version 1.2.2). [Online] Available: http://physics.nist.gov/Star [25 February 2005]. National Institute of Standards and Technology, Gaithersburg, MD.

4. S. M. Seltzer and M. J. Berger, Nucl. Instrum. Methods Phys. Res. B **12**, 95 (1985).

5. R. H. Pratt *et al*., At. Data Nucl. Data Tables **20**, 175 (1977).

6. J. D. Jackson, *Classical Electrodynamics*, 2nd ed. (Wiley, New York, 1975).

7. C. J. Powell, Rev. Mod. Phys. **48**, 33 (1976).

Laser Channeling in Millimeter-Scale Underdense Plasmas of Fast-Ignition Targets

Ignition in inertial confinement fusion (ICF) starts in a hot spot in the core of compressed fuel pellets. In conventional ICF schemes, the hot spot—a small region with a temperature of ~10 keV—is created through a highly symmetric compression driven by multiple laser beams that illuminate the target from all directions.[1] In fast ignition (FI) a separate ignition pulse is used to create the hot spot after the core has been compressed, thereby relaxing symmetry requirements and leading to higher gain.[2] There are several scenarios for getting the ignition pulse close to the compressed core. In the so-called "hole-boring" scenario of FI, the ignition pulse is to first propagate through a millimeter (mm)-scale underdense plasma to reach a critical surface with a critical density $n_c = \omega_0^2 m_e / (4\pi e^2)$ (m_e and e are electron mass and charge, respectively, and ω_0 is the pulse frequency). There the ignition pulse may continue to push forward into the overdense plasma through its ponderomotive pressure (hole-boring) and relativistic transparency. As the intense laser interacts with the overdense plasma, it generates energetic electrons that must eventually reach the dense core region where their energy is to be absorbed to create the hot spot. An alternative way to move the ignition pulse closer to the core region is to use fuel pellets with a hollow gold cone attached to one side. The compression beams illuminate the target from all directions except those within the opening of the cone. The asymmetric compression still leads to a dense core and has the potential to lead to a clear path for the ignition pulse to propagate up to a very overdense plasma. The first integrated FI experiments with the coned targets showed a 10^3 times fusion neutron increase.[3] However, the hole-boring scenario is still being actively pursued for its more symmetric compression and its absence of radiation loss associated with the gold cone.

Many factors affect the overall efficiency of converting the ignition pulse energy to the hot-spot energy, including the conversion efficiency to the energetic electrons at the critical surface,[4–6] the angular spread of these electrons,[7,8] and the slowing-down and scattering of the electrons as they propagate to the core.[9] Of particular concern to the hole-boring scenario is the loss of ignition pulse energy through laser–plasma inter-actions in the mm-scale underdense plasma.[10] While a small-amplitude electromagnetic wave can linearly propagate through densities less than n_c without much loss, the petawatt (PW) ignition pulse can interact with the plasma in a highly nonlinear manner, leading to processes such as laser self-focusing[11,12] and filamentation,[13,14] as well as scattering[15] and significant plasma heating and density modification.[14,16] Energy lost in this region will not be available for hole boring and energetic electron generation at the critical surface. A channeling pulse, which could be the prepulse of the ignition pulse or a separate pulse, has been proposed[2] to produce a low-density channel to reduce the nonlinear interactions of the ignition pulse in the underdense region. Plasma density channels were created using lasers with intensities of $I = 10^{17–19}$ W/cm^2 in experiments of laser–solid target or laser–gas jet interactions.[17–20] Increased transmission of a trailing $I = 10^{20}$ W/cm^2 in the density channel was also observed.[19] Two dimensional (2-D) and three-dimensional (3-D) particle-in-cell (PIC) simulations of these experiments showed laser self-focusing in the plasma and channel generation through the ponderomotive force and resulting shock expansion.[18,21,22] Most of these previous experiments and simulations were done in 100-μm-scale plasmas.

The underdense region of an actual FI target, however, is about 1000 μm long. The residual plasma in the channel can continue to interact with the latter part of the channeling pulse and the ignition pulse. Later stages of the nonlinear evolution of the pulses and the channel need to be studied with full spatial scale simulations to obtain values of critical parameters such as the channeling time (T_c) and the required channeling pulse energy (E_c) and their scaling with the laser intensity I. These are needed to assess the viability of the hole-boring scheme and to plan for integrated experiments on next-generation FI facilities. This article presents results from 2-D PIC simulations with the code $OSIRIS$[23] showing that channeling in mm-scale plasmas is a highly nonlinear and dynamic process involving laser self-focusing and filamentation, channel generation via shock waves, longitudinal plasma snowplowing, laser hosing, and channel bifurcation and self-correction. As a result, the channeling speed oscillates and is much less than the laser

linear group velocity. We find that it eventually asymptotes to the expression obtained by conservation of momentum even for densities less than the critical density.

In our 2-D PIC simulations, a channeling pulse of wavelength λ_0 is launched from the left boundary of the simulation box with a peak intensity between $I = 10^{18}$ and 10^{20} $(1 \mu m/\lambda_0)^2$ W/cm^2 and a rise time of 150 laser periods, after which the pulse amplitude is kept constant. The transverse profile is Gaussian with a full-width-at-half-maximum intensity spot size of $r_0 = 16$ to $47 \lambda_0$ ($1/e$ spot size for the electric field, $w_0 = 90$ to 264 c/ω_0). It is focused onto a surface $600 \lambda_0$ away from the left boundary. Both s- and p-polarizations are used to infer 3-D effects. The initial plasma density profile used is $n_0 = 0.1$ n_c exp(x/L) with $L = 430 \lambda_0$. (Length and time in these simulations are normalized to λ_0 and $1/\omega_0$, respectively, but $\lambda_0 = 1 \mu m$ is assumed so that the density scale length L is comparable to that of FI targets.) The ion-to-electron mass ratio is $m_i/m_e = 4590$, thereby approximating a DT plasma. The electron and ion temperatures are $T_e = T_i = 1$ keV. We simulate the region of $n_0 = 0.1$ to 1.02 n_c ($x = 0$ to $1000 \lambda_0$) in two different setups. In the first setup we simulate the whole region in two separate simulations, one for $n_0 = 0.1$ to 0.3 n_c and the other for $n_0 = 0.3$ to 1 n_c. The simulation box size is $L_x = 477 \lambda_0$ (longitudinal) and $L_y = 262 \lambda_0$ (transverse) for the low-density portion and $L_x = 523 \lambda_0$ and $L_y = 262 \lambda_0$ for the high-density portion. The grid resolution in these simulations is $\Delta_x = 0.314$ c/ω_0 and $\Delta_y = 0.628$ c/ω_0. Ten particles per cell are used for each species in this setup. In the second setup we simulate the entire region in one simulation with a box size of $L_x = 987 \lambda_0$ and $L_y = 401 \lambda_0$ (totaling 19740×4010 cells). The grid resolution is kept the same but one particle per cell is used for each species.

We now describe general features of the channeling process using results from a simulation where $I = 10^{19}$ W/cm^2, $r_0 = 16 \mu m$, and the laser was p-polarized. Other simulations with different intensities and/or with an s-polarized laser display similar features. The channeling pulse power P greatly exceeds the power threshold for relativistic self-focusing P_c (Ref. 4). For $n/n_c = 0.1$, $P/P_c = 300P/(10^{12}$ W) $n/n_c \approx 780 \gg 1$ and r_0 is 32 c/ω_p. Therefore, relativistic whole-beam self-focusing and filamentation of the pulse[5] occur before significant plasma density perturbations arise. This initial phase is dominated by filamentation that is seeded by the Gaussian transverse profile since the initial r_0 is 32 c/ω_p [Fig. 112.20(a)]. As the laser self-focuses and filaments, the laser normalized vector potential a within each filament increases and the radius of each filaments decreases. This causes the transverse ponderomotive force from each filament to increase so that significant electron density

depletion occurs.[5] The space charge force ultimately causes the ions to follow, leading to the formation of several microdensity channels, with $n_{max}/n_{min} \approx 6$ [Fig. 112.20(b)].

Due to the fact that the microdensity channels form at different times along the laser propagation direction, the walls of the channels develop a longitudinal modulation. As new laser energy flows straight toward the filaments, the ponderomotive forces snowplow away the microchannels, eventually destroying them. This leads to the merging of neighboring mini-channels, eventually forming a single density channel centered along the axis of the laser [Fig. 112.20(c)]. At the end of this stage, a high-mach-number ion-acoustic shock is launched, causing the walls of the channel to move radially outward at a fairly constant speed of 0.03 c. The channel eventually becomes much wider than r_0.

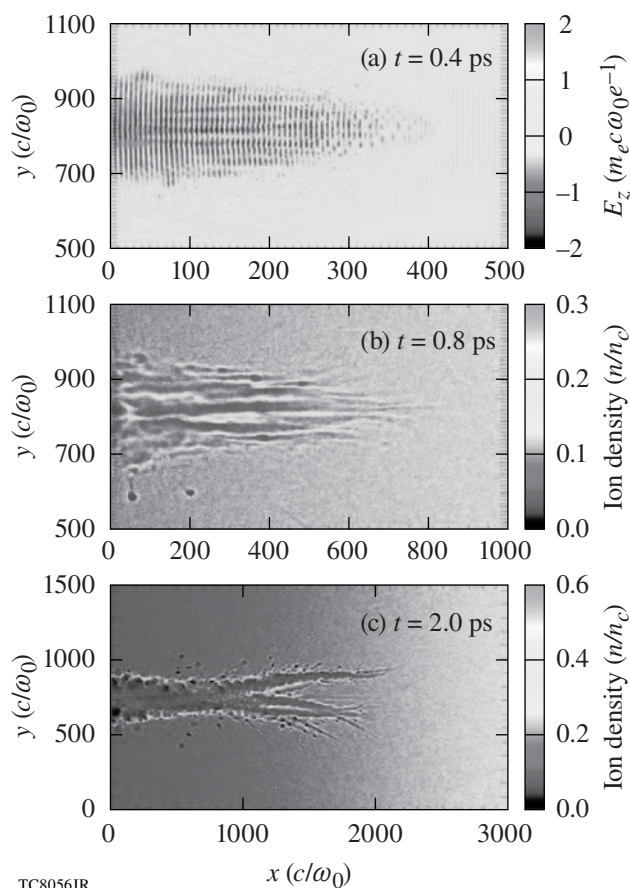Figure 112.20
Results from a simulation with an $I = 10^{19}$ W/cm^2, p-polarized laser and $n_0 = 0.1$ to 0.3 n_c. (a) Laser E-field at $t = 0.4$ ps showing relativistic self-focusing and filamentation; (b) ion density at $t = 0.8$ ps showing the formation of microchannels; (c) ion density at $t = 2.0$ ps showing the formation of a single channel at the center for $x < 1000$ c/ω_0.

This entire process repeats as the laser and the head of the channel gradually advance toward the critical surface. Additionally, at the head of the channel, the density piles up to a value several times the local value of the initial density (Fig. 112.21). The density buildup grows as the channel digs into higher density. At regions of $n_0 > 0.55\ n_c$, the density compression exceeds n_c [Fig. 112.21(b)], thus making the subsequent pulse propagation similar to the hole-boring process, slower than the linear group velocity for the initial local density $v_g \equiv \sqrt{1 - n_0/n_c}$. While the transverse expansion is regular, the advance of the head of the channel is dynamic and intermittent. The channel can bend away from its center due to a long-wavelength hosing instability. This is seeded by hosing of the head of the laser on the electron time scale as it propagates up the density gradient. For a finite-width pulse in a uniform plasma, the hosing instability[24] is caused by upward or downward tilting of local wavefronts due to a transverse phase velocity difference across the wavefronts. The phase velocity gradient is caused by the plasma density perturbation driven by the ponderomotive force of the hosing pulse.[25] The channel bends because of the hosing pulse, whose first occurrence is at $t \approx 3$ ps in the simulation with $n_0 = 0.1$ to $0.3\ n_c$ [Fig. 112.22(a)]. With the initial pulse parameters $a = 2.7$, $w = 90\ c/\omega_0$, and observed $k_h = (\pi/500)\ \omega_0/c$, the predicted growth rate in the long-wavelength regime,[25,26] $\gamma_{\mathrm{hu}} = \left(a/\sqrt{8}\right)\left(c/\omega_0 w\right)k_h c \approx 0.13\ \mathrm{ps}^{-1}$ may seem too slow for this observed time. However, self-focusing makes a larger and w smaller than their initial values and can increase γ_h. There is another channel-bending instability caused by the plasma pressure, but its growth rate $\gamma_{\mathrm{hp}} \sim C_{\mathrm{sk}_h} \sim 0.07\ \mathrm{ps}^{-1}$ (Ref. 27) is too small even for $T_e = 1$ MeV.

As the channel hoses, the radius of curvature gradually increases. At some point the curvature becomes too severe to trap all of the incoming energy. As a consequence, some of

TC8057JR
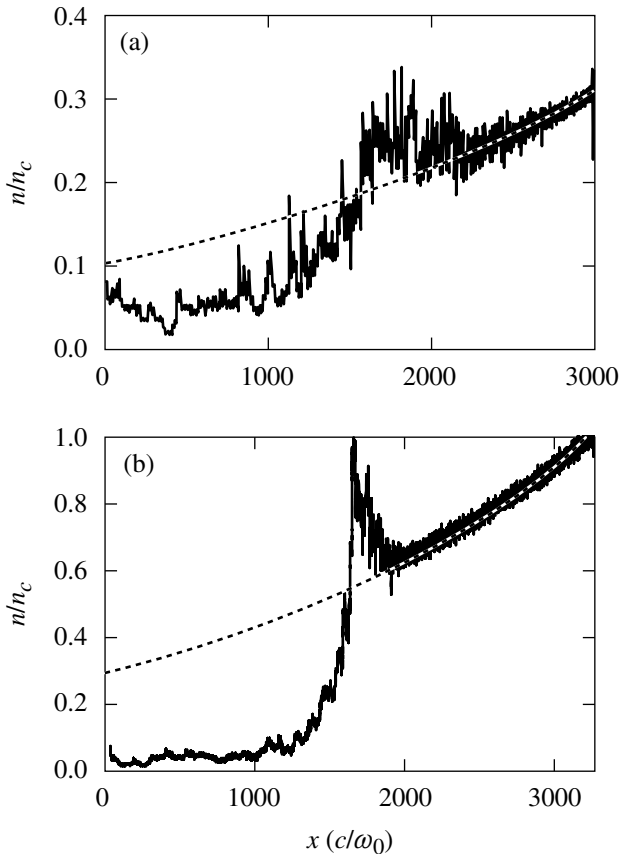
Figure 112.21
Average channel density plots for (a) $n_0 = 0.1$ to $0.3\ n_c$ at $t = 8.2$ ps and (b) $n_0 = 0.3$ to $1.0\ n_c$ at $t = 8$ ps showing the density pile-up. The dotted lines are the initial density profiles.

TC8058JR

Figure 112.22
Results from a simulation with an $I = 10^{19}$ W/cm^2, p-polarized laser and $n_0 = 0.1$ to $0.3\ n_c$. (a) Laser E-field showing laser hosing; (b) ion density showing channel bifurcation at $t = 3.4$ ps; (c) ion density at $t = 7.2$ ps showing channel self-correction.

the laser energy breaks out of the channel to form a second branch of the channel that bends in the opposite direction. This process stalls the channel formation process. Both branches then adva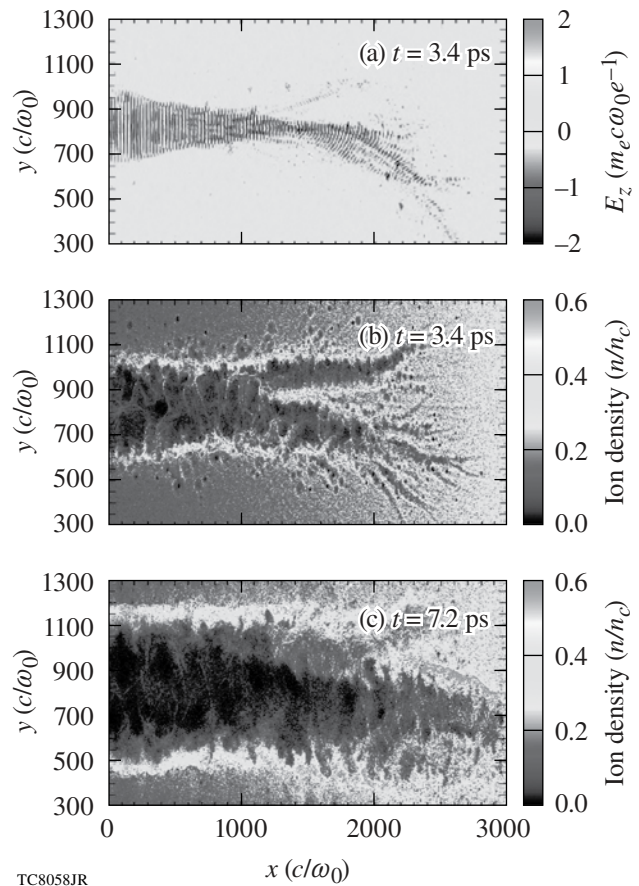nce deeper into the plasma, leaving a narrow plasma "island" in the middle of the entire channel [Fig. 112.22(b)]. Eventually, the island is pushed away by the ponderomotive force of the incoming laser energy and the two branches merge to form again a single channel [Fig. 112.22(c)]. This process of bifurcation and self-correction can repeat in a simulation lasting ~10 ps and provides a mechanism for the head of the channel to advance in propagation caused by the hosing-bending instability. Over time, the channel direction remains along the pulse propagation direction in our simulations.

Residual densities in the channel vary for different pulse intensities, from 0.1 n_c for $I = 10^{18}$ W/cm^2 to 0.04 n_c for $I = 10^{20}$ W/cm^2. To determine T_c, the time needed for the channel to reach the critical surface, under different pulse intensities, we define the channel as any location where the average plasma density is less than $n_r = 0.1\ n_c$. The average density, rather than the lowest density, in the channel is more relevant for the transmission of the ignition pulse. Specifically, the density is averaged transversely around the pulse center y_c, y_c–$w/2 < y < y_c + w/2$. The channel front X_c is defined as the location when the average density decreases to n_r and the channel advance speed is defined as $v_c = dX_c/dt$. Figure 112.23 plots the time for the channel to reach different density surfaces for three pulse intensities, measured from the one-particle-per-cell and p-polarization runs, and the resulting v_c for the $I = 10^{19}$ W/cm^2 case. It shows that v_c generally decreases as n_0 increases; however, v_c also oscillates as the channel advances, reflecting the underlying bifurcation and

self-correction process seen in Figs. 112.22(b) and 112.22(c). We emphasize that v_c describes the speed of the density modification rather than the speed at which the laser energy advances. Figure 112.23(b) shows that v_c is much less than v_g and asymptotes to the ponderomotive hole-boring velocity [Eq. (1)]

$$v_{hb} = 0.6\ c \sqrt{\frac{n_c}{n_0} \frac{m_e}{m_i} \frac{I\lambda_0^2}{10^{18}\ \text{W}\mu\text{m}^2/\text{cm}^2}}\ , \qquad (1)$$

as the front density buildup exceeds n_c. At the end of these simulations, the channel did not reach the critical surface. We estimate T_c by fitting and extrapolating the data in Fig. 112.23(a) and find $T_c = 283$, 72, and 15 ps for $I = 10^{18}$, 10^{19}, and 10^{20} W/cm^2, respectively. An intensity scaling can be found from this limited data set,

$$T_c \approx 2.9 \times 10^2 \left(I/10^{18}\ \text{W}/\text{cm}^2\right)^{-0.64}\ \text{ps}\ , \qquad (2)$$

which enables us to obtain an intensity scaling for the total energy needed to reach the critical surface,

$$E_c \approx 1.7 \left(I/10^{18}\ \text{W}/\text{cm}^2\right)^{0.36}\ \text{kJ}. \qquad (3)$$

From this scaling we can see that the channeling pulse intensity should be kept as low as possible to minimize the total energy used in the channeling process. However, the ignition process needs to be completed within ~100 ps, which sets a lower bound for the channeling intensity to $I \approx 5 \times 10^{18}$ W/cm^2. If the self-focusing and other nonlinear interactions were neglected and channeling were taken to be the hole-boring process described
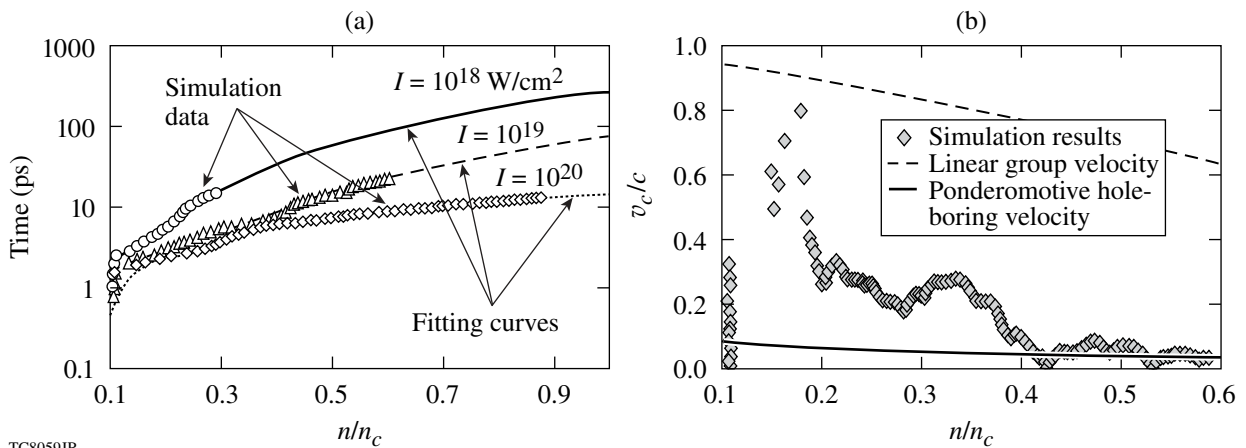

Figure 112.23
(a) Time for the channel to reach different initial densities under different pulse intensities and the corresponding fitting curves. Data were taken from the one-particle-per-cell and $n_0 = 0.1$ to 1.0 n_c runs. (b) The channeling speed v_c in the $I = 10^{19}$ W/cm^2 case.

by Eq. (1) from the beginning, analytical expressions for T_c and E_c can be obtained for density profiles dn/dx,

$$T_c^{\text{(hb)}} = \int dn (dn/dx)^{-1} / v_{\text{hb}}$$
$$= 2.2 \times 10^2 \left(I / 10^{18} \text{ W} / \text{cm}^2 \right)^{-0.5} \text{ ps,}$$

and $E_c^{\text{(hb)}} \approx 1.3 (I/10^{18} \text{ W/cm}^2)^{0.5} \text{ kJ}$ for these simulations. That $T_c^{\text{(hb)}}$ and $E_c^{\text{(hb)}}$ are close to those from Eqs. (2) and (3) shows that despite the complexity of the channel formation, the channeling in these parameter regimes eventually becomes largely a ponderomotive process.

The scalings of Eqs. (2) and (3) are based on the available data set with p-polarization. The s-polarization data show a slightly larger v_c but similar scalings with intensities. The difference in v_c is due to less laser absorption in the channel walls in the s-polarization case than in the p-polarization case. In reality, the difference in the laser absorption at the channel walls in the directions perpendicular and parallel to the polarization may cause different expansion rates in the two directions, resulting in a noncircular channel cross section. In addition, self-focusing is stronger in 3-D than in 2-D, which may lead to a larger channeling speed in 3-D. These effects will be studied in future 3-D simulations with reduced scales; however, currently, full-scale 3-D simulations are not feasible even on the largest computers available.

In summary, channeling in the mm-scale underdense plasma of fast-ignition targets is a highly nonlinear and dynamic process. The channel expands transversely from density perturbations created by the relativistic and ponderomotive pulse self-focusing and filamentation. The density buildup near the channel front can eventually reach above the critical density, making the channeling speed much less than the linear group velocity of an electromagnetic wave. The channeling speed approaches estimates based on momentum conservation and 100% reflection of the laser at the density pile-up at the channel front[10] (although the second of these assumptions is not met). The scaling of the channeling time obtained from the PIC simulations indicates that a low-intensity channeling pulse is preferred to minimize the total channeling energy, but the intensity cannot be much lower than $I \approx 5 \times 10^{18} \text{ W/cm}^2$ if the channeling is to be completed within 100 ps. It is worth pointing out that for a typical fast-ignition target, the critical surface for 1-μm light will be roughly 600 μm in front of the target center. One way to move the channel closer to the core would be to use blue light ($\lambda = 0.35 \mu$m) for both the channeling and ignition pulses.

REFERENCES

1. J. D. Lindl, Phys. Plasmas **2**, 3933 (1995).

2. M. Tabak *et al.*, Phys. Plasmas **1**, 1626 (1994).

3. R. Kodama *et al.*, Nature **412**, 798 (2001); *ibid*. **418**, 933 (2002).

4. S. C. Wilks *et al.*, Phys. Rev. Lett. **69**, 1383 (1992).

5. A. Pukhov and J. Meyer-ter-Vehn, Phys. Rev. Lett. **79**, 2686 (1997).

6. C. Ren *et al.*, Phys. Rev. Lett. **93**, 185004 (2004).

7. C. Ren *et al.*, Phys. Plasmas **13**, 056308 (2006).

8. J. C. Adam, A. Héron, and G. Laval, Phys. Rev. Lett. **97**, 205006 (2006).

9. C. K. Li and R. D. Petrasso, Phys. Rev. E **70**, 067401 (2004).

10. K-C. Tzeng, W. B. Mori, and C. D. Decker, Phys. Rev. Lett. **76**, 3332 (1996).

11. C. Max, J. Arons, and A. B. Langdon, Phys. Rev. Lett. **33**, 209 (1974).

12. G.-Z. Sun *et al.*, Phys. Fluids **30**, 526 (1987).

13. P. Kaw, G. Schmidt, and T. Wilcox, Phys. Fluids **16**, 1522 (1973).

14. A. B. Langdon and B. F. Lasinski, Phys. Rev. Lett. **34**, 934 (1975).

15. D. W. Forslund, J. M. Kindel, and E. L. Lindman, Phys. Fluids **18**, 1002 (1975).

16. W. B. Mori *et al.*, Phys. Rev. Lett. **60**, 1298 (1988).

17. M. Borghesi *et al.*, Phys. Rev. Lett. **78**, 879 (1997).

18. J. Fuchs *et al.*, Phys. Rev. Lett. **80**, 1658 (1998).

19. A. J. Mackinnon *et al.*, Phys. Plasmas **6**, 2185 (1999).

20. K. A. Tanaka *et al.*, Phys. Rev. E **60**, 3283 (1999).

21. A. Pukhov and J. Meyer-ter-Vehn, Phys. Rev. Lett. **76**, 3975 (1996).

22. Y. Sentoku *et al.*, Fusion Sci. Technol. **49**, 278 (2006).

23. R. G. Hemker, "Particle-in-Cell Modeling of Plasma-Based Accelerators in Two and Three Dimensions," Ph.D. thesis, University of California, 2000; R. A. Fonseca, L. O. Silva, F. S. Tsung, V. K. Decyk, W. Lu, C. Ren, W. B. Mori, S. Deng, S. Lee, T. Katsouleas, and J. C. Adam, in *Computational Science—ICCS 2002*, edited by P. M. A. Sloot *et al.*, Lecture Notes in Computer Science (Springer, Berlin, 2002), pp. 343–351.

24. G. Shvets and J. S. Wurtele, Phys. Rev. Lett. **73**, 3540 (1994); P. Sprangle, J. Krall, and E. Esarey, Phys. Rev. Lett. **73**, 3544 (1994).

25. C. Ren and W. B. Mori, Phys. Plasmas **8**, 3118 (2001).

26. B. J. Duda and W. B. Mori, Phys. Rev. B **61**, 1925 (2000); B. J. Duda *et al*., Phys. Rev. Lett. **83**, 1978 (1999).

27. E. Valeo, Phys. Fluids **17**, 1391 (1974).

Optimizing a Cleaning Process for Multilayer Dielectric (MLD) Diffraction Gratings

Introduction

The OMEGA EP Laser System consists of four beamlines, two of which will provide 1054-nm pulses having multikilo-joule energies, picosecond pulse widths, petawatt powers, and ultrahigh intensities exceeding 10^{20} W/cm^2 (Ref. 1). These two beams can be directed into the existing OMEGA laser's target chamber for (1) fast-ignition experiments, which use a pulse of energetic electrons to heat the compressed fuel, thus igniting the fusion reaction,[2] and for (2) production of short pulses of x rays to "backlight" imploding fusion targets for diagnostic purposes.

The picosecond pulses are created by chirped-pulse ampli-fication (CPA),[3] as shown in Fig. 112.24. To amplify the laser pulse without damaging the amplifier, a short pulse from the source is first chirped, or stretched into a longer, lower-power pulse in which the longer wavelengths travel at the front. The pulse is expanded in diameter, amplified, and then compressed by a series of four diffraction gratings. The compression occurs as the longer (red) wavelengths at the front of the amplified pulse are diffracted more and, therefore, forced to travel longer paths than the shorter (blue) ones. As a result, all wavelengths in the pulse arrive at the fourth grating at the same time. The fourth grating in the series experiences the shortest pulse length and is subjected to the highest fluence. The damage resistance of this last grating is the limiting element on the amount of energy that can be obtained in the compressed laser pulse. The last grating must be of a very high optical quality and have a high laser-damage threshold. The primary require-ments for these large-aperture (43 cm $\times$ 47 cm) gratings are a high diffraction efficiency greater than 95%, peak-to-valley wavefront quality of less than λ/10 waves, and a high laser-induced-damage threshold greater than 2.7 J/cm^2 at 10-ps measured beam normal.

The multilayer dielectric (MLD) grating consists of a film of SiO$_2$, etched to form a grating structure with 1740 lines per mil-limeter. This structure resides on top of a multilayer dielectric high-reflector stack composed of alternating layers of SiO$_2$ and HfO$_2$. It is the cleanliness of this structure that is of paramount importance to survivability. Previous work at LLE has evalu-ated several candidate MLD cleaning protocols.[4] This article describes the results of an investigation to further optimize a final MLD-diffraction-grating cleaning process called "piranha clean" to increase laser-damage resistance.

Piranha Clean

Piranha solution is a mixture of sulfuric acid and hydrogen peroxide. This chemically aggressive agent has been used in the semiconductor industry for many years as the primary means of removing heavy organics like photoresist from wafers and photomasks. Typically, mixtures of H$_2$SO$_4$ (>95 wt%) and H$_2$O$_2$ (30 wt%) in volume ratios of 2 to 4:1 are used at tem-peratures of 80°C and higher. When hydrogen peroxide and sulfuric acid are mixed, "Caro's acid" [i.e., monopersulfuric acid (H$_2$SO$_5$)] is formed [Eq. (1)]. Caro's acid is the active etchant in a piranha bath.[5]
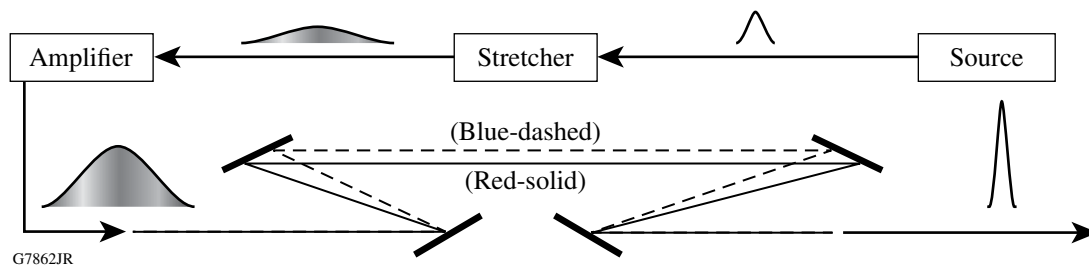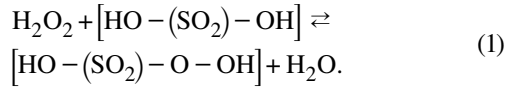

Figure 112.24
Diagram of chirped-pulse amplification. The pulse is amplified and then compressed by a series of four tiled-grating assemblies.

$$H_2O_2 + \left[HO - (SO_2) - OH\right] \rightleftarrows$$
$$\left[HO - (SO_2) - O - OH\right] + H_2O. \tag{1}$$

As shown in Eq. (1), water is produced in the reaction between hydrogen peroxide and sulfuric acid. The presence of excess water in the mixture shifts the equilibrium toward the reactants, minimizing the production of Caro's acid. Therefore, using highly concentrated hydrogen peroxide (85 to 90 wt%) optimizes the production of Caro's acid; however, the use of highly concentrated hydrogen peroxide is extremely dangerous. For safety reasons, a lower concentration (30 wt%) is used. The excess water in 30-wt% H_2O_2 shifts the reaction away from the formation of H_2SO_5. The use of H_2O_2 in a low concentration also leads to significant heating of the piranha solution when the reactants are mixed. Caro's acid, which is heat sensitive, subsequently breaks down, resulting in a low-equilibrium concentration of this oxidizing acid. So, the mixture of H_2SO_4 and H_2O_2 requires higher temperatures to be effective in removing heavy organic materials like photoresist.

Experimental

Small (100-mm-diam) MLD diffraction gratings were fabricated at Plymouth Grating Laboratories (Fig. 112.25) by the following process steps:

1. *E*-beam deposit a 1053-nm, high-reflectivity multilayer coating of hafnium dioxide (HfO_2) and silicon dioxide (SiO_2) on a BK7 substrate.

2. Meniscus-coat a bottom organic antireflective coating (BARC) to the multilayer stack to eliminate standing wave effects; then meniscus-coat a PFI 88 (Sumitomo) positive photoresist layer.

3. Expose (pattern) the photoresist layer using a scanning-beam interference-lithography (Nanoruler) method. (The Nanoruler was developed by Dr. Mark Schattenburg at MIT. This exposure system moves a small UV laser beam over the substrate in overlapping scans to create a pattern of parallel lines in the photoresist. The gratings were patterned for 1740 lines/mm.)

4. Develop the patterned photoresist layer using an OPD262 developer.

5. Selectively remove the BARC layer with an O_2 reactive ion-beam-etch (RIBE) process.

6. Etch the SiO_2 grating layer using an Ar/O$_2$/CHF$_3$ RIBE process.

After step 6 above, gratings were shipped to LLE to evaluate the piranha clean process for removing (e.g., stripping) all photoresist and cleaning the grating surface. Two variables were examined: the ratio of H_2SO_4 to H_2O_2, and the treatment temperature.

1. Coat substrate with MLD, BARC, and photoresist

2. Pattern grating by SBIL and develop

3. Etch BARC by oxygen RIBE

4. Etch MLD top layer by fluorine RIBE

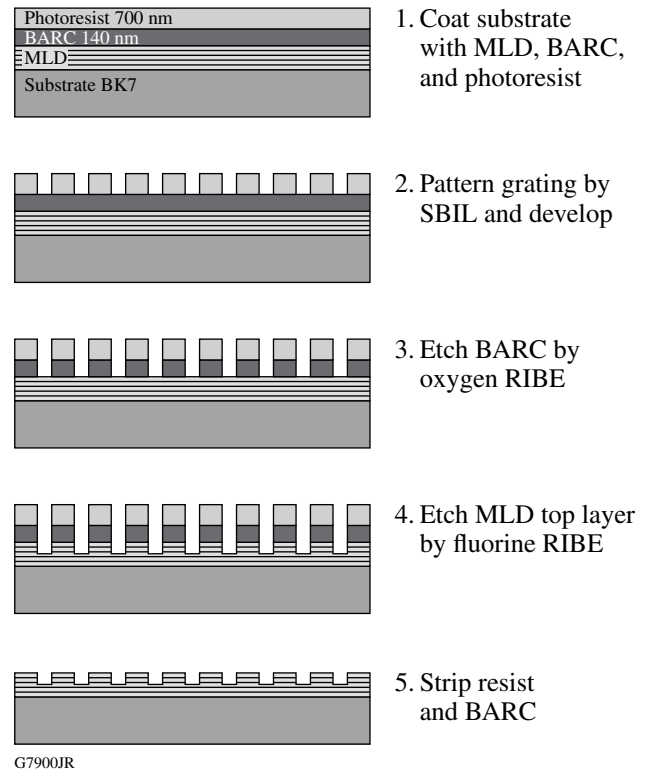5. Strip resist and BARC

G7900JR

Figure 112.25
MLD grating fabrication process (figure not drawn to scale).

A sufficient number of gratings were cut into quarters to generate nine parts. A design-of-experiments (DOE) test was conducted with these parts to evaluate the influence of piranha solution composition and temperature on laser-damage threshold. The piranha clean process is shown schematically in Fig. 112.26. At a given treatment temperature, a part was immersed in a piranha bath of a given concentration and stirred for 20 min to strip the resist (step 1), subjected to a piranha rinse for less than 1 min (step 2), cleaned again for 10 min (step 3), rinsed in de-ionized water for approximately 3 min (step 4), then cooled to ~22°C and blown dry with filtered N_2 gas (step 5). Dried parts were evaluated for cleanliness by determining their laser-damage thresholds.
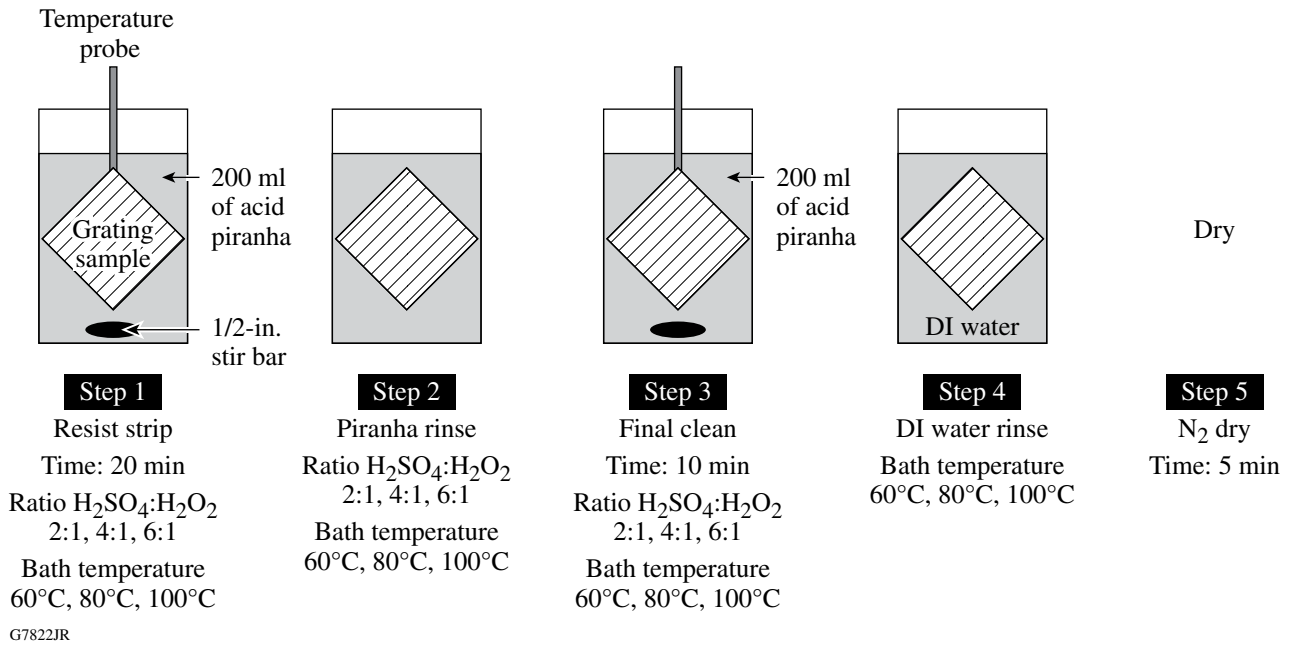
G7822JR

Figure 112.26
Piranha process. The variables within the experiment were the ratio of H_2SO_4 to H_2O_2 and the temperature of the piranha mixture.

Results

1. Laser-Damage Threshold

Laser-damage testing was conducted using a 10-ps-pulse, *s*-polarized laser operating at 1053 nm with an incident beam angle of 61° (diffracted beam of 72°). Both 1-on-1 and *N*-on-1 laser-induced-damage tests were performed. For 1-on-1 testing, individual sites on the grating are irradiated once with increasing energies until visible damage is observed. For *N*-on-1 testing, a single site is irradiated at increasing energies until damage is observed. The LLE specification for the damage threshold of our MLD gratings is >2.7 J/cm^2 at 10-ps pulse length (for both 1-on-1 and *N*-on-1).

Figures 112.27 and 112.28 show the results of the damage-threshold tests that were measured for the different piranha clean processes. These results indicate that the temperature of the piranha mixture was the main variable, while the ratio of H_2SO_4 to H_2O_2 had a lesser effect. For both 1-on-1 and *N*-on-1
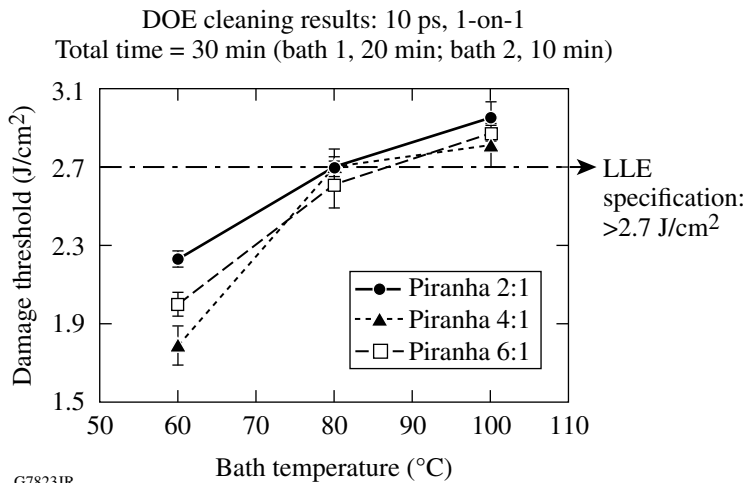

G7823JR

Figure 112.27
10-ps, 1-on-1 damage threshold at 1053 nm.

DOE cleaning results: 10 ps, *N*-on-1
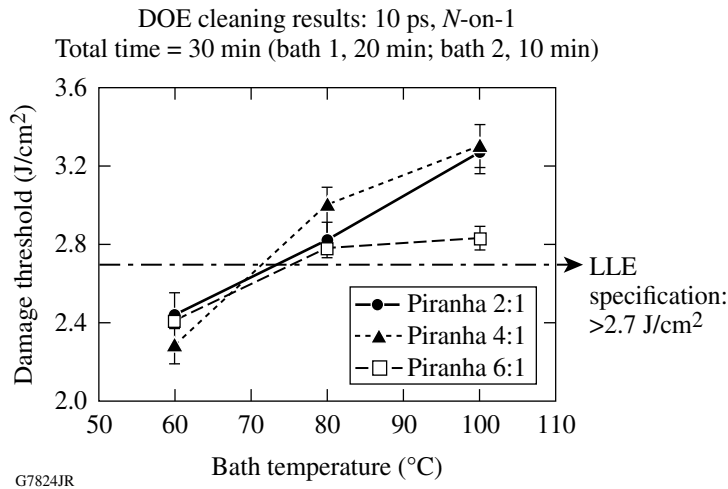Total time = 30 min (bath 1, 20 min; bath 2, 10 min)

G7824JR

Figure 112.28
10-ps, *N*-on-1 damage threshold at 1053 nm.

tests, increasing the piranha temperature caused the grating laser-damage threshold to increase. This observation supports the discussion earlier in this article regarding the need to generate sufficient Caro's acid for efficient etch-cleaning. One could expect that further increases in bath temperatures would lead to even more enhanced laser-damage thresholds. Other work (not described here) has shown that higher process temperatures create thermal shock issues for small test gratings. The full-size grating elements used in OMEGA EP, consisting of 10-cm-thick plates of BK-7 glass, will not be subjected to cleaning process temperatures greater than 100°C. (Preliminary work to model this issue is reported elsewhere.[6])

2. SEM Analysis

Scanning electron microscopy (SEM) images were collected and analyzed for the highest (2:1, 100°C) and lowest (4:1, 60°C) damage-threshold MLD gratings that were cleaned in this study. The SEM images of the piranha 2:1, 100°C and

piranha 4:1, 60°C processes indicate there is no visual residual contamination within either of the grating trenches. The SEM images, along with the associated laser-damage-threshold data for these gratings, are shown in Fig. 112.29. Since neither sample had visual contamination, SEM analysis is not useful in determining the root cause for the differences in damage-threshold values.

3. ToF-SIMS Analysis

The ToF-SIMS analysis was performed at Surface Science Western, University of Western Ontario. The instrument used was an ION-TOF (GmbH), TOF-SIMS IV, with a mass range of 1 to 1000 amu. To acquire positive and negative "shallow" depth profiles (i.e., meaning probing a few tens of nanometers into the surface), a 3-keV Cs^+ sputter ion beam was used for the negative secondary-ion profiles, while a 3-keV O_2^+ sputter ion beam was used for the positive secondary-ion profiles. The sputter-beam raster area was 500×500 μm^2. Each sputter beam
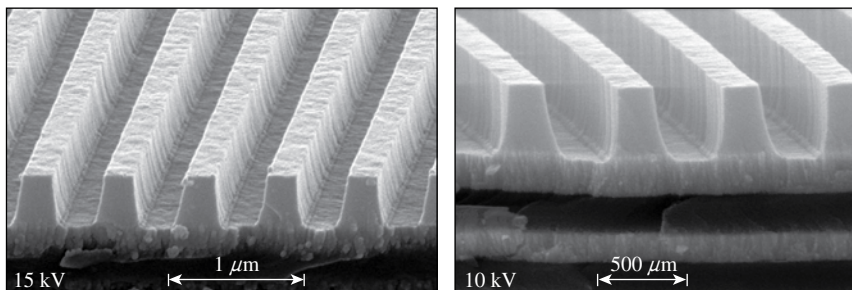
Piranha 2:1, 100°C, 30 min
Damage threshold:
    10 ps, *N*-on-1: 3.27 J/cm^2
    10 ps, 1-on-1: 2.95 J/cm^2

Piranha 4:1, 60°C, 30 min
Damage threshold:
    10 ps, *N*-on-1: 2.29 J/cm^2
    10 ps, 1-on-1: 1.79 J/cm^2

G7827JR

Figure 112.29
SEM images of the highest- and lowest-damage-threshold samples (piranha 2:1, 100°C; piranha 4:1, 60°C process). Laser-damage-threshold standard deviation for these samples is ±5%.

enhanced the secondary-ion yield through a reactive-ion effect for the given secondary-ion polarity. The Bi_3^+ analysis area was centered within this sputter crater, with a raster size of $200 \times 200 \ \mu m^2$. (Using a smaller raster size for analysis rather than the sputter crater size allows one to avoid edge effects during depth profiling.) By alternating the Bi_3^+ analysis and Cs^+/O_2^+ sputter beams, and inserting an electron flood-gun pulse in between for charge neutralization, a depth profile into the surface was acquired.[7]

A ToF-SIMS "shallow"-depth-profile analysis was conducted on the highest (piranha 2:1, 100°C) and lowest (piranha 4:1, 60°C) damage-threshold samples to determine if there was a correlation between higher contaminant ions and lower damage-threshold values. The relative intensities of the positive and negative ions detected versus the sputter time for the two samples were plotted to examine the differences between the two samples.

The data (see Fig. 112.30) indicate that there were significant levels of salt ions remaining within the lowest-damage-threshold samples (piranha 4:1, 60°C). The potassium (K^+) and sodium (Na^+) ions were the most abundant at the surface and into the grating. These salt ions are thought to have come from multiple contamination sources, including, possibly, the rinse water, developer, materials used during cleaning (beakers), and general handling.

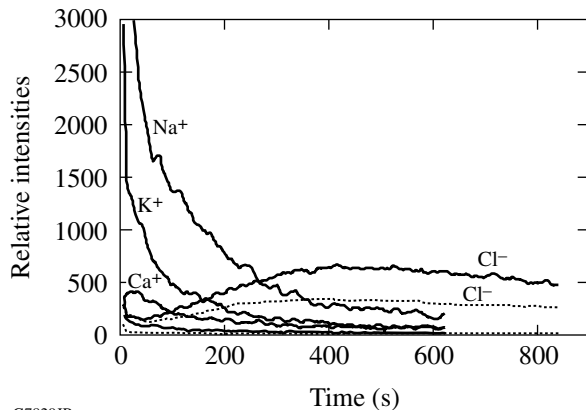| Piranha process	10-ps, 1-on-1 (J/cm^2)	10-ps, N-on-1 (J/cm^2)
— 2:1 at 100°C	2.95	3.27
···· 4:1 at 60°C	1.79	2.29

G7829JR

Figure 112.30
Salt-containing species. Piranha 4:1, 100°C has significant levels of salt remaining after clean. Laser-damage-threshold standard deviation for these samples is ±5%.

The carbon-ion species are shown in Fig. 112.31. The carbon ions are associated with the photoresist that was used in the fabrication process. This graph indicates that there were carbon (i.e., photoresist) species remaining at the surface and within the grating. The 4:1, 60°C sample had a much higher level of carbon ions than the 2:1, 100°C sample. There was also a high level of carbon implanted within the gratings. Since the top SiO_2 grating layer is amorphous, the resist was being driven into this surface. This correlates well with the damage-threshold values measured on these samples. Low-temperature piranha (with lower ratio) creates less Caro's acid and is ultimately less effective in removing organic contamination. This temperature effect can be seen clearly within our ToF-SIMS results.

Piranha process	10-ps, 1-on-1 (J/cm^2)	10-ps, N-on-1 (J/cm^2)
— 2:1 at 100°C	2.95	3.27
···· 4:1 at 60°C	1.79	2.29

G7830JR
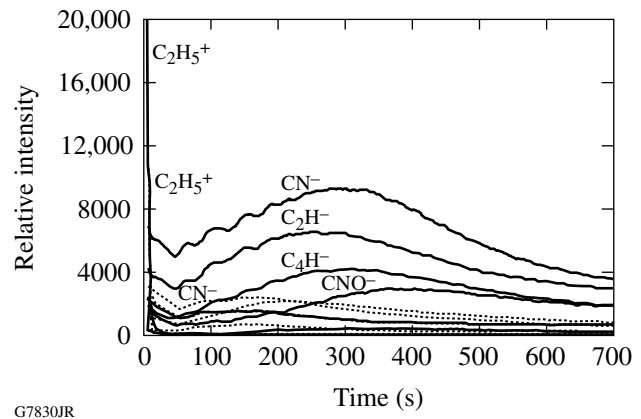
Figure 112.31
Carbon-containing species. Piranha 4:1, 100°C has significant levels of carbon (photoresist species) remaining after clean. Laser-damage-threshold standard deviation for these samples is ±5%.

Poor rinsing and neutralization of the piranha chemistry can over time cause problems at the grating surface. Residual sulfur-containing ions on or within the surface can cause surface haze (a common soft defect in the photomask industry). Figure 112.32 indicates that we did not completely rinse the piranha chemistry from the surface of the grating. The 4:1, 60°C sample had a much higher level of remaining sulfur ions than the 2:1, 100°C sample. This may be due to the lower-temperature piranha mixture not reacting completely with the carbon-resist species on the surface. The final rinse step to remove all of the piranha mixture will be very important in our final clean process to prevent the growth of sulfur-type haze.

Piranha process	10-ps, 1-on-1 (J/cm^2)	10-ps, N-on-1 (J/cm^2)
— 2:1 at 100°C	2.95	3.27
···· 4:1 at 60°C	1.79	2.29
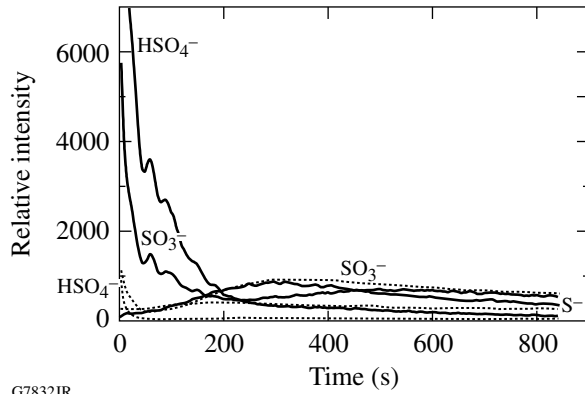
G7832JR

Figure 112.32
Sulfuric-containing species from incomplete rinse of the piranha mixture. Laser-damage-threshold standard deviation for these samples is ±5%.

Conclusions

Final clean removes any resist or particle contaminants that remain on the MLD diffraction grating after patterning and etch. Contaminant-removal efficiency in this step is critical to the performance of the grating within the laser system. The final clean employs a piranha mixture and DI water rinse to remove residual organic and other particulate and molecular contaminants. This final clean process must leave the surface free of unwanted contaminants and be able to produce high-damage-threshold gratings.

Using the 100-mm-diam MLD gratings fabricated at Plymouth Grating Laboratories, the final piranha cleaning process was optimized to achieve the OMEGA EP specification of >95% optical-diffraction efficiency and >2.7-J/cm² laser-damage threshold. The two main variables in the piranha process were the ratio of H_2SO_4 and H_2O_2 and the temperature of the mixture. Post-clean laser-damage threshold was measured for each cleaned sample. Additionally, scanning electron microscopy (SEM) and time-of-flight secondary ion-mass spectrometry (ToF-SIMS) "shallow"-depth-profile analysis was used to evaluate what type of contamination remained after the final clean process.

The laser-damage-threshold results indicate that as the ratio of H_2SO_4 to H_2O_2 increases within the piranha mixture, the damage threshold increases. Additionally, as the temperature is increased, the laser-damage threshold increases. From our data, there is a stronger correlation with the temperature of the piranha mixture.

ToF-SIMS shallow-depth-profile analysis provides an understanding of the contaminants on the surface as well as how far these contaminants are implanted into the grating surface. The analysis determined that the lowest-damage-threshold sample (4:1, 60°C) had considerably more contaminants on the surface and implanted into the grating. The low ratio and temperature piranha mixture was also unable to effectively rid the surface of the organic (i.e., photoresist) material and left considerable amounts of salts on the surface. Incomplete rinse and removal of the piranha mixture will leave sulfur-containing groups on the grating that may cause haze defects. LLE will use the information obtained in this study to scale up the piranha clean process to full-size gratings ($43 \times 47 \times 10$ cm).

REFERENCES

1. L. J. Waxer, D. N. Maywar, J. H. Kelly, T. J. Kessler, B. E. Kruschwitz, S. J. Loucks, R. L. McCrory, D. D. Meyerhofer, S. F. B. Morse, C. Stoeckl, and J. D. Zuegel, Opt. Photonics News **16**, 30 (2005).

2. M. Tabak *et al.*, Phys. Plasmas **1**, 1626 (1994).

3. D. Strickland and G. Mourou, Opt. Commun. **56**, 219 (1985).

4. B. Ashe, K. L. Marshall, C. Giacofei, A. L. Rigatti, T. J. Kessler, A. W. Schmid, J. B. Oliver, J. Keck, and A. Kozlov, in *Laser-Induced Damage in Optical Materials: 2006*, edited by G. J. Exarhos *et al.* (SPIE, Bellingham, WA, 2007), Vol. 6403, p. 64030O.

5. S. Verhaverbeke and K. Christenson, in *Contamination-Free Manufacturing for Semiconductors and Other Precision Products*, edited by R. P. Donovan (Marcel Dekker, New York, 2001), pp. 317–332.

6. Y. Zhang, Y. Wu, H. Liu, and J. C. Lambropoulos, in *Optical Manufacturing and Testing VII*, edited by J. H. Burge, O. W. Faehnle, and R. Williamson (SPIE, Bellingham, WA, 2007), Vol. 6671, p. 66710H.

7. Dr. J. Francis, Surface Science Western, ToF-SIMS Report, email reports and private communication (9 August 2006).

Shock Ignition of Thermonuclear Fuel with High Areal Densities

The energy gain[1] G of a direct-drive implosion is defined as the ratio between the thermonuclear energy yield and the laser energy on target. The gain is directly related to the capsule implosion velocity $G = \left(1/V_I^2\right)\eta_h \theta E_f / m_i$, where V_I is the implosion velocity, $\eta_h = E_K/E_L$ is the hydrodynamic efficiency representing the ratio between the shell kinetic energy and the laser energy on target, $E_f = 17.6$ MeV is the energy of the fusion products for a DT fusion reaction, and $m_i = 2.5\, m_H$ is the average ion mass. The function θ represents the fraction of burned fuel depending on the fuel areal density $\rho R \equiv \int_0^R \rho dr$. The function $\theta = \theta(\rho R)$ is commonly approximated[1] by $\theta \approx (1 + 7/\rho R)^{-1}$, where ρR is given in g/cm^2. The hydrodynamic efficiency of direct-drive implosions scales[2] as $\eta_h \sim V_I^{0.75}/I_L^{0.25}\lambda_L^{0.5}$, where I_L is the laser intensity on target and λ_L is the laser wavelength. It follows that the target gain scales as $G \sim 1/V_I^{1.25}$, indicating that high gains require low-velocity implosions. This is because low velocities are achieved by imploding massive shells and compressing large amounts of thermonuclear fuel. Since the areal densities are approximately independent of the implosion velocities,[2] the burn-up fraction depends only on the laser energy and fuel adiabat. Thus, low-velocity implosions of massive shells lead to high gains, provided that the fuel is ignited. However, the energy required to trigger ignition grows rapidly as the implosion velocity decreases. As shown in Ref. 3, the shell kinetic energy required for ignition scales as $E_K^{\text{ign}} \sim 1/V_I^6$ and low-velocity implosions fail to ignite at moderate driver energies. Large lasers in the 1-MJ energy range, such as at the National Ignition Facility, are expected to ignite relatively thin shells (initial aspect ratio ~5) driven at high velocities, ~4×10^7 cm/s, to achieve moderate gains of ~40 (Ref. 4). The performance of such implosions is sensitive to the growth of the Rayleigh–Taylor (RT) instability on the ablation front. The RT modes that can cause shell breakup during the acceleration phase have an inverse wave number $1/k$ comparable to the in-flight shell thickness $d(kd \sim 1)$. The number of e-foldings of growth for such modes is about $\sqrt{\text{IFAR}}$, where IFAR is the in-flight aspect ratio, which scales[1] as ~$V^2/\alpha^{0.6}I_L^{0.27}$.

The parameter α represents the shell's in-flight adiabat defined as the ratio of the pressure to the Fermi pressure of a degenerate electron gas. For a fully ionized DT plasma, the adiabat is given by $\alpha = P(\text{Mb})/2.3\rho(\text{g/cc})^{5/3}$. To maximize the burn-up fraction (and the areal density), the adiabat must be kept low. It follows that the shell stability can be improved by lowering the IFAR through reducing the implosion velocity. Low-velocity implosions with low IFAR's have good stability properties during the acceleration phase. However, despite their good stability properties and potential for high gains, slow targets would fail to ignite for moderate driver energies because the hot-spot temperature and pressures are too low. For example, ignition at implosion velocities of ~2×10^7 cm/s and adiabats of $\alpha \sim 1$ require large multimegajoule laser drivers.

Here we show that a spherically convergent shock wave propagating through the shell during the coasting phase of the implosion enhances the compression of the hot spot, thus significantly improving the ignition conditions.[5] The ignitor shock is launched at the end of the laser pulse and must collide with the return shock near the inner shell surface. The return shock is the shock wave driven by the hot-spot pressure propagating outward through the shell. After the ignitor and return shock collide, a third shock wave, resulting from the collision, propagates inward, leading to further compression of the hot spot. The final fuel assembly develops a peaked pressure profile with its maximum in the center. Such non-isobaric assemblies exhibit a lower ignition threshold than standard isobaric ones.[5] This mechanism is effective only in thick-shell implosions, where the ignitor shock wave significantly increases its strength as it propagates through the converging shell.

This effect can be observed in simulations of realistic ICF implosions of thick shells like the one in Fig. 112.33 showing a thick wetted-foam shell with an outer radius of 852 μm, a 106-μm-thick layer of wetted foam CH(DT)$_6$ and a 240-μm-thick layer of DT ice. The initial shell aspect ratio (average shell radius/thickness) is about 2. One-dimensional simulations of a direct-drive implosion of such shells are carried out for the two 350-kJ, $\lambda_L = 0.35$-μm laser pulses shown in Fig. 112.34. The dashed curve represents a standard laser pulse, while the solid curve represents a shock-ignition laser pulse with a power

spike at the end of the pulse used to drive the ignitor shock. Both laser pulses use an intensity picket at the beginning of the pulse to shape the adiabat profile and to improve the target stability. The in-flight adiabat of the shell is $\alpha \approx 1$, the implosion velocity is $V = 2.5 \times 10^7$ cm/s, and the IFAR ≈ 17. The ultralow IFAR indicates that the integrity of the shell is not significantly affected by the Rayleigh–Taylor instability. The simulation of the implosions for the two laser pulses is carried out using the hydrocode *LILAC*. Figure 112.35 compares the pressure and density profiles at the time of peak compression for the standard pulse shape (dashed) and the shock-ignition pulse shape (solid). Notice that the hot-spot pressure for the
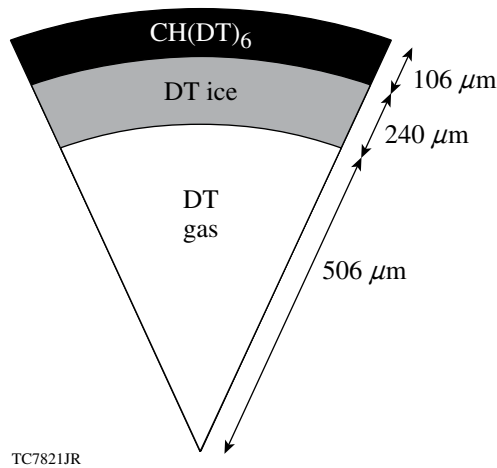
shock-ignition pulse shape is about twice as high as for the standard pulse shape. While the target driven by the standard pulse is far from ignition, the shock-ignited target is at marginal ignition. Marginal ignition for a shock-ignited target is estimated by the size of the shock-launching-time ignition window, i.e., the time interval during which the ignitor shock needs to be launched to trigger ignition. If the ignition window is very narrow (only tens of picoseconds), the shock-ignited target is close to marginal ignition. To exceed the marginal ignition conditions and to widen the ignition window, the total laser energy needs to be increased.

Figure 112.33
Thick wetted-foam target used in the shock-ignition simulations.
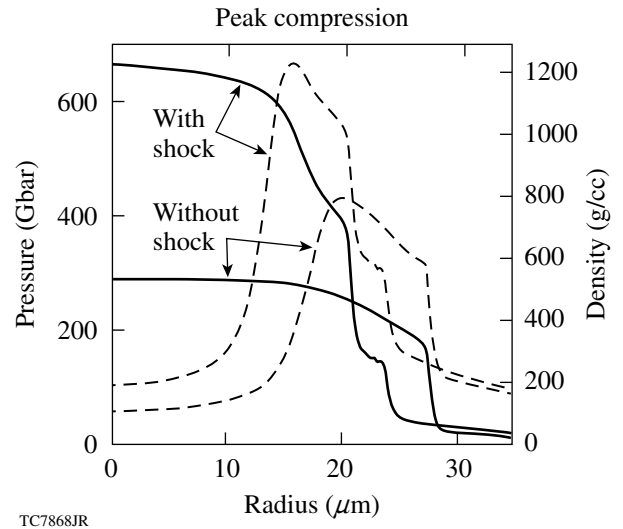
Figure 112.35
Density (dashed) and pressure (solid) profiles at peak compression for the standard and shock-ignition pulse shape.

Figure 112.34
UV 350-kJ standard pulse shape (dashed) and shock-ignition pulse shape (solid).

Since the laser intensity during the power spike is considerably higher than during the assembly pulse, hot electrons can be generated in the corona by laser–plasma instabilities. In standard implosions, hot electrons can preheat the shell, thus raising the adiabat, reducing the final compression, and preventing the ignition of the hot spot. In shock ignition, hot electrons generated during the power spike may have a positive effect on the implosions. Since the areal density grows rapidly in time during the final stages of the implosion, the range of the hot electrons from the intensity spikes is less than the shell thickness. In this case, the hot electrons are stopped on the shell surface and help drive the ignitor shock. Figure 112.36 shows a plot of the laser intensity (solid curve) and the areal density evolution (dashed curve) during the power spike. Since the ρR range of 100-keV electrons in DT (about 17 mg/cm^2, dashed line in Fig. 112.36) is much smaller than the shell areal density (50 to 80 mg/cm^2)

Figure 112.36
Evolution of the laser intensity (solid) and the areal density (dashed) during the power spike.

during the spike, the hot electrons of moderate energy (~100 keV) are stopped before penetrating deep into the shell, thus augmenting the strength of the ignitor shock. The effects of hot electrons are included in the simulations through a multigroup diffusion model for the hot electrons as described in Ref. 6. In the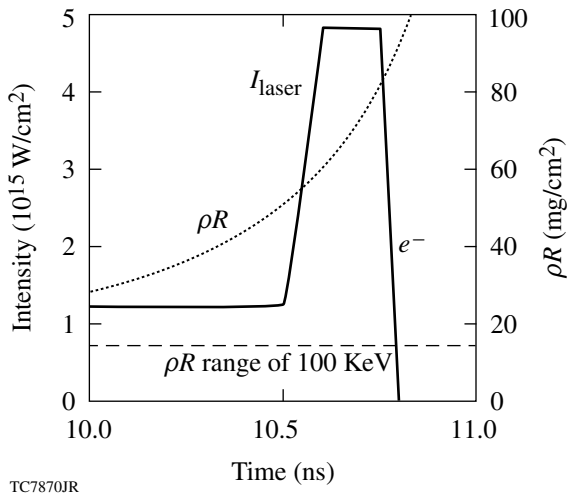 simulations, the hot electrons are generated isotropically during the power spike in the corona with their birth temperature set at 150 keV and with a Maxwellian distribution function. The total energy into hot electrons is assumed to be 25% of the laser energy during the power spike. As shown in Fig. 112.37,
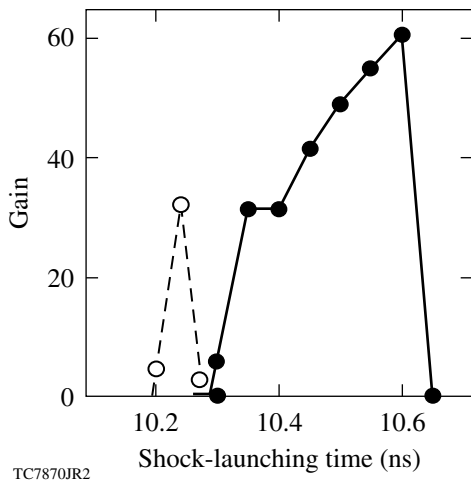

Figure 112.37
Shock-launching-time ignition window with (solid) and without (dashed) hot electrons.

the ignition window is considerably wider when the effects of hot electrons are included in the simulation, thus showing that hot electrons can indeed benefit the shock-ignition scheme as long as their range does not exceed the shell thickness.

Another important effect to be included in shock-ignition targets is the long mean free path of the thermal coronal electrons heated to high temperatures during the power spike. The power spike raises the coronal electron temperatures to about 7 keV, causing the heat-carrying electrons to free-stream to the ablation front, thus enhancing heat conduction. A nonlocal heat-conduction model is, therefore, required to adequately model the electron heat transfer during the power spike. To estimate the effects of nonlocal heat transport, the model of Ref. 7 is included in the simulations of the ignitor-shock generation during the power spike. The new conditions for ignition and gain are computed in terms of the ignition window and shown in Fig. 112.38. As expected, the long-mean-free-path electrons augment the heat transfer during the power spike, thus driving a stronger ignitor shock. The ignition window is widened by nonlocal transport, and the gain is higher than without nonlocal effects.
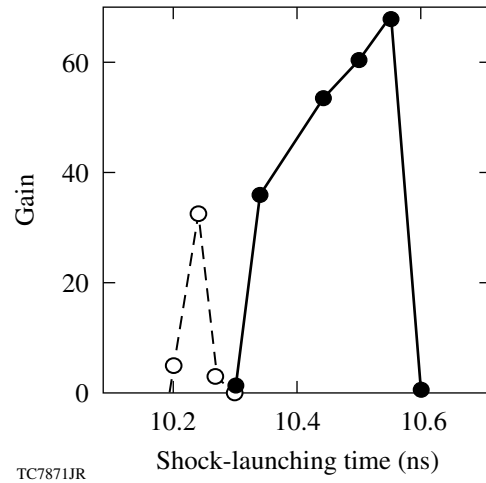
Figure 112.38
Ignition window with (solid) and without (dashed) nonlocal heat transport.

It is shown that a two-step ignition scheme can be configured by combining a fuel-assembly laser pulse and a shock-driving power spike. The ignitor shock enhances the compression of the hot spot, thus leading to a significant reduction of the energy required for ignition and high gains. A powerful laser pulse or particle beam can be used to drive the ignitor shock to trigger ignition at relatively low driver energies.

REFERENCES

1. J. D. Lindl, *Inertial Confinement Fusion: The Quest for Ignition and Energy Gain Using Indirect Drive* (Springer-Verlag, New York, 1998).

2. R. Betti and C. Zhou, Phys. Plasmas **12**, 110702 (2005).

3. M. C. Herrmann, M. Tabak, and J. D. Lindl, Nucl. Fusion **41**, 99 (2001).

4. P. W. McKenty, V. N. Goncharov, R. P. J. Town, S. Skupsky, R. Betti, and R. L. McCrory, Phys. Plasmas **8**, 2315 (2001).

5. R. Betti, C. D. Zhou, K. S. Anderson, L. J. Perkins, W. Theobald, and A. A. Solodov, Phys. Rev. Lett. **98**, 155001 (2007).

6. J. Delettrez and E. B. Goldman, Laboratory for Laser Energetics, University of Rochester, Rochester, NY, LLE Report No. 36 (1976).

7. G. P. Schurtz, Ph. D. Nicolaï, and M. Busquet, Phys. Plasmas **7**, 4238 (2000).

LLE's Summer High School Research Program

During the summer of 2007, 14 students from Rochester-area high schools participated in the Laboratory for Laser Energetics' Summer High School Research Program. The goal of this program is to excite a group of high school students about careers in the areas of science and technology by exposing them to research in a state-of-the-art environment. Too often, students are exposed to "research" only through classroom laboratories, which have prescribed procedures and predictable results. In LLE's summer program, the students experience many of the trials, tribulations, and rewards of scientific research. By participating in research in a real environment, the students often become more excited about careers in science and technology. In addition, LLE gains from the contributions of the many highly talented students who are attracted to the program.

The students spent most of their time working on their individual research projects with members of LLE's technical staff. The projects were related to current research activities at LLE and covered a broad range of areas of interest including experimental diagnostic development and analysis, computational modeling of implosion hydrodynamics and electron transport, database development, materials science, computational chemistry, and solid-state switch development (see Table 112.IV).

The students attended weekly seminars on technical topics associated with LLE's research. Topics this year included laser physics, fusion, holographic optics, fiber optics, liquid crystals, error analysis, and global warming. The students also received safety training, learned how to give scientific presentations, and were introduced to LLE's resources, especially the computational facilities.

The program culminated on 29 August with the "High School Student Summer Research Symposium," at which the students presented the results of their research to an audience including parents, teachers, and LLE staff. The students' written reports will be made available on the LLE Web site and bound into a permanent record of their work that can be cited in scientific publications.

Two hundred and eighteen high school students have now participated in the program since it began in 1989. This year's students were selected from approximately 50 applicants.

At the symposium it was announced that Mr. Christian Bieg, a physics teacher at Fairport High School, is the recipient of the eleventh annual William D. Ryan Inspirational Teacher Award. This award is presented to a teacher who motivated one of the participants in LLE's Summer High School Research Program to study science, mathematics, or technology and includes a $1000 cash prize. Teachers are nominated by alumni of the summer program. Mr. Bieg was nominated by Rui Wang, a participant in the 2006 Summer Program and a finalist in the 2007 Intel Science Talent Search. "I have moved around the globe during my years of primary and secondary education," Rui wrote in her nomination letter, "yet the teacher whose dedication to science and education has inspired me the most is Mr. Bieg … Mr. Bieg was not only passionate about physics and teaching, but also knew exactly how to bring out the curious side in everyone … He had promised us on the first day that we would never see the world the same way after each class, and, of course, he kept his promise." Mr. David Paddock, principal of Fairport High School, added, "Chris Bieg is an outstanding teacher … He has the ability to make the subject interesting and fun to all students, even those who may not generally favor science. Chris … serves as a wonderful role model for his students."

Table 112.IV: High School Students and Projects—Summer 2007.

Name	High School	Supervisor	Project Title
Joshua Bell	Churchville-Chili	W. R. Donaldson	Development of a GaAs Photoconductive Switch for the Magneto-Inertial Fusion Electrical Discharge System
Margaret Connolly	Mercy	T. C. Sangster, M. McCluskey, S. Roberts	Response of CR-39 to Heat Exposure
Juraj Culak	Brighton	P. B. Radha	Neutron Imaging of Inertial Confinement Fusion Implosions
Daniel Fleischer	Brighton	R. Boni, P. A. Jaanimagi	ROSS Performance Optimization
Jean Gan	Pittsford Sutherland	K. L. Marshall	Patterned Photoresist Spacers and Photo-Induced Alignment Coatings for Liquid Crystal Waveplates and Polarizers
Roy Hanna	Williamsville	J. A. Delettrez	Extension of the Modeling of Blooming and Straggling of the Electron Beam in the Fast-Ignition Scenario
Katherine Manfred	Fairport	R. S. Craxton	Polar-Direct-Drive Simulations for a Laser-Driven HYLIFE-II Fusion Reactor
Richard Marron	Allendale Columbia	R. Kidder	Creation of an Ontology for the OMEGA EP Laser System
Alan She	Pittsford Mendon	R. S. Craxton	Thermal Conductivity of Cryogenic Deuterium
Benjamin Smith	Webster Schroeder	L. M. Elasky	Expansion of Search Capabilities for the Target Fabrication Database
Alexander Tait	Allendale Columbia	W. A. Bittle	Data Analysis for Electro-Magnetic Pulse Measurements
Ernest Wang	Pittsford Mendon	K. L. Marshall	Computational Modeling of Spectral Properties of Azobenzene Derivatives
Eric Welch	Livonia	J. P. Knauer	Design of an X-Ray Photoconductive Device Spectrometer
Andrew Yang	Fairport	R. Epstein	Unfolding X-Ray Spectra from a Multichannel Spectrometer

FY07 Laser Facility Report

The OMEGA Facility conducted 1514 target shots for a variety of users in FY07 (see Table 112.V). A total of 27 D_2 and 17 DT low-adiabat cryogenic target implosions that required high-contrast pulse shapes were performed. Such pulse shapes are typically characterized by a narrow picket pulse on top of a low-intensity foot pulse, followed by a high-intensity drive pulse (see Fig. 112.39). Substantial strides have been made with low-adiabat-drive pulse shapes and shock timing. Small picket timing and intensity changes have been demonstrated to effect cryogenic target areal-density measurements in agreement with theory. OMEGA Availability and Experimental Effectiveness averages for FY07 were 92.8% and 95.9%, respectively. Highlights of other achievements for FY07 include the following:

- An offline OMEGA frequency-conversion-crystal (FCC) tuning test bed was developed and activated to tune new OMEGA and OMEGA EP FCC's. This facility supports the ongoing refurbishment of OMEGA crystals and is used to precisely characterize the performance of OMEGA EP FCC's.

- More than 25 new or significantly modified target-diagnostic systems were qualified for use on the OMEGA Experimental
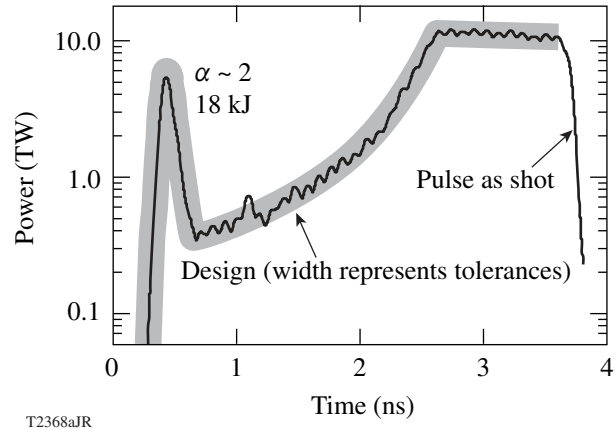
Figure 112.39
OMEGA single-beam pulse shape from a low-adiabat cryogenic target implosion (shot 47206) using pulse shape HE363001p.

Facility in FY07. These diagnostics supported LLE, LLNL, LANL, AWE, and CEA experiments and all were supported by LLE and the cognizant laboratory. Diagnostic improvements in FY 2007 include

- integration of the LLNL/OMEGA high-resolution velocimeter (OHRV) diagnostic,

Table 112.V: The OMEGA target shot summary for FY07.

Laboratory	Planned Number of Target Shots	Actual Number of Target Shots	IDI NIC	DDI NIC	Total NIC	Non-NIC
LLE	629	698	174	502	676	22
LLNL	386	422	235	0	235	187
LANL	158	192	73	0	73	119
NLUF	117	121	0	0	0	121
CEA	40	40	0	0	0	40
AWE	20	26	0	0	0	26
SNL	11	15	15	0	15	0
Total	1361	1514	497	502	999	515

   – upgrade of the active shock breakout (ASBO) diagnostic with a new long-pulse laser system, two ROSS streak cameras, and an off-axis telescope option,

   – integration of an electromagnetic interference (EMI) monitor system to provide baseline and operational data to support short-pulse operations,

   – activation of the magneto inertial fusion energy delivery system (MIFEDS), and

   – qualification of nine x-ray imaging and spectrometer diagnostics.

Significant modifications were made to the OMEGA Laser Facility in FY07 to integrate the OMEGA EP short-pulse beam into the OMEGA target chamber. These modifications include the following:

• Ten-inch manipulator #2 was modified for near-vertical operation and moved from port H7 to port H3.

• The gated microchannel-plate x-ray imager (GMXI) was modified and moved from port H9 to port H12.

• The turning mirror structure and surrounding platform were extensively modified to accommodate the short-pulse beam tube (SPBT) and the off-axis parabola inserter/manipulator (OAPI/M); these modifications include replacing two segments of the personnel platform and the addition of a new two-level platform to provide personnel access.

• The bore diameter of port H7 was increased to provide clearance for the off-axis parabola.

• The SPBT connecting the OMEGA target chamber to the OMEGA EP grating compressor chamber (GCC) was installed.

National Laser Users' Facility and External Users' Programs

During FY07, 826 target shots were taken on OMEGA for external users' experiments, accounting for 54.6% of the total OMEGA shots for the year. The external users during this year included six collaborative teams participating in the National Laser Users' Facility (NLUF) program and many collaborative teams from the national laboratories (LLNL, LANL, and SNL), the Commissariat à l'Énergie Atomique (CEA) of France, and the Atomic Weapons Establishment (AWE) of the United Kingdom.

FY07 NLUF Experiments

FY07 was the first of a two-year period of performance for the NLUF projects approved for the FY07–FY08 funding and OMEGA shots (see Table 112.VI). Six of these NLUF projects were allotted OMEGA shot time and received a total of 131 shots on OMEGA in FY07. Some of this work is summarized in this section.

Recreating Planetary Core States on OMEGA in FY07

Principal Investigator: R. Jeanloz (University of California, Berkeley)

Co-investigators: J. H. Eggert, P. M. Celliers, S. Brygoo, D. G. Hicks, and G. W. Collins (LLNL); P. Loubeyre (CEA); T. R. Boehly (LLE); S. McWilliams and D. Spaulding (U.C. Berkeley)

The approach to recreate planetary core states in the laboratory involves driving a laser-induced shock through a sample already precompressed in a diamond-anvil cell (Fig. 112.40). This combines the benefits of static and dynamic high-pressure experiments, allowing the final pressure–volume–temperature (P–V–T) state of the sample to be tuned across a broad range of thermodynamic conditions. Much higher densities are achieved through this approach than through traditional shock-wave
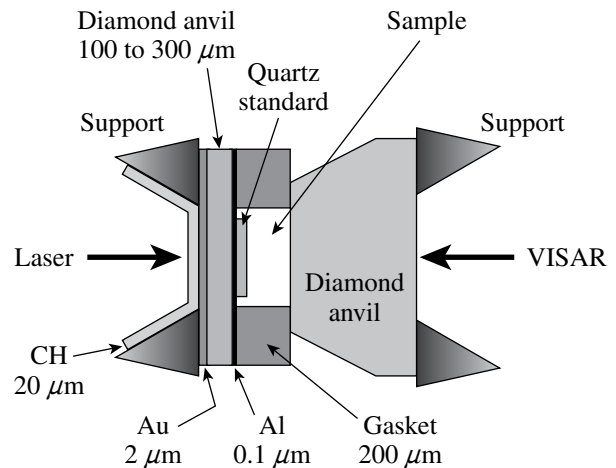
U660JR

Figure 112.40

Schematic cross section of the diamond cell. The diamond anvil on the entry (drive laser) side must be thin in order to minimize attenuation of the shock front before it enters the sample, and diagnostics include velocity interferometry system for any reflector (VISAR) as well as pyrometry (not shown) collected through the thicker anvil on the exit side.

Table 112.VI: FY07–FY08 NLUF Experiments.

Principal Investigator	Affiliation	Proposal Title
R. Jeanloz	University of California, Berkeley	Recreating Planetary Core States on OMEGA in FY07
R. P. Drake	University of Michigan	Experimental Astrophysics on the OMEGA Laser
P. Hartigan	Rice University	Laboratory Experiments on Supersonic Astrophysical Flows Interacting with Clumpy Environments
R. Mancini	University of Nevada, Reno	Multiview Tomographic Study of OMEGA Direct-Drive-Implosion Experiments
R. D. Petrasso, C. K. Li	Massachusetts Institute of Technology	Monoenergetic Proton Radiography of Laser–Plasma-Generated Fields and ICF Implosions
R. Falcone, H. J. Lee	University of California, Berkeley	X-Ray Compton Scattering on Compressed Matter

(Hugoniot) measurements because thermal effects come to dominate the latter but are suppressed by the precompression.

Thus, states directly relevant to the deep interiors of giant planets are reproduced, and we can study interatomic-bonding forces at much closer packing than is otherwise possible through laboratory experiments. This is important both for planetary science and for validating (and extending) the condensed-matter theory based on first-principles quantum-mechanical calculations.

This year we developed a technique that uses quartz as a reference standard for Hugoniot, temperature, and reflectivity measurements of planetary fluids.[1] This new technique greatly reduces the uncertainty of shock-compression data, and measurements were completed for He.[2] This work establishes how the compressibility changes with ionization and interparticle interaction and will serve as a key benchmark for models of the evolution and structure of solar and extra-solar giant planets. Temperature and reflectivity measurements on He were also finished this year, and we have collected the highest-density and -pressure data for He.[3]

In addition to He, we have finished collecting shocked precompressed data on H_2 and D_2. While the deuterium data, for samples that start at the same density as liquid deuterium, have the same compressibility as impedance-matched liquid deuterium, contrasting H_2 and D_2 measurements reveals an interesting isotope dependence for the compressibility. In

essence, the hydrogen shows a larger compressibility than deuterium at the same precompressed pressure. This is likely because the compressibility is sensitive to the excitation of degrees of freedom that increases the compressibility and the interparticle interaction that increases pressure and reduces the compressibility. In fact, all the tabular equation-of-state (EOS) models show this signature, with the maximum compressibility decreasing with precompression (still, the final density increases with precompression). Hydrogen, which has a larger zero-point volume because of its smaller mass, behaves like deuterium, having a lower initial density.

The reflectivity and temperature data for hydrogen reveal that contours of constant reflectance are nearly parallel to the predicted plasma phase transition derived from Saumon and Chabrier[4] and from Bonev's density functional calculations[5] (Fig. 112.41).

Finally we have finished our first set of measurements on He/H_2 mixtures, finding that the temperature and optical reflectivity are between those of He and H_2. The reflectivity of He increases slowly with shock pressure as compared to H_2. At the same time, the temperature of He increases rapidly with shock pressure as compared to H_2. These two observations are related: the reason H_2 stays colder with increasing shock pressure compared to He (over the pressure range studied) is because H_2 dissociates; also, it ionizes at much lower shock pressure than He, and the dissociation and ionization (which leads to enhanced optical reflectance) lower the shock tempera-
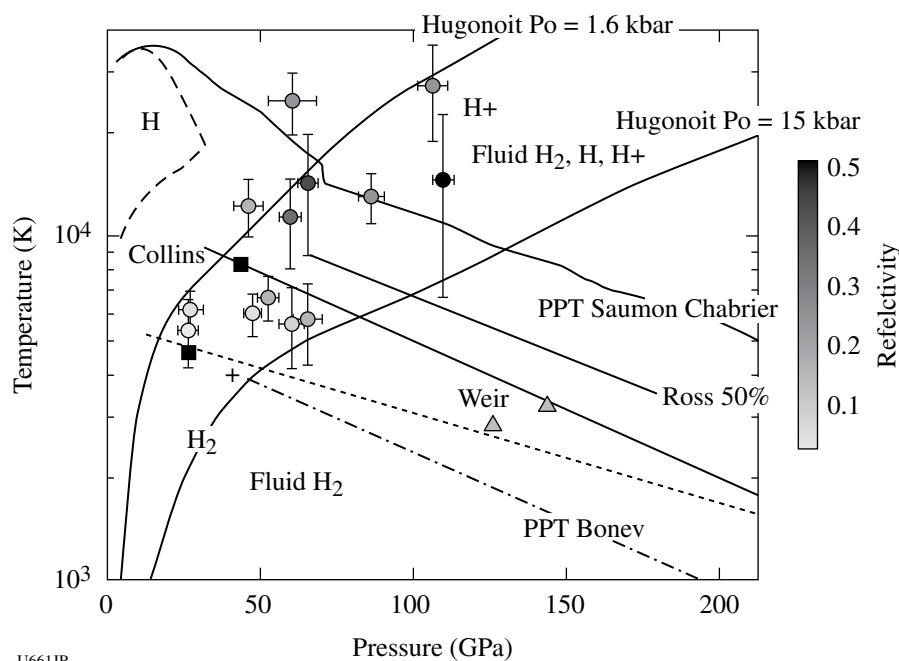

Figure 112.41
Reflectivity versus temperature and pressure for shocked precompressed H_2. Data show a continuous transition between the molecular and plasma phases in this range of temperature and pressure.

U661JR

ture. Over the same pressure range (0.1 to 2 Mbar), He exhibits much lower ionization. Therefore, increasing shock pressure rapidly increases shock temperature.

The 50/50 mixture of He/H_2 shows that the temperature and shock reflectivity lie between those of H_2 and He, suggesting that the mixture can be modeled as ideal (Figs. 112.42 and 112.43). These data suggest that over the warm, dense matter states tested here, which are relevant to the outer 20% of Jupiter, the mixture does not phase separate. This is an important result, providing new constraints on models of the interior structure and evolution of giant planets. It warrants further analysis, both to refine our understanding of the experimental observations and to fully understand the implications for the evolution, hence formation, of planets.
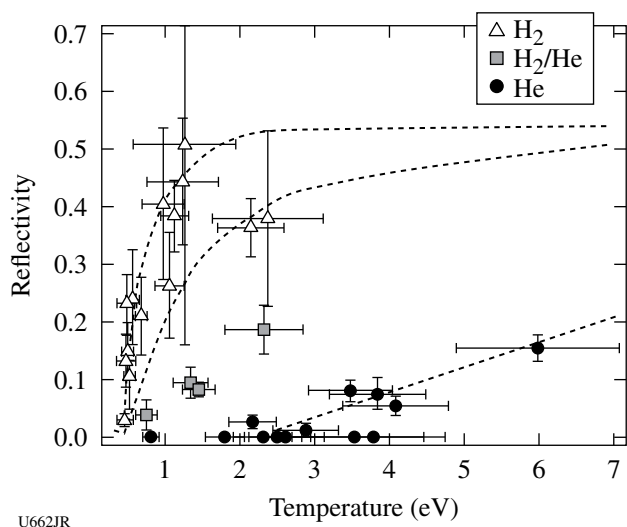

Figure 112.42
Reflectivity versus temperature for H_2, He, and a 50/50 mixture of H_2/He. These data start off at very different initial densities but, since the reflectivity is largely temperature dependent, the reflectivity for each material follows a specific trend. The reflectivity (and the temperature versus pressure) for the mixture is intermediate between that of H_2 and He.

In summary, we completed 23 experiments in two shot days, filling out our database for H_2, He, and one mixture of He/H_2. We have characterized key properties of dense planetary fluids and have documented an interesting isotope effect in the compressibility of H_2 relative to D_2. Helium becomes electronically conducting at ~1 Mbar and 1 eV, largely by a thermally activated process. The $He/H2$ mixture seems to behave like an ideal solution up to ~1 Mbar and 2 eV. Several papers are published or are in the process of publication,[1–3,6–9] and this work has ignited an explosion of papers on He, H_2, and mixtures at planetary-core conditions.
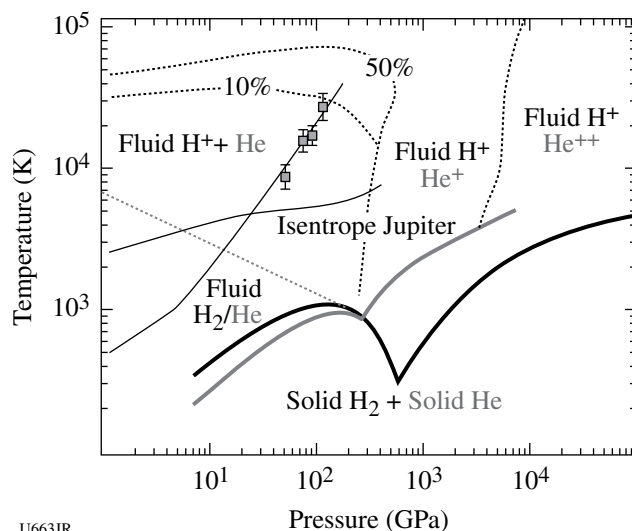

Figure 112.43
Temperature versus pressure for He/H_2. These are the first high-temperature, high-pressure data collected for this mixture that provide key information on the properties of the H_2–He mixtures dominating giant planetary interiors.

Experimental Astrophysics on the OMEGA Laser

Principal Investigator: R. P. Drake (University of Michigan)
Co-investigators: D. Arnett (University of Arizona); T. Plewa (Florida State University); A. Calder, J. Glimm, Y. Zhang, and D. Swesty (SUNY Stony Brook); M. Koenig (LULI, Ecole Polytechnique, France); C. Michaut (Observatorie de Paris, France); M. Busquet (France); J. P. Knauer and T. R. Boehly (LLE); P. Ricker (University of Illinois); B. A. Remington, H. F. Robey, J. F. Hansen, A. R. Miles, R. F. Heeter, D. H. Froula, M. J. Edwards, and S. H. Glenzer (LLNL)

The OMEGA laser is able to produce processes similar to those that occur in astrophysics because it can generate extremely high energy densities, corresponding to pressures greater than 10 Mbar in millimeter-scale targets. This project is focused on two such issues in astrophysics: the contribution of hydrodynamic instabilities to the structure in supernovae and the dynamics of radiative shock waves. To explore hydro-dynamic instabilities in supernovae, it was necessary to develop new radiographic diagnostics capable of improved imaging in two orthogonal directions. We have accomplished this goal and are proceeding to study the contributions of various initial modes to the enhanced spike penetration.

In the experiment, ten OMEGA laser beams irradiate a plastic disk with UV light for 1 ns. The total energy of the beams is ~5 kJ and the average irradiance is ~9.5×10^{14} W/cm^2, producing an ablation pressure of ~50 Mbar in the plastic layer

of the target. This large pressure creates a strong shock in the plastic material, which evolves into a blast wave. The blast wave crosses a perturbed interface into a lower-density material. This process is similar to what occurs in a supernova explosion. In the experiment, we monitor the unstable evolution of the interface between the two materials using x-ray radiography.

Figure 112.44 shows data from the latest experiments to obtain physics data using simultaneous, orthogonal, point-projection backlighting. The data are obtained by using a brief (1-ns) x-ray source to project a signal onto an exposed piece of x-ray film. This experiment was imaged 21 ns after the initial laser beams had been pulsed. One can see on these images the structures that have evolved from an initial condition defined by
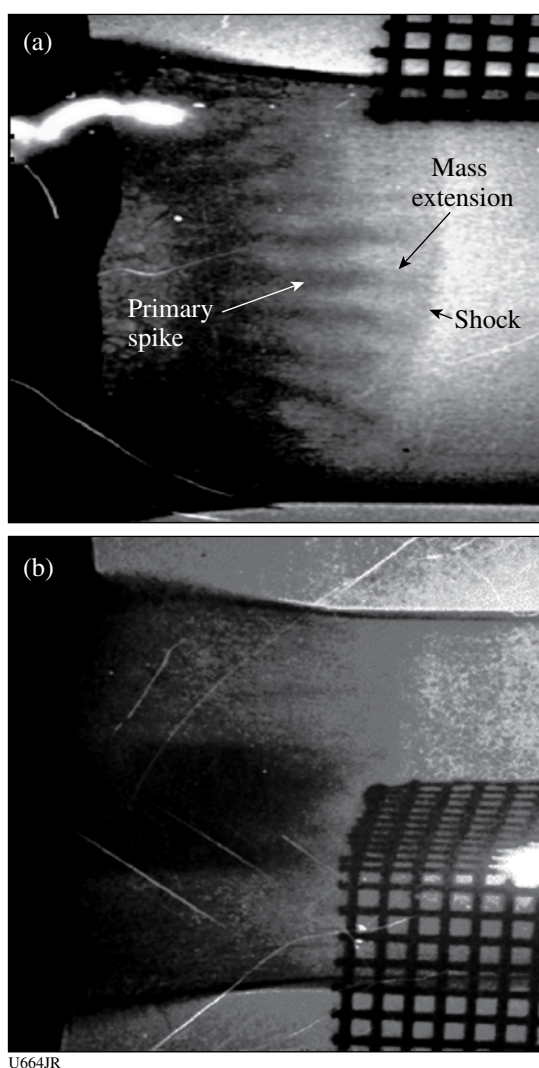

Figure 112.44
Simultaneous, orthogonal, point-projection x-ray backlighting images (a) and (b) of blast wave propagation in plastic material.

$a_0 \sin(kx)\sin(ky)$, where $a_0 = 2.5$ μm and $k_x = k_y = 2\pi/(71$ μm). Image (a) shows mass extensions that extend from the primary spike toward the shock. This phenomenon has not been previously observed. We have also studied the impact of a selected range of initial conditions. In the next year we plan to do an experiment that will investigate initial conditions more realistic to an actual supernova.

Laboratory Experiments on Supersonic Astrophysical Flows Interacting with Clumpy Environments

Principal Investigator: P. Hartigan (Rice University)
Co-investigators: R. Carver (Rice University); A. Frank (University of Rochester); P. A. Rosen, J. M. Foster, and R. Williams (AWE, UK); B. H. Wilde and R. Coker (LANL); B. E. Blue (LLNL)

Supersonic directed jets and outflows are important components of many astrophysical systems. Their interaction with surrounding matter results in the creation of spectacular bow shocks and the entrainment of dense clumps of interstellar material; it may also result in significant deflection of the collimated jet. The objective of this sequence of NLUF experiments is to develop a laboratory platform to study the hydrodynamics of these processes; the laboratory work is complementary to astrophysical observations using the Hubble Space Telescope (HST) and the Kitt Peak National Observatory (KPNO); furthermore, the same computer codes will be used to interpret both the laboratory and astrophysical observations.

In previous experiments on OMEGA, we have developed an experimental platform to create a dense, supersonic, titanium-plasma jet propagating through low-density foam,[10] and we have studied the deflection of this jet by a localized density perturbation.[11] During the past year, two shot days were allocated to this project: we investigated structure potentially seeded in the jet by granularity of the foam medium used in the OMEGA experiments (no significant effect was found), and we progressed further into our project by beginning our study of the interaction of a strong shock with a spherical density discontinuity in the foam. Excellent experimental data were obtained (Fig. 112.45), thereby laying the foundations for further work to study the interaction of shocks and jets with multiple clumps of material—phenomena also being observed in ongoing work using HST and KPNO. The OMEGA experiments were an important component of the case for these further astronomical observations, and our aim is to build a synergistic relationship between experiments, observation, and modeling that will provide new insight into these complex phenomena.
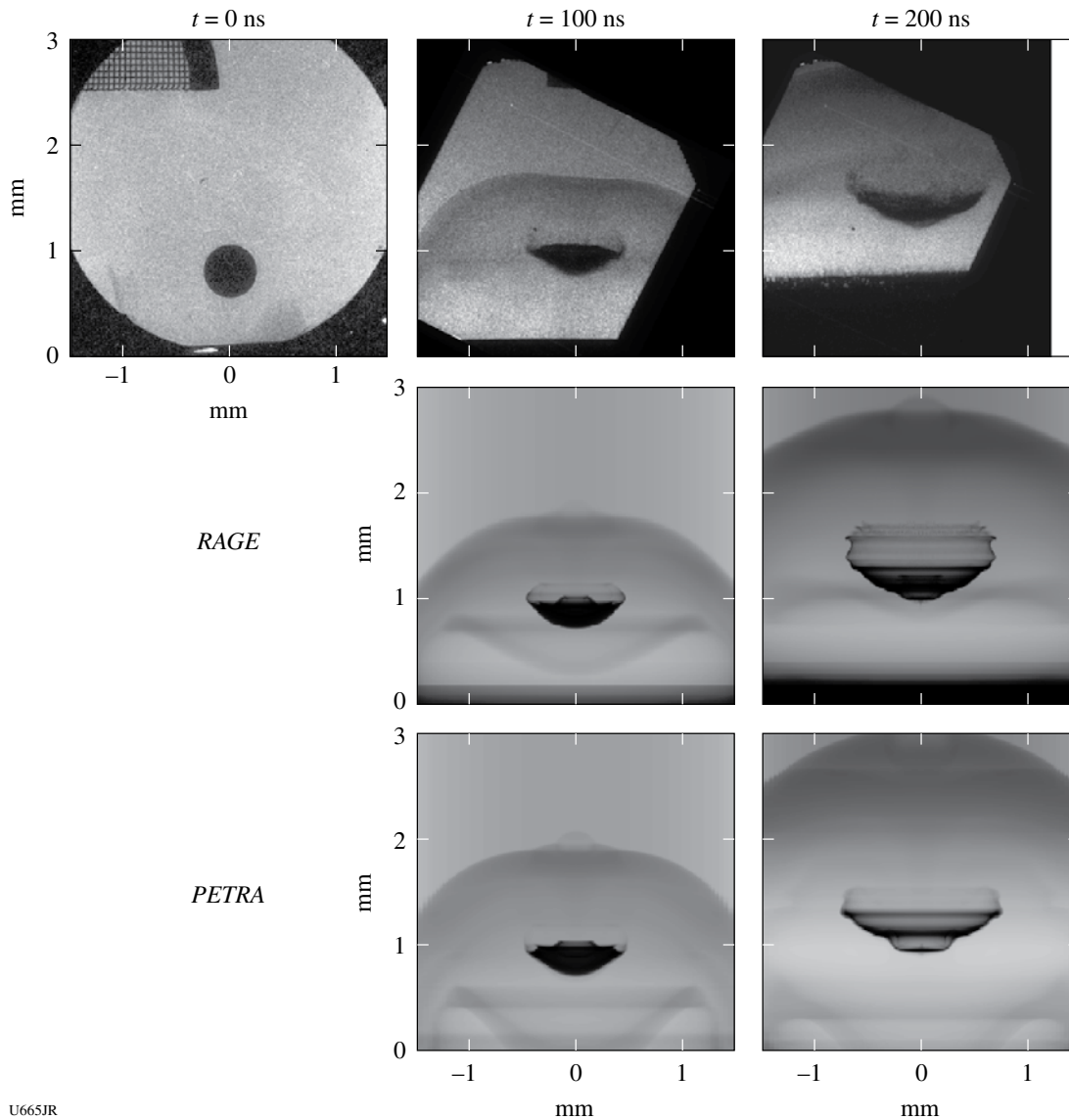
Figure 112.45

Interaction of a strong shock with a density "clump." The OMEGA laser drives a shock through hydrocarbon foam containing a 500-μm-diam sapphire sphere. The sequence of experimental images (top) at 0, 100, and 200 ns shows the shock-driven distortion and entrainment of the sphere by the hydrodynamic flow. The data are compared with modeling (center and bottom) using the *RAGE* and *PETRA* hydrocodes. These phenomena are analogous to those observed in Hubble Space Telescope images of astrophysical jets propagating through interstellar matter.

Multiview Tomographic Study of OMEGA Direct-Drive-Implosion Experiments

Principal Investigator: R. Mancini (University of Nevada, Reno)
Co-investigators: R. Tommasini, N. Izumi, and J. A. Koch (LLNL);
I. E. Golovkin (PRISM); D. A. Haynes and G. A. Kyrala (LANL);
J. A. Delettrez, S. P. Regan, and V. A. Smalyuk (LLE)

The determination of the spatial structure of inertial confinement fusion implosion cores is an important problem of high-energy-density physics. To this end, three identical multi-monochromatic imagers (MMI) have been designed, built, and fielded in OMEGA implosion experiments to perform observations along three quasi-orthogonal lines of sight (LOS). The implosions were driven with 60 OMEGA beams—23 kJ of UV energy in a 1-ns-duration square laser pulse; the targets were gas-filled plastic shells. At the collapse of the implosion, the hot, dense core plasma achieved temperatures in the 1- to 2-keV range and electron number densities between 1×10^{24} cm^{-3} and

2×10^{24} cm^{-3}. X-ray K-shell line emission from the argon dopant added to the fuel is a suitable spectroscopy diagnostic for this temperature and density range. In addition, x-ray absorption from a titanium tracer layer embedded in the plastic yields information about the state of the compressed shell.

Core images recorded by MMI instruments are formed by a large array of 10-μm-diam pinholes with an ~100-μm separation between pinholes and are reflected off a depth-graded WB$_4$C multilayer mirror with an average bilayer thickness of 15 Å. The instrument is equipped with 10-cm-long mirrors that permit the observation of narrowband x-ray images over a photon energy range from 3 to 5 keV. They have a magnification of 8.5, provide spatial resolution of approximately 10 μm, and record gated (framed) images characteristic of a 50-ps time interval. The broad photon energy range, afforded by the use of long mirrors, covers the K-shell line emission from argon ions as well as the K-shell line absorption from titanium L-shell ions. As an illustration of the data recorded by MMI, Fig. 112.46 displays a time history (i.e., three frames) of narrowband x-ray core images from OMEGA shot 47485 recorded along one LOS

at the collapse of the implosion; also shown are examples of narrowband image reconstruction from the data for several spectral features. The data effectively resolve time, space, and photon energy, and show several argon line emissions, namely Ly$_\alpha$ ($1s\,^2S$–$2p\,^2P$, $h\nu = 3320$ eV), He$_\alpha$ ($1s^2\,^1S$–$1s2p\,^1P$, $h\nu = 3140$ eV), Ly$_\beta$ ($1s\,^2S$–$3p\,^2P$, $h\nu = 3936$ eV), and He$_\beta$ ($1s^2\,^1S$–$1s3p\,^1P$, $h\nu = 3684$ eV). The photon energy range of these images is given by the (mainly) Stark broadening widths of the line shapes, which is 60 eV to 70 eV for the plasma conditions achieved in these cores. Core dimensions are in the 60- to 120-μm range. In addition, x-ray absorption in the shell due to titanium ions is also observed. These absorption features are formed by line transitions from $n = 1$ to $n = 2$ in L-shell titanium ions (e.g., F-like, O-like, etc.) in the photon energy range from 4500 to 4750 eV driven by continuum radiation emitted in the core, and their analysis permits the characterization of the compressed shell. It is interesting to observe the differences in distribution of brightness associated with the line-based core images, which depends on both temperature and density conditions in the core. Detailed spectral modeling and analysis of the emissivity and opacity of the argon x-ray
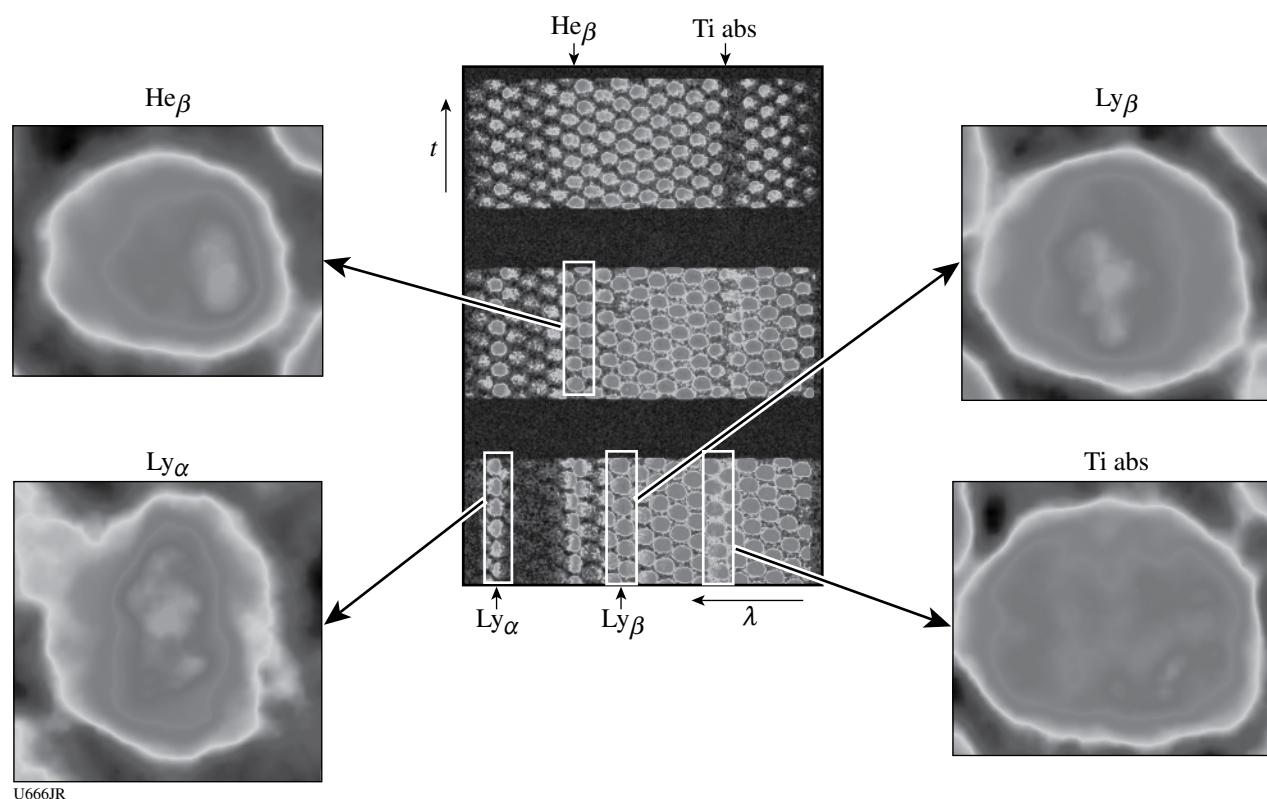

Figure 112.46
Time history (three center frames) of narrowband, x-ray core images recorded by MMI and four narrowband image reconstructions from this data (OMEGA shot 47485).

emission permit a reconstruction of the spatial structure of the core plasma. Several analysis methods are currently being investigated that simultaneously consider data observed along several lines of sight.

Monoenergetic Proton Radiography of Laser–Plasma-Generated Fields and ICF Implosions

Principal Investigators: R. D. Petrasso and C. K. Li (Massachusetts Institute of Technology)
Co-investigators: J. A. Frenje and F. H. Séguin (MIT); J. P. Knauer and V. A. Smalyuk (LLE); R. P. J. Town (LLNL)

MIT's NLUF program has continued an ongoing series of experiments using monoenergetic charged-particle radiography to study transient electromagnetic fields generated by the interaction of OMEGA laser beams with plastic foils. This work, involving novel studies of time evolution, field instabilities, and magnetic reconnection, has resulted in the publication of three Physical Review Letters publications[12–14] and two invited talks at APS conferences.[15,16]

Figure 112.47 shows the basic experimental setup.[17] One or more OMEGA laser beams interact with a plastic foil, generating plasma bubbles, **B** fields, and **E** fields. A special backlighter and matched imaging detector are used to create a radiographic image of the resultant plasma/field structure. The backlighter is a glass-shell ICF capsule filled with D^3He gas and imploded by 20 OMEGA laser beams, producing D^3He protons (14.7 MeV), DD protons (3 MeV), D^3He alpha particles (3.6 MeV), and a few other fusion products. CR-39 nuclear track detectors are used in conjunction with appropriate filters and processing techniques to record individual charged particles and their energies in the detector plane. Since the burn duration of the D^3He implosion is short (~130 ps) relative to the nanosecond-scale duration of
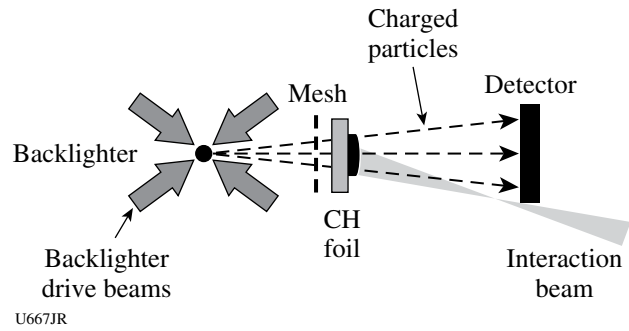

Figure 112.47
Schematic illustration of the experiment setup and the physical relationship between the proton backlighter (imploded D^3He-filled capsule), mesh, CH foil, CR-39 imaging detector, and OMEGA laser beams. Distances of the components from the backlighter were 0.8 cm for mesh, 1 cm for foil, and 30 cm for detector. The hole-to-hole spacing in the mesh was 150 μm.

the foil illumination and subsequent evolution, and since the relative timing of the backlighter and the foil illumination was adjustable, it is possible to record images at different times relative to the foil illumination. A metal mesh is interposed between the backlighter and the foil to divide the incident particle flux into beamlets; distortion in the mesh pattern at the detector shows how the particle trajectories were deflected by the fields generated by laser–plasma interactions at the foil.

In one series of experiments (Fig. 112.48), field evolution and instabilities were studied with 14.7-MeV proton radiography when a single interaction beam was used. While the 1-ns interaction beam was on, the plasma bubble and its surrounding megagauss **B** field expanded symmetrically and roughly linearly, but then became increasingly asymmetric as expansion continued and field strength decayed. We believe this is the first direct observation and evidence of the pressure-driven, resistive-interchange instability in laser-produced high-energy-

Figure 112.48
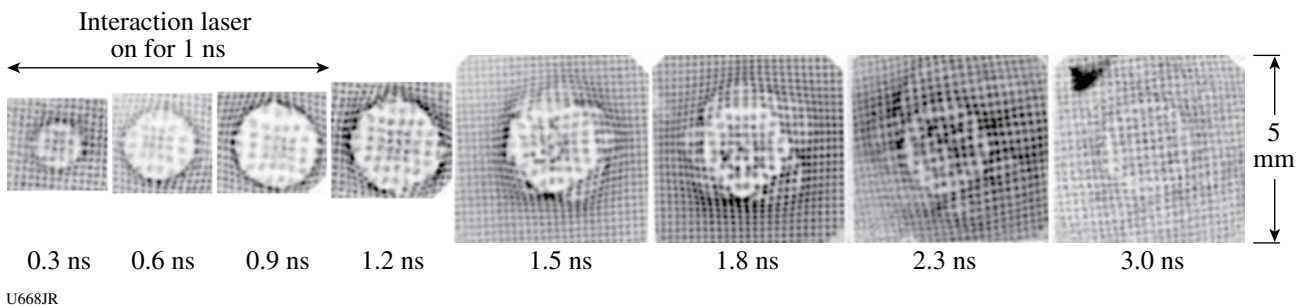Radiographs showing the spatial structure and temporal evolution of the **B** fields generated by laser–plasma interactions. Each image, made with 14.7-MeV protons, is labeled by the time interval between the arrival at the foil of the interaction beam and the arrival of the imaging protons, and each image corresponds to an area about 5 mm by 5 mm at the foil. Note that the laser was on for only 1 ns.

density plasmas. Details and quantitative analysis are given in Ref. 13. In a second series of experiments utilizing 14.7-MeV-proton radiography, multiple laser interaction beams were used simultaneously and resulted in the first direct observation of field reconnection in the high-energy-density regime. Figure 112.49 shows plasma bubbles resulting from two interaction lasers at a time when the bubbles have expanded just enough to contact each other. Quantitative field maps derived from the radiographs revealed precisely and directly, for the first time, the changes in the magnetic topology that resulted from reconnection. Details may be found in Ref. 14.
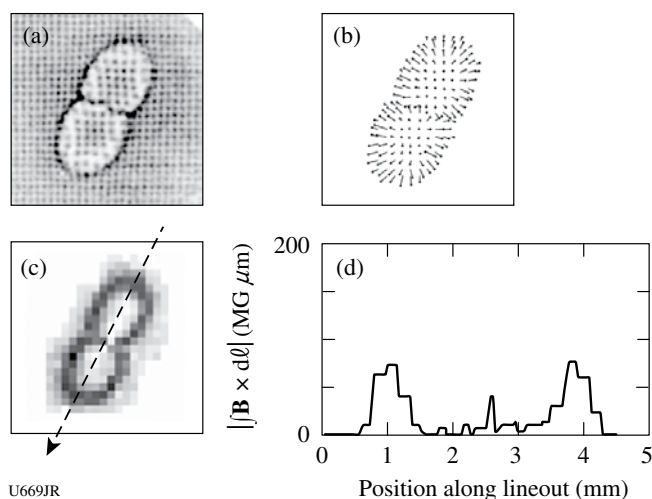

Figure 112.49

A monoenergetic proton radiograph of two plasma bubbles generated in a foil by two interaction lasers was used to deduce a map of the **B** field at the foil. In (a), the location of each beamlet can be compared with the location it would have had with no **B** fields (beamlets on the image edges define the grid of "undeflected" locations); (b) shows displacement vectors. The displacement amplitudes are shown as an image in (c), where each pixel represents one beamlet, with value proportional to displacement. Displacement is proportional to $\int \mathbf{B} \times d\ell$ along the particle trajectory, so the lineout along the arrow in (c) provides quantitative measurements of $\left| \int \mathbf{B} \times d\ell \right|$ at the foil location (d), showing the loss of field energy where the bubbles collided and magnetic reconnection occurred.

X-Ray Compton Scattering on Compressed Matter
Principal Investigators: R. Falcone and H. J. Lee (University of California), P. Neumayer, O. L. Landen, and S. H. Glenzer (LLNL)

These experiments are aimed to measure exact electron density (n_e), temperature (T_e), and ionization (Z) of dense matter with the development of the Compton-scattering technique on the OMEGA Laser Facility. Since an x-ray source can propagate through the critical electron density ~10^{22} cm^{-3},

x-ray Compton scattering has been the most useful diagnostic of local plasma conditions of dense matter with solid density and above. The Compton-scattering cross-section diagnostic is related to the dynamic structure factor $S(k,\omega)$, which presents the Fourier transform of total electron-density fluctuation. It has been understood by decomposing total density distribution: the sum of the motion of electrons and the motion of ions.

Two types of a planar Be target coupled with Mn backlighter are designed for the x-ray Compton-scattering technique with 90° and 25° scattering angles at the OMEGA Laser Facility. The target consists of 250-μm-thick Be, 50-μm-thick plastic substrate coated with 3 μm of Mn, 50 μm of Ta with a slot window, and two Au/Fe shields, as shown Fig. 112.50(a). Eleven heater beams of 4-ns flat pulse, $I_{av} \sim 2 \times 10^{14}$ W/cm^2 at 531 nm, are focused symmetrically onto solid Be with an ~800-μm
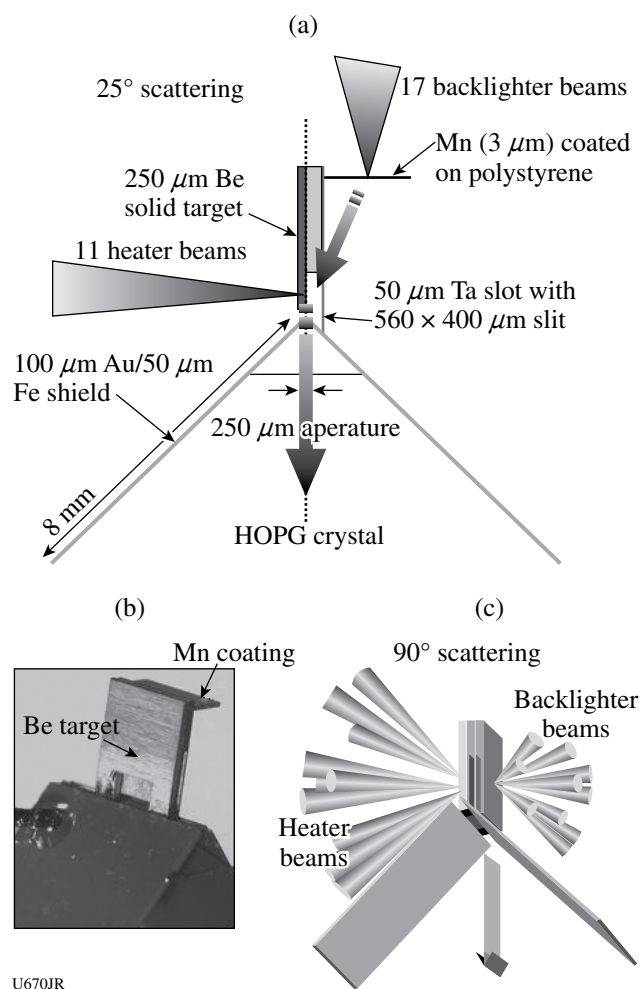

Figure 112.50
(a) Schematic of the target details for 25° scattering; (b) a real image of the target; (c) target schematic for 90° scattering.

spot. To create ~6.18-keV Mn He$_\alpha$ x-ray photons, we applied 12 backlighter beams to Mn-coated plastic for 25° scattering (17 backlighter beams for 90° scattering) with a focal spot of 200 μm. Figures 112.50(b) and 112.50(c) present a photograph of 25° scattering target and an image for 90° scattering target that has a Mn backlighter parallel to Be. A highly oriented pyrolytic graphite (HOPG) crystal coupled to an x-ray framing camera with 500-ps gating time in TIM3 has been used as a spectrometer and a detector.

Figures 112.51(a) and 112.51(b) show scattering spectra (black lines) and fits (thick white lines) to the data of 90° and 25° scattering geometries. In the noncollective scattering regime of 90°, the spectrum shows Compton down-shifted peaks in addition to the elastic-scattering peaks at E_{01} = 6.18-keV Mn He$_\alpha$ and E_{02} = 6.15-keV intercombination x-ray lines. With the broadening by the thermal motion of electrons, the intensity and shape of Compton peak are sensitive to T_e and n_e. For the analysis, we calculated $S(k,\omega)$, theoretical x-ray scattering spectra using random phase approximation. The calculated spectrum with n_e = 7.5 × 10^{23} cm^{-3}, T_e = 13 eV, and Z = 2 for a Fermi temperature of E_F = 30 eV gives a best fitting to the data. The 25° forward scattering independently provides a unique data set on the n_e and Z of compressed matter. In the collective scattering regime, the probing wavelength is larger than Debye screening length and scattered spectrum is dominated by plasmon resonance, which is associated with electron

plasma wave resonance. The measured spectra of Fig. 112.51(b) show downshifted plasmon peaks; the position of the peak is very sensitive to n_e. The thick white line presents a best fitting to the data. The n_e and T_e measured from the plasmon peak show very good agreement with the parameters obtained from the backscattering spectra as well as from the hydrodynamic calculation on compressed Be plasmas.

Through this project, we successively measured the Compton and plasmon resonance on shock-compressed Be. With the comparison to the theoretical calculation, we find that compressed plasmas of n_e = 7.5 × 10^{23} cm^{-3}, T_e = 13 eV, and Z = 2 within ~10% error bars could be reached under the pressure in the range of 20 to 30 Mbar. From these experiments, we have proved that the x-ray Compton-scattering technique is a precise experimental tool for determining the exact densities and temperatures in compressed matter and characterized compressed states of matter.

FY07 LLNL OMEGA Experimental Programs

In FY07 Lawrence Livermore National Laboratory (LLNL) led 404 target shots on the OMEGA Laser System. This total represents a shot rate approximately 8% higher than nominal (373 shots scheduled for the year). This is an improvement over last year's operations (4% above nominal) and is especially noteworthy considering that programmatic needs frequently require complex configuration changes both overnight and mid-day.

National Ignition Campaign (NIC) Experiments: About 57% of the LLNL shots were dedicated to advancing the National Ignition Campaign in preparation for future experiments at the National Ignition Facility (NIF). This represents a slight percentage decrease from the prior year, as effort transitions to NIF itself. Campaigns on OMEGA had many objectives, including studies of the laser–plasma interaction (LPI) physics in physical conditions relevant for the NIF ignition targets, improving the diagnostic suite for ignition, and studying dense-plasma physics via collective x-ray scattering; however, this year there was a special emphasis on assessing the physical characteristics of proposed ignition capsule materials.

A variety of LPI experiments were conducted in FY07, some in collaboration with CEA, typically using gas-filled hohlraums arranged so that one OMEGA beam (beam 30) could be used as an on-axis probe beam.

In work now submitted for publication, experiments demonstrated a significant reduction of stimulated Brillouin scattering (SBS) by polarization smoothing in conditions (T_e ~
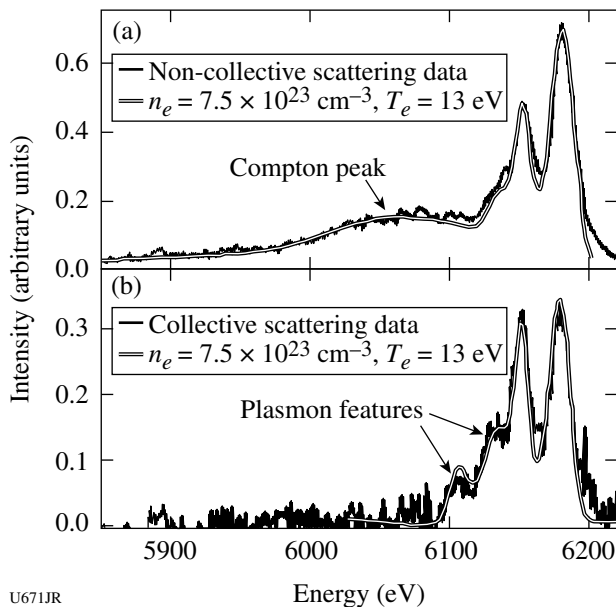

Figure 112.51
Experimental scattering data (black line) and fitting results (thick white line) of (a) 90° scattering geometry and (b) 25° scattering geometry.

U671JR

3 keV) with no ponderomotive and thermal filamentation (see Fig. 112.52). Measurements showed that adding polarization smoothing increases the intensity threshold for SBS by a factor of 1.7. For intensities less than 2×10^{15} W/cm^2, more than an order of magnitude reduction in the backscattered power is observed. This reduction in backscatter was shown to increase the total transmission through a plasma for conditions that are comparable to those in current ICF target designs. A simple model relevant to ICF plasma conditions is able to explain a direct effect on the SBS gain exponent and, consequently, the threshold for when SBS becomes energetically important.
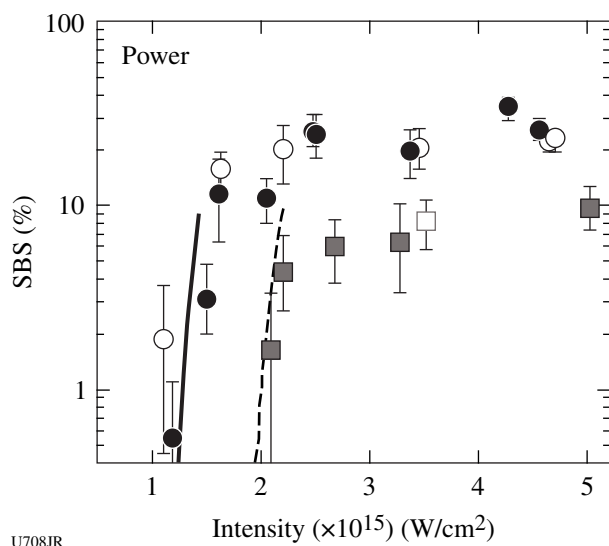

Figure 112.52
The measured instantaneous SBS reflectivity at $t = 700$ ps is plotted as a function of the interaction beam intensity; three laser-smoothing conditions are shown: continuous phase plates (CPP's, circles), CPP's plus polarization smoothing (squares), and with 3-Å SSD (open circles). The calculated reflectivities using an analytical model reproduce the measured thresholds and a factor-of-1.7 reduction in the SBS threshold when polarization smoothing is applied to a CPP smoothed laser beam. An analytical model that calculates the thresholds is shown for the CPP only (solid curve) and when polarization smoothing is applied (dashed curve).

Another experimental result now submitted for publication, and detailed in Fig. 112.53, extends the limits of plasma length in inertial fusion laser–plasma interaction experiments. Laser-beam propagation and low backscatter were demonstrated in laser-produced hohlraum plasmas of ignition plasma length. At intensities $<5 \times 10^{14}$ W/cm^2, greater than 80% of the energy in a blue (351-nm) laser is transmitted through an $L = 5$-mm-long, high-temperature ($T_e = 2.5$ keV), high-density ($n_e = 5 \times 10^{20}$ cm^{-3}) plasma. For an intensity of $I = 6 \times 10^{14}$ W/cm^2, these experiments also show that the backscatter scales exponentially with plasma length, from <0.05% at a 1.3-mm length to >10%
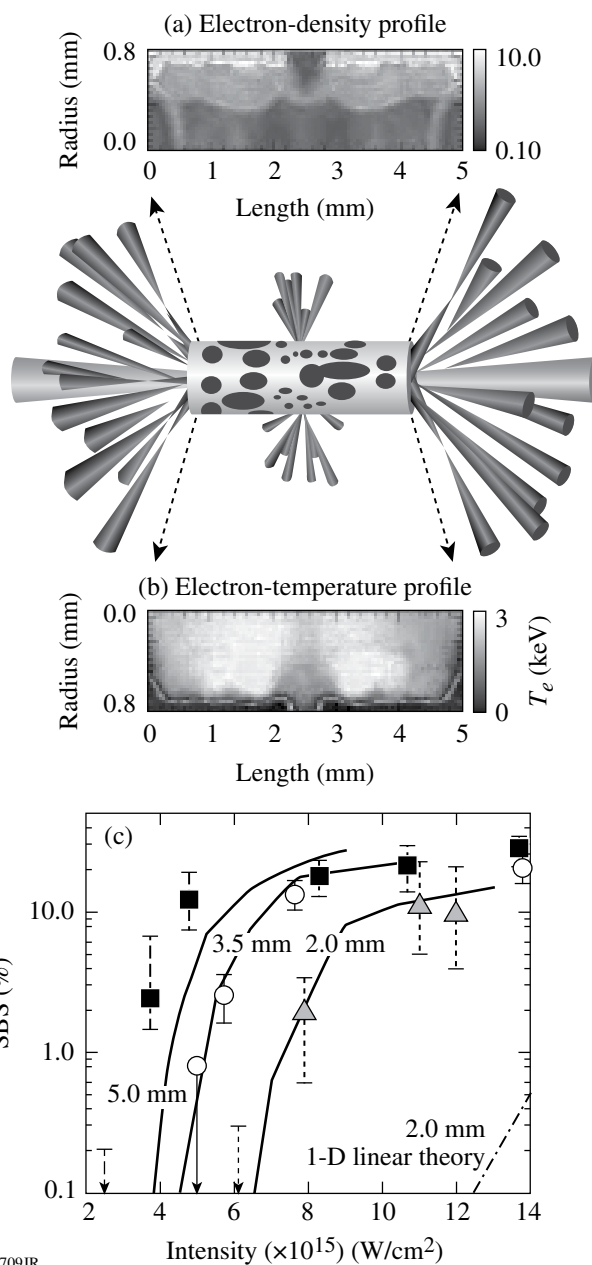
Figure 112.53
(a) Simulated electron-density and electron-temperature profiles for a 5-mm-long LPI hohlraum at peak electron temperature (900 ps after the heater beams turn on). Three LEH's are equally spaced around the hohlraum equator to allow the addition of 17 laser beams. In total, 53 laser beams irradiate the hohlraum wall, producing electron temperature T_e along the axis in excess of 2.5 keV. The interaction beam is aligned along the axis of the hohlraum, interacting with a uniform 5×10^{20}-cm^{-3} plasma plateau. (b) The measured instantaneous SBS reflectivity is plotted as a function of vacuum intensity for the three target lengths: 2 mm (triangles), 3.5 mm (circles), and 5 mm (squares). The solid curves are simulations performed by SLIP. For reference, a curve is shown (dashed) calculated using linear theory for the 2-mm-long targets where a gain of $\Gamma_s \beta_s = 11$, for an intensity of 1×10^{15} W/cm^2, is determined by post processing the hydrodynamic parameters.

at a 4.0-mm length. This result is consistent with linear theory. The backscatter calculated by a new steady-state, 3-D laser–plasma interaction code (SLIP) developed for large ignition plasmas is in good agreement with the measurements. These results span the gap between previous studies ($L < 2$ mm, $T_e = 2.5$ keV) and future ignition hohlraum plasmas ($L = 5$ mm, $T_e > 3$ keV) and indicate that backscatter can be controlled at ignition plasma conditions and intensities.

Additional laser–plasma interaction experiments on the high-electron-temperature gas-filled hohlraum target platform demonstrated the effectiveness of Landau damping in multiple-ion species plasmas to reduce backscatter. By adding hydrogen to a CO_2 gas fill, the SBS reflected power was suppressed from >30% to ~1%, while SRS was below the detection threshold (Fig. 112.54). Improved heater beam coupling into the hohlraum by suppression of the total backscatter resulted in an increase in measured hohlraum radiation temperature. As a result of these findings, a multiple-ion-species gas fill is now included in the NIC hohlraum point design.
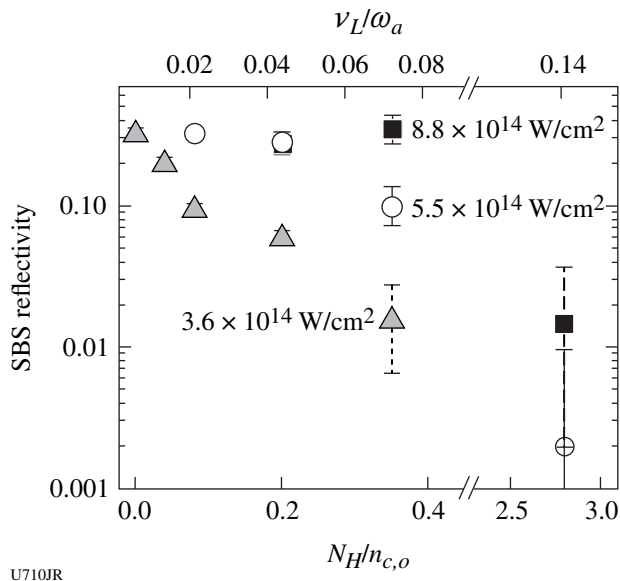

Figure 112.54
The SBS reflectivity is reduced from >30% to ~1% when increasing Landau damping by adding hydrogen to the CO_2 hohlraum gas fill (probe-beam intensities of 3.6, 5.5, and 8.8×10^{14} W/cm^2).

In pursuit of a more precise understanding of hohlraum energetics, and to develop methods for diagnosing possible ignition failure modes, half of an extended day was dedicated to a series of shots designed to study the impact of x-ray flux originating from outside the laser entrance hole (LEH) of a laser-heated hohlraum—measured with the OMEGA DANTE diagnostic—

on the interpretation of the observed radiation temperature inside the hohlraum. An empty gold hohlraum was heated with 38 beams using a 2.6-ns-long pulse. In addition, two beams were used to illuminate the hohlraum outside of the LEH. One beam had a large spot size, mimicking the effect of LEH closure during the heating; the second beam had a small spot size, providing an indicator of the x-ray emission due to a mispointed heater beam. A soft x-ray imager was used to identify the various sources of x-ray emission, and Fig. 112.55 shows a set of images for three different x-ray regimes, i.e., around 250 eV, 750 eV, and above 2 keV. For this particular shot, the start times of the cone 2 and cone 3 heater beams were tuned to also study the spot formation. The series of shots indicated that without correcting the x-ray flux measured by DANTE with respect to its origin, the derived radiation temperature was about 1% higher.
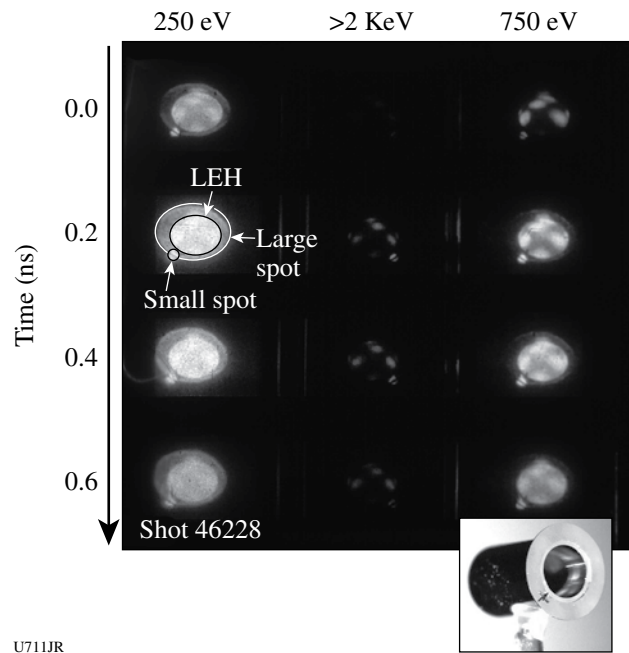
Figure 112.55
Soft x-ray images taken from the laser-heated Au hohlraum, together with a picture of the target. The x-ray images show the emission from the LEH with various spots from the heater beams. Additional x-ray emission originates from a large beam spot and a small beam spot, which hit the gold washer and provide the required emission area outside of the LEH to mimic the "LEH closure" scenario. The washer also contains a spatial fiducial (cross hair).

Progress also continued in characterizing the physical properties of warm, dense matter. Experiments studying x-ray scattering on radiatively heated solid-density beryllium at different scattering angles provided a first direct test of dense matter theories describing ion–ion correlations at long scalelengths in dense matter, as shown in Fig. 112.56.

$n_e = 2.8 \times 10^{23}$ cm^{-3}; $T_e = T_i = 12$ eV

U712JR
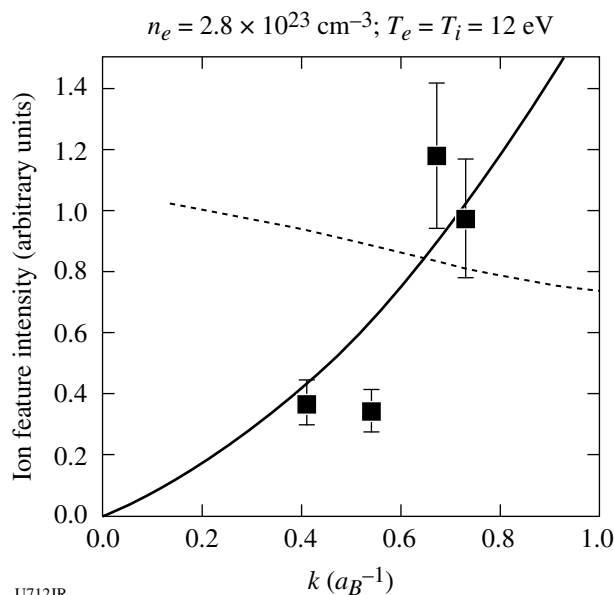
Figure 112.56
Comparison of measured elastic scattering feature with theoretical predictions, showing better agreement with the HNC TCP calculations.

Ignition capsules face challenging physics requirements since they must transmit shocks into the DT ignition fuel without also producing hydrodynamic instabilities that would dilute the fuel with higher-Z ablator material. This translates into requirements for very low surface roughness and specific shock response properties. In FY07, the physical properties of capsules based on copper-doped beryllium and high-density carbon (synthetic diamond) were studied extensively, using new techniques that significantly extend previous work on, e.g., Rayleigh–Taylor growth measurements, imploding-capsule radiography, and velocity interferometry of shocked surfaces.

Simulations predict that residual microstructure and velocity fields in melted Be could still seed some hydrodynamic instabilities upon shock breakout, but at a level below that expected and acceptable from growth of known surface imperfections. To validate these expectations, we have designed OMEGA experiments that amplify their perturbation seeding using high-growth-factor [GF ~ exp($\gamma\tau$)] Rayleigh–Taylor instability drives. To achieve this, an 8- to 10-ns-long drive has been developed [see Fig. 112.57(b)], which for a given achievable radiographic accuracy, ΔGF/GF $= \tau\Delta\gamma$, leads to an improved growth-rate accuracy $\Delta\gamma \sim 1/\tau$. This drive also provides sufficient sensitivity to directly measure, through x-ray radiography, 3-D growth from BeCu planar foils with a level of surface roughness equal to the NIF ignition design surface-roughness tolerance [see Fig. 112.57(c)]. The results—when compared to simulations that ignore possible growth from Be microstructure

(a) Acceleration

(b)

(c)

Box is 50-μm square

U713JR

Figure 112.57
(a) Experimental setup for ablation-front Rayleigh–Taylor growth measurement; (b) measured versus calculated x-ray drive T_r; (c) 4.3-keV radiograph of growth of NIF-surface roughness on Be(Cu) foil at 8.2 ns.

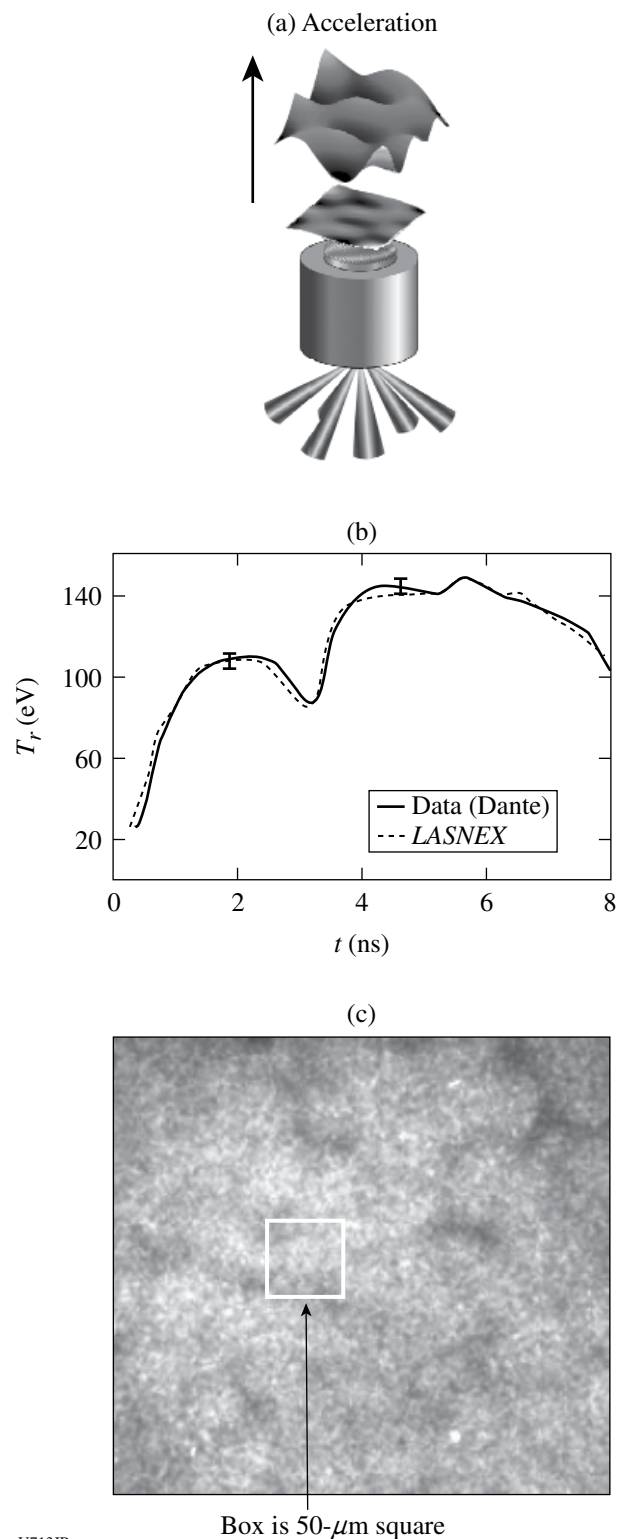and, hence, consider only growth from surface perturbations—suggest that, at least for ablation-front instability growth, microstructure is not important.

Determining ablator performance during an implosion is a critical part of the NIF tuning campaign. In particular, it is vital to have accurate, time-resoved, in-flight measurements of the velocity, areal density, and mass of the ablator as it converges. In tests on OMEGA we have developed a new technique that achieves time-resolved measurements of all these parameters in a single, area-backlit, streaked radiograph of an indirectly driven capsule. This is accomplished by first extracting the radial density profile at each time step from the measured radiograph; then scalar quantities such as the average position, thickness, areal density, and mass of the ablator are determined by taking integral moments of this density profile. Results from implosions of Cu-doped Be capsules are shown in Fig. 112.58.
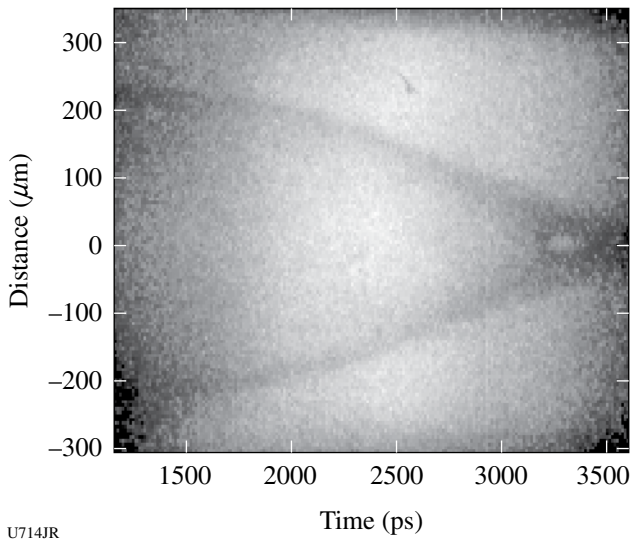
Figure 112.58
Streaked radiograph showing converging capsule leading up to bang time at 3300 ps.

Synthetic diamond is a promising ablator material for ICF capsules because of its low-Z and high density. It is important, however, to know the high-pressure phase diagram of diamond since the tuning design for ICF capsules requires that the first-shock state remain completely solid and the second-shock state be completely melted. Having successfully measured first-shock melting of diamond on OMEGA last year, a new method was developed this year to detect second-shock melting. This involved launching a first shock into diamond between 2 to 4 Mbar, followed by a strong second shock between

15 and 25 Mbar. As shown in Fig. 112.59, by measuring the thermal emission of the second shock through the transparent first shock, it was possible to determine the temperature of the second-shock Hugoniot versus pressure. Evidence of melting was found in the discontinuity in the second-shock Hugoniot above 20 Mbar.
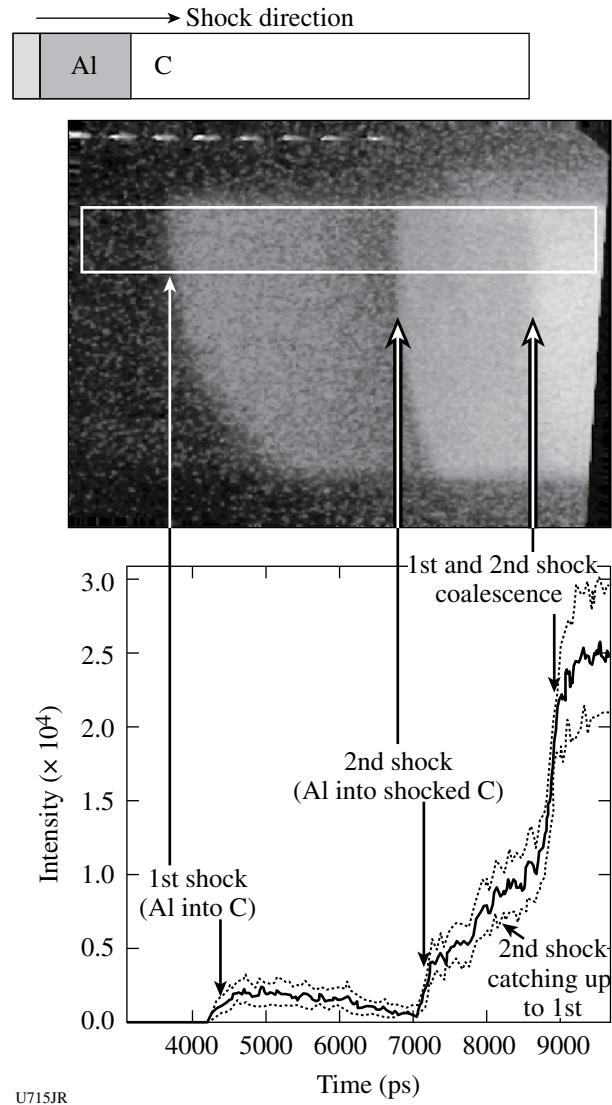
Figure 112.59
Streaked, space-resolved measurement of the thermal emission from a doubly shocked Al/diamond sample.

Determining the level of velocity uniformities created by microscopic perturbations in NIF ablator materials is a challenging measurement task. The measurement diagnostic must detect these nonuniformities at a level of a few parts in 10,000 to be relevant to the NIF requirements. The CAPSEED campaigns were fielded to make these measurements with a

new technique. During FY07 a high-resolution velocity interferometer was fielded on the TIM 6 diagnostic location. The instrument, called the OMEGA High-Resolution Velocimeter (OHRV), is a 2-D space-resolving "velocity interferometer from the surface of any reflector" (VISAR), which probes the velocity distribution across a moving reflecting surface with 2-μm spatial resolution and few-m/s velocity resolution in a single 2-D snapshot. It's main mission is to measure the seed-level nonuniformities in NIF capsule ablator candidate materials and to verify that the seed levels are consistent with current model predictions of capsule performance. Assembly and qualification of the instrument took place during the summer, commissioning in early September, followed by a successful experimental campaign in October (Fig. 112.60). Experiments testing Be(Cu), high-density carbon, and Ge-doped plastic ablators are continuing in FY08.

High-Energy-Density Science (HEDS) Experiments: About 43% of the LLNL shots were dedicated to HEDS campaigns, including quasi-isentropic compression experiments (ICE), dynamic hohlraums, opacity measurements of hot plasmas in local thermodynamic equilibrium (LTE), and non-LTE implosion physics. High-temperature hohlraums, long-duration point backlighter sources, and foam-walled hohlraums were also studied to develop HED experimental platforms for future NIF experiments.

LLNL has for some time been developing laser-based experimental platforms that can compress materials quasi-isentropically to very high pressures at ultrahigh strain rates. This laser-driven, ramped (shockless) drive is used to study material properties such as strength, equation of state, phase, and phase-transition kinetics under extreme conditions. In FY07 an effort was launched to develop a platform compatible with NIF, based on ICE drive by indirect x-ray illumination from a hohlraum onto a reservoir/package assembly on the side of the hohlraum at the midplane.

Development of such a hohlraum-driven ICE platform requires an understanding of the hydrodynamics of hohlraum radiation coupling to the ICE pressure, planarity of the pressure drive on the package, hohlraum filling at late times for package radiography, and potential preheat of the reservoir and package by the hohlraum M band.

Initial experiments used the normal OMEGA VISAR (ASBO) system and a tilted target package (since the VISAR does not have a view orthogonal to a standard hohlraum axis). This approach provided helpful information on obtaining VISAR data from hohlraum packages, but it resulted in hard-to-model 3-D effects on the drive and insufficient planarity. A new tilted ASBO telescope was developed that is able to measure packages normal to the hohlraum axis. It has now
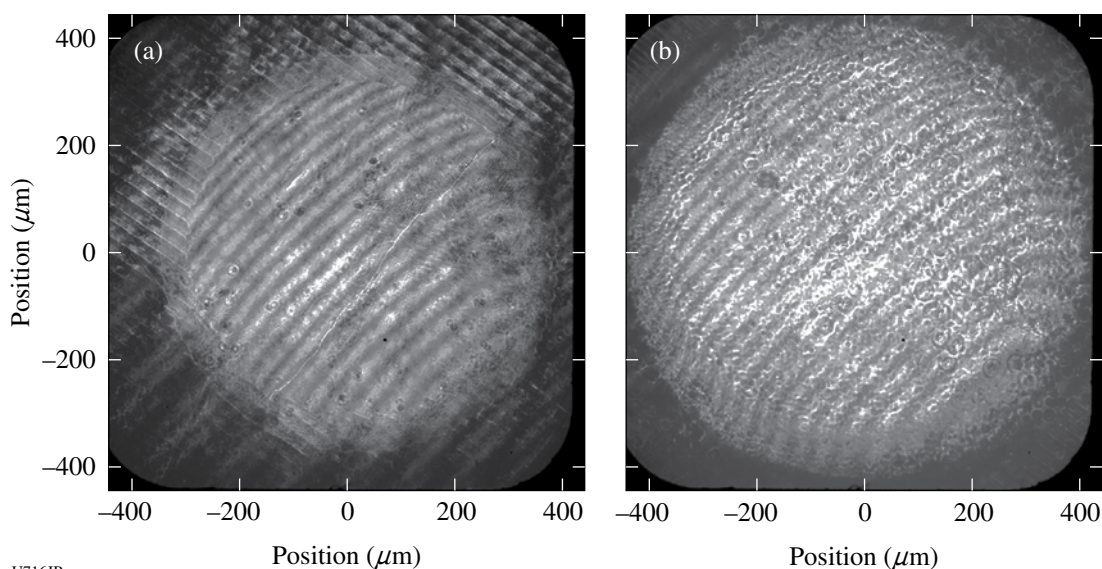
Figure 112.60

(a) Two-dimensional interferogram of a shock front emerging from a Be(Cu) ablator sample approximately 200 ps after breakout into a plastic layer (central 600-μm-diam circular region). Bias fringes run from bottom left to top right; a preimposed ripple machined into the Be surface is visible in the edges of the image (periodic pattern oriented perpendicular to the fringes). (b) Velocity interferogram of a shock front emerging from a diamond ablator into a plastic layer, approximately 1 ns after breakout. The high-frequency spatial modulations superimposed on the fringe pattern indicate nonuniformities in the shock front.

been tested and fully qualified for the next set of experiments, presently scheduled for January 2008.

A parallel set of experiments studied the hohlraum plasma filling at late times. Hohlraums with and without thin CH liners were probed using a 6.7-keV Fe backlighter. The radiographic data were used to assess the Au filling from the walls at late times ($t = 20$, 60, and 80 ns after the hohlraum drive); these results agreed well with 2-D simulations. The hohlraum stays open at late times with minimal filling, providing support for future ICE-driven Rayleigh–Taylor radiography experiments at late times on the NIF.

To understand the drive on the reservoir, the radiation temperatures of different types of hohlraums were studied and compared with *LASNEX* 2-D simulations. Figure 112.61 shows the Dante measurements and *LASNEX* simulations from both CH-lined and non-CH-lined hohlraums. The peak radiation temperature data are in good agreement with the simulation, but the simulation shows the radiation temperature remaining higher later in time than the data indicate. This might be caused by the on-axis stagnation effect, which is more pronounced in the symmetric 2-D simulation as opposed to the experiments, which have enough 3-D effects to reduce the axial stagnation. The study of late-time hohlraum energetics is significant for multiple HEDS campaigns and will continue in FY08.

U717JR
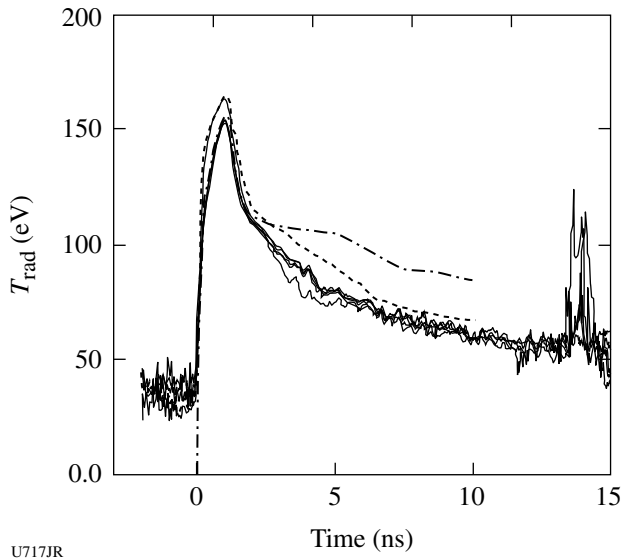
Figure 112.61
Dante radiation-temperature measurements (solid) from scale 1.37 hohlraums driven with 12.5 kJ in a 1-ns square pulse, compared with 2-D *LASNEX* simulations (dashed).

Over the past year, LLNL has continued experiments with laser-driven dynamic hohlraums (LDDH's). These experiments have compared the neutron yield and the areal fuel density produced by "standard" xenon-filled LDDH's (see Fig. 112.62) to those of capsules where the xenon is replaced by neopentane; the latter gas fill replicates the hydrodynamics of a xenon-filled LDDH but does not create the high-Z radiation-trapping cavity (hohlraum), thus making it possible to measure the difference in yield and fuel density due to the hohlraum effect. Analysis of this data is underway. Additional LDDH experiments have explored the robustness of dynamic hohlraums when driven by laser beams in a polar configuration, such as would be necessary on the NIF; the experiment showed that repointing the laser beams along the polar axis can compensate for the nonuniform laser drive.

U608JR
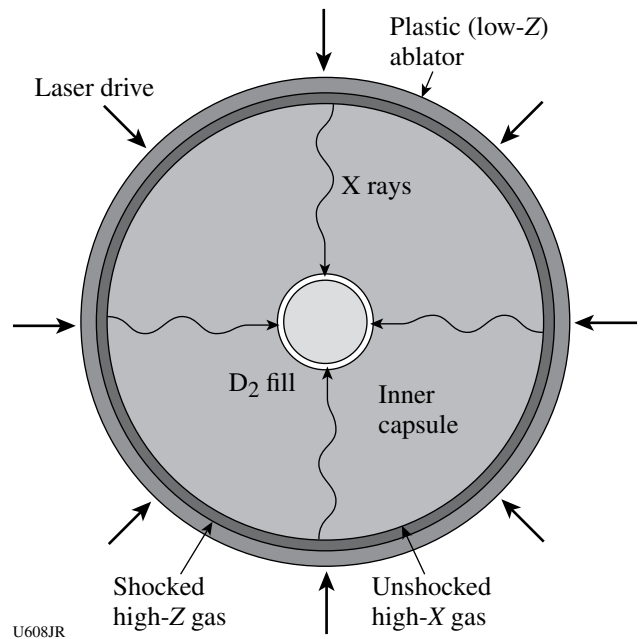
Figure 112.62
Concept of "dynamic hohlraum:" shock-heated Xe gas between shells radiates x rays that ablatively implode inner shell. Data obtained include x-ray-streaked images of the self-emitted x rays, multiple x-ray images, charged-particle information (collaboration with MIT), and multiple standard OMEGA neutron diagnostics.

Prior results having shown that LDDH's emit very bright, spectrally smooth bursts of multi-keV x rays, it was decided to explore whether LDDH's might scale down for use as bright, broadband backlighters suitable for absorption spectroscopy experiments. Early in FY07, a set of small, Kr-filled plastic capsules were imploded using ten polar direct-drive beams and produced bright continuum emission at photon energies up to at least 5.5 keV (Fig. 112.63). These capsules proved bright enough

to use as backlighters for spectroscopic transmission measurements of hot plasmas. Previous continuum x-ray sources either required too many beams (so that the hot plasmas could not be produced) or did not work at photon energies above ~3500 eV (Ref. 18). In a follow-up experiment, initial data were obtained for $n = 1$ to $n = 2$ absorption of Ti samples at LTE conditions near 100 eV inside hohlraums. LLNL plans to use this new capability to measure the temperatures of high-temperature LTE opacity samples in FY08.
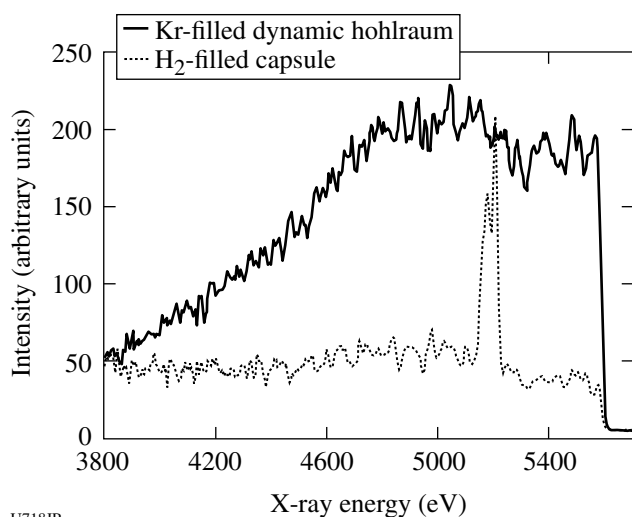
Figure 112.63

Gated spectra produced by an H_2-filled capsule (dotted) and a Kr-filled capsule (solid). Instrument configurations were identical for both shots; Dante data for this band show a factor-of-2 increase in peak x-ray yield. The lines near 5200 eV in the H_2 spectrum are from a vanadium dopant in the shell for that capsule.

The goal of the nonlocal thermodynamic equilibrium (NLTE) campaign is to build a platform to study energy balance in implosions by measuring ion, electron, and radiation temperatures as a function of high-Z dopant concentration. In the FY07 experiments, all 60 beams of the OMEGA Laser Facility were used for direct-drive implosions of thin (4 μm) glass capsules filled with 10 atm of D^3He gas and 0.01 atm of Kr gas as a spectroscopic tracer. We used Xe as the high-Z dopant gas, with concentrations from 0 to 0.06 atm. As a time-resolved electron-temperature (T_e) diagnostic, we fielded a new mica conical crystal spectrometer (Fig. 112.64), which was coupled to a streak camera, and viewed K-shell emission lines from the Kr dopant. Time-integrated spectra were also recorded with the HENEX spectrometer developed by NIST/NRL. The time-resolved spectra show that the addition of Xe reduces T_e proportionally, in agreement with simulations. Time-dependent ion temperatures (T_i), inferred from proton and neutron emission time histories and spectra, also show a reduction in the compression-phase T_i with increasing Xe concentra-
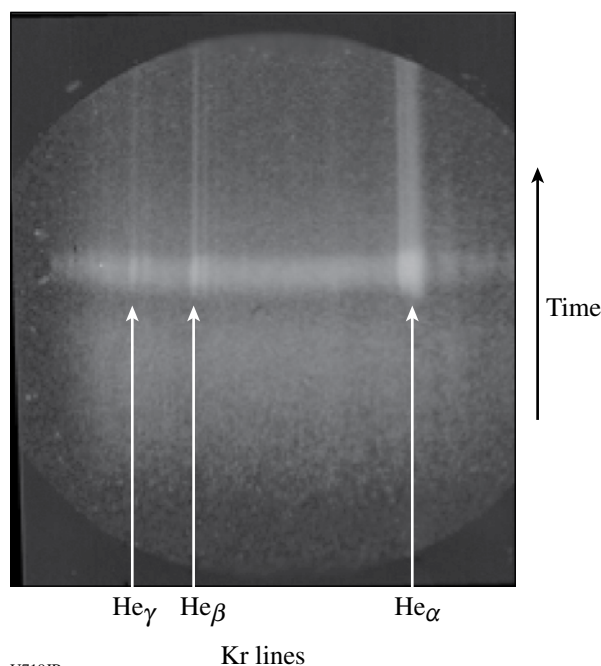
Figure 112.64

Typical time-resolved spectrum from the mica conical crystal spectrometer for a capsule without Xe dopant.

tions. Finally, secondary neutron measurements as well as gated x-ray pinhole images show a dramatic reduction in areal density and core size as the Xe concentration is increased.

One of the campaigns planned for the NIF will study the opacities of high-temperature plasmas in LTE conditions. Present-generation long-pulse facilities produce LTE plasmas in the range of 100 to 180 eV, and the intent is to extend this range upward on the NIF. To do so, it is desirable to optimize the coupling of high-intensity laser radiation to produce x rays from small targets, which in turn heat samples in LTE conditions. In FY07 the high-temperature hohlraum development campaign began studying the utility of rear-wall burnthrough radiation from the back of a small halfraum as a technique for radiatively heating samples several hundred microns away. Figure 112.65 shows data from plastic (carbon) and chromium samples diagnosed with x-ray spectroscopy. Surprisingly, the samples were cooler (under-ionized) relative to what was predicted. Future work will focus on improving the modeling to match the observations and then looking for ways to optimize the experimental configuration.

To produce multiple radiographic images with a single NIF shot, with a minimum number of NIF beams devoted to the backlighter, it is desirable to have a long-duration point-projection backlighter source. To this end, a few half-days
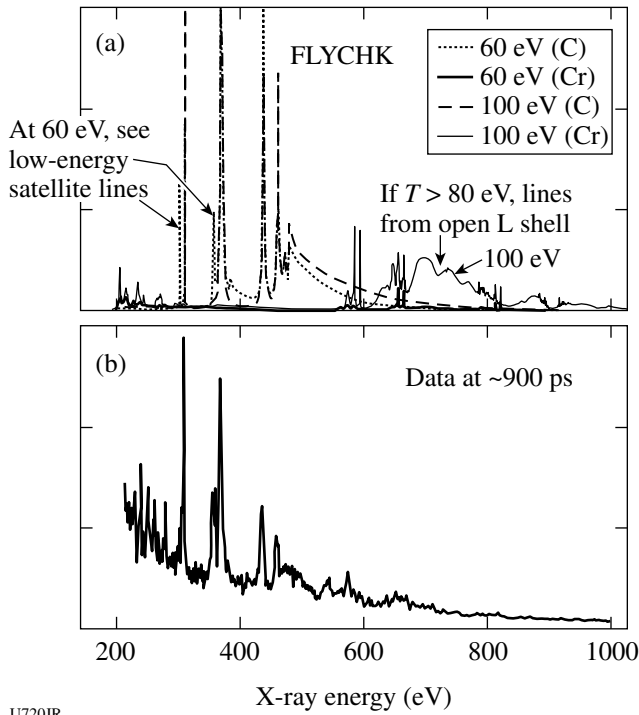
Figure 112.65

(a) Spectroscopic data from a target radiatively heated by the thin back wall of a tiny holraum. (b) Comparison with modeling indicates target temperature is 60 to 70 eV at this time.

were devoted to developing a long-duration, pinhole-apertured, point-projection zinc K-shell backlighter to diagnose NIF experiments. Current laser experiments use pulses of typically 0.2 to 1.0 ns. Extending the backlighter duration out to the desired 8 ns for the NIF leads to issues of pinhole closure and signal strength. Initial experiments using a streak camera with an open slit showed a significant contribution to the background from the streak camera's retrace signal. Subsequent experiments (Fig. 112.66) showed that increasing the laser intensity on the backlighter and using zinc filtering to block unwanted low-energy radiation was sufficient to produce adequate signal above the retrace and other backgrounds. The continuation of this campaign in FY08 will explore pinhole closure time and new backlighter designs aimed at increasing the signal-to-noise ratio without sacrificing resolution.

To further improve hohlraum heating efficiency and reduce plasma filling (which obscures radiographic views of HED material samples), hohlraum development experiments have been conducted using laser-driven cylindrical hohlraums whose walls were machined from Ta_2O_5 foams of 100-mg/cc and 4-g/cc densities. Measurements of the radiation temperature, shown in Fig. 112.67, demonstrate that the lower-density walls
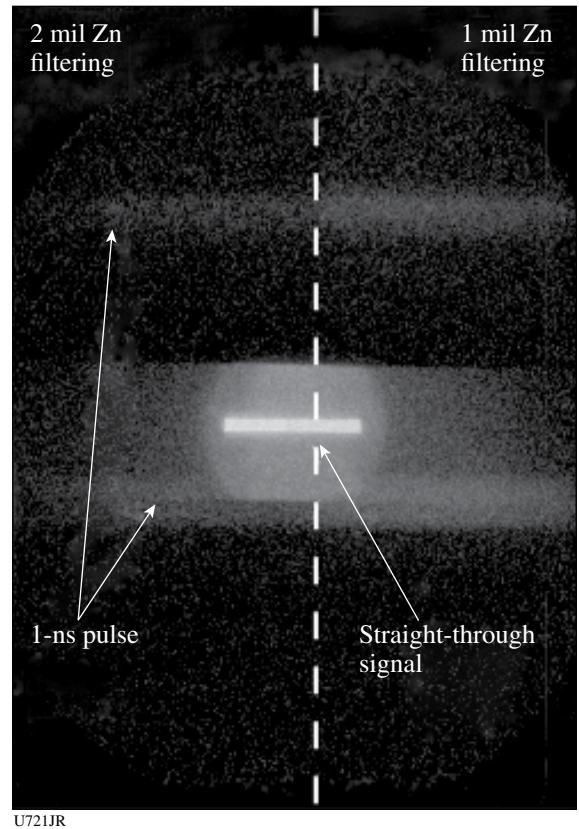
Figure 112.66

Streak measurement of Zn backlighter radiation from multiple OMEGA laser pulses, demonstrating adequate signal-to-test, long-duration backlighter concepts for the NIF.
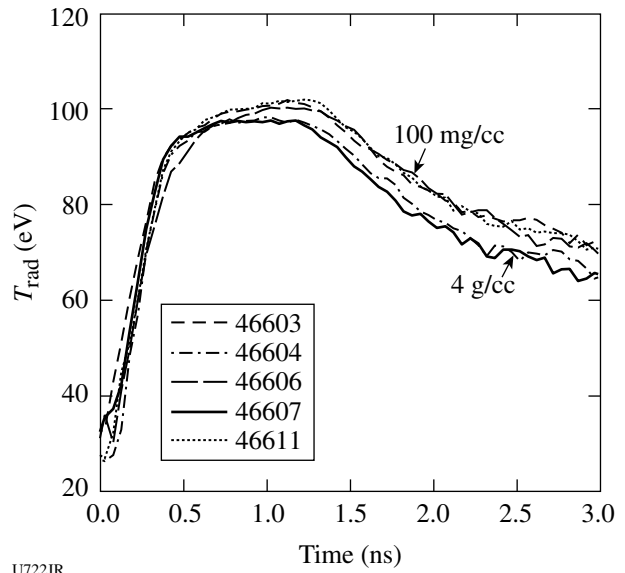
Figure 112.67

Radiation temperature from Dante measurements for five foam-walled hohlraums.

produce higher radiation temperatures than the higher-density walls. The difference in temperature is determined by the difference in energy lost to the walls. For higher-density walls, the radiation front propagates subsonically, so the density seen by the front is dominated by the density profile established by the rarefaction wave. For lower densities the radiation-front velocity is supersonic so the energetics of the wall are determined by the equation of state and the opacity of the wall material.

FY07 LANL OMEGA Experimental Programs

During FY07 Los Alamos National Laboratory (LANL) successfully fielded a range of experiments on OMEGA to study the physics relevant to inertial confinement fusion (ICF) and high-energy-density laboratory plasmas (HEDLP) in support of the national program. LANL conducted a total of 192 target shots on OMEGA, 22% higher than the nominal allocation. Collaborations with LLNL, LLE, MIT, and AWE remain an important component of LANL's program on OMEGA. In particular, the LANL-led symergy campaign has provided a better understanding of symmetry control for the future NIF ignition experiments.

Radiation Transport in Inhomogenous Media: The inhomogeneous radiation flow experiment was allotted a single shot day in FY07. This experiment studies the transport of radiation through inhomogeneously mixed media, that is, where discrete particles of random size are randomly dispersed in a host material. For a constant gold fraction, the effective opacity of the mixture is expected to increase as the particle size decreases, thereby slowing the radiation propagation in the media. Many models describe this phenomenon,[19–24] but it has not been demonstrated that these models are implemented correctly in our codes.

The radiation source for these experiments is a hohlraum nominally heated by 7.5 kJ of laser energy to a peak temperature of about 210 eV (Fig. 112.68). The radiation from the hohlraum drives a temperature front into a gold-loaded foam. The foams are nominally 55 to 60 mg/cm^3 of triacrylate ($C_{15}H_{20}O_6$) foam containing nominally 12% by atom gold particles. The size of the gold particles is varied during these experiments to observe how the particle size impacts the temperature-front propagation.

An example of the effect the gold particle size has on the temperature-front propagation is shown in Fig. 112.69. The data clearly show this effect for the temperature-front propagation for two gold particle cases: 5-μm diameter and atomic mix. At early times, the temperature-front propagation is similar;

(2) Temperature front propagates through gold-loaded foam

(3) Temperature front tracked via soft x-ray emission

(1) Hohlraum creates temperature front

U672JR
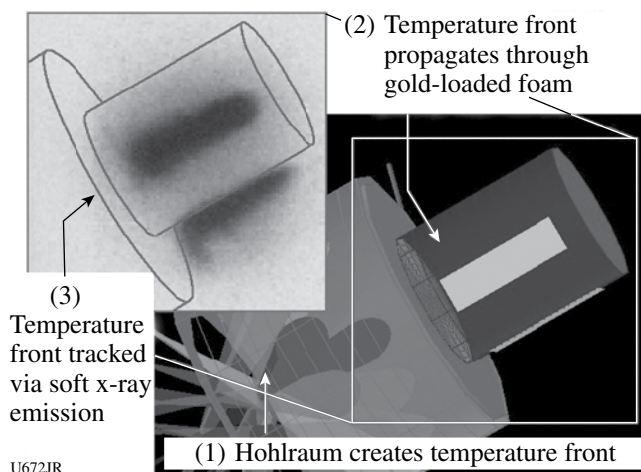
Figure 112.68
A schematic of the inhomogeneous radiation flow platform.

U673JR
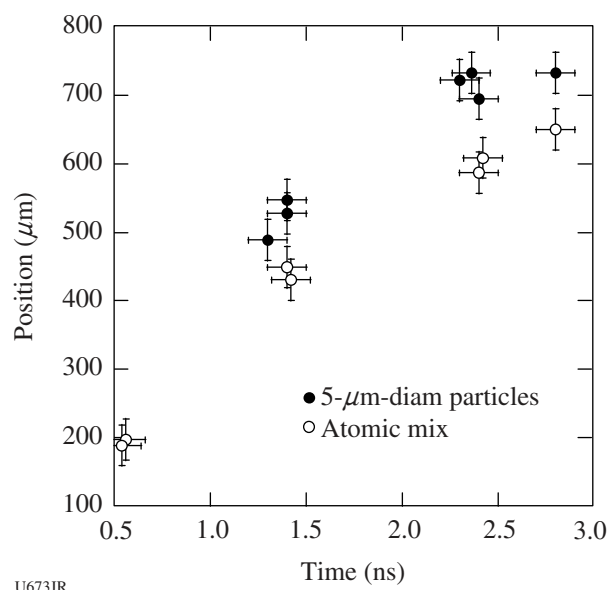
Figure 112.69
Experimentally determined temperature-front position showing the differences between foams loaded with 5-μm-diam gold particles and an atomic mix with gold particles. By 2.5 ns, the temperature front has propagated 100 μm farther in the 5-μm particle case than in the atomic mix case.

however, at 2.5 ns there is roughly a 100-μm difference between the two cases. Also, simulations with the Langrangian radiation hydrodynamics code NYM[25] (Fig. 112.70) show excellent agreement with the experimental data in the atomic mix case.

Off-Hugoniot Experiments: Recent experiments by LANL on OMEGA explored the hydrodynamic evolution of embedded layers subject to radiative heating. These experiments, focusing
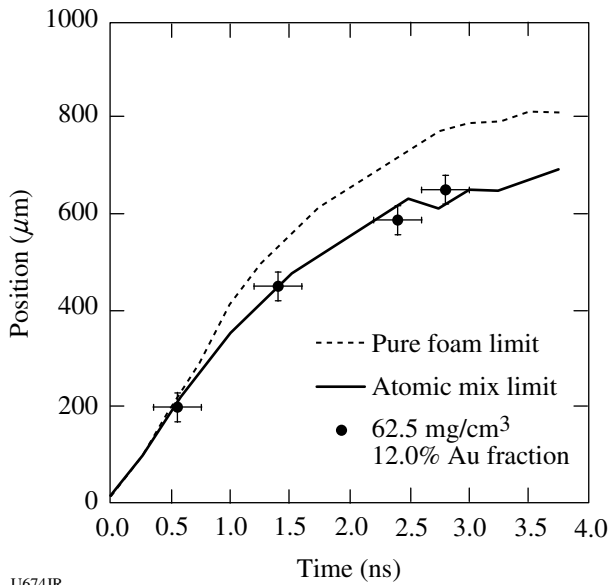
Figure 112.70

A comparison of the simulation in the pure foam and the atomic mix limit versus the experimental data. The atomic mix simulation is in excellent agreement with the experimental results.

on hydrodynamic evolution, are being used for quantitative validation of 3-D Advanced Scientific Computing (ASC) calculations of both large- and small-scale hydrodynamic motion. In contrast to traditional shock interaction experiments, the material conditions are constantly changing with time before and during the shock interaction process. The complex material and density gradients developed during the heating phase significantly change the shock evolution from what it would be

with the initial "as-built" profile. Thus far, the types of embedded features fielded include planar disks, rectangular gaps, and, most recently, single-mode sinusoids. This campaign began in 2004 and continues today with significant collaboration from the Atomic Weapons Establishment (AWE). Current efforts have shifted from data collection to analysis and quantitative comparison with simulations. In FY07 LANL conducted two days of shots on OMEGA that yielded high-quality images of both heated and shocked-gap targets as well as newly fielded sinusoid targets (Figs. 112.71 and 112.72). Data from the sinusoid targets show a recurring phase inversion of the sinusoid pattern as predicted by 3-D ACS calculations.
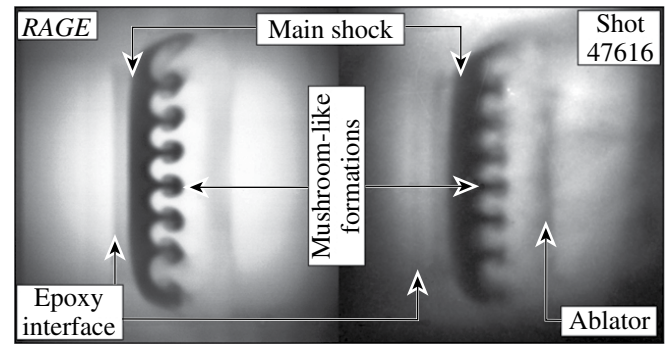
Figure 112.72

Comparison of 3-D ASC *RAGE* calculation (left) with experimental data (right) of heated and shocked sinusoid targets.

NIF Platform #5: The NIF Platform #5 (NIF 5) Campaign is developing x-ray diagnostic techniques to measure tempera-
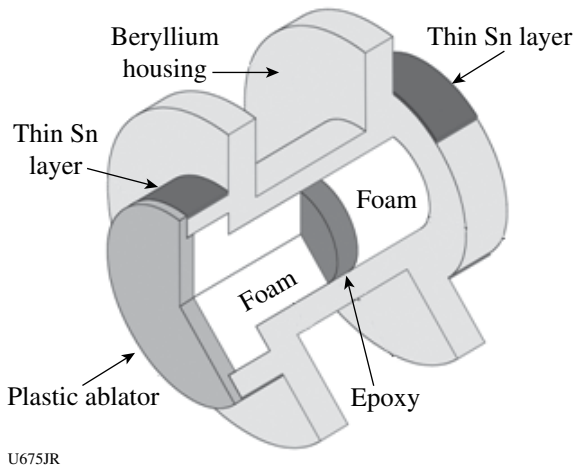
Figure 112.71

Targets consist of a Be housing with epoxy between 60-mg/cm^3 foam parts. A plastic ablator is used to generate shocks. Full target characterization is performed before shots including radiographic images (right) to determine part alignment and material impurities.
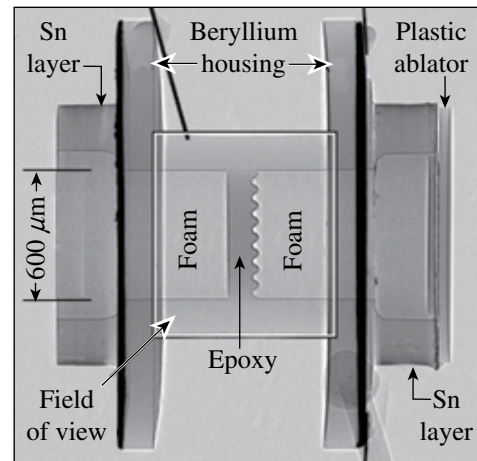
ture in radiation-transport experiments on the future National Ignition Facility (NIF). In FY07 NIF 5 had 1.5 shot days and obtained extremely useful data. This year NIF 5 met both of its main objectives: to measure the spectrum of a suitable backlighter source and to determine the temperature of a foam that had been radiatively driven.

The NIF 5 platform (Fig. 112.73) utilizes a quasi-continuum backlighter and a hohlraum to heat a low-density foam. In some configurations, the backlighter alone is used to measure its x-ray emission spectrum.
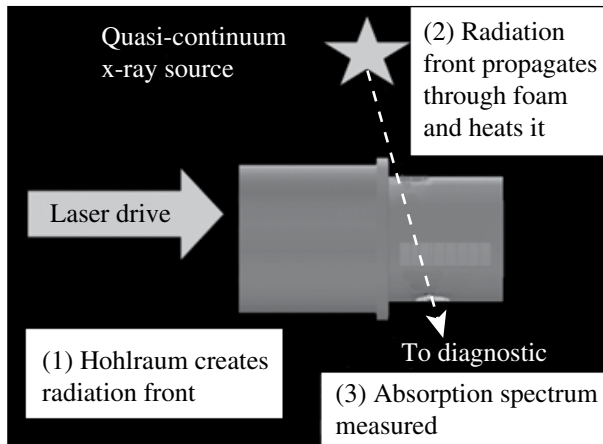
Figure 112.73
A schematic of the NIF 5 platform experimental configuration.

Figure 112.74 displays an example of the absorption data obtained. The emission present is due to the M-band emission of the gold backlighter. The backlighter emission was initiated before the foam was heated and continued during the heating phase of the foam. As the foam heats, the absorption spectrum profile changes, which is captured by the data.
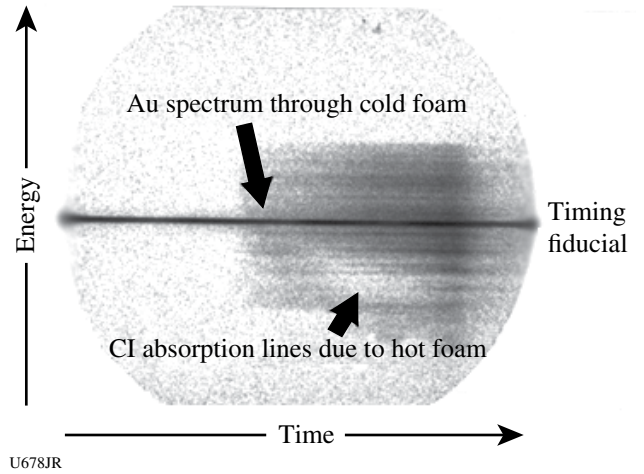
Figure 112.74
Measured absorption spectrum due to a heated foam. The vertical axis is the spectral energy (increasing to the top) and the horizontal axis is time (increasing to the right). The emission is due to the M band of the gold backlighter.

Synergy: LANL fielded two days of OMEGA experiments to test the concept of using thin shells to quantify asymmetry during the foot of the NIF pulse in support of the National Ignition Campaign. Figure 112.75 shows the ~0.7-scale NIF hohlraum geometry used for these experiments. Three cones of beams enter the hohlraum from each side with a 3-ns laser pulse to produce a peak radiation temperature of ~115 eV, comparable to the foot pulse incident on an ignition capsule.

The emission levels from the capsule implosions (Fig. 112.76) proved the concept of thin-shell capsules as a symmetry diagnostic for the NIF. Furthermore, the variation in symmetry with beam cone pointing shows that one-way capsule asymmetries could be corrected at the NIF. These quantitative results showed that we can now proceed to tune asymmetry in the foot of a full-scale the NIF ignition capsule using the 96-beam configuration in FY08!
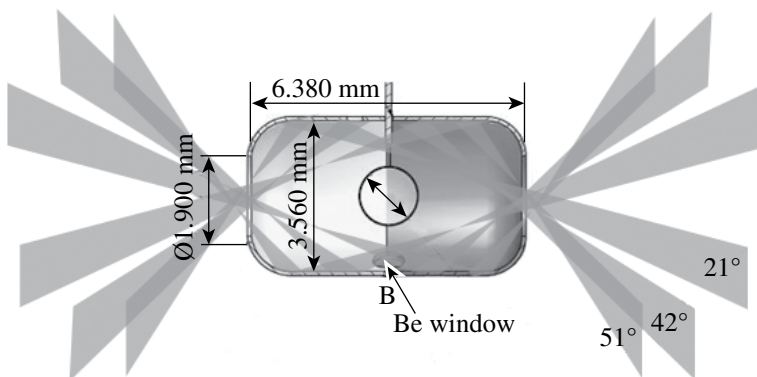
Figure 112.75
Gold hohlraum with an x-ray diagnostic port used in thin-shell symmetry capsule experiments. The capsule is a 1400-μm-diam, 15-μm-thick CH shell filled with 1 atm of D2.
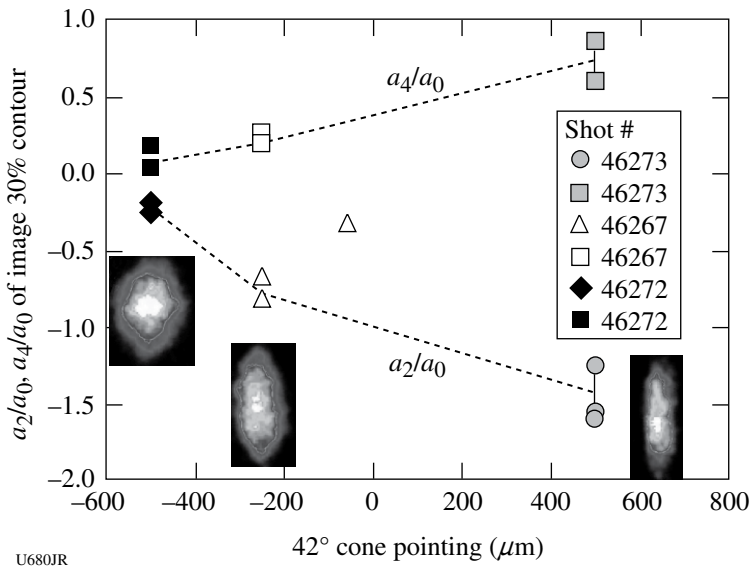
Figure 112.76
Observed time-integrated x-ray images and corresponding P2 and P4 asymmetries as the pointing of the 42° cone is moved along the hohlraum axis.

U680JR

Convergent Ablator: Two shots days were dedicated to investigating the slowing of protons from the D + ^{3}He reaction to diagnose the ablator remaining at ignition in a NIF target in collaboration with MIT. Capsules were imploded in a 3/4-scale OMEGA hohlraum driven by 19 kJ in a 1-ns square pulse with hohlraum temperatures peaking at ~270 eV. By driving different thicknesses of CH capsules we could obtain different final ablator and fuel ρR's to test our ability to observe and calculate downshifts of the 14.7-MeV proton by up to ~1.5 MeV.

The results of this campaign confirmed our predictions of hohlraum temperature and our ability to observe gated images in self-emission of the imploding capsules. Figure 112.77 shows the observed neutron yields from nine capsules for capsule wall thicknesses varying from 25 to 55 μm thick. The points labeled "Nom 70% LEH" are calculated yields without mix. The triangles include expected degradation by mix as the capsules converge more with increasing initial thickness. Observed x-ray images for all but the 55-μm-thick capsules were round. MIT is now analyzing the charged-particle detectors to obtain total proton yield and spectra from emitted protons. Initial results with a 35-μm-thick capsule had enough yield to obtain a spectra, and calculations agreed with the measured energy shift.

In a similar experiment,[26] abundant hard x-rays were measured indicative of hot-electron production. By varying laser energy in each of the three laser cones, we were able to determine that hard x rays were being produced almost entirely by the innermost cone, and that hot-electron temperatures were >100 keV. The particle temporal diagnostic (PTD) and neutron temporal diagnostic (NTD) instruments, modi-

U681JR
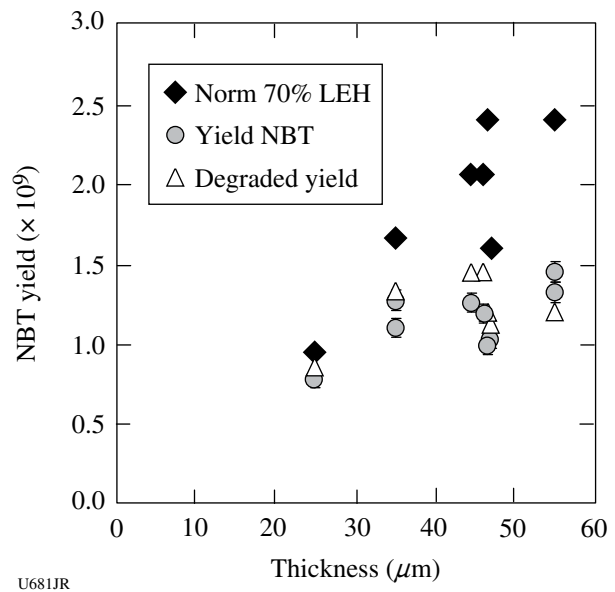
Figure 112.77
Observed and calculated D + D neutron yields from the convergent ablator experiment.

fied to become hard x-ray detectors, showed peak emission at ~0.7 ns and a subsequent decrease, within the 1-ns laser pulse. In calculations this corresponded to the appearance of a quarter-critical-density surface between hohlraum wall and capsule ablator expansions. We showed increased x-ray production when the plastic-capsule ablator was changed to beryllium from CH, and no 3/2ω radiation from either type. These results are still being analyzed but suggest that Raman scattering plays an important role in hot-electron production, as suggested from laser-instability postprocessing of the *LASNEX* hohlraum calculations.

Laser–Plasma Interactions: Gas-filled hohlraums are often used for high-energy-density laser experiments including inertial confinement fusion. While the gas fill is needed to provide a hot ionized plasma whose pressure prevents the ablated wall material from filling the hohlraum, it can also potentially lead to large laser–plasma instability growth since a long-scale-length quasi-homogeneous plasma is often created. One instability that may be detrimental to gas-filled hohlraum experiments is stimulated Raman scattering (SRS), which occurs when intense laser light resonantly decays into an electron-plasma wave and a backscattered light wave. Two strategies for mitigating SRS were investigated in FY07 on the OMEGA laser using gas-filled hohlraums.

The first strategy uses a small amount of a high-Z dopant in the low-Z gas fill, which had previously been observed to reduce SRS in experiments at the Helen laser and last year on the OMEGA laser. These experiments, which were a continuation of experiments started in FY06, heated a 1.6-mm-diam, 2.0-mm-length, Au gas-filled hohlraum. The hohlraum is filled with ~1 atm C_5H_{12} gas and has 0.25-μm-thick polyimide windows over the 0.8-mm-diam laser entrance holes (LEH's). The target is aligned along the B30 axis and heated with up to 12 kJ using 32 beams in three cones in a 1-ns pulse. After plasma formation, B30 is used to interact with the long-scale-length plasma with an intensity ~10^{15} W/cm^2, smoothed with a 150-μm CPP and full-bandwidth SSD. The 3ω transmitted-beam diagnostic (TBD) measures the transmitted light, and the full-aperture backscatter station (FABS) measures SRS and SBS growth. For this set of experiments, a small amount of Xe dopant was added to the gas fill and systematically varied up to 9% atomic fraction. These experiments indicate greater than a factor-of-2 decrease in SRS reflectivity when the Xe dopant is 1%. Experiments with a B30 intensity of 1.8×10^{15} W/cm^2 with SSD on or at 10^{15} W/cm^2 with SSD off show little change in SRS with 1% Xe. Comparison of these results with radiation hydrodynamic calculations is ongoing and will help rule out whether the effect can be simply explained by an increase in inverse Bremsstrahlung absorption, or whether competition of SRS with beam spray is the mechanism responsible for the observed decrease in SRS.

The second strategy examined this year used lower-density gas fills to increase Landau damping via the dimensionless parameter $k\lambda_D$, where k is the wave number and λ_D is the Debye wavelength. To examine the effects of high-$k\lambda_D$ regimes on SRS, the critical onset intensity for SRS is measured. A critical onset occurs theoretically for a random-phase-plate–smoothed laser beam with a distribution of intensities with a well-defined spatial correlation length (speckle length). As the average laser intensity increases, the calculated SRS gain diverges, leading to a saturated reflectivity. This is experimentally determined by measuring a sharp increase from no reflectivity to large reflectivity for a small increase in laser intensity. As $k\lambda_D$ increases, Landau damping of the electron-plasma wave increases, thus increasing the SRS critical onset intensity. In these experiments, mixtures of C_5H_{12} and C_3H_8 were used at different pressures to vary the electron density. B30 was used at an intensity of 10^{15} W/cm^2 with SSD to interact with the preformed hohlraum plasma and drive SRS. As the electron density is lowered, the critical onset for SRS occurs at a higher intensity, qualitatively consistent with theory. In Fig. 112.78, the presence of large SRS (>10%) is plotted in the gray circles, and the presence of small SRS (<1%) is plotted as open circles. For a small change in plasma density at a fixed laser intensity, or a small change in laser intensity at a fixed plasma density, SRS increases rapidly to a saturated state. The dashed line is plotted as a guide to indicate the demarcation of the measured critical onset.
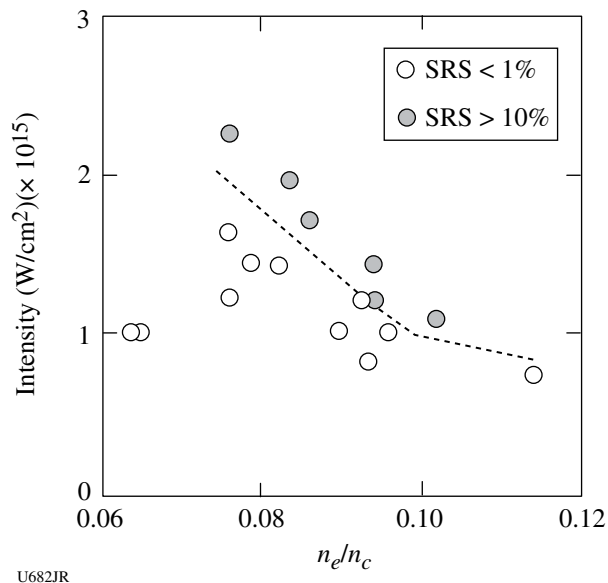
Figure 112.78
SRS levels as a function of n_e/n_c. The dashed line is plotted as a guide to indicate the demarcation of the measured critical onset.

Hi-Z: To better understand the effects of instability growth and the resulting mix, we need to be able to calculate the performance of capsule implosions with known quantities of preimposed mix. Two days of directly driven implosions on the OMEGA laser in 2007 have tested the effects of pre-mix of Ar, Kr, and Xe in $D_2 + {}^3$He–filled glass microballoons. In FY07 we focused on the effects of argon pre-mix, while earlier

experiments explored Kr and Xe. Diagnostics included D + D and D + T neutron yields, D + ^{3}He proton yields and spectra, Doppler-broadened ion temperatures, time-dependent neutron and proton burn rates, and time-gated, high-energy filtered x-ray images. Simulated yields agree better with the experiment when calculated by XSN LTE[27] than by non-LTE atomic physics packages.

Measured yields with a small amount of pre-mix, atom fractions of ~5 × 10^{-3} for Ar, 2 × 10^{-3} for Kr, and 5 × 10^{-4} for Xe are more degraded than calculated, while the measured ion temperatures are the same as without pre-mix. There is also a decrease in fuel ρR. The neutron burn histories suggest that the early yield coming before the reflected shock strikes the incoming shell is undegraded, with yield degradation occurring afterward. Adding 20%-by-atom ^{3}He to pure-D fuel seems to produce a similar degradation. This ^{3}He degradation was previously observed in directly driven plastic shells by Rygg et al.[28] Figure 112.79 shows how calculated gated x-ray images agree in radius with observed when the reflected shock strikes the incoming shell at 1.18 ns but are smaller than observed afterward. This lack of convergence and lower fuel density partially explains the yield degradation as well as the low fuel and whole capsule ρR's observed in secondary T + D neutrons and slowing of the D + ^{3}He protons. Neither LTE on non-LTE captures the degradation by ^{3}He or with low Ar, Kr, and Xe pre-mix levels, nor matches the large shell radii after impact of the reflected shocks.[29]

Reaction History: In October 2006, LANL conducted the *Reaction History Structure Using a Double Laser Pulse* experiment to study the effects of time-dependent mix in a DT capsule implosion. Two temporally separated laser pulses, as seen in Fig. 112.80(a), were used to obtain double peaks in the fusion reaction history as determined by deconvolved measurements from the gamma-based gas Cherenkov detector (GCD) and the neutron temporal diagnostic (NTD) are shown in Fig. 112.80(b). The expected double-peak character of the reaction history is well resolved by the GCD. The first laser pulse contained 10 kJ in 40 beams and the second 5 kJ in 20 beams. Each was a square 600-ps pulse. This

U683JR

Figure 112.79
X-ray-image radius with (shot 47857) and without (shot 47863) ^{3}He versus simulated using LTE and non-LTE.
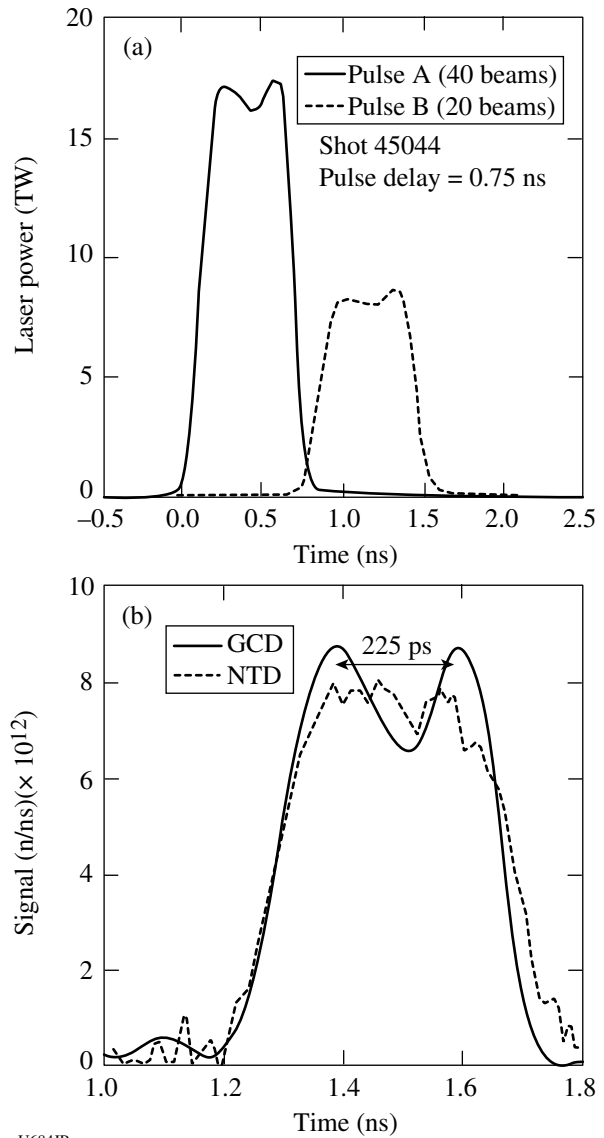
U684JR

Figure 112.80
(a) Double-pulse laser waveforms; (b) double-pulse reaction history.

shorter-than-the-usual 1-ns laser pulse allows the shock and compression fusion burn components to be separated in time. Comparisons with modeling are indicating that the first peak is dominated by shock yield and the second peak, a result of compression burn, becomes significant only when the delays between pulses are less than 800 ps. This is contrary to the leading mix models, such as Scannapieco and Cheng, which predict a dominant compression burn, and is requiring us to invoke the harsh mix of a fall-line mix model to explain these observations.

DTRat: In June 2007, LANL conducted the *DT Ratio-3He Addition* experiment to investigate the effect of ^{3}He on the yield and reaction history of DT implosions. The DTRat experiment also used 600-ps laser pulses, but at 50% more energy: 15 kJ versus 10 kJ in the first pulse of the *Double Pulse* experiment. As seen in Fig. 112.81, the absolute DT fusion gamma and neutron yields are consistent with each other and dropped by 80% in going from 0 to 33% ^{3}He addition (i.e., 5 atm ^{3}He). The shock and compression burns agree with the Scannapieco and Cheng mix model relatively well as determined by the GCD-measured reaction history shown in Fig. 112.82, so there was no need to resort to fall-line mix in this case. In both calculations and experiment, the compression burn is clearly much more degraded by the addition of ^{3}He than is shock burn. The MIT group had previously determined that the addition of ^{3}He to DD in thick plastic shells resulted in approximately a factor-of-2 anomalous drop in scaled yield [i.e., yield over clean (YOC)] at 50% ^{3}He by

atom as compared to pure DD or nearly pure ^{3}He, as seen in Fig. 112.83 (Ref. 27). While a drop in scaled yield with the addition of ^{3}He was observed for DT, it was not nearly as significant as reported for DD. These data are the first of a planned series to study the effects of ^{3}He concentration on implosion yield and reaction history using DT capsules.
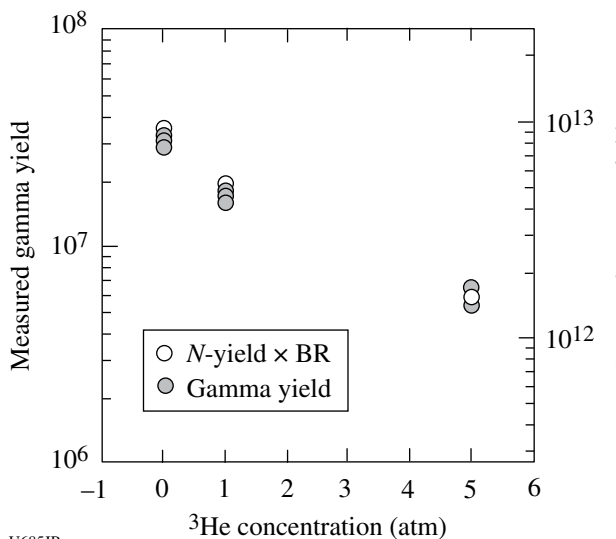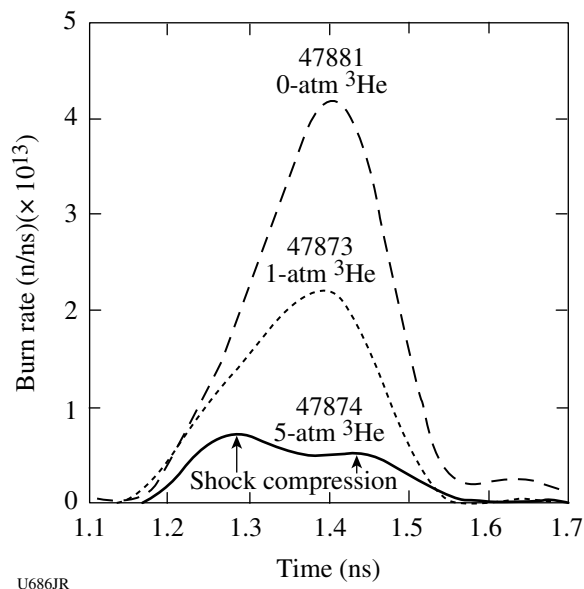

Figure 112.82
Burn history versus ^{3}He concentration.

Figure 112.81
Neutron and γ-ray yields versus ^{3}He concentration shows a decrease in yield as the ^{3}He concentration is increased.
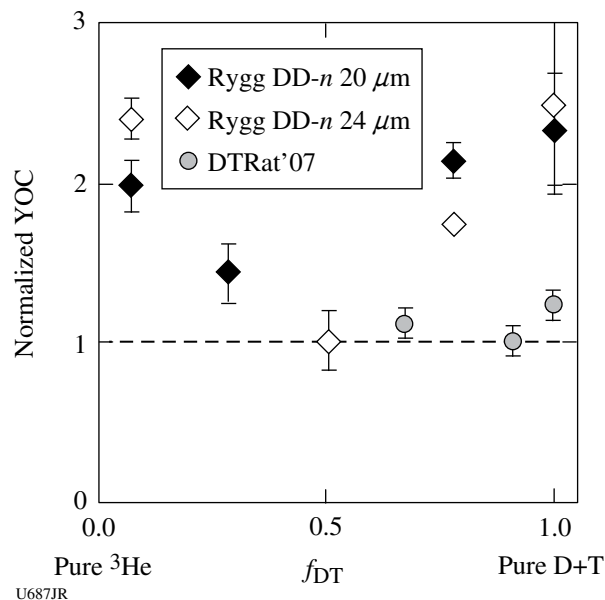
Figure 112.83
Scaled neutron yield normalized to 1 at the minimum for 20- and 24-μm plastic shells (Rygg) and 4.7-μm glass shells (DTRat'07).

Beta Mix: Ignition experiments at megajoule/terawatt laser facilities will take the field of high-energy-density science into new frontiers, in terms of both physics and diagnostic capabilities. In particular, understanding the nature and amount of mix caused by hydrodynamic instabilities in inertial confinement fusion (ICF) targets is important from a fundamental physics perspective as well as for optimizing target performance. A radiochemical diagnostic to measure the amount of mix is being developed at Los Alamos National Laboratory. Figure 112.84 shows a conceptual diagram of how the diagnostic would be implemented. Neutrons produced in deuterium and tritium fusion interactions traverse the fuel to the ablator interface where they can upscatter tritons to MeV energies. Given the electron density or temperature (T_e) in this region, the triton range is quite short. Thus, the probability for $^9Be(t,x)$ interactions will depend strongly on the amount of mix that has occurred.

The diagnostic proposed for the National Ignition Facility is to collect and measure ^8Li atoms produced in $^9Be(t,\alpha)$ interactions. Short-lived radiochemical signatures, such as ^8Li (half-life of 840 ms, and a Q_β of 13.4 MeV), provide a distinguishable signature for measuring mix, as MeV-scale backgrounds from prompt activation at the millisecond and greater timescales should be small. Further, this approach is not subject to systematic uncertainties from nontarget backgrounds from which stable and metastable isotope techniques can suffer. The two keys to executing this diagnostic are the ability to collect target debris after the implosion and the ability to begin counting the radionuclide decays of interest within this collected debris.

To gain insight into the issues surrounding radionuclide counting after a high-yield ICF shot, experiments were performed on OMEGA. Detectors were located both on the target chamber wall and inside a re-entrant tube to provide a prompt, high-fluence flash of radiation that must be addressed prior to initiating counting. The prompt radiation burst was also used as an activation source for counting experiments. Activation targets were located directly in front of the counters and included graphite and ^{15}N-enriched NH_4Cl. The graphite provided a source of ^{12}B atoms ($\tau_{1/2} = 20.2$ ms, $Q_\beta = 13.4$ MeV) through $^{12}C(n,p)^{12}B$ interactions, while the ammonium chloride was a source of ^{15}C atoms ($\tau_{1/2} = 2.45$ ms, $Q_\beta = 4.5$ and 9.8 MeV) through $^{15}N(n,p)^{15}C$ interactions. Figure 112.85 shows the results of measurements made with the graphite target. The data were collected using a scintillation telescope, with a Pilot-B
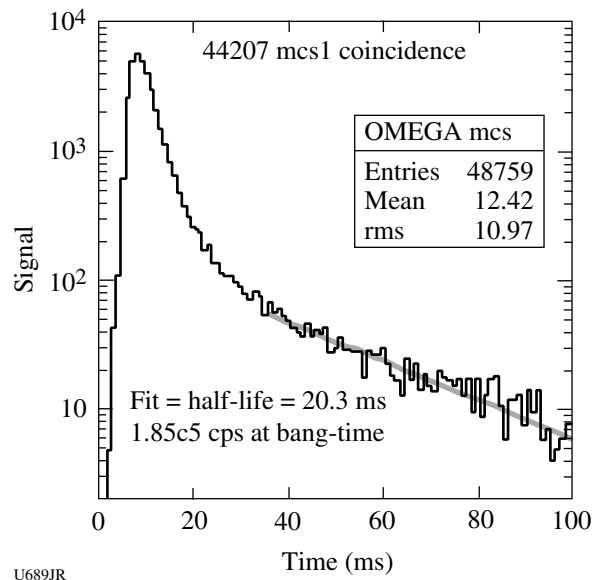
Figure 112.85
Counting data from a Pilot-B coincidence telescope. The half-life fit to the data is consistent with ^{12}B, and the resulting abundance is used to calculate a $^{12}C(n,p)^{12}B$ cross section of 14.1 MeV of 300 ± 30 μb.
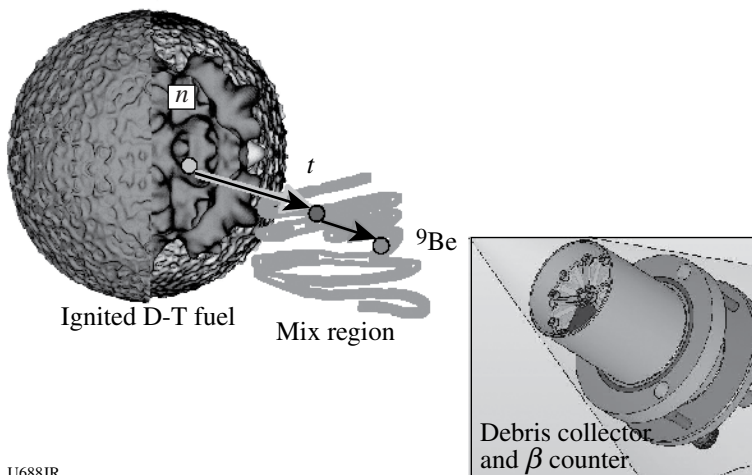
Figure 112.84
Illustration of the "beta-mix" diagnostic concept. Fast neutrons upscatter tritons in the fuel–ablator mix region. Triton–ablator reactions produce unstable daughters with millisecond to second half-lives that are collected and counted by a distant detector.

scintillator and Burle 8575 photomultiplier tubes (PMT's). The PMT bases were custom bases that included a gating circuit to reverse bias the photocathode of the PMT to partially blind the tube during the prompt radiation burst. The anode signals from each PMT were discriminated, subjected to a coincidence requirement, and recorded in a multchannel scaler. The scaler data were then fit in the region of the ^{12}B decay, and an abundance calculation was made. From this abundance measurment, and a Geant 4 simluation to estimate efficiency and acceptance, it is possible make a preliminary ^{12}C$(n,p)^{12}$B cross-section measurement at 14.1 MeV of 300±30 μb.

Debris collection appears to be the most challenging of the two key issues for this diagnostic. A number of attempts have been made to collect target debris at various laser facilities around the world, including OMEGA, but with mixed results. Although gas-collection schemes appear to have been successful, they are not practicable for short half-life counting diagnostics. Figure 112.86 illustrates why it is challenging to collect solid debris on direct-drive experiments. In an effort to improve efficiency of collection within a diagnostic cone, it is desirable to place collector materials as close to the target as possible. Unfortunately, in yield-producing direct-drive shots, two precursor shock waves strike the collector prior to the debris of interest. The first shock is due to the x rays produced at maximum compression. The second, and more damaging, shock in direct-drive scenarios is produced by the ions ablated from the target during laser illumination. The ions are calculated to have ~40 keV of kinetic energy, and if the collector is located close enough to the target, the energy density delivered to the surface of the collector is sufficient to eject a significant amount of mass from this collector. This ejected material drifts with velocities in the cm/μs range normal to the surface. Ejecta formation is illustrated in Fig. 112.87, which shows the surface profile of a 0.004-in. Ti collector foil that was exposed

to three direct-drive shots. The foil was positioned 15 cm from the targets and partially covered. Approximately 160 nm of Ti foil was removed from the exposed portion of the foil on each shot. Disassembled target material, which would carry the mix signal of interest in putative experiments, follows the precursor shock materials with kinetic energies calculated to be ~10 keV. Stopping calculations estimate the mean implantation depth of the ~10-keV ions in room-temperature, solid-density Ti is of the order of ~20 nm, which is 8 times less than the thickness of material removed by the ablated material shock. These dynamics may explain why past solid collection schemes have met with marginal success.
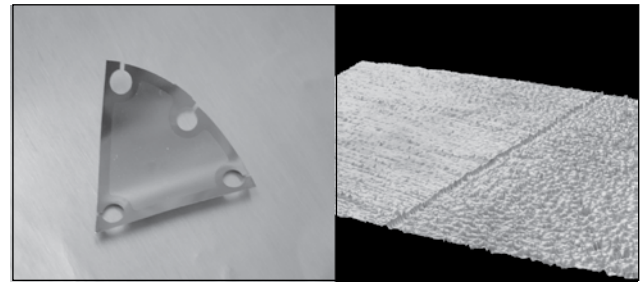
U691JR

Figure 112.87
A Ti debris-collector foil exposed to three direct-drive shots of CH shells filled with 5 atm of D_2. The right panel shows the difference between exposed and unexposed surfaces. Approximately 160 nm of material was removed on each shot.

During the past year, both counting detector optimization and debris collection experiments have been performed on OMEGA, in support of the Mix in Inertial Confinement Fusion, LDRD DR at Los Alamos National Laboratory. The experiments have shown that it is straightforward to count millisecond half-life decays of radionuclides following high-yield implosions on OMEGA. Further, studies are underway to optimize
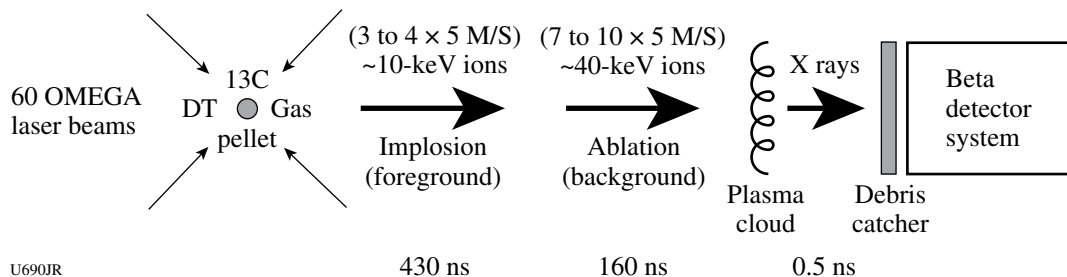
U690JR

Figure 112.86
Illustration of the shock fronts impinging a debris collector in direct-drive ICF implosions. For a mix diagnostic, the signal is carried in the third shock front to strike the collector.

the performance of the counting scheme and to understand the issues to implement such a system in an environment appropriate for megajoule/terawatt-class laser facilities. Debris collection studies have also been initiated. The dynamics of solid debris collection are beginning to be understood, and work during FY08 is focused on furthering understanding of the dynamics and implementing mitigation strategies to optimize the collector efficiency.

FY07 Sandia National Laboratories OMEGA Experimental Programs

HDC Ablation-Rate Measurements in Planar Geometry: Accurate knowledge of the x-ray ablation rates of low-Z capsule materials will be essential for successful indirect-drive ICF ignition experiments. As part of the U.S. National Ignition Campaign, we have over the past few years performed experiments to measure the x-ray ablation rates in beryllium, copper-doped beryllium, polystyrene (CH), germanium-doped CH, and polyimide. In FY07, we performed the first measurements of the x-ray ablation rates of the diamond-like high-density-carbon (HDC) ablator that has been proposed as a NIF ignition capsule material.[30] The experimental tech-

nique for ablation rate measurements in planar geometry is illustrated in Fig. 112.88 (details in Ref. 31). Basically, ablator samples are placed over an opening on the end of a halfraum. Laser beams that enter through the LEH provide the input power required to maintain the radiation field. The Dante array of K- and L-edge filtered photocathodes views the hohlraum wall through the LEH, and a time- and spectrally resolved measurement of the hohlraum radiation field is obtained from this data. An x-ray framing camera views the interior surface of the ablator sample, and the relative x-ray re-emission of the ablator versus the Au wall is determined. The streaked x-ray imager (SXI) diagnostic views the exterior surface of the ablator sample. The SXI employs an imaging slit, a transmission grating, an offset slit, and a streak camera to provide a highly time resolved streaked image of the x-ray burnthrough flux on the exterior-facing side of the sample (as shown in Fig. 112.88). The combined information from these three measurements over a series of experiments is used to determine the mass ablation rate (mg/cm^2/ns) as a function of hohlraum radiation temperature. In previous work, we found that the ablation rates in beryllium range from about 3 to 12 mg/cm^2/ns for hohlraum radiation

(a) X-ray framing camera (XRFC) (b) OMEGA halfraum (c) Streaked x-ray imager (SXI)
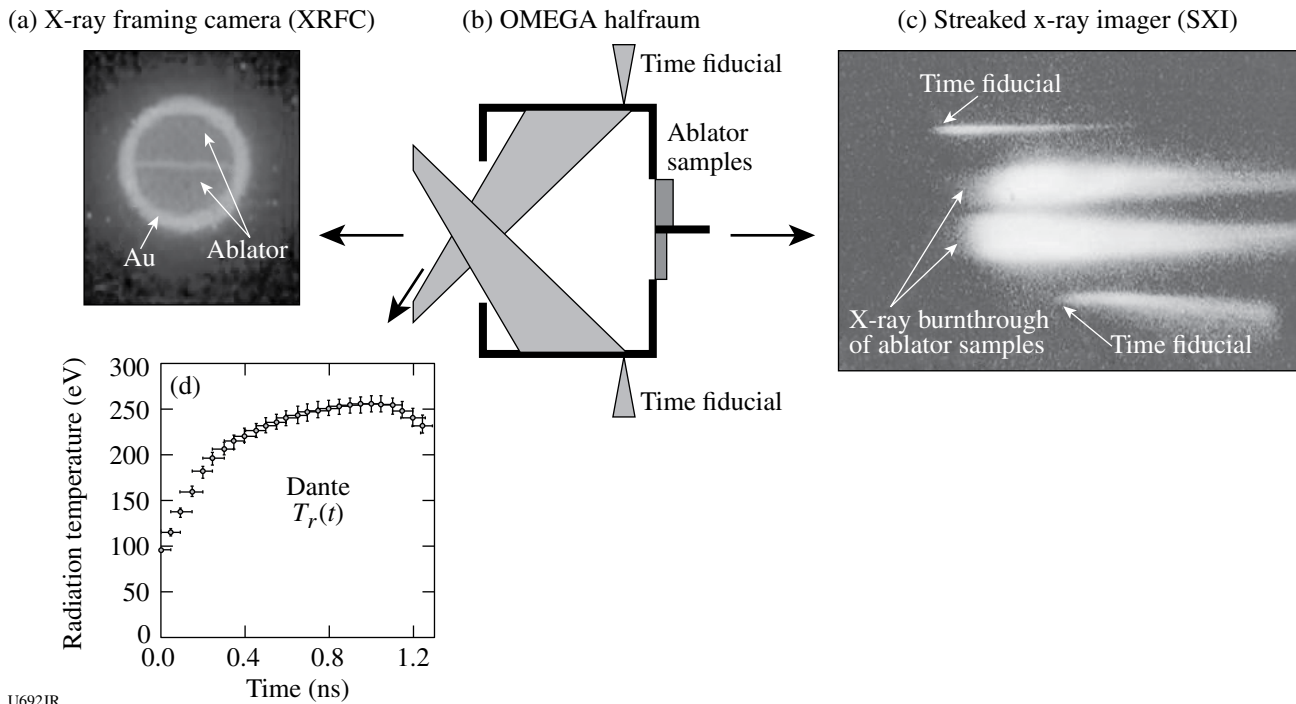
Figure 112.88
(a) The x-ray framing camera (XRFC) provides an x-ray re-emission flux relative to the re-emission of the Au wall (and, therefore, an estimate of the absorbed x-ray flux). (b) Schematic of the burnthrough experiment. (c) The streaked x-ray imager (SXI) measures burnthrough time for each ablator sample thickness. (d) The Dante provides a time-resolved hohlraum radiation temperature.

temperatures in the range of 160 to 250 eV [Fig. 112.89(a)]. As expected, the HDC ablation rates are a bit lower, in the range of 2 to 9 mg/cm^2/ns for temperatures in the range of 170 to 260 eV [Fig. 112.89(b)]. The corresponding implied ablation pressures are in the range of 40 to 160 Mbar for beryllium and 20 to 140 Mbar for diamond (Fig. 112.90). Our post-shot computational simulations (shown as squares on the Fig. 112.89 plots) are mostly within the uncertainties of the ablation rate measurements. An iterative rocket model has been developed and used to relate the planar ablation rate
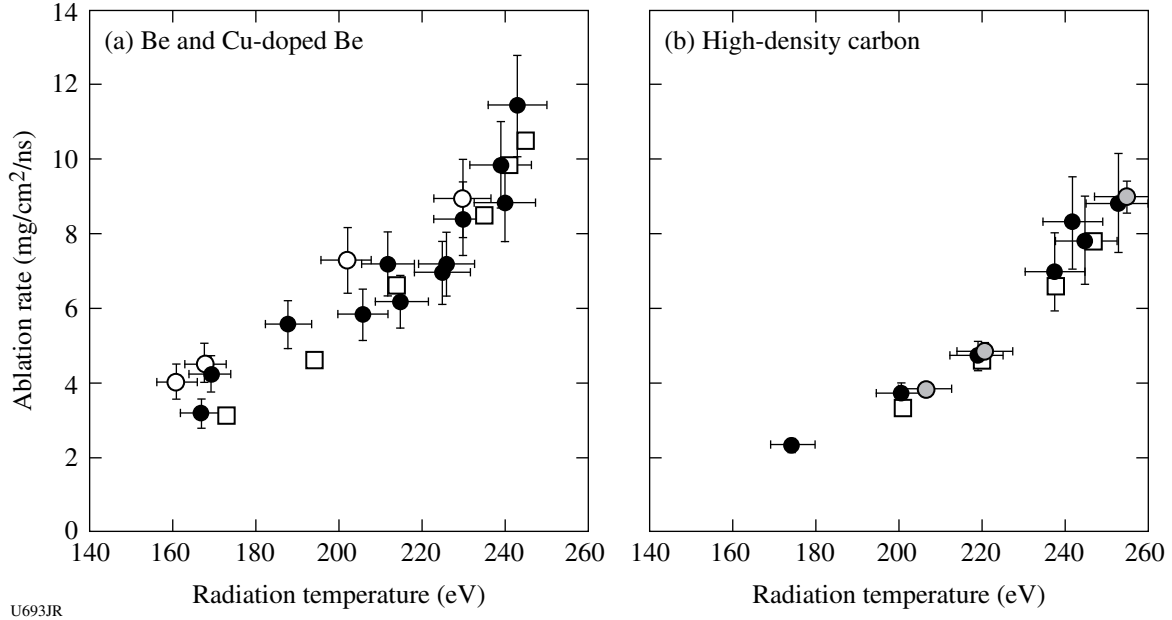
Figure 112.89
Ablation rates measured for radiation temperatures in the range of 160 to 260 eV for (a) Be and Cu-doped Be and (b) high-density carbon.
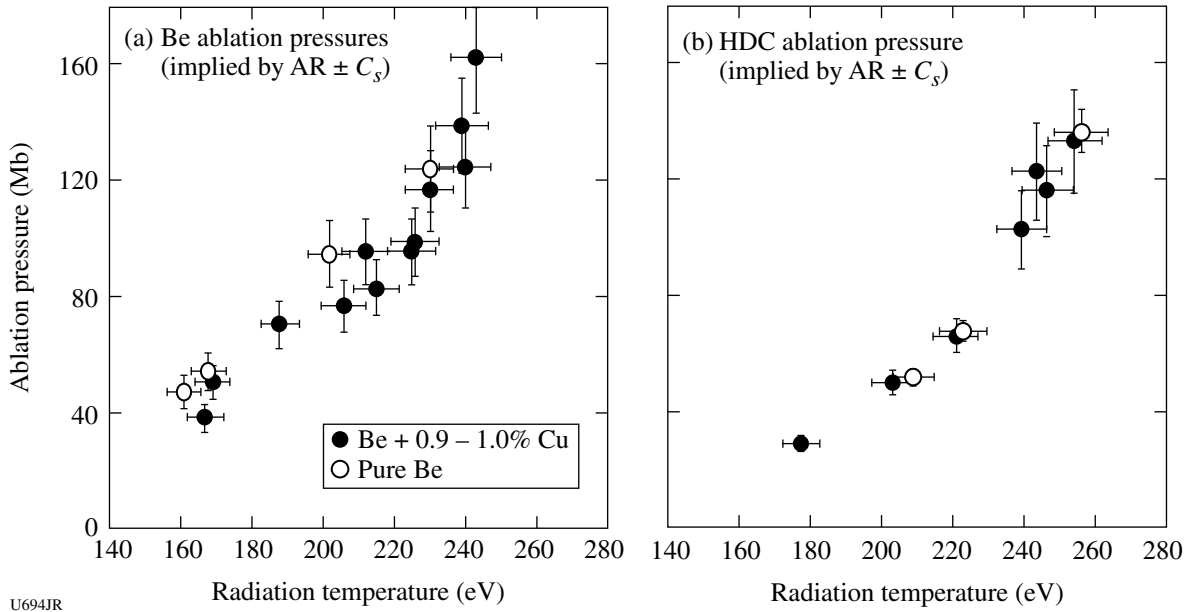
Figure 112.90
Corresponding ablation pressures implied by the data of Fig. 112.89. The Be and HDC ablators approximately follow a $Pr \sim T^{3.5}$ scaling.

data to convergent OMEGA ablation rate experiments and also to full-scale NIF ignition capsule calculations.

FY07 CEA OMEGA Experimental Programs

Wall-Motion Experiment: Measurements of wall and laser-spot motion in a cylindrical hohlraum were obtained on the OMEGA Laser Facility on 11 September 2007. Wall motion was measured using axial imagery with an x-ray framing camera (XRFC) in the axis of the hohlraum while laser-spot motion was measured using an x-ray streak camera (SSCA) looking through a thinned wall of the target (Fig. 112.91).
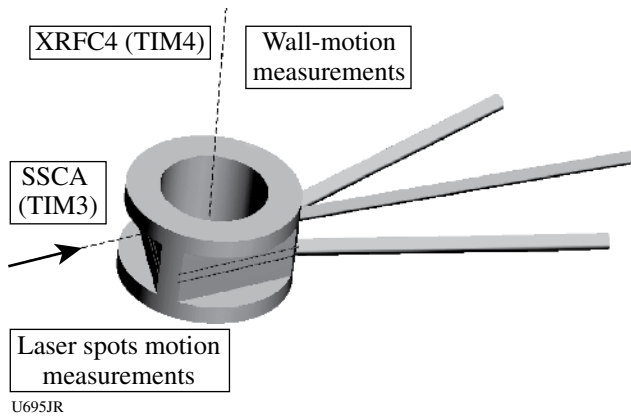
Figure 112.91
Schematic of experimental configuration for OMEGA wall-motion experiments.

Empty hohlraums, CH-lined hohlraums, and a propane-filled hohraum were shot. Axial imagery (Fig. 112.92) shows that plasma striction comes early in empty hohlraums, while lined and gas-filled targets restrict wall expansion during the PS26 laser irradiation.

Streak images corroborate these results by showing a quicker expansion of laser spots in the case of an empty Au hohlraum (Fig. 112.93).

Neutron Imaging on OMEGA: In a directly driven implosion of a DT capsule, the CEA neutron imaging[32] system uses a penumbral coded aperture to cast an image of the neutron source onto a detector. The system now routinely provides neutron images with 20-μm resolution. Recently, the system has been used for the first time ever during the implosion of a DT cryo target. An image of the DT cryo implosion is shown in Fig. 112.94(a); an image of a gas-filled target imploded during the same shot day is shown in Fig. 112.94(b) for comparison.

On the diagnostic technique, the last step of development is to achieve a more valuable measurement with a 10-μm resolu-
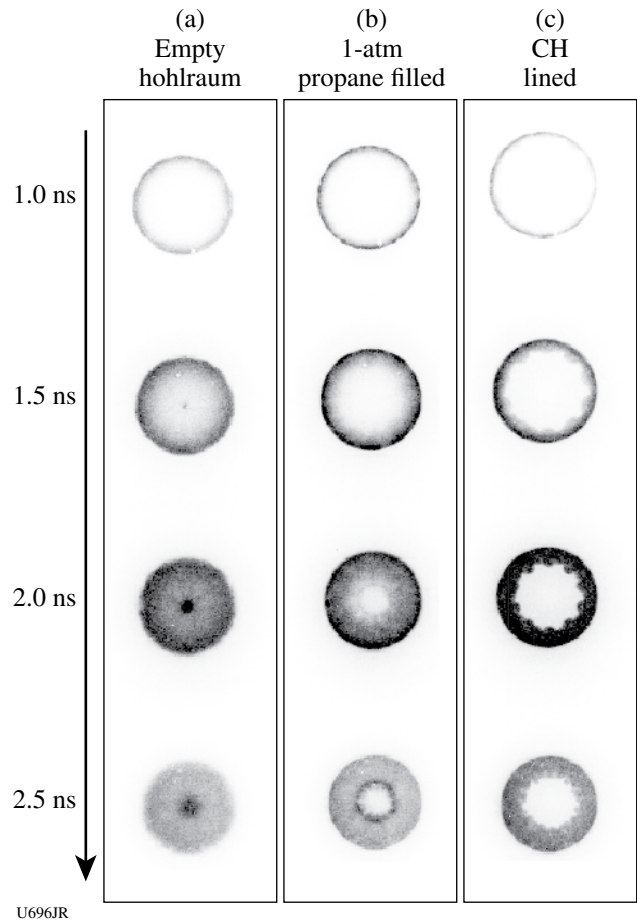
Figure 112.92
Axial x-ray framing camera images of wall motion in (a) empty, (b) 1-atm-propane–filled, and (c) CH-lined hohlraums, respectively.
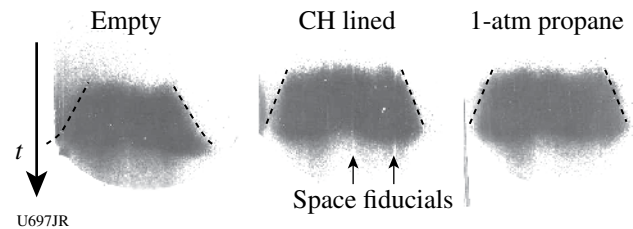
Figure 112.93
Spatially resolved streak-camera images of laser-spot motions in (a) empty, (b) CH-lined, and (c) gas-filled hohlraums.

tion at the source. Novel detectors made of capillaries filled with a liquid scintillator now reach a few-hundred-microns spatial resolution, which moderates the required magnification ratio of the system and reduces the diagnostic line of path to a more practical distance (<30 m). A high-resolution diagnostic
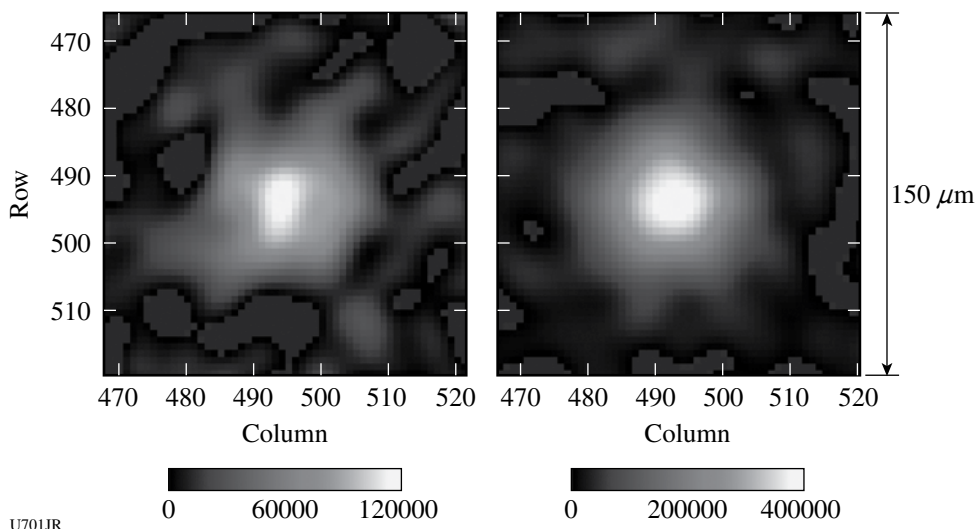
Figure 112.94

(a) Image of DT cryo implosion (shot 47575) yielding 1.1×10^{12} neutrons; (b) image of a DT(15)CH[15] implosion (shot 47551) producing 1.5×10^{13} neutrons.

design now appears to be achievable but still requires addressing the resolution and the transmission across the field of view of the neutron aperture. As an example for the penumbral technique, a neutron point source transmitted through the aperture material cast a finite penumbra whose shape depends on the source location in the aperture field of view. This can result in an image distortion as classical unfolding methods assume a constant response across the field of view. These issues have been addressed this year both experimentally on OMEGA and with Monte Carlo calculation.

Our work is performed with a penumbral aperture made by a pair of intersecting cones on the same axes (Fig. 112.95).
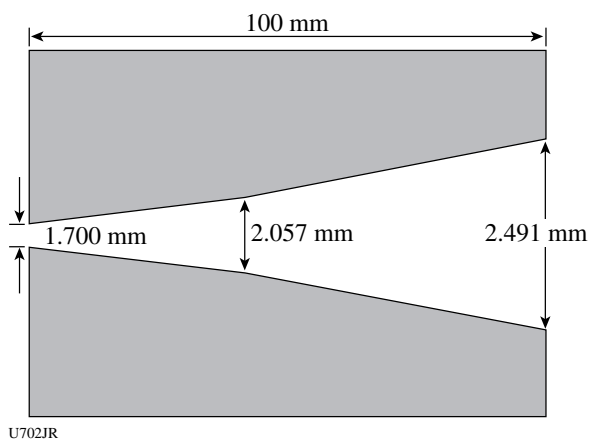
Figure 112.95

Penumbral aperture with a biconical shape made of tungsten.

The middle of the aperture is set at 260 mm from the target chamber center and has a ± 100-μm field of view. Using the Monte Carlo code Geant 4, neutrons are transported through the biconical penumbral aperture. The neutron originates from a 50-μm-diam source, and penumbral images are generated for different locations of the source in the aperture field of view. Each of these images is unfolded using our standard autocorrelation method.[33] The reconstructed images present large distortions when the entire source is out of the field of view (see Fig. 112.96). However, when the source is at the edge of the field of view, there is clear distortion in the images.

Such distortions have also been investigated experimentally on OMEGA. The implosion of DT(15)CH[15] capsules produce an intense neutron source. Several neutron images using penumbral or annular apertures have shown a reproducible spherical source of 50-μm mean diameter. Therefore, the penumbral aperture was displaced between various shots performed with this target. The reconstructed sources are presented in Fig. 112.97 and agree with the conclusion deduced from the Geant 4 calculations. The ± 100-μm field of view defined by the intersection of the two cones of the penumbral aperture appears to be very effective.

In the future, we plan to reproduce these experiments with a ring aperture as Monte Carlo calculations predict enhanced image distortion with the source position in the field of view. Also, the construction of a 150-mm-diam camera will allow us to record the image at a finer spatial resolution.
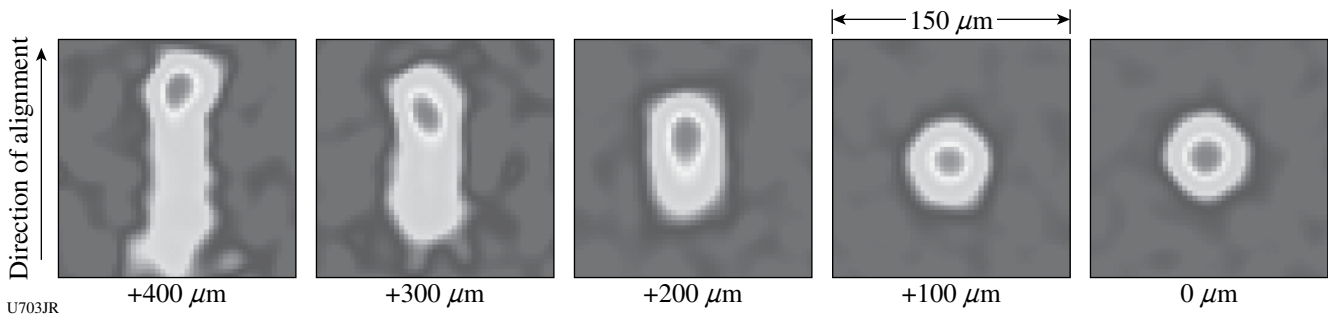
Figure 112.96
A 50-μm-diam neutron source at different locations in the field of view of a penumbral aperture using the Monte Carlo code Geant 4.
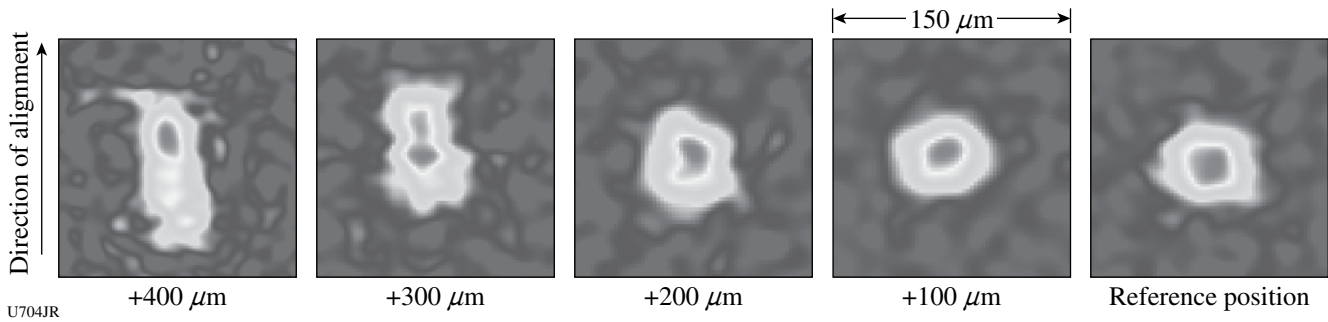
Figure 112.97
Experimental neutron images recorded at different positions in the field of view of a penumbral aperture. All images were recorded on a DT(15)CH[15] target implosion.

Neutron Flux and Duration Emission Measured with CVD Diamond Detectors: A series of chemical-vapor-deposition (CVD) diamond detectors have been implemented on OMEGA during a directly driven implosion of a DT capsule yielding 10^{13} to 10^{14} neutrons. These detectors discriminate neutrons by the time-of-flight technique and can provide a neutron-yield measurement after a calibration with the usual copper activation diagnostic. Neutron bang time and ion temperature measurement can also be deduced from the probed signal as long as the diamond detectors exhibit temporal properties in the 100-ps range. Here the diamond devices used were grown and fabricated by CEA with controlled impurity levels (nitrogen, oxygen) that affect the sensitivity and the response time of the diamond detectors.[34] The relation between the level and nature of impurities with respect to the detector performances is, to date, empirical and has therefore required an experimental approach. These experiments have aimed at identifying the relevant characteristics of the diamond detectors to be suitable for neutron-yield, bang-time, and ion-temperature diagnostics.

Diamond detectors were inserted at distances of 30 cm, 1 m, and 2 m from the target chamber center using the TIM diagnostic insertion mechanisms. The distances and neutron-yield range

provide the ability to probe the performances of the detectors within two decades of the neutron flux (n/cm^2). The detectors exhibit a linear response over the dynamic range explored. Sensitivity was also found reproducible on the A281103 diamond device tested in December 2005 and March 2007 (Fig. 112.98).
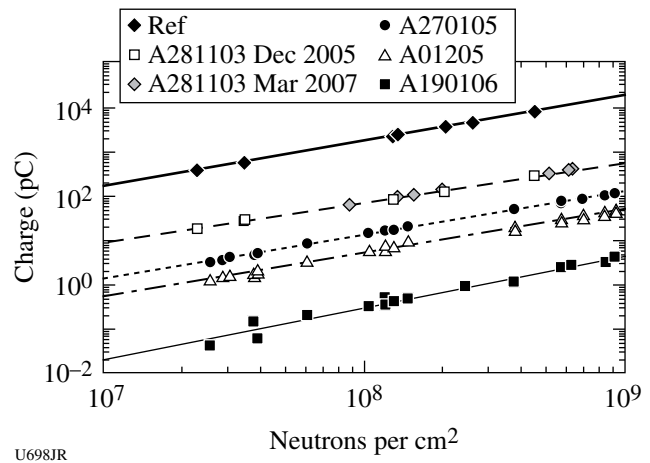
Figure 112.98
Linear response of a chemical vapor deposition (CVD) diamond measured on OMEGA.

Further, the diamond sensitivity can vary by a factor of 10^4 (Table 112.VII), which is mainly attributed to the material nature and the contribution of the added impurities since the geometrical dimensions of all detectors remained almost equal (3×3-mm^2 surface, 200 to 400 μm thick). Such results are essential to determine the required diamond detector characteristics as a function of location and detection volumes as NIF and LMJ experiments will require the neutron diagnostics to operate in the 10^{12} to 10^{18} neutron yield range.[35]

The relative sensitivity between the diamonds as measured with the 14-MeV neutrons was also probed for comparison with 16-MeV electrons produced on a Linac accelerator at CEA (Bruyères le Châtel) (Fig. 112.99). A simple test on an electron accelerator will make it possible to classify the diamond detectors prior to their installation on large ICF facilities.

The temporal properties of the detectors, such as rise time, FWHM, and decay time, were also measured from the short duration (25 ps) of the Linac electron pulses. Several diamond detectors show a 10% to 90% rise time below 100 ps and a subnanosecond decay time (Table 112.VIII). On OMEGA, the 150-ps-long neutron pulse makes it possible to measure the main temporal characteristics of the diamond detectors.

The detector signal propagates through 30 m of cable before reaching a 7-GHz-bandwidth single-shot oscilloscope (IN7100). After software removal of the dispersion caused by this cable, the diamond detector exhibits a signal duration at FWHM and a decay time comparable to those measured using the 16-MeV electrons. The signal rise time observed during DT implosions is, however, somewhat different since the neutron pulse duration at the detector position is determined by the 150-ps duration of the neutron source, convoluted with the temporal broadening induced by the DT ion's main energy at bang time. This ion temperature effect is clearly observed on the signal rise time by probing the response at varying distances—37 cm, 100 cm, or 200 cm—from the target (see Fig. 112.100—probed on the detector A270105).

Table 112.VII: Diamond sensitivity measured with a pulse of 14-MeV neutrons.

Chemical Vapor Deposition	Type	Thickness	Size	Gold Contact	High Voltage	Sensitivity $(C.n^{-1})$
Ref	Monocrystalline	225 μm	4×4 mm	3×3 mm	–100 V	2.03×10^{-16}
A040406	Monocrystalline	260 μm	3×3 mm	2×2 mm	–750 V	4.15×10^{-18}
A281103	Polycrystalline	260 μm	5×5 mm	4×4 mm	–750 V	5.84×10^{-18}
A270105	Polycrystalline	250 μm	5×5 mm	4×4 mm	–750 V	1.06×10^{-18}
A010205	Polycrystalline	630 μm	5×5 mm	4×4 mm	–360 V	4.53×10^{-19}
A190106	Polycrystalline	450 μm	5×5 mm	4×4 mm	–500 V	2.70×10^{-20}

U699JR
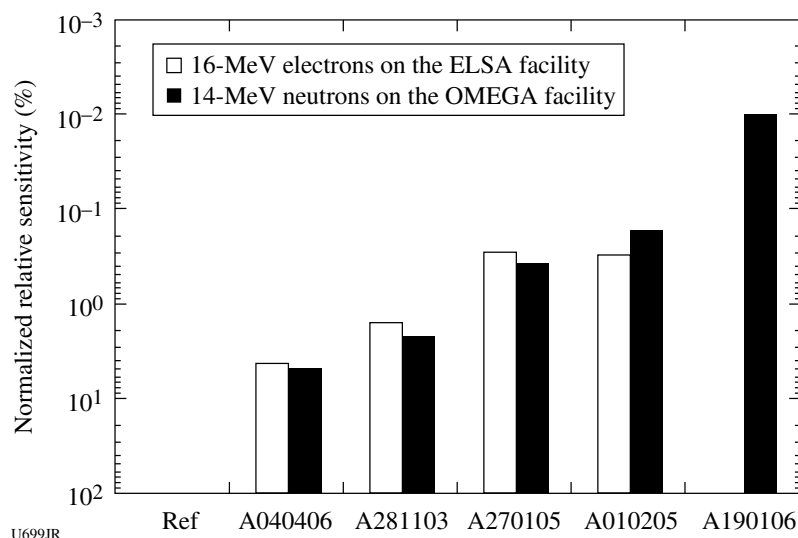
Figure 112.99
Comparison of electron and neutron relative sensitivity. All data are normalized by the most sensitive diamond "Ref."

Table 112.VIII: Temporal properties of diamond detectors as measured under 16-MeV electron pulses of 25-ps duration and 14-MeV neutron pulses of 150-ps duration.

Diamond Reference	ELSA Facility 16-MeV Electrons			OMEGA Facility 14-MeV Neutrons		
	Rise (ps)	FWHM (ps)	Decay (ps)	Rise (ps)	FWHM (ps)	Decay (ps)
Ref	219	2870	4228	461	3508	4075
A040406	85	265	627	260	367	1340
A281103	134	434	772	226	442	688
A270105	73	297	608	164	318	601
A010205	86	178	540	133	241	322
A190106	n/a	n/a	n/a	150	266	917
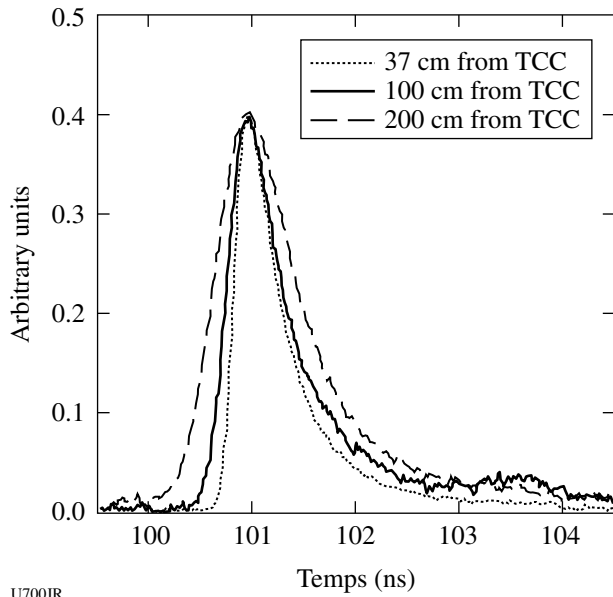
U700JR

Figure 112.100
Doppler broadening of the neutron pulse.

Using the signal processing technique already used in the NTD diagnostics,[36] we deduce the neutron duration at 2 m from the target, which is mainly determined by the Doppler broadening produced by the ions. The resulting ion temperature and measured time duration are shown on the two last columns of Table 112.IX. For comparison, Table 112.IX also shows the ion temperature measured with the standard OMEGA system, performed at 5 m with a fast scintillator and an MCP photomultiplier. From these values, the time broadening (Δt) is deduced for a measurement at 2 m from TCC. The measured ion temperatures deduced from the CVD diamond at 2 m from the target are in good agreement with the standard OMEGA measurement.

A low-sensitivity CVD diamond with a high level of nitrogen impurity (A190106) demonstrates that diamond detectors can measure very-high-yield neutron for the NIF and LMJ. The development of faster low-sensitivity CVD diamond detectors will continue with CEA-LIST and OMEGA. Ion-temperature measurement with CVD diamonds will be strengthened with future experiments.

Table 112.IX: Ion-temperature measurement at 2 m from TCC.

OMEGA Measurement			CVD Measurement		
N° Tir	T_i LLE ($\pm$0.5 keV)	Δt	Reference CVD	T_i Measured	Δt Measured
47539	3.4 keV	446 ps	A270105	3.8 keV	474 ps
			A010205	3.6 keV	456 ps
47540	3.6 keV	459 ps	A270105	3.5 keV	450 ps
			A010205	3.4 keV	449 ps
47549	5.4 keV	562 ps	A270105	5.5 keV	565 ps
			A010205	5.7 keV	576 ps
47550	5.1 keV	547 ps	A270105	5.0 keV	542 ps
			A010205	5.0 keV	542 ps

One new challenging task will be to demonstrate the capability of a large, sensitive CVD diamond to measure the downscattered neutron yield for ρR determination.

FY07 AWE OMEGA Experimental Program

Radiation transport through enclosed spaces with inwardly moving walls is a key component of the physics of laser-heated hohlraums. It arises in the laser-heated cavity itself (where inward motion of the wall results in late-time stagnation of dense plasma on the hohlraum axis[37]) and also in the laser-entry and diagnostic holes (where an understanding of hole closure is important to hohlraum design and the interpretation of diagnostic data[38]). To better understand these phenomena, AWE (in collaboration with LLNL and General Atomics) successfully led two days of experiments on OMEGA during FY07.

A laser-heated hohlraum was used (Fig. 112.101) to illuminate annular slits machined in samples of solid-density tantalum and low-density, tantalum-oxide foam. In the first day of experiments (November 2006), the transmitted energy was measured indirectly (by measuring the temperature rise of a "calorimeter" hohlraum), directly (by measuring the emission from the tantalum-oxide component, using a target in which the calorimeter hohlraum was omitted), and by x-ray gated imaging of the slit. In the second series of experiments (May 2007), x-ray point-projection backlighting was used to determine the density distribution of plasma within a radiatively driven slit in solid-density tantalum. Figure 112.102 shows the measured temperature rise of the calorimeter hohlraum in comparison with radiation hydrocode simulation, for slits of
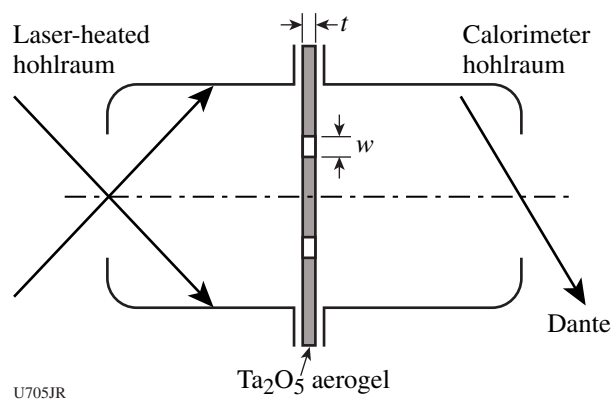
Figure 112.101
Schematic of the experiment to measure radiation transport through slits in low-density tantalum oxide and solid-density tantalum. One surface of the slit is heated by a scale-1.4 hohlraum target, and the transmitted energy either heats a "calorimeter" hohlraum or is measured directly (calorimeter not present). Radiographic measurements of the slit closure are made by point-projection backlighting along the hohlraum axis.

two different widths and also for a sample of tantalum-oxide foam with no slit. Heating of the calorimeter arises from two sources: (1) x-ray transmission through the closing slit and (2) radiation burnthrough of the surrounding tantalum-oxide foam material. Both phenomena are modeled well by the simulation. Figure 112.103 shows point-projection radiographs of an annular slit in solid-density tantalum foil and comparison with a simulation in simplified (2-D Eulerian) geometry. The simulation approximately reproduces the deceleration shock and axial stagnation region at the center of the slit, as well as the complex shock interactions in the neighborhood of the
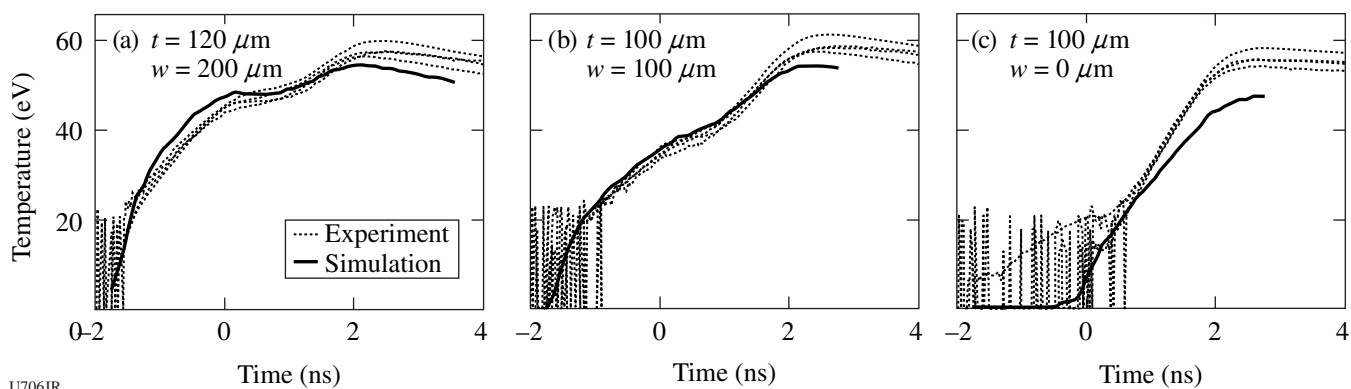
Figure 112.102
Temperature of the calorimeter hohlraum for experiments using low-density (0.25 g cm^{-3}) tantalum-oxide slits of (a) 120-μm thickness and 200-μm width, (b) 100-μm thickness and 100-μm width, and (c) 100-μm thickness with no slit. In each case the temperature inferred from four channels of the Dante diagnostic (a filtered x-ray diode array) is compared with simulation.
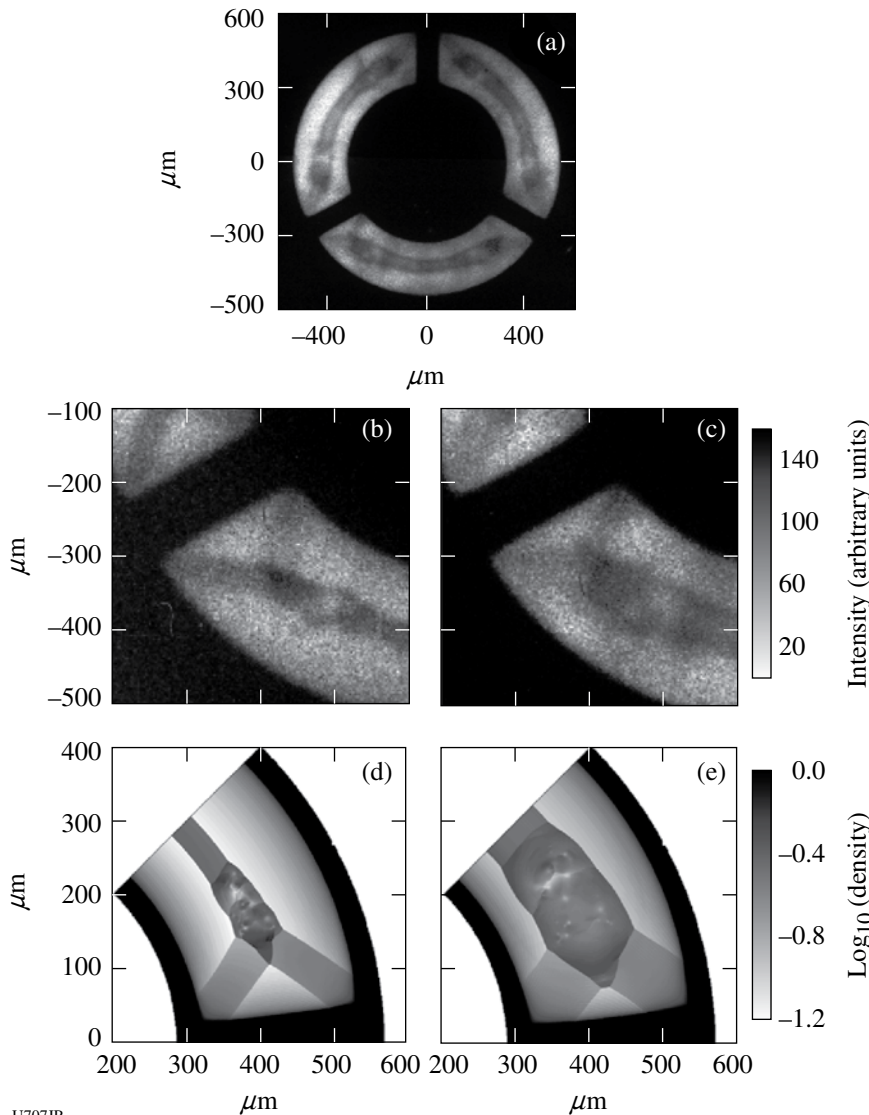
Figure 112.103
Point-projection radiographs of the closure of a 200-μm-wide slit in 50-μm-thick solid-density tantalum. (a) The deceleration shock and axial stagnation region within the slit are clearly visible. Images (b) and (c) are separated by 1.3 ns in time and show detail of the complex shock interactions in the corners bounded by the sides of the slit and the radial spokes supporting the central disk. Radiation hydrocode simulations (d) and (e) approximately reproduce this structure.

radial spokes supporting the central disk. It is interesting to note that "N-wave" distributions of density, similar to the central stagnation region, also occur, in the astrophysical context, in stellar atmospheres[39,40] and that experiments of this type offer a potential laboratory platform for their investigation.

REFERENCES

1. S. Brygoo *et al*., "Development of Quartz as an Impedance-Match Standard for Laser Shock Measurements in the Diamond Anvil Cell," submitted to the Journal of Applied Physics.

2. J. Eggert *et al*., "Hugoniot Data for Helium in the Mbar Regime," to be published in Physical Review Letters.

3. G. W. Collins, Lawrence Livermore National Laboratory, private communication (2007).

4. D. Saumon and G. Chabrier, Phys. Rev. Lett. **62**, 2397 (1989).

5. S. A. Bonev, B. Militzer, and G. Galli, Phys. Rev. B **69**, 014101 (2004).

6. R. Jeanloz *et al*., Proc. Natl. Acad. Sci. USA **104**, 9172 (2007).

7. L. Stixrude and R. Jeanloz, "Fluid Helium at Conditions of Giant Planetary Interiors," submitted to the Proceedings of the National Academy of Sciences of the United States of America.

8. M. Ross, R. Boehler, and D. Errandonea, Phys. Rev. B **76**, 184117 (2007).

9. P. Celliers, Lawrence Livermore National Laboratory, private communication (2007).

10. J. M. Foster, B. H. Wilde, P. A. Rosen, R. J. R. Williams, B. E. Blue, R. F. Coker, R. P. Drake, A. Frank, P. A. Keiter, A. M. Khokhlov, J. P. Knauer, and T. S. Perry, Astrophys. J. Lett. **634**, L77 (2005).

U707JR

11. R. F. Coker *et al.*, Astrophys. Space Sci. **307**, 57 (2007).

12. C. K. Li, F. H. Séguin, J. A. Frenje, J. R. Rygg, R. D. Petrasso, R. P. J. Town, P. A. Amendt, S. P. Hatchett, O. L. Landen, A. J. Mackinnon, P. K. Patel, V. A. Smalyuk, T. C. Sangster, and J. P. Knauer, Phys. Rev. Lett. **97**, 135003 (2006).

13. C. K. Li, F. H. Séguin, J. A. Frenje, J. R. Rygg, R. D. Petrasso, R. P. J. Town, P. A. Amendt, S. P. Hatchett, O. L. Landen, A. J. Mackinnon, P. K. Patel, M. Tabak, J. P. Knauer, T. C. Sangster, and V. A. Smalyuk, Phys. Rev. Lett. **99**, 015001 (2007).

14. C. K. Li, F. H. Séguin, J. A. Frenje, J. R. Rygg, R. D. Petrasso, R. P. J. Town, O. L. Landen, J. P. Knauer, and V. A. Smalyuk, Phys. Rev. Lett. **99**, 055001 (2007).

15. C. K. Li, presented at the Fifth International Conference on Inertial Fusion Sciences and Applications, Kobe, Japan, 9–14 September 2007 (invited) (Paper ThO4.1).

16. R. Petrasso, Bull. Am. Phys. Soc. **52**, 97 (2007) (invited).

17. C. K. Li, F. H. Séguin, J. A. Frenje, J. R. Rygg, R. D. Petrasso, R. P. J. Town, P. A. Amendt, S. P. Hatchett, O. L. Landen, A. J. Mackinnon, P. K. Patel, V. Smalyuk, J. P. Knauer, T. C. Sangster, and C. Stoeckl, Rev. Sci. Instrum. **77**, 10E725 (2006).

18. J. F. Hansen, Lawrence Livermore National Laboratory, private communication (2007).

19. B. L. Henke *et al.*, J. Opt. Soc. Am. B **1**, 818 (1984).

20. D. Vanderhaegen, J. Quant. Spectrosc. Radiat. Transf. **36**, 557 (1986).

21. G. C. Pomraning, J. Quant. Spectrosc. Radiat. Transf. **40**, 479 (1988).

22. G. C. Pomraning, *Linear Kinetic Theory and Particle Transport in Stochastic Mixtures*, Series on Advances in Mathematics for Applied Sciences, Vol. 7 (World Scientific, Singapore, 1991).

23. O. Haran, D. Shvarts, and R. Theiberger, Phys. Rev. E **61**, 6183 (2000).

24. C. C. Smith, J. Quant. Spectrosc. Radiat. Transf. **81**, 451 (2003).

25. P. D. Roberts *et al.*, J. Phys. D: Appl. Phys. **13**, 1957 (1980).

26. P. Amendt *et al.*, Bull. Am. Phys. Soc. **49**, 26 (2004).

27. W. A. Lokke and W. H. Grasberger, Lawrence Livermore National Laboratory, Livermore, CA, Report UCRL-52276, NTIS Order No. UCRL-52276 (1977).

28. J. R. Rygg, J. A. Frenje, C. K. Li, F. H. Séguin, R. D. Petrasso, J. A. Delettrez, V. Yu. Glebov, V. N. Goncharov, D. D. Meyerhofer, S. P. Regan, T. C. Sangster, and C. Stoeckl, Phys. Plasmas **13**, 052702 (2006).

29. D. C. Wilson *et al.*, "The Effects of High Z Pre-Mix on Burn in ICF Capsules," submitted to the *Proceedings of the Fifth International Conference on Inertial Fusion Science and Applications (2007)* [to be published by Journal of Physics: Conference Series (Institute of Physics), London, England].

30. D. Ho *et al.*, Bull. Am. Phys. Soc. **51**, 213 (2006).

31. R. E. Olson, R. J. Leeper, A. Nobile, J. A. Oertel, G. A. Chandler, K. Cochrane, S. C. Dropinski, S. Evans, S. W. Haan, J. L. Kaae, J. P. Knauer, K. Lash, L. P. Mix, A. Nikroo, G. A. Rochau, G. Rivera, C. Russell, D. Schroen, R. J. Sebring, D. L. Tanner, R. E. Turner, and R. J. Wallace, Phys. Plasmas **11**, 2778 (2003).

32. L. Disdier, A. Rouyer, I. Lantuéjoul, O. Landoas, J. L. Bourgade, T. C. Sangster, V. Yu. Glebov, and R. A. Lerche, Phys. Plasmas **13**, 056317 (2006).

33. A. Rouyer, Rev. Sci. Instrum. **74**, 1234 (2003).

34. P. Bergonzo, D. Tromson, and C. Mer, Semicond. Sci. Technol. **18**, S105 (2003).

35. V. Yu. Glebov, D. D. Meyerhofer, T. C. Sangster, C. Stoeckl, S. Roberts, C. A. Barrera, J. R. Celeste, C. J. Cerjan, L. S. Dauffy, D. C. Eder, R. L. Griffith, S. W. Haan, B. A. Hammel, S. P. Hatchett, N. Izumi, J. R. Kimbrough, J. A. Koch, O. L. Landen, R. A. Lerche, B. J. MacGowan, M. J. Moran, E. W. Ng, T. W. Phillips, P. M. Song, R. Tommasini, B. K. Young, S. E. Caldwell, G. P. Grim, S. C. Evans, J. M. Mack, T. Sedillo, M. D. Wilke, D. C. Wilson, C. S. Young, D. Casey, J. A. Frenje, C. K. Li, R. D. Petrasso, F. H. Séguin, J. L. Bourgade, L. Disdier, M. Houry, I. Lantuejoul, O. Landoas, G. A. Chandler, G. W. Cooper, R. J. Lepeer, R. E. Olson, C. L. Ruiz, M. A. Sweeney, S. P. Padalino, C. Horsfield, and B. A. Davis, Rev. Sci. Instrum. **77**, 10E715 (2006).

36. R. A. Lerche, D. W. Phillion, and G. L. Tietbohl, Rev. Sci. Instrum. **66**, 933 (1995).

37. R. T. Eagleton *et al.*, Rev. Sci. Instrum. **68**, 834 (1997).

38. R. E. Chrien *et al.*, Rev. Sci. Instrum. **70**, 557 (1999).

39. D. Mihalas and B. Weibel-Mihalas, *Foundations of Radiation Hydrodynamics* (Oxford University Press, New York, 1984).

40. T. K. Suzuki, Astrophys. J. **578**, 598 (2002).

Publications and Conference Presentations

Publications

B. Ashe, K. L. Marshall, C. Giacofei, A. L. Rigatti, T. J. Kessler, A. W. Schmid, J. B. Oliver, J. Keck, and A. Kozlov, "Evaluation of Cleaning Methods for Multilayer Diffraction Gratings," in *Laser-Induced Damage in Optical Materials: 2006*, edited by G. J. Exarhos, A. H. Guenther, K. L. Lewis, D. Ristau, M. J. Soileau, and C. J. Stolz (SPIE, Bellingham, WA, 2007), Vol. 6403, pp. 64030O.

V. Bagnoud, J. D. Zuegel, N. Forget, and C. Le Blanc, "High-Dynamic-Range Temporal Measurements of Short Pulses Amplified by OPCPA," Opt. Exp. **15**, 5504 (2007).

R. Betti, K. Anderson, T. R. Boehly, T. J. B. Collins, R. S. Craxton, J. A. Delettrez, D. H. Edgell, R. Epstein, V. Yu. Glebov, V. N. Goncharov, D. R. Harding, R. L. Keck, J. H. Kelly, J. P. Knauer, S. J. Loucks, J. A. Marozas, F. J. Marshall, A. V. Maximov, D. N. Maywar, R. L. McCrory, P. W. McKenty, D. D. Meyerhofer, J. Myatt, P. B. Radha, S. P. Regan, C. Ren, T. C. Sangster, W. Seka, S. Skupsky, A. A. Solodov, V. A. Smalyuk, J. M. Soures, C. Stoeckl, W. Theobald, B. Yaakobi, C. Zhou, J. D. Zuegel, J. A. Frenje, C. K. Li, R. D. Petrasso, and F. H. Séguin, "Progress in Hydrodynamics Theory and Experiments for Direct-Drive and Fast Ignition Inertial Confinement Fusion," Plasma Phys. Control. Fusion **48**, B153 (2006) (invited).

R. Betti and J. Sanz, "Bubble Acceleration in the Ablative Rayleigh–Taylor Instability," Phys. Rev. Lett. **97**, 205002 (2006).

R. Betti, A. A. Solodov, J. A. Delettrez, and C. Zhou, "Gain Curves for Direct-Drive Fast-Ignition at Densities Around 300 g/cc," Phys. Plasmas **13**, 100703 (2006).

R. Betti, C. D. Zhou, K. S. Anderson, J. L. Perkins, W. Theobald, and A. A. Solodov, "Shock Ignition of Thermonuclear Fuel with High Areal Density," Phys. Rev. Lett. **98**, 155001 (2007).

P. Brijesh, T. J. Kessler, J. D. Zuegel, and D. D. Meyerhofer, "Demonstration of a Horseshoe-Shaped Longitudinal Focal Profile," J. Opt. Soc. Am. B **24**, 1 (2007).

J. Bromage, C. Dorrer, I. A. Begishev, N. G. Usechak, and J. D. Zuegel, "Highly Sensitive, Single-Shot Characterization for Pulse Widths from 0.4 to 85 ps Using Electro-Optic Shearing Interferometry," Opt. Lett. **31**, 3523 (2006).

I. Carusotto, S. X. Hu, L. A. Collins, and A. Smerzi, "Bogoliubov-Čerenkov Radiation in a Bose-Einstein Condensate Flowing Against an Obstacle," Phys. Rev. Lett. **97**, 260403 (2006).

A. C.-A. Chen, J. U. Wallace, K. P. Klubek, M. B. Madaras, C. W. Tang, and S. H. Chen, "Device Characteristics of Organic Light-Emitting Diodes Comprising Terfluorene Modified with Triphenyltriazine," Chem. Mater. **19**, 4043 (2007).

T. J. B. Collins, J. A. Marozas, R. Betti, D. R. Harding, P. W. McKenty, P. B. Radha, S. Skupsky, V. N. Goncharov, J. P. Knauer, and R. L. McCrory, "One-Megajoule, Wetted-Foam Target-Design Performance for the National Ignition Facility," Phys. Plasmas **14**, 056308 (2007) (invited).

J. E. DeGroote, A. E. Marino, J. P. Wilson, A. L. Bishop, and S. D. Jacobs, "Material Removal Rate Model for Magneto-rheological Finishing (MRF) of Optical Glasses with Nano-diamond MR Fluid," in *Optifab 2007: Technical Digest*, SPIE Technical Digest (SPIE, Bellingham, WA, 2007), Vol. TD04, pp. TF040F.

C. Dorrer, "High-Speed Characterization for Optical Telecommunication Signals," in *Commercial and Biomedical Applications of Ultrafast Lasers VII*, edited by J. Neev, S. Nolte, A. Heisterkamp, and C. B. Schaffer (SPIE, Bellingham, WA, 2007), Vol. 6460, p. 64600L (invited).

C. Dorrer, I. A. Begishev, A. V. Okishev, and J. D. Zuegel, "High-Contrast Optical-Parametric Amplifier as a Front End of High-Power Laser Systems," Opt. Lett. **32**, 2143 (2007).

C. Dorrer, A. V. Okishev, I. A. Begishev, J. D. Zuegel, V. I. Smirnov, and L. B. Glebov, "Optical Parametric Chirped-Pulse–Amplification Contrast Enhancement by Regenerative Pump Spectral Filtering," Opt. Lett. **32**, 2378 (2007).

C. Dorrer and J. D. Zuegel, "Design and Analysis of Binary Beam Shapers Using Error Diffusion," J. Opt. Soc. Am. B **24**, 1268 (2007).

C. Dorrer and J. D. Zuegel, "Optical Testing Using the Transport-of-Intensity Equation," Opt. Express **15**, 7165 (2007).

D. H. Edgell, R. S. Craxton, L. M. Elasky, D. R. Harding, S. J. Verbridge, M. D. Wittman, and W. Seka, "Three-Dimensional Characterization of Spherical Cryogenic Targets Using Ray-Trace Analysis of Multiple Shadowgraph Views," Fusion Sci. Technol. **51**, 717 (2007).

K. A. Fletcher, B. Apker, S. Hammond, J. Punaro, F. J. Marshall, J. Laine, and R. Forties, "Detection of Charged Particles with Charge Injection Devices," Rev. Sci. Instrum. **78**, 063301 (2007).

V. Yu. Glebov, D. D. Meyerhofer, T. C. Sangster, C. Stoeckl, S. Roberts, C. A. Barrera, J. R. Celeste, C. J. Cerjan, L. S. Dauffy, D. C. Eder, R. L. Griffith, S. W. Haan, B. A. Hammel, S. P. Hatchett, N. Izumi, J. R. Kimbrough, J. A. Koch, O. L. Landen, R. A. Lerche, B. J. MacGowan, M. J. Moran, E. W. Ng, T. W. Phillips, P. M. Song, R. Tommasini, B. K. Young, S. E. Caldwell, G. P. Grim, S. C. Evans, J. M. Mack, T. J. Sedillo, M. D. Wilke, D. C. Wilson, C. S. Young, D. Casey, J. A. Frenje, C. K. Li, R. D. Petrasso, F. H. Séguin, J. L. Bourgade, L. Disdier, M. Houry, I. Lantuejoul, O. Landoas, G. A. Chandler, G. W. Cooper, R. J. Leeper, R. E. Olson, C. L. Ruiz, M. A. Sweeney, S. P. Padalino, C. Horsfield, and B. A. Davis, "Development of Nuclear Diagnostics for the National Ignition Facility," Rev. Sci. Instrum. **77**, 10E715 (2006) (invited).

V. Yu. Glebov, C. Stoeckl, T. C. Sangster, C. Mileham, S. Roberts, and R. A. Lerche, "High-Yield Bang Time Detector for the OMEGA Laser," Rev. Sci. Instrum. **77**, 10E712 (2006).

G. Gol'tsman, O. Minaeva, A. Korneev, M. Tarkhov, I. Rubstova, A. Divochiy, I. Milostnaya, G. Chulkova, N. Kaurova,

B. Voronov, D. Pan, J. Kitaygorsky, A. Cross, A. Pearlman, I. Komissarov, W. Slysz, M. Wegrzecki, P. Grabiec, and R. Sobolewski, "Middle-Infrared to Visible-Light Ultrafast Superconducting Single-Photon Detectors," IEEE Trans. Appl. Supercond. **17**, 246 (2007).

W. Guan and J. R. Marciante, "Dual-Frequency Operation in a Short-Cavity Ytterbium-Doped Laser," IEEE Photonics Technol. Lett. **19**, 261 (2007).

W. Guan and J. R. Marciante, "Single-Polarisation, Single-Frequency, 2 cm Ytterbium-Doped Fibre Laser," Electron. Lett. **43**, 558 (2007).

M. Haurylau, S. P. Anderson, K. L. Marshall, and P. M. Fauchet, "Electrically Tunable Silicon 2-D Photonic Bandgap Structures," IEEE J. Quantum Electron. **12**, 1527 (2006).

B. Hu, R. Betti, and J. Manickam, "Kinetic Stability of the Internal Kink Mode in ITER," Phys. Plasmas **13**, 112505 (2006).

S. X. Hu, "Producing Ultracold and Trappable Antihydrogen Atoms," Phys. Rev. Lett. **75**, 010501(R) (2007).

S. X. Hu, "Quantum Study of Slow Electron Collisions with Rydberg Atoms," Phys. Rev. A **74**, 062716 (2006).

S. X. Hu, "Three-Body Recombination of Atomic Ions with Slow Electrons," Phys. Rev. A **98**, 133201 (2007).

H. Huang and T. Kessler, "Tiled-Grating Compressor with Uncompensated Dispersion for Near-Field-Intensity Smoothing," Opt. Lett. **32**, 1854 (2007).

I. V. Igumenshchev, V. N. Goncharov, W. Seka, D. Edgell, and T. R. Boehly, "The Effect of Resonance Absorption in OMEGA Direct-Drive Designs and Experiments," Phys. Plasmas **14**, 092701 (2007).

S. D. Jacobs, "Manipulating Mechanics and Chemistry in Precision Optics Finishing," Sci. Technol. Adv. Mater. **8**, 153 (2007).

Z. Jiang and J. R. Marciante, "Mode-Area Scaling of Helical-Core, Dual-Clad Fiber Lasers and Amplifiers Using an Improved Bend-Loss Model," J. Opt. Soc. Am. B **23**, 2051 (2006).

A. Jukna, I. Barboy, G. Jung, A. Abrutis, S. S. Banerjee, X. Li, D. Wang, and R. Sobolewski, "Noise Evidence for Intermit-

tent Channeled Vortex Motion in Laser-Processed YBaCuO Thin Films," in *Noise and Fluctuations in Circuits, Devices, and Materials*, edited by M. Macucci, L. K. J. Vandamme, C. Ciofi, and M. B. Weissman (SPIE, Bellingham, WA, 2007), Vol. 6600, pp. 66001C.

M. Khafizov, X. Li, Y. Cui, X. X. Xi, and R. Sobolewski, "Mechanism of Light Detection in Current-Biased Superconducting MgB_2 Microbridges," IEEE Trans. Appl. Supercond. **17**, 2867 (2007).

J. Kitaygorsky, I. Komissarov, A. Jukna, D. Pan, O. Minaeva, N. Kaurova, A. Divochiy, A. Korneev, M. Tarkhov, B. Voronov, I. Milostnaya, G. Gol'tsman, and R. Sobolewski, "Dark Counts in Nanostructured NbN Superconducting Single-Photon Detectors and Bridges," IEEE Trans. Appl. Supercond. **17**, 275 (2007).

J. P. Knauer, F. J. Marshall, B. Yaakobi, D. Anderson, B. A. Schmitt, K. M. Chandler, S. A. Pikuz, T. A. Shelkovenko, M. D. Mitchell, and D. A. Hammer, "Response Model for Kodak Biomax-MS Film to X Rays," Rev. Sci. Instrum. **77**, 10F331 (2006).

A. Korneev, O. Minaeva, A. Divochiy, A. Antipov, N. Kaurova, B. Seleznev, B. Voronov, G. Gol'tsman, D. Pan, J. Kitaygorsky, W. Slysz, and R. Sobolewski, "Ultrafast and High Quantum Efficiency Large-Area Superconducting Single-Photon Detectors," in *Photon Counting Applications, Quantum Optics, and Quantum Cryptography*, edited by I. Prochazka, A. L. Migdall, A. Pauchard, M. Dusek, M. S. Hillery, and W. P. Schleich (SPIE, Bellingham, WA, 2007), Vol. 6583, pp. 65830I.

T. Z. Kosc, C. J. Coon, G. V. Babcock, K. L. Marshall, A. Trajkovska-Petkoska, and S. D. Jacobs, "Exploring Motion Reversal in Polymer Cholesteric-Liquid-Crystal Devices," in *Liquid Crystals X*, edited by I.-C. Khoo (SPIE, Bellingham, WA, 2006), Vol. 6332, p. 633209.

T. Z. Kosc, A. A. Kozlov, and A. W. Schmid, "Formation of Periodic Microstructures on Multilayer Dielectric Gratings Prior to Total Ablation," Opt. Express **14**, 10,921 (2006).

T. Z. Kosc, K. L. Marshall, A. Trajkovska-Petkoska, C. J. Coon, K. Hasman, G. V. Babcock, R. Howe, M. Leitch, and S. D. Jacobs, "Development of Polymer Cholesteric Liquid Crystal Flake Technology for Electro-Optic Devices and Particle Displays," in *Emerging Liquid Crystal Technologies II*, edited

by L.-C. Chien (SPIE, Bellingham, WA, 2007), Vol. 6487, p. 64870L.

B. E. Kruschwitz, J. H. Kelly, M. J. Shoup III, L. J. Waxer, E. C. Cost, E. T. Green, Z. M. Hoyt, J. Taniguchi, and T. W. Walker, "High-Contrast Plasma-Electrode Pockels Cell," Appl. Opt. **46**, 1326 (2007).

N. N. Lepeshkin, S. G. Lukishova, R. W. Boyd, and K. L. Marshall, "Feedback-Free, Single-Beam Pattern Formation by Nanosecond Pulses in Dye-Doped Liquid Crystals," in *Liquid Crystals X*, edited by I.-C. Khoo (SPIE, Bellingham, WA, 2006), Vol. 6332, p. 63320A.

X. Li, M. Khafizov, Š. Chromik, M. Valerianova, V. Štrbík, P. Odier, and R. Sobolewski, "Ultrafast Photoresponse Dynamics of Current-Biased Hg-Ba-Ca-Cu-O Superconducting Microbridges," IEEE Trans. Appl. Supercond. **17**, 3648 (2007).

S. G. Lukishova, A. W. Schmid, R. Knox, P. Freivald, L. J. Bissell, R. W. Boyd, C. R. Stroud, Jr., and K. L. Marshall, "Room Temperature Source of Single Photons of Definite Polarization," J. Mod. Opt. **54**, 417 (2007).

J. R. Marciante, W. R. Donaldson, and R. G. Roides, "Averaging of Replicated Pulses for Enhanced-Dynamic-Range Single-Shot Measurement of Nanosecond Optical Pulses," IEEE Photon. Technol. Lett. **19**, 1344 (2007).

J. A. Marozas, "Fourier Transform–Based Continuous Phase-Plate Design Technique: A High-Pass Phase-Plate Design as an Application for OMEGA and the National Ignition Facility," J. Opt. Soc. Am. A **24**, 74 (2007).

F. J. Marshall, J. P. Knauer, D. Anderson, and B. L. Schmitt, "Absolute Calibration of Kodak Biomax-MS Film Response to X Rays in the 1.5- to 8-keV Energy Range," Rev. Sci. Instrum. **77**, 10F308 (2006).

K. L. Marshall, A. G. Noto, G. Painter, and N. Tabiryan, "Computational Chemistry Methods for Predicting the Chiroptical Properties of Liquid Crystal Systems. II. Application to Chiral Azobenzenes," in *Liquid Crystals X*, edited by I.-C. Khoo (SPIE, Bellingham, WA, 2006), Vol. 6332, p. 63320C.

R. L. McCrory, "Highlights of the History of the University of Rochester," in *Inertial Confinement Nuclear Fusion: A Historical Approach by Its Pioneers*, edited by G. Velarde

and N. Carpintero-Santamaria (Foxwell & Davies (UK) Ltd., London, 2007), pp. 127–166.

R. L. McCrory, D. D. Meyerhofer, R. Betti, T. R. Boehly, R. S. Craxton, T. J. B. Collins, J. A. Delettrez, R. Epstein, V. Yu. Glebov, V. N. Goncharov, D. R. Harding, R. L. Keck, J. H. Kelly, J. P. Knauer, S. J. Loucks, L. D. Lund, J. A. Marozas, P. W. McKenty, F. J. Marshall, S. F. B. Morse, P. B. Radha, S. P. Regan, S. Roberts, W. Seka, S. Skupsky, V. A. Smalyuk, C. Sorce, C. Stoeckl, J. M. Soures, R. P. J. Town, B. Yaakobi, J. A. Frenje, C. K. Li, R. D. Petrasso, F. H. Séguin, K. Fletcher, S. Padalino, C. Freeman, and T. C. Sangster, "Direct-Drive Inertial Confinement Fusion Research at the Laboratory for Laser Energetics," in *Current Trends in International Fusion Research—Proceedings of the Fourth Symposium*, edited by C. D. Orth and E. Panarella (NRC Research Press, Ottawa, Canada, 2007), pp. 367–386.

P. W. McKenty, M. D. Wittman, and D. R. Harding, "Effect of Experimentally Observed Hydrogenic Fractionation in Inertial Confinement Fusion Ignition Target Performance," J. Appl. Phys. **100**, 073302 (2006).

J. E. Miller, T. R. Boehly, A. Melchior, D. D. Meyerhofer, P. M. Celliers, J. H. Eggert, D. H. Hicks, C. M. Sorce, J. A. Oertel, and P. M. Emmel, "A Streaked Optical Pyrometer System for Laser-Driven Shock-Wave Experiments on OMEGA," Rev. Sci. Instrum. **78**, 034903 (2007).

J. Myatt, W. Theobald, J. A. Delettrez, C. Stoeckl, M. Storm, T. C. Sangster, A. V. Maximov, and R. W. Short, "High-Intensity Laser Interactions with Mass-Limited Solid Targets and Implications for Fast-Ignition Experiments on OMEGA EP," Phys. Plasmas **14**, 056301 (2007) (invited).

A. V. Okishev, C. Dorrer, V. I. Smirnov, L. B. Glebov, and J. D. Zuegel, "Spectral Filtering in a Diode-Pumped Nd:YLF Regenerative Amplifier Using a Volume Bragg Grating," Opt. Express **15**, 8197 (2007).

A. V. Okishev and J. D. Zuegel, "Intracavity-Pumped Raman Laser Action in a Mid-IR, Continuous-Wave (cw) MgO:PPLN Optical Parametric Oscillator," Opt. Express **14**, 12,169 (2006).

D. Pan, W. Donaldson, and R. Sobolewski, "Femtosecond Laser–Pumped Source of Entangled Photons for Quantum Cryptography Applications," in *Photon Counting Applications, Quantum Optics, and Quantum Cryptography*, edited

by M. Dusek, M. S. Hillery, W. P. Schleich, A. L. Migdall, A. Pauchard, and I. Prochazka (SPIE, Bellingham, WA, 2007), Vol. 6583, pp. 65830K.

S. Papernov and A. W. Schmid, "Using Gold Nanoparticles as Artificial Defects in Thin Films: What Have We Learned About Laser-Induced Damage Driven by Localized Absorbers?" in *Laser-Induced Damage in Optical Materials: 2006*, edited by G. J. Exarhos, A. H. Guenther, K. L. Lewis, D. Ristau, M. J. Soileau, and C. J. Stolz (SPIE, Bellingham, WA, 2007), Vol. 6403, pp. 64030D (invited).

G. P. Pepe, M. Amanti, C. De Lisio, R. Latempa, N. Marrocco, L. Parlato, G. Peluso, A. Barone, R. Sobolewski, and T. Taneda, "Ultrafast Photoresponse of Superconductor/Ferromagnet Nb/ NiCu Heterostructures," Phys. Stat. Sol. C **3**, 2968 (2006).

J. Qiao, A. Kalb, M. J. Guardalben, G. King, D. Canning, and J. H. Kelly, "Large-Aperture Grating Tiling by Interferometry for Petawatt Chirped-Pulse–Amplification Systems," Opt. Express **15**, 9562 (2007).

S. P. Regan, R. Epstein, V. N. Goncharov, I. V. Igumenshchev, D. Li, P. B. Radha, H. Sawada, W. Seka, T. R. Boehly, J. A. Delettrez, O. V. Gotchev, J. P. Knauer, J. A. Marozas, F. J. Marshall, R. L. McCrory, P. W. McKenty, D. D. Meyerhofer, T. C. Sangster, D. Shvarts, S. Skupsky, V. A. Smalyuk, B. Yaakobi, and R. C. Mancini, "Laser-Absorption, Mass Ablation Rate, and Shock Heating in Direct-Drive Inertial Confinement Fusion," Phys. Plasmas **14**, 056305 (2007) (invited).

E. Reiger, S. Dorenbos, V. Zwiller, A. Korneev, G. Chulkova, I. Milostnaya, O. Minaeva, G. Gol'tsman, J. Kitaygorsky, D. Pan, W. Słysz, A. Jukna, and R. Sobolewski, "Spectroscopy With Nanostructured Superconducting Single Photon Detectors," J. Sel. Top. Quantum Electron. **13**, 934 (2007).

T. C. Sangster, R. Betti, R. S. Craxton, J. A. Delettrez, D. H. Edgell, L. M. Elasky, V. Yu. Glebov, V. N. Goncharov, D. R. Harding, D. Jacobs-Perkins, R. Janezic, R. L. Keck, J. P. Knauer, S. J. Loucks, L. D. Lund, F. J. Marshall, R. L. McCrory, P. W. McKenty, D. D. Meyerhofer, P. B. Radha, S. P. Regan, W. Seka, W. T. Shmayda, S. Skupsky, V. A. Smalyuk, J. M. Soures, C. Stoeckl, B. Yaakobi, J. A. Frenje, C. K. Li, R. D. Petrasso, F. H. Séguin, J. D. Moody, J. A. Atherton, B. D. MacGowan, J. D. Kilkenny, T. P. Bernat, and D. S. Montgomery, "Cryogenic DT and D_2 Targets for Inertial Confinement Fusion," Phys. Plasmas **14**, 058101 (2007) (invited tutorial).

T. C. Sangster and J. M. Soures, "Validation of Direct-Drive Ignition Target Design on OMEGA," American Nuclear Society, Fusion Energy Division Newsletter (June 2006), p. 10.

W. Seka, P. Rechmann, J. D. B. Featherstone, and D. Fried, "Laser Ablation of Dental Hard Tissue," J. Laser Dent. **15**, 61 (2007).

S. N. Shafrir, J. C. Lambropoulos, and S. D. Jacobs, "A Magnetorheological Polishing-Based Approach for Studying Precision Microground Surfaces of Tungsten Carbides," Precision Engineering **31**, 83 (2007).

S. N. Shafrir, J. C. Lambropoulos, and S. D. Jacobs, "Micromechanical Contributions to Material Removal and Surface Finish," in *Optifab 2007: Technical Digest*, SPIE Technical Digest (SPIE, Bellingham, WA, 2007), Vol. TD04, pp. TF0407.

S. N. Shafrir, J. C. Lambropoulos, and S. D. Jacobs, "Subsurface Damage and Microstructure Development in Precision Microground Hard Ceramics Using Magnetorheological Finishing Spots," Appl. Opt. **46**, 5500 (2007).

A. Simon, "Comment on 'Magnetic Field Effects on Gas Discharge Plasmas' [Phys. Plasmas **13**, 063511 (2006)]," Phys. Plasmas **14**, 084703 (2007).

W. Słysz, M. Węgrzecki, J. Bar, P. Grabiec, M. Górska, E. Reiger, S. Dorenbos, V. Zwiller, I. Milostnaya, O. Minaeva, A. Antipov, O. Okunev, A. Korneev, K. Smirnov, B. Voronov, N. Kaurova, G. N. Gol'tsman, J. Kitaygorsky, D. Pan, A. Pearlman, A. Cross, I. Komissarov, and R. Sobolewski, "Fiber-Coupled NbN Superconducting Single-Photon Detectors for Quantum Correlation Measurements," in *Photon Counting Applications, Quantum Optics, and Quantum Cryptography*, edited by I. Prochazka, A. L. Migdall, A. Pauchard, M. Dusek, M. S. Hillery, and W. P. Schleich (SPIE, Bellingham, WA, 2007), Vol. 6583, pp. 65830J.

W. Słysz, M. Węgrzecki, J. Bar, P. Grabiec, M. Górska, V. Zwiller, C. Latta, P. Böhi, A. J. Pearlman, A. S. Cross, D. Pan, J. Kitaygorsky, I. Komissarov, A. Verevkin, I. Milostnaya, A. Korneev, O. Minayeva, G. Chulkova, K. Smirnov, B. Voronov, G. N. Gol'tsman, and R. Sobolewski, "Fibre-Coupled, Single Photon Detector Based on NbN Superconducting Nanostructures for Quantum Communications," J. Mod. Opt. **54**, 315 (2007).

V. A. Smalyuk, R. Betti, J. A. Delettrez, V. Yu. Glebov, V. N. Goncharov, D. Y. Li, D. D. Meyerhofer, S. P. Regan, S. Roberts,

T. C. Sangster, C. Stoeckl, W. Seka, J. A. Frenje, C. K. Li, R. D. Petrasso, and F. H. Séguin, "Experimental Studies of Direct-Drive, Low-Intensity, Low-Adiabat Spherical Implosions on OMEGA," Phys. Plasmas **14**, 022702 (2007).

V. A. Smalyuk, S. B. Dumanis, J. A. Delettrez, V. Yu. Glebov, D. D. Meyerhofer, S. P. Regan, T. C. Sangster, and C. Stoeckl, "Hot-Core Assembly in Cryogenic D$_2$ Direct-Drive Spherical Implosions," Phys. Plasmas **13**, 104502 (2006).

V. A. Smalyuk, V. N. Goncharov, K. S. Anderson, R. Betti, R. S. Craxton, J. A. Delettrez, D. D. Meyerhofer, S. P. Regan, and T. C. Sangster, "Measurements of the Effects of the Intensity Pickets on Laser Imprinting for Direct-Drive, Adiabat-Shaping Designs on OMEGA," Phys. Plasmas **14**, 032702 (2007).

A. A. Solodov, R. Betti, J. A. Delettrez, and C. D. Zhou, "Gain Curves and Hydrodynamic Simulations of Ignition and Burn for Direct-Drive Fast-Ignition Fusion Targets," Phys. Plasmas **14**, 062701 (2007).

C. Stoeckl, V. Yu. Glebov, P. A. Jaanimagi, J. P. Knauer, D. D. Meyerhofer, T. C. Sangster, M. Storm, S. Sublett, W. Theobald, M. H. Key, A. J. MacKinnon, P. Patel, D. Neely, and P. A. Norreys, "Operation of Target Diagnostics in a Petawatt Laser Environment," Rev. Sci. Instrum. **77**, 10F506 (2006) (invited).

S. Sublett, J. P. Knauer, I. V. Igumenshchev, A. Frank, and D. D. Meyerhofer, "Double-Pulse Laser-Driven Jets on OMEGA," Astrophys. Space Sci. **307**, 47 (2007).

L. Sun and J. R. Marciante, "Filamentation Analysis in Large-Mode-Area Fiber Lasers," J. Opt. Soc. Am. B. **24**, 2321 (2007).

T. Taneda, G. P. Pepe, L. Parlato, A. A. Golubov, and R. Sobolewski, "Time-Resolved Carrier Dynamics and Electron-Phonon Coupling Strength in Proximized Weak Ferromagnet/Superconductor Nanobilayers," Phys. Rev. B **75**, 174507 (2007).

W. Theobald, J. E. Miller, T. R. Boehly, E. Vianello, D. D. Meyerhofer, T. C. Sangster, J. H. Eggert, and P. M. Celliers, "X-Ray Preheating of Window Materials in Direct-Drive Shock-Wave Timing Experiments," Phys. Plasmas **13**, 122702 (2006).

A. Trajkovska, C. Kim, K. L. Marshall, T. H. Mourey, and S. H. Chen, "Photoalignment of a Nematic Liquid Crystal Fluid and Glassy–Nematic Oligofluorenes on Coumarin-Containing Polymer Films," Macromolecules **39**, 6983 (2006).

D. Wang, A. Cross, G. Guarino, S. Wu, R. Sobolewski, and A. Mycielski, "Time-Resolved Dynamics of Coherent Acoustic Phonons in CdMnTe Diluted-Magnetic Single Crystals," Appl. Phys. Lett. **90**, 211905 (2007).

S. Wu, P. Geiser, J. Jun, J. Karpinski, and R. Sobolewski, "Femtosecond Optical Generation and Detection of Coherent Acoustic Phonons in GaN Single Crystals," Phys. Rev. B **76**, 085210 (2007).

S. Wu, P. Geiser, J. Jun, J. Karpinski, D. Wang, and R. Sobolewski, "Time-Resolved Intervalley Transitions in GaN Single Crystals," J. Appl. Phys. **101**, 043701 (2007).

L. Zheng, A. W. Schmid, and J. C. Lambropoulos, "Surface Effects on Young's Modulus and Hardness of Fused Silica by Nanoindentation Study," J. Mater. Sci. **42**, 191 (2007).

C. D. Zhou and R. Betti, "Hydrodynamic Relations for Direct-Drive Fast-Ignition and Conventional Inertial Confinement Fusion Implosions," Phys. Plasmas **14**, 072703 (2007).

C. D. Zhou, W. Theobald, R. Betti, P. B. Radha, V. A. Smalyuk, D. Shvarts, V. Yu. Glebov, C. Stoeckl, K. S. Anderson, D. D. Meyerhofer, T. C. Sangster, C. K. Li, R. D. Petrasso, J. A. Frenje, and F. H. Séguin, "High-ρR Implosions for Fast-Ignition Fuel Assembly," Phys. Rev. Lett. **98**, 025004 (2007).

OMEGA External Users' Publications

K. U. Akli, M. H. Key, H. K. Chung, S. B. Hansen, R. R. Freeman, M. H. Chen, G. Gregori, S. Hatchett, D. Hey, N. Izumi, J. King, J. Kuba, P. Norreys, A. J. Mackinnon, C. D. Murphy, R. Snavely, R. B. Stephens, C. Stoeckel, W. Theobald, and B. Zhang, "Temperature Sensitivity of Cu K$_\alpha$ Imaging Efficiency Using a Spherical Bragg Reflecting Crystal," Phys. Plasmas **14**, 023102 (2007).

A. Benuzzi-Mounaix, M. Koenig, A. Ravasio, T. Vinci, N. Ozaki, M. Rabec le Gloahec, B. Loupias, G. Huser, E. Henry, S. Bouquet, C. Michaut, D. Hicks, A. MacKinnon, P. Patel, H. S. Park, S. Le Pape, T. Boehly, M. Borghesi, C. Cecchetti, M. Notley, R. Clark, S. Bandyopadhyay, S. Atzeni, A. Schiavi, Y. Aglitskiy, A. Faenov, T. Pikuz, D. Batani, R. Dezulian, and K. Tanaka, "Laser-Driven Shock Waves for the Study of Extreme Matter States," Plasma Phys. Control. Fusion **48**, B347 (2006).

E. G. Blackman, "Distinguishing Propagation vs. Launch Physics of Astrophysical Jets and the Role of Experiments," Astrophys. Space Sci. **307**, 7 (2007).

R. F. Coker, B. H. Wilde, J. M. Foster, B. E. Blue, P. A. Rosen, R. J. R. Williams, P. Hartigan, A. Frank, and C. A. Back, "Numerical Simulations and Astrophysical Applications of Laboratory Jets at OMEGA," Astrophys. Space Sci. **307**, 57 (2007).

A. Frank, "Hypersonic Swizzle Sticks: Protostellar Turbulence, Outflows and Fossil Outflow Cavities," Astrophys. Space Sci. **307**, 35 (2007).

D. H. Froula, L. Divol, N. B. Meezan, S. Dixit, J. D. Moody, P. Neumayer, B. B. Pollack, J. S. Ross, and S. H. Glenzer, "Ideal Laser-Beam Propagation Through High-Temperature Ignition Hohlraum Plasmas," Phys. Rev. Lett. **98**, 085001 (2007).

D. H. Froula, L. Divol, N. B. Meezan, S. Dixit, P. Neumayer, J. D. Moody, B. B. Pollock, J. S. Ross, L. J. Suter, and S. H. Glenzer, "Laser Beam Propagation Through Inertial Confinement Fusion Hohlraum Plasmas," Phys. Plasmas **14**, 055705 (2007) (invited).

S. H. Glenzer, O. L. Landen, P. Neumayer, R. W. Lee, K. Widmann, S. W. Pollaine, R. J. Wallace, G. Gregori, A. Höll, T. Bornath, R. Thiele, V. Schwarz, W.-D. Kraeft, and R. Redmer, "Observations of Plasmons in Warm Dense Matter," Phys. Rev. Lett. **98**, 065002 (2007).

J. F. Hansen, M. J. Edwards, D. H. Froula, A. D. Edens, G. Gregori, and T. Ditmire, "Laboratory Observation of Secondary Shock Formation Ahead of a Strongly Radiative Blast Wave," Astrophys. Space Sci. **307**, 219 (2007).

J. F. Hansen, H. F. Robey, R. I. Klein, and A. R. Miles, "Experiment on the Mass-Stripping of an Interstellar Cloud in a High Mach Number Post-Shock Flow," Phys. Plasmas **14**, 056505 (2007).

J. F. Hansen, H. F. Robey, R. I. Klein, and A. R. Miles, "Mass-Stripping Analysis of an Interstellar Cloud by a Supernova Shock," Astrophys. Space Sci. **307**, 147 (2007).

J. Hawreliak, J. Colvin, J. Eggert, D. H. Kalantar, H. E. Lorenzana, S. Pollaine, K. Rosolankova, B. A. Remington, J. Stölken, and J. S. Wark, "Modeling Planetary Interiors in Laser Based Experiments Using Shockless Compression," Astrophys. Space Sci. **307**, 285 (2007).

J. Honig, J. Halpin, D. Browning, J. Crane, R. Hackel, M. Henesian, J. Peterson, D. Ravizza, T. Wennberg, H. Rieger, and J. Marciante, "Diode-Pumped Nd:YAG Laser with 38 W Average Power and User-Selectable, Flat-in-Time Subnanosecond Pulses," Appl. Opt. **46**, 3269 (2007).

C. J. Horsfield, S. E. Caldwell, C. R. Christensen, S. C. Evans, J. M. Mack, T. Sedillo, C. S. Young, and V. Yu. Glebov, "γ-Ray 'Bang-Time' Measurements with a Gas-Cherenkov Detector for Inertial-Confinement Fusion Experiments," Rev. Sci. Instrum. **77**, 10E724 (2006).

I. Kang and C. Dorrer, "Method of Optical Pulse Characterization Using Sinusoidal Optical Phase Modulations," Opt. Lett. **32**, 2538 (2007).

P. A. Keiter, S. C. Laffite, G. A. Kyrala, J. R. Fincke, J. H. Cooley, and D. C. Wilson, "A Planar-Geometry Platform for the Experimental Investigation of Be Jets," Phys. Plasmas **14**, 034501 (2007).

M. Koenig, A. Ravasio, A. Benuzzi-Mounaix, B. Loupias, N. Ozaki, M. Borghesi, C. Cecchetti, D. Batani, R. Dezulian, S. Lepape, P. Patel, H. S. Park, D. Hicks, A. McKinnon, T. Boehly, A. Schiavi, E. Henry, M. Notley, R. Clark, and S. Bandyopadhyay, "Density Measurements of Shock Compressed Matter Using Short Pulse Laser Diagnostics," Astrophys. Space Sci. **307**, 257 (2007).

C. C. Kuranz, B. E. Blue, R. P. Drake, H. F. Robey, J. F. Hansen, J. P. Knauer, M. J. Grosskopf, C. Krauland and D. C. Marion, "Dual, Orthogonal, Backlit Pinhole Radiography in OMEGA Experiments," Rev. Sci. Instrum. **77**, 10E327 (2006).

C. C. Kuranz, R. P. Drake, T. L. Donajkowski, K. K. Dannenberg, M. Grosskopf, D. J. Kremer, C. Krauland, D. C. Marion, H. F. Robey, B. A. Remington, J. F. Hansen, B. E. Blue, J. Knauer, T. Plewa, and N. Hearn, "Assessing Mix Layer Amplitude in 3D Decelerating Interface Experiments," Astrophys. Space Sci. **307**, 115 (2007).

G. A. Kyrala, D. C. Wilson, J. F. Benage, M. Gunderson, K. Klare, J. Frenje, R. Petrasso, W. Garbett, S. James,

V. Glebov, and B. Yaakobi, "Effect of Higher z Dopants on Implosion Dynamics: X-Ray Spectroscopy," High Energy Density Phys. **3**, 163 (2007).

K. L. Lancaster, J. S. Green, D. S. Hey, K. U. Akli, J. R. Davies, R. J. Clarke, R. R. Freeman, H. Habara, M. H. Key, R. Kodama, K. Krushelnick, C. D. Murphy, M. Nakatsutsumi, P. Simpson, R. Stephens, C. Stoeckl, T. Yabuuchi, M. Zepf, and P. A. Norreys, "Measurements of Energy Transport Patterns in Solid Density Laser Plasma Interactions at Intensities of 5×10^{20} W cm^{-2}," Phys. Rev. Lett. **98**, 125002 (2007).

O. L. Landen, S. H. Glenzer, D. H. Froula, E. L. Dewald, L. J. Suter, M. B. Schneider, D. E. Hinkel, J. C. Fernandez, J. L. Kline, S. R. Goldman, D. G. Braun, P. M. Celliers, S. J. Moon, H. S. Robey, N. E. Lanier, S. G. Glendinning, B. E. Blue, B. H. Wilde, O. S. Jones, J. Schein, L. Divol, D. H. Kalantar, K. M. Campbell, J. P. Holder, J. W. McDonald, C. Niemann, A. J. Mackinnon, G. W. Collins, D. K. Bradley, J. H. Eggert, D. G. Hicks, G. Gregori, R. K. Kirkwood, B. K. Young, J. M. Foster, J. F. Hansen, T. S. Perry, D. H. Munro, H. A. Baldis, G. P. Grim, R. F. Heeter, M. B. Hegelich, D. S. Montgomery, G. A. Rochau, R. E. Olson, R. E. Turner, J. B. Workman, R. L. Berger, B. I. Cohen, W. L. Kruer, A. B. Langdon, S. H. Langer, N. B. Meezan, H. A. Rose, C. H. Still, E. A. Williams, E. S. Dodd, M. J. Edwards, M.-C. Monteil, R. M. Stevenson, B. R. Thomas, R. F. Coker, G. R. Magelssen, P. A. Rosen, P. E. Stry, D. Woods, S. V. Weber, P. E. Young, S. Alvarez, G. Armstrong, R. Bahr, J.-L. Bourgade, D. Bower, J. Celeste, M. Chrisp, S. Compton, J. Cox, C. Constantin, R. Costa, J. Duncan, A. Ellis, J. Emig, C. Gauntier, A. Greenwood, R. Griffith, F. Holdner, G. Holtmeier, D. Hargrove, T. James, J. Kamperschroer, J. Kimbrough, M. Landon, F. D. Lee, R. Malone, M. May, S. Montelongo, J. Moody, E. Ng, A. Nikitin, D. Pellinen, K. Piston, M. Poole, V. Rekow, M. Rhodes, R. Shepherd, S. Shiromizu, D. Voloshin, A. Warrick, P. Watts, F. Weber, P. Young, P. Arnold, L. Atherton, G. Bardsley, R. Bonanno, T. Borger, M. Bowers, R. Bryant, S. Buckman, S. Burkhart, F. Cooper, S. N. Dixit, G. Erbert, D. C. Eder, R. E. Ehrlich, B. Felker, J. Fornes, G. Frieders, S. Gardner, C. Gates, M. Gonzalez, S. Grace, T. Hall, C. A. Haynam, G. Heestand, M. A. Henesian, M. Hermann, G. Hermes, S. Huber, K. Jancaitis, S. Johnson, B. Kauffman, T. Kelleher, T. Kohut, A. E. Koniges, T. Labiak, D. Latray, A. Lee, D. Lund, S. Mahavandi, K. R. Manes, C. Marshall, J. McBride, T. McCarville, L. McGrew, J. Menapace, E. Mertens, J. Murray, J. Neumann, M. Newton, P. Opsahl, E. Padilla, T. Parham, G. Parrish, C. Petty, M. Polk, C. Powell, I. Reinbachs, R. Rinnert, B. Riordan, G. Ross, V. Robert, M. Tobin, S. Sailors, R. Saunders, M. Schmitt,

M. Shaw, M. Singh, M. Spaeth, A. Stephens, G. Tietbohl, J. Tuck, B. M. Van Wonterghem, R. Vidal, P. J. Wegner, P. Whitman, K. Williams, K. Winward, K. Work, R. Wallace, A. Nobile, M. Bono, B. Day, J. Elliott, D. Hatch, H. Louis, R. Manzenares, D. O'Brien, P. Papin, T. Pierce, G. Rivera, J. Ruppe, D. Sandoval, D. Schmidt, L. Valdez, K. Zapata, B. J. MacGowan, M. J. Eckart, W. W. Hsing, P. T. Springer, B. A. Hammel, E. I. Moses, and G. H. Miller, "The First Target Experiments on the National Ignition Facility," Eur. Phys. J. D **44**, 273 (2007).

C. K. Li, F. H. Séguin, J. A. Frenje, J. R. Rygg, R. D. Petrasso, R. P. J. Town, P. A. Amendt, S. P. Hatchett, O. L. Landen, A. J. Mackinnon, P. K. Patel, V. A. Smalyuk, J. P. Knauer, T. C. Sangster, and C. Stoeckl, "Monoenergetic Proton Backlighter for Measuring E and B Fields and for Radiographing Implosions and High-Energy Density Plasmas," Rev. Sci. Instrum. **77**, 10E725 (2006) (invited).

C. K. Li, F. H. Séguin, J. A. Frenje, J. R. Rygg, R. D. Petrasso, R. P. J. Town, P. A. Amendt, S. P. Hatchett, O. L. Landen, A. J. Mackinnon, P. K. Patel, M. Tabak, J. P. Knauer, T. C. Sangster, and V. A. Smalyuk, "Observation of the Decay Dynamics and Instabilities of Megagauss Field Structures in Laser-Produced Plasmas," Phys. Rev. Lett. **99**, 015001 (2007).

C. K. Li, F. H. Séguin, J. A. Frenje, J. R. Rygg, R. D. Petrasso, R. P. J. Town, O. L. Landen, J. P. Knauer, and V. A. Smalyuk, "Observation of Megagauss-Field Topology Changes Due to Magnetic Reconnection in Laser-Produced Plasmas" Phys. Rev. Lett. **99**, 055001 (2007).

N. B. Meezan, R. L. Berger, L. Divol, D. H. Froula, D. E. Hinkel, O. S. Jones, R. A. London, J. D. Moody, M. M. Marinak, C. Niemann, P. B. Neumayer, S. T. Prisbrey, J. S. Ross, E. A. Williams, S. H. Glenzer, and L. J. Suter, "Role of Hydrodynamics Simulations in Laser-Plasma Interaction Predictive Capability," Phys. Plasmas **14**, 056304 (2007) (invited).

M. J. Moran, R. A. Lerche, G. Mant, V. Yu. Glebov, T. C. Sangster, and J. M. Mack, "Optical Lightpipe as a High-Bandwidth Fusion Diagnostic," Rev. Sci. Instrum. **77**, 10E718 (2006).

T. Nagayama, R. C. Mancini, L. A. Welser, S. Louis, I. E. Golovkin, R. Tommasini, J. A. Koch, N. Izumi, J. A. Delettrez, F. J. Marshall, S. P. Regan, V. Smalyuk, D. Haynes, and G. Kyrala, "Multiobjective Method for Fitting Pinhole Image Intensity Profiles of Implosion Cores Driven by a Pareto Genetic Algorithm," Rev. Sci. Instrum. **77**, 10F525 (2006).

A. B. Reighard and R. P. Drake, "The Formation of a Cooling Layer in a Partially Optically Thick Shock," Astrophys. Space Sci. **307**, 121 (2007).

A. B. Reighard, R. P. Drake, J. E. Mucino, J. P. Knauer, and M. Busquet, "Planar Radiative Shock Experiments and Their Comparison to Simulations," Phys. Plasmas **14**, 056504 (2007).

P. A. Rosen, J. M. Foster, M. J. Taylor, P. A. Keiter, C. C. Smith, J. R. Finke, M. Gunderson, and T. S. Perry, "Experiments to Study Radiation Transport in Clumpy Media," Astrophys. Space Sci. **307**, 213 (2007).

J. R. Rygg, J. A. Frenje, C. K. Li, F. H. Séguin, R. D. Petrasso, J. A. Delettrez, V. Yu. Glebov, V. N. Goncharov, D. D. Meyerhofer, P. B. Radha, S. P. Regan, and T. C. Sangster, "Nuclear Measurements of Fuel-Shell Mix in Inertial Confinement Fusion Implosions on OMEGA," Phys. Plasmas **14**, 056306 (2007).

J. R. Rygg, J. A. Frenje, C. K. Li, F. H. Séguin, R. D. Petrasso, V. Yu. Glebov, D. D. Meyerhofer, T. C. Sangster, and C. Stoeckl, "Time-Dependent Nuclear Measurements of Mix in Inertial Confinement Fusion," Phys. Rev. Lett. **98**, 215002 (2007).

M. B. Schneider, D. E. Hinkel, O. L. Landen, D. H. Froula, R. F. Heeter, A. B. Langdon, M. J. May, J. McDonald, J. S. Ross, M. S. Singh, L. J. Suter, K. Widmann, B. K. Young, H. A. Baldis, C. Constantin, R. Bahr, V. Yu. Glebov, W. Seka, and C. Stoeckl, "Plasma Filling in Reduced-Scale Hohlraums Irradiated with Multiple Beam Cones," Phys. Plasmas **13**, 112701 (2006).

F. H. Séguin, J. L. DeCiantis, J. A. Frenje, C. K. Li, J. R. Rygg, C. D. Chen, R. D. Petrasso, J. A. Delettrez, S. P. Regan, V. A. Smalyuk, V. Yu. Glebov, J. P. Knauer, F. J. Marshall, D. D. Meyerhofer, S. Roberts, T. C. Sangster, C. Stoeckl, K. Mikaelian, H. S. Park, H. F. Robey, and R. E. Tipton, "Measured Dependence of Nuclear Burn Region Size on Implosion Parameters in Inertial Confinement Fusion Experiments," Phys. Plasmas **12**, 082704 (2006).

L. Welser, R. C. Mancini, T. Nagayama, R. C. Tommasini, J. A. Koch, N. Izumi, J. A. Delettrez, F. J. Marshall, S. P. Regan, V. A. Smalyuk, I. E. Golovkin, D. A. Haynes, and G. Kyrala, "Spatial Structure Analysis of Direct-Drive Implosion Cores at OMEGA Using X-Ray Narrow-Band Core Images," Rev. Sci. Instrum. **77**, 10E320 (2006).

L. Welser-Sherrill, R. C. Mancini, D. A. Haynes, S. W. Haan, I. E. Golovkin, J. J. MacFarlane, P. B. Radha, J. A. Delettrez, S. P. Regan, J. A. Koch, N. Izumi, R. Tommasini, and V. A. Smalyuk, "Development of Two Mix Model Postprocessors for the Investigation of Shell Mix in Indirect Drive Implosion Cores," Phys. Plasmas **14**, 072705 (2007).

L. Welser-Sherrill, R. C. Mancini, J. A. Koch, N. Izumi, R. Tommasini, S. W. Haan, D. A. Haynes, I. E. Golovkin, J. A. Delettrez, F. J. Marshall, S. P. Regan, and V. A. Smalyuk, "Development of Spectroscopic Tools for the Determination of Temperature and Density Spatial Profiles in Implosion Cores," High Energy Density Phys. **3**, 287 (2007).

Conference Presentations

The following presentations were made at the 17th Target Fabrication Meeting, San Diego, CA, 1–5 October 2006:

D. H. Edgell, R. S. Craxton, L. M. Elasky, D. R. Harding, S. J. Verbridge, M. D. Wittman, and W. Seka, "Three-Dimensional Characterization of Cryogenic Targets Using Systems Identification Techniques with Multiple Shadowgraph Views."

L. M. Elasky, S. J. Verbridge, A. Weaver, D. H. Edgell, and D. R. Harding, "Developments in Layering OMEGA D_2 Cryogenic Targets."

L. M. Elasky, A. Weaver, S. J. Verbridge, R. Janezic, and W. T. Shmayda, "Tritium Migration in MCTC's During DT Introduction."

R. Q. Gram and D. R. Harding, "Thermal Conductivity of Condensed D_2 and D_2 in RF Foam Using the 3-ω Method."

D. R. Harding, L. M. Elasky, S. J. Verbridge, A. Weaver, and D. H. Edgell, "Forming Cryogenic DT Ice Layers for OMEGA."

R. Janezic, "Operational Challenges in Filling and Transferring Cryogenic DT Targets."

R. Janezic, "Performance of the Tritium Removal Systems at LLE."

A. K. Knight and D. R. Harding, "Evaluating the Dependence of the Roughness of Polyimide Capsules and Processing Conditions."

L. D. Lund, D. Jacobs-Perkins, D. H. Edgell, R. Orsagh, J. Ulreich, and R. Early, "Cryogenic Target Positioning and Stability on OMEGA."

S. Scarantino, M. Bobeica, and D. R. Harding, "Performance of the Cryogenic Test Facility Used to Simulate the Effect of Injecting an Inertial Fusion Energy Target into a Hot Target Chamber."

W. T. Shmayda, M. J. Bonino, D. R. Harding, P. S. Ebey, and D. C. Wilson, "Hydrogen Isotope Exchange in Plastic Targets."

D. Turner, M. J. Bonino, J. Ulreich, and R. Orsagh, "Measuring and Optimizing the Dynamics of Spherical Cryogenic Targets on OMEGA."

M. D. Wittman and D. R. Harding, "Isotopic Fractionation During Solidification and Sublimation of Hydrogen-Isotope Mixtures."

———

The following presentations were made at Frontiers in Optics 2006/Laser Science XXII, Rochester, NY, 8–12 October 2006:

W. Guan and J. R. Marciante, "Gain Apodization in Highly Doped Fiber DFB Lasers."

W. Guan and J. R. Marciante, "Single-Frequency, 2-cm, Yb-Doped Silica Fiber Laser."

Z. Jiang and J. R. Marciante, "Loss Measurements for Optimization of Large-Mode-Area, Helical-Core Fibers."

A. V. Okishev and J. D. Zuegel, "Highly Stable, Long-Pulse, Diode-Pumped Nd:YLF Regenerative Amplifier."

L. Sun and J. R. Marciante, "Filamentation Analysis in Large-Area-Mode Fiber Lasers."

J. D. Zuegel, J. H. Kelly, L. J. Waxer, V. Bagnoud, I. A. Begishev, J. Bromage, C. Dorrer, B. E. Kruschwitz, T. J. Kessler, S. J. Loucks, D. N. Maywar, R. L. McCrory, D. D. Meyerhofer, S. F. B. Morse, J. B. Oliver, A. L. Rigatti, A. W. Schmid, C. Stoeckl, S. Dalton, L. Folnsbee, M. J. Guardalben, R. Jungquist, J. Puth,

M. J. Shoup III, and D. Weiner, "New and Improved Technologies for the OMEGA EP High-Energy Petawatt Laser" (invited).

———————

D. D. Meyerhofer, "Research Using Chirped-Pulse–Amplification Lasers at the University of Rochester," OSA Annual Meeting and APS Laser Science Meeting, Rochester, NY, 8–12 October 2006 (invited).

———————

The following presentations were made at Optical Fabrication and Testing, Rochester, NY, 9–11 October 2006:

J. E. DeGroote, A. E. Marino, A. L. Bishop, and S. D. Jacobs, "Using Mechanics and Polishing Particle Properties to Model Material Removal for Magnetorheological Finishing (MRF) of Optical Glasses."

J. E. DeGroote, J. P. Wilson, T. M. Pfunter, and S. D. Jacobs, "Adding Chemistry and Glass Composition Data into a Mechanical Material Removal Model for Magnetorheological Finishing (MRF)."

———————

S. N. Shafrir, J. C. Lambropoulos, and S. D. Jacobs, "A Magnetorheological Polishing-Based Approach for Studying Magnetic/Nonmagnetic WC Hard Metals," ASPE 21st Annual Meeting, Monterey, CA, 15–20 October 2006.

———————

T. C. Sangster, R. L. McCrory, V. N. Goncharov, D. R. Harding, S. J. Loucks, P. W. McKenty, D. D. Meyerhofer, S. Skupsky, B. A. Hammel, J. D. Lindl, E. Moses, J. Atherton, G. B. Logan, S. Yu, J. D. Kilkenny, A. Nikroo, H. Wilken, K. Matzen, R. Leeper, R. Olsen, J. Porter, C. Barnes, J. C. Fernandez, D. Wilson, J. D. Sethian, and S. Obenschain, "Overview of Inertial Fusion Research in the United States," 21st IAEA Fusion Energy Conference, Chendu, China, 16–21 October 2006.

———————

S. D. Jacobs, "Manipulating Mechanics and Chemistry in Precision Optics Finishing," International 21st Century COE Symposium on Atomistic Fabrication Technology, Osaka, Japan, 19–20 October 2006.

———————

W. Guan and J. R. Marciante, "Dual-Frequency Ytterbium-Doped Fiber Laser," LEOS 2006, Montreal, Quebec, Canada, 29 October–2 November 2006.

———————

The following presentations were made at the 48th Annual Meeting of the APS Division of Plasma Physics, Philadelphia, PA, 30 October–3 November 2006:

K. S. Anderson, R. Betti, P. W. McKenty, P. B. Radha, and M. M. Marinak, "2-D Simulations of OMEGA Fast-Ignition Cone Targets."

R. Betti, K. S. Anderson, C. Zhou, L. J. Perkins, M. Tabak, P. Bedrossian, and K. N. LaFortune, "Shock Ignition of Thermonuclear Fuel with High Areal Density."

T. R. Boehly, V. N. Goncharov, D. D. Meyerhofer, J. E. Miller, T. C. Sangster, V. A. Smalyuk, P. M. Celliers, G. W. Collins, D. Munro, and R. E. Olson, "Direct- and Indirect-Drive Shock-Timing Experiments on the OMEGA Laser."

D. T. Casey, J. A. Frenje, C. K. Li, J. R. Rygg, F. H. Séguin, R. D. Petrasso, V. Yu. Glebov, B. Owens, D. D. Meyerhofer, T. C. Sangster, P. Song, S. W. Haan, S. P. Hatchett, R. A. Lerche, M. J. Moran, D. C. Wilson, R. Leeper, and R. E. Olson, "Diagnosing Cryogenic DT Implosions Using the Magnetic Recoil Spectrometer (MRS)."

T. J. B. Collins, J. A. Marozas, R. Betti, D. R. Harding, P. W. McKenty, P. B. Radha, S. Skupsky, V. N. Goncharov, J. P. Knauer, and R. L. McCrory, "One-Megajoule, Wetted-Foam Target Design Performance for the NIF" (invited).

J. A. Delettrez, J. Myatt, C. Stoeckl, and D. D. Meyerhofer, "Hydrodynamic Simulations of Integrated Fast-Ignition Experiments Planned for the OMEGA/OMEGA EP Laser Systems."

D. H. Edgell, R. S. Craxton, L. M. Elasky, D. R. Harding, L. S. Iwan, R. L. Keck, L. D. Lund, S. J. Verbridge, A. Weaver, M. D. Wittman, and W. Seka, "Layering and Characterization of Cryogenic-DT Targets for OMEGA."

R. Epstein, H. Sawada, V. N. Goncharov, D. Li, P. B. Radha, and S. P. Regan, "K-Shell Absorption Spectroscopy at Low Temperatures in Preheat Conditions."

J. A. Frenje, D. T. Casey, C. K. Li, J. R. Rygg, F. H. Séguin, R. D. Petrasso, P. B. Radha, V. Yu. Glebov, D. D. Meyerhofer, and T. C. Sangster, "Diagnosing Cryogenic D_2 and DT Implosions on OMEGA Using Charged-Particle Spectroscopy."

M. Ghilea, D. D. Meyerhofer, T. C. Sangster, D. J. Lonobile, A. Dillenbeck, R. A. Lerche, and L. Disdier, "Developmental Status of a Liquid-Freon Bubble Chamber for Neutron Imaging."

V. Yu. Glebov, T. C. Sangster, P. B. Radha, W. T. Shmayda, M. J. Bonino, D. R. Harding, D. C. Wilson, P. S. Ebey, A. Nobile, Jr., R. A. Lerche, and T. W. Phillips, "Measurement of the Neutron Energy Spectrum in T-T Inertial Confinement Fusion."

V. N. Goncharov, V. A. Smalyuk, W. Seka, T. R. Boehly, R. L. McCrory, I. A. Igumenshchev, J. A. Delettrez, W. Manheimer, and D. Colombant, "Thermal Transport Modeling in ICF Direct-Drive Experiments."

O. V. Gotchev, M. D. Barbero, N. W. Jang, J. P. Knauer, and R. Betti, "A Compact, TIM-Based, Pulsed-Power System for Magnetized Target Experiments on OMEGA."

S. Hu, V. N. Goncharov, V. A. Smalyuk, J. P. Knauer, and T. C. Sangster, "Analysis of the Compressibility Experiments Performed on the OMEGA Laser System."

I. V. Igumenshchev, V. N. Goncharov, V. A. Smalyuk, W. Seka, D. H. Edgell, T. R. Boehly, and J. A. Delettrez, "Effects of Resonant Absorption in Direct-Drive Experiments on OMEGA."

N. W. Jang, R. Betti, J. P. Knauer, O. V. Gotchev, and D. D. Meyerhofer, "Theory and Simulation of Laser-Driven Magnetic-Field Compression."

J. P. Knauer, P. W. McKenty, K. S. Anderson, T. J. B. Collins, and V. N. Goncharov, "Direct-Drive, Foam-Target ICF Implosions."

C. K. Li, F. H. Séguin, J. A. Frenje, J. R. Rygg, R. D. Petrasso, R. P. J. Town, P. A. Amendt, S. P. Hatchett, D. G. Hicks, O. L. Landen, V. A. Smalyuk, T. C. Sangster, and J. P. Knauer, "Measuring E and B Fields in Laser-Produced Plasmas Through Monoenergetic Proton Radiography."

D. Li, I. V. Igumenshchev, and V. N. Goncharov, "Effects of the Ion Viscosity on the Shock Yield and Hot-Spot Formation in ICF Targets."

G. Li, C. Ren, V. N. Goncharov, and W. B. Mori, "The Channeling Effect in the Underdense Plasma."

J. A. Marozas, P. W. McKenty, P. B. Radha, and S. Skupsky, "Imprint Simulations of 1.5-MJ NIF Implosions Using a Refractive 3-D Laser Ray Trace with an Analytic SSD Model."

F. J. Marshall, R. S. Craxton, M. J. Bonino, R. Epstein, V. Yu. Glebov, D. Jacobs-Perkins, J. P. Knauer, J. A. Marozas, P. W. McKenty, S. G. Noyes, P. B. Radha, W. Seka, S. Skupsky, and V. A. Smalyuk, "Optimized Polar-Direct-Drive Experiments on OMEGA."

A. V. Maximov, J. Myatt, and R. W. Short, "Laser–Plasma Coupling Near Critical Density in Direct-Drive ICF Plasmas."

P. W. McKenty, J. A. Marozas, V. N. Goncharov, K. S. Anderson, R. Betti, D. D. Meyerhofer, P. B. Radha, T. C. Sangster, S. Skupsky, and R. L. McCrory, "Numerical Investigation of Proposed OMEGA Cryogenic Implosions Using Adiabat-Shaping Techniques."

D. D. Meyerhofer, T. C. Sangster, K. S. Anderson, R. Betti, R. S. Craxton, J. A. Delettrez, D. H. Edgell, R. Epstein, V. Yu. Glebov, V. N. Goncharov, D. R. Harding, R. L. Keck, J. D. Kilkenny, J. P. Knauer, S. J. Loucks, L. D. Lund, F. J. Marshall, R. L. McCrory, P. W. McKenty, P. B. Radha, S. P. Regan, W. Seka, V. A. Smalyuk, J. M. Soures, C. Stoeckl, S. Skupsky, J. A. Frenje, C. K. Li, R. D. Petrasso, and F. H. Séguin, "Studies of Adiabat Shaping in Direct-Drive, Cryogenic-Target Implosions on OMEGA."

J. E. Miller, T. R. Boehly, A. Melchior, and D. D. Meyerhofer, "Thermal and Kinetic Equation-of-State Experiments Using Decaying Shock Waves."

J. Myatt, A. V. Maximov, and R. W. Short, "Positron–Electron, Pair-Plasma Production on OMEGA EP."

J. Myatt, W. Theobald, J. A. Delettrez, C. Stoeckl, M. Storm, T. C. Sangster, A. V. Maximov, and R. W. Short, "High-Intensity Laser Interactions with Solid Targets and Implications for Fast-Ignition Experiments on OMEGA EP" (invited).

P. Nilson, "Magnetic Reconnection and Plasma Dynamics in Two Beam Laser–Solid Interactions."

R. D. Petrasso, C. K. Li, F. H. Séguin, J. A. Frenje, J. R. Rygg, M. Manuel, V. A. Smalyuk, R. Betti, R. S. Craxton, J. P. Knauer,

F. J. Marshall, D. D. Meyerhofer, J. Myatt, P. B. Radha, T. C. Sangster, W. Theobald, R. P. J. Town, P. A. Amendt, P. M. Celliers, S. P. Hatchett, D. G. Hicks, O. L. Landen, J. Cobble, N. M. Hoffman, and J. D. Kilkenny, "Monoenergetic Particle Backlighter for Radiography and Measuring E and B Fields and Plasma Areal Density."

P. B. Radha, V. Yu. Glebov, V. N. Goncharov, D. D. Meyerhofer, T. C. Sangster, S. Skupsky, J. A. Frenje, and R. D. Petrasso, "Inferring Areal Density in OMEGA DT-Cryogenic Implosions."

S. P. Regan, R. Epstein, V. N. Goncharov, I. V. Igumenshchev, D. Li, P. B. Radha, H. Sawada, T. R. Boehly, J. A. Delettrez, O. V. Gotchev, J. P. Knauer, J. A. Marozas, F. J. Marshall, R. L. McCrory, P. W. McKenty, D. D. Meyerhofer, T. C. Sangster, S. Skupsky, V. A. Smalyuk, B. Yaakobi, and R. Mancini, "Laser-Energy Coupling, Mass Ablation Rate, and Shock Heating in Direct-Drive Inertial Confinement Fusion" (invited).

S. P. Regan, D. D. Meyerhofer, T. C. Sangster, R. Epstein, L. J. Suter, O. S. Jones, N. B. Meezan, M. D. Rosen, S. Dixit, C. Sorce, O. L. Landen, J. Schein, and E. L. Dewald, "Hohlraum Energetics with Elliptical Phase Plates on OMEGA."

J. R. Rygg, J. A. Frenje, C. K. Li, F. H. Séguin, R. D. Petrasso, and V. N. Goncharov, "Time-Dependent Nuclear Measurements of Fuel–Shell Mix in ICF Implosions."

T. C. Sangster, R. Betti, R. S. Craxton, J. A. Delettrez, D. H. Edgell, L. M. Elasky, V. Yu. Glebov, V. N. Goncharov, D. R. Harding, D. Jacobs-Perkins, R. Janezic, R. L. Keck, J. P. Knauer, S. J. Loucks, L. D. Lund, F. J. Marshall, R. L. McCrory, P. W. McKenty, D. D. Meyerhofer, P. B. Radha, S. P. Regan, W. Seka, W. T. Shmayda, S. Skupsky, V. A. Smalyuk, J. M. Soures, C. Stoeckl, B. Yaakobi, J. A. Frenje, C. K. Li, R. D. Petrasso, F. H. Séguin, J. D. Moody, J. A. Atherton, B. D. MacGowan, J. D. Kilkenny, T. P. Bernat, and D. S. Montgomery, "Cryogenic DT and D_2 Targets for Inertial Confinement Fusion" (invited tutorial).

T. C. Sangster, R. S. Craxton, J. A. Delettrez, D. H. Edgell, R. Epstein, V. Yu. Glebov, V. N. Goncharov, D. R. Harding, R. L. Keck, J. D. Kilkenny, J. P. Knauer, S. J. Loucks, L. D. Lund, J. A. Marozas, F. J. Marshall, R. L. McCrory, P. W. McKenty, D. D. Meyerhofer, P. B. Radha, S. P. Regan, W. Seka, V. A. Smalyuk, J. M. Soures, C. Stoeckl, S. Skupsky, J. A. Frenje, C. K. Li, R. D. Petrasso, and F. H. Séguin, "Implosion

Performance of Fully β-Layered Cryogenic-DT Targets on OMEGA" (invited).

J. Sanz and R. Betti, "Bubble Acceleration in the Ablative Rayleigh–Taylor Instability."

H. Sawada, S. P. Regan, R. Epstein, D. Li, V. N. Goncharov, P. B. Radha, D. D. Meyerhofer, T. R. Boehly, V. A. Smalyuk, T. C. Sangster, B. Yaakobi, and R. Mancini, "Investigation of Direct-Drive Shock Heating Using X-Ray Absorption Spectroscopy."

F. H. Séguin, C. K. Li, J. A. Frenje, J. R. Rygg, R. D. Petrasso, V. A. Smalyuk, R. S. Craxton, J. P. Knauer, F. J. Marshall, T. C. Sangster, S. Skupsky, A. Greenwood, and J. D. Kilkenny, "Using Target Shimming to Compensate for Asymmetric Drive in ICF Implosions."

W. Seka, V. N. Goncharov, J. A. Delettrez, D. H. Edgell, I. V. Igumenshchev, R. W. Short, A. V. Maximov, J. Myatt, and R. S. Craxton, "Time-Dependent Absorption Measurements in Direct-Drive Spherical Implosions."

R. W. Short and J. Myatt, "Instabilities of Relativistic Electron Beams in Plasmas: Spatial Growth and Absolute Instability."

S. Skupsky, "Nonlocal Ion-Heat Transport in ICF Implosions."

A. A. Solodov, R. Betti, J. A. Delettrez, and C. Zhou, "Gain Curves for Fast-Ignition Inertial Confinement Fusion."

J. M. Soures, T. R. Boehly, V. N. Goncharov, S. Hu, D. D. Meyerhofer, J. E. Miller, T. C. Sangster, W. Seka, and V. A. Smalyuk, "Spherical Shock-Breakout Measurements on OMEGA."

C. Stoeckl, J. Bromage, J. H. Kelly, T. J. Kessler, B. E. Kruschwitz, S. J. Loucks, R. L. McCrory, D. D. Meyerhofer, S. F. B. Morse, A. L. Rigatti, T. C. Sangster, W. Theobald, L. J. Waxer, and J. D. Zuegel, "Status of the OMEGA EP High-Energy Petawatt Laser Facility."

M. Storm, J. Myatt, and C. Stoeckl, "Characterization of Fast-Electron Beam Propagation Through Solid-Density Matter by Optical-Transition Radiation."

S. Sublett, J. P. Knauer, D. D. Meyerhofer, I. V. Igumenshchev, T. J. B. Collins, and A. Frank, "Influence of Episodic Mass Ejection on Hydrodynamic Jet Evolution."

W. Theobald, C. Stoeckl, C. Zhou, R. Betti, S. Roberts, V. A. Smalyuk, V. Yu. Glebov, J. A. Delettrez, T. C. Sangster, D. D. Meyerhofer, C. K. Li, and R. D. Petrasso, "High-Areal-Density Fuel-Assembly Experiments for the Fast-Ignitor Concept."

C. Zhou and R. Betti, "Fast-Ignition Fuel-Assembly Scaling Laws: Theory and Experiments."

––––––––––

The following presentations were made at the 9th International Fast Ignition Workshop, Cambridge, MA, 3–5 November 2006:

K. S. Anderson, R. Betti, P. W. McKenty, P. B. Radha, and M. M. Marinak, "2-D Simulations of OMEGA Fast-Ignition Cone Targets."

J. A. Delettrez, J. Myatt, C. Stoeckl, D. D. Meyerhofer, and M. G. Haines, "Hydrodynamic Simulations of Integrated Fast-Ignition Experiments Planned for the OMEGA/OMEGA EP Laser Systems."

D. D. Meyerhofer, R. Betti, V. N. Goncharov, D. H. Edgell, D. R. Harding, J. H. Kelly, T. J. Kessler, S. J. Loucks, L. D. Lund, R. L. McCrory, S. F. B. Morse, T. C. Sangster, W. Seka, C. Stoeckl, W. Theobald, L. J. Waxer, and J. D. Zuegel, "Preparations for Integrated Cryogenic Fast-Ignition Experiments on OMEGA/OMEGA EP" (invited).

J. Myatt, A. V. Maximov, and R. W. Short, "Laboratory Demonstration of e$^+$e$^-$ Pair-Plasma Production on OMEGA EP."

J. Myatt, W. Theobald, J. A. Delettrez, C. Stoeckl, M. Storm, T. C. Sangster, A. V. Maximov, and R. W. Short, "High-Intensity Laser Interactions with Solid Targets and Implications for Fast-Ignition Experiments on OMEGA EP" (invited).

P. Nilson, "Optical Probing of Underdense Laser–Plasma Interactions Using the Vulcan Petawatt Laser."

A. A. Solodov, R. Betti, J. A. Delettrez, and C. Zhou, "Gain Curves for Fast-Ignition Inertial Confinement Fusion."

C. Stoeckl, S.-W. Bahk, J. Bromage, V. Yu. Glebov, O. V. Gotchev, P. A. Jaanimagi, D. D. Meyerhofer, P. Nilson, T. C. Sangster, M. Storm, S. Sublett, W. Theobald, and J. D. Zuegel, "Diagnostics for Fast-Ignitor Experiments on OMEGA/ OMEGA EP."

W. Theobald, C. Stoeckl, K. S. Anderson, R. Betti, T. R. Boehly, J. A. Delettrez, R. Epstein, V. Yu. Glebov, J. H. Kelly, T. J. Kessler, B. E. Kruschwitz, S. J. Loucks, R. L. McCrory, D. N. Maywar, D. D. Meyerhofer, J. E. Miller, S. F. B. Morse, J. Myatt, P. B. Radha, A. L. Rigatti, T. C. Sangster, V. A. Smalyuk, L. J. Waxer, B. Yaakobi, J. C. Zhou, J. D. Zuegel, R. D. Petrasso, C. K. Li, C. A. Back, G. Hund, R. B. Stephens, S. P. Hatchett, M. H. Key, A. J. MacKinnon, H.-S. Park, P. K. Patel, K. L. Lancaster, and P. A. Norreys, "Fast-Ignition Research at the Laboratory for Laser Energetics."

C. Zhou and R. Betti, "Fast-Ignition Fuel-Assembly Scaling Laws."

––––––––––

The following presentations were made at SPIE Photonics West, San Jose, CA, 20–25 January 2007:

C. Dorrer, "High-Speed Characterization for Optical Telecommunication Signals" (invited).

T. Z. Kosc, K. L. Marshall, A. Trajkovska-Petkoska, C. J. Coon, K. Hasman, G. V. Babcock, R. Howe, M. Leitch, and S. D. Jacobs, "Development of Polymer Cholesteric Liquid Crystal Flake Technology for Electro-Optic Devices and Particle Displays" (invited).

––––––––––

The following presentations were made at ASSP 2007, Vancouver, Canada, 28–31 January 2007:

I. A. Begishev, V. Bagnoud, C. Dorrer, and J. D. Zuegel, "Suppression of Optical Parametric Generation in the High-Efficient OPCPA System."

Z. Jiang and J. R. Marciante, "Impact of Spatial-Hole Burning on Beam Quality in Large-Mode-Area Fibers."

J. R. Marciante, "Effectiveness of Radial Gain Tailoring in Large-Mode-Area Fiber Lasers and Amplifiers."

A. V. Okishev and J. D. Zuegel, "Intracavity-Pumped Raman Laser Action in a Mid-IR CW MgO:PPLN Optical Parametric Oscillator."

––––––––––

J. M. Soures and D. D. Meyerhofer, "High-Energy-Density Physics Research at NLUF with the OMEGA and OMEGA EP Lasers," 2007 Stewardship Science Academic Alliance Program Symposium, Washington, DC, 5–7 February 2007.

———————

R. L. McCrory, D. D. Meyerhofer, S. J. Loucks, S. Skupsky, K. S. Anderson, R. Betti, T. R. Boehly, M. J. Bonino, R. S. Craxton, T. J. B. Collins, J. A. Delettrez, D. H. Edgell, R. Epstein, V. Yu. Glebov, V. N. Goncharov, D. R. Harding, R. L. Keck, J. H. Kelly, T. J. Kessler, J. P. Knauer, L. D. Lund, D. Jacobs-Perkins, J. R. Marciante, J. A. Marozas, F. J. Marshall, A. V. Maximov, P. W. McKenty, S. F. B. Morse, J. Myatt, S. G. Noyes, P. B. Radha, T. C. Sangster, W. Seka, V. A. Smalyuk, J. M. Soures, C. Stoeckl, W. Theobald, K. A. Thorp, M. D. Wittman, B. Yaakobi, C. D. Zhou, J. D. Zuegel, C. K. Li, R. D. Petrasso, J. A. Frenje, and F. H. Séguin, "Inertial Confinement Fusion Research at the Laboratory for Laser Energetics," 7th Symposium on Current Trends in International Fusion Research: A Review, Washington, DC, 5–9 March 2007.

———————

J. R. Marciante, "Fiber Technologies for Terawatt Lasers," Optical Fiber Communication Conference 2007, Anaheim, CA, 25–29 March 2007.

———————

The following presentations were made at SPIE Europe: Optics and Optoelectronics, Prague, Czech Republic, 16–19 April 2007:

D. Pan, W. R. Donaldson, and R. Sobolewski, "Femtosecond Laser-Pumped Source of Entangled Photons for Quantum Cryptography Applications."

R. Sobolewski, "Fiber-Coupled NbN Superconducting Single-Photon Detectors for Quantum Correlation Measurements."

———————

The following presentations were made at CLEO/QELS 2007, Baltimore, MD, 6–11 May 2007:

P. Brijesh, T. J. Kessler, J. D. Zuegel, and D. D. Meyerhofer, "Spatially Shaping the Longitudinal Focal Distribution into a Horseshoe-Shaped Profile."

W. R. Donaldson, D. N. Maywar, and J. H. Kelly, "Measurement of the Self-Phase-Modulation–Induced Bandwidth in a 30-kJ-Class Laser-Amplifier System."

C. Dorrer, "Pulse Shaping Using Binary Sequences Designed with Error Diffusion."

C. Dorrer and J. D. Zuegel, "Characterization of High-Frequency Surface Modulation Using the Transport-of-Intensity Equation."

J. R. Marciante, "Effectiveness of Radial Index Tailoring in Large-Mode-Area Fiber Lasers and Amplifiers."

J. R. Marciante, "Gain Filtering for Single-Spatial-Mode Operation of Large-Mode-Area Fiber Amplifiers."

J. Qiao, D. Canning, G. King, M. J. Guardalben, J. Price, A. Kalb, R. Jungquist, A. L. Rigatti, and J. H. Kelly, "Interferometric Tiling for Large-Aperture Gratings for Petawatt Laser Systems."

———————

The following presentations were made at Optifab 2007, Rochester, NY, 14–17 May 2007:

J. E. DeGroote, A. E. Marino, J. P. Wilson, A. L. Bishop, and S. D. Jacobs, "Material Removal Rate Model for Magnetorheological Finishing (MRF) of Optical Glasses with Nanodiamond MR Fluid."

S. N. Shafir, J. C. Lambropoulos, and S. D. Jacobs, "Surface Finish and Subsurface Damage in Polycrystalline Optical Materials."

———————

K. L. Marshall, K. Hasman, M. Leitch, G. Cox, T. Z. Kosc, A. Trajkovska-Petkoska, and S. D. Jacobs, "Doped Multilayer Polymer Cholesteric-Liquid-Crystal (PCLC) Flakes: A Novel Electro-Optical Medium for Highly Reflective Color Flexible Displays," SID 2007 Symposium, Long Beach, CA, 20–25 May 2007.

———————

K. L. Marshall, V. Rapson, Y. Zhang, G. Mitchell, and A. L. Rigatti, "Contaminant Resistant Sol-Gel Coatings for High

Peak Power Laser Applications," Optical Interference Coatings (OSA-OIC), Tucson, AZ, 3–8 June 2007.

———

S. G. Lukishova, L. J. Bissell, S. K. H. Wei, A. W. Schmid, Z. Shi, H. Shin, R. Knox, P. Freivald, R. W. Boyd, C. R. Stroud, Jr., S.-H. Chen, and K. L. Marshall, "Room-Temperature Single Photon Sources with Fluorescent Emitters in Liquid Crystal Hosts," International Conference on Quantum Information, Rochester, NY, 13–15 June 2007.

———

The following presentations were made at the 15th APS Topical Conference on Shock Compression of Condensed Matter, Fairmont Orchard, HI, 24–29 June 2007:

T. R. Boehly, J. E. Miller, J. H. Eggert, D. G. Hicks, P. M. Celliers, D. D. Meyerhofer, and G. W. Collins, "Measurements of the Release of Alpha Quartz: A New Standard for Impedance-Match Experiments."

S. Brygoo, J. H. Eggert, P. Loubeyre, R. S. McWilliams, D. G. Hicks, P. M. Celliers, T. R. Boehly, R. Jeanloz, and G. W. Collins, "The Equation of State and Optical Conductivity of Warm Dense He and H_2."

J. Eggert, D. Bradley, P. Celliers, G. Collins, D. Hicks, D. Braun, S. Prisbey, R. Smith, and T. Boehly, "Ramp Compression of Diamond to Over 1000 GPa."

D. Hicks, J. Eggert, P. Celliers, H.-S. Park, S. LePape, P. Patel, B. Maddox, G. Collins, T. Boehly, and B. Barbrel, "Measurement of Shock Wave Density Using Quantitative X-Ray Phase Contrast Imaging."

J. E. Miller, T. R. Boehly, D. D. Meyerhofer, J. H. Eggert, S. C. Wilks, J. H. Satcher, and J. F. Poco, "Equation-of-State Measurements in Ta_2O_5 Aerogel."

———

The following presentations were made at the ITER-LMJ-NIF International Workshop, Cadarache, France, 27–29 June 2007:

V. Yu. Glebov, T. C. Sangster, C. Stoeckl, S. Roberts, M. Cruz, C. Mileham, M. J. Moran, R. A. Lerche, J. M. Mack, H. Herrmann, C. S. Young, J. L. Bourgade, O. Landoas, J. Raimbourg, G. A.

Chandler, and K. Miller, "Environmental Challenges for the Nuclear Diagnostics on the NIF and LMJ."

W. T. Shmayda, "Tritium Management on OMEGA."

———

A. Trajkovska-Petkoska, T. Z. Kosc, K. L. Marshall, and S. D. Jacobs, "Electro-Optics of Polymer Cholesteric Liquid Crystal Flakes: Applications Toward Electronic Paper," ECLC 2007, 9th European Conference on Liquid Crystals, Lisbon, Portugal, 2–6 July 2007.

———

K. L. Marshall, A. Trajkovska-Petkoska, K. Hasman, M. Leitch, G. Cox, T. Z. Kosc, and S. D. Jacobs, "Polymer Cholesteric Liquid Crystal (PCLC) Flake/Fluid Host Electro-Optic Suspensions and Their Applications in Color Flexible Reflective Displays," International Display Manufacturing Conference 2007, Taipei, Taiwan, 3–6 July 2007.

———

T. Z. Kosc, A. Trajkovska-Petkoska, K. L. Marshall, S. D. Jacobs, K. Hasman, and C. Coon, "Polymer Cholesteric Liquid Crystal Flakes: A Novel Medium for Electro-Optical Particle-Based Technologies," Particles 2007, Toronto, Canada, 18–21 August 2007.

———

The following presentations were made at SPIE Optics and Photonics 2007, San Diego, CA, 26–30 August 2007:

J. E. DeGroote, A. E. Marino, J. P. Wilson, A. L. Bishop, and S. D. Jacobs, "The Role of Nanodiamonds in the Polishing Zone During Magnetorheological Finishing (MRF)."

K. L. Marshall, Z. Culakova, B. Ashe, C. Giacofei, A. L. Rigatti, T. J. Kessler, A. W. Schmid, J. B. Oliver, and A. Kozlov, "Vapor-Phase–Deposited Organosilane Coatings as 'Hardening' Agents for High Peak Power Laser Optics."

K. L. Marshall, R. Wang, M. Coan, A. G. Noto, K. Leskow, R. Pauszek, and A. Moore, "Using Time-Dependent Density Functional Theory (TDDFT) in the Design and Development of Near-IR Dopants for Liquid Crystal Device Applications."

C. Miao, K. M. Bristol, A. E. Marino, S. N. Shafrir, J. E. DeGroote, and S. D. Jacobs, "Magnetorheological Fluid Tem-

plate for Basic Studies of Mechanical-Chemical Effects During Polishing."

S. N. Shafrir, J. C. Lambropoulos, and S. D. Jacobs, "MRF Spotting Technique for Studying Subsurface Damage in Deterministic Microground Polycrystalline Alumina."

———————

The following presentations were made at the 37th Anomalous Absorption Conference, Maui, HI, 27–31 August 2007:

J. A. Delettrez, V. N. Goncharov, P. B. Radha, C. Stoeckl, A. V. Maximov, T. C. Sangster, D. Shvarts, R. D. Petrasso, and J. A. Frenje, "Simulations of the Effect of Energetic Electrons Produced from Two-Plasmon Decay in the 1-D Hydrodynamics Code *LILAC*."

D. H. Edgell, W. Seka, J. A. Delettrez, R. S. Craxton, V. N. Goncharov, I. V. Igumenshchev, J. Myatt, A. V. Maximov, R. W. Short, T. C. Sangster, and R. E. Bahr, "Time-Dependent Spectral Shifts of Scattered Laser Light in Direct-Drive Inertial Confinement Fusion Implosion Experiments."

D. H. Edgell, W. Seka, V. N. Goncharov, I. V. Igumenshchev, R. S. Craxton, J. A. Delettrez, J. Myatt, A. V. Maximov, and R. W. Short, "Time-Resolved Scattered-Light Spectroscopy in Direct-Drive Implosion Experiments."

M. G. Haines and J. Myatt, "Competition Between the Resistive Weibel Instability and the Electrothermal Instability in Fast Ignition."

A. V. Maximov, J. Myatt, R. W. Short, W. Seka, and C. Stoeckl, "Modeling of Two-Plasmon-Decay Instability Under Incoherent Laser Irradiation."

J. Myatt, P. Nilson, W. Theobald, M. Storm, A. V. Maximov, and R. W. Short, "Determination of Hot-Electron Conversion Efficiency and Isochoric Heating of Low-Mass Targets Irradiated by the Multi-Terawatt Laser."

W. Seka, D. H. Edgell, J. P. Knauer, C. Stoeckl, V. N. Goncharov, I. V. Igumenshchev, J. A. Delettrez, J. Myatt, A. V. Maximov, R. W. Short, and T. C. Sangster, "Laser–Plasma Interaction Processes Observed in Direct-Drive Implosion Experiments."

R. W. Short and J. Myatt, "Modeling the Filamentation Instability of Relativistic Electron Beams for Fast Ignition."

D. Shvarts, V. A. Smalyuk, R. Betti, J. A. Delettrez, D. H. Edgell, V. Yu. Glebov, V. N. Goncharov, R. L. McCrory, P. W. McKenty, D. D. Meyerhofer, F. J. Marshall, P. B. Radha, T. C. Sangster, W. Seka, S. Skupsky, C. Stoeckl, B. Yaakobi, J. A. Frenje, C. K. Li, R. D. Petrasso, and F. H. Séguin, "The Role of Fast-Electron Preheating in Low-Adiabat Cryogenic and Plastic (CH) Shell Implosions on OMEGA."

V. A. Smalyuk, D. Shvarts, R. Betti, J. A. Delettrez, D. H. Edgell, V. Yu. Glebov, V. N. Goncharov, S. X. Hu, F. J. Marshall, R. L. McCrory, P. W. McKenty, D. D. Meyerhofer, P. B. Radha, T. C. Sangster, W. Seka, S. Skupsky, C. Stoeckl, B. Yaakobi, J. A. Frenje, C. K. Li, R. D. Petrasso, and F. H. Séguin, "Effects of Hot-Electron Preheat in Direct-Drive Experiments on OMEGA."

A. A. Solodov, K. S. Anderson, R. Betti, V. Gotcheva, J. Myatt, J. A. Delettrez, and S. Skupsky, "Integrated Simulation of Fast-Ignition ICF."

———————

The following presentations were made at IFSA 2007, Kobe, Japan, 9–14 September 2007:

R. Betti, W. Theobald, C. D. Zhou, K. S. Anderson, P. W. McKenty, D. Shvarts, and C. Stoeckl, "Shock Ignition of Thermonuclear Fuel with High Areal Densities."

V. N. Goncharov, P. B. Radha, R. Betti, T. J. B. Collins, J. A. Delettrez, R. Epstein, S. X. Hu, I. V. Igumenshchev, R. L. McCrory, P. B. McKenty, D. D. Meyerhofer, S. P. Regan, T. C. Sangster, W. Seka, S. Skupsky, V. A. Smalyuk, and D. Shvarts, "Modeling High-Compression, Direct-Drive ICF Experiments."

D. R. Harding, D. D. Meyerhofer, T. C. Sangster, S. J. Loucks, R. L. McCrory, R. Betti, J. A. Delettrez, D. H. Edgell, L. M. Elasky, R. Epstein, V. Yu. Glebov, V. N. Goncharov, S. X. Hu, I. V. Igumenshchev, D. Jacobs-Perkins, R. J. Janezic, J. P. Knauer, L. D. Lund, J. R. Marciante, F. J. Marshall, D. N. Maywar, P. W. McKenty, P. B. Radha, S. P. Regan, R. G. Roides, W. Seka, W. T. Shmayda, S. Skupsky, V. A. Smalyuk, C. Stoeckl, B. Yaakobi, J. D. Zuegel, D. Shvarts, J. A. Frenje, C. K. Li, R. D. Petrasso, and F. H. Séguin, "Cryogenic Target-Implosion Experiments on OMEGA."

D. N. Maywar, J. H. Kelly, L. J. Waxer, S. F. B. Morse, I. A. Begishev, J. Bromage, C. Dorrer, J. L. Edwards, L. Folnsbee, M. J. Guardalben, S. D. Jacobs, R. Jungquist, T. J. Kessler, R. W. Kidder, B. E. Kruschwitz, S. J. Loucks, J. R. Marciante,

R. L. McCrory, D. D. Meyerhofer, A. V. Okishev, J. B. Oliver, G. Pien, J. Qiao, J. Puth, A. L. Rigatti, A. W. Schmid, M. J. Shoup, III, C. Stoeckl, K. A. Thorp, and J. D. Zuegel, "OMEGA EP High-Energy Petawatt Laser: Progress and Prospects."

P. W. McKenty, T. J. B. Collins, J. A. Marozas, S. Skupsky, D. R. Harding, J. D. Zuegel, D. Keller, A. Shvydky, D. D. Meyerhofer, and R. L. McCrory, "Multidimensional Numerical Investigation of NIF Polar-Direct-Drive Designs with Full Beam Smoothing."

S. P. Regan, T. C. Sangster, D. D. Meyerhofer, W. Seka, R. Epstein, S. J. Loucks, R. L. McCrory, C. Stoeckl, V. Yu. Glebov, O. S. Jones, D. Callahan, P. A. Amendt, N. B. Meezan, L. J. Suter, M. D. Rosen, O. L. Landen, E. L. DeWald, S. H. Glenzer, C. Sorce, S. Dixit, R. E. Turner, and B. MacGowan, "Hohlraum Energetics and Implosion Symmetry with Elliptical Phase Plates Using a Multi-Cone Beam Geometry on OMEGA."

D. Shvarts, V. A. Smalyuk, R. Betti, J. A. Delettrez, D. H. Edgell, V. Yu. Glebov, V. N. Goncharov, R. L. McCrory, P. W. McKenty, D. D. Meyerhofer, F. J. Marshall, P. B. Radha, S. P. Regan, T. C. Sangster, W. Seka, S. Skupsky, C. Stoeckl, B. Yaakobi, J. A. Frenje, C. K. Li, R. D. Petrasso, and F. H. Séguin, "The Role of Fast-Electron Preheating in Low-Adiabat Cryogenic Implosions on OMEGA."

S. Skupsky, V. N. Goncharov, and D. Li, "Nonlocal Ion-Heat and Momentum Transport in ICF Implosions."

———————

A. V. Okishev, C. Dorrer, V. I. Smirnov, L. B. Glebov, and J. D. Zuegel, "ASE Suppression in a Diode-Pumped Nd:YLF Regenerative Amplifier Using a Volume Bragg Grating," Frontiers in Optics 2007/Laser Science XXIII, San Jose, CA, 16–20 September 2007.

———————

The following presentations were made at the 8th International Conference on Tritium Science and Technology, Rochester, NY, 16–21 September 2007:

T. Duffy, R. Janezic, and W. T. Shmayda, "LLE's High-Pressure DT-Fill-Process Control System."

R. T. Janezic, W. T. Shmayda, G. P. Wainwright, P. Regan, K. Lintz, D. R. Harding, and S. J. Loucks, "Operational Experience of Tritium Handling During LLE's Cryogenic Target Filling Operation."

W. T. Shmayda, S. J. Loucks, R. T. Janezic, G. P. Wainwright, and T. Duffy, "Tritium Management on OMEGA at the Laboratory for Laser Energetics."

W. T. Shmayda, C. R. Shmayda, C. Waddington, and R. D. Gallagher, "Operation of a 2.6-Mg/Year Heavy-Water Detritiation Plant."

G. P. Wainwright, W. T. Shmayda, R. T. Janezic, and P. Regan, "Tritium Capture with Getter-Bed Technology at the Laboratory for Laser Energetics."

———————

D. N. Maywar, "Optical Control of Flip-Flops Based on Resonant-Type SOA's," University of Tokyo Seminar, Tokyo, Japan, 18 September 2007.

———————

The following presentations were made at the Boulder Damage Symposium, Boulder, CO, 24–26 September 2007:

B. Ashe, C. Giacofei, G. Myhre, and A. W. Schmid, "Optimizing a Cleaning Process for Multilayer Dielectric (MLD) Diffraction Gratings."

S. Papernov, A. W. Schmid, J. B. Oliver, and A. L. Rigatti, "Damage Thresholds and Morphology of the Front- and Back-Irradiated SiO_2 Thin Films Containing Gold Nanoparticles as Artificial Absorbing Defects."